

16 May 2014 | \$10

# Science



## Evolution on Parallel Paths

Stick insect genomes  
show similar adaptations  
in early speciation

## EDITORIAL

- 672 Think Outside the Lab  
Marcia McNutt

## NEWS OF THE WEEK

- 676 A roundup of the week's top stories

## NEWS & ANALYSIS

- 678 Crippling Virus Set to Conquer Western Hemisphere
- 679 Needed: More Females in Animal and Cell Studies
- 680 Bones From a Watery 'Black Hole' Confirm First American Origins  
>> Report p. 750
- 681 Job Change Lands Egyptian Scientist in Legal Battle
- 683 No Stopping the Collapse of West Antarctic Ice Sheet  
>> Report p. 735

## NEWS FOCUS

- 684 Beyond the Temples
- 687 The Hunt for Missing Genes

## LETTERS

- 691 China's Soil Pollution: Farms on the Frontline  
R. Chen et al.
- China's Soil Pollution: Urban Brownfields  
H. Yang et al.
- Scientific Justification for Animal Capture  
J. Cooke et al.
- Public Credibility Drives Vaccination Decisions  
B. Penders

## BOOKS ET AL.

- 694 The Oldest Living Things in the World  
R. Sussman; reviewed by J. Farmer
- 695 The Gap  
T. Suddendorf; reviewed by B. Sim

## POLICY FORUM

- 696 A Call for Deep-Ocean Stewardship  
K. J. Mengerink et al.

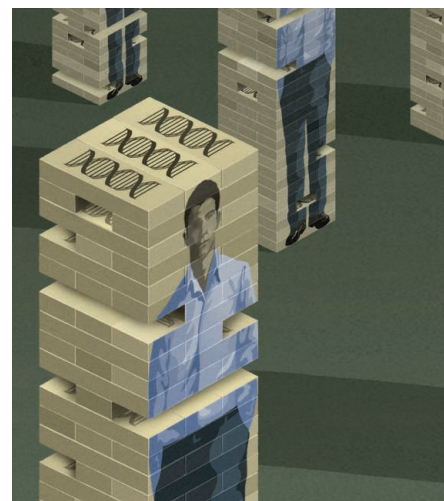
## PERSPECTIVES

- 699 Making Hunger Yield  
C. R. McClung
- 700 Recognizing Foreshocks from the 1 April 2014 Chile Earthquake  
E. E. Brodsky and T. Lay
- 702 Electronic Control of Circularly Polarized Light Emission  
J. Zaumseil  
>> Report p. 725
- 703 New Tricks for an Old Dimer  
J. A. Wells and A. A. Kossiakoff  
>> Research Article p. 710
- 705 Imaging Crystallization  
P. Dandekar and M. F. Doherty  
>> Report p. 729
- 706 Toward Recyclable Thermosets  
T. E. Long  
>> Report p. 732
- 707 Cas9 Targeting and the CRISPR Revolution  
R. Barrangou

## REVIEW

- 709 Lignin Valorization: Improving Lignin Processing in the Biorefinery  
A. J. Ragauskas et al.  
Review Summary; for full text:  
<http://dx.doi.org/10.1126/science.1246843>

CONTENTS continued >>



page 687



page 694

## ON THE WEB THIS WEEK

### >> Science Podcast

On this week's show: avoiding quantum back-action effects and a roundup of stories from our daily news site.

### >> Find More Online

Check out *Science Express*, the weekly podcast, videos, daily news, our research journals, and *Science Careers* at [www.sciencemag.org](http://www.sciencemag.org).



## COVER

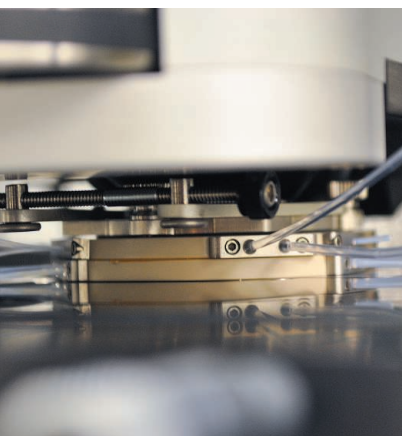
A male stick insect (*Timema knulli*) sitting on its host redwood (*Sequoia sempervirens*) in the Landels-Hill Big Creek Reserve, Big Sur, California. The process of *Timema* populations adapting to different hosts has repeatedly initiated parallel genetic changes in this group of insects. In turn, these replicate instances of differentiation have resulted in predictable and repeatable patterns of genome divergence by natural selection. See page 738.

Photo: © Moritz Muschick

## DEPARTMENTS

- 671 This Week in *Science*
- 673 Editors' Choice
- 674 Science Staff
- 765 New Products
- 766 Science Careers





pages 705 &amp; 729



pages 680 &amp; 750

## RESEARCH ARTICLES

- 710** Mechanism of Activation of Protein Kinase JAK2 by the Growth Hormone Receptor  
*A. J. Brooks et al.*  
A molecular mechanism for transmembrane signaling by the growth hormone receptor is elucidated.  
*Research Article Summary; for full text:*  
<http://dx.doi.org/10.1126/science.1249783>  
>> *Perspective p. 703*
- 711** Border Control—A Membrane-Linked Interactome of *Arabidopsis*  
*A. M. Jones et al.*  
A membrane and signaling protein interaction network for gene discovery and hypothesis generation is identified in *Arabidopsis*.
- 717** Oxidation Products of Biogenic Emissions Contribute to Nucleation of Atmospheric Particles  
*F. Riccobono et al.*  
Experiments in the CLOUD chamber at CERN reproduce particle nucleation rates observed in the lower atmosphere.

## REPORTS

- 722** Transverse Demagnetization Dynamics of a Unitary Fermi Gas  
*A. B. Bardoun et al.*  
The diffusion of spin orientation is observed in a gas of potassium atoms in a magnetic field gradient.
- 725** Electrically Switchable Chiral Light-Emitting Transistor  
*Y. J. Zhang et al.*  
The valley degree of freedom in  $WSe_2$  is used to realize an electrically switchable, circularly polarized light source.  
>> *Perspective p. 702*
- 729** In Situ Imaging of Silicalite-1 Surface Growth Reveals the Mechanism of Crystallization  
*A. I. Lupulescu and J. D. Rimer*  
Silicalite-1 growth occurs via the addition of silica molecules and precursors, confirming both main theories.  
>> *Perspective p. 705*
- 732** Recyclable, Strong Thermosets and Organogels via Paraformaldehyde Condensation with Diamines  
*J. M. García et al.*  
A strong polymer formed by heating can be digested with strong acid to recover and recycle its bisaniline monomers.  
>> *Perspective p. 706*

- 735** Marine Ice Sheet Collapse Potentially Under Way for the Thwaites Glacier Basin, West Antarctica  
*I. Joughin et al.*  
The onset of rapid collapse of the Thwaites Glacier in West Antarctica is likely within the next 200 to 1000 years.  
>> *News story p. 683*
- 738** Stick Insect Genomes Reveal Natural Selection's Role in Parallel Speciation  
*V. Soria-Carrasco et al.*  
Parallel speciation in insects shows both convergent and divergent selection after one generation.
- 742** NMR Spectroscopy of Native and in Vitro Tissues Implicates PolyADP Ribose in Biomineralization  
*W. Y. Chow et al.*  
An in vitro model of developing bone from a mouse model is amenable to nuclear magnetic resonance analysis.
- 747** Genomic Diversity and Admixture Differs for Stone-Age Scandinavian Foragers and Farmers  
*P. Skoglund et al.*  
Population dynamics of Scandinavian Mesolithic and Neolithic hunter-gatherers differ from those of early farmers.
- 750** Late Pleistocene Human Skeleton and mtDNA Link Paleoamericans and Modern Native Americans  
*J. C. Chatters et al.*  
The differences between Paleoamericans and Native Americans likely resulted from local evolution.  
>> *News story p. 680*
- 754** Neurosensory Perception of Environmental Cues Modulates Sperm Motility Critical for Fertilization  
*K. McKnight et al.*  
Nematode pheromones modulate a neuroendocrine pathway that converts dietary fats into sperm-attracting prostaglandins.
- 757** Sulfur Oxidation Genes in Diverse Deep-Sea Viruses  
*K. Anantharaman et al.*  
Host-derived viral auxiliary metabolic genes for sulfur oxidation play a key biogeochemical role in the dark ocean.
- 760** Positive Feedback Within a Kinase Signaling Complex Functions as a Switch Mechanism for NF- $\kappa$ B Activation  
*H. Shinohara et al.*  
The molecular basis of an all-or-none response in B cells is revealed.

SCIENCE (ISSN 0036-8075) is published weekly on Friday, except the last week in December, by the American Association for the Advancement of Science, 1200 New York Avenue, NW, Washington, DC 20005. Periodicals Mail postage (publication No. 484460) paid at Washington, DC, and additional mailing offices. Copyright © 2014 by the American Association for the Advancement of Science. The title SCIENCE is a registered trademark of the AAAS. Domestic individual membership and subscription (51 issues): \$153 (\$74 allocated to subscription). Domestic institutional subscription (51 issues): \$1282; Foreign postage extra: Mexico, Caribbean (surface mail) \$55; other countries (air assist delivery) \$85. First class, airmail, student, and emeritus rates on request. Canadian rates with GST available upon request, GST #1254 88122. Publications Mail Agreement Number 1069624. Printed in the U.S.A.

Change of address: Allow 4 weeks, giving old and new addresses and 8-digit account number. Postmaster: Send change of address to AAAS, P.O. Box 96178, Washington, DC 20090-6178. Single-copy sales: \$10.00 current issue, \$15.00 back issue prepaid includes surface postage; bulk rates on request. Authorization to photocopy material for internal or personal use under circumstances not falling within the fair use provisions of the Copyright Act is granted by AAAS to libraries and other users registered with the Copyright Clearance Center (CCC) Transactional Reporting Service, provided that \$30.00 per article is paid directly to CCC, 222 Rosewood Drive, Danvers, MA 01923. The identification code for Science is 0036-8075. Science is indexed in the Reader's Guide to Periodical Literature and in several specialized indexes.

## Out of the Air

New-particle formation from gaseous precursors in the atmosphere is a complex and poorly understood process with importance in atmospheric chemistry and climate. Laboratory studies have had trouble reproducing the particle formation rates that must occur in the natural world. **Riccobono et al.** (p. 717) used the CLOUD (Cosmics Leaving Outdoor Droplets) chamber at CERN to recreate a realistic atmospheric environment. Sulfuric acid and oxidized organic vapors in typical natural concentrations caused particle nucleation at similar rates to those observed in the lower atmosphere.

## Controlling Chiral Light Emission

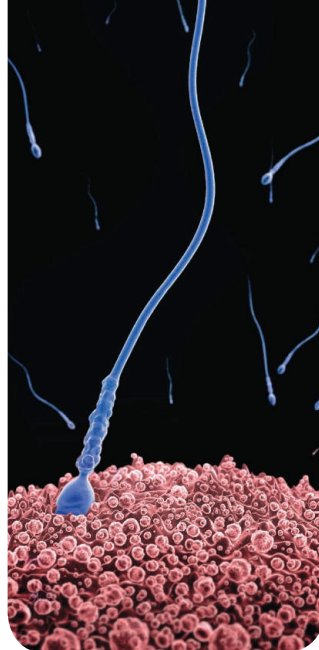
Circularly polarized light plays important roles in a number of applications such as displays, communication, and sensing. Thus, the ability to produce compact and readily controllable polarized light sources is important, and dichalcogenide materials such as tungsten diselenide may provide a route to such sources. **Zhang et al.** (p. 725, published online 17 April; see the Perspective by **Zaumseil**) formed an electric-double-layer transistor structure with  $\text{WSe}_2$  and used a gated ionic liquid to control the carrier density. Electrical control of the output light was achieved with the polarization being switched by reversing the polarity of the applied field and injected charge.

## Recyclable Thermoset Polymers

The high mechanical strength and durability of thermoset polymers are exploited in applications such as composite materials, where they form the matrix surrounding carbon fibers. The thermally driven polymerization reaction is usually irreversible, so it is difficult to recycle the constituent monomers and to remove and repair portions of a composite part. **García et al.** (p. 732; see the Perspective by **Long**) now describe a family of polymers formed by condensation of paraformaldehyde with bisanilines that could form hard thermoset polymers or, when more oxygenated, produce self-healing gels. Strong acid digestion allowed recovery of the bisaniline monomers.

## Stick to the Bush

Can the underlying genetic changes driving the divergence of populations into new species be predicted or repeated? **Soria-Carrasco et al.** (p. 738) investigated the genetic changes observed



## << Scents and Sperm

Once sperm enter the female reproductive tract, they have an arduous task to find an egg at a distant, often concealed, location. **McKnight et al.** (p. 754) show that *Caenorhabditis elegans* make this task more or less difficult, depending on pheromones in the external environment. Pheromones perceived by female sensory neurons modulate the synthesis of ovarian prostaglandins, which provide sperm positional information. Thus, environmental cues can indirectly impact sperm function even when the sperm themselves are not directly exposed.

after one generation when stick insect (*Timema cristinae*) populations were transplanted from their preferred host plants to alternative hosts. Diverged genetic regions were relatively small, with most loci showing divergence in a single population pair. However, the number of loci showing parallel divergence was greater than expected by chance. Thus, selection can drive parallel phenotypic evolution via parallel genetic changes.

## Fundamentals of Bone Formation

In vitro models can help guide research for tissue engineering or drug delivery, but the extent to which results from in vitro experiments may mimic in vivo ones will depend on the robustness of the model. For complex tissues like the extracellular matrix or bone, this means matching the chemical organization of the tissue at both the atomic scale and the structural level. **Chow et al.** (p. 742) used nuclear magnetic resonance (NMR) spectroscopy to analyze a sample on both these length scales. First an isotope-enriched mouse was produced to enhance the NMR signal. Samples from these mice were then used to study the extracellular matrix of developing bone and the calcification front during fetal bone growth.

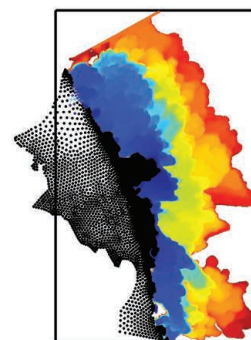
## American Beauty

Modern Native American ancestry traces back to an East Asian migration across Beringia. However, some Native American skeletons from the late Pleistocene show phenotypic characteristics more similar to other, more geographically distant, human populations. **Chatters et al.** (p. 750) describe a skeleton with a Paleoamerican phenotype from the eastern

Yucatan, dating to approximately 12 to 13 thousand years ago, with a relatively common extant Native American mitochondrial DNA haplotype. The Paleoamerican phenotype may thus have evolved independently among Native American populations.

## Antarctic Collapse

The West Antarctic Ice Sheet (WAIS) is particularly vulnerable to ocean warming-induced collapse. The Thwaites Glacier of West Antarctica is one of the largest WAIS regional contributors to sea level rise, and has been considered to be potentially unstable for many years. **Joughin et al.** (p. 735) used a combination of a numerical model and observations of its recent geometry and movement to investigate the stability of the Thwaites Glacier. The glacier has already entered the early stages of collapse, and rapid and irreversible collapse is likely in the next 200 to 1000 years.



## Virus-Enhanced Sulfur Oxidation

How do microbial viruses affect subsurface microbial communities? **Anantharaman et al.** (p. 757, published online 1 May) investigated the interactions between ubiquitous marine lithotrophs found at hydrothermal vents and their viruses. The genes for sulfur oxidation in viruses that infect abundant marine chemosynthetic sulfur-oxidizing bacteria enhanced sulfur oxidation, thereby influencing the biogeochemical sulfur cycle.



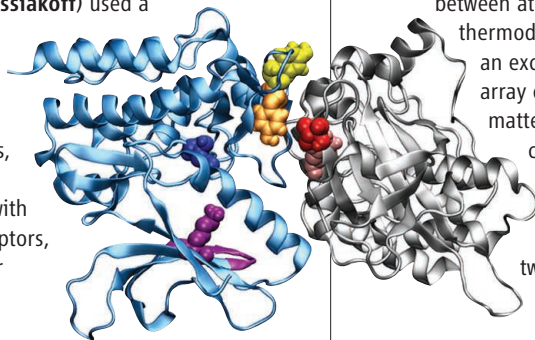
## Additional summaries

## The Lignin Landscape

Lignin is a chemically complex polymer that lends woody plants and trees their rigidity. Humans have traditionally either left it intact to lend rigidity to their own wooden constructs, or burned it to generate heat and sometimes power. With the advent of major biorefining operations to convert cellulosic biomass into ethanol and other liquid fuels, researchers are now exploring how to transform the associated leftover lignin into more diverse and valuable products. **Ragauskas *et al.*** (p. 709) review recent developments in this area, ranging from genetic engineering approaches that tune lignin properties at the source, to chemical processing techniques directed toward extracting lignin in the biorefinery and transforming it into high-performance plastics and a variety of bulk and fine chemicals.

## The Hormone's Message

The receptor for growth hormone is a well-studied representative of a family of cytokine receptors through which binding of hormone molecules at the cell surface is converted into a biochemical signal within the cell. **Brooks *et al.*** (p. 710; see the Perspective by **Wells and Kossiakoff**) used a combination of crystal structures, biophysical measurements, cell biology experiments with modified receptors, and molecular dynamics and modeling to decipher how the receptor actually transmits the information that a hormone molecule is bound. The results suggest that the receptors exist in inactive dimeric complexes in which two associated JAK2 protein kinase molecules interact in



an inhibitory manner. Binding of growth hormone causes a structural change in the receptor that results in movement of the receptor intracellular domains apart from one another. This relieves the inhibition of the JAK2 molecules and allows them to activate one another, thus initiating the cellular response to the hormone.

## Degrees of Separation

Proteins embedded in membranes represent an interesting point of communication between the cell and its environment, but their localization to membranes can make them difficult to study. **Jones *et al.*** (p. 711) found an approach to catalog thousands of interactions involving membrane proteins and membrane-associated signaling machinery—including many previously uncharacterized proteins. With a focus on the model plant *Arabidopsis*, several of the identified interactions fill gaps in important signal transduction chains, while others point to functions for enigmatic unknown proteins.

## Untwisting the Spin Spiral

Ultracold Fermi gases in the so-called unitary regime—where the diverging interactions between atoms make their thermodynamics universal—are an excellent test bed for an array of strongly interacting matter systems. The transport characteristics in this regime are particularly intriguing, and a discrepancy between two- and three-dimensional transport coefficients has been observed. **Bardon *et al.*** (p. 722) studied the demagnetization dynamics of a three-dimensional Fermi gas. The gas was initially polarized along a single direction and was noninteracting. An applied magnetic field gradient then caused a spin spiral to form; as the gas relaxed from this state, the authors extracted the diffusion coefficient and observed the buildup of interactions between the atoms.

## Crystal Growth

Two main routes for the growth of crystalline species are either via molecule-by-molecule attachment to existing nuclei or via the addition of preformed metastable precursors, but do these mechanisms need to be mutually exclusive? **Lupulescu and Rimer** (p. 729; see the Perspective by **Dandekar and Doherty**) developed an in situ atomic force microscopy (AFM) technique to study the crystallization of materials under extreme conditions of temperature (25° to 300°C) and alkalinity (up to a pH of 13). The growth of the zeolite silicalite-1 involved both the attachment of metastable precursors and of individual molecules.

## Hunters and Farmers

The Neolithic period in Europe saw the transition from a hunter-gatherer lifestyle to farming. Previous genetic analyses have suggested that hunter-gatherers were replaced by immigrant farmers. **Skoglund *et al.*** (p. 747, published online 24 April) sequenced one Mesolithic and nine Neolithic Swedish individuals to examine the transition from hunter-gatherers to farmers. Substantial genetic differentiation was observed between hunter-gatherers and farmers: There was lower genetic diversity within the hunter-gatherers and gene flow from the hunter-gatherers into the farmers but not vice versa.

## Signaling Dynamics

The signaling pathways that activate the transcription factor NF- $\kappa$ B are key regulatory pathways in cells of the immune system, and their dynamic properties are still being elucidated. In B cells, analysis of single-cell responses has shown that the stimulation of the B cell receptor causes a “digital” all-or-none response of cells to a stimulus. **Shinohara *et al.*** (p. 760) used a combination of mathematical modeling and experiments to show that this property of the system results from the presence of a positive feedback loop among the signaling components activated in response to the receptor. Studies in cells expressing mutated signaling components resolved key phosphorylation events that provide the threshold responses observed and identified potential molecular modifications that might modify the threshold or other aspects of the dynamic response.

# Think Outside the Lab

LAST MONTH, THE U.S. NATIONAL SCIENCE FOUNDATION (NSF) RELEASED A REPORT\* WITH SOME grim news that confirmed what is painfully obvious to recent Ph.D. graduates in science, technology, engineering, and mathematics (STEM) fields: Unemployment for this cohort is on the rise (at 2.4% in 2010, up nearly a percentage point since 2008). Although it remains below the U.S. national average for all workers (8.2%), for bright students who have invested many years in specialized education and training, the outlook is discouraging. Furthermore, according to an NSF survey, in 2008 only 16% of Ph.D.'s in science, engineering, and health fields held positions in academia within 3 years of earning a doctorate.† Prospects for employment can be improved, however, for STEM Ph.D.'s who make a concerted effort to learn about positions outside the lab and prepare themselves for alternative paths.

Recently, I participated in a *Science Careers* Webinar that offered advice on nonresearch employment. The timeliness of this topic was reflected in the number of registrants signed up in advance for the Webinar: 6000, far above the average for other Webinars hosted by this career resource. I was joined by Dr. Lori Conlan, director of Office of Postdoctoral Services at the U.S. National Institutes of Health, and Dr. Anish Goel, director of Geopolitical Affairs for Boeing Commercial Airplanes. We all agreed that our nonlab positions had allowed us the ability to follow our passions, forge our own paths, and provide us with flexibility to balance work and family life. Regardless of when we had made the move to a nonresearch career, no one expressed any regrets; but we agreed that the move can be challenging. It requires one to thoughtfully research career options and invest sufficient time in networking to build bridges to new communities.

Webinar participants asked about skills that are not sufficiently covered in most traditional science Ph.D. programs that are highly valued in many nonlab positions. Communications skills are near the top of our list, particularly the ability to explain complex scientific concepts to diverse audiences. Related to that is the ability to listen, which is the first step in understanding how the application of science can help meet the needs of others. Also high on the list is an understanding of people: how to recognize their strengths and shortcomings, to motivate them to achieve their best, and to assemble diverse teams that achieve what no individual could ever accomplish. Surprisingly, many Ph.D. scientists do not realize that much of their training and experience has imbued them with such skills and that they are better qualified for positions outside the lab than they think. Collaborating with interdisciplinary colleagues on projects over long distances, writing successful research proposals, planning the logistics for complex field experiments, analyzing large data sets, and contributing in meaningful ways to committee activities require skills that are relevant to the nonlab working world.

A Ph.D. in a STEM field opens doors, rather than closes them, but opening those doors is not easy. Before applying for any position, candidates should consider the breadth of their experience and make an honest assessment of themselves. Are they better suited to working alone, as part of a team, or as a team leader? What do they value most: that they solved the right problem, that they solved the problem correctly, that they got the job done, or how everyone felt about the job? A good place to start is with an Individual Development Plan (<http://myidp.sciencereaders.org>), an online resource to help scientists examine their skills, interests, and values; explore scientific career paths to find which ones are a best fit; and set strategic goals for the coming year.

If you are considering making the move from the lab, you are not alone. This transition is taking place at all career levels, spurred by different motivations. Whatever the reason, many have successfully taken this road, and so can you.

— Marcia McNutt

10.1126/science.1255745

\*[www.nsf.gov/statistics/infbrief/nsf14310/?WT.mc\\_id=USNSF\\_179](http://www.nsf.gov/statistics/infbrief/nsf14310/?WT.mc_id=USNSF_179). †[www.nsf.gov/statistics/seind12/c3/tt03-20.htm](http://www.nsf.gov/statistics/seind12/c3/tt03-20.htm).



Marcia McNutt is Editor-in-Chief of *Science*.



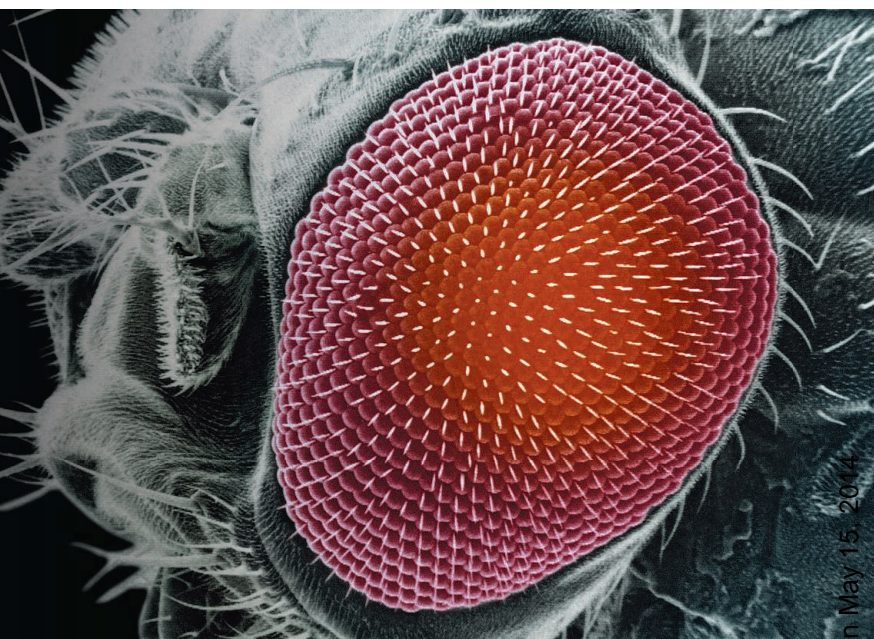


## NEURODEVELOPMENT

## Neural Circuits One Step At a Time

How do simple neurons come together to form a complicated circuit? To answer this question, Pecot *et al.* studied a well-defined circuit in the eye of the fruit fly *Drosophila melanogaster*, which is composed of two different types of neurons, to learn the intricate steps in the circuit-building dance. The fruit fly's eye is built of repetitive units made up of eight photoreceptor neurons and five lamina neurons each. Each unit perceives light and transmits chemical signals into the fly's brain. But before the unit can work, the circuit needs to form. That happens step by step, as one neuron signals to another. Photoreceptor neurons of type 1 through 6 send a chemical signal to lamina neuron 3. Lamina neuron 3 in turn sends out a homing beacon to guide photoreceptor neuron 8 to its correct destination. Without the correct signals, lamina neuron 3 dies, and without the lamina homing beacon, photoreceptor neuron 8 remains lost in no-man's land. — PJH

*Neuron* 82, 320 (2014).

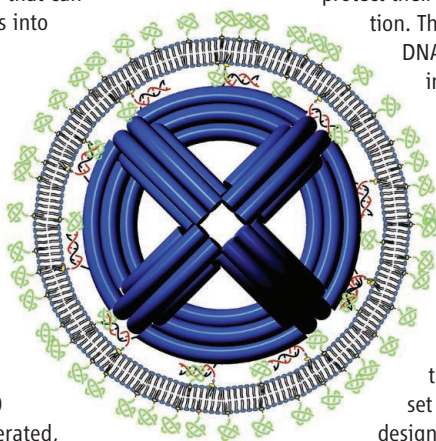


## MATERIALS SCIENCE

## Perpetual Heart Throb

Many cardiac conditions require the implantation of a pacemaker or defibrillator to help regulate the contractions of the heart. While these devices are extremely helpful in extending and improving the quality of a person's life, they need to be replaced every few years, primarily because of the limited life span of the batteries. One potential solution may come from energy-harvesting materials that can convert small mechanical motions into electrical energy, and thus could exploit cardiac motion, muscle contractions, and relaxation, or blood circulation as the driving source for power generation. Hwang *et al.* created a self-powered artificial pacemaker using single, crystalline PMN-PT  $[(1-x)\text{Pb}(\text{Mg}_{1/3}\text{Nb}_{2/3})\text{O}_3 - x\text{PbTiO}_3]$  placed on a thin plastic substrate. Through low-frequency flexing of the substrate back and forth, a current of more than 100 microamperes at 8 volts was generated, enough to power a string of commercial LED lights or recharge a coin battery. A sample device was implanted into the cardiac muscle of an anesthetized rat and enabled real-time electrical stimulation. The next step for the authors is to test a stack of devices to see if they can harvest energy from the heart of a larger animal such as a pig. — MSL

*Adv. Mat.* 10.1002/adma.201400562 (2014).



## BIOMATERIALS

## Viral Envelopes Built Better

Drawing inspiration from virus structure has the potential to make nanoparticles more stable and better at hiding from the immune system which might help researchers expand the uses of nanoparticles in the clinic. Nanotechnology can enhance drug targeting and improve the engineering of nanoscale medical devices. Perrault and Shih mimicked the strategy viruses use to protect their genetic information. They fabricated a

DNA cage structure in the form of a nanooctahedron with a diameter of 50 nm. The structure had "handles" made from single-stranded DNA on the inside and outside of the cage. The inner set of handles was designed to attach to fluorophore-conjugated oligonucleotides, providing a visible marker for the structure. The outer set of handles was designed to attach to lipid-conjugated oligonucleotides, so that the researchers could then assemble a lipid bilayer around the DNA cage. The resulting particles were 76 nm in diameter and resembled enveloped virus structures. The particles were more resistant to nucleases in vitro and caused

immune cells isolated from mouse spleens to produce much lower levels of the inflammatory cytokines IL-6 and IL-12. The particles also stayed in the bodies of injected mice for longer times than unencapsulated DNA cages. — BJ

*ACS Nano.* 10.1021/nn5011914 (2014).

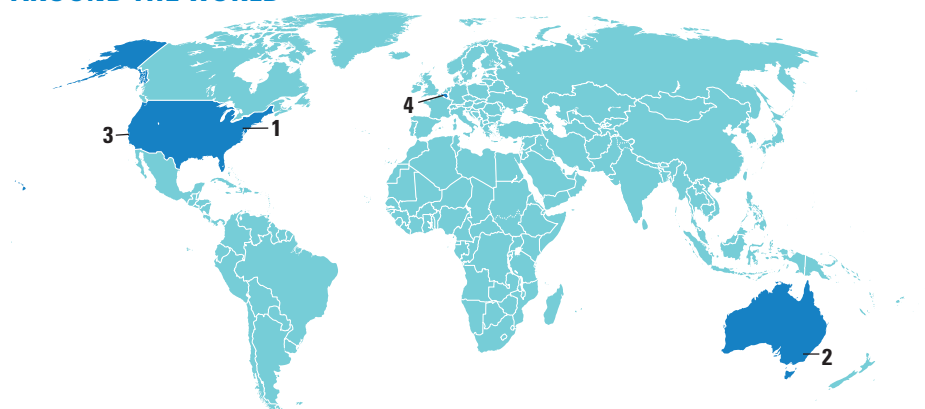
## PALEOCLIMATE

## Too Short to Show

During the last ice age, the climate of Greenland (and much of the Northern Hemisphere) jumped between cold intervals (called stadials) and warm ones. Records from ice cores show that the concentration of carbon dioxide in the atmosphere rose during the longer stadials, but how it may have changed during the shorter ones was unclear due to a lack of highly time-resolved  $\text{CO}_2$  measurements. Ahn and Brooks constructed a detailed time series of atmospheric  $\text{CO}_2$  from an ice core in Antarctica, which shows that  $\text{CO}_2$  concentrations changed during the longer stadials but not during the shorter ones. The authors therefore suggest that during short Greenlandic stadials, changes in ocean circulation large enough to cause the transfer of large amounts of  $\text{CO}_2$  from the deep ocean to the atmosphere did not occur, unlike during longer stadials when the effect is clearly apparent. This, in turn, may imply that the climate links between the Antarctic and the high-latitude Northern Hemisphere could have been controlled by shallow oceanic or atmospheric processes, whereas  $\text{CO}_2$  changes were controlled by deep oceanic and Southern Ocean ones. — HJS

*Nat. Commun.* 10.1038/ncomms4723 (2014).

## AROUND THE WORLD

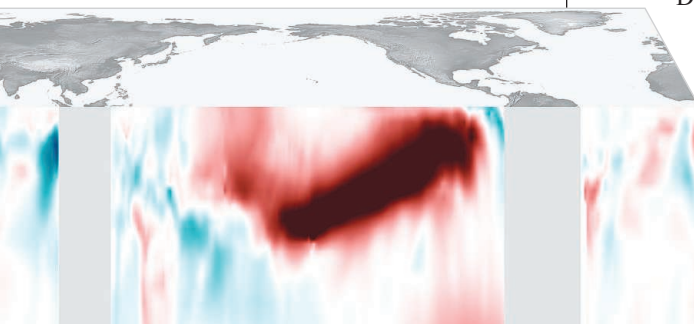


College Park, Maryland 1

**El Niño Coming Back**

El Niño, a periodic warming in the eastern tropical Pacific Ocean, has a 58% chance of emerging in the next 3 months, according to an 8 May forecast by the Climate Prediction Center (CPC) of the National Oceanic and Atmospheric Administration. That likelihood rises to 78% by the early fall, CPC found.

If strong, the El Niño event could wreak havoc on weather around the world, kick-



**Trouble arising?** Warm water (red) in the Pacific Ocean could trigger El Niño if it reaches the surface.

ing off weather patterns that can cause droughts, storms, fires, and floods. The last El Niño occurred in 2009 to 2010, and the last big one, in 1997 to 1998, caused billions of dollars of damage worldwide.

A strong El Niño event could also trigger a resumption of global warming, seemingly stalled for the last 15 years. The Pacific Decadal Oscillation (PDO), a 20- to 30-year climate cycle, has been in a cool phase for nearly 20 years. But a strong El Niño event could push the PDO back into a warm phase, allowing heat from the ocean to reach the atmosphere—and causing a jump in atmospheric global warming. <http://scim.ag/elnino2014>

Canberra 2

**Budget Slashes Science Funding**

Australia's new conservative government released its first federal budget on 13 May, with major cuts to science funding outside of biomedical research. Spending at major science agencies will be at least AU\$420 million less than envisioned by government projections: The Commonwealth Scientific and Industrial Research Organisation, for instance, would lose AU\$111.4 million, the Defence Science and Technology Organisation AU\$120 million, the Australian Nuclear Science and Technology Organisation AU\$27.6 million, and the Australian Institute of Marine Science AU\$7.8 million.

The big winner in the budget is biomedical research; the government will establish a Medical Research Future Fund, and AU\$42 million will go to expand the Australian Institute of Tropical Health and Medicine at James Cook University. <http://scim.ag/AUbud>

Palo Alto, California 3

**Stanford Strips Coal Investments From Endowment**

Advocates of reducing fossil fuel use are lauding Stanford University's announcement last week that it will sell stock in 100 publicly traded firms focused on coal extraction that are part of its \$18.7 billion endowment. Stanford is the most prominent school to announce divestment from fossil fuels; 11 other schools have announced divestment policies, says nonprofit activist organization 350.org, which is coordinating the divestment movement. "[C]oal is one of the most

carbon-intensive methods of energy generation," said Stanford President John Hennessy in a statement, calling the move "a small, but constructive, step" toward developing "broadly viable sustainable energy solutions."

How much impact Stanford's divestment will have on the environment or the university itself is unclear, however, as the school didn't say how much the holdings are worth. Some skeptics, including the National Association of College and University Business Officers, say the move amounts to a drop in the bucket, or that others will invest in coal if universities pull out.

Brussels 4

**E.U. Unveils University Ranking System**

The European Commission has launched an online tool to rate universities worldwide. "U-Multirank" provides a sophisticated alternative to cruder rankings by letting users select rating criteria out of 30 indicators, identifying top performers for each one rather than providing overall scores in a single table, project leader Frank Ziegele said at the launch event on 13 May.

U-Multirank relies in part on the same publicly available data as other rankings, including citation rates or patent figures. But it also introduces fresh indicators, such as publications involving several disciplines and joint publications with industry, and collects data from student surveys and universities themselves. Next year, U-Multirank plans to add more universities to its list of 879 and to add three disciplines to the current four. <http://scim.ag/UMultirank>

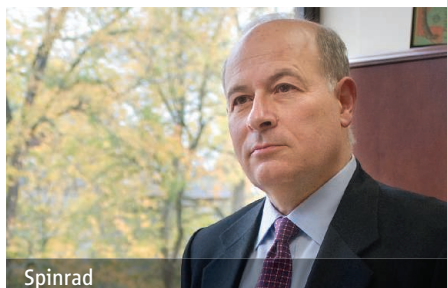
## NEWSMAKERS

**NOAA Gets Chief Scientist**

President Barack Obama on 8 May announced his plan to appoint oceanographer **Richard "Rick" Spinrad** to become the next chief scientist of the National Oceanic and Atmospheric Administration (NOAA). Spinrad would be the agency's first chief scientist since former astronaut and earth scientist Kathryn Sullivan—now NOAA's administrator—held the job in the mid-1990s.

The move marks the administration's second effort to fill the post, which it reestablished in 2009 as a presidential appointment requiring confirmation by the U.S. Senate. (Previous administrations downgraded, eliminated, or refused to fill





Spinrad

the position.) The White House's initial nominee, geochemist Scott Doney, withdrew his name in 2012 after a 2-year battle with Republicans in the U.S. Senate. Because of changes to federal personnel rules, Spinrad will not need Senate confirmation.

Now the vice president for research at Oregon State University (OSU), Corvallis, Spinrad served as NOAA's assistant administrator for research from 2005 to 2010 and led its oceans and coastal zone programs from 2003 to 2005. From 1987 to 2003, he worked for the U.S. Navy, including as technical director for the oceanographer of the Navy. He earned his doctorate at OSU. <http://scim.ag/Spinrad>

## FINDINGS

### Progeria Drug May Extend Lifespan

An experimental drug to treat the fatal disease progeria slightly increased the lifespan of dozens of children afflicted with the disease, reports the Progeria Research Foundation (PRF), which funded the first trials of the drug. The genetic mutation behind progeria causes symptoms resembling premature aging: hair and weight loss; joint stiffness; and atherosclerosis, which causes heart attacks that kill most patients in their teens.

Leslie Gordon, medical director of PRF, and colleagues reported in 2012 that patients taking the drug, lonafarnib, showed small weight gains and reductions in blood vessel stiffness. In a paper published online on 2 May in *Circulation*, her team now reports that the drug added, on average, 19 months to their lifespans.

Because so few children have progeria and the disease is invariably fatal, the trial did not include a placebo group. The researchers compared the treated group to historical records and published case reports, but such comparisons are "notoriously unreliable," because different studies may use different criteria for including patients, says Donald Berry, a biostatistician at the

University of Texas MD Anderson Cancer Center in Houston. Other factors, he notes, could therefore contribute to differences in lifespan. [http://scim.ag/\\_progeria](http://scim.ag/_progeria)

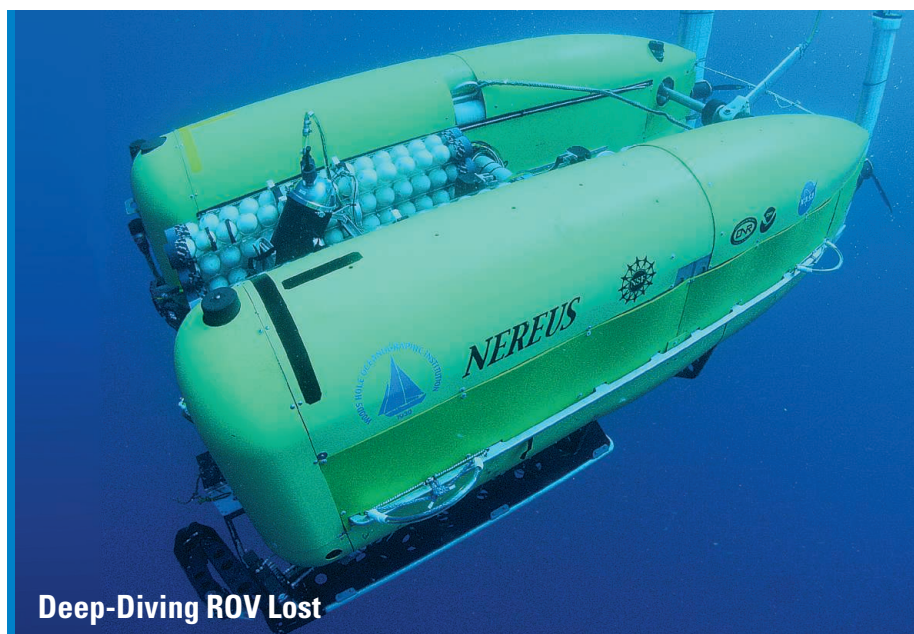
### Many Genes Helped Tame Wild Rabbits

Charles Darwin wrote that no animal is more difficult to tame than a young wild rabbit—and no animal is tamer than a young domesticated bunny. That behavioral about-face arises from thousands of subtle genetic differences, and not—as researchers thought—from big changes in just one or two genes, Nima Rafati and Leif Andersson from Uppsala University in Sweden reported last week at the Biology of Genomes meeting in Cold Spring Harbor, New York.



With most domesticated animals, it's difficult to pin down a domestication gene: Humans tamed them so long ago that the wild ancestors are hard to identify. But rabbits came under our control just 1400 years ago, and their ancestors still thrive in Europe's Iberian Peninsula. After sequencing 20 wild and domesticated rabbit

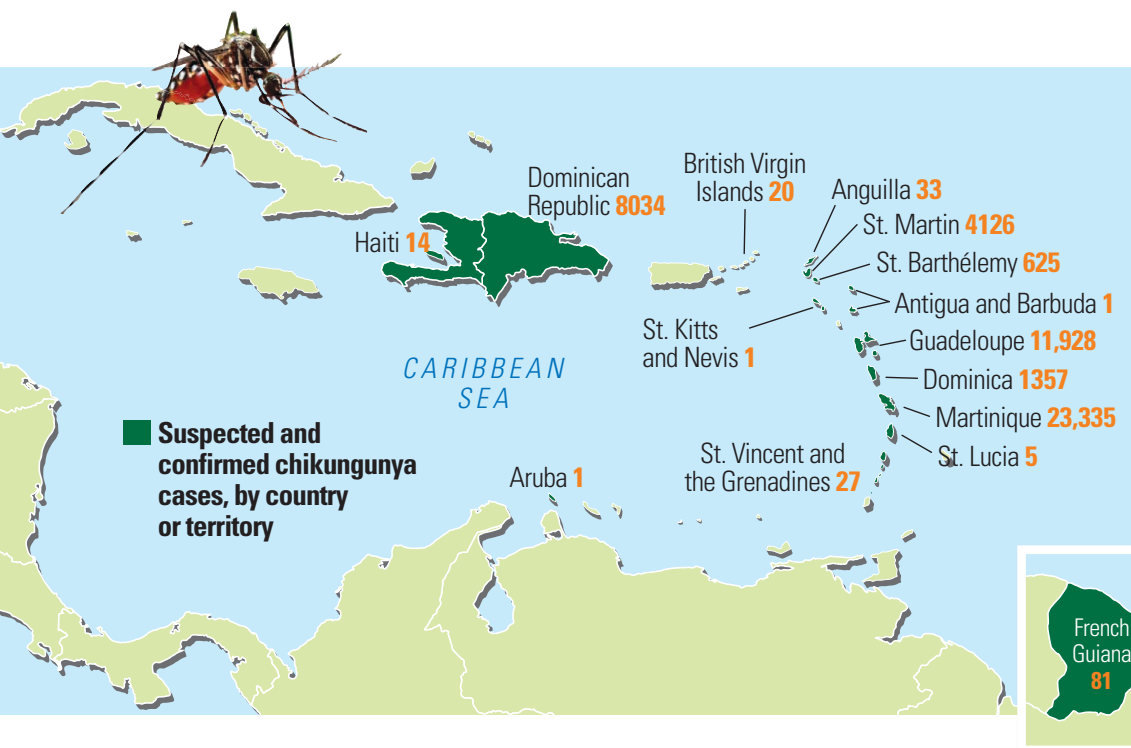
genomes, the researchers observed shifts in the frequency of different versions of genes in the two types of rabbits. Often the shifts were associated with genes and regulatory DNA involved in development, particularly of the nervous system. "The message coming from the rabbit is that it's just a large number of small changes," says Princeton University evolutionary geneticist Peter Andolfatto, who was not involved in the study. [http://scim.ag/\\_rabdom](http://scim.ag/_rabdom)



### Deep-Diving ROV Lost

*Nereus*, the Woods Hole Oceanographic Institution's hybrid remotely operated vehicle (ROV) that was an integral part of a mission to explore the little-known ecosystems in some of the deepest parts of the ocean, was confirmed lost on 10 May during one of its deepest dives. Seven hours into a planned 9-hour dive to a depth of 9990 meters in the Kermadec Trench northeast of New Zealand, researchers lost contact with *Nereus*. They later spotted debris on the water thought to belong to the missing ROV, suggesting a "catastrophic implosion" due to pressures as great as 110 megapascals at those water depths, the mission's blog noted.

*Nereus*, designed to operate either as a free-swimming vehicle or connected to an optical fiber tether, had previously survived a plunge into the deepest point of the ocean, Challenger Deep in the Mariana Trench. The \$8 million ROV was just 30 days into the current mission, the inaugural research cruise of a 3-year National Science Foundation-funded program to systematically study life in deep-ocean trenches, also called the hadal depths (*Science*, 18 April, p. 241).



**Island hopping.** Chikungunya, whose main vector is the *Aedes aegypti* mosquito, is spreading fast in the Caribbean.

Chikungunya remained obscure until about a decade ago, in part because most cases occurred in Africa. Then in 2004, a big outbreak in East Africa spilled over into islands in the Indian Ocean; among them was La Réunion, a French *département* and a popular tourist destination, where almost 40% of the population fell ill in a matter of months. That helped raise global awareness and research euros (*Science*, 21 December 2007, p. 1860). Since then, the virus has been on a global rampage. Outbreaks in India have sickened millions; the

virus has also moved into Southeast Asia and some islands in the Pacific.

The massive spread was fueled in part by genetic changes that enabled the virus to replicate efficiently in a second vector, *A. albopictus*, better known as the Asian tiger mosquito. That species has invaded countries around the world over the past 3 decades (*Science*, 16 May 2008, p. 864), so the mutations gave the virus a ticket to many new destinations. The tiger mosquito is the predominant vector in parts of India, for instance. And in two villages in northeast Italy—which has massive *A. albopictus* infestations—217 people were sickened in 2007 after a patient brought in the virus from India.

One of the surprises of the Caribbean outbreak is that the strain responsible isn't the one adapted to the tiger mosquito, but a different one, most likely originating in East Asia, says virologist Scott Weaver of the University of Texas Medical Branch in Galveston. That's little consolation for most of the hemisphere, because *A. aegypti* is so widespread. But in the United States, *A. aegypti* occurs only in the southernmost parts of the country, which could limit the spread.

There are no drugs for chikungunya, but several vaccine candidates are in various stages of development, and the Caribbean outbreak has revived industry attention, Weaver says. Weaver's own team has designed a live vaccine, based on a weakened

## INFECTIOUS DISEASES

# Crippling Virus Set to Conquer Western Hemisphere

The world of infectious diseases is full of unpleasant surprises. But the explosive outbreak of a virus called chikungunya now happening on a string of Caribbean islands isn't one of them. Scientists have said for years that the virus was bound to come to the Western Hemisphere. And now that it has, they have another prediction: Mosquitoes will almost certainly spread it far and wide, from the southern United States to Argentina. Big, dense cities will be especially vulnerable to the virus, which can cause rashes, fever, and agonizing, sometimes lasting, pain in fingers, wrists, elbows, toes, ankles, and knees. Millions will likely get sick.

The reason experts felt so certain—and the Pan American Health Organization warned countries to prepare in 2011—is that the virus was causing huge outbreaks elsewhere, and its main vector, the *Aedes aegypti* mosquito, is widespread in the Americas. Health authorities in the United States, Canada, and Brazil were already seeing a steady stream of imported cases; all it took for the disease to take off was for one of them to be bitten by a local mosquito. “Nothing feasible could have been done to prevent this from happening,” says Roger

Nasci, who heads the Arboviral Diseases Branch of the Centers for Disease Control and Prevention in Fort Collins, Colorado.

In early December, health authorities on the French side of St. Martin reported a cluster of locally transmitted chikungunya cases. Martinique, St. Barthélemy, and Guadeloupe soon followed suit, as did French Guiana in South America. This year, the virus hit Dominica, St. Lucia, Aruba, the U.K. Virgin Islands, and the Dominican Republic. Haiti joined the list just last week. So far, more than 4000 cases have been confirmed in the lab, but the number of suspected cases—people with acute fever and severe, unexplained joint pains—exceeded 45,000 early this week.

The *A. aegypti* mosquito also transmits dengue, a disease that has similar symptoms but is more often deadly. Dengue's global reach has expanded massively in the past 30 years, and it has caused major outbreaks in Latin America. Wherever the disease occurs, chikungunya can spread as well, Nasci says. Tourism in the Caribbean region could help the spread to the mainland; the tens of thousands of soccer fans traveling to Brazil for the World Cup in June and July may also give the virus a leg up.



version of the chikungunya virus, licensed to Japanese pharma company Takeda. Animal studies suggest that one shot of the vaccine will provide long-lasting protection, and Takeda is keen on beginning human studies, Weaver says. But expensive preclinical studies will be needed first, for instance to make sure the vaccine virus won't revert to a more pathogenic form. Another vaccine candidate, developed at the Vaccine Research Center of the National Institutes of Health and licensed to Merck, consists of viruslike particles—empty protein shells resembling the virus that trigger immunity. It has already passed safety studies in humans.

Testing a vaccine's ability to prevent chikungunya in the real world is difficult,

however. Once an epidemic has roared through a population, the virus still infects people now and then, but the scattered cases often aren't diagnosed, or are mistaken for dengue. That makes it hard for companies to decide how many people to enroll in a trial—and how much they need to spend—to show that a vaccine actually works, Weaver says.

One solution would be to set up a trial that kicks off just before a massive wave of cases starts rolling in, rather than afterward—for instance, in a city in Latin America, where the virus now seems set to strike. Because a significant part of the population will get sick, “you could probably do an efficacy study in a small number of people for a small

amount of money,” Weaver says. Whether there is enough time to do this soon with any of the vaccines is unclear, however.

Absent a vaccine, it's tough to contain chikungunya—just as it has been with dengue. *Aedes* mosquitoes breed in little pools of water around the house—in flowerpots, plastic containers, and old tires, for example—and these have proven very hard to eliminate, Nasci says. Even an island like Martinique, which had a reputation for good vector control, had a big dengue outbreak in 2010, notes Paul Reiter, a medical entomologist at the Institut Pasteur in Paris. “There is just very little we can do about it,” Reiter says. “The mosquito wins.”

—MARTIN ENSERINK

NATIONAL INSTITUTES OF HEALTH

## Needed: More Females in Animal and Cell Studies

Hoping to end the reliance on male animals in research, the National Institutes of Health (NIH) announced this week that it will soon require grant applicants to balance the sex of animals and cells they intend to study—or explain why they won't. The new policy, said two top NIH officials who described it in a commentary in *Nature*, is critical because work in cells and animals guides therapies that move into humans.

Sex “really has to be considered as a fundamental variable” when designing experiments, says Janine Clayton, director of the Office of Research on Women's Health. She wrote the *Nature* commentary along with her boss, NIH Director Francis Collins. Not every experiment needs to include the same number of males and females, Clayton says, but in general, “if we don't pay upfront we will pay later.”

NIH addressed male bias in human studies more than 20 years ago, but that rebalancing hasn't trickled down. Researchers often avoid female animals because they're considered more variable due to their estrous cycle. Many scientists don't know the sex of the cells they're probing, and despite growing evidence to the contrary, they tend to assume that it doesn't matter whether cells come with a Y chromosome or not.

“You have this real lack of understanding of female biology,” says Annaliese Beery, a neuroendocrinologist at Smith College in Northampton, Massachusetts. In a 2010 paper, she and Irving Zucker of the University of California, Berkeley, surveyed almost 2000 animal studies. They found that eight of 10 disciplines favored male animals, and the bias was most pronounced in neuroscience; for every study using only females, 5.5 used only males. A startling 75% of papers in three top immunology

neuroendocrinologist at the University of Maryland School of Medicine in Baltimore. Eighty percent of genes in the liver, she points out, are expressed differently in male and female cells.

A key reason for excluding female animals—that they are more variable than males—may be unfounded, recent research suggests. Zucker and two colleagues pored over nearly 300 mouse studies, looking at behavioral, physiological, and other traits. In an analysis published earlier this year in *Neuroscience & Biobehavioral Reviews*, they found that male biology was just as variable as that of their female counterparts. For example, whether the males were housed alone or with others had an impact on results.

The new policy, which the agency will begin rolling out in October, might increase costs, Clayton acknowledges—in certain cases, a study might need extra animals, or a researcher who for years has relied on an XX cell line to study a particular pathway might need to find or create one that is XY.

Those who have long lamented the dominance of the XY cohort are thrilled by the change. “On a 1 to 10 scale of how happy this makes me, it's a 10,” says Jeffrey Blaustein, a neuroendocrinologist at the University of Massachusetts, Amherst, who as editor-in-chief of *Endocrinology* made waves a couple of years ago when he required that authors disclose the sex of animals. “When NIH speaks, people listen.”

—JENNIFER COUZIN-FRANKEL



**Sex “really has to be considered as a fundamental variable.”**

—JANINE CLAYTON,  
Office of Research  
on Women's Health

journals didn't even report whether their animals were male or female.

“We're making conclusions about females based on studies that don't support that,” Beery says. Among many other examples of male-female variation, Clayton and Collins point out that female rats respond differently to stress than males do.

Differences between XX and XY cells haven't been studied as thoroughly, but “the more people look, the more they're finding,” says Margaret McCarthy, a



**Naia the nymph.** The skeleton of a teenage girl was found in a Mexican underwater cave.

## PALEOANTHROPOLOGY

# Bones From a Watery 'Black Hole' Confirm First American Origins

In May 2007, Alberto Nava, a diver based in California, was exploring an underwater cave in Mexico's Yucatán Peninsula with two Mexican colleagues. They swam more than a kilometer down a narrow tunnel, which suddenly opened up into a huge, dark chamber. "The floor disappeared under us and we could not see across to the other side," Nava says. They dubbed the chamber Hoyo Negro, Spanish for "black hole."

About 2 months later, the threesome returned to Hoyo Negro to explore it further with powerful underwater lights, revealing a bell-shaped amphitheater some 60 meters in diameter. On its boulder-strewn floor, the divers began to see the bones of large mammals; then, Nava says, they spotted "a human skull resting on the top of a small ledge. It was lying upside down, carrying a perfect set of teeth and with dark eye sockets looking back at us."

On page 750 of this week's issue of *Science*, Nava and an international team of anthropologists, archaeologists, geneticists, geologists, and dating experts report that the skull, along with other bones found nearby, belonged to a teenage girl who lived as early as 13,000 years ago. The girl—whom the team calls Naia, which means "water nymph" in Greek—bore the typical skull and facial features of some of the earliest known

prehistoric Americans, including a long and high skull and pronounced forehead. These differ markedly from those of today's Native Americans, who tend to have broader and rounder skulls. Yet Naia's genetic profile, which the team determined by partially sequencing mitochondrial DNA (mtDNA) extracted from one of her molars, is common among Native Americans today.

The researchers say that this finding shows that Native Americans are descended from the earliest Paleoamericans, who beginning about 15,000 years ago migrated from Asia to the New World across the Bering Strait, then a vast tract of exposed land that researchers call Beringia. It is another strike against the idea that today's Native Americans derive from a different source population in Asia or even in Europe. Jennifer Raff, an anthropologist at the University of Texas, Austin, says that the study "is a very simple and direct test of two competing hypotheses about Paleoamerican ancestry," in which the early Beringian origins hypothesis clearly wins.

But she and other researchers caution that, so far, the Naia team has identified only one genetic marker—called mtDNA haplogroup D1—that ties the skeleton to modern Native Americans. "The skeleton is cool," says Tom Dillehay, an anthropologist at Vanderbilt

University in Nashville, but he and others think the new study breaks little new ground. They say it serves mostly as confirmation of a recent, major study reporting the complete nuclear genome sequence of the 12,700-year-old Anzick child from Montana.

The paper does represent a personal about-face for its lead author, James Chatters, a forensic anthropologist based in Bothell, Washington. Chatters was the first researcher to study Kennewick Man, a 9000-year-old skeleton found in Washington in 1996. Kennewick Man also showed the skull features typical of earlier Paleoamericans, and Chatters originally sided with anthropologists who argued that Native Americans were the descendants of later migrants. Now, he fully embraces the genetic continuity model. "As more genetic information came in," Chatters says, it became clear that Paleoamericans and Native Americans came from "the same root population."

Naia can only confirm the single-origin hypothesis, however, if she really does represent an early Paleoamerican population. "Dating is critical to the significance of the paper," says Dennis O'Rourke, a geneticist at the University of Utah in Salt Lake City. And that was no easy task. The team thinks that the girl, roughly 15 or 16 years old when she died, fell into a shallow pool that led to one of the cave's upper passages, and drifted down into Hoyo Negro.

After thousands of years deep underwater, her bones contained little of the collagen protein needed for direct radiocarbon dating. So the team's dating experts, including geochemist Yemane Asmerom of the University of New Mexico, Albuquerque, used multiple approaches to bracket her age. They knew that Naia was unlikely to be very much younger than 13,000 years, because the large animals whose bones littered the cave floor nearby, including elephantlike gomphotheres and ground sloths, were mostly extinct by that time. Meanwhile, uranium-thorium dating of calcite that had encrusted Naia's bones showed it was up to 12,000 years old. The bones had to be older than that—thus bracketing their age between 13,000 and 12,000 years.

If ancient Paleoamericans were the ancestors of later Native Americans, how and why did the anatomical differences arise? Chatters speculates that Paleoamericans, with their large skulls and more forward-projecting faces, represented



a human “wild type” and that Native Americans, with rounder and flatter faces, reflect a more “domesticated” form as the Beringians settled down in the Americas and shifted from hunting and gathering to farming.

But Raff, along with archaeologist David Meltzer of Southern Methodist University, Dallas, in Texas, argues that the changes could simply be the result of random

“genetic drift” over thousands of years. And Rolando González-José, an anthropologist at the National Scientific and Technical Research Council in Puerto Madryn, Argentina, contends that the differences are actually the result of a broad genetic and anatomical diversity that developed during the so-called Beringian standstill—a proposed interlude of thousands of years when migrants from northeast Asia paused

in Beringia before moving on to the Americas (*Science*, 28 February, p. 961).

For the moment, Naia, from her watery grave deep in Hoyo Negro, has said all she can about the origins of the first Americans. But this might not be her last word: The team, Chatters says, will now try to sequence her nuclear DNA, in search of still more answers.

—MICHAEL BALTER

## UNIVERSITIES

# Job Change Lands Egyptian Scientist in Legal Battle

Rania Siam thought she was putting her troubles behind her when she left Misr University for Science & Technology (MUST) near Cairo. It was June 2005, and the microbiologist had spent four tumultuous months as a lecturer there, quarreling with administrators and fellow faculty over working conditions and research support. That September, she landed a tenure-track position at the American University in Cairo (AUC). But just when things were looking up, MUST sued her.

In what observers call an unprecedented case in Egypt, MUST claimed that Siam's departure caused “damage to MUST's reputation and its scientific credibility,” and “lost [MUST] the scientific and educational benefits, which [it] would have gained from [Siam's] research.” MUST took particular umbrage at missing out on a grant that Siam had applied for during her brief stay at the university and demanded \$3 million in damages.

After 9 years of legal maneuvering, an Egyptian judge in March ordered Siam to pay MUST \$49,000—the sum of the forfeited grant—in addition to court and attorney fees, and more than \$14,000 in damages. Last week, Siam filed an appeal with the Court of Cassation, Egypt's highest judicial authority.

The feud highlights the question of whether universities can claim compensation when a promising faculty member jumps ship. In the United States, for example, a university that poaches a star faculty member on sabbatical will often agree to pay the former employer a portion of that person's salary. The issue is of acute interest to Egypt's private universities, which have sprung up in large numbers to meet a growing demand for higher education. With scant resources available from the Egyptian government, fledgling private institutions have struggled to build research programs.

In late 2004, Siam was working in a biotechnology firm in San Diego, California,



**Embroided.** Rania Siam's former university sued her for resigning.

when she decided to return to her native Egypt to be closer to her 11-year-old son, who was living with his father in Cairo. In January 2005, she responded to an advertisement for a vacant faculty position at MUST. In a job interview, she recalls, MUST President Morad Abou-Sabe, who has since retired, discussed his hopes for improving research at the university. She liked what she heard.

Siam started at MUST that February, and by April she had submitted a grant proposal to the International Centre for Genetic Engineering and Biotechnology (ICGEB), a U.N.-affiliated research outfit that aims to advance research in the developing world. Siam proposed working with ICGEB molecular geneticist Carlo Bruschi, based in Trieste, Italy, on a study of proteins involved in yeast cell division. But after

submitting the proposal, Siam realized that carrying out the research in her allotted lab space would be a challenge.

In her response filed with the court, she says she was especially irked by an expectation that she should store yeast cell lines in the same incubators as mammalian cells—which she saw as a recipe for contamination. Siam also maintains that she was not permitted to buy essential reagents or hire a technician.

A former research assistant in another lab at MUST echoes Siam's complaints. Hany Fanous told *Science* that he had to wait 6 months for approval to order reagents. When the reagents finally arrived, MUST administrators gave other university researchers permission to use them, Fanous claims. “We filed a complaint” with the university, he says. “It was rejected.” MUST refused to comment on the complaints.

Fed up, Siam resigned. In September, the same month that she joined AUC, she learned that she had won the ICGEB grant. But when she informed ICGEB of her change of affiliation, she was told that she could not transfer the funds to another institution. That same day, Siam was served the court papers detailing MUST's case against her. “I thought about leaving Egypt,” she says. But she stayed to contest the suit, she says, because she enjoys working at AUC.

Over the next several years, Siam broadened her research to look at microbial communities that thrive in hot, salt-rich pools on the Red Sea floor. She has since received more than \$6 million in funding from various institutions and ascended the ranks of AUC's biology department, which she now

chairs. “She is one of our young stars,” says Tarek Shawki, AUC’s dean of the School of Sciences and Engineering. The lawsuit, however, cast a shadow. Rumors that she had stolen grant money were rife, Siam says.

In November 2012, a court found in Siam’s favor, stating that because MUST hadn’t given her an employment contract, she was free to leave. MUST appealed and on 16 March, Cairo’s Court of Appeal overturned the lower court’s verdict, ruling that Siam had nevertheless broken “authentic academic values” in not fulfilling her research duties. The \$14,000 in damages, the judgment states, is compensation for “the loss of hope to the university and

society” and for “moral damage incurred [by] MUST.”

“[The case] seems completely unreasonable to me,” says Gregory Marczynski, a biochemist at McGill University in Montreal, Canada, and Siam’s former graduate adviser, who describes her work as “cutting-edge” and “highly collaborative.” Although the order to compensate MUST for missing out on the grant may be in the “realm of reason,” adds Aly El Shalakany, a partner at the Shalakany Law Office in Cairo who is not involved in the case, “I don’t think it’s fair.” No hearing date has been set yet for Siam’s appeal.

MUST officials did not respond to questions from *Science*. In a statement to

*Science*, Maged Said, a senior associate in the Tahoun Law Office, the Giza, Egypt–based firm representing MUST, repeated the initial claim that Siam had violated her obligations to the university by depriving it of the grant.

If the verdict is upheld, it would “seriously undermine researchers’ willingness to file grants” if they were even considering a career move, says Lisa Rasmussen, a research ethicist at the University of North Carolina, Charlotte. If scientists are not free to leave a university, she says, they are merely “agents of their institutions, rather than independent scientists.”

—JENNIFER CARPENTER

Jennifer Carpenter is a writer in Toronto, Canada.

## CLIMATE CHANGE

# No Stopping the Collapse of West Antarctic Ice Sheet

A disaster may be unfolding—in slow motion. Earlier this week, two teams of scientists reported that Thwaites Glacier, a key-stone holding the massive West Antarctic Ice Sheet together, is starting to collapse. In the long run, they say, the entire ice sheet is doomed. Its meltwater would raise sea levels by more than 3 meters.

One team combined data on the recent retreat of the 182,000-square-kilometer Thwaites Glacier with a model of the glacier’s dynamics to forecast its future. In a paper on page 735, they report that in as few as 2 centuries Thwaites Glacier’s edge will recede past an underwater ridge now stalling its retreat. Their models suggest that the glacier will then cascade into rapid collapse. The second team, writing in *Geophysical Research Letters* (GRL), describes recent radar mapping of West Antarctica’s glaciers and confirms that the 600-meter-deep ridge is the final obstacle before the bedrock underlying the glacier dips into a deep basin.

Because inland basins connect Thwaites Glacier to other major glaciers in the region, both research teams say its collapse would flood West Antarctica with seawater, prompting a near-complete loss of ice in the area over hundreds of years. “The next stable state for the West Antarctic Ice Sheet might be no ice sheet at all,” says the *Science* paper’s lead author, glaciologist Ian Joughin of the University of Washington (UW), Seattle.

“Very crudely, we are now committed to global sea level rise equivalent to a permanent Hurricane Sandy storm surge,” says glaciologist Richard Alley of Pennsylvania

State University, University Park, referring to the storm that ravaged the Caribbean and the U.S. East Coast in 2012. Alley was not involved in either study.

Where Thwaites Glacier meets the Amundsen Sea, deep warm water burrows under the ice sheet’s base, forming an ice shelf from which icebergs break off. When melt and iceberg creation outpace fresh snowfall farther inland, the glacier shrinks. According to the radar mapping released this week in GRL from the European Remote Sensing satellite, from 1992 to 2011 Thwaites

result: In all but the most conservative melt scenarios, a glacial collapse has already started. In 200 to 500 years, once the glacier’s “grounding line”—the point at which the ice begins to float—retreats past the ridge, the glacier’s face will become taller and, like a tower of blocks, more prone to collapse. The retreat will then accelerate to more than 5 kilometers per year, the team says. “On a glacial timescale, 200 to 500 years is the blink of an eye,” Joughin says.

And once Thwaites is gone, the rest of West Antarctica would be at risk.

Eric Rignot, a climate scientist at the University of California, Irvine, and the lead author of the GRL study, is skeptical of Joughin’s timeline because the computer model used estimates of future melting rates instead of calculations based on physical processes such as changing sea temperatures. “These simulations ought to go to the next stage and include realistic ocean forcing,” he says. If they do, he says, they might predict an even more rapid retreat.

Antarctic history confirms the danger, Alley says: Core samples drilled into the inland basins that connect Thwaites Glacier with its neighbors have revealed algae preserved beneath the ice sheet, a hint that seawater has filled the basins within the past 750,000 years. That past flooding shows that modest climate warming can cause the entire ice sheet to collapse, Alley says. “The possibility that we have already committed to 3 or more meters of sea level rise from West Antarctica will be disquieting to many people, even if the rise waits centuries before arriving.”

—THOMAS SUMNER

### Linchpin.

Thwaites Glacier is connected with its neighbors in ways that threaten a wholesale collapse.



Glacier retreated 14 kilometers. “Nowhere else in Antarctica is changing this fast,” says UW Seattle glaciologist Benjamin Smith, co-author of the *Science* paper.

To forecast Thwaites Glacier’s fate, the team plugged satellite and aircraft radar maps of the glacier’s ice and underlying bedrock into a computer model. In simulations that assumed various melting trends, the model accurately reproduced recent ice-loss measurements and churned out a disturbing





# Beyond the Temples

**Turning their backs on spectacular monuments, archaeologists are studying ordinary households to uncover the daily rhythms of long-lost cities**

**TAPACHULA, MEXICO**—Kneeling in the cacao tree–shaded ruins of a 2000-year-old house, Rebecca Mendelsohn carefully scrapes soil off the fractured edge of a red ceramic plate and into a plastic bag. The archaeology graduate student from the University at Albany, State University of New York (SUNY), will bring hundreds of such samples to a lab in the mountain city of San Cristóbal de las Casas, where she will analyze them for traces of the food that the mysterious residents of Izapa, one of Mesoamerica’s earliest cities, prepared and ate.

Izapa, 10 kilometers outside of the modern city of Tapachula in the Soconusco region of Chiapas state, arose around 850 B.C.E., possibly as people moved north from the

Guatemalan coast to take advantage of a better climate for growing maize. Over at least the next 800 years, Izapa became the major economic and cultural hub along a trade route linking Olmec cities of the Gulf Coast and Maya strongholds in Central America.

Why Izapa flourished and who its inhabitants were are riddles that Mendelsohn hopes to solve from the bottom up. By excavating in several places around Izapa’s periphery, she aims to compare the jobs, possessions, diet, and economic well-being of the city’s residents, and how those patterns changed over time. And by plotting that information on a map that she and her adviser, Robert Rosenswig, created by surveying the site with an airborne laser, Mendelsohn hopes to

uncover something that past archaeologists never expected to find in the region’s ancient settlements: neighborhoods.

Studying pyramids and deciphering cryptic writing systems have helped archaeologists piece together the political, cultural, and religious characteristics of many Mesoamerican civilizations. But ceremonial architecture and official records may not reveal how societies actually work. “Tell me what the normal people were doing,” Mendelsohn says. “That won’t be on your monuments.” Mapping lost neighborhoods can help archaeologists see an ancient city through the eyes of its residents, rather than through its leaders. What Mendelsohn and others are discovering through their





**Heart of the city.** Mexico's Teotihuacan had distinct neighborhoods outside its majestic downtown.

But many other settlements in the ancient world don't fit the high-density, modern sense of a city. The Maya capitals Tikal and Copán, for example, were long thought to consist of unoccupied temples and administrative buildings surrounded by a haphazard smattering of villages spread across vast swaths of landscape. But as archaeologists studied sprawling ancient cities in Africa and in Southeast Asia, including Cambodia's Angkor Wat, they developed a concept of low-density urbanism, which defines a city not by size or density, but by what Smith calls its "urban function": the economic, political, or religious effect it has on a hinterland, or what is today known as a metropolitan area. A city, in other words, casts a spell over an entire region.

This idea raised a tantalizing possibility for Mayanists and other Mesoamerican archaeologists working at sites other than Teotihuacan: What if the landscape around a ceremonial center were not wasteland, but hinterland? What if the clusters of households weren't independent, self-governing villages, but rather interconnected nodes in a complex network of neighborhoods—one that was just as urban as high-density Teotihuacan?

### Hidden patterns

At Izapa, Mendelsohn is looking for signs of those neighborhoods. On a map, she points to a cluster of small structures near a larger mound far to the southeast of downtown. These are the households she's excavating in the cacao field. Another of her field teams is excavating a mound a few hundred meters to the west. Mendelsohn hopes to discern, 2000 years later, whether these were separate neighborhoods.

Preliminary findings hint at a major lifestyle gap. The ceramics and grinding stones found in the cacao-shaded dwellings suggest an abode of commoners. The pits at the mound to the west have yielded valuable jade beads, imported obsidian, and high-status pottery. Quite simply, Mendelsohn says, it "seems like rich people were here."

That may not mean, however, that all their neighbors were well-to-do. In Teotihuacan, for example, neighborhoods were economically mixed, says Ian Robertson, an archaeologist who studied Teotihuacan at Stanford University in California. Elite residences, temples, and administrative buildings were scattered throughout the ancient city, and the poor lived alongside the wealthy.

Some archaeologists believe Teotihuacan's economic mosaic offers a clue to its political structure. Based on 8 years of excavations in the center of an economically diverse neighborhood dubbed Teopancazco, Linda Manzanilla, an archaeologist at the National Autonomous University of Mexico in Mexico City, has proposed that Teotihuacan operated as a collection of "house societies," in which neighborhood leaders commanded the labor and loyalty of nearby lower status residents. This relationship resembled the feudal system of medieval Europe, she explains.

If it holds up under future excavations, the house society model may explain how Teotihuacan first formed, Robertson says. "Compared to most other cities,



**Neighborhood watch.** Clusters of houses are being excavated far from Izapa's city center.

[Teotihuacan] was there very fast"—faster than the city's birthrate could account for. That means that people must have been migrating to the new city in droves. "I imagine that sometimes what you had were whole towns pulling up stakes, moving into Teotihuacan, and reproducing their own social structure in the new urban center," he proposes. As time went on, those uprooted towns likely morphed into neighborhoods.

Marilyn Masson, an archaeologist at the University at Albany, SUNY, sees a similar

bottom-up approach to places like Izapa are cities that look like nothing found in the modern world.

### The new urbanism

Cities, and therefore neighborhoods, were once considered a rarity in ancient Mesoamerica. Scholars have long defined cities as places with large, densely packed populations, intertwined economic activities—trades such as tailors, jewelers, soldiers, or manual laborers—and, often, a splash of cultural diversity, says Michael Smith, an archaeologist at Arizona State University, Tempe. "That definition makes sense because it fits our preconceptions of what cities are like today."

Teotihuacan, which lies 50 kilometers northeast of Mexico City and was occupied from roughly 100 B.C.E. to 650 C.E., was one of the few Mesoamerican cities that conformed to those expectations. Centered on the imposing Pyramids of the Sun and the Moon, it was laid out on a grid, and its more than 100,000 residents, many living in apartment buildings, were crammed into just 20 square kilometers.

CREDIT: LIZZIE WADE





**Pay dirt.** Rebecca Mendelsohn (left) and Saskia Kuchnicki unearthing high-status ceramics in Izapa.

pattern in Mayapán, an ancient city in the dry interior of the Yucatán Peninsula. From the early 1200s C.E. to its collapse in the 1400s, Mayapán was the political and economic capital of the Maya area. Spanish accounts of Mayapán's history suggest that as the city consolidated, its rulers—who came from all over the peninsula—"forcibly relocated" people to populate the new center, Masson says. Mayapán's first neighborhoods, therefore, probably would have resembled the uprooted villages.

Masson believes she's found the primary way order was imposed on Mayapán's unruly melting pot: walls. Walls were everywhere in the city, and after years of fieldwork and a laser mapping survey in 2013, Masson and Timothy Hare, an anthropologist at Morehead State University in Kentucky, have mapped every single one. "With the walls, [the city] starts making sense," Hare says.



Not only did Mayapán boast a defensive wall surrounding a dense 4-square-kilometer downtown, but smaller walls also separated houses from one another, demarcated roads, and, overall, organized how people moved through the city. They also dictated how buildings were oriented, a key feature of neighborhoods. "When people walk out of the front door of their houses, what do they see?" Masson asks. Likely, the dwellings would be facing their neighborhood's "most important symbol." Downtown, she says, that would be the temples and administrative buildings in Mayapán's ceremonial center.



But farther out—and especially in low-density areas beyond the city's defensive wall—the buildings tend to be oriented toward complexes of elite residences and smaller ritual buildings. According to Masson, those secondary centers probably played a role in knitting the surrounding households into neighborhood communities, and perhaps served as landmarks to help residents navigate the city.

### Ethnic diversity

Back in the cacao field, Mendelsohn points out an odd feature of the mound she's excavating: The dwellings here are arranged around a shared patio. This architectural pattern is more common in the Maya area to the south and east. She wonders if she might be looking at an ethnic enclave. Izapa's location along a major trade route meant that Maya and Olmec people probably passed through frequently, and it's possible some of them stayed. "It would be completely reasonable to find a Maya neighborhood or an Olmec neighborhood" in Izapa, Mendelsohn says.

Although most archaeologists, including Mendelsohn, doubt that artifacts can reliably distinguish their owners' ethnicity thousands of years later, at least two ethnic enclaves have been identified at Teotihuacan. A cluster of apartment compounds on the city's western edge contained ceramics resembling those made by the Zapotecs, who lived 500 kilometers to the south in modern-day Oaxaca. These out-of-place cooking tools and ritual objects were made of local clay but fired using an Oaxacan technique that darkened the pottery. Later excavations of the area uncovered an ornate Zapotec-style tomb and a temple clearly modeled after its cousins in Oaxaca—structures that, according to Michael Spence, an archaeologist at the University of Western Ontario in London, Canada, have "got no business being in Teotihuacan." Meanwhile, a separate cluster of similarly anomalous pottery styles from the Gulf Coast and the Maya region was found in apartment compounds on the other side of the city. The two enclaves were the first neighborhoods identified in Teotihuacan.

At Izapa, neighborhood outlines are more elusive. Its city plan is still coming into view; Rosenswig's laser survey doubled the early city's estimated size, revealing dozens of hidden mounds. And now Mendelsohn's excavations hint that Izapa may have been occupied far longer than anyone thought. Its neighborhoods had centuries to shift borders and change character, adding texture to the city—and intrigue to its ruins. **—LIZZIE WADE**

CREDITS: (PHOTOS) KELLY RICH; (INSET) LIZZIE WADE





# The Hunt for Missing Genes

Identifying healthy human “knockouts”—people completely lacking a specific gene—may suggest new biomedical treatments

Daniel MacArthur’s quest for the genes we can live without began with two sick boys. In 2000, as an undergraduate student, he began working in the laboratory of Kathryn North, a geneticist who studies rare, mysterious muscle diseases. Her group at the University of Sydney in Australia had recently published the possible cause of two brothers’ early-onset form of muscular dystrophy. They suspected a pair of faulty copies of *ACTN3*, a gene that codes for a protein in the fast-twitch muscles that generate short bursts of power.

But later, the group tested the parents to confirm what seemed obvious: that each had two versions of *ACTN3*—a working copy and a broken one—and both had passed on the latter to their ill children. To the team’s surprise, the parents, like their sons, both lacked any functioning copy of the gene or any trace of its protein in their muscles. Yet both mother and father appeared healthy.

North’s group eventually did find another mutated gene responsible for the boys’ disease, but at the time they also realized they had documented something significant. “It was actually incredibly exciting,” says MacArthur, who joined the lab soon after the misstep was recognized. “It was one of the first examples of a gene that should be important” but that people can live without.

Nor was that family a rarity: North’s group found that about 16% of the global population had two broken copies of the gene, without obvious disease as a result. As he continued in North’s lab into graduate school, MacArthur and co-workers also discovered that the functional version of the gene was more prevalent in Australia’s elite sprinters and jumpers.

But MacArthur became most intrigued by the prospect that hidden in the human population were people who lacked certain genes yet remained healthy. Researchers

routinely disable, or “knock out,” a specific gene in mice to learn what the gene does, but the results don’t always translate into people. Ethically, knocking out genes in humans is off-limits. But the sick children’s parents offered another route—finding natural human knockouts and looking for differences between their physiology and that of people with the intact gene. “I became fascinated by the idea that these individuals serve as experiments of nature,” says MacArthur, now at Massachusetts General Hospital (MGH) in Boston and the Broad Institute in Cambridge, Massachusetts.

Those natural experiments could have biomedical payoffs. Researchers often seek new drug targets by identifying genes that cause disease when mutated and looking for molecules that can compensate. Healthy knockouts suggest a different approach: hunting for genes that, when missing, actually confer a health benefit, then trying to mimic



## Select Human Knockouts

Gene	Missing protein's role	Effect of loss	Knockout frequency	Biomedical promise
<b>PCSK9</b>	Enzyme triggers LDL receptor degradation	Lower LDL cholesterol, reduced heart disease	Extremely rare (2% of African-Americans lack one copy)	PCSK9 inhibitors in trials for heart disease
<b>CCR5</b>	Cell surface receptor	Protected against HIV	1% of northern Europeans	Drug, modified stem cell transplant
<b>ACTN3</b>	Acts in fast-twitch muscles	Associated with reduced sprinting ability, greater endurance	16% of global population	Unknown
<b>CASP12</b>	Immune response to bacteria	Resistance to sepsis	Most non-Africans	Unknown
<b>SCN9A</b>	Sodium channel in nerve cells	Insensitive to pain	Extremely rare	New class of pain drugs

that effect by blocking the normal gene's protein. AIDS researchers have already found that certain people lacking a working gene for a specific cell surface protein suffer no ill effects and are resistant to HIV; that protein is now a drug target and figures into other anti-HIV strategies. More recently, pharmaceutical firms began developing a potential new blockbuster class of cholesterol-lowering drugs, inspired by a woman missing a cholesterol-regulating gene.

In a survey of scores of human genomes 2 years ago, MacArthur and co-workers caught a glimpse of a bigger universe of missing genes. The survey showed that the average healthy person has about 20 genes knocked out. Now, he and several other groups want to similarly comb through many more thousands of people's genomes for missing genes to seed what MacArthur calls the Human Knockout Project.

Such an effort may be the only way to fully understand the function of many of our genes, he and others contend. But identifying missing genes is only the start of the challenge. Then, investigators have to link a dispensable gene to the human knockout's phenotype—their health measures and other traits—and that information is costly and time-consuming to collect. "Getting good phenotypes makes genome sequencing look cheap (and easy)," says cardiovascular disease researcher Helen Hobbs of the University of Texas (UT) Southwestern Medical Center in Dallas.

### The poster gene

Hobbs speaks from experience. About a decade ago, she and her UT Southwestern colleague Jonathan Cohen wondered if mutations that hampered or disabled a gene called *PCSK9* explained why some people

in the Dallas Heart Study had unusually low levels of harmful cholesterol. Recent studies had suggested that the gene's product, an enzyme, might regulate the body's blood levels of low-density lipoprotein (LDL) cholesterol, the type that raises the risk of heart disease.

The pair's hypothesis proved to be correct. They even found one 34-year-old woman who was a *PCSK9* knockout—she completely lacked the enzyme due to mutations in both the genes for it. She had the lowest LDL cholesterol levels of all, yet was perfectly healthy. Based on the team's work, drug companies realized that blocking the *PCSK9* enzyme might lower cholesterol levels alone or in combination with the immensely popular statins.

That hunch is paying off in clinical trials of *PCSK9*-inhibiting drugs; early results suggest they can lower blood cholesterol levels by up to 57%. *PCSK9* has become the poster child for the idea that genes whose absence confers some benefit can be an extremely attractive drug target. The very existence of a healthy knockout shows that the gene isn't essential, so blocking its protein to mimic the beneficial effect should not cause harmful side effects. The human knockout is "a shortcut. You know you could inhibit" the gene's protein, says human geneticist David Altshuler of the Broad Institute.

Until recently, however, no one knew how many genes like *PCSK9* existed. That's why MacArthur did his initial survey. After moving from Australia to a postdoc at the Sanger Institute in the United Kingdom, MacArthur and his team scanned the genomes of 185 individuals who were part of a study of human genetic variation. They homed in on DNA errors that incapacitate a

gene, known as loss-of-function mutations. Because not all DNA alterations do so—and many apparent DNA errors are actually sequencing mistakes—identifying true gene knockouts was a huge analytical task.

This laborious effort paid off, revealing that the average person carries about 100 incapacitated genes—and in 20 of those cases, both the maternal and paternal copies of a gene are missing, creating a complete knockout, the team reported 2 years ago in *Science* (17 February 2012, p. 823). "More than a few of us were surprised" by such a large number, says human geneticist David van Heel of Queen Mary, University of London.

Many of the more common missing genes were involved in smell; they may have been important for helping our ancestors find food, but are unlikely to affect a modern human's fitness. Others belonged to families of related genes that serve similar functions, suggesting the missing genes were not needed because the cell has backups.

Still, that left a small, but not insignificant, number of missing genes that just might protect against disease. Other scientists took notice. National Institutes of Health (NIH) Director Francis Collins remarked at a meeting that MacArthur's study suggested "a systematic, comprehensive way of identifying where the other several dozen *PCSK9*s might be out there."

### Hunting for gold

Even before MacArthur's paper, other disease researchers had followed Hobbs and Cohen's example and begun looking at the genomes of people who seem protected against disease by missing genes. For example, earlier this year, Altshuler and others reported finding a gene that, when one copy

is nonfunctional, lowers a person's risk of type 2 diabetes—by a stunning 65%.

Now, MacArthur and other knockout seekers plan to widen the search. They will sequence the DNA of a large number of healthy people, see who lacks potentially interesting genes, then study whether those individuals are somehow protected—if they're less prone to heart attacks or high blood pressure, for example—or if they are unusual in some other unexpected way. This strategy “allows you to discover things you didn't know were there,” says a fan of the idea, human geneticist Leslie Biesecker of NIH.

The most efficient way to do this is not to look in the general population; novel knocked-out genes will be too rare. A faster way may be to study historically isolated populations, such as the Finns. Some 4000 years ago, presumably when a small number of settlers moved to Finland, that population passed through a bottleneck. Because of this initial small gene pool, the frequency of some loss-of-function mutations is “enriched,” says Aarno Palotie of the Broad Institute and the University of Helsinki. As part of a project pooling samples and data on 200,000 Finns from various biobanks, he and Mark Daly of MGH and the Broad Institute led a pilot study in which they scoured the protein-coding portions of the genome, or exomes, of 3000 Finns; they found twice as many knocked-out genes as in a northern European comparison group.

Marrying that work with DNA data and health records for 35,000 Finns has already led to potential gold: 227 individuals entirely lacked a gene called *LPA* that codes for a blood lipoprotein implicated in cardiovascular disease. These people had a significantly lower risk of heart attacks and stroke, according to a retrospective analysis that the team presented last fall at the annual meeting of the American Society of Human Genetics.

“This is a proof of concept that, indeed, you can find protective loss-of-function variants using isolated populations,” Palotie says. “The excitement is that we can find many more of these.” Finland's vast electronic system of medical and death records should give the team an advantage in the hunt.

Cultural traditions may also help the search for knockouts. In some cultures, it is common practice for relatives as close as first cousins to marry. That increases the odds a child will inherit two copies of the exact same nonfunctioning genetic variant, says Yale University human geneticist Richard Lifton. This has a downside if the mutations are in necessary genes—countries such as Turkey

and Saudi Arabia have relatively high rates of inherited genetic diseases—but it ups the odds of finding beneficial cases.

To take advantage of this, van Heel and Richard Trembath, his colleague at Queen Mary, University of London, along with MacArthur and others, plan to sequence the exomes of up to 25,000 adults of Pakistani and Bangladeshi descent living in East London. They are now engaging with community leaders to build support for the Wellcome Trust-funded project and plan to begin the search next year. In a pilot study looking at the genomes of 1103 healthy British Pakistani individuals, they've already found about 200 potentially interesting knocked-out genes that differ from the ones found in other studies. “Some 20 are reportedly lethal in mice [if knocked out], but clearly these fit adults are doing just fine,” van Heel says.

In another effort, starting this summer, a team in Saudi Arabia will collect blood samples and basic clinical data from volunteers recruited in public areas such as malls and parks—“places where healthy

**“I became fascinated by the idea that these individuals serve as experiments of nature.”**

—DANIEL MACARTHUR,  
MGH AND THE BROAD INSTITUTE

people are likely to go,” says study leader Fowzan Alkuraya of King Faisal Specialist Hospital and Research Center in Riyadh. The goal is to enroll 10,000 people whose parents are first cousins and sequence their exomes over the next year; it is a subproject of the country's recently announced 100,000 genomes project. Like other knockout hunters, the team plans to later recall individuals with interesting loss-of-function genes for more clinical testing. “I'm pretty sure we're going to find something as exciting as the *PCSK9* story,” Alkuraya says.

#### **A lofty goal**

Not everybody thinks that the search for knockouts should focus exclusively on healthy people. Lifton suggests that more drug targets will come from people in whom

a missing gene causes a disease or some kind of obvious abnormality. He cites a gene involved in making a neurotransmitter that causes narcolepsy when both copies are disabled. Studying this gene has led to a new kind of sleeping pill, now awaiting regulatory approval. Another example is the rare individuals who feel no pain because they lack a gene for a particular cell receptor. The gene could eventually result in a new class of painkillers.

Hobbs and Cohen add that sequencing large groups of healthy people without having good clinical information to guide the search may lead nowhere. They credit their success at identifying the *PCSK9* knockout and several others to having years of detailed clinical data on people they have studied. When they find a mutation, they can immediately know a lot about the medical consequences, the pair says.

That is especially important because the consequences of missing a gene won't always be straightforward. The missing gene may have no effect in some people; or it may matter only later in life, or when the person eats certain plants or is exposed to a specific disease, Hobbs says.

MacArthur has heard the warnings, and he plans to bring together both healthy knockouts and those linked to disease, along with as much clinical data as he can amass, in one loss-of-function mutation database—the foundation, he hopes, for an eventual Human Knockout Project. Besides gathering published data on diseases caused by nonfunctioning genes, his group is building a list of novel knocked-out genes by combing through the exomes of more than 80,000 ill and healthy people sequenced for disease studies at the Broad Institute and other research centers. Eventually, he hopes other researchers, including those working in the United Kingdom, Finland, and Saudi Arabia, will contribute their knockouts, along with data on clinical consequences.

The proposal is “massively ambitious,” MacArthur acknowledges, and will require buy-in from the broader genetics community. For now, he adds, “This is the beginning of an idea.”

For all the voices of caution, few doubt that tallying up the world's human knockouts is a worthy goal. “We think the key is to have an outstanding, centralized database,” Hobbs and Cohen note in an e-mail, “that contains systematic phenotypic information in each human knockout.” Adds Lifton: “It's an obvious thing to do.” —JOCELYN KAISER





## LETTERS

edited by Jennifer Sills

## China's Soil Pollution: Farms on the Frontline

CHINA'S SOIL POLLUTION IS MUCH WORSE THAN PREVIOUSLY THOUGHT ("CHINA GETS SERIOUS about its pollutant-laden soil," C. Larson, *News & Analysis*, 28 March, p. 1415). A report released on 17 April admitted that 16.1% of the Chinese soil was polluted, including 19.4% of farmland, 10.0% of forest land, 10.4% of grassland, and 11.4% of unused land (1). Of the contaminated soil samples, 82% contained toxic inorganic pollutants, the most common being heavy metals such as cadmium, mercury, arsenic, chromium, and lead, which can cause chronic health problems. Moreover, levels of organic pollutants such as dichlorodiphenyltrichloroethane (DDT), polycyclic aromatic hydrocarbons (PAHs), and hexachlorocyclohexanes (HCHs) are also very high, and samples above established safety levels account for 1.9%, 1.4%, and 0.5%, respectively, of all tested soil samples, which covered 6.3 million square kilometers. Aside from industrial plant waste and mining operations, the report states that the unsustainable use of chemical fertilizers and pesticides is a main human cause of widespread soil pollution (1).

China's food production is affected by soil pollution but also creates much pollution itself. China consumes nearly one-third of the world's fertilizer, and the pesticide usage per unit area is 2.5 times the world average (2). The quality of cultivated land should be guaranteed. Farmers should be subsidized to improve fertilizer use efficiency and encouraged to adopt organic and biodynamic farming methods that are not reliant on heavy input of chemicals. Soil remediation projects should be implemented to improve the polluted soil gradually. Finally, there is a need to change cultural habits relating to consumption so as to reduce food waste nationwide.

RUISHAN CHEN,<sup>1\*</sup> ALEX DE SHERBININ,<sup>2</sup> CHAO YE,<sup>3</sup> GUOQING SHI<sup>1</sup>

<sup>1</sup>School of Public Administration, Hohai University, Nanjing, 210098, China. <sup>2</sup>Center for International Earth Science Information Network (CIESIN), Columbia University, Palisades, NY 10964, USA. <sup>3</sup>College of Geographic Sciences, Nanjing Normal University, Nanjing 210023, China.

\*Corresponding author. E-mail: chenrsh04@gmail.com

## References

1. Ministry of Environmental Protection and Ministry of Land and Resources of P.R. China, "Reports on China's Soil Pollution Survey" (2014); [www.zhb.gov.cn/gkml/hbb/qt/201404/t20140417\\_270670.htm](http://www.zhb.gov.cn/gkml/hbb/qt/201404/t20140417_270670.htm) [in Chinese].
2. "Establish a long-term mechanism for sustainable agricultural development," *China People's Daily* (22 January 2014); [http://paper.people.com.cn/rmrb/html/2014-01/22/nw.D110000renmr\\_b\\_20140122\\_1-02.htm#fin](http://paper.people.com.cn/rmrb/html/2014-01/22/nw.D110000renmr_b_20140122_1-02.htm#fin) [in Chinese].



## China's Soil Pollution: Urban Brownfields

CHINA'S PLANS TO TACKLE FARMLAND POLLUTION and improve food safety are to be welcomed ("China gets serious about its pollutant-laden soil," C. Larson, *News & Analysis*, 28 March, p. 1415). However, the country faces equally serious urban soil and water pollution.

As a result of unparalleled urbanization over recent decades, many polluting and energy-intensive activities, including steel, coke, pesticide, and chemical industries, have relocated from urban areas to peripheral or rural areas (1). The legacy is more than 5000 brownfields—sites polluted, or potentially polluted, by hazardous substances—in China's major cities (2). A recently released ambitious urbanization plan will move more polluting plants from cities, leaving more brownfield sites (3). Brownfields pose health and environmental hazards in densely populated cities and are obstacles to urban and economic development. Soil concentrations of pollutants, including heavy metals, persistent organic pollutants, and benzene, can be hundreds of times the regulated limits (4). Seepage will also result in groundwater contamination.

Many brownfields have been used for housing. Without adequate survey and remediation of toxic brownfields, construction has already resulted in acute poisoning incidents. For example, workers were hospitalized during construction on sites at former pesticide factories in Beijing and Wuhan (4). Residents of newly built houses are often unaware of pollution beneath their properties. The Guangzhou Asia Games Village site was changed due to soil pollution from fertilizer factories, but housing for local people is being built in the area (5).

The Chinese Premier vowed to declare "war on pollution." However, government spending on environmental protection and energy conservation decreased by 9.7% between 2012 and 2013 (6). Funding and

technology may limit remediation of Chinese brownfields, but information should be made publicly available to raise awareness and facilitate wider participation in brownfield management. Experience from elsewhere, such as the U.S. “Brownfield Act” (7), should be deployed to demonstrate commitment to tackling the growing problem of soil pollution.

HONG YANG,<sup>1\*</sup> XIANJIN HUANG,<sup>2</sup>

JULIAN R. THOMPSON,<sup>3</sup> ROGER J. FLOWER<sup>3</sup>

<sup>1</sup>Centre for Ecological and Evolutionary Synthesis, Department of Biosciences, University of Oslo, Blindern, 0316, Oslo, Norway. <sup>2</sup>School of Geographic and Oceanographic Science, Xianlin Campus, Nanjing University, Nanjing 210023, China. <sup>3</sup>Wetland Research Unit/Environmental Change Research Centre, UCL Department of Geography, University College London, London, WC1E 6BT, UK.

\*Corresponding author. E-mail: hongyanghy@gmail.com

#### References

1. H. Yang, R. J. Flower, J. R. Thompson, *Nature* **490**, 342 (2012).
2. East Asia Infrastructure Division of the World Bank, *China Waste Management: Problems and Suggestions* (World Bank, 2005).
3. The Central People's Government of the People's Republic of China, 2014 ([www.gov.cn/zhengce/2014-03/16/content\\_2640075.htm](http://www.gov.cn/zhengce/2014-03/16/content_2640075.htm)) [in Chinese].
4. M. Jin, *Ecol. Econ.* **258**, 18 (2012).
5. S. Gao, K. Wang, *Caijing Mag.* **323**, 1 (2012).
6. Ministry of Finance of the People's Republic of China,

2014 ([www.mof.gov.cn/zhengwuxinxi/caizhengxinwen/201403/t20140306\\_1052323.html](http://www.mof.gov.cn/zhengwuxinxi/caizhengxinwen/201403/t20140306_1052323.html)) [in Chinese].

7. Y. Gong, *International Experience in Policy and Regulatory Frameworks for Brownfield Site Management* (World Bank, 2010).

## Scientific Justification for Animal Capture

IN THE NEWS & ANALYSIS STORY “COURT slams Japan’s scientific whaling” (4 April, p. 22), V. Morell recounts the recent judgment of the International Court of Justice that the second Japanese scientific whaling program in the Antarctic (JARPA II) shall cease. This decision has given extra weight to a principle that is already contained in most existing scientific and ethical guidelines for research involving the taking of wild animals: Sample sizes (numbers of animals taken) must be justified in advance in relation to the specific objectives of the research.

Wisely, the court did not try to answer the broader question of what constitutes legitimate scientific research, but it faulted the absence of explanation or analysis as to how the specified numbers of whales to be

caught would have contributed to the objectives of the JARPA II program. The ruling has implications for Japan’s whaling program in the North Pacific (JARPN II). An Expert Panel appointed by the International Whaling Commission to review Japan’s whaling in the North Pacific, which targeted up to 100 sei whales, 50 Bryde’s whales, 220 minke whales, and 10 sperm whales a year (1), also noted the absence of a scientific justification for the number of whales killed in relation to quantifiable research objectives (2).

While not restricting the freedom of scientific research, the International Court of Justice ruling highlights the importance of careful analysis and clear justification of the study duration and of the sample sizes required to meet research objectives, in advance of any take of wild animals.

JUSTIN COOKE,<sup>1</sup> VASSILI PAPASTAVROU,<sup>2</sup>

RUSSELL LEAPER,<sup>3\*</sup> SIDNEY HOLT<sup>4</sup>

<sup>1</sup>Centre for Ecosystem Management Studies, Windenreute, 79312, Germany. <sup>2</sup>Department of Biology, University of Bristol, Bristol, BS8 2LR, UK. <sup>3</sup>School of Biological Sciences, University of Aberdeen, Aberdeen, AB24 2TZ, UK. <sup>4</sup>Voc Palazzetta 68, Paciano PG, 06060, Italy.

\*Corresponding author. E-mail: r.c.leaper@abdn.ac.uk



### References

1. International Whaling Commission, *J. Cetacean Res. Manage.* **11** (suppl.), 405 (2010).
2. Government of Japan, "Revised research plan for cetacean studies in the western North Pacific under Special Permit (JARPN II)," Paper SC/56/O1 presented to IWC Scientific Committee, Sorrento, Italy (2004).

## Public Credibility Drives Vaccination Decisions

IN THEIR EDITORIAL "ADDRESSING VACCINE hesitancy" (25 April, p. 339), B. R. Bloom, E. Marcuse, and S. Mnookin identify a need to combat antivaccination messages with evidence-based strategies to best communicate the importance of vaccination. "The crux of the problem," they write, "is our inability to demonstrate to skeptical parents that vaccinations save lives."

This inability is not due to a lack of evidence. Rather, it is a struggle between public health officials and vaccination skeptics for public credibility. Public debate is frequently guided by particulars: singular cases and narratives of inexplicable deaths or illness following vaccination. These par-



ticulars are delivered by voices that skeptical parents trust. A well-calibrated display of particulars allows many people to relate to such stories (1).

This suggests that public credibility is not the result of experts telling the truth as they see it. It is the result of a demonstrated ability to solve problems (2), to build trust amongst one's audience (3), and to take doubts seriously rather than rejecting them as ignorant

(4). After all, beyond the boundaries of the lab, trust and narratives contribute as much as truth and data to public credibility.

**BART PENDERS**

School for Public Health and Primary Care (Caphri), Maastricht University, Maastricht, 6200MD, Netherlands.  
E-mail: b.penders@maastrichtuniversity.nl

### References

1. S. Shapin, in *Public Science in Liberal Democracy*, P. W. B. Phillips, Ed. (Univ. of Toronto Press, Toronto, 2007), pp. 33–39.
2. E. Freidson, *Profession of Medicine: A Study of the Sociology of Applied Knowledge* (Univ. of Chicago Press, Chicago, 1988).
3. E. v. Rijnswoud, *Nature* **460**, 571 (2009).
4. G. A. Poland, R. M. Jacobsen, *N. Engl. J. Med.* **364**, 97 (2011).

## Letters to the Editor

Letters (~300 words) discuss material published in *Science* in the past 3 months or matters of general interest. Letters are not acknowledged upon receipt. Whether published in full or in part, Letters are subject to editing for clarity and space. Letters submitted, published, or posted elsewhere, in print or online, will be disqualified. To submit a Letter, go to [www.submit2science.org](http://www.submit2science.org).

## NATURAL HISTORY

## The Art of Longevity

Jared Farmer

Rachel Sussman, a photographer who first earned wide attention through a 2010 TED talk, spent ten years taking portraits of organisms that have lived longer than two millennia. The result, *The Oldest Living Things in the World*, is not a Guinness Book of Longevity. Sussman is an artist, neither a cataloger nor a scientist, and certainly not in league with peakbaggers and “doom tourists” who want to gain access to exotica just because they’re there or preen about having seen things before they’re gone. Rather, for her, the number 2000 is simply an organizing principle for contemplating persistence in a time of climate change. Almost accidentally, her path of personal discovery became an exercise in biological inquiry and environmental humanism.

Her photographs, shot in natural light with a medium-format film camera, are more evocative than informational. Sussman favors the medium-wide-angle view from a moderate distance—a perspective that approximates a person’s ocular coverage while standing in front of a tree. In this way, she humanizes her specimens even though her pictures include no people. Unlike 19th-century photographers such as Carleton Watkins or contemporary tree-climbers with *National Geographic*, Sussman has no desire to capture—optically conquer—an entire giant sequoia (*Sequoiadendron giganteum*).

Some of her arboreal subjects are charismatic; others, like *Welwitschia mirabilis*, look weird; just as many are hauntingly nondescript. Going well beyond trees, Sussman seeks out lesser-known marvels: monster mushrooms, luxuriant seagrass, ultra-green tuffets of Atacaman parsley (*Azorella compacta*), Arctic lichens, Antarctic moss, sculptural stromatolites, and permafrost extremophiles that may be half a million years old.

The reviewer is at the Department of History, State University of New York, Stony Brook, NY, 11794, USA. E-mail: jared.farmer@stonybrook.edu

The only animals in her cabinet of curiosities are corals that by themselves look like art.

Sussman hasn’t (yet) shown in a major art museum, but her book essentially functions as an exhibition catalog. As such, it is a gorgeous thing: oversized dimensions, glossy pages, and whole-page color plates. The accompanying text—a series of science-inflected travel essays—enhances or distracts from the art depending on one’s bias. Although Sussman writes

forthrightly with style and wit, not everyone will relate to the travel and relationship issues of a self-identified 30-something, single, female, Jewish, atheist, freelance acrobat-turned-photographer based in Brooklyn.

As a memoir, the book might have been improved if it were even more personal and organized chronologically like a journal—one decade of a life spent contemplating multimillennial lives. Instead, Sussman divides her work into seven parts by continents (starting, conventionally, with North America and giant sequoia). For scientists, at least, the material would have been more interesting arranged along different axes: natural versus human-assisted longevity, mild versus extreme environments, terrestrial versus aquatic species, plants versus nonplants, fast versus slow growers, individuals ver-

sus clonal colonies, and multicellular versus single-celled organisms.

It’s easy to name deserving specimens, species, and habitats unvisited by Sussman. Some of these she appends as a to-do list. In the meantime, dendrophiles can refer to a more formal—and nicely illustrated—compendium published in association with the Royal Botanic Gardens, Kew (*1*).

Susmann neglects to mention that the search for the oldest living thing is itself quite old and includes great names (and egos) in the history of biology, such as Candolle, Adanson, Humboldt, Agassiz, Lindley, and Gray. In the 19th century, the documentation of ancient trees (both living and fossilized) contributed to the great debates over Earth’s age and the historicity of the Bible. European yew (*Taxus baccata*) was widely considered the oldest until the 1853 publicity about *Sequoiadendron giganteum*, which was definitively superseded in the 1950s by Great Basin bristlecone pine (*Pinus longaeva*).

More recently, botanists have determined that the megaflores of the Sierra Nevada are mostly younger than advertised and that extreme longevity is more common than once suspected—and hardly restricted to single-trunked woody dicots. The hitch is that scientists can only estimate the ages of various clonal life forms using a combination of radiocarbon dating and growth rate analysis. As Sussman admits, her given date ranges may yet be revised. Many of her subjects were discovered only in the past 30 years as researchers have paid increased attention to polar, desert, and oceanic organisms that may function as advance indicators of climate change. It’s heartening to read

about the many experts who volunteered their time—inviting Sussman to the field, guiding her to specimens—after an e-mail exchange.

What can scientists take from this work? Perhaps it will inspire new interest in the evolutionary ecology of senescence. It would be good to know if certain environmental conditions favor endurance across species, populations, and individuals—and whether there are “hot spots” for longevity as well as biodiversity. Or, like Edward O. Wilson (who contributes a blurb), one can simply appreciate Sussman’s biophilic sense of wonder. Stewart Brand (provider of another endorsement) represents a different audience.

## The Oldest Living Things in the World

by Rachel Sussman  
University of Chicago Press,  
Chicago, 2014.  
304 pp. \$45, £31.50. ISBN  
9780226057507.



La Llaretas #0308-23B26. Llaretas (*Azorella compacta*), a member of the celery family from Chile’s Atacama Desert, reaches ages of up to 3000 years.



Founding editor of the *Whole Earth Catalog*, contrarian champion of nuclear power, and driving force behind the Long Now Foundation, Brand has lately advocated for de-extinction and human life extension. One wonders if Sussman's art of longevity might unwittingly motivate technophilic oligarchs to fund bioengineering projects following Google's antiaging initiative, Calico.

Sussman has humbler, nobler designs: creating additional art and advocating for UNESCO recognition for all ancient organisms. God bless her. We need more artists, musicians, dancers, and poets to give humanistic expression to the pursuit of environmental knowledge. I wish major research institutions supported artist-in-residence programs alongside labs. Sussman believes that "[t]he best art and science projects enhance and extend each other, bringing something new to both; they are not about simply making the research pretty, or making artworks using novel scientific tools." By this measure, *The Oldest Living Things in the World* is a work for the ages.

#### References

1. E. Parker, A. Lewington, *Ancient Trees: Trees That Live for a Thousand Years* (Batsford, London, 2012).

10.1126/science.1254361

## COGNITIVE SCIENCE

# How Great a Separation?

Bryan Sim

In *The Gap*, Thomas Suddendorf offers a cogent analysis of how the mental lives of humans differ from those of other animals. He claims that the gap lies in animals' inability to imagine the future or "read" the minds of others. Suddendorf (a psychologist at the University of Queensland) distills research that spans domains of memory, mental time travel, mind-reading, and morality. For each topic, he spells out psychological feats that most humans can perform and details explorations of the same traits in other animals. He supplements his summaries with research highlights: case studies of individuals who lack episodic memory, tests of self-awareness that expose animals with rouge on their noses to mirrors, arguments for mental

time travel in animals that store tools for later use, and inferring morality from apes' sign language.

Following a simple and predictable menu, Suddendorf's chapters simmer "what the science of the mind has taught us about the human faculties," serve up our knowledge of the "animal capacities in these domains that challenge claims of human uniqueness," and finally blend in a short discussion that melds these ingredients. He serves up a clear and unbiased account. More important, Suddendorf's conclusions are restrained and his analyses prudent.

Attempting to appease those with short attention spans, the author sprinkles *The Gap* with tidbits about current understanding and research methodology that range from mildly interesting to quite fascinating. Many of us assume, for example, that puberty marks the last major spurt in our growth and that any further cognitive advances trickle rather than flow. However, our brains do not fully reach maturity until young adulthood: When asked to simply look in the opposite direction of a light that appears on a screen, participants stumble as adolescents, then gradually get better as they grow up and learn to toe the line.

Suddendorf starts his quest to delineate the boundaries between human and animal brains with an assertion that some will find difficult to swallow: we are not that unique. We are "the last humans" simply because our nearest relatives have all died out. This perspective serves to map the rest of our journey: Because the forces of nature (or, as some argue, we) have killed off the hominids that would otherwise be most closely related to us, the best source of information about our ancestral conditions comes from apes and monkeys. Suddendorf vividly describes these creatures, including anecdotes of monkeys swinging off his arms. The book then walks us through humans' intellectual aspirations. Here readers encounter cats with rouge on their noses walking into mirrors, chimpanzees playing with paintbrushes, and orangutans trying to determine which cup (the noisy or quiet one) contains the nuts. In summarizing the results of these studies, Suddendorf discusses two contrasting perspectives: "rich" and "lean" explanations of animal behavior. For any set of findings, there can be rich interpretations that "ascribe complex, human-like abilities to animals" and lean explanations that defer



to simpler learning processes. For instance, Australian crows (*Corvus orru*) that have learned to eat poisonous crane toads (*Rhinella marina*) safely by flipping them over and pecking at their harmless belly demonstrate flexible problem-solving. But given the seemingly much greater intellectual flexibility of humans, what significance should we attribute to the crows' capability? The contrasting interpretations arise because the science is not objective. In our attempts to demarcate the gap between humans and other animals, our humanness confounds our understanding of nature—the romantics and skeptics among us reach rich and lean explanations, respectively. To his credit, Suddendorf gives equal voice to both.

Its foibles aside, the book provides a new lens through which to see the world. Read it, and you might never look at yourself or your household pets in the same light. One starts to realize how strange our own behaviors are as Suddendorf ratchets up our collective self-consciousness by offering snapshots of the insane world we seem to have created for ourselves. Referring to the abstract roles of "[r]eferees, idols, CEOs, officers, priests, [and] banks," he notes that "[a]nimals cannot perceive them. We merely imagine them together and act as if they are real. And so, for us, they are."

Ultimately, Suddendorf does not deliver a feel-good story. The book did not leave me feeling fuzzy inside, nor could I divine a moral or take-home message. The ideas presented are fascinating; the presentation, less so. *The Gap*, however, provides an honest account of an extremely interesting topic and a candid view of the research behind our understanding. The narrative is not always pretty, but why should science be?

#### The Gap

The Science of What Separates Us from Other Animals

By Thomas Suddendorf

Basic Books, New York, 2013.  
366 pp. \$29.99, C\$34.50.  
ISBN 9780465030149.

The reviewer is at the Department of Psychology, New York University, 6 Washington Place, New York, NY 10003, USA. E-mail: bryan.sim@nyu.edu

10.1126/science.1254362

# A Call for Deep-Ocean Stewardship

The precautionary approach and collaborative governance must balance deep-ocean use and protection.

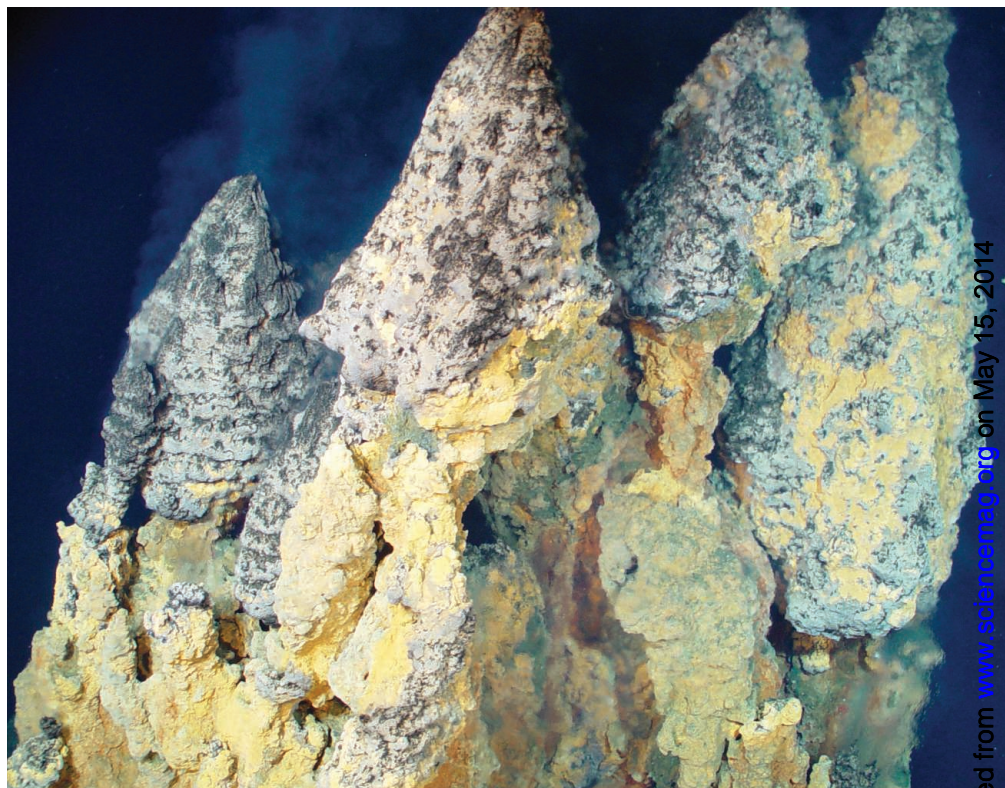
Kathryn J. Mengerink,<sup>1,2</sup> Cindy L. Van Dover,<sup>3</sup> Jeff Ardron,<sup>4</sup> Maria Baker,<sup>5</sup>  
Elva Escobar-Briones,<sup>6</sup> Kristina Gjerde,<sup>7</sup> J. Anthony Koslow,<sup>2</sup> Eva Ramirez-Llodra,<sup>8</sup>  
Ana Lara-Lopez,<sup>9</sup> Dale Squires,<sup>10</sup> Tracey Sutton,<sup>11</sup> Andrew K. Sweetman,<sup>12</sup> Lisa A. Levin<sup>2\*</sup>

Covering more than half the planet, the deep ocean sequesters atmospheric CO<sub>2</sub> and recycles major nutrients; is predicted to hold millions of yet-to-be-described species; and stores mind-boggling quantities of untapped energy resources, precious metals, and minerals (1). It is an immense, remote biome, critical to the health of the planet and human well-being. The deep ocean (defined here as below a typical continental shelf break, >200 m) faces mounting challenges as technological advances—including robotics, imaging, and structural engineering—greatly improve access. We recommend a move from a frontier mentality of exploitation and single-sector management to a precautionary system that balances use of living marine resources, energy, and minerals from the deep ocean with maintenance of a productive and healthy marine environment, while improving knowledge and collaboration.

We have an opportunity to make smart decisions now about the future of the deep ocean ahead of expanding and emerging uses—decisions that weigh benefits of use against both direct costs of extraction and external costs that include damage to sensitive and unknown ecosystems and their services that would be difficult to repair or replace.

## Expanding Use, Fragmented Governance

The deep ocean already experiences impacts from activities such as fishing; oil and gas development; waste disposal; and land-based pollution, including greenhouse gases (2). On the horizon is industrial-scale mining combined with impacts from CO<sub>2</sub> emissions, which will alter temperature, pH, O<sub>2</sub>, and food supply to the deep (3). Together, these will inflict a spectrum of impacts that, if not managed wisely, may irreversibly damage essential ecosystem functions, processes, and services (see the figure).



**Minerals from the deep.** Active “smoker” chimneys precipitating iron, copper, and zinc sulfides from 230°C fluid in the Mariana Arc region, Western Pacific Ocean.

Industrial fishing in the deep ocean is moving inexorably deeper; the mean depth of fishing activity has increased by 350 m since 1950 (4) and is largely unsustainable, removing long-lived, low-productivity species that cannot recover on reasonable time scales (5). Bottom trawling in effect “clear-cuts” hundred-year-old fishes and thousand-year-old corals on seamounts and continental margins. One-fifth of the continental slope (4.4 million km<sup>2</sup>), which largely occurs below 200 m, has been trawled at least once and often multiple times (6). Only a few countries benefit briefly from the yield, but habitat loss is widespread and

largely permanent in human time scales (2). In response to the recognized devastation caused by trawling in the deep ocean, the European Parliament recently took measures to restrict such trawling in the northeast Atlantic, building on calls by the United Nations for urgent action. Many believe that the actions do not go far enough and advocate a complete ban.

Since the 1970s, the oil and gas industry has drilled almost 2000 deep-ocean exploration wells (7). The probability of accidents increases markedly with water depth, about 8.5% with every ~30 m of platform depth (8). Although the footprint of any individual drilling operation may be small, the Deepwater Horizon spill has demonstrated a worst-case-scenario oil disaster at great depths (9). This event highlighted the paucity of baseline data for deep-ocean ecosystems in the Gulf of Mexico and elsewhere. Such data are fundamental for evaluating impacts to, protecting, and restoring lost resources.

<sup>1</sup>Environmental Law Institute, Washington, DC 20036, USA. <sup>2</sup>Center for Marine Biodiversity and Conservation, Scripps Institution of Oceanography, La Jolla, CA 92093–0202, USA. <sup>3</sup>Marine Laboratory, Duke University, Beaufort, NC 28516, USA. <sup>4</sup>Institute for Advanced Sustainability Studies, Potsdam, Germany. <sup>5</sup>National Oceanography Centre, University of Southampton, Southampton, UK. <sup>6</sup>Universidad Nacional Autónoma de México, ICML, México. <sup>7</sup>Wycliffe Management, 05510 Warsaw, Poland. <sup>8</sup>Norwegian Institute for Water Research (NIVA), Oslo, Norway. <sup>9</sup>Institute for Marine and Antarctic Studies, University of Tasmania, Hobart, Australia. <sup>10</sup>University of California San Diego, La Jolla, CA 92093, USA. <sup>11</sup>Oceanographic Center, College of Oceanography, Nova Southeastern University, Dania Beach, FL 33004, USA. <sup>12</sup>International Research Institute of Stavanger, Norway. \*Corresponding author. E-mail: llevin@ucsd.edu

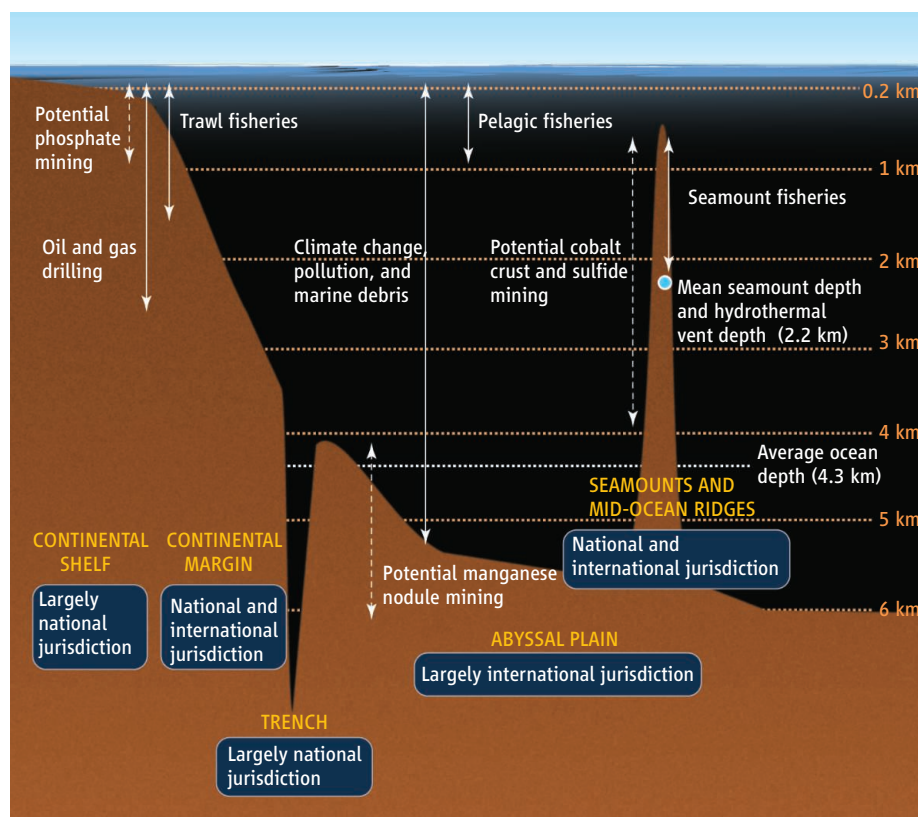


Deep-ocean mining is an emerging industry with national and international regulations under development now. Already, the International Seabed Authority has entered into eleven 15-year contracts with nations leasing an area more than twice the size of Germany (883,000 km<sup>2</sup>) in the abyssal central Pacific (>3500 m) for polymetallic nodule exploration. Mining companies and nations also have leases in national and international areas to explore hydrothermal vents for deposits of massive polymetallic sulfides, seamounts for cobalt crusts, and margin sediments for phosphates. (See the photo and the figure.)

The deep ocean has served as an intentional dumping ground for radioactive waste, sewage, toxic chemicals, and terrestrial mine tailings (2). It is now being considered as a long-term storage site for CO<sub>2</sub> to combat climate change (10). The deep ocean is also the unintended final resting place for an array of land-based anthropogenic debris and pollutants (2).

Expanding use brings cumulative impacts and conflicts that will likely grow as we identify new ways to exploit the deep ocean. Already, fishing and mineral or energy extraction industries clash over exploitation (11). Deep-water phosphate deposits off Namibia, New Zealand, and Mexico are being targeted for use as fertilizer. These phosphates occur in waters that support productive coastal fisheries important to local economies and communities. Such overlapping uses and multisector activities generate cumulative impacts that are difficult to monitor and quantify in the deep ocean (2). Conflict also arises between those wishing to exploit resources and those seeking to preserve species and habitats.

Governance in the deep ocean is fragmented. The water column and the seabed below 200 m are interconnected, extending across national and international jurisdictions (see the figure), but are managed on a single-sector basis, if at all. The 1982 United Nations Convention on the Law of the Sea (UNCLOS) is an umbrella framework for international ocean management. Multilateral regional fishery management organizations regulate commercial fisheries harvest; the International Maritime Organization manages shipping; and the International Seabed Authority regulates mining of the international seabed. Management of other activities (dumping, laying submarine cables, and military activities) that affect the deep ocean is similarly a single-sector approach. In some arenas, like marine genetic resource management, agreements and institutions are substantially lacking (12). These single-sector



Existing and potential uses and impacts in the deep ocean.

approaches, necessary for managing specific activities, are not sufficient to ensure balanced resource use and sustainability. An example of the challenge is playing out now on the Chatham Rise in New Zealand: the site proposed for deep-ocean phosphate mining overlaps with an existing “benthic protection area” that prohibits bottom trawling under New Zealand fisheries requirements.

#### A Path Forward

In the face of uncertainty, a growing number of international treaties and other instruments adopt the precautionary approach (13), which as explained in the 1992 United Nations Rio Declaration on Environment and Development, recognizes that “[w]here there are threats of serious or irreversible damage, lack of full scientific certainty shall not be used as a reason for postponing cost-effective measures to prevent environmental degradation.” The deep ocean is challenged by threats of irreversible damage where there are slow rates of substrate formation (manganese nodules may precipitate a few mm per million years) and slow growth and maturation of the deep biota. The task for deep-ocean management in national and international areas is to achieve appropriate precaution while enabling use of living and nonliving resources. Here, we propose three directions

to advance deep-ocean stewardship: (i) protection and mitigation, (ii) research, and (iii) collaborative governance.

(i) Protection and mitigation. We recognize the great expense and near impossibility of restoring many deep-ocean ecosystems (14). These facts alone demand a precautionary approach that includes appropriate protection of areas that are representative of targeted habitat as well as ecologically, biologically, and scientifically important. An expert-driven planning process has been used to delineate a network of appropriate sites for protection in the manganese nodule-covered Clarion Clipperton Fracture Zone of the Central Pacific Ocean (15), an approach that could be adopted for other regions.

Representative protected areas that have the same geomorphic, physical, chemical, and biological characteristics as existing and planned exploitation areas should be established as effective refuges and as a source of brood stock for species likely to be affected. The International Seabed Authority has established as part of its management plan for the Central Pacific Ocean, nine “Areas of Particular Environmental Interest” that have many of these features; however, the designations are so far not permanent and apply only to mining. In addition, established control areas are required for baseline mea-

surements and as a reference for monitoring impact and mitigation. To be effective, protected areas must be multisector in application to avoid damage by one sector when protected by another.

Typically, mitigation includes avoiding or minimizing harm and, where harm is unavoidable, restoring key ecosystem services. With known sensitive resources, avoiding and minimizing harm can be achieved through buffer zones or heightened siting standards. For

sal distance, demographics, connectivity, and the many factors that affect community diversity. Modeling is required to estimate vulnerability to impacts and resilience after disturbance, as is valuation of deep-ocean ecosystem services.

One way to develop the requisite knowledge base is to establish funding mechanisms as part of leasing, licensing, mitigation, and liability systems under national and international frameworks (19). For example,

## *The International Seabed Authority has entered into eleven 15-year contracts with nations leasing an area more than twice the size of Germany ... in the abyssal central Pacific ... for polymetallic nodule exploration.*

example, U.S. oil and gas guidance calls upon those operating below 300 m to establish 76- to 610-m buffer zones around deep-sea corals and chemosynthetic communities, depending on the activity. New research on plume effects and other impacts will be required to understand buffer-zone requirements for deep-sea mining activities.

When harm is unavoidable and the ecosystem will be damaged, compensatory restoration can help address loss. However, the impracticality of restoration in the deep ocean in most instances calls for a different approach. In lieu of restoration in the classic sense (e.g., fixing injured resources or establishing new sites with the same features), deep-ocean managers should focus on protection and expansion of knowledge as restoration tools. Yet-to-be-discovered species, habitats and functions must be safeguarded while scientific understanding required for ecosystem-based management and mitigation techniques (14) are developed. "Research as restoration" is an approach with precedence; the *Exxon Valdez* oil spill restoration plan included the development of a research fund (16). A similar approach has been called for in the Deepwater Horizon oil spill (17). Although these examples arise from catastrophic spills, the approach is relevant to mitigation for planned injury, as occurs with permitted activities like fishing and mining. In addition, U.S. law allows preservation (protected areas) as a form of compensatory mitigation when other approaches are not feasible (18).

(ii) Research. For most deep-sea ecosystems, we lack basic information on species composition and distribution ranges, their natural variability and dynamics, disper-

sal distance, demographics, connectivity, and the many factors that affect community diversity. Modeling is required to estimate vulnerability to impacts and resilience after disturbance, as is valuation of deep-ocean ecosystem services.

U.S. law requires electricity revenues from the Bonneville dam to fund a fish and wildlife program, including scientific research to mitigate impacts. Beyond information generation, such funding should support a global deep-ocean data repository, such as the Ocean Biogeographic Information System (OBIS).

(iii) Collaborative governance. Overcoming fragmented governance requires improved collaboration. Marine spatial planning efforts recognize the need for interdisciplinary, transboundary, and multisector management to ensure that cumulative effects are minimized and explicit trade-offs made. Among these trade-offs are the environmental, social, and economic trade-offs between deep-ocean and terrestrial resource extraction. For example, deep-ocean minerals can occur at higher concentrations, are closer to the sediment surface, and will likely require less permanent mining infrastructure for extraction than terrestrial minerals. Weighing against deep-ocean mining is the lack of knowledge about mining impacts and ecosystem resilience, the likelihood of slow to no recovery for many habitat types, the lack of ability to monitor and restore damaged systems, and the potential disturbance to seafloor and water-column life far beyond mining sites.

Marine spatial planning approaches provide a template for deep-ocean management and will require formal procedures for improved information-sharing among governance institutions, industry, civil society, and researchers; collectively agreed-upon goals and objectives; careful monitoring and reporting; improved compliance and enforcement; and transparent, partici-

patory processes. For international waters and seabed, a new implementing agreement to UNCLOS for the conservation and sustainable use of marine biodiversity beyond national jurisdiction, as has been proposed by many nations to the United Nations, could provide a platform for international collaboration, coordinated management, and precaution.

Given our substantial knowledge gaps, any future exploitation of deep-ocean resources must be balanced with lasting protection of habitats, biodiversity, and services.

### References and Notes

1. E. Ramirez-Llodra *et al.*, *Biogeosciences* **7**, 2851 (2010).
2. E. Ramirez-Llodra *et al.*, *PLoS ONE* **6**, e22588 (2011).
3. C. Mora *et al.*, *PLoS Biol.* **11**, e1001682 (2013).
4. R. A. Watson, T. Morato, *Fish. Res.* **140**, 63 (2013).
5. E. Norse *et al.*, *Mar. Policy* **36**, 307 (2012).
6. P. Puig *et al.*, *Nature* **489**, 286 (2012).
7. Global offshore oil-1: Exploration trends show continued promise in world's offshore basins. *Oil Gas J.* (5 March 2007); <http://www.ogj.com/articles/print/volume-105/issue-9.html>.
8. L. Muehlenbachs, M. A. Cohen, T. Gerarden, *Energy Policy* **55**, 699 (2013).
9. H. K. White *et al.*, *Proc. Natl. Acad. Sci. U.S.A.* **109**, 20303 (2012).
10. K. Z. House, D. P. Schrag, C. F. Harvey, K. S. Lackner, *Proc. Natl. Acad. Sci. U.S.A.* **103**, 12291 (2006).
11. A. Blanchard *et al.*, *Mar. Policy* **43**, 313 (2014).
12. F. Lehmann, *N.Z. J. Environ. Law* **11**, 33 (2007).
13. Seabed Disputes Chamber of the International Tribunal for the Law of the Sea, Case No. 17 (2011); [www.itlos.org/index.php?id=109](http://www.itlos.org/index.php?id=109).
14. C. Van Dover *et al.*, *Mar. Policy* **44**, 98 (2014).
15. L. M. Wedding *et al.*, *Proc. Biol. Sci.* **280**, 20131684 (2013).
16. *Exxon Valdez* Oil Spill Trustee Council, Restoration Plan; [www.evostc.state.ak.us/index.cfm?FA=facts.restorationPlan](http://www.evostc.state.ak.us/index.cfm?FA=facts.restorationPlan).
17. Ocean Conservancy and the Gulf of Mexico University Research Collaborative, Marine Restoration Priorities & Science Principles: Results of the Expert Panel Workshop. Marine Restoration Workshop, St. Petersburg, Florida, 24–25 April 2012.
18. Code of Federal Regulations, 40 C.F.R. §230.93 (2014).
19. E. B. Barbier *et al.*, *Nature* **505**, 475 (2014).

**Acknowledgments:** The ideas behind this paper arose during the inaugural Deep-Ocean Stewardship Initiative (DOSI) workshop held in Mexico City in 2013 ([www.indeep-project.org/deep-ocean-stewardship-initiative](http://www.indeep-project.org/deep-ocean-stewardship-initiative)), cohosted by Instituto de Ciencias del Mar y Limnología at Universidad Nacional Autónoma de México, Center for Marine Biodiversity and Conservation at Scripps Institution of Oceanography, and the International Network for Scientific Investigation of Deep-sea Ecosystems (INDEEP). Support for the workshop was provided by the J. M. Kaplan Fund, INDEEP (funded by Fondation Total), the National Commission for Knowledge and Use of Biodiversity (México), and La Comisión Nacional de Áreas Naturales Protegidas (México). C.L.V.D. has been supported by Nautilus Minerals. M.B. and E.R.-L. have been supported by Fondation Total. E.E.-B. serves on the International Seabed Authority Legal and Technical Commission. K.G. and A.K.S. have been supported by EU FP7 MIDAS project, contract number 603418; A.K.S. is also supported by U.K. Seabed Resources. T.S. has been supported by Industrial Economics Inc. L.A.L. has been supported by or has advised Nautilus Minerals, Neptune Minerals, Odyssey Marine Explorations Inc., and Namibian Coast Conservation and Management (NACOMA) Project.

10.1126/science.1251458



## PLANT SCIENCE

# Making Hunger Yield

C. Robertson McClung

The human population reached 1 billion in the early 1800s, roughly 12,000 years after the dawn of agriculture. However, exponential growth in the ensuing 200 years resulted in the global population exceeding 7 billion, placing enormous demands on modern agriculture. Over the past half-century, the human population has doubled but food production has more than kept pace, and the fraction of people with insufficient food has declined dramatically, from 60% in 1960 to about 15% in 2010 (1). Nonetheless, ~1 billion people remain chronically underfed and another ~2 billion suffer from micronutrient deficiencies (1, 2). It is imperative, then, to accelerate increases in agricultural production.

Although the human growth rate peaked in the early 1960s, the human population is still growing and will likely plateau at around 9 billion in the middle of this century (3). Associated with this decline in growth rate is increased wealth, which boosts demand for preferred cereals such as wheat and rice and subsequently, for meat, fish, and dairy products (1). Thus, growth in population and in per capita consumption will require continued increase in agricultural production, necessitating an estimated doubling of crop production between 2005 and 2050 (4).

Multiple issues compound the challenge of increasing food production. The focus will likely be on a limited set of crops, as there is a trend to homogenize the global food supply (5). Thus, the sources of larger yields must be found within or developed from a reduced base of genetic and agronomic diversity. In addition, a sizable fraction of the available arable land is lost each year to development, salinity, or nutritional degradation, and simply cultivating more land is unattractive due to the release of greenhouse gases associated with the conversion of new land into agriculture (2). There is also a need to make agriculture more sustainable—excess water use, unsustainable soil management, and fertilizer leaching all must be addressed (2). Moreover, climate change, particularly rising temperatures, is likely to slow increases in agricultural production (6).



**Overachieving crop.** Submergent-tolerant rice was generated through DNA marker–assisted breeding (15).

Given the enormity of the challenge, it is instructive to examine the reasons behind the dramatic rise in agricultural yield over the past 70 years. The manipulation of plant architecture has been a major focus. The “Green Revolution” between the 1940s and 1960s saw the development of wheat varieties that combined resistance to rust fungus with semi-dwarfism. Shorter, stronger stems boosted grain yield from increased nitrogen inputs, and permitted increased allocation of biomass to the seed rather than the vegetative parts (harvest index) without lodging (collapse of the stem when it can no longer support the seed weight) (7). A similar strategy produced greater rice and maize yields. In part, these increases resulted from nitrogen fertilization, but another key factor has been a steady rise in planting densities. Newer varieties do not yield more grain per plant, but greater planting density yields more grain per field. A critical contribution of genetic improvement through conventional breeding has been the ability of newer varieties to tolerate the biotic and abiotic stresses associated with increased planting density (8).

These advances were achieved without knowledge of the molecular mechanisms responsible for the improvements in plant growth and productivity. However, it is now known that the reduced plant stature of wheat

A combination of approaches to develop crops with improved yields is needed to address the demands of a growing population.

and rice resulted from alterations in hormone signaling pathways (7). Understanding the underlying molecular mechanism(s) and alleles (alternate versions of the same gene) that confer trait(s) of interest makes possible the determination of combinations of alleles from multiple genes that confer the desired combination of traits in a single plant variety. This DNA-marker-assisted breeding has been enabled by genomic technologies that facilitate the integration of high-throughput determination of allele combinations (genotyping) with high-throughput trait measurement (phenotyping) (9). This approach allows efficient genetic identification of plants that carry desired traits and is now being used to improve maize, rice, soybean, and wheat (see the figure).

The availability of genomic resources enables conventional breeding, but also transgenic modification. The introduction of a single transgene (a gene from a different organism or a modified version of a gene from the same organism) can confer a desired property, such as herbicide or pest resistance; without appropriate control measures, crop losses to diseases, weeds, and pests, both before and after harvest, can total 50% or more (10). By conventional breeding, individual resistance genes are introduced from wild varieties, but resistance often

Department of Biological Sciences, Dartmouth College, Hanover, NH, USA. E-mail: c.robertson.mcclung@dartmouth.edu

breaks down rapidly as the pests or pathogens evolve to evade or overcome the resistance gene. Transgenic approaches allow the simultaneous introduction of multiple different resistance genes (stacking) into a single plant variety, which generates more durable resistance in a desired variety. This strategy is analogous to the use of drug combinations (cocktails) when treating diseases like tuberculosis and HIV infection, and has proven effective both in disease treatment and in preventing the emergence of multidrug-resistant bacteria and viruses.

Transgenic modification also permits the alteration of specific biochemical pathways and genetic networks. Examples can be found among efforts to enhance nutrition, including the genetic modification of “golden rice” to increase its beta-carotene content (11). The overexpression of a transcription factor from the flowering plant *Arabidopsis thaliana* in soybean dramatically boosts grain yield by extending the length of time of vegetative development. The result is a larger plant capable of supporting greater seed yield (12). Improved water-use and nitrogen-use efficiencies are attractive targets to increase yields while

reducing unsustainable inputs such as irrigation water and nitrogen fertilizer (6). More audacious goals include the transgenic engineering of rice (and other  $C_3$  crops) to introduce  $C_4$  metabolism—a more efficient carbon fixation pathway—and thereby increase photosynthetic capacity (13).

Although the “intelligent breeding” approach that is guided by DNA markers has been much less controversial, there remains considerable public opposition to the deployment of genetically modified organisms (GMOs), especially in the food supply. One consequence has been the focus of regulatory agencies on the technology to develop the plant rather than on the properties of the engineered plant itself. This regulatory morass has delayed the availability of golden rice more than a decade at a probable cost of tens of millions of lives (6, 14). Efforts to address concerns about the safety of GMOs have chiefly focused on evidence-based refutation of claims of real and potential adverse outcomes (6), but have not alleviated concerns. The scientific community is understandably reluctant to move beyond evidence-based logic, but must explore new approaches to advocate GMOs.

In seeking new crops to sustainably feed an expanding world population, there is compelling need for a multipronged approach that includes traditional breeding, molecular breeding, and genetic modification. We need to accelerate this new green revolution in the lab, in the field, and through better communication outside the scientific community if we are to address the nearly 3 billion chronically undernourished people worldwide.

#### References

1. H. C. J. Godfray *et al.*, *Science* **327**, 812 (2010).
2. H. C. J. Godfray, T. Garnett, *Philos. Trans. R. Soc. Lond. B Biol. Sci.* **369**, 20120273 (2014).
3. W. Lutz, S. K. C., *Philos. Trans. R. Soc. Lond. B Biol. Sci.* **365**, 2779 (2010).
4. D. Tilman, C. Balzer, J. Hill, B. L. Befort, *Proc. Natl. Acad. Sci. U.S.A.* **108**, 20260 (2011).
5. C. K. Khoury *et al.*, *Proc. Natl. Acad. Sci. U.S.A.* **111**, 4001 (2014).
6. N. V. Fedoroff *et al.*, *Science* **327**, 833 (2010).
7. P. Hedden, *Trends Genet.* **19**, 5 (2003).
8. D. N. Duvick, *Maydica* **50**, 193 (2005).
9. L. Cabrera-Bosquet *et al.*, *J. Integr. Plant Biol.* **54**, 312 (2012).
10. J. D. G. Jones *et al.*, *Philos. Trans. R. Soc. Lond. B Biol. Sci.* **369**, 20130087 (2014).
11. T. Johns, P. B. Eyzaguirre, *Food Policy* **32**, 1 (2007).
12. S. B. Preuss *et al.*, *PLOS ONE* **7**, e30717 (2012).
13. S. von Caemmerer *et al.*, *Science* **336**, 1671 (2012).
14. B. Alberts *et al.*, *Science* **341**, 1320 (2013).
15. J. Bailey-Serres *et al.*, *Rice* **3**, 138 (2010).

10.1126/science.1254135

## GEOPHYSICS

# Recognizing Foreshocks from the 1 April 2014 Chile Earthquake

Emily E. Brodsky and Thorne Lay

Are there measurable, distinctive precursors that can warn us in advance of the planet's largest earthquakes? Foreshocks have long been considered the most promising candidates for predicting earthquakes. At least half of large earthquakes have foreshocks, but these foreshocks are difficult or even impossible to distinguish from non-precursory seismic activity. The foreshocks for the 1 April 2014 Chile event and other recent large earthquakes suggest that observable precursors may exist before large earthquakes.

Statistical models of interacting earthquakes suggest that big earthquakes are most likely to happen when regional earthquake activity is already high (1–4). However, the same models also indicate that the

probability of any given earthquake being a foreshock is low, because small earthquakes are often not followed by large ones.

Data for the 2011  $M_w$  9.0 Tohoku, Japan, earthquake suggest that detectable precursory processes may occur for some large plate boundary earthquakes. Twenty-three days before the earthquake, a series of smaller earthquakes began, migrating toward the future mainshock hypocentral region at a rate of several kilometers per day; then, 2 days before the mainshock, a  $M_w$  7.3 earthquake struck within 10 km of the mainshock nucleation site (see the figure, panel A). Data from geodetic instruments recovered from the sea floor after the  $M_w$  9.0 earthquake showed that the fault had slipped slowly during the foreshock sequence (5, 6). No additional slow slip was detected on the fault immediately before the mainshock (7). Bouchon *et al.* have recently suggested that ~70% of interplate earthquakes are preceded

Seismic activity preceding recent large earthquakes, including the 1 April 2014 earthquake in Chile, hints that some large earthquakes may potentially be predictable.

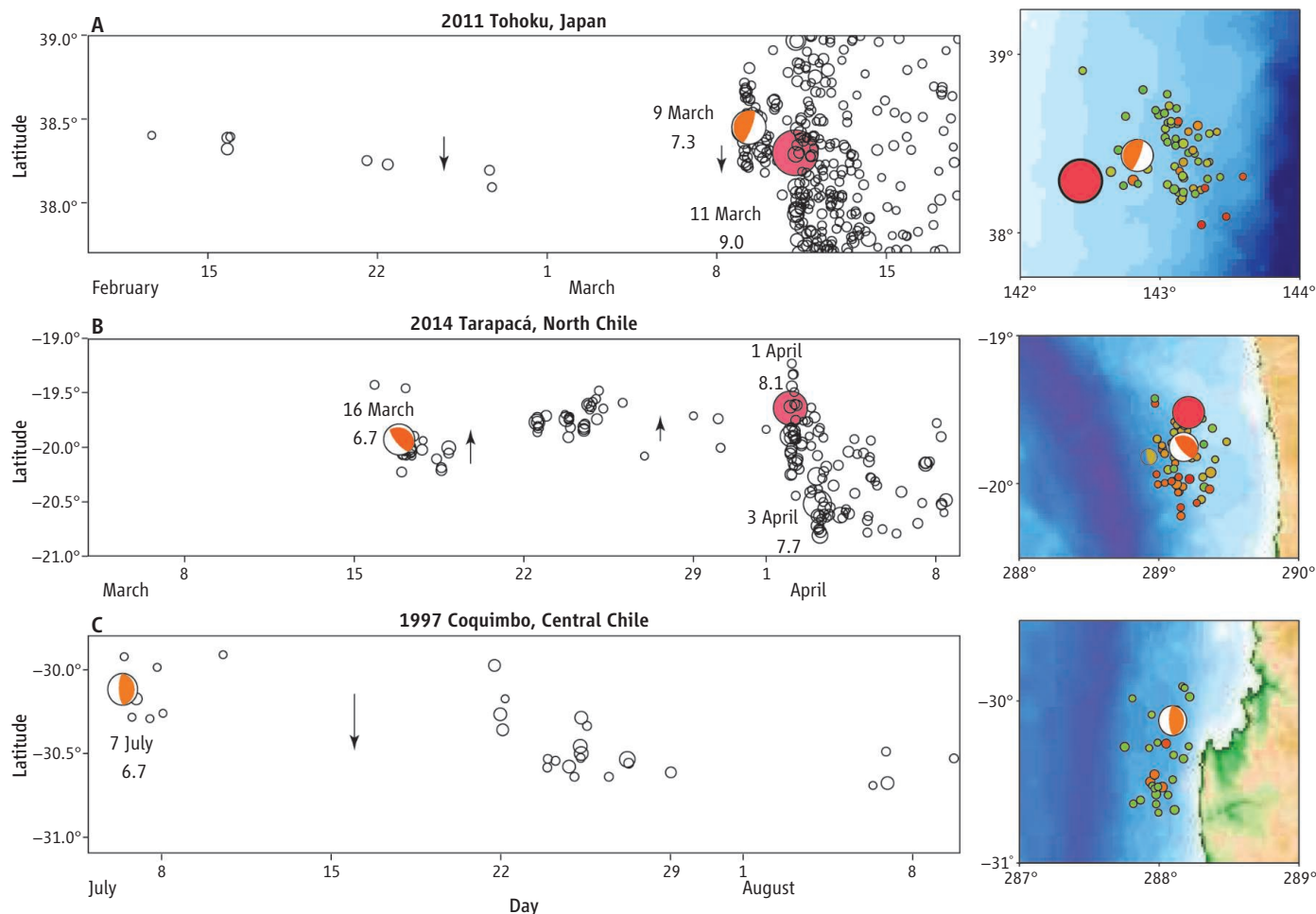
by similar sequences extending to months prior to mainshocks (8). It seems that some large earthquakes might be predictable.

This newfound optimism is tempered by two major scientific and practical concerns. First, it remains difficult to distinguish elevated earthquake activity prior to a mainshock from earthquake swarms that do not culminate in a major event (9). The foreshocks of Tohoku may have been a random cluster that then triggered the mainshock (10). If so, the predictive value of the foreshocks is limited because such random clusters will often not trigger large mainshocks. However, the slow slip inferred from the sea-floor geodetic data is a more widespread, and hence potentially more predictable, precursory process. Unfortunately, the sea-floor data are too sparse to allow a unique interpretation of the apparent slip.

The scarcity of ocean floor measurements highlights the second, practical bar-

Department of Earth and Planetary Sciences, University of California, Santa Cruz, CA 95064, USA. E-mail: brodsky@pmc.ucsc.edu; tlay@ucsc.edu





rier to uncovering possibly subtle signals of precursory subduction zone fault activity. The tantalizing offshore geodetic data for the Tohoku event were not available until ships could retrieve the instrumentation after the earthquake. Real-time telemetry of offshore ocean floor deformation data for subduction zones is critical to any hope of using these signals in prospective forecasting. Building and maintaining such offshore networks is technically possible but would require substantial infrastructure development (11–13).

The difficulties in evaluating possible earthquake precursors came to the forefront in the 1 April 2014  $M_w$  8.1 earthquake in north Chile. The mainshock was preceded by nearly 2 weeks of moderate to large offshore earthquakes on the plate boundary fault (megathrust). Similar to the Tohoku activity, the sequence migrated over about 2 weeks at a rate of several kilometers per day to the location of the 1 April mainshock initiation (see the figure, panel B). The sequence was located in a recognized seismic gap (a region that has not had large earthquakes for a long time, but is known to be capable of them).

The last large earthquake rupturing the plate boundary in this region occurred in 1877.

Both the local population and the scientific community reacted to the foreshock sequence with trepidation. Without a firm scientific footing for assessing the migrating sequence, the authorities could only communicate general concern about the unusual seismic activity and remind people that they should always be prepared for a major earthquake in this region (14). Relatively few casualties resulted from the earthquake. The potential remains for a much larger event to rupture the remaining ~80% of the seismic gap in this region.

The dilemma confronting the geophysical and local communities is exemplified by comparing the north Chile and Tohoku sequences (see the figure, panels A and B) with the Coquimbo earthquake sequence that struck central Chile in 1997 (panel C). The 1997 earthquakes were similar in size, number, and faulting geometry to those along north Chile in 2014 and occurred in a seismic gap that last ruptured in 1943. However, as yet, no large earthquake has followed.

**Precursors or not?** Plate boundary thrust sequences for the 2011  $M_w$  9.0 earthquake in Tohoku, Japan (A), the 1 April 2014  $M_w$  8.1 earthquake in north Chile (B), and the 1997 central Chile sequence (C). Red dots indicate great earthquake epicenters. The fault geometries of large foreshocks are indicated by orange focal mechanisms (the 1997 sequence was not followed by a great event). Arrows indicate migration direction. In the maps on the right of each panel, color denotes depth of foreshocks (red, 5 to 15 km; brown, 15 to 25 km; green, 25 to 35 km).

Combining the seismic signals with the tectonic context may provide a guide as to whether such sequences are foreshocks preceding an imminent mainshock rupture. All three earthquake sequences lasted for a few weeks, migrated along the plate boundary at a rate of a few kilometers per day, had shallow depths of ~20 km on the megathrust with interplate slip, and released a total seismic energy equivalent to  $M_w$  6.8 or larger. However, two features distinguish Tohoku and north Chile from central Chile. Geodetic data indicate that the Tohoku and north Chile sequences were on regions of the plate boundary that were frictionally locked. Both regions had not experienced a

large earthquake for over a century, so large strains should have accumulated in these regions. Geodetic measurements near the central Chile sequence indicate that the megathrust is not as strongly locked as in the other regions (15). With a relatively short time (54 years) since the last large event, less strain should have built up. It is unclear whether slow slip of the plate boundary occurred for either of the Chile sequences, because no offshore geodetic instrumentation exists for detecting it.

Whether earthquakes are predictable or not is still an open question, but perhaps there is now some cause for optimism. Preparatory processes of slow slip and seismic

migration before large plate boundary earthquakes can be monitored with a combination of seismic and geodetic observations, both on-shore and off-shore, if investments are made in instrumentation. More data will be needed to establish whether such observations can lead to confident assessment of imminent earthquake potential.

#### References

1. L. Jones, P. Molnar, *Nature* **262**, 677 (1976).
2. R. Abercrombie, J. Mori, *Nature* **381**, 303 (1996).
3. A. Helmstetter, D. Sornette, *J. Geophys. Res.* **108**, 2457 (2003).
4. K. R. Felzer, R. Abercrombie, G. Ekström, *Bull. Seismol. Soc. Am.* **94**, 88 (2004).
5. Y. Ito et al., *Tectonophysics* **600**, 14 (2013).
6. A. Kato et al., *Science* **335**, 705 (2012).
7. R. Hino et al., *Mar. Geophys. Res.* **10.1007/s11001-013-9208-2** (2013).
8. M. Bouchon, V. Durand, D. Marsan, H. Karabulut, J. Schmittbuhl, *Nat. Geosci.* **6**, 299 (2013).
9. S. G. Holtkamp, M. E. Pritchard, R. B. Lohman, *Geophys. J. Int.* **187**, 128 (2011).
10. D. Marsan, B. Enescu, *J. Geophys. Res.* **117**, B06316 (2012).
11. C. R. Barnes et al., *IEEE J. Oceanic Eng.* **38**, 144 (2013).
12. R. Monastersky, *Nature* **483**, 144 (2012).
13. R. Bürgmann, D. Chadwell, *Annu. Rev. Earth Planet. Sci.* **42**, 140317115936006 (2014).
14. A. Smith, "Experts in Chile fear catastrophe as 300 quakes hit in one week," NBC News, 25 March 2014; [www.nbcnews.com/storyline/chile-earthquake/experts-chile-fear-catastrophe-300-quakes-hit-one-week-n61531](http://www.nbcnews.com/storyline/chile-earthquake/experts-chile-fear-catastrophe-300-quakes-hit-one-week-n61531).
15. C. Vigny et al., *Phys. Earth Planet. Inter.* **175**, 86 (2009).

10.1126/science.1255202

#### APPLIED PHYSICS

## Electronic Control of Circularly Polarized Light Emission

Jana Zaumseil

Circularly polarized (CP) light has many applications, including circular dichroism spectroscopy (to determine the secondary structure of proteins), three-dimensional (3D) displays, spintronics, and even quantum computation. However, CP light is usually created with optical filters, and changing the handedness (left or right) of the polarization requires mechanical rotation of the filters. Alternatively, chiral organic light-emitting diodes with a fixed circular polarization or spin light-emitting diodes, which require an external magnetic field, could be used. On page 725 of this issue, Zhang et al. (1) demonstrate CP electroluminescence from monolayers and multilayers of tungsten diselenide ( $\text{WSe}_2$ ) and other transition metal dichalcogenides (TMDs). The handedness of the CP light is directly controlled by the direction of the in-plane electric field. This effect is not only interesting for applications, but also reveals the "valley" properties of the electronic bands of 2D TMDs.

Unlike bulk TMDs, monolayers of TMDs lack inversion symmetry and exhibit a direct band gap. The electronic structure is usually described by how the energy changes with carrier momentum, and the direct gap occurs at two points with the same energy but different momenta, called  $K$  and  $K'$ —the so-called

valleys. The lack of inversion symmetry and the strong spin-orbit coupling in monolayer TMDs also leads to distinctive optical selection rules. Specifically, electronic transitions near the  $K$  and  $K'$  points couple only to right- or left-handed CP light, respectively. Single-layer  $\text{MoS}_2$  shows CP photoluminescence when excited with CP light (2).

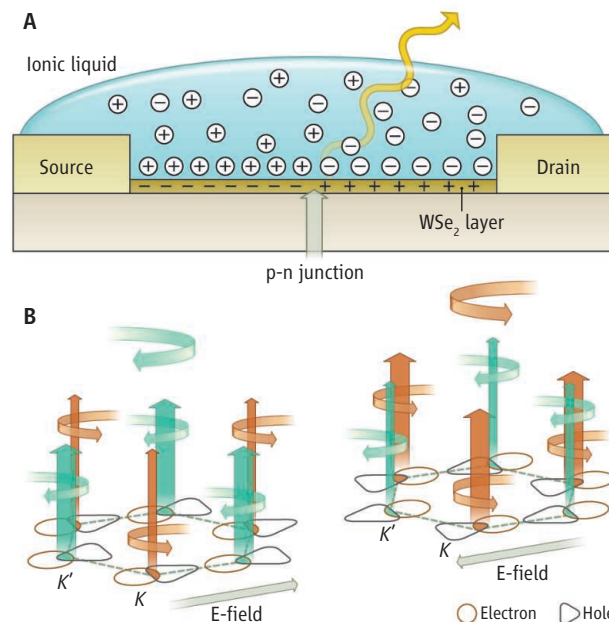
Current-driven or electroluminescent CP light emission would be the next step toward a practical device and requires creating a p-n junction where electron-hole recombination

The handedness of circularly polarized light, which is normally controlled by rotating filters, was switched by the electric field direction in a light-emitting device.

occurs. The TMD flakes cannot be easily doped, so the hole- and electron-rich regions must be induced electrostatically. One possibility is a field-effect transistor (FET) structure with two gate electrodes underneath the channel, one to induce holes and the other to induce electrons. The resulting p-n junction is rectifying, and electron-hole recombination and light emission take place, as has been shown for  $\text{WSe}_2$  monolayers (3–5). However, with emission efficiencies of 0.01 to 1%, they are far from being competitive with thin-film organic light-emitting diodes, which regu-

#### A bias for circularly polarized light.

(A) Zhang et al. created a p-n junction within a thin flake of  $\text{WSe}_2$  that generates light through charge recombination. A frozen ionic liquid electrolyte acts as the gate electrode, causing both holes and electrons to accumulate within the transistor channel. (B) Because of the large in-plane electric field, the hole and electron distributions (triangular and circular contours) are shifted in opposite directions in momentum space. This shift creates a different electron-hole overlap for the  $K$  and  $K'$  valleys and unequal generation of left- and right-handed circularly polarized light. The net handedness can be changed by reversing the applied bias.



Department of Materials Science and Engineering, Friedrich-Alexander-Universität Erlangen-Nürnberg, 91058 Erlangen, Germany. E-mail: jana.zaumseil@fau.de



larly reach external quantum efficiencies of around 20% (6).

An alternative to separate gates, which require careful photolithographic fabrication, is electrolyte gating. The dielectric is replaced by an ionic liquid (an organic salt that is liquid at room temperature) as an electrolyte. When a gate voltage is applied, the cations and anions of the electrolyte move toward the gate electrode and semiconductor surface, respectively, to form electric double layers with very large capacitances (7). The resulting large effective gate field breaks inversion symmetry for multilayer TMDs, so their electronic response is like that of monolayers, and also enables ambipolar transport (8). In the ambipolar regime of a FET, both hole and electron accumulation zones exist within the channel and form a tunable p-n junction where charge recombination and light emission take place, as was shown for several materials (9).

Simple electrolyte gating of WSe<sub>2</sub> monolayers leads to ambipolar transport and electroluminescence (10), but Zhang *et al.* went further and froze the p-n junction by cooling the sample below 100 K, which stopped ionic movement. They then increased the forward bias, and thus the in-plane electric field,

across the p-n junction (see the figure, panel A). The emitted light showed a net circular polarization of up to 45% at 40 K. By reversing the direction of the p-n junction, the net polarization could be reversed as well.

The large electric field causes holes and electrons to move in opposite directions in momentum space (see the figure, panel B). The distributions of holes and electrons around the *K* and *K'* points are not isotropic, so these shifts lead to different electron-hole overlap for the two valleys and unequal contributions to light emission. Thus, depending on the direction of the in-plane electric field, the emitted light has a larger component of either left- or right-handed CP light, hence a net circular polarization.

The degree of polarization depends on the exact orientation of the 2D TMD crystal with respect to the field. Tuning the direction of the field by means of electrodes at different positions also affects the degree of polarization. The orientation of mechanically exfoliated TMD flakes is random, and the observed degree of polarization varies strongly from sample to sample. However, given the fast progress of growth of large triangular TMD monolayers by chemical vapor deposition (11), which enables perfect align-

ment between the electrodes and the crystal, this problem may be solved soon.

The demonstration of CP electroluminescence from monolayers and multilayers of TMDs by Zhang *et al.* shows that valley symmetry is broken in these materials, and also constitutes a first step toward “valleytronics.” If the external quantum efficiencies can be improved and the operating temperatures increased, these devices could become useful as switchable CP light sources.

## References

1. Y. J. Zhang, T. Oka, R. Suzuki, J. T. Ye, Y. Iwasa, *Science* **344**, 725 (2014).
2. H. Zeng, J. Dai, W. Yao, D. Xiao, X. Cui, *Nat. Nanotechnol.* **7**, 490 (2012).
3. J. S. Ross *et al.*, *Nat. Nanotechnol.* **9**, 268 (2014).
4. A. Pospischil, M. M. Furchi, T. Mueller, *Nat. Nanotechnol.* **9**, 257 (2014).
5. B. W. H. Baugher, H. O. H. Churchill, Y. Yang, P. Jarillo-Herrero, *Nat. Nanotechnol.* **9**, 262 (2014).
6. C. Murawski, K. Leo, M. C. Gather, *Adv. Mater.* **25**, 6801 (2013).
7. S. H. Kim *et al.*, *Adv. Mater.* **25**, 1822 (2013).
8. Y. J. Zhang, J. T. Ye, Y. Yomogida, T. Takenobu, Y. Iwasa, *Nano Lett.* **13**, 3023 (2013).
9. M. Muccini, W. Koopman, S. Toffanin, *Laser Photonics Rev.* **6**, 258 (2012).
10. S. Jo, N. Ubrig, H. Berger, A. B. Kuzmenko, A. F. Morpurgo, *Nano Lett.* **14**, 2019 (2014).
11. A. M. van der Zande *et al.*, *Nat. Mater.* **12**, 554 (2013).

10.1126/science.1254496

## CELL BIOLOGY

# New Tricks for an Old Dimer

James A. Wells<sup>1</sup> and Anthony A. Kossiakoff<sup>2</sup>

Much of multicellular biology depends on communication through extracellular signaling molecules that bind to membrane receptors and trigger intracellular signaling events and cell behaviors. One of the first paradigm systems for understanding how polypeptide hormones bind and activate their receptors was human growth hormone (hGH). The molecular details of how hGH binds to its receptor and activates components within the cell started to illuminate over 20 years ago based on biophysical, mutational, and high-resolution structural studies showing that a single hGH molecule binds to two identical molecules of the hGH receptor (1, 2). On page 710 of this issue, Brooks *et al.* (3) propose a fascinating multistep

scissor-like mechanical model in which clamping, rotating, tilting, and the splaying apart of different regions of the transmembrane receptor dimer ultimately lead to receptor activation.

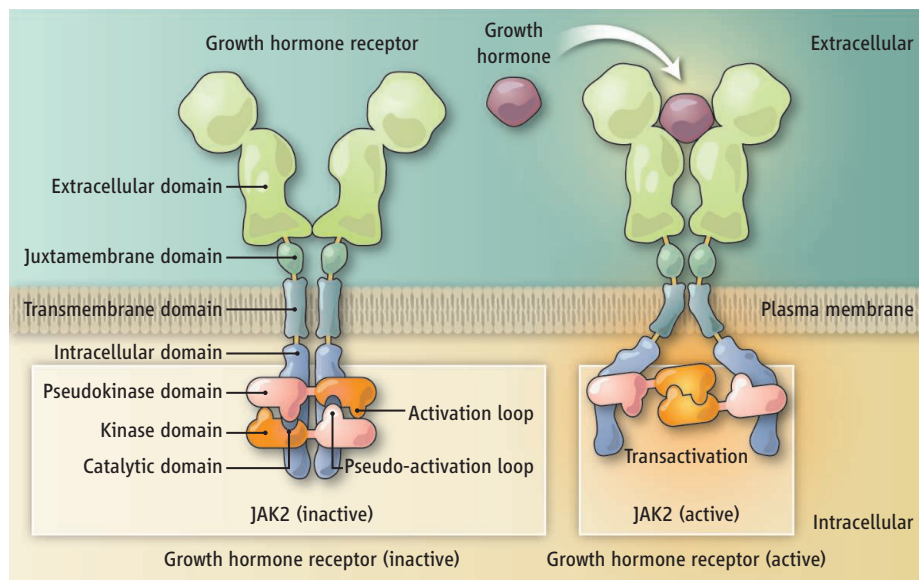
The 1:2 hGH-hGH receptor structure has been a paradigm for other cytokine receptors, as hGH is structurally similar to cytokines that affect hematopoietic cell viability, differentiation, and function. A single hGH hormone binds sequentially to the extracellular domain of each monomer of the receptor (at binding sites 1 and 2 on the hormone) (1, 2). Mutations that block binding to the second monomer (G120R, in which glycine at position 120 in hGH is replaced with arginine) inhibit signaling (4). This insight led to the development of pegmisorvant (trade name Somavert), an hGH receptor antagonist now used to treat acromegaly, a deadly condition of chronic hGH excess. The most straightforward model to explain these data was based on proximity: hGH binding sim-

The receptor for human growth hormone is poised like scissors to transmit signals across the cell membrane when activated.

ply brought together receptors on the cell surface, thereby drawing together the intracellular domains (ICDs) so that they could associate with signaling molecules inside the cell. Some of these intracellular molecules were revealed with the discovery that binding of hGH induced phosphorylation of the receptor ICDs by Janus kinase-2 (JAK2), an event that transferred a signal to a transcription factor called signal transducer and activator of transcription 5 (STAT-5) (5).

Several years ago, the simple proximity model for hGH and homologous cytokine signaling was superseded by data indicating that the receptors for erythropoietin, prolactin, and thrombopoietin, as well as the hGH receptor, were preimerized in the membrane (6–8). Moreover, JAK2 is a large multidomain protein containing protein interaction domains, a pseudokinase domain, and the kinase domain (9). The pseudokinase domain inhibits JAK2 enzymatic activity, but just how this effect is mediated was not

<sup>1</sup>Pharmaceutical Chemistry; Cellular and Molecular Pharmacology, University of California, San Francisco, 1700 4th Street, San Francisco, CA 94158, USA. <sup>2</sup>Biochemistry and Molecular Biology, University of Chicago, Chicago, IL 60637, USA. E-mail: jim.wells@ucsf.edu; koss@bsd.uchicago.edu



**Scissor model.** The hGH receptor exists as an inactive dimer in which the two subunits are held together through weak interactions in the TMD and poised in the inactive state through electrostatic repulsion in the JMD and pseudokinase inhibition in the associated JAK2 dimer (left). Binding of hGH to the receptor (right) clamps the JMD such that it avoids the electrostatic repulsion and mechanically alters the TMD such that the ICD is splayed outward. Splaying pulls on the JAK2 molecules to align their kinase domains. This triggers a wave of phosphorylation events critical in receptor signaling.

known. This spurred many important questions about how predimerized hGH receptor is kept in its off-state, how hormone binding induces its on-state, and how binding outside the cell activates JAK2 signaling inside the cell.

Brooks *et al.* systematically evaluated the roles of the juxtamembrane domain (JMD) and transmembrane domain (TMD) of the hGH receptor dimer in transmitting conformational changes induced by hormone binding to the inside of the cell. A series of mutational analyses, including cysteine-scanning mutagenesis and disulfide cross-linking, coupled with a transcriptional output assay, show that the TMDs of the hGH receptor form a weak dimer in the membrane in the absence of hGH. Interestingly, addition of hGH increased JMD cysteine cross-linking, leading to constitutive activation, yet with little change in the conformation of the TMD. This suggests a larger organization in the JMD than in the TMD. The authors also observed that when each receptor extracellular domain (ECD) was replaced with a “leucine zipper”—a structural motif that functions as a dimerization domain—there was stronger receptor activation as the location of the zipper was placed closer to the TMD. This suggests that enforced dimerization of the JMD is critical for signaling and strongest in its effect when closest to the TMD. The authors further show that electrostatic

repulsion in the JMD is important for hindering basal receptor activation.

JAK2 binds to a site in the receptor ICD that is within the so-called box 1 region. A key observation made by Brooks *et al.* is that when fluorescence resonance energy transfer (FRET) sensors are placed at the carboxyl-terminal end of the JAK2 binding site, they move farther apart as the dimerizing zipper motif enforces stronger receptor signaling. The box 1 motif in the ICD is structurally linked to the TMD as part of an extended  $\alpha$  helix, thus rigidly connecting motions imparted by hormone binding a TMD “hinge” to the JAK2 binding site. Binding of hGH to the full-length receptor causes similar reduction in the FRET signal (which indicates that the FRET sensors have moved apart from each other), and this does not occur in the case of the hGH antagonist, G120R, which has a functional binding site 1, but not site 2.

JAK2 is only competent for signaling when associated with the box 1 motif in the ICD (10). Brooks *et al.* provide data suggesting that JAK2 exists in solution as a head-to-tail dimer in which the pseudokinase domain in one subunit inhibits the kinase domain of its partner. They speculate that if hormone binding results in the receptor ICDs splaying apart, this can effectively pull apart the JAK2 dimer, sliding the carboxyl-terminal kinase domains into registry. This would allow transphosphorylation

of each other and the receptor, thereby activating the receptor (see the figure) (11). The authors support this idea by showing that FRET sensors attached to the carboxyl terminus of JAK2 move closer together upon binding hGH, whereas they move further away when placed near the pseudokinase domain, as predicted. Ironically, this mechanism implies that the function of hormone binding is to separate the JAKs, not to move them together, as was the basis of the original dimerization model. Moreover, if the JAK2 proteins are expressed such that they have the same orientation to the receptor—so that their kinase domains are aligned—the receptor is constitutively active, even in the absence of hGH ligand.

The scissor model for hGH receptor activation is further supported by the authors’ detailed structural model. It explains how the inactive receptor dimer is poised for signaling and how activation relies on relieving electrostatic inhibition in the JMD and pseudokinase inhibition in JAK2. Further testing is required, and the generalities to other cytokine receptors need to be explored owing to their very diverse TMDs and JMD sequences. But like the hGH receptor, disulfide bond formation in the JMD of the erythropoietin receptor constitutively activates the receptor (12), and JAK2 tightly associates with the box 1 region of this receptor as well (13). The scissor model suggests new ways to modulate the hGH receptor. From outside the cell, one can imagine antibodies that clamp the JMD and activate the receptor. Another approach might be to activate JAK2 by disrupting the pseudokinase interactions with small molecules, while preserving kinase-kinase interactions. Clearly, this old dimer is full of new and potentially useful tricks.

## References

1. B. C. Cunningham *et al.*, *Science* **254**, 821 (1991).
2. A. M. de Vos, M. Ultsch, A. A. Kossiakoff, *Science* **255**, 306 (1992).
3. A. J. Brooks *et al.*, *Science* **344**, 1249783 (2014); 10.1126/science.1249783.
4. G. Fuh *et al.*, *Science* **256**, 1677 (1992).
5. L. S. Argetsinger *et al.*, *Cell* **74**, 237 (1993).
6. O. Livnah *et al.*, *Nat. Struct. Biol.* **5**, 993 (1998).
7. J. Gent, P. van Kerkhof, M. Roza, G. Bu, G. J. Strous, *Proc. Natl. Acad. Sci. U.S.A.* **99**, 9858 (2002).
8. S. L. Gadd, C. V. Clevenger, *Mol. Endocrinol.* **20**, 2734 (2006).
9. D. Ungureanu *et al.*, *Nat. Struct. Biol.* **18**, 971 (2011).
10. K. He *et al.*, *Mol. Endocrinol.* **17**, 2211 (2003).
11. View animation at <http://web-services.imb.uq.edu.au/waters/hgh.html>.
12. X. Lu, A. W. Gross, H. F. Lodish, *J. Biol. Chem.* **281**, 7002 (2006).
13. M. Funakoshi-Tago, S. Pelletier, H. Moritake, E. Parganas, J. N. Ihle, *Mol. Cell. Biol.* **28**, 1792 (2008).

10.1126/science.1254799

CREDIT: H. McDONALD/SCIENCE



## MATERIALS SCIENCE

# Imaging Crystallization

Preshit Dandekar and Michael F. Doherty

The invention of the atomic force microscope (AFM) (1) created a revolution in the imaging of crystal growth processes. Surface features can now be visualized and measured in three dimensions so that step heights, terrace widths, and other surface features can be measured with subnanometer-scale resolution. The current generation of commercial AFM instruments is robust and capable of angstrom-scale [and even single atom-scale (2)] resolution. During the 1990s, the AFM flow cell was introduced (3), which allows for real-time imaging as crystals grow, thereby providing insight into the time evolution of surface structure (4). On page 729 of this issue, Lupulescu and Rimer (5) report another exciting development in AFM imaging science—the ability to monitor the crystallization process in real time and under realistic growth conditions.

Understanding the mechanism of crystal growth remains an active area of research in a diversity of fields, including geology, biomineralization, catalysis, and pharmaceuticals. Classical growth mechanisms include the spiral growth model (6) and the birth-and-spread model (7). Both mechanisms assume that the growth units are individual molecules or ions that attach on monomolecular steps present on a crystal surface. Aggregative growth of oriented nanoparticle precursors is a nonclassical crystallization pathway that has been widely observed since the late 1990s

(8). In situ transmission electron microscopy images have shown that these precursors may be crystalline and that the aggregation yields single crystals (9). Lupulescu and Rimer have developed an AFM instrument capable of imaging in situ, time-resolved crystal growth under extreme conditions of temperature (up to 300°C) and pH (from 10 to 12). Also, they have overcome the challenges associated with long imaging times (~40 hours) in these difficult experiments.

Lupulescu and Rimer observed real-time crystal growth on the (010) face of silicalite-1 crystals and identified the attachment of two types of growth units: silica molecules and silica nanoparticle precursors on the zeolite crystal surface [see figure 1A of (5)]. The temporal profile of the measured height of the growth features on the surface is convincing evidence that both species are involved in the growth process. They have found that the deposition of silica molecules on the AFM tip is a major challenge associated with the in situ AFM imaging of silicalite-1 crystal growth. They verified that the error in the measurement of size of growth features due to this deposition is appreciable only for the lateral directions ( $<100>$ ) and that the height of the features that attach on the (010) crystal surface is accurately measured. The agreement between the size of the precursor particles in the solution (from x-ray scattering) and on the (010) surface (from time-resolved AFM measurements) demonstrates that the precursor particles indeed attach on the crystal surface.

The attachment of precursors on the terraces of a crystal surface could affect the

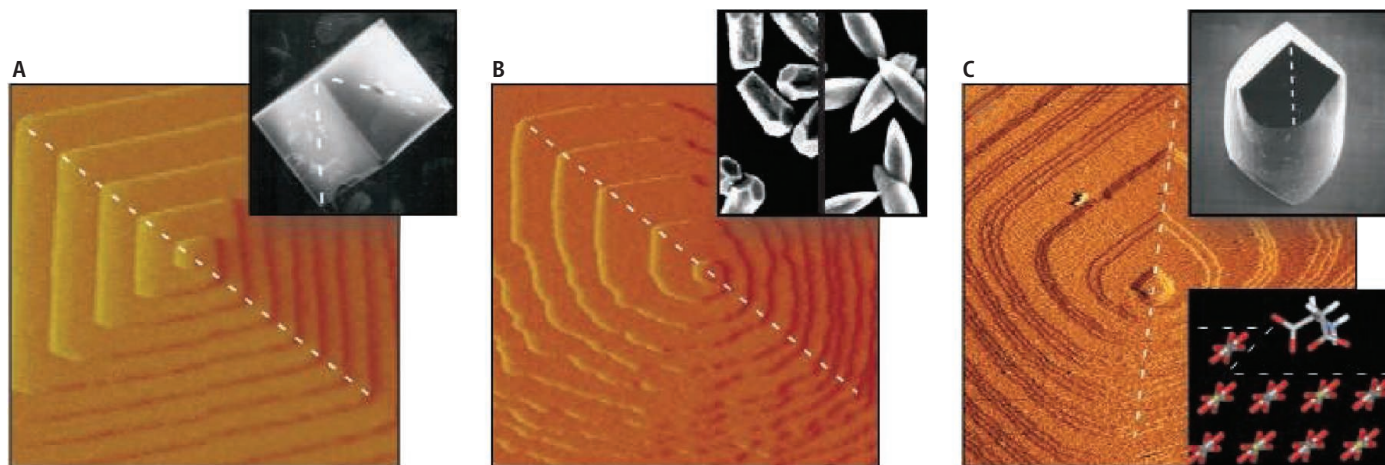
Real-time atomic force microscopy provides insights into complex processes associated with crystal growth.

growth kinetics. These nanoparticles would provide more favorable sites for individual molecules to attach onto the surface, thereby promoting growth. However, structural rearrangement of the deposited nanoparticles to match the structure of the underlying surface (5) could impede the overall growth kinetics. A mechanistic growth model for zeolite crystals such as silicalite-1 must account for these competing effects of precursor deposition.

In situ AFM imaging can elucidate the effect of impurity or additive molecules on crystal growth kinetics. These species may disrupt the crystal growth process in one or more ways (10). Time-resolved motion of the steps on crystal surfaces reveals the specific action of a particular additive species (see the figure) (11). Identification of the additive species that modify the crystal growth kinetics in the most desirable and efficient manner could lead to the rational design of crystalline materials with specific functionality.

One of the remaining mysteries in crystal growth is the mechanism by which polar crystal faces stabilize and grow (12). Polar crystals have a nonzero net electrostatic

**Watching it grow.** The effect of additive species on spiral growth and the shape of calcite crystals. Each panel shows an AFM image of spiral growth hillocks (main image) and a scanning electron microscope image of the crystal shape (inset), with dashed lines to indicate the glide plane symmetry. (A) Pure calcite. (B) Calcite plus  $Mg^{2+}$ . The inset shows crystals grown at  $Mg^{2+}:Ca^{2+}$  mole ratios of 1.5 (left) and 2.0 (right). (C) Calcite plus D-aspartic acid; a snapshot of a D-aspartic acid molecule binding to a particular step on calcite crystal surface.



Department of Chemical Engineering, University of California Santa Barbara, Santa Barbara, CA 93106, USA. E-mail: mfd@engineering.ucsb.edu

dipole moment in their unit cell (e.g., wurtzite structure) that results in asymmetric crystal shapes. Polar crystal faces find application in semiconductors (e.g., zinc oxide) and catalysis. It has been impossible to observe the growth of such crystals in real time under typical synthesis conditions ( $T \sim 100^\circ\text{C}$ ), but now there is reason for optimism that such important crystallizations can be tempted to reveal their secrets.

## References

1. G. Binnig, C. F. Quate, Ch. Gerber, *Phys. Rev. Lett.* **56**, 930 (1986).
2. G. Meyer, N. M. Amer, *Appl. Phys. Lett.* **56**, 2100 (1990).
3. S. Manne *et al.*, *Science* **251**, 183 (1991).
4. J. D. Rimer *et al.*, *Science* **330**, 337 (2010).
5. A. I. Lupulescu, J. D. Rimer, *Science* **344**, 729 (2014).
6. W. K. Burton, N. Cabrera, F. C. Frank, *Phil. Trans. Roy. Soc. A* **243**, 299 (1951).
7. M. Ohara, R. Reid, *Modeling Crystal Growth Rates from Solution* (Prentice-Hall, Upper Saddle River, NJ, 1973).
8. R. L. Penn, J. F. Banfield, *Science* **281**, 969 (1998).
9. D. Li *et al.*, *Science* **336**, 1014 (2012).
10. N. Cabrera, D. Vermilyea, *Growth and Perfection of Crystals*, R. Doremus, B. Roberts, D. Turnbull, Eds. (Wiley, New York, 1958).
11. J. J. De Yoreo, P. M. Dove, *Science* **306**, 1301 (2004).
12. J. Goniakowski *et al.*, *Rep. Prog. Phys.* **71**, 016501 (2008).

**Acknowledgments:** Financial support was provided by the Dow Chemical Company through a doctoral fellowship (P.D.) and by the National Science Foundation through CBET-1159746 (M.F.D.).

10.1126/science.1254259

## MATERIALS SCIENCE

# Toward Recyclable Thermosets

Timothy E. Long

Recycling codes on plastic food and beverage packaging serve to guide consumers' daily decisions about the disposal of used packaging. However, technological obstacles remain for the recycling of more sophisticated polymeric packaging, ranging from multilayered food packaging to composite polymeric materials for electronic packaging. Moreover, many electronic devices contain heat-resistant, chemically stable polymers called thermosets that are not amenable to conventional collecting and recycling. On page 732 of this issue, García *et al.* (1) report a crucial step toward recyclable thermosets with the synthesis of ductile, insulating, temperature-resistant, and chemically inert thermosets that can be returned to their monomeric state through a pH trigger.

Thermoplastics are polymers that become pliable or moldable at elevated temperatures, but return to a solid state when cooled. These polymers can thus be readily processed or reprocessed upon heating, and are therefore widely used in food and beverage packaging. In contrast, thermosets are chemically crosslinked polymers, networks, or gels with chemical bonds between chains that do not thermally dissociate, even at high temperature. They are ideal for high-temperature electronic or automotive applications, but cannot be reprocessed or recycled either by melting or by solution processing. Many researchers are now challenging this classical definition with concepts of recyclable networks, reworkable encapsulants, reversible gels, self-healing polymeric coatings, and stimuli-responsive polymeric structures (2, 3). The goal is to create reversible thermosets

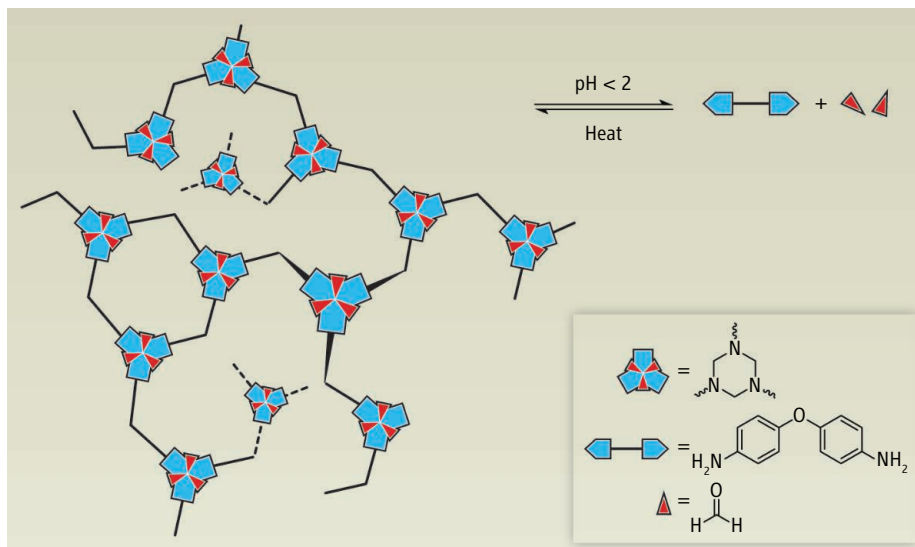
that combine the desirable thermal and chemical stability of conventional thermosets with recyclability and reprocessability.

For several decades, the microelectronics, aerospace, and automotive industries have used a relatively small number of thermally stable and mechanically ductile thermosets. A nitrogen-containing heterocycle exemplifies a desirable chemical linkage in polymeric thermosets due to thermal stability and restricted rotation that provides high glass transition temperatures (4, 5). However, many polymerization processes for thermosets require high temperatures and long reaction times. Researchers are therefore trying to develop chemical processes that require less energy. The microelectronics and automotive industries also demand higher performance, including increased modulus, improved

toughness, and flame resistance. Use of existing monomers in new synthetic methods can also lead to novel compositions with desirable properties.

García *et al.*'s novel thermoset-forming reaction is based on the well-established reactivity of monofunctional aromatic and aliphatic amines with paraformaldehyde. A monofunctional amine in combination with paraformaldehyde readily forms a low-molar mass triazine. Use of a difunctional amine enabled the in situ formation of a triazine cross-link point that is the basis of the polymeric network of García *et al.*'s thermosets (see the figure). The use of a multifunctional amine for making high-performance triazine polymeric networks is unprecedented.

The authors first created a family of low-temperature, hemiaminal-based thermosets,



**Reversible thermoset plastics.** García *et al.* show that the formation of a trifunctional cross-link point through reaction of a diamine and paraformaldehyde leads to a thermally stable and mechanically ductile thermoset. Low pH triggers the reversal of the thermoset architecture to the corresponding monomers.

Department of Chemistry, Macromolecules and Interfaces Institute, Virginia Tech, Blacksburg, VA 24061, USA. E-mail: telong@vt.edu

CREDIT: K. ZHANG/VIRGINIA TECH



which are chemically and thermally stable to modest temperatures (<150°C). Treatment with an acidic (pH = 2) aqueous solution leads to dissociation, allowing recovery of the starting materials. Heating of the hemiaminal-containing thermoset led to a second class of higher-temperature triazine thermosets. The tensile properties of these triazine thermosets exceed conventional polyimide benchmarks; as for the low-temperature thermosets, they quantitatively reverse to the starting diamine monomer upon treatment with an acidic solution.

In the search for processable and reprocessable thermosets, other researchers have combined thermoreversible physical cross-linking with nanoscale phase separation (6). For example, Meijer *et al.* have created supramolecular reversible thermosets based on temperature-sensitive multiple hydrogen bonding (7). Rowan *et al.* have used noncovalent interactions of metals with polymer end groups to create thermoreversible thermosets with potential applications in sensors, scratch-resistant coatings, and reversible adhesives (8).

However, these earlier studies use temperature as the stimulus for reversibility. Given that temperatures vary in many commercial applications and that thermosets must be able to withstand very high temperatures in the microelectronics, transportation, and aerospace industries, a thermo-responsive thermoset is not always suitable. A covalent network as defined by García *et al.* provides a more thermally stable structure; the challenge is to preserve the thermal stability while allowing for reversibility. Alternatives include photo-reversible thermosets (9) and thermosets that are reversible upon the application of mechanical stress (10, 11). García *et al.*'s demonstration of pH reversibility of a class of thermosets with mechanical properties and thermal stabilities that exceed traditional benchmarks is an important advance.

Synthetic strategies for making thermally stable thermosets for high-performance applications often require high temperatures and complex synthetic methods. The search for thermally stable bond-forming reactions at lower temperatures is aided by computational modeling analysis (12). García *et al.* use density functional theory (DFT) to understand the thermodynamics of cyclization and hexahydrotriazine formation. DFT calculations also elucidated the role of water and dipolar aprotic solvents in the stabilization of the intermediate. The synthetic strategies involve reactions that occur quickly (10 to 30 min) at modest temperatures (50° to 185°C), with water as a by-product.

Polymeric materials will continue to play a role in addressing the global challenges of our times, from energy generation and storage to novel therapeutics and water scarcity (13). However, technological progress should go hand in hand with minimizing negative impact on the environment. The emerging genre of stimuli-responsive chemical recycling—exemplified by the pH-dependent reversibility of García *et al.*'s thermosets—allows recovery of the original starting monomers in sufficient purity for conversion to a new product. Furthermore, thermosets with improved thermomechanical properties also enable longer product lifetimes and may require less plastic to achieve similar performance. Integration of nanoscale fillers may further enhance properties without compromising reversibility. Future research should aim to demonstrate quantitative thermoset reversal and isolation of pure monomers, identify more environmentally friendly

monomers, and confirm that recycled monomers can be used in subsequent thermosets without compromising performance.

## References

1. J. M. García *et al.*, *Science* **344**, 732 (2014).
2. T. Aida, E. W. Meijer, S. I. Stupp, *Science* **335**, 813 (2012).
3. D. Chen, H. Liu, T. Kobayashi, H. Yu, *J. Mater. Chem.* **20**, 3610 (2010).
4. J. L. Hedrick, J. W. Labadie, W. Volksen, J. G. Hilborn, *Adv. Polym. Sci.* **147**, 61 (1999).
5. J. E. McGrath, D. L. Dunson, S. J. Mechem, J. L. Hedrick, *Adv. Polym. Sci.* **140**, 61 (1999).
6. D. G. Bucknall, H. L. Anderson, *Science* **302**, 1904 (2003).
7. R. P. Sijbesma *et al.*, *Science* **278**, 1601 (1997).
8. J. R. Kumpfer *et al.*, *Macromolecules* **45**, 473 (2012).
9. G. Kaur, P. Johnston, K. Saito, *Polym. Chem.* **5**, 2171 (2014).
10. C. M. Kingsbury *et al.*, *J. Mater. Chem.* **21**, 8381 (2011).
11. D. A. Davis *et al.*, *Nature* **459**, 68 (2009).
12. C. M. Breneman *et al.*, *Adv. Funct. Mater.* **23**, 5746 (2013).
13. D. F. Sanders *et al.*, *Polymer (Guildf.)* **54**, 4729 (2013).

10.1126/science.1254401

## RNA EVENTS

# Cas9 Targeting and the CRISPR Revolution

Uncovering how an RNA-protein molecular scalpel targets DNA will advance our ability to engineer genomes.

Rodolphe Barrangou

The ability to add, remove, or change DNA sequences is essential to studies that investigate the genetic underpinning of phenotypic traits. With its unprecedented efficiency and stunning ease of use, DNA editing technology based on the prokaryotic CRISPR (clustered regularly interspersed short palindromic repeats)–Cas9 system is completely revolutionizing genome engineering. In little more than a year, CRISPR–Cas9 editing has been implemented in a multitude of model organisms and cell types (1) and has already started to supplant incumbent genome editing technologies, such as TALENs (transcription activator-like effector nucleases) and ZFNs (zinc finger nucleases).

The CRISPR–Cas9 editing technology is derived from the CRISPR adaptive immune system of bacteria (2) and consists of an RNA-guided endonuclease (Cas9 being one example) harnessed for specific targeting and cleavage of DNA by means of a single program-

mable RNA molecule (3). Following precise DNA cleavage of the sequence of interest, mutations are surgically inserted using error-prone DNA repair mechanisms or designed templates, generating altered genotypes (4–6). To further harness this versatile technology platform for scalable genome editing, transcriptional control, DNA labeling, and so forth, as well as to minimize possible off-target effects, a more precise molecular understanding of how Cas9 targets and interacts with DNA is required. Recent work by Sternberg *et al.* (7) revealed the molecular mechanisms by which the endonuclease Cas9 interrogates DNA, providing a basis for improving the specificity and efficiency of CRISPR technologies for genome editing and beyond.

In the CRISPR–Cas9 adaptive immune system, the Cas9 endonuclease is guided by an RNA duplex (8), including the CRISPR RNA (crRNA), which directs sequence-specific double-stranded DNA (dsDNA) cleavage (9). After R-loop formation, where the crRNA displaces one of the DNA strands and forms a short DNA–RNA segment with the other DNA strand, the HNH nuclease

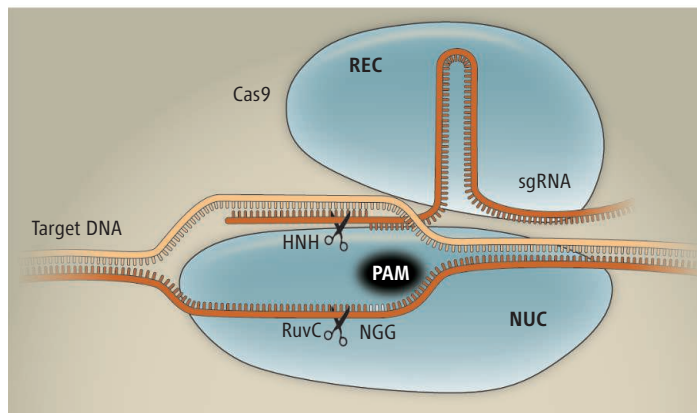
Department of Food, Bioprocessing and Nutrition Sciences,  
North Carolina State University, Raleigh, NC 27695, USA.  
E-mail: rbarran@ncsu.edu

domain of Cas9 nicks the DNA strand complementary to the guide RNA, while the RuvC domain cleaves the displaced DNA strand, yielding a double-strand break (3, 10) (see the figure). Specificity is determined by the crRNA sequence, which targets complementary DNA, flanked by a short proto-spacer adjacent motif (PAM). A single guide RNA (sgRNA) molecule can be engineered to replace the native RNA duplex (3), and the resulting sgRNA-Cas9 system can be readily deployed for sequence-specific DNA cleavage of virtually any sequence of interest (4–6), because the three-nucleotide NGG PAM consensus associated with the widely used *Streptococcus pyogenes*

Cas9 (SpyCas9) is present at high frequency in random DNA sequences. Yet how Cas9 specifically and efficiently localizes a single DNA target in the vast maze of a genome has remained enigmatic.

Using single-molecule and bulk biochemical experiments, Sternberg *et al.* have unraveled the molecular mechanisms by which Cas9 programmed with sgRNA scans DNA molecules, localizes the cleavage target, and specifically interacts with PAM sequences. Using tethered “curtains” of single DNA molecules together with fluorescence microscopy, they visualized labeled Cas9 interacting with phage DNA. Cas9 programmed with sgRNA complementary to various sites in the tethered DNA localized almost exclusively at the predicted target sites. Facilitated diffusion by sliding along the DNA was not important for specific Cas9-DNA interactions; rather, targets were identified through three-dimensional collisions between Cas9 and DNA, with PAM distribution and density playing a critical role in both Cas9 localization and binding lifetimes. PAM binding by Cas9 is long-lived in the presence of the target sequence, whereas the interaction is transient with rapid dissociation in the absence of target sequences. The critical role of the PAM in initiating the interaction between DNA and Cas9 is best illustrated by the absence of binding to substrates that contain the target sequence but lack a flanking PAM. This is consistent with short-lived Cas9 interactions with molecules that have high PAM densities but lack sgRNA complementarity.

Once DNA interrogation is initiated by Cas9 at the PAM site, the RNA guide is unzipped and inserted into the DNA duplex



**Targeting a molecular scalpel.** The CRISPR-Cas9 nuclease, programmed with sgRNA, specifically targets a short DNA sequence “tag” (the PAM) and unzips DNA complementary to the sgRNA to create a sgRNA–target DNA heteroduplex, triggering R-loop formation. Two nuclease domains (RuvC, HNH) each nick one DNA strand, generating a double-strand break. Structurally, the Cas9 recognition (REC) domain interacts with the sgRNA, while the nuclease (NUC) lobe drives interaction with the PAM and target DNA.

to directionally unwind the complementary dsDNA double helix toward the distal end of the target sequence, creating a sgRNA–target DNA heteroduplex and triggering R-loop formation. Following target dsDNA destabilization at the PAM, a stretch of several complementary bases between the sgRNA and the target DNA is critical to ensure sustainable unwinding and heteroduplex extension. Once established, this interaction catalytically activates the two nickase domains of the endonuclease to specifically generate a double-strand break in the target DNA molecule, exactly three nucleotides into the sequence homologous to the guide.

Until recently, the crRNA sequence was thought to be all-important for Cas9 targeting of complementary DNA. Sternberg *et al.* have now established that PAMs are the key drivers of target DNA interrogation, helping to initiate the interaction, and that the sgRNA subsequently directs cleavage only of complementary DNA sequences. Results indicate that Cas9 remains bound to both ends of the cleaved DNA molecules, perhaps extending the lifetime of cleaved termini and allowing recruitment of the DNA repair machinery.

Recent structural studies have shed light on the detailed molecular interactions between Cas9 and the sgRNA, as well as Cas9 and the target DNA (11, 12). Cas9 has a distinct bilobed architecture, with a sgRNA-binding target recognition lobe and a nuclease domain, which is hypothesized to carry the PAM interaction domain. The sgRNA–target DNA heteroduplex is formed in the groove located between these two lobes. The structural understanding of these interactions will facilitate structure-based rational design of optimal

guides by defining the elements that drive PAM specificity, binding fidelity, and mismatch tolerance for various Cas9 protein families, as well as the similarities and differences between different CRISPR systems.

An intriguing question is whether there are nucleotide preferences within PAM sequences that could optimize Cas9 efficiency and/or specificity and thereby minimize potential off-target cleavage. This problem has already been partially addressed by using multiplexing, dual nicking guides, and short sgRNAs (13). The study by Sternberg *et al.* indicates that off-target concerns should be exclusively limited to sites homologous to sgRNA sequences that are flanked by a PAM.

Major factors underlying the CRISPR-Cas9 genome editing revolution include the compactness, simplicity, and targeting flexibility afforded by this system (13). The implications for enhanced Cas9 targeting specificity and binding efficiency are exciting and establish a basis for the further optimization of the Cas9-sgRNA system and the development of next-generation CRISPR tools. Future studies will determine the potential of various natural or engineered Cas9 proteins, sgRNA molecules, and their respective PAM sequences for increased sequence recognition specificity and DNA binding efficiency, and possibly the generation of short Cas9 homologs for convenient packaging and delivery. Notwithstanding the CRISPR craze of 2013 (1), this dynamic field is off to an effervescent start for 2014, and these latest findings open new engineering avenues for CRISPR-Cas9 and set the stage for further applications in synthetic biology, translational research, and next-generation genome engineering.

## References

1. E. Pennisi, *Science* **341**, 833 (2013).
2. R. Barrangou *et al.*, *Science* **315**, 1709 (2007).
3. M. Jinek *et al.*, *Science* **337**, 816 (2012).
4. L. Cong *et al.*, *Science* **339**, 819 (2013).
5. P. Mali *et al.*, *Science* **339**, 823 (2013).
6. W. Jiang *et al.*, *Nat. Biotechnol.* **31**, 233 (2013).
7. S. H. Sternberg *et al.*, *Nature* **507**, 62 (2014).
8. E. Deltcheva *et al.*, *Nature* **471**, 602 (2011).
9. J. E. Garneau *et al.*, *Nature* **468**, 67 (2010).
10. G. Gasiunas, R. Barrangou, P. Horvath, V. Siksnys, *Proc. Natl. Acad. Sci. U.S.A.* **109**, E2579 (2012).
11. M. Jinek *et al.*, *Science* **343**, 6176 (2014).
12. H. Nishimasu *et al.*, *Cell* **156**, 935 (2014).
13. J. D. Sander, J. K. Joung, *Nat. Biotechnol.* **32**, 347 (2014).

10.1126/science.1252964





READ THE FULL ARTICLE ONLINE  
<http://dx.doi.org/10.1126/science.1246843>

Advances in biotechnology and chemistry hold promise for greatly expanding the scope of products derived from lignin.

# Lignin Valorization: Improving Lignin Processing in the Biorefinery

Arthur J. Ragauskas,\* Gregg T. Beckham, Mary J. Biddy, Richard Chandra, Fang Chen, Mark F. Davis, Brian H. Davison, Richard A. Dixon, Paul Gilna, Martin Keller, Paul Langan, Amit K. Naskar, Jack N. Saddler, Timothy J. Tschaplinski, Gerald A. Tuskan, Charles E. Wyman

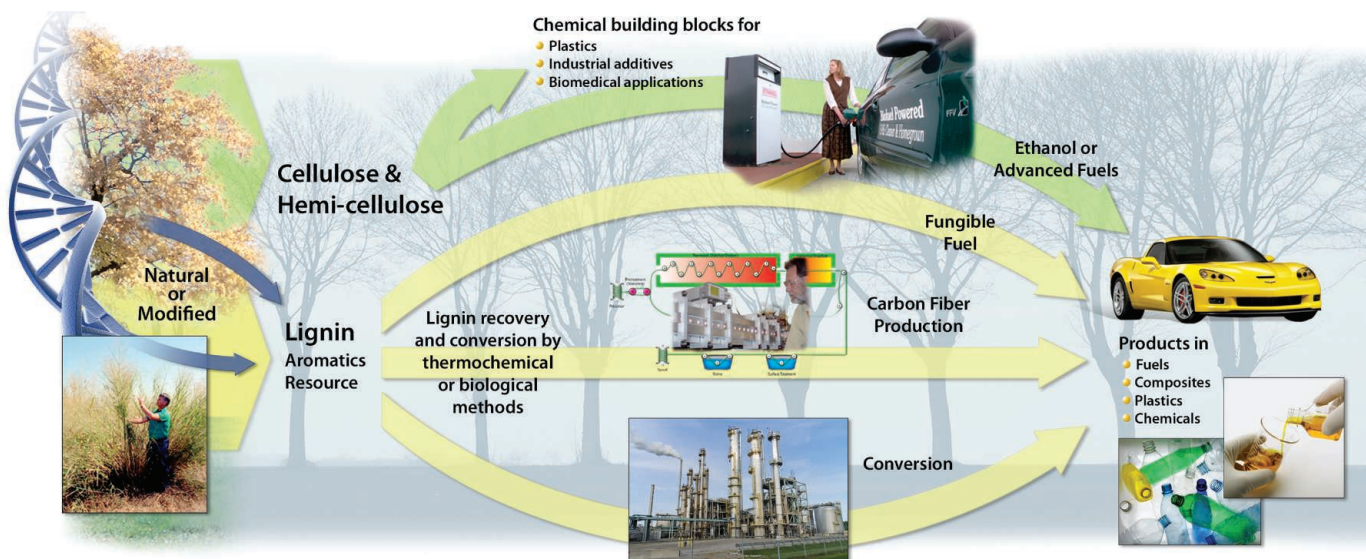


**Background:** Lignin, nature's dominant aromatic polymer, is found in most terrestrial plants in the approximate range of 15 to 40% dry weight and provides structural integrity. Traditionally, most large-scale industrial processes that use plant polysaccharides have burned lignin to generate the power needed to productively transform biomass. The advent of biorefineries that convert cellulosic biomass into liquid transportation fuels will generate substantially more lignin than necessary to power the operation, and therefore efforts are underway to transform it to value-added products.

**Advances:** Bioengineering to modify lignin structure and/or incorporate atypical components has shown promise toward facilitating recovery and chemical transformation of lignin under biorefinery conditions. The flexibility in lignin monomer composition has proven useful for enhancing extraction efficiency. Both the mining of genetic variants in native populations of bioenergy crops and direct genetic manipulation of biosynthesis pathways have produced lignin feedstocks with unique properties for coproduct development. Advances in analytical chemistry and computational modeling detail the structure of the modified lignin and direct bioengineering strategies for targeted properties. Refinement

of biomass pretreatment technologies has further facilitated lignin recovery and enables catalytic modifications for desired chemical and physical properties.

**Outlook:** Potential high-value products from isolated lignin include low-cost carbon fiber, engineering plastics and thermoplastic elastomers, polymeric foams and membranes, and a variety of fuels and chemicals all currently sourced from petroleum. These lignin coproducts must be low cost and perform as well as petroleum-derived counterparts. Each product stream has its own distinct challenges. Development of renewable lignin-based polymers requires improved processing technologies coupled to tailored bioenergy crops incorporating lignin with the desired chemical and physical properties. For fuels and chemicals, multiple strategies have emerged for lignin depolymerization and upgrading, including thermochemical treatments and homogeneous and heterogeneous catalysis. The multifunctional nature of lignin has historically yielded multiple product streams, which require extensive separation and purification procedures, but engineering plant feedstocks for greater structural homogeneity and tailored functionality reduces this challenge.



**Production of biofuels from cellulosic biomass requires separation of large quantities of the aromatic polymer lignin.** In planta genetic engineering, enhanced extraction methods, and a deeper understanding of the structure of lignin are yielding promising opportunities for efficient conversion of this renewable resource to carbon fibers, polymers, commodity chemicals, and fuels. [Credit: Oak Ridge National Laboratory, U.S. Department of Energy]

The list of author affiliations is available in the full article online.

\*Corresponding author. E-mail: [arthur.ragauskas@chemistry.gatech.edu](mailto:arthur.ragauskas@chemistry.gatech.edu)

Cite this article as A. J. Ragauskas *et al.*, *Science* **344**, 1246843 (2014). DOI: 10.1126/science.1246843

# Lignin Valorization: Improving Lignin Processing in the Biorefinery

Arthur J. Ragauskas,<sup>1\*</sup> Gregg T. Beckham,<sup>2</sup> Mary J. Biddy,<sup>2</sup> Richard Chandra,<sup>3</sup> Fang Chen,<sup>4</sup> Mark F. Davis,<sup>5</sup> Brian H. Davison,<sup>6</sup> Richard A. Dixon,<sup>4</sup> Paul Gilna,<sup>6</sup> Martin Keller,<sup>7</sup> Paul Langan,<sup>8</sup> Amit K. Naskar,<sup>9</sup> Jack N. Saddler,<sup>3</sup> Timothy J. Tschaplinski,<sup>6</sup> Gerald A. Tuskan,<sup>6</sup> Charles E. Wyman<sup>10</sup>

Research and development activities directed toward commercial production of cellulosic ethanol have created the opportunity to dramatically increase the transformation of lignin to value-added products. Here, we highlight recent advances in this lignin valorization effort. Discovery of genetic variants in native populations of bioenergy crops and direct manipulation of biosynthesis pathways have produced lignin feedstocks with favorable properties for recovery and downstream conversion. Advances in analytical chemistry and computational modeling detail the structure of the modified lignin and direct bioengineering strategies for future targeted properties. Refinement of biomass pretreatment technologies has further facilitated lignin recovery, and this coupled with genetic engineering will enable new uses for this biopolymer, including low-cost carbon fibers, engineered plastics and thermoplastic elastomers, polymeric foams, fungible fuels, and commodity chemicals.

**T**ranslational biorefinery research and development has become a near-global effort in response to a variety of drivers, including energy security, rural development, and environmental concerns. The approved Summary for Policymakers in the Intergovernmental Panel on Climate Change (IPCC) Working Group I Fifth Assessment Report report states that “Human influence on the climate system is clear. This is evident from the increasing greenhouse gas concentrations in the atmosphere, positive radiative forcing, observed warming, and understanding of the climate system.” These findings add urgency to the need to develop viable, sustainable, biorefining technologies that maximize yields of renewable fuels, chemicals materials, and biopower (1). Recent results have demonstrated that biomass conversion into biofuels can deliver a sustainable and renewable energy source for liquid transportation fuels (2–4). For

the United States alone, a recent study suggested that more than 1.3 billion tons annually of biomass could be sustainably produced from agricultural and forestry sources (5). Indeed, coupling advanced ‘biomass-conversion technologies with land-use changes could meet the nation’s need for liquid transportation fuels without affecting food, feed, and fiber production (6). Although widespread, cost-competitive biofuels production at the industrial scale must overcome multiple technical and economic challenges (7), several commercial cellulosic ethanol plants have been commissioned (8), and the first plant now generates 75 million l year<sup>-1</sup> of cellulosic ethanol in Italy (9).

Currently, most integrated biologically based biorefinery concepts comprise four major core sections: feedstock harvest and storage, pretreatment, enzymatic hydrolysis, and sugar fermentation to ethanol or other fuels (10). Lignin, the second most abundant terrestrial polymer on Earth after cellulose, is underutilized in these first-generation cellulosic projects, with about 60% more lignin generated than is needed to meet internal energy use by its combustion (11, 12). Therefore, new processes are needed that generate value-added products from lignin (13). Lignin is the only large-volume renewable feedstock that is composed of aromatics (14). The U.S. Energy Security and Independence Act of 2007 mandates the development of 79 billion liters of second-generation biofuels annually by 2022. Assuming a yield of 355 liters per dry ton of biomass, 223 million tons of biomass will be used annually, producing about 62 million tons of lignin (15). Without new product streams, the lignin produced would far exceed the current world market for lignin used in specialty products (16).

Although fundamental research has historically focused on converting lignin to chemicals,

materials, and fuels, very little of this effort has been translated into commercial practice. So what has changed to address this paradigm? In brief, research and commercialization efforts surrounding cellulosic ethanol have tilted the tables through several important developments: (i) bioengineering of lignin to modify and/or incorporate atypical components that reduce recalcitrance of the cell walls to bioprocessing and facilitate ease of recovery and conversion; (ii) advances in analytical chemistry and computational modeling that couple developments in genetic engineering of lignin to targeted physical and chemical properties; and (iii) biomass pretreatment technologies that facilitate lignin recovery and catalytic modifications that yield tailored chemical and/or physical properties.

## Lignin Biosynthesis

Lignin is derived from the radical polymerization of substituted phenyl propylene units. Figure 1 highlights the relative amounts of lignin and plant polysaccharides in several key agroenergy plants and woody resources.




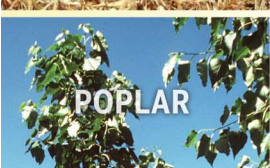
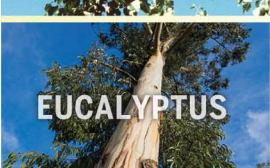

Lignin modification in plants has been extensively investigated to reduce lignin levels or to alter its structure to facilitate pulping, improve forage digestibility, or overcome recalcitrance for bioenergy feedstocks (17, 18). The biosynthetic pathway to the three classical monolignol building blocks of lignin was thought to be understood more than 10 years ago (19), although a recent revision suggests that we may still have more to learn (20, 21). Eleven recognized enzymes are involved in the conversion of L-phenylalanine to the primary monolignols, p-coumaryl alcohol, coniferyl alcohol, and sinapyl alcohol that generate the hydroxyphenyl (H), guaiacyl (G), and syringyl (S) lignin subunits, respectively (Fig. 2), and most of these enzymes have been targeted for down-regulation to generate plants with reduced lignin levels (22–24). Lignin levels can also be effectively reduced by targeting pathways to precursors for monolignol biosynthesis, such as C1 metabolism to supply methyl groups (25), manipulation of transcription factors (26), or introduction of engineered enzymes that generate monolignol analogs incapable of polymerization (27). In many cases, the digestibility or saccharification potential of biomass has been considerably enhanced (28), sometimes at the expense of plant growth (29–31). In some studies, reduction of lignin by ~50% or less from the wild-type levels has made pretreatment unnecessary for efficient saccharification (32).

Gymnosperm lignins lack S units and, as a result, are generally more branched than the classical G/S-rich lignin of angiosperms, which are rich in β-O-aryl ether linkages and cross-linked to cell wall polysaccharides via coupling of feruloylated xyans to lignin or by nucleophilic addition of cell wall sugars to lignin quinone-methide intermediates yielding ether-linked lignin carbohydrate linkages (33). Ferulates and

<sup>1</sup>BioEnergy Science Center, School of Chemistry and Biochemistry, Institute of Paper Science and Technology, Georgia Institute of Technology, Atlanta, GA 30332, USA. <sup>2</sup>National Bioenergy Center and National Advanced Biofuels Consortium, National Renewable Energy Laboratory (NREL), Golden, CO 80402, USA. <sup>3</sup>Department of Wood Science, University of British Columbia, Vancouver, BC V6T 1Z4, Canada. <sup>4</sup>BioEnergy Science Center, Department of Biological Sciences, University of North Texas, Denton, TX 76203, USA. <sup>5</sup>BioEnergy Science Center and National Advanced Biofuels Consortium, National Renewable Energy Laboratory, Golden, CO 80402, USA. <sup>6</sup>BioEnergy Science Center, Biosciences Division, Oak Ridge National Laboratory (ORNL), Oak Ridge, TN 37831, USA. <sup>7</sup>Energy and Environmental Science Directorate, Oak Ridge National Laboratory, Oak Ridge, TN 37831, USA. <sup>8</sup>Biology and Soft Matter Division, Oak Ridge National Laboratory, Oak Ridge, TN 37831, USA. <sup>9</sup>Materials Science and Technology Division, Oak Ridge National Laboratory, Oak Ridge, TN 37831, USA. <sup>10</sup>BioEnergy Science Center, Center for Environmental Research and Technology and Department of Chemical and Environmental Engineering, University of California, Riverside, CA 92507, USA.

\*Corresponding author. E-mail: arthur.ragauskas@chemistry.gatech.edu



Plant resource	% Hemicellulose	% Cellulose	% Lignin*
 MISCANTHUS	24-33	45-52	9-13
 SWITCHGRASS	26-33	37-32	17-18
 CORN STOVER	31	37	18
 POPLAR	16-22	42-48	21-27
 EUCALYPTUS	24-28	39-46	29-32
 PINE	23	46	28

\*Typical aromatic polymer containing:

**Syringyl** C

COc1cc(Cc2cc(C)cc(C)c2)c(O)c1

**Guaiacyl** C

COc1cc(Cc2cc(C)cc(C)c2)cc(O)c1

**Hydroxyphenyl**

Oc1cc(Cc2cc(C)cc(C)c2)cc(O)c1

Depending on the bioresource and isolation methodology, molecular weights for native lignin have been reported from 78,400 [in spruce (118)] to 8300 [in Miscanthus (119)] g mol<sup>-1</sup>, which are derived from C9 monolignols as described in Fig. 2.

**Fig. 1. Typical biomass constituents for select plant resources.** Information for miscanthus is from (120); switchgrass, (121); corn stover, (122); poplar, (123); eucalyptus, (124); pine, (125). [Photo credits: R. Kaltschmidt, Lawrence Berkeley National Laboratory, DOE (eucalyptus); Oak Ridge National Laboratory, DOE (all other photos)]

coumarates are particularly abundant in the cell walls of grasses (34). These lignin properties contribute to recalcitrance by hindering the accessibility of cellulose microfibrils to microorganisms and enzymes but also affect coproduct value. Interruption of the monolignol pathway can alter the H/G/S ratios (35) and reduce the degree of polymerization to benefit lignin removal during pretreatment (36). Furthermore, studies on both natural and engineered lignins have demonstrated that lignin biosynthesis, and therefore structure, is more adaptable than originally believed, with variations tolerated in both the aromatic ring and side chain. For example, by up-regulating ferulate-5-hydroxylase (F5H) (Fig. 2), the entry point to S lignin biosynthesis, while simultaneously down-regulating the enzyme that O-methylates the product of F5H, *Arabidopsis* can be generated with the bulk of the lignin as 5-hydroxyguaiacyl

(5HG) units (Fig. 2, structure B) (37), and this approach would appear to be widely applicable. Such lignins have recently been shown to occur naturally in the seed coats of a limited number of species of cacti (38), and trace levels of 5HG units likely occur in lignins of perennial angiosperms. By restoring growth to plants harboring a loss-of-function mutation in the 4-coumaroyl shikimate 3'-hydroxylase gene (Fig. 2) as a result of disrupting components of the Mediator complex, it was possible to recover *Arabidopsis* plants in which the lignin was essentially comprised of only H units (21).

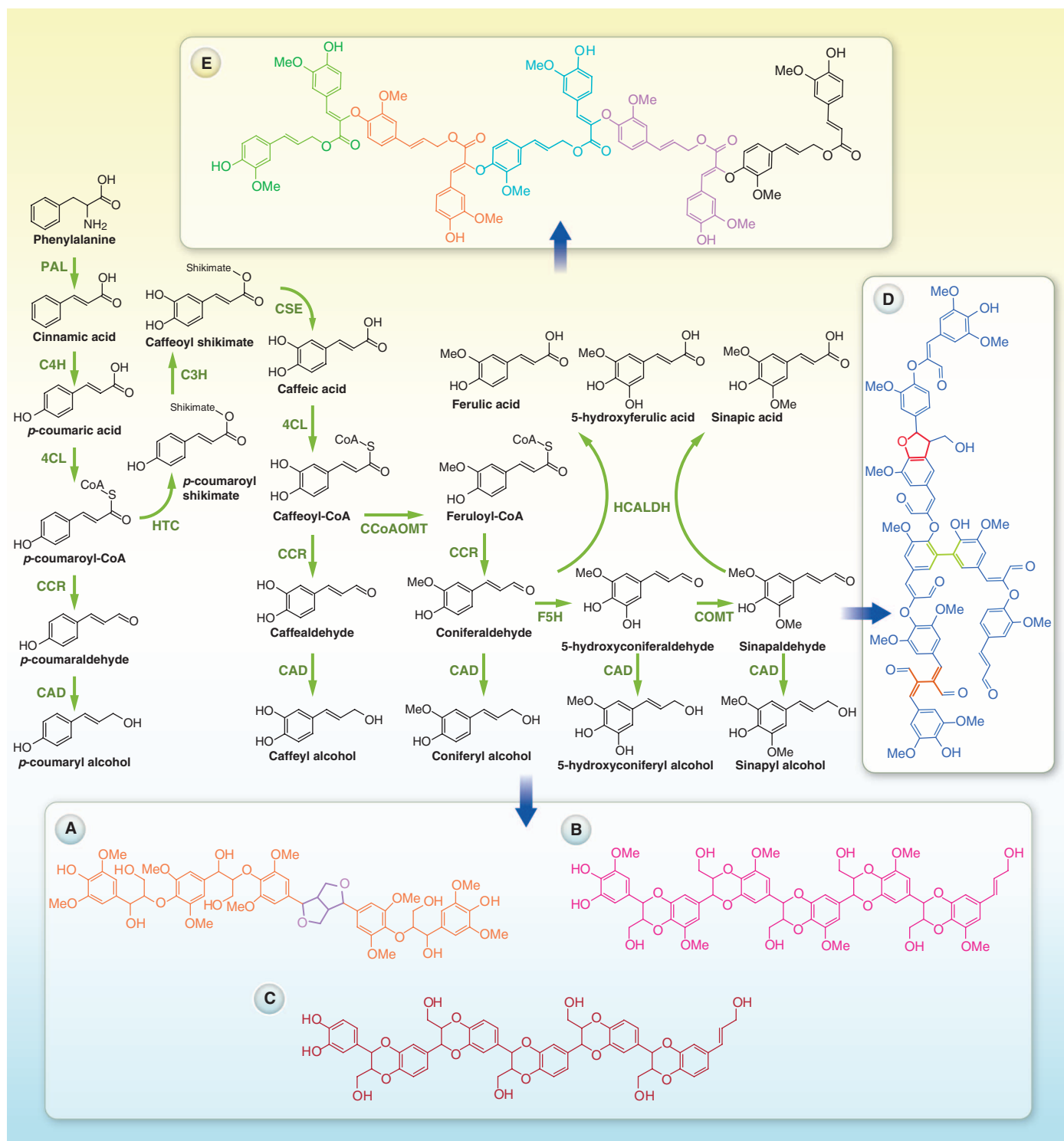
The seed coats of a larger number of unrelated and relatively exotic plant species, both monocots and dicots, contain a lignin comprising only catechyl alcohol units that are completely non-methylated and form a linear homopolymer (Fig. 2, structure C) (39, 40). In species examined

so far in which this C lignin coexists with G/S lignin, it is not attached to the classical lignin polymer (41). Down-regulation of cinnamyl alcohol dehydrogenase results in an increased aldehyde signature in lignin (42, 43), and mutants of barrel medic (*Medicago truncatula*), in which the cinnamyl alcohol dehydrogenase 1 (CADI) gene has been disrupted, contain lignin that is almost exclusively composed of hydroxycinnamaldehydes rather than hydroxycinnamyl alcohol units (Fig. 2, structure D) (44), suggesting that monolignol side chains can exhibit variation without seriously compromising the lignification process. Unnatural monomers can also be introduced that will result in formation of more cleavable interunit bonds (Fig. 2, structure E) (45). Genetic engineering to incorporate unnatural lignin monomers with shortened side chains (40) reduces the degree of polymerization and facilitates biomass processing. An alternative approach was recently reported by Wilkerson *et al.* (46) whereby coniferyl ferulate feruloyl-coenzyme A (CoA) monolignol transferase was expressed in poplar. This transformation facilitated the incorporation of monolignol ferulate conjugates into lignin, which yields lignin with elevated ester linkages that are predisposed to mild alkaline depolymerization.

This flexibility in lignin monomer composition is potentially useful for reducing recalcitrance, enhancing extraction, and developing lignin as a high-value coproduct. For example, unlike the G lignin found in gymnosperms with complex interunit linkages, predominantly S lignin molecules engineered by overexpression of F5H (Fig. 2, structure A) have fewer interunit linkage types, facilitating separation of lignin from biomass and significantly reducing recalcitrance (47).

To date, linear C lignin has only been reported in seed coats. Simultaneous mutations in the two monolignol O-methyltransferases that should theoretically accumulate the precursor for formation of catechyl alcohol units do not lead to substantial accumulation of C lignin in stems of transgenic plants; rather, the plants are dwarfed, fail to develop properly, and contain mainly H lignin (48). The presence of naturally high levels of C lignin in *Jatropha curcas* seed coats (39), a high volume by-product of biodiesel production from the seed oil of this species, suggests a near-term resource for exploitation of this polymer.

Further development of modified lignins as feedstocks for industrial products will require a high level of production of such lignins as coproducts in lignocellulosic bioenergy crops. Considerable variation in lignin content exists in natural populations (49), but most attempts to increase lignin levels in plants by simply overexpressing one or more enzymes in the monolignol pathway have been unsuccessful. In fact, in an association study of 1100 sequenced black cottonwood (*Populus trichocarpa*) genotypes, representing the main geographic distribution of the species, none of the extreme variants in lignin



**Fig. 2. Pathways for the biosynthesis of monolignols, recently discovered nonclassical lignins, and modified lignin structures that can be obtained through genetic engineering.** The enzymatic steps (green arrows) are catalyzed by PAL, L-phenylalanine ammonia-lyase; C4H, cinnamate 4-hydroxylase; 4CL, 4-coumarate:CoA ligase; CCR, cinnamoyl-CoA reductase; CAD, cinnamyl alcohol dehydrogenase; HCT, hydroxycinnamoyl CoA:shikimate/ quinate hydroxycinnamoyl transferase; C3'H, 4-coumaroyl shikimate 3-hydroxylase; CCoAOMT, caffeoyl-CoA 3-O-methyltransferase; COMT, caffeic acid/5-hydroxyconiferaldehyde 3-O-methyltransferase; CSE, caffeoyl shikimate esterase; F5H, ferulate/coniferaldehyde 5-hydroxylase. After transport of

monolignols to the apoplast, polymerization (blue arrows) is catalyzed by laccases (essential for initiation of polymerization *in vivo*) and peroxidases. The different lignin structures (showing only portions of the complete polymers) are A, all syringyl (S) lignin from poplar (*Populus*) overexpressing F5H; B, all 5-hydroxyguaiacyl lignin from poplar overexpressing F5H and down-regulated in COMT; C, all catechyl lignin (C lignin) from the seed coats of species within families including the Cactaceae, Cleomaceae, and Orchidaceae; D, lignin constructed from hydroxycinnamaldehydes, as found in the *M. truncatula cad-1* mutant; E, a hypothetical ester-linked linear lignin. Me, methyl group.



content, S/G ratio, or degree of polymerization contained naturally occurring mutations in the 11 enzymes of the lignin biosynthetic pathway (50). Genes controlling lignin content, molecular weight, and composition include copper transporters, vesicular trafficking genes, shikimate pathway genes, and transcription factors. Similarly, several independent mutations exist in the model species *Arabidopsis thaliana*, mostly in genes encoding transcription factors that lead to ectopic lignin deposition (51, 52). Mining natural lignin variants within existing bioenergy crops may reveal further variants in lignin composition that will favorably impact lignin as a primary biofeedstock, allowing for generation of extreme variants with unique chemical composition and physical properties that can be industrially exploited. Given the plasticity of the lignin biosynthetic pathway, unique lignins can be expected to be common rather than exceptional. Alternatively, ectopic lignin production, particularly in pith tissue that neither provides mechanical support nor enables vascular function, might facilitate the plant's accumulation of forms of lignin optimized as coproducts. However, that approach will not functionally replace classical lignins, thus allowing the tolerance of lignin for compositional diversity to be more fully exploited. Strategies have been reported for activating lignification in pith tissues in dicotyledonous plants through repression of transcription factors (53).

Two factors are critical for realizing the value of lignin in the biorefinery: ease of extraction of a lignin stream, which is generally facilitated by manipulations that reduce cross-linking to other cell wall polymers, and a structure that facilitates downstream processing, as to be discussed.

### Lignin Characterization

The ability to genetically engineer new lignin structures and control lignin deposition in plants has developed in parallel with powerful new methods for imaging lignin and analyzing its chemical structure. For example, coherent anti-Stokes Raman scattering (CARS) provides a label-free method for chemical imaging of lignin with greatly enhanced sensitivity over state-of-the-art confocal Raman scattering microscopy at a spatial resolution of about 200 nm (54). Although not as sensitive as CARS, time-of-flight secondary ion mass spectrometry (ToF-SIMS) spectral imaging can provide lignin chemical distribution maps for intact and processed biomass samples (55). Select ion monitoring in ToF-SIMS experiments makes it readily possible to visualize the distribution of S and G units in plant cross sections (56) within a single cell wall of *P. trichocarpa*. Alternatively, lignification in *A. thaliana* and *Pinus radiata* has been studied by using fluorescence-tagged monolignol analogs that penetrate plant tissue and incorporate into cell wall lignin to reveal insights into lignin deposition (57). Immunological techniques for lignin analysis have also been devel-

oped such that monoclonal antibodies can be used to detect phenylcoumaran and resinol-like structures (58) in biomass. Although still early in development, mode-synthesizing atomic force microscopy (AFM) promises to combine the analytical resolution of AFM with spectroscopy (59).

Structural analysis of lignin has become almost a subdiscipline of its own, with several textbooks written on the topic (60). One of the most promising high-throughput methods for lignin analysis is pyrolysis molecular beam mass spectrometry, which requires minimal sample amounts and routinely provides analysis of hexose and pentose sugars, lignin content, and S/G ratios (53). Structural analysis of interunit linkages of lignin is often accomplished by using advanced one- and two-dimensional (2D) nuclear magnetic resonance (NMR) (61). Likewise, detection of lignin-carbohydrate complexes increasingly relies on NMR methodologies (62). Whole-cell NMR techniques using the resolving power of 2D NMR to make structural assignments and relative signal intensity measurements have replaced the more laborious methodology that required preisolation of the lignin (63). Selective chemical fragmentation of lignin by thioacidolysis or derivatization followed by reductive cleavage and gas chromatography-mass spectrometry (GC-MS) analysis has been equally informative at identifying the main interunit linkages of lignin (64). This methodology is especially attractive for sample-size-limited lignin-related material. Regardless of the methodologies used, critically important detailed sequencing of extended interunit linkage frequencies (65, 66) and lignin carbohydrate complexes (67, 68) remains challenging.

Neutron scattering represents an emerging complementary approach to characterize lignin's structural properties. In particular, small-angle neutron scattering (SANS) provides structural information over the nm- to  $\mu\text{m}$ -length scale range, which can be interpreted by computational methods to provide an atomic-level predictive understanding of physical properties. For example, large computational atomistic simulations of models of the plant cell wall, informed by SANS, have revealed some of the fundamental physical processes involved in the phase separation of lignin from other plant matrix polymers and subsequent lignin aggregation during various types of acidic thermal treatments of biomass (69). Molecular dynamics simulations indicated that low-temperature lignin collapse is thermodynamically driven by an increase in translational entropy and solvation effects (70). The temperature dependence of the structure and dynamics of individual softwood lignin polymers was examined by using extensive molecular dynamics simulations. Lignin was found to transition from glassy, compact to mobile, extended states at temperatures above 150°C. This result is consistent with in situ SANS experiments showing lignin phase separation and aggregation to occur during the heating phase of pretreatment

(69, 71). Computational modeling offers complementary insights to advanced experimental approaches. These computational models represent a predictive tool that can help guide changes to biomass and pretreatment processes to improve the properties of extracted lignin and accelerate its separation.

### Lignin Recovery

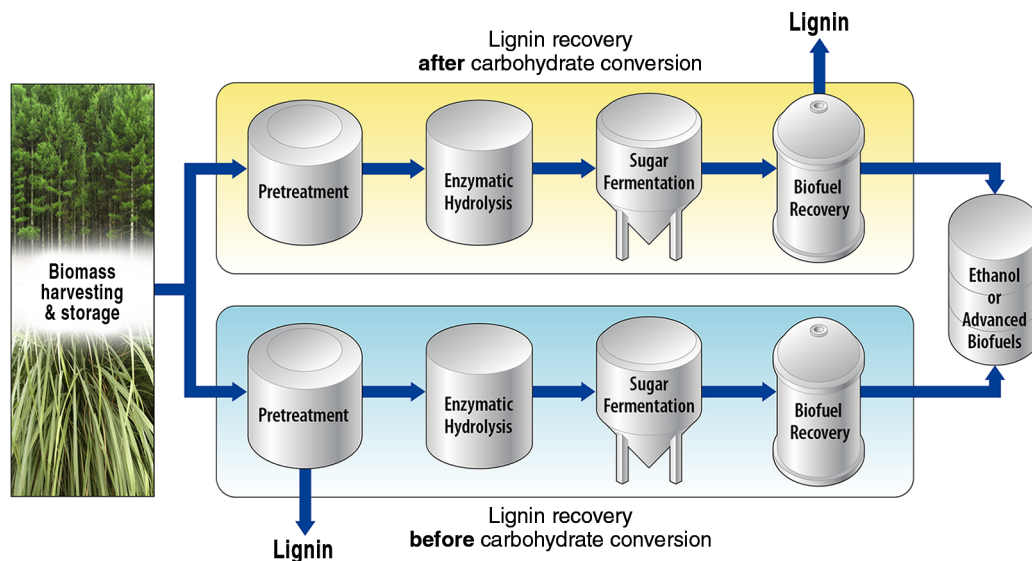
Currently, most lignocellulosic biorefineries using enzymes to deconstruct plant polysaccharides will yield lignin-rich streams by either (i) extracting the plant carbohydrates to leave most of the lignin in the solid residue (72) or (ii) applying pretreatments to fractionate biomass to extract lignin (73) before carbohydrate conversion (Fig. 3).

Some pretreatments use dilute sulfuric or other acids, or simply hot water (hydrothermal), to break down hemicellulose to sugars and to increase cellulose accessibility for enzymatic hydrolysis, after which most of the lignin is left in the solid residue (74). Others use high pH conditions by adding calcium, sodium, or potassium hydroxide to remove a large portion of the lignin and some of the hemicellulose. Ammonia (high pH) disrupts but does not necessarily remove lignin, while still making biomass more accessible to enzymes.

Pretreatment by dilute acid or hot water is known to alter the physical and chemical structure of lignin and deposit altered hemicellulose and lignin products on pretreated solids. Lignin isolated after enzymatic deconstruction currently also contains some recalcitrant polysaccharides, proteins, and mineral salts, a mixture generally viewed as limiting suitability for direct material applications. Recently, this perspective has been challenged by the use of *N,N*-dimethyl formamide to extract lignin from the solid residue of enzymatically hydrolyzed poplar (75). These separation challenges will certainly be simplified in the future as biorefinery engineering advances take hold. For example, although industrial lignocellulosic pretreatment is mostly envisioned to use plug-flow type reactors, improved benefits from flowthrough pretreatments could facilitate lignin recovery free of proteins (76, 77). Historically, this process has been challenged by excessive energy and water consumption, but some of these concerns have been addressed by using a countercurrent flowthrough design to recover less-degraded xylans and 40 to 80% of the lignin, depending on feedstock and reactor conditions (78).

Pretreatments that specifically target lignin extraction frequently have their technical origins in the chemical pulp industry. For example, alkaline pretreatments can fragment and solubilize lignin, thus providing a biomass product with highly reactive polysaccharides for biofuels production, with lignin recovery from these alkaline streams in various stages of commercial development. Alternatively, organosolv approaches treat biomass with a mixture of water and organic solvents, such as ethanol or methanol, along with

**Fig. 3. Simplified process flow diagram illustrating paths to recover lignin.** This can happen either after removal of most of the carbohydrates by hydrolysis and fermentation operations (top sequence) or by pretreatment (126, 127) before downstream carbohydrate conversion (bottom sequence). [Courtesy of Oak Ridge National Laboratory, DOE]



addition of a catalyst at 140° to 200°C. Organosolv pretreatment typically results in more than 50% lignin removal through cleavage of lignin-carbohydrate bonds and  $\beta$ -O-4 interunit linkages and subsequent solubilization in the organic solvent (79). After pretreatment, lignin is precipitated and recovered from the concentrated liquor (80). Organosolv-derived lignin is sulfur-free, rich in functionality including phenolics, exhibits a narrow polydispersity, and has limited carbohydrate contamination (81). Ionic liquids provide an alternative path for lignin removal to classical organosolv pretreatment for enhancements of subsequent enzymatic hydrolysis. For example, 1-ethyl-3-methylimidazolium acetate was used to extract lignin from promising biorefining feedstocks, such as poplar and birch, at elevated temperatures; the lignin was then recovered with the addition of an antisolvent (82). Although some changes in lignin structure were noted, most structural features were retained (83). More aggressive changes in the structure of lignin can be accomplished by using acidic ionic liquids, such as 1-*H*-3-methylimidazolium chloride, which will hydrolyze ether linkages (84). Future developments will focus on selective lignin extraction and functionalization and minimization of process costs for recovery and recycling.

Postfermentation recovery of lignin is expected to be used for low-value markets, such as process heat and electricity, because of the presence of deconstruction enzymes and fermentation components that would require additional purification for higher value uses. Lignin utilization in value-added markets that take advantage of its unique material properties can more likely afford the extra costs for prerecovery by such pretreatments as flowthrough, organosolv and ionic liquids, provided that these processes are not overly capital intensive. As discussed previously, the extraction of lignin from transgenic plants with reduced structural diversity or labile interunit linkages (i.e., esters) can further

simplify the overall extraction process in the future.

#### Lignin Valorization: Materials

One of the greatest challenges in biorefining is to engineer lignin structures to not only reduce biomass recalcitrance but also enable lignin valorization (i.e., conversion to higher value compounds). Although low-market volume chemical additives can be derived from lignin, the amount of lignin from an industrial cellulosic ethanol plant will range from ~100,000 to 200,000 tons year<sup>-1</sup>; this scale disparity will shape lignin valorization research and development (85).

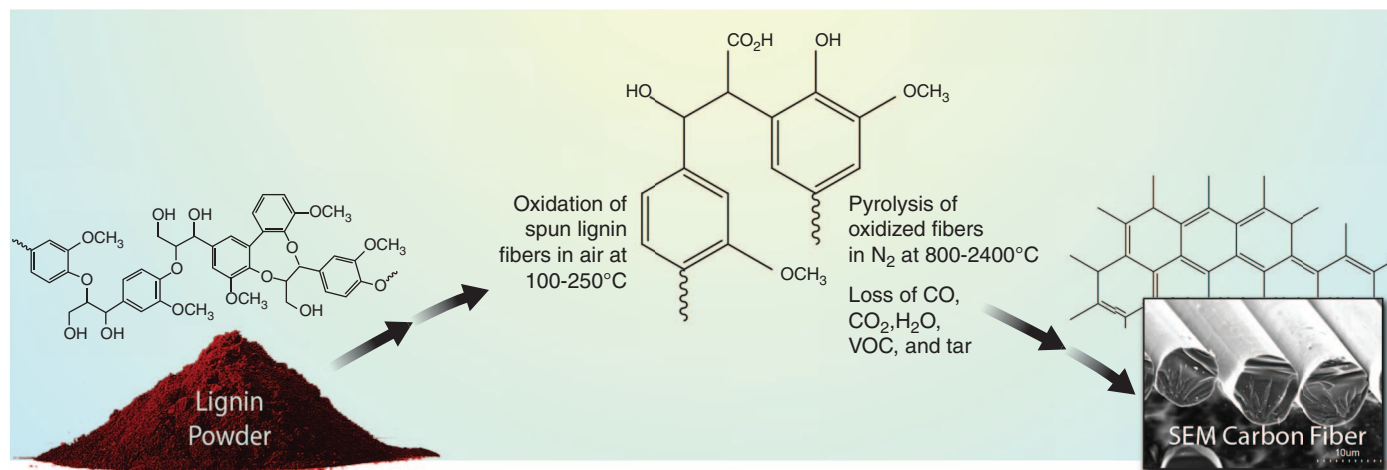
A promising lignin product platform is the global development of energy-efficient lightweight vehicles. A body-in-white design-based model has demonstrated that over 40 to 50% of the structural steel mass in a vehicle could be replaced with carbon fiber composite materials (86). However, to realize this goal, low-cost manufacturing of carbon fibers (~300 × 10<sup>6</sup> kg year<sup>-1</sup>) is needed at the commercial scale, but commercial carbon-fiber precursors derived from polyacrylonitrile (PAN) are too costly for most such applications. Lignin from cellulosic biorefining operations could become an ideal precursor for carbon fiber synthesis, as highlighted in Fig. 4, but our understanding of the fundamental chemistry involved in this process is limited, hindering advances in this process to some extent.

To obtain lignin-derived carbon fiber, isolated lignin is first processed into fibers by extruding filaments from a melt or solvent swollen gel. Then the spun fibers are thermally stabilized in air where the lignin fiber is oxidized. At this stage, the filaments become pyrolyzable without melting or fusion. During pyrolysis under nitrogen or inert atmosphere, the fibers become carbonized through the elimination of hydrocarbon volatiles, their oxidized derivatives, carbon monoxide, carbon dioxide, and moisture. Figure 4 shows a scanning electron micrograph of car-

bonized filaments with a rough cross section. The final morphology of the carbon materials depends not only on carbon precursor chemistry but also on processing methodology. So far, lignin-based carbon fibers largely derived from Kraft pulping liquors have not exhibited good mechanical properties, mainly because of fiber porosity and lack of oriented graphitic structure. Softwood and hardwood lignins, obtained from the pulping process, can be melt-processed to fibers after eliminating the high-molecular-weight fractions by solvent extraction or molecular fractionation using membranes (87, 88). Softwood lignin precursor fibers manifest more rapid oxidative cross-linking than hardwood lignin fibers, a desirable characteristic for high-yield cost-competitive carbonized derivatives. The use of lignin from switchgrass and other agricultural resources has not been explored as extensively, although recent reviews and patent claims have highlighted its potential, and future studies will undoubtedly further define this opportunity (89, 90).

Lignin-based carbon fibers currently have poor mechanical properties compared with petroleum-derived counterparts. PAN-based fibers exhibit graphitic stacking that is so far difficult to achieve in lignin-derived carbon. The disordered carbon synthesized from natural lignins is thought to be related to its original morphology. The partially globular structure of lignin in nature forms glassy carbon during thermal pyrolysis (91). The formation of rigid oxidized segments during lignin thermal treatment is supported by a gradual increase in the glass transition temperature of the precursor with increasing thermal treatment (92). Although oxidation and cross-linking helps to increase char content in a pyrolyzed polymer (93), extensive cross-linking could be detrimental to structural carbon order (94). Therefore, new chemical modifications of lignin and/or innovative biosynthesis strategies are needed to produce linear-fiber-forming lignin, with controlled monomer ratios and chemical architectures that facilitate





**Fig. 4. Highlights of thermal chemistry involved in converting lignin to carbon fiber.** See (88, 128) for more information. [Courtesy of Oak Ridge National Laboratory, DOE]

rapid chemical transformation to infusible mass and formation of planar graphitic structure during pyrolysis.

Minimization of reactive C-O bonds in interunit lignin linkages, such as  $\beta$ -O-aryl ether, is anticipated to yield a more favorable lignin for structural carbon-fiber production (95). This type of lignin manipulation has already been accomplished in transgenic alfalfa lines down-regulated in the expression of enzymes involved in lignin biosynthesis, which exhibited higher amounts of H-lignin and consequently yielding less C-O-C reactive interunit linkages and more C-C linkages that are chemically less reactive (96). Such lignin modifications could be beneficial for high carbon yield and formation of long-range order in high-temperature carbonized filaments.

Another high-volume lignin application is plant-derived plastics and composites. The synthesis of engineering plastics and thermoplastic elastomers, polymeric foams, and membranes from lignin with comparable properties to those from petroleum products has been reported for some time (97). The most frequent lignin source for these past studies has been from chemical pulping operations that are directed primarily at lignin removal from cellulosic fibers through a series of alkaline depolymerization or lignin sulfonation reactions. Although the lignin structure from such operations may be far removed from that needed for most high-value material applications, these sources have found commercial markets, such as an additive for cement, dust suppression, and drilling fluids for oil recovery (98). A few notable exceptions have been published: for example, the intrinsic structure of select lignosulfonates has facilitated their use for expanders for lead acid batteries (99) and other select applications (100). However, process impurities, variable molecular weights, and poor processability hinder the value of most current industrial pulping lignins for composite products. Despite these concerns, oxypropylation of lignin has been shown to yield a promising

polyol for polyurethane synthesis, yielding excellent physical strength properties (101). In contrast, the application of lignin in thermoplastics has been challenging; for example, blending ~5 to 20% of hydroxyl propyl lignin with poly(methyl methacrylate) provided up to a 200-MPa increase in Young's modulus over the pure polymer but exhibited detrimental embrittlement (102). Hilburg *et al.* presented an alternative approach using a controlled polymerization of nanolignin particles with styrene or methyl methacrylate, which provided a 10-fold increase in toughness over a lignin/polymer blend equivalent (103). The latter results illustrate the potential for utilizing lignin in composites provided the structures are engineered on the molecular scale.

Future development of green lignin-based polymers pivots on new processing technologies coupled to tailor-made bioenergy crops containing lignin with desired chemical and physical properties for a host of lignin-based material applications. For example, mild isolation of C lignin (Fig. 2, structure C) could readily provide a lignin feedstock that addresses many of the current processing issues. Alternatively, lignin composed partially or exclusively of hydroxycinnamaldehydes, such as the lignin from the *Medicago cad1* mutant (Fig. 2, structure D), provides a new functional group as a natural avenue to explore formation of formaldehyde-free resins or plastics by using the intrinsic reactivity of the aldehyde for cross-linking.

#### Lignin Valorization: Fuels and Chemicals

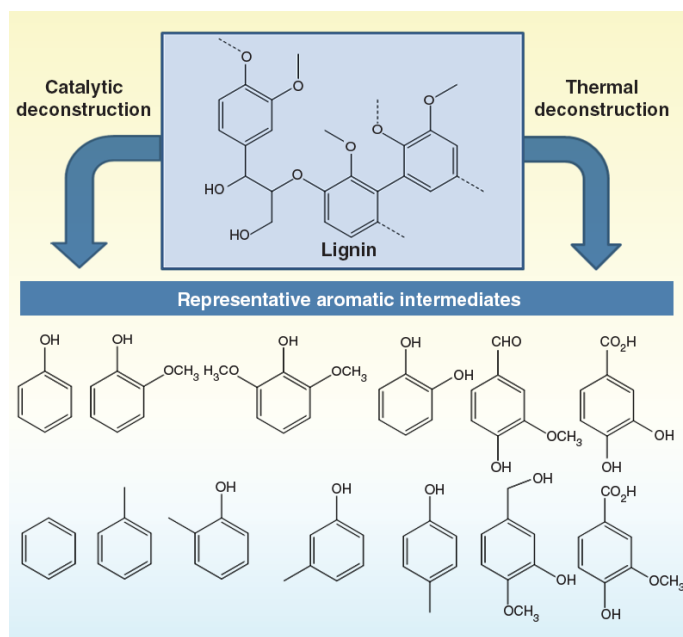
Despite the anticipated improvements in engineered lignin structures and tailored pretreatment chemistries, some lignin fractions from a biorefinery are not expected to be suitable for material applications but can still be valuable for conversion into fuels and chemicals. Lignin depolymerization is challenging given the broad distribution of bond strengths in the various C-O and C-C linkages in lignin and the tendency for

low-molecular-weight species to undergo recondensation, often to more recalcitrant species (Fig. 5). Resulting streams are subsequently difficult to upgrade, given the heterogeneity of low-molecular-weight species, which often possess diverse functional groups.

These challenges will be substantially diminished as plant feedstocks are engineered to have predominant G, H, C, or S lignin. The latter would certainly favor thermal or chemical depolymerization, because methoxy groups at the 3 and 5 positions of the aromatic ring (structure A in Fig. 2) diminish relatively unreactive carbon-carbon (C-C) interunit linkages, yielding a lignin more reactive to thermal and catalytic fragmentation. To date, multiple strategies have emerged for lignin depolymerization and upgrading, including thermochemical treatments, homogeneous and heterogeneous catalysis, and biological depolymerization.

Transition metal catalysts have long been used for lignin hydrogenolysis and hydrodeoxygenation upgrading at high hydrogen pressures, either as single- or two-step processes (104). These approaches have received substantial academic and industrial attention for production of gasoline-range aromatics, as well as benzene, toluene, and xylene. A recent review provides a comprehensive list of the reductive depolymerization and upgrading strategies used to date (105). Most have required high temperature and pressure (>200°C and >5 MPa) in combination with catalysts developed for petroleum processing, such as Ni-Mo or Co-Mo/ $\text{Al}_2\text{O}_3$ , with the primary function being removal of sulfur and nitrogen heteroatoms. Despite substantial research, lignin depolymerization via hydrogenolysis remains a major technical challenge, primarily because the diverse reactivities of lignin-derived low-molecular-weight species limit yields of single products and their presence in biomass-derived streams poisons metal catalysts. Additionally, hydrodeoxygenation catalysis for the production of fuels and chemicals from

**Fig. 5. Generalized catalytic and thermal fragmentation of lignin to low-molecular-weight compounds.**



lignin-derived intermediates often leads to catalyst deactivation through high coke formation, hydrothermal instability, and catalyst sintering (106). These challenges warrant development of more robust catalysts designed for diverse substrates and tolerant of harsh environments. For example, promising new catalysts to overcome these limitations, including designs with alternative supports and bimetallic functionalities, have been investigated with model compounds (107).

Oxidative processes for lignin depolymerization have also involved catalytic side-chain oxidation and fragmentation reactions (108). Many of the targeted products from lignin oxidation, wherein the aromatic character is preserved, are aromatic acids and aldehydes with smaller market volumes. However, oxidation can also enable production of ring-opened organic acids that an effective separation method could recover as potentially valuable products. Depolymerization of lignin in nature occurs primarily via oxidative enzymes, such as laccases and peroxidases, which are secreted by white-rot fungi and some bacteria (109, 110). Application of these natural strategies has been examined, such as a mild pretreatment of whole biomass or as a means to produce low-molecular-weight aromatic compounds (111). The utilization of these approaches for lignin depolymerization and subsequent upgrading will be predicated on minimizing the degradation of sugars and reductions in the need for potentially costly enzyme cofactors.

Purely thermal routes have also been explored for lignin depolymerization. Pyrolytic approaches yield low-molecular-weight species in the vapor phase, which undergo condensation reactions upon phase change to higher-molecular-weight oligomers (112). Coupling lignin pyrolysis with hydrodeoxygenation catalysis (113) for upgrading vapor-phase monomeric species potentially offers

a route to fuels and chemicals, but the primary technical barrier is the inability to continuously feed lignin to large-scale reactors (114), an issue that may be solved with commercial-scale ligno-cellulosic biorefineries.

For chemicals production, an underlying uncertainty is the ability to meet stringent product purity specifications. Thus, rather than targeting a single commodity chemical from lignin, a more direct solution may be to produce a blended petrochemical feedstock, such as reformat, that can be integrated and upgraded within an existing petrochemical complex. The primary trade-offs for this route are efficient oxygen removal, fuel quality (because of saturation of the high-octane aromatic blend stocks), and high hydrogen consumption (115). One of the largest challenges associated with lignin valorization is whether there are economic pathways for conversion of lignin to value-added fuels and chemicals. A recent design study that focused on the biological conversion of cellulosic sugars to fuels showed that potential routes for the conversion of lignin to chemicals may lead to improvements in overall economics and sustainability for an integrated biorefinery (116). For example, the conversion of lignin to 1,4-butanediol and adipic acid improved the overall process economics and potentially reduced the greenhouse gas emissions by an order of magnitude relative to production of electricity from lignin. The well-established commercial production of vanillin from lignin provides a strong precedent for future innovative advances in this field (117).

### The Present and Future

Lignin is a major component of terrestrial ligno-cellulosic biomass. The effective utilization of lignin is critical for the accelerated development and deployment of the advanced cellulosic bio-

refinery. However, we acknowledge that, despite some markets and uses of lignin which stretch back decades, it has been long said in the pulp industry that “one can make anything from lignin except money.” This review set out to describe a set of developments over the past few years that we suggest, when taken together, represent a tipping point in the prospects for lignin as a viable, commercially relevant sustainable feedstock for a new range of materials and uses.

First, the advent of new cellulosic biorefineries will introduce an excess supply of different, nonsulfonated, native and transgenically modified lignins into the process streams. Future research will continue to establish to what extent the lignin structure in plants can be altered to yield a product that can be readily recovered via pretreatment and has the appropriate tailored structures to be valorized for materials, chemicals, and fuels. Third, although lignin sequencing remains a vision, approaches based largely on NMR, high-performance liquid chromatography–mass spectrometry (LC-MS) or GC-MS, and specific binding antibodies have greatly improved our knowledge of the structures of lignin and its products. These results need to be further integrated into improved force fields and high-performance computational modeling to provide a predictive tool of lignin’s chemical and physical properties and reactivities in multiple environments. Such insights may help redesign lignin within its cross-linked complex biological matrix to meet subsequent process and end product goals. Overall, the need to understand and manipulate lignin from its assembly within plant cell walls to its extraction and processing into value-added products aligns with our potential to obtain a deeper understanding of complex biological structures. This is especially true because the valorization of lignin cannot come at the expense of the effective utilization of other biopolymers, such as cellulose and hemicellulose.

### References and Notes

1. T. F. Stocker *et al.*, Eds., *Climate Change 2013: The Physical Science Basis, Summary for Policymakers* (IPCC, Geneva, 2014); [www.ipcc.ch/report/ar5/wg1/docs/WGIAR5\\_SPM\\_brochure\\_en.pdf](http://www.ipcc.ch/report/ar5/wg1/docs/WGIAR5_SPM_brochure_en.pdf).
2. A. P. C. Faaij, Bio-energy in Europe: Changing technology choices. *Energy Policy* **34**, 322–342 (2006). doi: [10.1016/j.enpol.2004.03.026](https://doi.org/10.1016/j.enpol.2004.03.026)
3. U.S. Department of Energy, Office of the Biomass Program, 30 x 30 Workshop, Washington, DC (2014); [www.30x30workshop.biomass.govtools.us](http://www.30x30workshop.biomass.govtools.us).
4. U.S. Department of Energy, Office of the Biomass Program (OBP), Biomass Multi-Year Program Plan (2014); [www1.eere.energy.gov/bioenergy/pdfs/mypp\\_april\\_2011.pdf](http://www1.eere.energy.gov/bioenergy/pdfs/mypp_april_2011.pdf).
5. R. D. Perlack, B. J. Stokes, U.S. Department of Energy, *U.S. Billion-Ton Update: Biomass Supply for a Bioenergy and Bioproducts Industry* (Oak Ridge National Laboratory Report ORNL/TM-2011/224, Oak Ridge, TN, 2011).
6. S. Nonhebel, Renewable energy and food supply: Will there be enough land? *Renew. Sustain. Energy Rev.* **9**, 191–201 (2005). doi: [10.1016/j.rser.2004.02.003](https://doi.org/10.1016/j.rser.2004.02.003)
7. M. E. Himmel *et al.*, Biomass recalcitrance: Engineering plants and enzymes for biofuels production. *Science* **315**,



- 804–807 (2007). doi: [10.1126/science.1137016](https://doi.org/10.1126/science.1137016); pmid: [17289988](https://pubmed.ncbi.nlm.nih.gov/17289988/)
8. [www1.eere.energy.gov/bioenergy/integrated\\_biorefineries.html](http://www1.eere.energy.gov/bioenergy/integrated_biorefineries.html) (2014).
9. J. Lane, Beta renewables: Biofuels digest's 2014 5-minute guide. *Biofuels Digest* (2014); [www.biofuelsdigest.com/bdigest/2014/02/24/beta-renewables-biofuels-digests-2014-5-minute-guide](http://www.biofuelsdigest.com/bdigest/2014/02/24/beta-renewables-biofuels-digests-2014-5-minute-guide).
10. B. E. Dale, R. G. Ong, Energy, wealth, and human development: Why and how biomass pretreatment research must improve. *Biotechnol. Prog.* **28**, 893–898 (2012). doi: [10.1002/btpr.1575](https://doi.org/10.1002/btpr.1575); pmid: [22718309](https://pubmed.ncbi.nlm.nih.gov/22718309/)
11. P. Sannigrahi, A. J. Ragauskas, Characterization of fermentation residues from the production of bio-ethanol from lignocellulosic feedstocks. *J. Biobased Mat. Bioeng* **5**, 514–519 (2011). doi: [10.1166/jbmb.2011.1170](https://doi.org/10.1166/jbmb.2011.1170)
12. W. Boerjan, J. Ralph, M. Baucher, Lignin biosynthesis. *Annu. Rev. Plant Biol.* **54**, 519–546 (2003). doi: [10.1146/annurev.arplant.54.031902.134938](https://doi.org/10.1146/annurev.arplant.54.031902.134938); pmid: [14503002](https://pubmed.ncbi.nlm.nih.gov/14503002/)
13. M. Kleinert, T. Barth, Towards a lignocellulosic biorefinery: Direct one-step conversion of lignin to hydrogen-enriched biofuel. *Energy Fuels* **22**, 1371–1379 (2008). doi: [10.1021/ef700631w](https://doi.org/10.1021/ef700631w)
14. C. O. Tuck, E. Pérez, I. T. Horváth, R. A. Sheldon, M. Poliakoff, Valorization of biomass: Deriving more value from waste. *Science* **337**, 695–699 (2012). doi: [10.1126/science.1218930](https://doi.org/10.1126/science.1218930); pmid: [22879509](https://pubmed.ncbi.nlm.nih.gov/22879509/)
15. M. Langholtz *et al.*, Lignin-derived carbon fiber as a co-product of refining cellululosic biomass. *SAE Int. J. Mater. Manuf* **7**, 115–121 (2014).
16. D. Stewart, Lignin as a base material for materials applications: Chemistry, application and economics. *Ind. Crops Prod.* **27**, 202–207 (2008). doi: [10.1016/j.indcrop.2007.07.008](https://doi.org/10.1016/j.indcrop.2007.07.008)
17. M. S. S. Reddy *et al.*, Targeted down-regulation of cytochrome P450 enzymes for forage quality improvement in alfalfa (*Medicago sativa* L.). *Proc. Natl. Acad. Sci. U.S.A.* **102**, 16573–16578 (2005). doi: [10.1073/pnas.0505749102](https://doi.org/10.1073/pnas.0505749102); pmid: [16263933](https://pubmed.ncbi.nlm.nih.gov/16263933/)
18. B. S. Dien *et al.*, Improved sugar conversion and ethanol yield for forage sorghum (*Sorghum bicolor* L. Moench) lines with reduced lignin contents. *Bioenerg. Res.* **2**, 153–164 (2009). doi: [10.1007/s12155-009-9041-2](https://doi.org/10.1007/s12155-009-9041-2)
19. J. M. Humphreys, C. Chapple, Rewriting the lignin roadmap. *Curr. Opin. Plant Biol.* **5**, 224–229 (2002). doi: [10.1016/S1369-5266\(02\)00257-1](https://doi.org/10.1016/S1369-5266(02)00257-1); pmid: [11960740](https://pubmed.ncbi.nlm.nih.gov/11960740/)
20. R. Vanholme *et al.*, Caffeoyl shikimate esterase (CSE) is an enzyme in the lignin biosynthetic pathway in *Arabidopsis*. *Science* **341**, 1103–1106 (2013). doi: [10.1126/science.1241602](https://doi.org/10.1126/science.1241602); pmid: [23950498](https://pubmed.ncbi.nlm.nih.gov/23950498/)
21. N. D. Bonawitz *et al.*, Disruption of Mediator rescues the stunted growth of a lignin-deficient *Arabidopsis* mutant. *Nature* (2014). doi: [10.1038/nature13084](https://doi.org/10.1038/nature13084); pmid: [24670657](https://pubmed.ncbi.nlm.nih.gov/24670657/)
22. R. Vanholme *et al.*, A systems biology view of responses to lignin biosynthesis perturbations in *Arabidopsis*. *Plant Cell* **24**, 3506–3529 (2012). doi: [10.1105/tpc.112.102574](https://doi.org/10.1105/tpc.112.102574); pmid: [23012438](https://pubmed.ncbi.nlm.nih.gov/23012438/)
23. R. Van Acker *et al.*, Lignin biosynthesis perturbations affect secondary cell wall composition and saccharification yield in *Arabidopsis thaliana*. *Biotechnol. Biofuels* **6**, 46 (2013). doi: [10.1186/1754-6834-6-46](https://doi.org/10.1186/1754-6834-6-46); pmid: [23622268](https://pubmed.ncbi.nlm.nih.gov/23622268/)
24. L. Li *et al.*, Combinatorial modification of multiple lignin traits in trees through multigene cotransformation. *Proc. Natl. Acad. Sci. U.S.A.* **100**, 4939–4944 (2003). doi: [10.1073/pnas.0831166100](https://doi.org/10.1073/pnas.0831166100); pmid: [12668766](https://pubmed.ncbi.nlm.nih.gov/12668766/)
25. B. Shen, C. Li, M. C. Tarczynski, High free-methionine and decreased lignin content result from a mutation in the *Arabidopsis* S-adenosyl-L-methionine synthetase 3 gene. *Plant J.* **29**, 371–380 (2002). doi: [10.1046/j.1365-3113X.2002.01221.x](https://doi.org/10.1046/j.1365-3113X.2002.01221.x); pmid: [11844113](https://pubmed.ncbi.nlm.nih.gov/11844113/)
26. H. Shen *et al.*, Functional characterization of the switchgrass (*Panicum virgatum*) R2R3-MYB transcription factor PvMYB4 for improvement of lignocellulosic feedstocks. *New Phytol.* **193**, 121–136 (2012). doi: [10.1111/j.1469-8137.2011.03922.x](https://doi.org/10.1111/j.1469-8137.2011.03922.x); pmid: [21988539](https://pubmed.ncbi.nlm.nih.gov/21988539/)
27. K. Zhang *et al.*, An engineered monolignol 4-O-methyltransferase depresses lignin biosynthesis and confers novel metabolic capability in *Arabidopsis*. *Plant Cell* **24**, 3135–3152 (2012). doi: [10.1105/tpc.112.101287](https://doi.org/10.1105/tpc.112.101287); pmid: [22851762](https://pubmed.ncbi.nlm.nih.gov/22851762/)
28. F. Chen, R. A. Dixon, Lignin modification improves fermentable sugar yields for biofuel production. *Nat. Biotechnol.* **25**, 759–761 (2007). doi: [10.1038/nbt1316](https://doi.org/10.1038/nbt1316); pmid: [17572667](https://pubmed.ncbi.nlm.nih.gov/17572667/)
29. L. Gallego-Giraldo, L. Escamilla-Trevino, L. A. Jackson, R. A. Dixon, Salicylic acid mediates the reduced growth of lignin down-regulated plants. *Proc. Natl. Acad. Sci. U.S.A.* **108**, 20814–20819 (2011). doi: [10.1073/pnas.1117873108](https://doi.org/10.1073/pnas.1117873108); pmid: [22123972](https://pubmed.ncbi.nlm.nih.gov/22123972/)
30. X. Li, N. D. Bonawitz, J.-K. Weng, C. Chapple, The growth reduction associated with repressed lignin biosynthesis in *Arabidopsis thaliana* is independent of flavonoids. *Plant Cell* **22**, 1620–1632 (2010). doi: [10.1105/tpc.110.074161](https://doi.org/10.1105/tpc.110.074161); pmid: [20511296](https://pubmed.ncbi.nlm.nih.gov/20511296/)
31. N. D. Bonawitz, C. Chapple, Can genetic engineering of lignin deposition be accomplished without an unacceptable yield penalty? *Curr. Opin. Biotechnol.* **24**, 336–343 (2013). doi: [10.1016/j.copbio.2012.11.004](https://doi.org/10.1016/j.copbio.2012.11.004); pmid: [23228388](https://pubmed.ncbi.nlm.nih.gov/23228388/)
32. C. Chapple, M. Ladisch, R. Meilan, Loosening lignin's grip on biofuel production. *Nat. Biotechnol.* **25**, 746–748 (2007). doi: [10.1038/nbt0707-746](https://doi.org/10.1038/nbt0707-746); pmid: [17621299](https://pubmed.ncbi.nlm.nih.gov/17621299/)
33. J. H. Grabber, How do lignin composition, structure, and cross-linking affect degradability? A review of cell wall model studies. *Crop Sci.* **45**, 820–831 (2005).
34. H. B. C. Molinari, T. K. Pellny, J. Freeman, P. R. Shewry, R. A. C. Mitchell, Grass cell wall feruloylation: Distribution of bound ferulate and candidate gene expression in *Brachypodium distachyon*. *Front. Plant Sci.* **4**, 50 (2013). doi: [10.3389/fpls.2013.00050](https://doi.org/10.3389/fpls.2013.00050); pmid: [23508643](https://pubmed.ncbi.nlm.nih.gov/23508643/)
35. R. Franke *et al.*, Changes in secondary metabolism and deposition of an unusual lignin in the ref8 mutant of *Arabidopsis*. *Plant J.* **30**, 47–59 (2002). doi: [10.1046/j.1365-3113X.2002.01267.x](https://doi.org/10.1046/j.1365-3113X.2002.01267.x); pmid: [11967092](https://pubmed.ncbi.nlm.nih.gov/11967092/)
36. A. Ziebell *et al.*, Increase in 4-coumaroyl alcohol units during lignification in alfalfa (*Medicago sativa*) alters the extractability and molecular weight of lignin. *J. Biol. Chem.* **285**, 38961–38968 (2010). doi: [10.1074/jbc.M110.137315](https://doi.org/10.1074/jbc.M110.137315); pmid: [20921228](https://pubmed.ncbi.nlm.nih.gov/20921228/)
37. J.-K. Weng, H. Mo, C. Chapple, Over-expression of F5H in COMT-deficient *Arabidopsis* leads to enrichment of an unusual lignin and disruption of pollen wall formation. *Plant J.* **64**, 898–911 (2010). doi: [10.1111/j.1365-3113X.2010.04391.x](https://doi.org/10.1111/j.1365-3113X.2010.04391.x); pmid: [21143672](https://pubmed.ncbi.nlm.nih.gov/21143672/)
38. F. Chen *et al.*, Novel seed coat lignins in the Cactaceae: structure, distribution and implications for the evolution of lignin diversity. *Plant J.* **73**, 201–211 (2013). doi: [10.1111/tpj.12012](https://doi.org/10.1111/tpj.12012); pmid: [22957702](https://pubmed.ncbi.nlm.nih.gov/22957702/)
39. F. Chen, Y. Tobimatsu, D. Havkin-Frenkel, R. A. Dixon, J. Ralph, A polymer of caffeoyl alcohol in plant seeds. *Proc. Natl. Acad. Sci. U.S.A.* **109**, 1772–1777 (2012). doi: [10.1073/pnas.1120992109](https://doi.org/10.1073/pnas.1120992109); pmid: [22307645](https://pubmed.ncbi.nlm.nih.gov/22307645/)
40. A. Eudes *et al.*, Biosynthesis and incorporation of side-chain-truncated lignin monomers to reduce lignin polymerization and enhance saccharification. *Plant Biotechnol. J.* **10**, 609–620 (2012). doi: [10.1111/j.1467-7652.2012.00692.x](https://doi.org/10.1111/j.1467-7652.2012.00692.x); pmid: [22458713](https://pubmed.ncbi.nlm.nih.gov/22458713/)
41. Y. Tobimatsu *et al.*, Coexistence but independent biosynthesis of catechyl and guaiacyl/syringyl lignin polymers in seed coats. *Plant Cell* **25**, 2587–2600 (2013). doi: [10.1105/tpc.113.113142](https://doi.org/10.1105/tpc.113.113142); pmid: [23903315](https://pubmed.ncbi.nlm.nih.gov/23903315/)
42. C. Lapierre *et al.*, Structural alterations of lignins in transgenic poplars with depressed cinnamyl alcohol dehydrogenase or caffeic acid O-methyltransferase activity have an opposite impact on the efficiency of industrial kraft pulping. *Plant Physiol.* **119**, 153–164 (1999). doi: [10.1104/pp.119.1.153](https://doi.org/10.1104/pp.119.1.153); pmid: [9880356](https://pubmed.ncbi.nlm.nih.gov/9880356/)
43. S. E. Sattler *et al.*, A nonsense mutation in a cinnamyl alcohol dehydrogenase gene is responsible for the Sorghum brown midrib6 phenotype. *Plant Physiol.* **150**, 584–595 (2009). doi: [10.1104/pp.109.136408](https://doi.org/10.1104/pp.109.136408); pmid: [19363091](https://pubmed.ncbi.nlm.nih.gov/19363091/)
44. Q. Zhao *et al.*, Loss of function of cinnamyl alcohol dehydrogenase 1 leads to unconventional lignin and a temperature-sensitive growth defect in *Medicago truncatula*. *Proc. Natl. Acad. Sci. U.S.A.* **110**, 13660–13665 (2013). doi: [10.1073/pnas.1312234110](https://doi.org/10.1073/pnas.1312234110); pmid: [23901113](https://pubmed.ncbi.nlm.nih.gov/23901113/)
45. R. Vanholme *et al.*, Metabolic engineering of novel lignin in biomass crops. *New Phytol.* **196**, 978–1000 (2012). doi: [10.1111/j.1469-8137.2012.04337.x](https://doi.org/10.1111/j.1469-8137.2012.04337.x); pmid: [23035778](https://pubmed.ncbi.nlm.nih.gov/23035778/)
46. C. G. Wilkerson *et al.*, Monolignol ferulate transferase introduces chemically labile linkages into the lignin backbone. *Science* **344**, 90–93 (2014). doi: [10.1126/science.1250161](https://doi.org/10.1126/science.1250161); pmid: [24700858](https://pubmed.ncbi.nlm.nih.gov/24700858/)
47. X. Li *et al.*, Lignin monomer composition affects *Arabidopsis* cell-wall degradability after liquid hot water pretreatment. *Biotechnol. Biofuels* **3**, 27 (2010). doi: [10.1186/1754-6834-3-27](https://doi.org/10.1186/1754-6834-3-27); pmid: [21126354](https://pubmed.ncbi.nlm.nih.gov/21126354/)
48. C.-T. Do *et al.*, Both caffeoyl Coenzyme A 3-O-methyltransferase 1 and caffeic acid O-methyltransferase 1 are involved in redundant functions for lignin, flavonoids and sinapoyl malate biosynthesis in *Arabidopsis*. *Planta* **226**, 1117–1129 (2007). doi: [10.1007/s00425-007-0558-3](https://doi.org/10.1007/s00425-007-0558-3); pmid: [17594112](https://pubmed.ncbi.nlm.nih.gov/17594112/)
49. M. H. Studer *et al.*, Lignin content in natural *Populus* variants affects sugar release. *Proc. Natl. Acad. Sci. U.S.A.* **108**, 6300–6305 (2011). doi: [10.1073/pnas.1009252108](https://doi.org/10.1073/pnas.1009252108); pmid: [21444820](https://pubmed.ncbi.nlm.nih.gov/21444820/)
50. I. Porth *et al.*, *Populus trichocarpa* cell wall chemistry and ultrastructure trait variation, genetic control and genetic correlations. *New Phytol.* **197**, 777–790 (2013). doi: [10.1111/nph.12014](https://doi.org/10.1111/nph.12014); pmid: [23278123](https://pubmed.ncbi.nlm.nih.gov/23278123/)
51. L. A. Rogers *et al.*, Comparison of lignin deposition in three ectopic lignification mutants. *New Phytol.* **168**, 123–140 (2005). doi: [10.1111/j.1469-8137.2005.01496.x](https://doi.org/10.1111/j.1469-8137.2005.01496.x); pmid: [16159327](https://pubmed.ncbi.nlm.nih.gov/16159327/)
52. H. Wang *et al.*, Mutation of WRKY transcription factors initiates pith secondary wall formation and increases stem biomass in dicotyledonous plants. *Proc. Natl. Acad. Sci. U.S.A.* **107**, 22338–22343 (2010). doi: [10.1073/pnas.1016436107](https://doi.org/10.1073/pnas.1016436107); pmid: [21135241](https://pubmed.ncbi.nlm.nih.gov/21135241/)
53. R. Sykes *et al.*, High-throughput screening of plant cell-wall composition using pyrolysis molecular beam mass spectroscopy. *Methods Mol. Biol.* **581**, 169–183 (2009). doi: [10.1007/978-1-60761-214-8\\_12](https://doi.org/10.1007/978-1-60761-214-8_12); pmid: [19768623](https://pubmed.ncbi.nlm.nih.gov/19768623/)
54. Y. Zeng, M. E. Himmel, S. Y. Ding, *Biomass Conversion, Methods and Protocols*, vol. 908 of *Methods in Molecular Biology* (Springer, New York, 2012), pp. 49–60.
55. S. Jung, M. Foston, U. C. Kalluri, G. A. Tuskan, A. J. Ragauskas, 3D chemical image using TOF-SIMS revealing the biopolymer component spatial and lateral distributions in biomass. *Angew. Chem. Int. Ed.* **51**, 12005–12008 (2012). doi: [10.1002/anie.201205243](https://doi.org/10.1002/anie.201205243); pmid: [23109300](https://pubmed.ncbi.nlm.nih.gov/23109300/)
56. C. Zhou, Q. Li, V. L. Chiang, L. A. Lucia, D. P. Griffiths, Chemical and spatial differentiation of syringyl and guaiacyl lignins in poplar wood via time-of-flight secondary ion mass spectrometry. *Anal. Chem.* **83**, 7020–7026 (2011). doi: [10.1021/ac200903y](https://doi.org/10.1021/ac200903y); pmid: [21851065](https://pubmed.ncbi.nlm.nih.gov/21851065/)
57. Y. Tobimatsu *et al.*, Visualization of plant cell wall lignification using fluorescence-tagged monolignols. *Plant J.* **76**, 357–366 (2013). doi: [10.1111/tpj.12299](https://doi.org/10.1111/tpj.12299); pmid: [23889038](https://pubmed.ncbi.nlm.nih.gov/23889038/)
58. S. Kiyoto *et al.*, Immunolocalization of 8-5' and 8-8' linked structures of lignin in cell walls of *Chamaecyparis obtusa* using monoclonal antibodies. *Planta* **237**, 705–715 (2013). doi: [10.1007/s00425-012-1784-x](https://doi.org/10.1007/s00425-012-1784-x); pmid: [23108661](https://pubmed.ncbi.nlm.nih.gov/23108661/)
59. L. Tetard, A. Passian, S. Jung, A. J. Ragauskas, B. H. Davison, Development of new methods in scanning probe microscopy for lignocellulosic biomass characterization. *Ind. Biotechnol. (New Rochelle N.Y.)* **8**, 245–249 (2012). doi: [10.1089/ind.2012.0017](https://doi.org/10.1089/ind.2012.0017)
60. C. Heitner, D. R. Dimmel, J. A. Schmidt, Eds., *Lignin and Lignans: Advances in Chemistry* (CRC, Boca Raton, FL, 2010).
61. M. Li *et al.*, Structural characterization of alkaline hydrogen peroxide pretreated grasses exhibiting diverse lignin phenotypes. *Biotechnol. Biofuels* **5**, 38 (2012). doi: [10.1186/1754-6834-5-38](https://doi.org/10.1186/1754-6834-5-38); pmid: [22672858](https://pubmed.ncbi.nlm.nih.gov/22672858/)
62. X. Du, G. Gellerstedt, J. Li, Universal fractionation of lignin-carbohydrate complexes (LCCs) from lignocellulosic biomass: An example using spruce wood. *Plant J.* **74**, 328–338 (2013). doi: [10.1111/tpj.12124](https://doi.org/10.1111/tpj.12124); pmid: [23332001](https://pubmed.ncbi.nlm.nih.gov/23332001/)

63. R. A. Chylla *et al.*, Plant cell wall profiling by fast maximum likelihood reconstruction (FMLR) and region-of-interest (ROI) segmentation of solution-state 2D 1H-13C NMR spectra. *Biotechnol. Biofuels* **6**, 45 (2013). doi: [10.1186/1754-6834-6-45](https://doi.org/10.1186/1754-6834-6-45); pmid: [23622232](https://pubmed.ncbi.nlm.nih.gov/23622232/)
64. K. M. Holtman, H. M. Chang, H. Jameel, J. F. Kadla, Elucidation of lignin structure through degradative methods: Comparison of modified DFRC and thioacidolysis. *J. Agric. Food Chem.* **51**, 3535–3540 (2003). doi: [10.1021/jf0340411](https://doi.org/10.1021/jf0340411); pmid: [12769520](https://pubmed.ncbi.nlm.nih.gov/12769520/)
65. S. G. A. Moinuddin *et al.*, Insights into lignin primary structure and deconstruction from *Arabidopsis thaliana* COMT (caffeic acid O-methyl transferase) mutant Atomt1. *Org. Biomol. Chem.* **8**, 3928–3946 (2010). doi: [10.1039/c004817h](https://doi.org/10.1039/c004817h); pmid: [20652169](https://pubmed.ncbi.nlm.nih.gov/20652169/)
66. K. Morreel *et al.*, Mass spectrometry-based sequencing of lignin oligomers. *Plant Physiol.* **153**, 1464–1478 (2010). doi: [10.1104/pp.110.156489](https://doi.org/10.1104/pp.110.156489); pmid: [20554692](https://pubmed.ncbi.nlm.nih.gov/20554692/)
67. A. Salanti, L. Zoia, E.-L. Tolpela, M. Orlandi, Chromatographic detection of lignin-carbohydrate complexes in annual plants by derivatization in ionic liquid. *Biomacromolecules* **13**, 445–454 (2012). doi: [10.1021/bm2014763](https://doi.org/10.1021/bm2014763); pmid: [22220942](https://pubmed.ncbi.nlm.nih.gov/22220942/)
68. M. Balakshin, E. Capanema, H. Gracz, H. M. Chang, H. Jameel, Quantification of lignin-carbohydrate linkages with high-resolution NMR spectroscopy. *Planta* **233**, 1097–1110 (2011). doi: [10.1007/s00425-011-1359-2](https://doi.org/10.1007/s00425-011-1359-2); pmid: [21298285](https://pubmed.ncbi.nlm.nih.gov/21298285/)
69. S. V. Pingali *et al.*, Breakdown of cell wall nanostructure in dilute acid pretreated biomass. *Biomacromolecules* **11**, 2329–2335 (2010). doi: [10.1021/bm100455h](https://doi.org/10.1021/bm100455h); pmid: [20726544](https://pubmed.ncbi.nlm.nih.gov/20726544/)
70. L. Petridis, R. Schulz, J. C. Smith, Simulation analysis of the temperature dependence of lignin structure and dynamics. *J. Am. Chem. Soc.* **133**, 20277–20287 (2011). doi: [10.1021/ja206839u](https://doi.org/10.1021/ja206839u); pmid: [22035184](https://pubmed.ncbi.nlm.nih.gov/22035184/)
71. S. E. Harton *et al.*, Evidence for Complex Molecular Architectures for Solvent-Extracted Lignins. *ACS Macro Lett.* **1**, 568–573 (2012). doi: [10.1021/mz300045e](https://doi.org/10.1021/mz300045e)
72. V. Poursorkhabi, M. Misra, A. K. Mohanty, Extraction of lignin from a co-product of the cellulosic ethanol industry and its thermal characterization. *BioResources* **8**, 5083–5101 (2013).
73. D. D. Laskar, J. Zeng, L. Yan, S. Chen, B. Yang, Characterization of lignin derived from water-only flowthrough pretreatment of Miscanthus. *Ind. Crops Prod.* **50**, 391–399 (2013). doi: [10.1016/j.indcrop.2013.08.002](https://doi.org/10.1016/j.indcrop.2013.08.002)
74. D. Humbird *et al.*, "Process design and economics for biochemical conversion of lignocellulosic biomass to ethanol: Dilute-acid pretreatment and enzymatic hydrolysis of corn stover," Technical Report NREL/TP-5100-47764, National Renewable Energy Laboratory, Golden, CO (2012).
75. P. Sannigrahi, A. J. Ragauskas, "Fundamentals of biomass pretreatment by fractionation," in *Aqueous Pretreatment of Plant Biomass for Biological and Chemical Conversion to Fuels and Chemicals*, C. E. Wyman, Ed. (Wiley, Oxford, 2013), pp. 201–222.
76. F. Hu, A. Ragauskas, Pretreatment and lignocellulosic chemistry. *Bioenergy Res* **5**, 1043–1066 (2012). doi: [10.1007/s12155-012-9208-0](https://doi.org/10.1007/s12155-012-9208-0)
77. H. L. Trajano *et al.*, The fate of lignin during hydrothermal pretreatment. *Biotechnol. Biofuels* **6**, 110 (2013). doi: [10.1186/1754-6834-6-110](https://doi.org/10.1186/1754-6834-6-110); pmid: [23902789](https://pubmed.ncbi.nlm.nih.gov/23902789/)
78. V. Archambault-Leger, X. Shao, L. R. Lynd, Integrated analysis of hydrothermal flow through pretreatment. *Biotechnol. Biofuels* **5**, 49 (2012). doi: [10.1186/1754-6834-5-49](https://doi.org/10.1186/1754-6834-5-49); pmid: [22812930](https://pubmed.ncbi.nlm.nih.gov/22812930/)
79. X. Zhao, K. Cheng, D. Liu, Organosolv pretreatment of lignocellulosic biomass for enzymatic hydrolysis. *Appl. Microbiol. Biotechnol.* **82**, 815–827 (2009). doi: [10.1007/s00253-009-1883-1](https://doi.org/10.1007/s00253-009-1883-1); pmid: [19214499](https://pubmed.ncbi.nlm.nih.gov/19214499/)
80. A. L. Macfarlane, R. Prestidge, M. M. Farid, J. J. Chen, Dissolved air flotation: A novel approach to recovery of organosolv lignin. *Chem. Eng. J.* **148**, 15–19 (2009). doi: [10.1016/j.cej.2008.07.036](https://doi.org/10.1016/j.cej.2008.07.036)
81. A. Berlin *et al.*, Inhibition of cellulase, xylanase and  $\beta$ -glucosidase activities by softwood lignin preparations. *J. Biotechnol.* **125**, 198–209 (2006). doi: [10.1016/j.jbiotec.2006.02.021](https://doi.org/10.1016/j.jbiotec.2006.02.021); pmid: [16621087](https://pubmed.ncbi.nlm.nih.gov/16621087/)
82. J. Y. Kim *et al.*, Structural features of lignin macromolecules extracted with ionic liquid from poplar wood. *Bioresour. Technol.* **102**, 9020–9025 (2011). doi: [10.1016/j.biortech.2011.07.081](https://doi.org/10.1016/j.biortech.2011.07.081); pmid: [21840709](https://pubmed.ncbi.nlm.nih.gov/21840709/)
83. J.-L. Wen, S.-L. Sun, B.-L. Xue, R.-C. Sun, Quantitative structures and thermal properties of birch lignins after ionic liquid pretreatment. *J. Agric. Food Chem.* **61**, 635–645 (2013). doi: [10.1021/jf3051939](https://doi.org/10.1021/jf3051939); pmid: [23265413](https://pubmed.ncbi.nlm.nih.gov/23265413/)
84. B. J. Cox, J. G. Ekerdt, Pretreatment of yellow pine in an acidic ionic liquid: Extraction of hemicellulose and lignin to facilitate enzymatic digestion. *Bioresour. Technol.* **134**, 59–65 (2013). doi: [10.1016/j.biortech.2013.01.081](https://doi.org/10.1016/j.biortech.2013.01.081); pmid: [23500560](https://pubmed.ncbi.nlm.nih.gov/23500560/)
85. C. E. Wyman, Potential synergies and challenges in refining cellulosic biomass to fuels, chemicals, and power. *Biotechnol. Progr.* **19**, 254–262 (2003). doi: [10.1021/bp025654j](https://doi.org/10.1021/bp025654j); pmid: [12675557](https://pubmed.ncbi.nlm.nih.gov/12675557/)
86. *Assessment of Fuel Economy Technologies for Light-Duty Vehicles* (National Research Council, National Academies Press, Washington, DC, 2011).
87. D. A. Baker, T. G. Rials, Recent advances in low-cost carbon fiber manufacture from lignin. *J. Appl. Polym. Sci.* **130**, 713–728 (2013). doi: [10.1002/app.39273](https://doi.org/10.1002/app.39273)
88. I. Norberg, Y. Nordström, R. Drougge, G. Gellerstedt, E. Sjöholm, A new method for stabilizing softwood kraft lignin fibers for carbon fiber production. *J. Appl. Polym. Sci.* **128**, 3824–3830 (2013). doi: [10.1002/app.38588](https://doi.org/10.1002/app.38588)
89. K. Lindsey, A. Johnson, P. Kim, S. Jackson, N. Labbé, Monitoring switchgrass composition to optimize harvesting periods for bioenergy and value-added products. *Biomass Bioenergy* **56**, 29–37 (2013). doi: [10.1016/j.biombioe.2013.04.023](https://doi.org/10.1016/j.biombioe.2013.04.023)
90. D. Argyropoulos, U.S. Patent US 20130255216 A1 20131003 (2013).
91. D. Saha, E. A. Payzant, A. S. Kumbhar, A. K. Naskar, Sustainable mesoporous carbons as storage and controlled-delivery media for functional molecules. *ACS Appl. Mater. Interfaces* **5**, 5868–5874 (2013). doi: [10.1021/am401661f](https://doi.org/10.1021/am401661f); pmid: [23731336](https://pubmed.ncbi.nlm.nih.gov/23731336/)
92. J. L. Braun, K. M. Holtman, J. F. Kadla, Lignin-based carbon fibers: Oxidative thermostabilization of kraft lignin. *Carbon* **43**, 385–394 (2005). doi: [10.1016/j.carbon.2004.09.027](https://doi.org/10.1016/j.carbon.2004.09.027)
93. J. W. Lawson, D. Srivastava, Formation and structure of amorphous carbon char from polymer materials. *Phys. Rev. B* **77**, 144209 (2008). doi: [10.1103/PhysRevB.77.144209](https://doi.org/10.1103/PhysRevB.77.144209)
94. R. H. Hurt, Z.-Y. Chen, Liquid crystals and carbon materials. *Phys. Today* **53**, 39–44 (2000). doi: [10.1063/1.883020](https://doi.org/10.1063/1.883020)
95. M. Foston *et al.*, NMR a critical tool to study the production of carbon fiber from lignin. *Carbon* **52**, 65–73 (2013). doi: [10.1016/j.carbon.2012.09.006](https://doi.org/10.1016/j.carbon.2012.09.006)
96. Y. Pu, F. Chen, A. Ziebell, B. Davison, A. J. Ragauskas, NMR characterization of C3H and HCT down-regulated alfalfa lignin for improved fermentable sugar yields. *BioEnergy Res.* **2**, 198–208 (2009). doi: [10.1007/s12155-009-9056-8](https://doi.org/10.1007/s12155-009-9056-8)
97. H. Chung, N. R. Washburn, Chemistry of lignin-based materials. *Green Mat.* **1**, 137–160 (2013). doi: [10.1680/jgmt.12.00009](https://doi.org/10.1680/jgmt.12.00009)
98. J. Lora, "Industrial commercial lignins: sources, properties and applications," in *Monomers, Polymers and Composites from Renewable Resources*, M. N. Belgacem, A. Gandini, Eds. (Elsevier, Oxford, 2008), pp. 225–241.
99. N. Hirai, S. Kubo, K. Magara, Combined cyclic voltammetry and in situ electrochemical atomic force microscopy on lead electrode in sulfuric acid solution with or without lignosulfonate. *J. Power Sources* **191**, 97–102 (2009). doi: [10.1016/j.jpowsour.2008.10.090](https://doi.org/10.1016/j.jpowsour.2008.10.090)
100. F. DeAngelis, S. Reale, Review – The lignin concept. *Chim. Ind. Mila* **88**, 58–65 (2006).
101. Y. Li, A. J. Ragauskas, Kraft lignin-based rigid polyurethane foam. *J. Wood Chem. Technol.* **32**, 210–224 (2012). doi: [10.1080/02773813.2011.652795](https://doi.org/10.1080/02773813.2011.652795)
102. S. L. Ciemniński, W. G. Glasser, Multiphase materials with lignin: 1. Blends of hydroxypropyl lignin with poly(methyl methacrylate). *Polymer* **29**, 1021–1029 (1988). doi: [10.1016/0032-3861\(88\)90010-9](https://doi.org/10.1016/0032-3861(88)90010-9)
103. S. L. Hilburg *et al.*, Washburn, A universal route towards thermoplastic lignin composites with improved mechanical properties. *Polymer* **55**, 995–1003 (2014). doi: [10.1016/j.polymer.2013.12.070](https://doi.org/10.1016/j.polymer.2013.12.070)
104. M. P. Pandey, C. S. Kim, Lignin depolymerization and conversion: A review of thermochemical methods. *Chem. Eng. Technol.* **34**, 29–41 (2011). doi: [10.1002/ceat.201000270](https://doi.org/10.1002/ceat.201000270)
105. J. Zakzeski, P. C. A. Bruijninx, A. L. Jongerius, B. M. Weckhuysen, The catalytic valorization of lignin for the production of renewable chemicals. *Chem. Rev.* **110**, 3552–3599 (2010). pmid: [20218547](https://pubmed.ncbi.nlm.nih.gov/20218547/)
106. H. M. Wang, J. Male, Y. Wang, Recent advances in hydrotreating of pyrolysis bio-oil and its oxygen-containing model compounds. *ACS Catal.* **3**, 1047–1070 (2013). doi: [10.1021/cs400069z](https://doi.org/10.1021/cs400069z)
107. D. M. Alonso, S. G. Wettstein, J. A. Dumesic, Bimetallic catalysts for upgrading of biomass to fuels and chemicals. *Chem. Soc. Rev.* **41**, 8075–8098 (2012). doi: [10.1039/c2cs35188a](https://doi.org/10.1039/c2cs35188a); pmid: [22872312](https://pubmed.ncbi.nlm.nih.gov/22872312/)
108. L. Das, P. Kolar, R. Sharma-Shivappa, Heterogeneous catalytic oxidation of lignin into value-added chemicals. *Biofuels* **3**, 155–166 (2012). doi: [10.4155/bfs.12.5](https://doi.org/10.4155/bfs.12.5)
109. Á. T. Martínez *et al.*, Biodegradation of lignocelluloses: Microbial, chemical, and enzymatic aspects of the fungal attack of lignin. *Int. Microbiol.* **8**, 195–204 (2005). pmid: [16200498](https://pubmed.ncbi.nlm.nih.gov/16200498/)
110. T. D. H. Bugg, M. Ahmad, E. M. Hardiman, R. Singh, The emerging role of bacteria in lignin degradation and bio-product formation. *Curr. Opin. Biotechnol.* **22**, 394–400 (2011). doi: [10.1016/j.copbio.2010.10.009](https://doi.org/10.1016/j.copbio.2010.10.009); pmid: [21071202](https://pubmed.ncbi.nlm.nih.gov/21071202/)
111. D. Salvachúa *et al.*, Fungal pretreatment: An alternative in second-generation ethanol from wheat straw. *Bioresour. Technol.* **102**, 7500–7506 (2011). doi: [10.1016/j.biortech.2011.05.027](https://doi.org/10.1016/j.biortech.2011.05.027); pmid: [21646018](https://pubmed.ncbi.nlm.nih.gov/21646018/)
112. P. R. Patwardhan, R. C. Brown, B. H. Shanks, Understanding the fast pyrolysis of lignin. *ChemSusChem* **4**, 1629–1636 (2011). doi: [10.1002/cssc.201100133](https://doi.org/10.1002/cssc.201100133); pmid: [21948630](https://pubmed.ncbi.nlm.nih.gov/21948630/)
113. W. Mu, H. Ben, A. Ragauskas, Y. Deng, Lignin pyrolysis components and upgrading – technology review. *Bioenerg. Res.* **6**, 1183–1204 (2013). doi: [10.1007/s12155-013-9314-7](https://doi.org/10.1007/s12155-013-9314-7)
114. D. J. Nowakowski, A. V. Bridgwater, D. C. Elliott, D. Meier, P. de Wild, Lignin fast pyrolysis: Results from an international collaboration. *J. Anal. Appl. Pyrolysis* **88**, 53–72 (2010). doi: [10.1016/j.jaap.2010.02.009](https://doi.org/10.1016/j.jaap.2010.02.009)
115. M. S. Talmadge *et al.*, A perspective on oxygenated species in the refinery integration of pyrolysis oil. *Green Chem.* **16**, 407–453 (2014). doi: [10.1039/c3gc41951g](https://doi.org/10.1039/c3gc41951g)
116. R. Davis *et al.*, "Process design and economics for the conversion of lignocellulosic biomass to hydrocarbons: Dilute-acid and enzymatic Deconstruction of biomass to sugars and biological conversion of Sugars to Hydrocarbons," NREL Report No. TP-5100-60223, Golden, CO (2013).
117. J. D. P. Araújo, C. A. Grande, A. E. Rodrigues, Vanillin production from lignin oxidation in a batch reactor. *Chem. Eng. Res. Des.* **88**, 1024–1032 (2010). doi: [10.1016/j.cherd.2010.01.021](https://doi.org/10.1016/j.cherd.2010.01.021)
118. A. Guerra *et al.*, Toward a better understanding of the lignin isolation process from wood. *J. Agric. Food Chem.* **54**, 5939–5947 (2006). doi: [10.1021/jf060722v](https://doi.org/10.1021/jf060722v); pmid: [16881698](https://pubmed.ncbi.nlm.nih.gov/16881698/)
119. R. El Hage *et al.*, Characterization of milled wood lignin and ethanol organosolv lignin from miscanthus. *Polym. Degrad. Stab.* **94**, 1632–1638 (2009). doi: [10.1016/j.polydegradstab.2009.07.007](https://doi.org/10.1016/j.polydegradstab.2009.07.007)
120. N. Brosse, A. Dufour, X. Meng, Q. Sun, A. Ragauskas, Miscanthus: A fast-growing crop for biofuels and chemicals production. *Biofuels Bioprod. Bior.* **6**, 580–598 (2012). doi: [10.1002/bbb.1353](https://doi.org/10.1002/bbb.1353)
121. K. David, A. J. Ragauskas, Switchgrass as an Energy Crop for Biofuel Production: A Review of Its Ligno-cellulosic Chemical Properties. *Energy Environ. Sci.* **3**, 1182–1190 (2010). doi: [10.1039/b926617h](https://doi.org/10.1039/b926617h)
122. B. C. Saha, T. Yoshida, M. A. Cotta, K. Sonomoto, Hydrothermal pretreatment and enzymatic saccharification of corn stover for efficient ethanol production. *Ind. Crops Prod.* **44**, 367–372 (2013). doi: [10.1016/j.indcrop.2012.11.025](https://doi.org/10.1016/j.indcrop.2012.11.025)



123. P. Sannigrahi, A. J. Ragauskas, G. A. Tuskan, Poplar as a Feedstock for Biofuels: A Review of Compositional Characteristics. *Biofuels Bioprod. Bior.* **4**, 209–226 (2010). doi: [10.1002/bbb.206](https://doi.org/10.1002/bbb.206)
124. C. A. Nunes, C. F. Lima, L. C. A. Barbosa, J. L. Colodette, P. H. Fidêncio, Determinação de constituintes químicos em madeira de eucalipto por Pi-CG/EM e calibração multivariada: Comparação entre redes neurais artificiais e máquinas de vetor suporte. *Quim. Nova* **34**, 279–283 (2011). doi: [10.1590/S0100-40422011000200020](https://doi.org/10.1590/S0100-40422011000200020)
125. F. Huang, A. Ragauskas, Extraction of Hemicellulose from Loblolly Pine Woodchips and Subsequent Kraft Pulping. *Ind. Eng. Chem. Res.* **52**, 1743–1749 (2013). doi: [10.1021/ie302242h](https://doi.org/10.1021/ie302242h)
126. C. E. Wyman *et al.*, “Comparative Performance of Leading Pretreatment Technologies for Biological Conversion of Corn Stover, Poplar Wood, and Switchgrass to Sugars,” in *Aqueous Pretreatment of Plant Biomass for Biological and Chemical Conversion to Fuels and Chemicals*, C. E. Wyman, Ed. (Wiley, Oxford, 2013), pp. 239–260.
127. N. Mosier *et al.*, Features of promising technologies for pretreatment of lignocellulosic biomass. *Bioresour. Technol.* **96**, 673–686 (2005). doi: [10.1016/j.biortech.2004.06.025](https://doi.org/10.1016/j.biortech.2004.06.025); pmid: [15588770](https://pubmed.ncbi.nlm.nih.gov/15588770/)
128. I. Brodin, M. Ernstsson, G. Gellerstedt, E. Sjöholm, Oxidative stabilisation of kraft lignin for carbon fiber production. *Holzforschung* **66**, 141–147 (2012). doi: [10.1515/HF.2011.133](https://doi.org/10.1515/HF.2011.133)

**Acknowledgments:** This work is supported by several agencies, including the Laboratory Directed Research and Development Programs at ORNL and NREL [ORNL is managed by UT-Battelle, LLC, for the U.S. Department of Energy (DOE); NREL is managed by Alliance for Sustainable Energy, LLC, for DOE]; Genomic Science Program, Office of Biological and Environmental Research, DOE, under FWP ERKP752; National Advanced Biofuels Consortium, which is funded by DOE BioEnergy Technologies Office through American Recovery and Reinvestment Act Funds, and DOE and the BioEnergy Science Center (BESC). BESC is a DOE Bioenergy Research Center supported by the Office of Biological and Environmental Research in the DOE Office of Science.

[10.1126/science.1246843](https://doi.org/10.1126/science.1246843)



READ THE FULL ARTICLE ONLINE  
<http://dx.doi.org/10.1126/science.1249783>

A molecular mechanism for transmembrane signaling by the growth hormone receptor is elucidated.

# Mechanism of Activation of Protein Kinase JAK2 by the Growth Hormone Receptor

Andrew J. Brooks,\* Wei Dai, Megan L. O'Mara, Daniel Abankwa, Yash Chhabra, Rebecca A. Pelekanos, Olivier Gardon, Kathryn A. Tunny, Kristopher M. Blucher, Craig J. Morton, Michael W. Parker, Emma Sieracki, Yann Gambin, Guillermo A. Gomez, Kirill Alexandrov, Ian A. Wilson, Manolis Doxastakis, Alan E. Mark, Michael J. Waters\*

## RELATED ITEMS IN SCIENCE

J. A. Wells, A. A. Kossiakoff, New tricks for an old dimer. *Science* **344**, 703–704 (2014).  
 DOI: 10.1126/science.1254799

**Introduction:** Class I cytokines regulate key processes such as growth, lactation, hematopoiesis, and immune function and contribute to oncogenesis. Although the extracellular domain structures of their receptors are well characterized, little is known about how the receptors activate their associated JAK (Janus kinase) protein kinases. We provide a mechanistic description for this process, focusing on the growth hormone (GH) receptor and its associated JAK2.

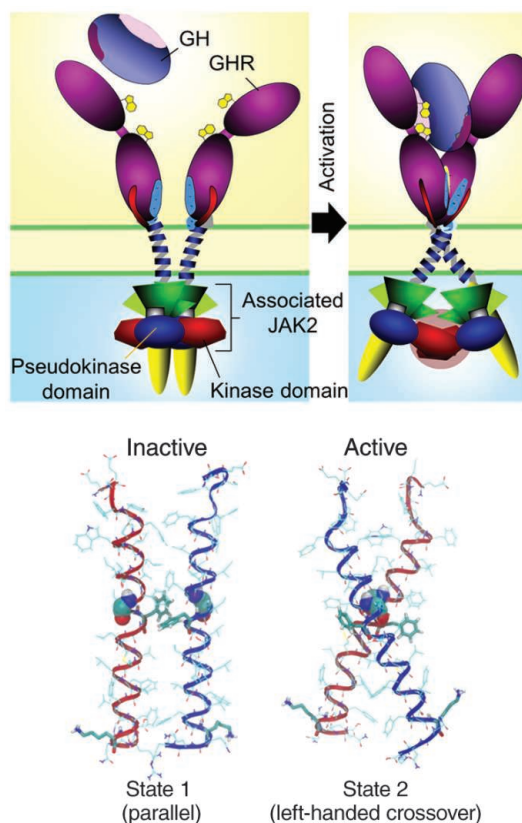
**Rationale:** We tested whether the receptor exists as a dimer in the inactive state by homo-FRET [fluorescence resonance energy transfer (FRET) between the proteins labeled with the same fluorophore] and other means. Then, to define receptor movements resulting from activation, we attached FRET reporters to the receptor below the cell membrane and correlated their movement with receptor activation, measured as increased cell proliferation. We controlled the position of the transmembrane helices with leucine zippers and mutagenesis, and we again monitored FRET and receptor activation. We used cysteine cross-linking data to define the faces of the transmembrane helices in contact in the basal state and verified this with molecular dynamics, which allowed us to model the activation process. We also used FRET reporters to monitor the movement of JAK2, and we matched this with molecular dynamics docking of the crystal structures of the kinase and its pseudokinase domains to derive a model for activation, which we then verified experimentally.

**Results:** We found that the GH receptor exists predominantly as a dimer in vivo, held together by its transmembrane helices. These helices are parallel in the

basal state, and binding of the hormone converts them into a left-hand crossover state that induces separation of helices at the lower transmembrane boundary (hence, Box1 separation). This movement is triggered by increased proximity of the juxtamembrane sequences, a consequence of locking together of the lower module of the extracellular domain on hormone binding.

Both this locking and the helix state transition require rotation of the receptors, but the key outcome is separation of the Box1 sequences. Because these sequences are bound to the JAK2 FERM (4.1, ezrin, radixin, moesin) domains, this separation results in removal of the pseudokinase inhibitory domain of one JAK2, which is blocking the kinase domain of the other JAK2, and vice versa. This brings the two kinase domains into productive apposition, triggering JAK2 activation. We verified this mechanism by kinase-pseudokinase domain swap, by changes in JAK2 FRET signal on activation, by showing association of pseudokinase-kinase domain pairs, and by docking of the crystal structures. An animation of our complete model of GH receptor activation is provided at <http://web-services.imb.uq.edu.au/waters/hgh.html>.

**Conclusion:** The proposed mechanism will be useful in understanding the many actions of GH, which include altered growth, metabolism, and bone turnover. We expect that it may extend to other members of this important receptor family. The mechanism provides a molecular basis for understanding the oncogenic JAK2 mutations responsible for polycythemia vera and certain other hematologic disorders and may thus be of value in the design of small-molecule inhibitors of clinical applicability.



**Receptor-JAK2 activation process. (Top)** Cartoons of the GH receptor basal state (state 1, left) and the active state (state 2, right) with **(Bottom)** transmembrane helix alignments for these states derived by modeling. GHR, GH receptor.

The list of author affiliations is available in the full article online.

\*Corresponding author. E-mail: m.waters@uq.edu.au (M.J.W.); a.brooks@uq.edu.au (A.J.B.)

Cite this article as A. J. Brooks *et al.*, *Science* **344**, 1249783 (2014). DOI: 10.1126/science.1249783



# Mechanism of Activation of Protein Kinase JAK2 by the Growth Hormone Receptor

Andrew J. Brooks,<sup>1\*</sup> Wei Dai,<sup>2</sup> Megan L. O'Mara,<sup>3</sup> Daniel Abankwa,<sup>1</sup> Yash Chhabra,<sup>1</sup> Rebecca A. Pelekanos,<sup>1</sup> Olivier Gardon,<sup>1</sup> Kathryn A. Tunny,<sup>1</sup> Kristopher M. Blucher,<sup>1</sup> Craig J. Morton,<sup>4</sup> Michael W. Parker,<sup>4,5</sup> Emma Sierecki,<sup>1</sup> Yann Gambin,<sup>1</sup> Guillermo A. Gomez,<sup>1</sup> Kirill Alexandrov,<sup>1</sup> Ian A. Wilson,<sup>6</sup> Manolis Doxastakis,<sup>2</sup> Alan E. Mark,<sup>1,3</sup> Michael J. Waters<sup>1\*</sup>

Signaling from JAK (Janus kinase) protein kinases to STAT (signal transducers and activators of transcription) transcription factors is key to many aspects of biology and medicine, yet the mechanism by which cytokine receptors initiate signaling is enigmatic. We present a complete mechanistic model for activation of receptor-bound JAK2, based on an archetypal cytokine receptor, the growth hormone receptor. For this, we used fluorescence resonance energy transfer to monitor positioning of the JAK2 binding motif in the receptor dimer, substitution of the receptor extracellular domains with Jun zippers to control the position of its transmembrane (TM) helices, atomistic modeling of TM helix movements, and docking of the crystal structures of the JAK2 kinase and its inhibitory pseudokinase domain with an opposing kinase-pseudokinase domain pair. Activation of the receptor dimer induced a separation of its JAK2 binding motifs, driven by a ligand-induced transition from a parallel TM helix pair to a left-handed crossover arrangement. This separation leads to removal of the pseudokinase domain from the kinase domain of the partner JAK2 and pairing of the two kinase domains, facilitating trans-activation. This model may well generalize to other class I cytokine receptors.

Class I cytokine receptors are key regulators of many processes, including post-natal growth, erythropoiesis, myelopoiesis, lactation, and metabolism. These receptors use the JAK-STAT (Janus kinase–signal transducers and activators of transcription) signaling pathway, which, when deregulated, becomes an important oncogenic pathway (1). Despite this, the molecular process responsible for activation of JAK2 tyrosine kinase by class I cytokine receptors has remained elusive.

Growth hormone (GH) and its receptor (Fig. 1) have been mechanistic exemplars for class I signaling molecules since publication of the crystal structure of the 2:1 complex of GH receptor (GHR) extracellular domains (ECDs) with the hormone (2). That structure and associated biophysical and mechanistic data (3, 4) led to a model of receptor activation wherein hormone-induced receptor dimerization resulted in close proximity of the receptor intracellular domains (ICDs) and

apposition of the activation loops within the catalytic domains of a pair of receptor-bound JAK2 protein tyrosine kinases, resulting in kinase activation (5). However, for the GHR and other related cytokine receptors such as the erythropoietin (EPO), prolactin, and thrombopoietin receptors, this model was superseded with the demonstration that these receptors exist largely as an inactive dimer in the absence of ligand (6–11). The transmembrane domains (TMDs) of these single-pass cytokine receptors have an important role in their constitutive dimerization, as shown by the ToxR assay for the EPO receptor (EPOR), as well as fluorescence resonance energy transfer (FRET) and coimmunoprecipitation studies with the GH and prolactin receptors. The existence of such dimers implies that a specific ligand-induced conformational change is required for signal transmission to the associated cytoplasmic JAK2 proteins.

Comparison of receptor subunit 1 in the crystal structure of the 2:1 complex of the GHR with GH bound with the unliganded crystal structure showed only minor conformational differences, implying that the signal is initiated by subunit realignment as a result of the asymmetric placement of the receptor binding sites on GH (7). How this realignment brings the dimeric receptor-associated JAK2 pair into productive interaction has remained elusive. Single-particle electron microscopic imaging of the homologous kinase JAK1 has not been able to resolve this issue thus far. The full crystal structure of JAK2 itself is not yet resolved (12). An appropriate model for JAK2 activation by its associated cytokine receptor should provide a means

of removing the inhibitory pseudokinase domain from the kinase domain of JAK2 and then aligning the kinase domains for their transactivation and signal initiation. The model should also account for the observation that mutations Val<sup>617</sup>→Phe<sup>617</sup> (V617F) and Tyr<sup>613</sup>→Glu<sup>613</sup> (Y613E) (13), which result in constitutively active JAK2 mutants, are only active at physiological expression levels in the presence of receptor dimers (14, 15). It should also encompass the finding that JAK2 binds to the juxtamembrane (JM) Box1 sequence of GHR through residues close to the end of the N-terminal FERM domain (16). We present a molecular model for activation of JAK2 by GH based on experimentation and molecular modeling (view animation at <http://web-services.imb.uq.edu.au/waters/hgh.html>).

## Results

### *GHR TMD Interaction Supports the Role of the TMD in Constitutive Dimer Formation and the Importance of Key Residues in TMD Helix Packing*

The GHR TMD is critical for ligand-independent receptor association (7). To characterize which interactions within the TMD contribute to constitutive GHR dimerization, we used the ToxR assay (17). This assay provides a colorimetric measure of TMD interactions from isolated TMDs expressed in the inner cell membrane of *Escherichia coli* (fig. S2) and has been used to demonstrate TMD association for the homologous EPOR and thrombopoietin receptor (TpoR or c-Mpl) (10, 18). The ToxR assay showed that GHR TMDs self-associate (Fig. 2A), although less strongly than do the homodimeric EPOR or the leucine zipper controls, but strongly compared with the noninteracting poly-alanine (alanine 16) control. The N-terminal, C-terminal, and central portions of the GHR TMD all interacted in this assay. Pro<sup>266</sup> and the first glycine (Gly<sup>274</sup>) of the GxxG motif [both of which are highly conserved (fig. S1)] appeared to weaken the TMD helix interaction, because interaction increased on conversion of these residues to Ile (Fig. 2, B and C). Substitution of individual residues within the TMD with alanine has negligible effect on helix interactions for these cytokine receptors (18), so we introduced disruptive Gly-Pro double substitutions at I272F and L282F. These substitutions decreased helix interaction [as they do for the EPOR TMD interaction, where they are thought to introduce a kink (19)]. Conversely, substitution of V280M with G280P had the opposite action, increasing interaction of GHR TMD helices (Fig. 2C). These results support the view that the GHR TMD helices do associate constitutively in a specific manner, but not so strongly as to preclude realignment as a result of ligand binding to the ECD.

Verification of constitutive dimer formation of GHR in mammalian cells was obtained by homo-FRET (FRET between the proteins labeled with the same fluorophore) with confocal microscopy

<sup>1</sup>The University of Queensland, Institute for Molecular Bioscience (IMB), St Lucia, Queensland 4072, Australia. <sup>2</sup>Department of Chemical and Biomolecular Engineering, University of Houston, Houston, TX 77004, USA. <sup>3</sup>The University of Queensland, School of Chemistry and Molecular Biosciences, St Lucia, Queensland 4072, Australia. <sup>4</sup>Biota Structural Biology Laboratory and Australian Cancer Research Foundation (ACRF) Rational Drug Discovery Centre, St Vincent's Institute of Medical Research, Fitzroy, Victoria 3065, Australia. <sup>5</sup>Department of Biochemistry and Molecular Biology and Bio21 Institute, University of Melbourne, Parkville, Victoria 3052, Australia. <sup>6</sup>Scripps Research Institute, La Jolla, CA 92037, USA.

\*Corresponding author. E-mail: m.waters@uq.edu.au (M.J.W.); a.brooks@uq.edu.au (A.J.B.)

anisotropy analysis at the cell surface (20, 21) (Fig. 2D). As controls for these experiments, we determined the FRET efficiency measured by fluorescence anisotropy of constitutive monomeric and dimeric versions of the receptor-type tyrosine-protein phosphatase  $\alpha$  (RTPT $\alpha$ ) transmembrane protein and compared it with that of the GHR fused to mCitrine (mCit) after residue 341, 37 residues after the Box1 sequence. For the monomeric RTPT $\alpha$  construct, the TMD was exchanged for the monomeric low-density lipoprotein receptor (22), whereas for the dimeric RTPT $\alpha$  construct, a constitutive disulfide bond was introduced in the extracellular domain adjacent to the TMD (23–25) (see supplementary materials). These data show that the GHR receptor exists primarily as a dimer at the surface of live cells.

#### Cysteine Scanning Analysis of GHR TMD Indicates Relative Orientation of Helices in the Receptor Dimer

Transmembrane domain association was verified by cysteine cross-linking of the TMD and JM residues. For these studies, a receptor construct was truncated in the intracellular domain after residue 388 and Cys<sup>259</sup> was converted to Ser<sup>259</sup>, resulting in a receptor without cysteines C-terminal of the lower cytokine domain. Within this construct, each amino acid from the top of the JM linker that joins the lower cytokine domain to the TMD, down to the end of the TMD (Leu<sup>251</sup> to Ser<sup>288</sup>), was individually mutated to cysteine, and cross-linking between receptors was examined. For these experiments, both intact cells and cell membranes were used. We cross-linked with either a cell-permeable 5 Å linker [methanethiosulfonate (MTS)] or through the formation of a disulfide bond with Cu-phenanthroline. Cross-linking with MTS in intact cells revealed dimeric and monomeric forms, with all of the N-terminal JM residues (Cys<sup>259</sup> to Phe<sup>265</sup>) cross-linking similarly, presumably reflecting flexibility in the absence of ligand, as shown for the EPOR (26). However, within the bulk of the TMD there was a helical periodicity evident in dimer formation, and when cross-linked residues were plotted on a helix wheel projection, an interaction interface (which included Ile<sup>272</sup> and Phe<sup>273</sup>, Ile<sup>275</sup> and Phe<sup>276</sup>, and Val<sup>280</sup>) was apparent, with cross-linking just visible at Phe<sup>283</sup> (Fig. 3, A and B). MTS has limited accessibility to residues buried deep in the bilayer where little reactive thiolate anion is present (27), which may account for the low efficiency of dimer formation toward the cytoplasmic side. This interface correlates well with the basal-state configuration predicted by molecular dynamics (MD) simulations (see below). The conserved GxxG motif appears not to participate in the TMD interaction in the basal state. Cross-linking of cell membranes with Cu-phenanthroline (which is less able to penetrate cell membranes) showed that cross-links could form from Thr<sup>258</sup> to Ileu<sup>268</sup> and again from Thr<sup>280</sup> to Leu<sup>286</sup> at the lower TMD boundary.

We investigated the extent of cross-linking in the presence or absence of human GH (hGH) in cell membrane preparations. Increased Cu-phenanthroline-induced cross-linking of D262C, located in the JM region, was evident in the presence of hGH (Fig. 3C), although other residues did not yield consistent results. This supports the view that ligand binding increases the proximity between JM residues in this conserved membrane proximal sequence and is consistent with hGH-induced formation of disulfide dimers at the adjacent Cys 259 residue in the native receptor (28).

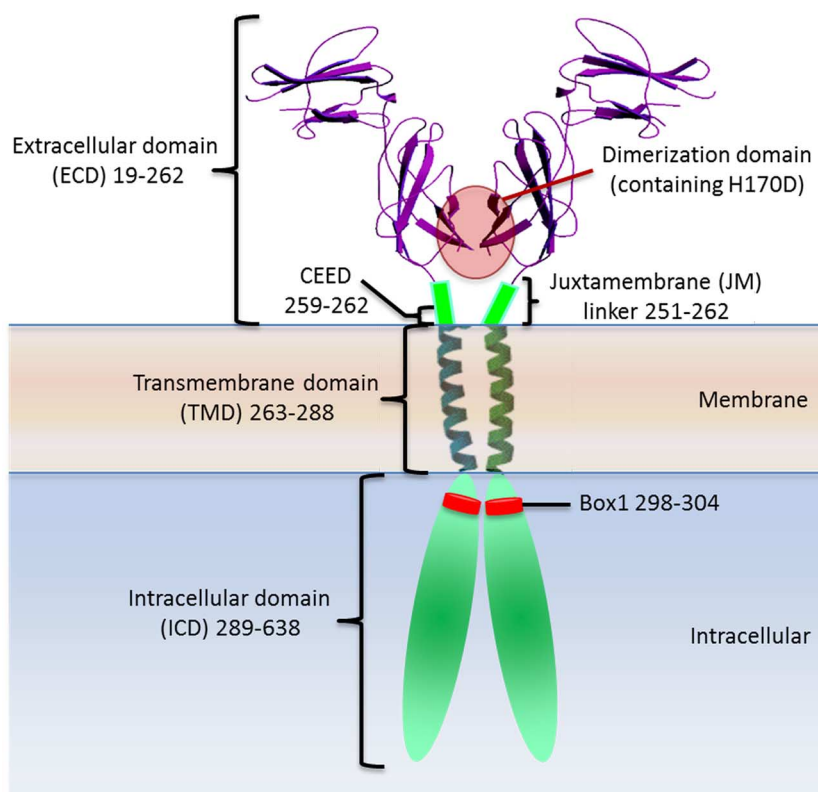
#### GHR Dimerization by Disulfide Bond Formation at the Extracellular JM and TMD Results in Constitutively Active Receptors

Growth hormone, like its structural homologs EPO and prolactin, has two asymmetrically placed receptor binding sites that would change the interaction geometry between the two receptor subunits on binding. To understand the nature of this change, we began with the observation that a minor fraction of the cysteine-substituted receptors described above form cross-linked dimers spontaneously in the absence of ligand (fig. S3). Hence, we could observe the activity of full-length dimerized receptor in the absence of ligand through cysteine substitution at cross-linked residues within the JM linker and upper TMD helix regions. For these experiments, we also mutated wild-type (WT) Cys<sup>259</sup> to Ser<sup>259</sup>. Transient expression in human embryonic kidney (HEK) 293 cells re-

vealed that constitutive cross-linking of the GHR with cysteine substitutions between Glu<sup>260</sup> and Leu<sup>269</sup> is accompanied by receptor activation (measured as STAT5 Tyr<sup>694</sup> phosphorylation), whereas above this, dimer formation and activation were weak. No evident dimer formation or signaling was seen with Cys<sup>259</sup> converted to serine, that is, when no JM or TMD free cysteines were present (Fig. 3D). Evidently dimerization within the upper TMD or the extracellular EED sequence can initiate signaling (i.e., close apposition of the upper TMD is sufficient to initialize signaling). Accordingly, introducing two disulfide bonds by cysteine substitution at E260C and I270C resulted in even stronger receptor activation (Fig. 3D).

#### Controlled Dimerization of GHR Reveals that Increased Receptor Activation Correlates with an Increase in Separation of the Box1 Motifs

To better understand the steric requirements for receptor activation we substituted the GHR ECD with a leucine zipper from the transcription factor c-Jun. This allowed us to control the positioning of the TMD without compensatory movements by the ECDs. The positioning of the cytoplasmic JAK2-binding Box1 motif and its downstream sequence were monitored by placing C-terminal FRET reporters (mCit or mCFP) 37 residues below the Box1 sequence. The receptor truncation and addition of FRET reporters did not prevent



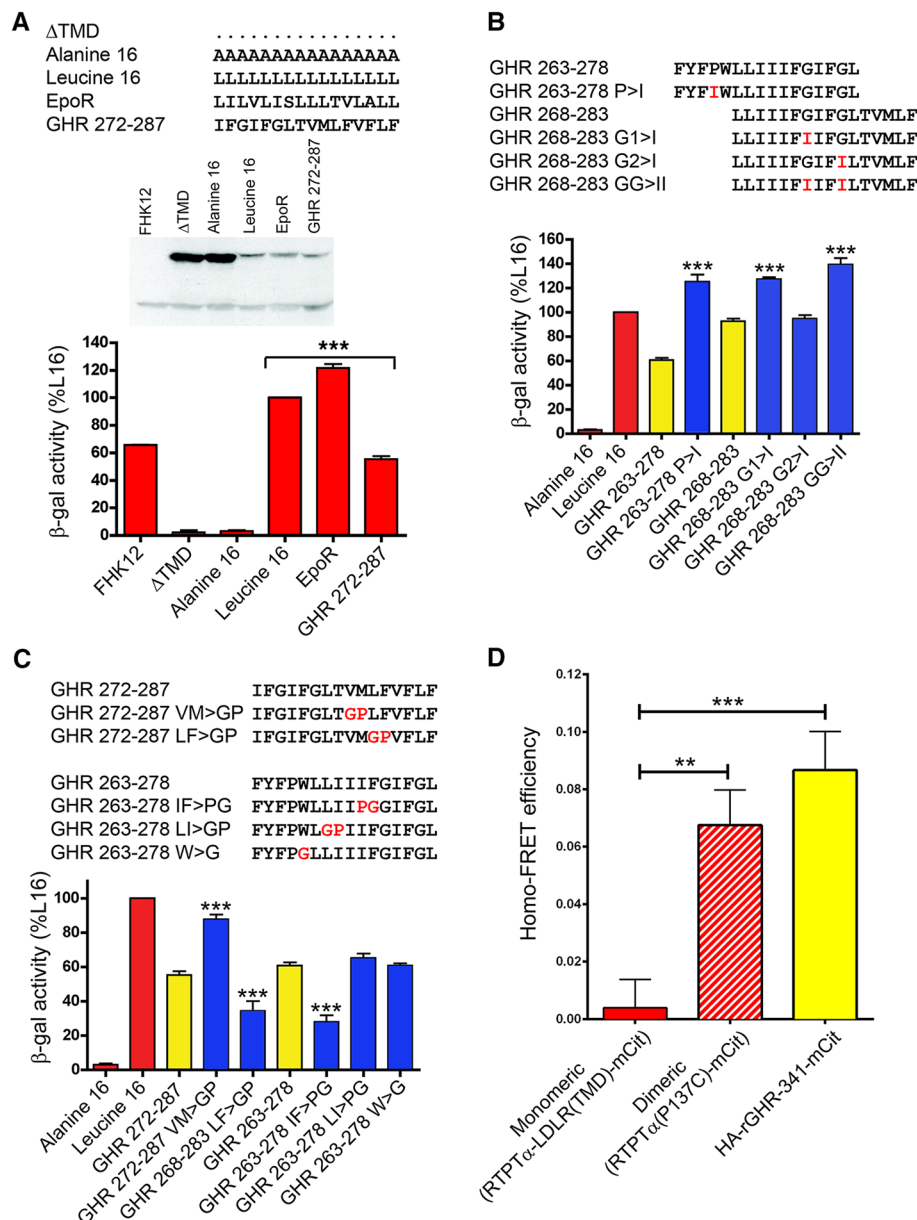
**Fig. 1. Cartoon of GHR showing key features with residue numbers.**



JAK2 binding, and GH addition activated JAK2 for these receptor constructs (fig. S4 and S5).

We first positioned the Jun zipper 12 residues above the presumed TMD boundary, where the GHR linker joins to the lower cytokine receptor domain. This construct results in some constitutive activation (29). Shortening the linker by

four residues at a time revealed that the closer the Jun zipper came to the TMD, the stronger the signal was, as measured by cell proliferation (Fig. 4, A and B). The strength of the signal correlated inversely with FRET ratio; that is, signal activation was associated with separation of the Box1 and its downstream sequence (Fig. 4, C to E).



**Fig. 2. Evidence of GHR dimers in cell surface membranes.** (A to C) GHR TMD association shown by ToxR assay. (A) ToxR assay showing self-association of GHR and EPOR TMDs with controls showing amino acid sequences used for each TMD construct, together with a maltose-binding protein (MBP) immunoblot of the ToxR-TMD-MBP chimeric proteins expressed in FHK12 *E. coli*, which was used to normalize the β-galactosidase values in Miller units (see fig. S2 for detail). (B and C) GHR TMD sequences showing mutations introduced to perturb TMD association, as monitored in the ToxR assay ( $n = 4$  to 17 independent experiments in triplicate, values expressed as percent L-16 value after normalization of β-galactosidase activity to MBP expression). Error bars in (A) to (C) denote average  $\pm$  SEM, with one-way ANOVA and Tukey's multiple comparison post-test (\*\* $P < 0.01$ , \*\*\* $P < 0.001$  compared to test constructs). (D) Homo-FRET efficiency for individual mCit-labeled proteins using confocal microscopy anisotropy analysis at the surface of live mammalian cells. Controls were constitutive monomeric and dimeric versions of the RTPTα transmembrane protein.

Next, the Jun zipper was placed at the upper TMD boundary, and the helices were rotated by inserting one to four alanines sequentially at the junction with the TMD. There was an optimum rotational position for signal activation, with the active and inactive positions adjacent. Again, the FRET ratio indicated that separation of the Box1 and downstream sequence occurs in the active rotational position (Fig. 4, F to H). To exclude the possibility that the changes in FRET ratio resulted from reorientation of the fluorophores rather than their separation, the comparison of the 3Ala and 4Ala Jun insertion constructs was repeated with the flexible linker RSIAT (Arg-Ser-Ile-Ala-Thr) (30) between the fluorophores and residue 341 of the receptor. This did not influence the FRET ratio comparison, from which we conclude that the decreased FRET ratio in the active states resulted from increased distance and not fluorophore rotation (fig. S6).

Because clamping the receptors together at the upper TMD interface, either by use of the Jun zipper (Fig. 4, A to E) or through disulfide bond formation (Fig. 3D), resulted in receptor activation, we examined the role of the conserved EED acidic sequence (fig. S1) positioned therein. It seemed likely that like-charge repulsion could maintain separation of the receptors and keep the receptor in an inactive state in the absence of ligand. Repulsion could then be overcome by ligand binding, inducing closer apposition of the receptors within the constitutive dimer. We explored this hypothesis by comparing the Jun-3Ala construct with an equivalent construct in which the three alanines were reverted to the WT E<sup>260</sup>ED sequence. The presence of the AAA sequence compared to EED substantially increased the proliferative activity and decreased the FRET ratio below the Box1 domain (Fig. 5A), again indicating that when the receptor dimer is clamped tighter together at the upper TMD interface, the Box1 motifs separate.

If this phenomenon applied to the full-length receptor, it could act as a point of control (gate) for receptor activation. We introduced the charge reversal mutations KKR in place of the EED sequence and transduced the full-length KKR construct alone or together with the WT construct into Ba/F3 cells and measured constitutive activity. Electrostatic attraction at this position partially activated the full-length receptor (Fig. 5B). This activation was again associated with separation of the Box1 and associated sequences below the membrane, as shown with GHR constructs that contained the full ECD with mCFP/mCit reporters placed after the Box1 motif (Fig. 5C). Expression of WT-GHR or KKR-GHR individually gave similar FRET values, whereas coexpression of both constructs gave a significantly lower FRET value, again demonstrating the inverse correlation between activation and separation of the Box1 motif.

We then used the full ECD WT-GHR FRET constructs to verify that the binding of hormone alone to the receptor on intact cells also resulted

in a decreased FRET ratio with membrane extracts from these cells (Fig. 5D). Introduction of the GHR D170H mutation (often referred to as D152H using numbering of the mature protein), which results in GH-insensitive Laron dwarfism (31), into these FRET constructs prevented the decrease in FRET seen with WT receptor in response to GH binding (Fig. 5D). The decrease in FRET ratio induced by WT GH was not seen with the clinical GH antagonist G120R hGH, and this also blocked the decrease in FRET ratio induced by WT GH (Fig. 5D).

Previous observations that hormone binding to GHR produced a transient increase in FRET signal (32) may have resulted from FRET reporters being placed at the C terminus. Given the relative immobilization of receptor-bound JAKs below the TMD, the lower cytoplasmic domains must move toward the JAKs for tyrosine phos-

phorylation to occur. This would be facilitated by an unstructured cytoplasmic domain, as is known to occur in the JAK1-gp130 couple (33).

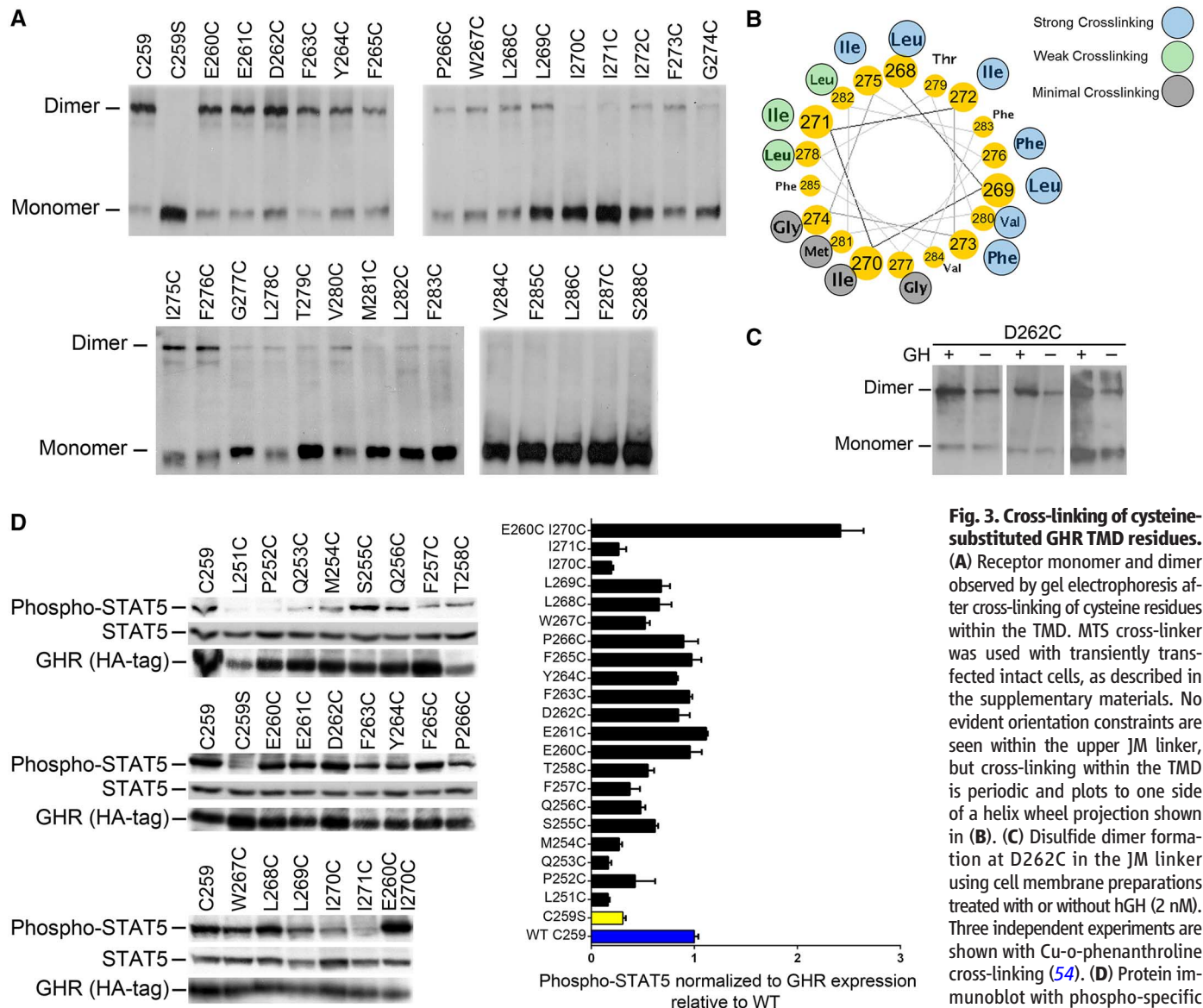
Role of Lys<sup>289</sup> at the GHR TMD-ICD Boundary in Receptor Activation

The data presented above are consistent with a gating mechanism at the upper TMD boundary that holds the receptors apart, minimizing activation in the absence of ligand. We investigated whether there are residues that hold the submembrane sequences together in the inactive state as there are in the TpoR, in which mutations within the conserved sequence above the Box1 domain result in constitutive activation and myeloproliferative neoplasms (34). Alanine substitution within the equivalent conserved SKQQRK sequence (fig. S1) in the GH receptor revealed that conversion

of the first lysine residue (Lys<sup>289</sup>) to alanine resulted in increased signaling (Fig. 5, E and F). The equivalent K507A mutant in TpoR also showed increased activation (30). Again, for K289A GHR, the submembrane FRET reporters indicate increased separation of the Box1 sequences (Fig. 5E) through movement of the JM  $\alpha$ -helical sequence (35).

Active and Inactive Dimer Orientations Identified by Molecular Simulations of GHR TMDs

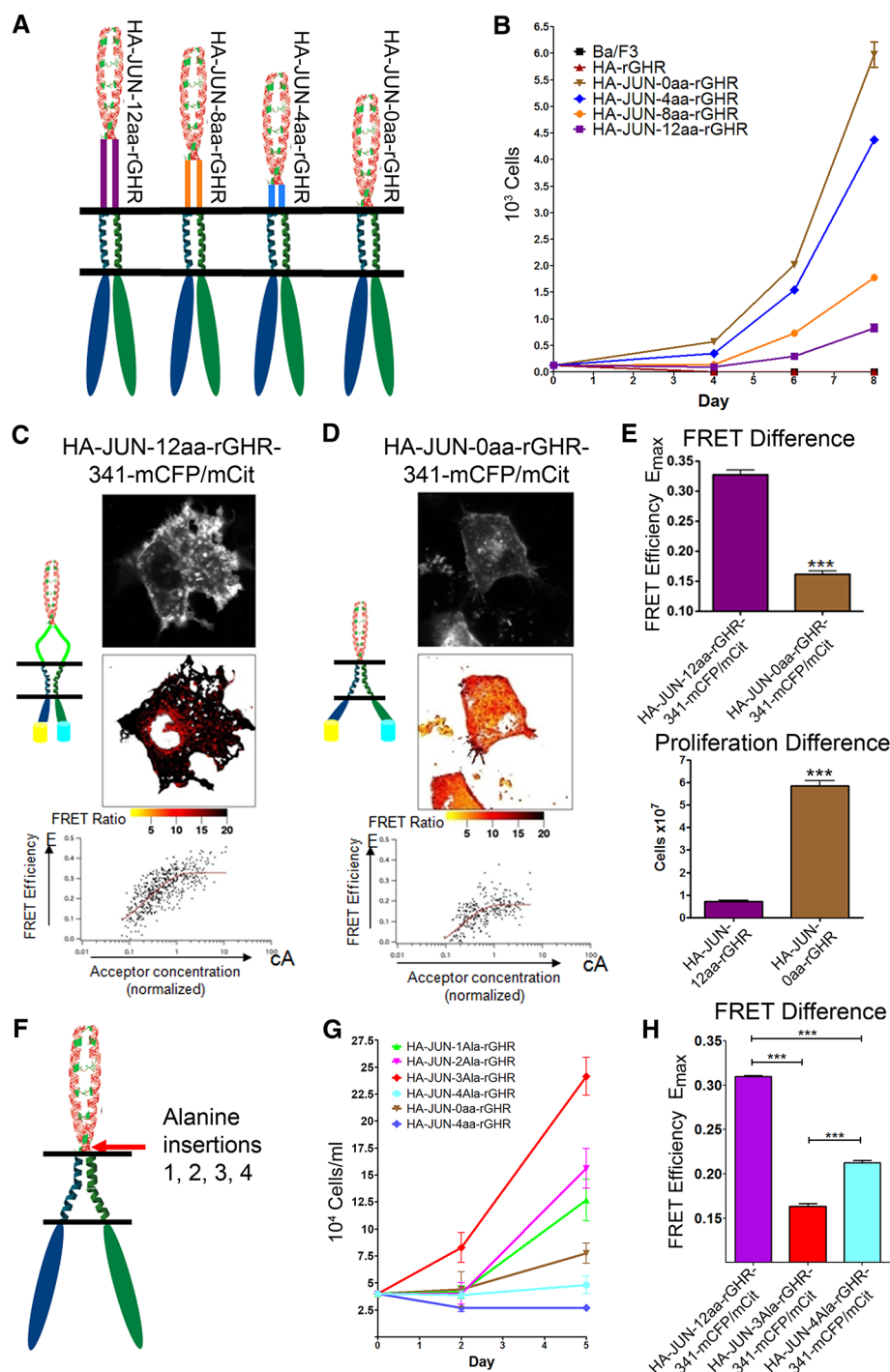
To understand the above experimental data in terms of a molecular model, we undertook extensive in silico modeling of the hGHR TMD helix dimers, initially assuming the helices were in a vacuum. Searches of helix rotation angles for both right- and left-handed crossing angles predicted a helix alignment corresponding to the cross-link data (Fig. 3A), with interactions between Phe<sup>276</sup>



**Fig. 3. Cross-linking of cysteine-substituted GHR TMD residues.** (A) Receptor monomer and dimer observed by gel electrophoresis after cross-linking of cysteine residues within the TMD. MTS cross-linker was used with transiently transfected intact cells, as described in the supplementary materials. No evident orientation constraints are seen within the upper JM linker, but cross-linking within the TMD is periodic and plots to one side of a helix wheel projection shown in (B). (C) Disulfide dimer formation at D262C in the JM linker using cell membrane preparations treated with or without hGH (2 nM). Three independent experiments are shown with Cu-o-phenanthroline cross-linking (54). (D) Protein immunoblot with phospho-specific antibodies for active STAT5 in tran-

siently transfected HEK293 cells. Levels of receptor expression are shown by corresponding blots for HA-tagged hGHR. The histogram shows the pSTAT5 level normalized to receptor protein expression for three replicate experiments [mean  $\pm$  SEM (error bars)].





**Fig. 4. Replacement of ECD with Jun zippers to enable analysis of orientational constraints in constitutive signaling by GHR.** (A) Shortening of the linker between the Jun zipper and the TMD results in (B) increased receptor activation in Ba/F3 cells stably expressing Jun fusion constructs (measured as increased cell number). (C and D) FRET efficiency images (top image, total fluorescence; lower image, FRET efficiency, where darkest is highest FRET efficiency, see color bar) by live-cell confocal microscopy, together with fluorescence-activated cell sorting (FACS) FRET analysis for individual cells showing an inverse relation between cell proliferation (measured as in Materials and Methods, with cell number shown at day 8) and FRET ratio for these constructs (E). (F) Rotation of the Jun-clamped TMD by insertion of one to four alanines into the HA-JUN-0aa-rGHR construct reveals an optimum orientation of the TMD helix for signaling, measured as cell proliferation (G), and this correlates with decreased FRET reporter signal below the TMD (H). Error bars in (B), (E), (G), and (H) denote SEM. \*\*\* $P < 0.001$ .

and Phe<sup>283</sup> (lowest free energy, cluster 1, fig. S7A). The rather different chicken GHR sequence was predicted to give a similar alignment (fig. S7C).

To understand the dynamics of receptor activation, we used MD simulations to model the behavior of the TMDs in a lipid bilayer (Fig. 6, A and B, and supplementary materials). A coarse-grained representation of the peptide, lipids, and solvent (36) was used to obtain the free-energy profile as a function of distance (PMF) between two TMDs by exhaustive Monte Carlo simulations of 128 replica pairs for a range of separations between the centers of mass of the helices (37). The fact that the PMF has a deep minimum at a separation of 0.7 to 0.8 nm with a predicted free energy of binding around 10 kcal/mol supports the finding that two TMDs interact strongly with minimal free monomer present (Fig. 6B).

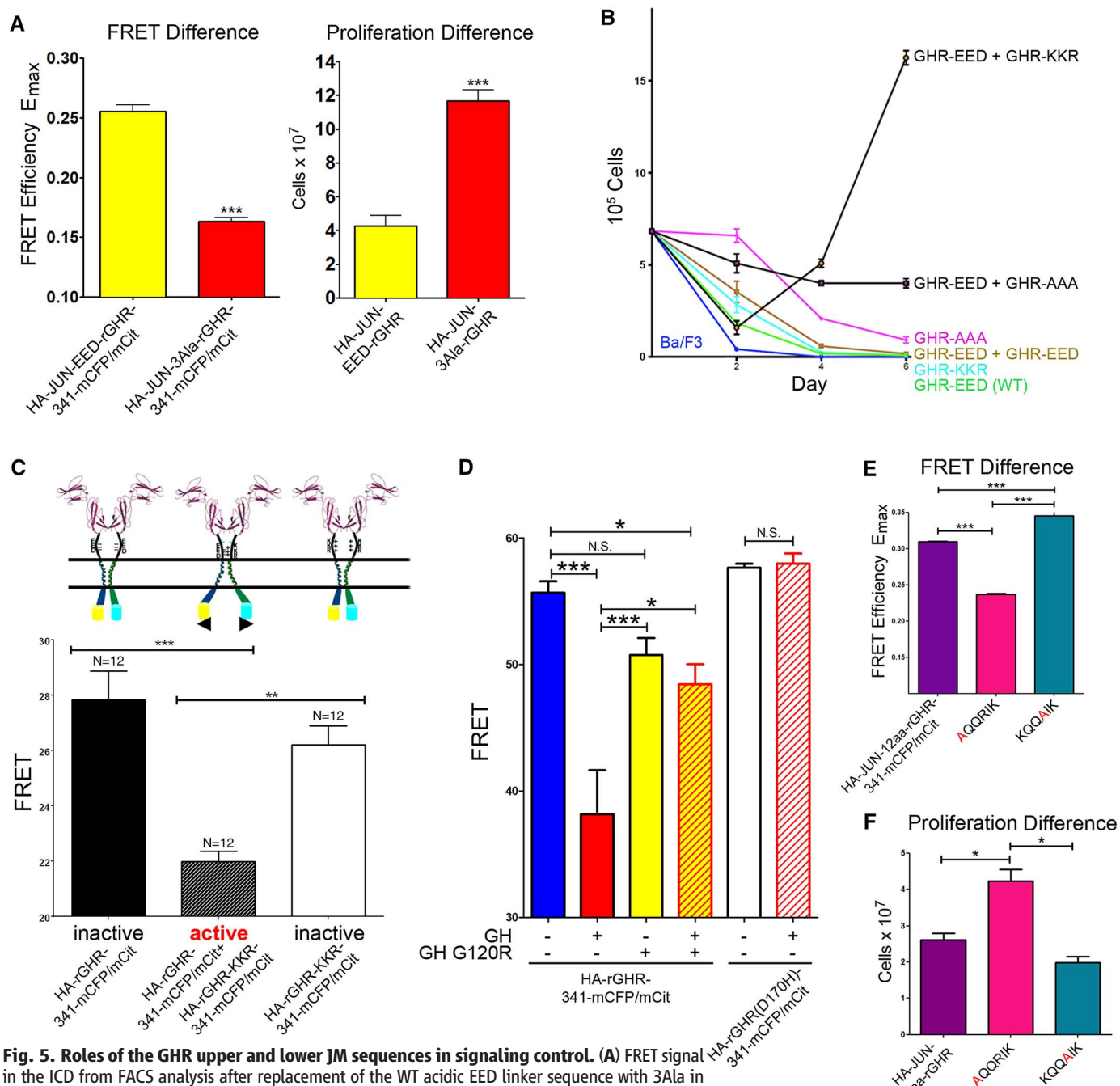
We sought measures to characterize our modeling data such as the crossing angle  $\Omega$  between the helix axes. We mapped the contacts between the two helices as they approach within a lipid bilayer (Fig. 6C). Helices tilt and interact first when the lateral separation of the centers of mass is  $\sim 2$  nm. Repulsive interactions at the N termini result in formation of an initial contact at the C termini. Subsequently, the TMDs follow a path that maximizes interactions between the Phe residues and Thr-Thr hydrogen bonding. This initially leads to an essentially parallel dimer (state 1 in Fig. 6D) with a low  $\Omega$  value but with many interactions. Closer approach of the helices (as could result from hormone binding) leads to a close-packed structure (state 2 in Fig. 6E) with increased tilting and  $\Omega$ , resulting in a left-handed crossover dimer with increased separation at the C terminus (see below). Both states 1 and 2 lie within the energy minimum (Fig. 6B), indicating a relatively facile state 1-to-state 2 transition. This transition has been observed for other TMDs using coarse-grained and atomistic simulations in simpler environments (38, 39). GHR TMDs form the left-handed dimer by rotating Phe<sup>276</sup> and Phe<sup>283</sup> out of the interface. Importantly, right-handed essentially parallel dimers at close separation readily rearrange to left-handed dimers (state 2) by substitution of disulfide bonds at Glu<sup>260</sup> and Ile<sup>270</sup> (Fig. 7, A and B), correlating with the constitutive receptor activation of such dimers (Fig. 3D). This is analogous to the activation seen by moving the Jun zipper down onto the cell surface (Fig. 4B).

To better identify structures correlated to activity, we needed to compare our predictions with mutation and cross-linking experiments. Therefore, atomistic models of helical TMDs were superimposed onto the structures from the coarse-grained simulations and subjected to MD in large lipid-bilayer systems. For state 1, three structures were each simulated for 0.3  $\mu$ s. Figure 6D shows a snapshot of one such dimer (state 1), together with an analysis of the separation between specific residues for which cysteine substitutions had been performed for each of the three trajectories. All three dimers fluctuated somewhat but maintained a separation of between 0.9 and 1.2 nm,

slightly tilted relative to the normal of the bilayer and in a parallel arrangement with low  $\Omega$ . These dimers are characterized by extensive interactions between Phe residues and appear to be stabilized by Lys<sup>289</sup>, which anchors the lower C termini at the water-hydrophobic region boundary. The pre-

dicted sulfur-sulfur separation distances closely resembled the experimental cross-link pattern seen with cysteine-cross-linking experiments in the absence of ligand, supporting state 1 as the inactive state. Gly<sup>274</sup> is far from the helix interface in the absence of hormone.

A 0.7- $\mu$ s full atomistic simulation for the most stable dimer predicted by the simpler coarse-grain model (state 2) showed that it remained helical throughout the simulation (Fig. 6E). Backbone atoms presented small fluctuations with an overall lateral separation of 0.8 nm. Helices tilted,



**Fig. 5. Roles of the GHR upper and lower JM sequences in signaling control.** (A) FRET signal in the ICD from FACS analysis after replacement of the WT acidic EED linker sequence with 3Ala in Jun GHR, and cell number for this construct stably expressed in Ba/F3 cells at day 8.  $E_{max}$ , FRET efficiency at high acceptor concentration. (B) Expression of full-length GHR in transduced Ba/F3 cells with WT GHR or GHR with the E<sup>260</sup>ED residues substituted to AAA or KKR. (C) Decreased FRET with membrane preparations when FRET reporters are placed below Box1. This activation correlates with increased proliferation. N, number of replicates. (D) FRET ratio in membrane preparations from transiently expressed rGHR-reporter constructs in HEK 293T cells treated with or without hGH (5 nM) or with G120R hGH (500 nM). Cells were also incubated with 500 nM G120R hGH for 10 min before treatment with 5 nM hGH. The GHR D170H Laron mutant showed no FRET change upon GH addition. N.S., not significant. (E and F) Substitution of Lys<sup>289</sup> with Ala promotes proliferative signaling in stably expressing Jun GHR Ba/F3 cells (shown for proliferation assay at day 3), and this correlates with decreased FRET from FACS analysis from reporters placed below Box1. ANOVA with Tukey post hoc test, \* $P < 0.05$ , \*\*\* $P < 0.001$ . Error bars in all panels denote SEM.

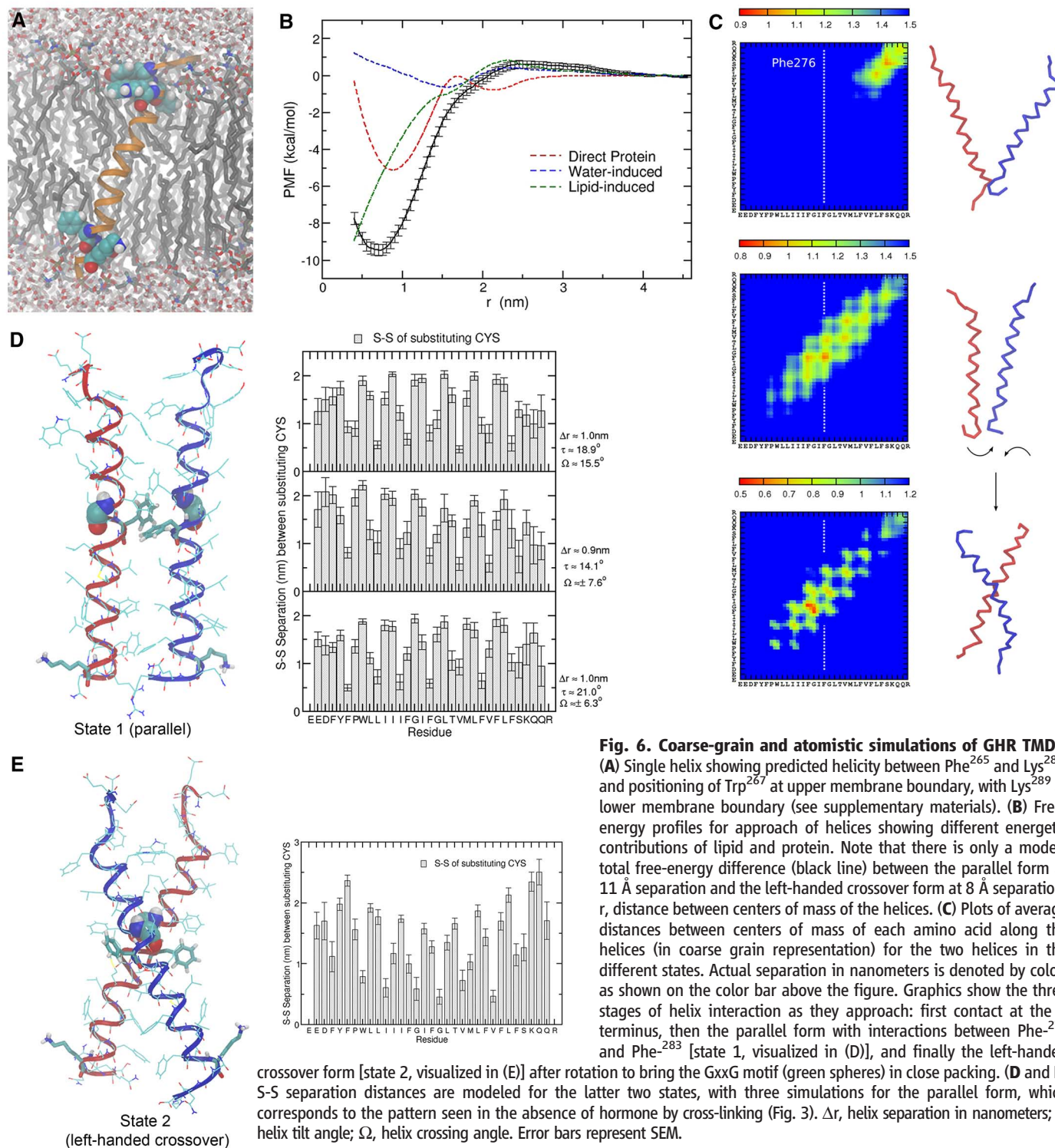


rotated, and packed against Gly<sup>274</sup> with a separation of substituted cysteines distinctively different from those obtained in experimental data for the inactive receptor. When the inactive state (Fig. 6D) was compared with the left-handed crossover form (Fig. 6E), separation between the C termini was increased (evident in the cysteine substitution sulfur-sulfur distances). The increased separation parallels our finding that activity

correlates with higher separation of the C termini, as monitored by FRET. Moreover, in the proposed active state 2 form, the N-terminal Trp<sup>267</sup> sits favorably at the membrane interface, facing outward to favor association, whereas the C-terminal Lys<sup>289</sup> is in an unfavorable configuration for helix interaction (allowing greater separation), consistent with nuclear magnetic resonance studies using model peptides (40). Thus, the model can

explain how alanine substitution of Lys<sup>289</sup> promotes the left-handed dimer form, correlating with the increased activation seen on conversion of Lys<sup>289</sup> to Ala (Fig. 5, E and F).

We constructed a chimeric model in which the proposed TMD dimer configurations were joined to the crystal structure of the human GH:ECD receptor complex [Protein Data Bank (PDB) ID: 3HHR]. Missing residues were generated with



State 1 (parallel)

State 2 (left-handed crossover)

the Modeller program ([http://salilab.org/modeller/about\\_modeller.html](http://salilab.org/modeller/about_modeller.html)). The overall best configuration based on Modeller's objective function for the linking amino acids (Fig. 7C) shows a good fit between the ECD positioning and the state 2 configuration and places the two Cys<sup>259</sup> residues in close enough proximity to form a disulfide bond, as shown experimentally after GH addition (28). We could also identify potential interreceptor hydrogen bonds in the linker that could assist in stabilizing the active configuration, between Glu<sup>260</sup> of receptor 1 and the amide of Trp<sup>267</sup> in receptor 2, as well as between the backbone carbonyl of Phe<sup>257</sup> and amide of Glu<sup>260</sup> in receptor 2. The ECDs without the hormone were attached to the parallel TMD (state1). This simulation

produced rotation of the ECDs, as described for isolated ECDs (41). In that simulation, the linker regions sat on the membrane, although the ECD domains did not separate. This observation is consistent with our inability to cross-link receptors above Cys<sup>259</sup> efficiently in the basal state. Potentially, this is related to repulsion between the acidic EED sequences.

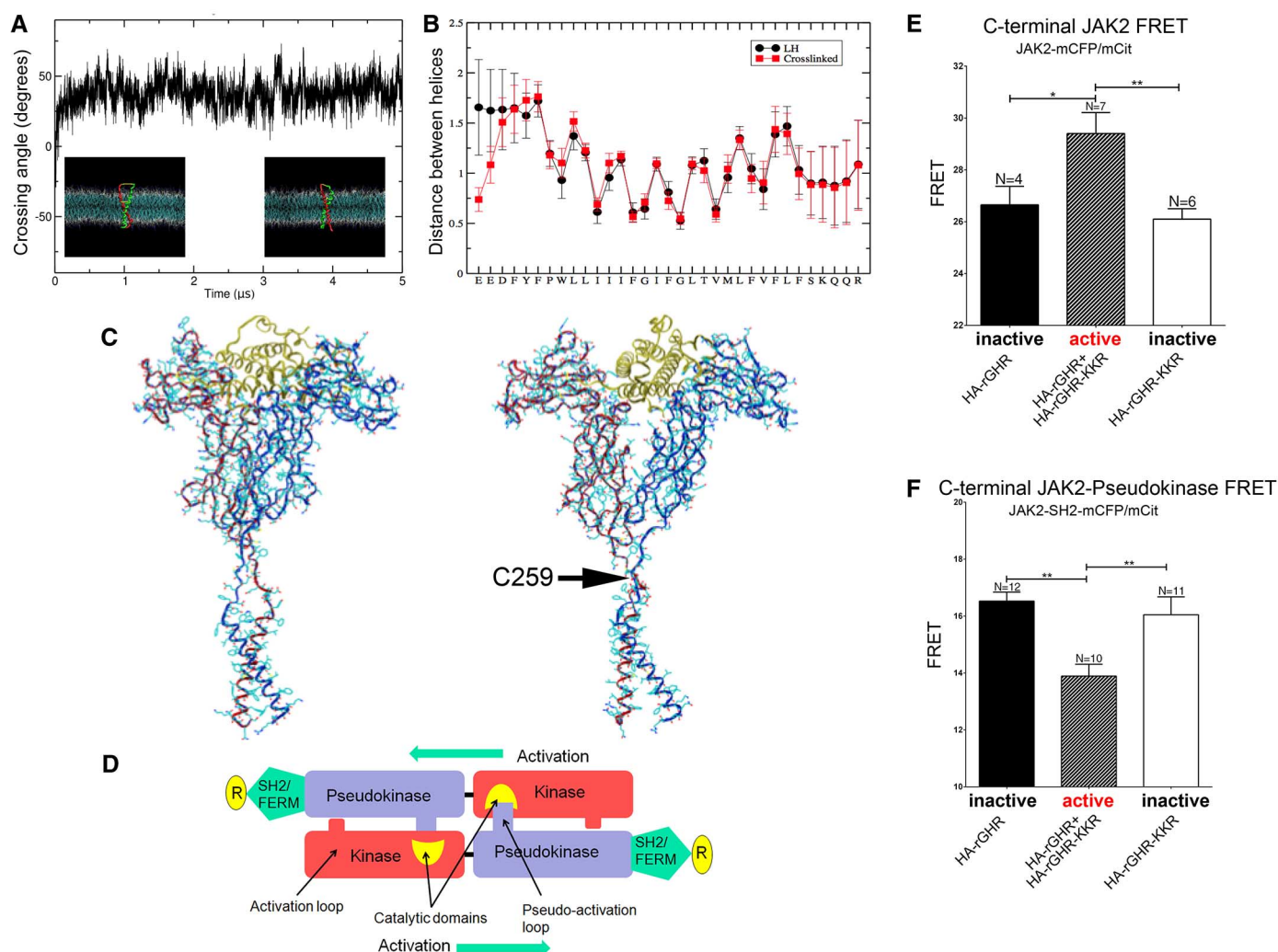
#### A Model for GHR Activation

The above findings are consistent with a model of receptor activation in which binding of GH through its asymmetrically placed binding sites (2) realigns the two receptors by relative rotation [as evident in MD simulations (41)] and, together with elevation of receptor 1, locks the two di-

merization domains in the ECD closely together. This locking is necessary for signal transduction (42, 43) and brings the upper TMD sequences close together by overcoming the electrostatic repulsion of the EED sequences. Closer apposition of the adjacent juxtamembrane sequences is presumably the reason for resistance to proteolytic attack on the receptor when GH is bound, in contrast to its sensitivity when the G120R hGH antagonist is bound (44). Closure of the upper TMD would promote the transition to the left-handed TMD form, with increased separation of the Box1 sequences.

#### A Model for JAK2 Activation by GH

Separation of the JAK2-binding Box1 sequences can provide a mechanism for JAK2 activation.



**Fig. 7. Validation of the GHR homology model.** Repositioning of JAK2 observed by FRET. (A) Disulfide bonding between cysteines substituted at Glu<sup>260</sup> and Ile<sup>270</sup> rapidly converts state 1 to state 2 in MD simulations, correlating with constitutive activation seen experimentally. (B) MD of the active disulfide dimer: Distances in nanometers between backbone residues of each amino acid to the corresponding residue of the other helix overlay closely on those for state 2. Error bars represent SEM. (C) Full-length simulations. The best model of the JM linker joined to the hGH:ECD receptor complex crystal structure (PDB ID: 3HHR) is shown. Note the proximity of

Cys<sup>259</sup> residues, which form a disulfide bond on addition of ligand. Between linkers, there are also two potential hydrogen bonds that could stabilize this conformation (see text). (D) Diagram of JAK2 dimer showing proposed movement of kinase and pseudokinase domains after receptor TMD separation in state 2. (E and F) FRET ratio measurements with activated receptor (WT + KKR charge reversal mutant as in Fig. 5, B and C) and KKR or WT receptor alone, showing convergence of kinase domains and separation of pseudokinase domains on activation. Error bars indicate SEM. \* $P < 0.05$ , \*\* $P < 0.01$ .



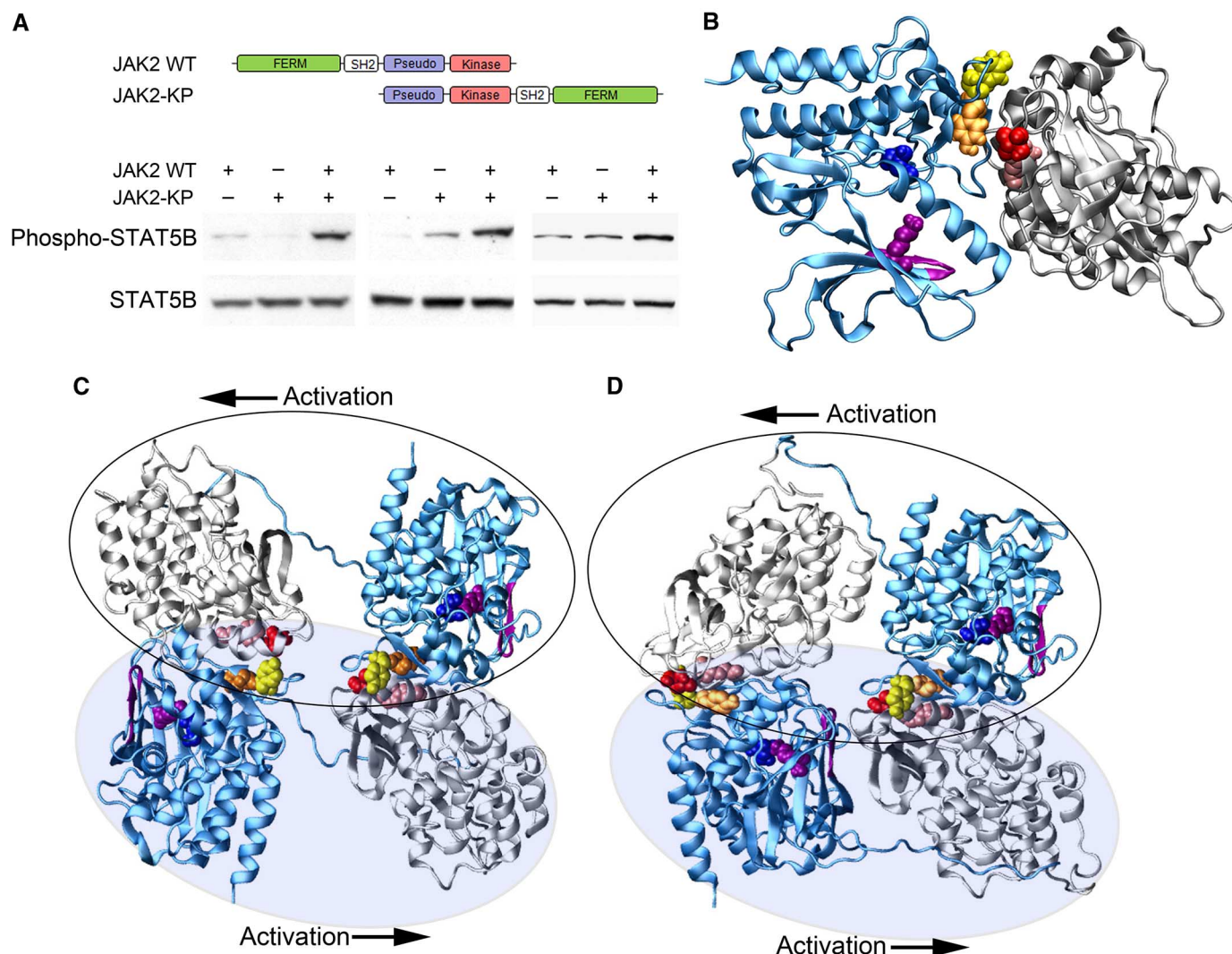
We have considered how such a separation might occur within a receptor dimer containing a JAK2 molecule bound to each receptor, given the finding that even constitutively activated oncogenic JAK2 mutants V617F, L611S, and Y613E require the presence of receptor for activity (14, 15); that is, the receptors need to be present to correctly appose the kinase domains for efficient transactivation. If the kinase domain of one JAK2 molecule is inhibited by the complementary pseudokinase domain of the second JAK2 and vice versa, then moving the JAK2 molecules apart in a sliding motion would remove the pseudokinase domain inhibitions and bring the

kinase domains into productive proximity (Fig. 7D and animation at <http://web-services.imb.uq.edu.au/waters/hgh.html>).

#### Activation of JAK2 by GH Through Removal of Trans-Inhibition

To provide experimental evidence for this model, we placed FRET reporters (mCFP or mCit) at strategic locations within JAK2 and then compared the FRET ratios when cells were transfected with WT rabbit GHR (rGHR), rGHR that had the EED-to-KKR substitution, or both. This strategy allowed measurement of FRET ratios when all receptors were fixed in an inactive basal

state or when a subset of receptors were fixed in an active orientation. FRET reporters were placed at the C terminus of JAK2, to monitor movement of the catalytic domains, or C-terminal to the SH2 domain at Asn<sup>533</sup>, in place of the pseudo-kinase domain. Reporter pairs were cotransfected (or transfected separately for FRET calculations) into HEK293T cells with the rGHR expression plasmids. Washed membrane preparations were then prepared from these cells (to reduce the background signal from free JAK2), and FRET ratios were determined. Although FRET ratio changes were small (Fig. 7, E and F), they were consistent. The small changes in FRET may result from



**Fig. 8. JAK2 domain swap.** (A) Diagram of JAK2 domain swap construct. Immunoblots showing constitutive activation of JAK2 when kinase and pseudokinase domains are swapped and the domain swap is cotransfected with WT JAK2. Result of three independent experiments shown with identical total JAK2 plasmid quantity. (B) The pseudokinase-kinase domain interface in the inactivated state after 40 ns of MD. The pseudokinase and kinase domains are shown in gray and blue ribbons, respectively. The following key residues are shown in space-fill representation: F595 (pink: required for V617F constitutive activation), V617 (red: mutation causing constitutive activation), substrate binding site D976 (blue), and activation loop phosphorylation residues Y1007

(yellow) and Y1008 (orange). The adenosine triphosphate (ATP) binding site and catalytic K882 are shown in purple ribbons and space-fill, respectively. View of the dimer interface from below shows that the ATP binding site is located in the center of residues implicated in constitutive activation. The dimer conformation derived from MD simulations can be used to construct two tetrameric orientations that fulfill the experimental data: (C) a stacked tetramer (D) or an inverse stacked tetramer, with each JAK2 circled. Arrows show proposed direction of movement induced by receptor separation below TMD, removing pseudokinase domain inhibition and bringing the kinase domains in proximity.

FRET observed between three receptor interaction possibilities when the KKR mutant is expressed with the WT receptor: WT-WT (inactive), KKR-KKR (inactive), and WT-KKR (active). The significant increase in FRET ratio for the C-terminal reporters (Fig. 7E) is consistent with the requirement for the kinase domains to trans-activate, whereas the reporters positioned in the location of the pseudokinase domain [i.e., C-terminal to the SH2 domain (Fig. 7F)] showed a decreased FRET ratio in accord with the model (Fig. 7D) and animation.

To further substantiate our JAK2 activation model, the kinase and pseudokinase domains were swapped (JAK2-KP) and then transfected together with a WT JAK2 construct and the GH receptor into JAK2-deficient human fibrosarcoma  $\gamma$ 2A cells. Our model would predict constitutive JAK2 activity only when these two JAK2 constructs are together, but not for either alone. Indeed, STAT5 phosphorylation by JAK2 was increased when WT JAK2 and JAK2-KP were present [in each experiment, the total amount of JAK2 transfected was the same (Fig. 8A)]. Overexpression of JAK2 leads to constitutive activation (45), which explains why some activated STAT5 is detectable when each JAK2 construct is transfected separately.

### Molecular Modeling of the Interaction of the JAK2 Kinase and Pseudokinase Domains

Currently, only the crystal structures of individual JAK2 kinase and pseudokinase domains are known (46, 47). To test if the proposed model is compatible with these structures, we docked the pseudokinase and kinase domain structures with the HADDOCK program. The resulting equilibrated dimer after 40 ns of unrestrained MD simulations (Fig. 8B) represents the interaction between the kinase of one molecule and the pseudokinase domain of another. In particular, the docked structures predict a close complementary interaction between the opposing kinase and pseudokinase domains. The structure shows proximity between the activation loops and Val<sup>617</sup> in the pseudokinase domain, which, when mutated, results in constitutive activation and oncogenesis. To make a model of the complete complex, we placed docked kinase and pseudokinase pairs in alternative orientations with another pair, and the cognate domains of each JAK2 were joined with their 30-residue interdomain linker. The two orientations and their movements were consistent with our experimental results (Fig. 8, C and D).

We verified that the pseudokinase-kinase pair can associate with a second such pair using AlphaScreen technology (fig. S9, A to C) based on cell-free expression of N-terminal enhanced green fluorescent protein (eGFP) or C-terminal mCherry-Myc tagged pairs. We supported this with single-molecule brightness coincidence results consistent with dimerization of GFP-tagged pseudokinase-kinase pairs in cell-free conditions (fig. S9D). Although the separate kinase domains do not associate under these condi-

tions, the pseudokinase-kinase pairs do associate effectively in trans (fig. S9, E and F).

### Discussion

We propose a mechanism for activation of JAK2 by the growth hormone receptor, an archetypal class I homomeric cytokine receptor. The receptor exists primarily as a constitutive dimer with its TMDs held in an inactive orientation in the absence of hormone. Activation of the receptor is associated with the separation of the membrane proximal signaling domains below the TMD, as assessed by FRET, and is consistent with MD modeling of the TMD.

In formulating a model to explain the increased separation of Box1 sequences on ligand binding, we were cognizant of our earlier finding that locking together of the ECD dimerization domains of the membrane proximal cytokine receptor module by specific hydrogen bonds and electrostatic bonds is essential for GH signaling (42). Based on MD modeling (41), this locking requires a relative rotation of receptor subunits of  $\sim 40^\circ$ , and disruption of this lock with the D170H mutation results in GH-insensitive (Laron) dwarfism (1). We had proposed that this locking resulted in activation of the receptor by relative rotation of the TMDs that was transmitted to the JAK2 binding Box1 sequence to allow contact of their catalytic kinase domains (7). However, when we introduced alanine insertions in the upper TMD of full-length receptor, we observed only weak receptor activation, indicating that some other ligand-induced movement was necessary for full activation.

We explored the geometry of activation by clamping the receptor signaling units (TMD and cytoplasmic domain) together and found that bringing the clamp down to the membrane surface gave the strongest activation, although concurrent insertion of alanines at the upper TMD boundary did show an optimum rotational position within that clamped receptor. Moreover, cross-linking at the EEDF sequence just above the TMD activated the receptor in an analogous manner to the Jun zipper clamp. Similar cross-linking results have been reported for the full-length EPOR (26, 48), and an optimum rotational position for activation has been reported for both EPOR (49) and TpoR (50). These findings suggest a common mechanism within related class I receptors involving both an optimum rotational position and the need to closely appose the upper JM sequences for activation, resulting in a tilt-and-twist movement of the TMDs. This is supported by the finding that the TMD and ICD of the granulocyte colony-stimulating factor receptor and GHR, both class I cytokine receptors, can be interchanged to produce signaling-competent receptors (51). This result implies that the conserved GxxG sequence of the GHR TMD is not necessary for receptor activation.

Our activation model requires separation of the Box1 motifs, resulting in activation of JAK2 bound by its FERM domain to the lower JM segment of each receptor. Current models of JAK2

assume that it exists as a monomer, where each JAK2 is autoinhibited by its own pseudokinase domain in the basal state (52). However, other studies (14, 15) show that constitutively active JAK2 point mutations require a receptor dimer to be active at physiologic levels. The original JAK2 structural model (53) has been superseded by the crystal structures of the JAK2 kinase and pseudokinase domains. We used these to determine if two kinase domains and two pseudokinase domains could pair in a complementary fashion such that an increased distance between the receptors and their attached JAK2 would slide the pseudokinase domains away from the kinase domains of their opposing counterpart and bring the two kinase domains together for trans-activation. We found optimized docked solutions that allowed this interaction, and we also located key residues known to be associated with constitutive activation of JAK2 (e.g., in myeloproliferative disorders) in the interface between the inhibitory pseudokinase domain and its kinase domain complement in the basal state. By placing FRET reporters either at the C terminus (kinase domain) or in place of the pseudokinase domain, we were able to show experimentally that the FRET ratio for the pseudokinase domains decreased on receptor activation, whereas the ratio for the catalytic domains increased, supporting a model in which the domains slide apart. Further, by exchanging the kinase and pseudokinase domains, we obtained strong experimental support for our model. When this domain-reversal mutant was expressed together with WT JAK2, constitutive activity was evident. Finally, we showed with single-molecule fluorescence brightness and AlphaScreen technology that the pseudokinase-kinase domain pair can associate in trans with another such pair. We anticipate that these findings will provide valuable insights into the design of cytokine receptor therapeutics and will facilitate understanding of relevant cytokine-related genetic disorders.

### Materials and Methods

#### ToxR Assay of TMD Interaction

This well-validated assay provides a means for testing the interaction of transmembrane helices that are placed in the inner membrane of bacteria. ToxR assays were performed essentially as previously described (17), using regions of the GHR TMD described in the Results section. See fig. S2 for the principle of this assay.

#### Cysteine Cross-Linking Studies

A series of N-terminal hemagglutinin (HA)-tagged hGHR mutants in pcDNA3.1 was constructed using QuikChange mutagenesis (Agilent Technologies), where every residue from Pro<sup>252</sup> to Ser<sup>288</sup> was converted to a cysteine after converting Cys<sup>259</sup> to serine. Two sets of these mutants were used: either truncated at residue 389 (for cross-linking studies) or full-length GHR (for STAT5 activation studies). These mutants were used for cross-linking according to Guo *et al.* (54) and for



immunoblotting or signal activation studies as detailed in the supplementary materials.

### Analysis of Proliferative Signal from GHR Constructs

The strength of constitutive proliferation signal from GHR constructs was assessed by starving Ba/F3 cells overnight in Ba/F3 starve media (see supplementary materials). Cultures were then counted using a Scepter with 40- $\mu$ M sensors (Millipore) and seeded at equal concentrations into three flasks for each sample and cultured in starve media. Cell concentration was subsequently counted on following days and plotted as shown.

### FRET Analysis

FRET measurements, using expression constructs detailed in the supplementary materials, were performed on single cells by confocal microscopy and flow cytometry essentially as previously described (55). Membrane extracts and FRET analysis with a fluorescence plate reader were essentially as described previously and detailed in the supplementary materials. Live cell membrane homo-FRET methods are described in the supplementary materials.

### Signaling Analysis of JAK2 Cotransfected with Kinase-Pseudokinase Domain Swap JAK2

Expression constructs for WT murine JAK2 and for JAK2 with the kinase domain and pseudokinase domain swapped [referred to as JAK2-KP corresponding to (Met<sup>1</sup>-Ile<sup>540</sup>)-(Asp<sup>840</sup>-Ala<sup>1132</sup>)-(Gly<sup>831</sup>-Arg<sup>839</sup>)-(Asn<sup>542</sup>-Gly<sup>834</sup>)] were constructed as described in the supplementary materials. JAK2-deficient (and STAT5-deficient)  $\gamma$ 2A cells (a gift from G. Stark, Imperial Cancer Research Fund, London) were transfected with expression plasmids for hGHR, STAT5B, and either WT-JAK2 or JAK2-KP separately, or WT-JAK2 and JAK2-KP cotransfected. In each set of experiments in which P-STAT5 signal from cotransfected WT-JAK2 and JAK2-KP was compared with each JAK2 construct transfected separately, the total amount of JAK2 transfected was identical. Details are given in the supplementary materials.

### JAK2 Interface Model

To construct a model of the interface between the pseudokinase and kinase domains of neighboring subunits, the crystal structures of the JAK2 pseudokinase (PDB ID: 4FVP) and kinase (PDB ID: 2B7A) domains were docked using the HADDOCK Web server with distance constraints between Tyr<sup>1007</sup> of the kinase domain and both Phe<sup>595</sup> and Val<sup>617</sup> of the pseudokinase domain. The docked model was then refined by simulating it for 40 ns in water. (Full details are given in the supplementary materials.) The actual interface between the two consecutive kinase-pseudokinase pairs is not known. To generate possible arrangements of JAK2 dimers that are consistent both with the 30-amino acid linker sequence and with our experimental data, a second copy of the MD conformation of the pseudokinase-kinase domain dimer was

positioned adjacent to the original pair. That this arrangement was possible was confirmed by modeling in the missing linker region. Note that although the proposed arrangement is possible, the model does not preclude the possibility of other arrangements being consistent with the data.

### Statistics

One-way analysis of variance (ANOVA) was undertaken with Tukey's multiple comparison test, whereas for comparisons of two groups, only unpaired Student's *t* test was used. Significance was shown as \**P* < 0.05, \*\**P* < 0.01, and \*\*\**P* < 0.001, with SEM.

### References and Notes

1. A. J. Brooks, M. J. Waters, The growth hormone receptor: Mechanism of activation and clinical implications. *Nat. Rev. Endocrinol.* **6**, 515–525 (2010). doi: [10.1038/nrendo.2010.123](#); pmid: [20664532](#)
2. A. M. de Vos, M. Ultsch, A. A. Kossiakoff, Human growth hormone and extracellular domain of its receptor: Crystal structure of the complex. *Science* **255**, 306–312 (1992). doi: [10.1126/science.1549776](#); pmid: [1549776](#)
3. B. C. Cunningham *et al.*, Dimerization of the extracellular domain of the human growth hormone receptor by a single hormone molecule. *Science* **254**, 821–825 (1991). doi: [10.1126/science.1948064](#); pmid: [1948064](#)
4. G. Fuh *et al.*, Rational design of potent antagonists to the human growth hormone receptor. *Science* **256**, 1677–1680 (1992). doi: [10.1126/science.256.5064.1677](#); pmid: [1535167](#)
5. J. A. Wells, Binding in the growth hormone receptor complex. *Proc. Natl. Acad. Sci. U.S.A.* **93**, 1–6 (1996). doi: [10.1073/pnas.93.1.1](#); pmid: [8552582](#)
6. J. Gent, P. van Kerkhof, M. Roza, G. Bu, G. J. Strous, Ligand-independent growth hormone receptor dimerization occurs in the endoplasmic reticulum and is required for ubiquitin system-dependent endocytosis. *Proc. Natl. Acad. Sci. U.S.A.* **99**, 9858–9863 (2002). doi: [10.1073/pnas.152294299](#); pmid: [12105275](#)
7. R. J. Brown *et al.*, Model for growth hormone receptor activation based on subunit rotation within a receptor dimer. *Nat. Struct. Mol. Biol.* **12**, 814–821 (2005). doi: [10.1038/nsmb977](#); pmid: [16116438](#)
8. K. F. Kubatzky *et al.*, Self assembly of the transmembrane domain promotes signal transduction through the erythropoietin receptor. *Curr. Biol.* **11**, 110–115 (2001). doi: [10.1016/S0960-9822\(01\)00018-5](#); pmid: [11231127](#)
9. S. L. Gadd, C. V. Clevenger, Ligand-independent dimerization of the human prolactin receptor isoforms: Functional implications. *Mol. Endocrinol.* **20**, 2734–2746 (2006). doi: [10.1210/me.2006-0114](#); pmid: [16840534](#)
10. E. E. Matthews *et al.*, Thrombopoietin receptor activation: Transmembrane helix dimerization, rotation, and allosteric modulation. *FASEB J.* **25**, 2234–2244 (2011). doi: [10.1096/fj.10-178673](#); pmid: [21402716](#)
11. O. Livnah *et al.*, An antagonist peptide-EPO receptor complex suggests that receptor dimerization is not sufficient for activation. *Nat. Struct. Biol.* **5**, 993–1004 (1998). doi: [10.1038/2965](#); pmid: [9808045](#)
12. P. J. Lupardus *et al.*, Structural snapshots of full-length Jak1, a transmembrane gp130/IL-6/IL-6R $\alpha$  cytokine receptor complex, and the receptor-Jak1 holocomplex. *Structure* **19**, 45–55 (2011). doi: [10.1016/j.str.2010.10.010](#); pmid: [21220115](#)
13. Single-letter abbreviations for the amino acid residues are as follows: A, Ala; C, Cys; D, Asp; E, Glu; F, Phe; G, Gly; H, His; I, Ile; K, Lys; L, Leu; M, Met; N, Asn; P, Pro; Q, Gln; R, Arg; S, Ser; T, Thr; V, Val; W, Trp; and Y, Tyr.
14. M. Funakoshi-Tago, S. Pelletier, H. Moritake, E. Parganas, J. N. Ihle, Jak2 FERM domain interaction with the erythropoietin receptor regulates Jak2 kinase activity. *Mol. Cell. Biol.* **28**, 1792–1801 (2008). doi: [10.1128/MCB.01447-07](#); pmid: [18160720](#)
15. X. Lu, L. J. Huang, H. F. Lodish, Dimerization by a cytokine receptor is necessary for constitutive activation of JAK2V617F. *J. Biol. Chem.* **283**, 5258–5266 (2008). doi: [10.1074/jbc.M707125200](#); pmid: [18158285](#)
16. K. He *et al.*, Janus kinase 2 determinants for growth hormone receptor association, surface assembly, and signaling. *Mol. Endocrinol.* **17**, 2211–2227 (2003). doi: [10.1210/me.2003-0256](#); pmid: [12920237](#)
17. D. Langosch, B. Brosig, H. Kolmar, H. J. Fritz, Dimerisation of the glycoporphin A transmembrane segment in membranes probed with the ToxR transcription activator. *J. Mol. Biol.* **263**, 525–530 (1996). doi: [10.1006/jmbi.1996.0595](#); pmid: [8918935](#)
18. W. Ruan, V. Becker, U. Klingmüller, D. Langosch, The interface between self-assembling erythropoietin receptor transmembrane segments corresponds to a membrane-spanning leucine zipper. *J. Biol. Chem.* **279**, 3273–3279 (2004). doi: [10.1074/jbc.M309311200](#); pmid: [14602718](#)
19. S. N. Constantinescu *et al.*, Ligand-independent oligomerization of cell-surface erythropoietin receptor is mediated by the transmembrane domain. *Proc. Natl. Acad. Sci. U.S.A.* **98**, 4379–4384 (2001). doi: [10.1073/pnas.081069198](#); pmid: [11296286](#)
20. A. N. Bader *et al.*, Homo-FRET imaging as a tool to quantify protein and lipid clustering. *ChemPhysChem* **12**, 475–483 (2011). doi: [10.1002/cphc.201000801](#); pmid: [21344588](#)
21. S. Ghosh, S. Saha, D. Goswami, S. Bilgrami, S. Mayor, Dynamic imaging of homo-FRET in live cells by fluorescence anisotropy microscopy. *Methods Enzymol.* **505**, 291–327 (2012). doi: [10.1016/B978-0-12-388448-0.00024-3](#); pmid: [22289460](#)
22. R. S. Kasai *et al.*, Full characterization of GPCR monomer-dimer dynamic equilibrium by single molecule imaging. *J. Cell Biol.* **192**, 463–480 (2011). doi: [10.1083/jcb.201009128](#); pmid: [21300851](#)
23. L. G. J. Tertoolen *et al.*, Dimerization of receptor protein-tyrosine phosphatase  $\alpha$  in living cells. *BMC Cell Biol.* **2**, 8 (2001). doi: [10.1186/1471-2121-2-8](#); pmid: [11401727](#)
24. G. Jiang *et al.*, Dimerization inhibits the activity of receptor-like protein-tyrosine phosphatase- $\alpha$ . *Nature* **401**, 606–610 (1999). doi: [10.1038/44170](#); pmid: [10524630](#)
25. G. Jiang, J. den Hertog, T. Hunter, Receptor-like protein tyrosine phosphatase  $\alpha$  homodimerizes on the cell surface. *Mol. Cell. Biol.* **20**, 5917–5929 (2000). doi: [10.1128/MCB.20.16.5917-5929.2000](#); pmid: [10913175](#)
26. K. F. Kubatzky *et al.*, Structural requirements of the extracellular to transmembrane domain junction for erythropoietin receptor function. *J. Biol. Chem.* **280**, 14844–14854 (2005). doi: [10.1074/jbc.M411251200](#); pmid: [15657048](#)
27. L. Guan, F. D. Murphy, H. R. Kaback, Surface-exposed positions in the transmembrane helices of the lactose permease of *Escherichia coli* determined by intermolecular thiol cross-linking. *Proc. Natl. Acad. Sci. U.S.A.* **99**, 3475–3480 (2002). doi: [10.1073/pnas.052703699](#); pmid: [11904412](#)
28. Y. Zhang, J. Jiang, J. J. Kopchick, S. J. Frank, Disulfide linkage of growth hormone (GH) receptors (GHR) reflects GH-induced GHR dimerization. Association of JAK2 with the GHR is enhanced by receptor dimerization. *J. Biol. Chem.* **274**, 33072–33084 (1999). doi: [10.1074/jbc.274.46.33072](#); pmid: [10551877](#)
29. S. N. Behncken *et al.*, Growth hormone (GH)-independent dimerization of GH receptor by a leucine zipper results in constitutive activation. *J. Biol. Chem.* **275**, 17000–17007 (2000). doi: [10.1074/jbc.275.22.17000](#); pmid: [10828073](#)
30. T. K. Kerppola, Design and implementation of bimolecular fluorescence complementation (BiFC) assays for the visualization of protein interactions in living cells. *Nat. Protoc.* **1**, 1278–1286 (2006). doi: [10.1038/nprot.2006.201](#); pmid: [17406412](#)
31. P. Duquesnoy *et al.*, A single amino acid substitution in the exoplasmic domain of the human growth hormone (GH) receptor confers familial GH resistance (Laron syndrome) with positive GH-binding activity by abolishing receptor homodimerization. *EMBO J.* **13**, 1386–1395 (1994). pmid: [8137822](#)

32. E. Biener-Ramanujan, V. K. Ramanujan, B. Herman, A. Gertler, Spatio-temporal kinetics of growth hormone receptor signaling in single cells using FRET microscopy. *Growth Horm. IGF Res.* **16**, 247–257 (2006). doi: [10.1016/j.ghir.2006.06.001](#); pmid: [16950496](#)
33. G. Skiniotis, P. J. Lupardus, M. Martick, T. Walz, K. C. Garcia, Structural organization of a full-length gp130/LIF-R cytokine receptor transmembrane complex. *Mol. Cell* **31**, 737–748 (2008). doi: [10.1016/j.molcel.2008.08.011](#); pmid: [18775332](#)
34. J. Staerk *et al.*, An amphipathic motif at the transmembrane-cytoplasmic junction prevents autonomous activation of the thrombopoietin receptor. *Blood* **107**, 1864–1871 (2006). doi: [10.1182/blood-2005-06-2600](#); pmid: [16249382](#)
35. M. J. Waters, H. N. Hoang, D. P. Fairlie, R. A. Pelekanos, R. J. Brown, New insights into growth hormone action. *J. Mol. Endocrinol.* **36**, 1–7 (2006). doi: [10.1677/jme.1.01933](#); pmid: [16461922](#)
36. L. Monticelli *et al.*, The MARTINI coarse-grained force field: Extension to proteins. *J. Chem. Theory Comput.* **4**, 819–834 (2008). doi: [10.1021/ct700324x](#)
37. L. Janosi, A. Prakash, M. Doxastakis, Lipid-modulated sequence-specific association of glycoporphin A in membranes. *Biophys. J.* **99**, 284–292 (2010). doi: [10.1016/j.bpj.2010.04.005](#); pmid: [20655857](#)
38. J. Hélin, A. Pohorille, C. Chipot, Insights into the recognition and association of transmembrane  $\alpha$ -helices. The free energy of  $\alpha$ -helix dimerization in glycoporphin A. *J. Am. Chem. Soc.* **127**, 8478–8484 (2005). doi: [10.1021/ja050581y](#); pmid: [15941282](#)
39. A. Prakash, L. Janosi, M. Doxastakis, GxxxG motifs, phenylalanine, and cholesterol guide the self-association of transmembrane domains of ErbB2 receptors. *Biophys. J.* **101**, 1949–1958 (2011). doi: [10.1016/j.bpj.2011.09.017](#); pmid: [22004749](#)
40. S. Özdirekcan, D. T. Rijkers, R. M. Liskamp, J. A. Killian, Influence of flanking residues on tilt and rotation angles of transmembrane peptides in lipid bilayers. A solid-state  $^2\text{H}$  NMR study. *Biochemistry* **44**, 1004–1012 (2005). doi: [10.1021/bi0481242](#); pmid: [15654757](#)
41. D. Poger, A. E. Mark, Turning the growth hormone receptor on: Evidence that hormone binding induces subunit rotation. *Proteins* **78**, 1163–1174 (2010). doi: [10.1002/prot.22636](#); pmid: [19927328](#)
42. C. Chen, R. Brinkworth, M. J. Waters, The role of receptor dimerization domain residues in growth hormone signaling. *J. Biol. Chem.* **272**, 5133–5140 (1997). doi: [10.1074/jbc.272.8.5133](#); pmid: [9030580](#)
43. B. Bernat, G. Pal, M. Sun, A. A. Kossiakoff, Determination of the energetics governing the regulatory step in growth hormone-induced receptor homodimerization. *Proc. Natl. Acad. Sci. U.S.A.* **100**, 952–957 (2003). doi: [10.1073/pnas.0235023100](#); pmid: [12552121](#)
44. P. van Kerkhof, M. Smeets, G. J. Strous, The ubiquitin-proteasome pathway regulates the availability of the GH receptor. *Endocrinology* **143**, 1243–1252 (2002). doi: [10.1210/endo.143.4.8755](#); pmid: [11897680](#)
45. O. Silvennoinen, J. N. Ihle, J. Schlessinger, D. E. Levy, Interferon-induced nuclear signalling by Jak protein tyrosine kinases. *Nature* **366**, 583–585 (1993). doi: [10.1038/366583a0](#); pmid: [7504785](#)
46. I. S. Lucet *et al.*, The structural basis of Janus kinase 2 inhibition by a potent and specific pan-Janus kinase inhibitor. *Blood* **107**, 176–183 (2006). doi: [10.1182/blood-2005-06-2413](#); pmid: [16174768](#)
47. R. M. Bandaranayake *et al.*, Crystal structures of the JAK2 pseudokinase domain and the pathogenic mutant V617F. *Nat. Struct. Mol. Biol.* **19**, 754–759 (2012). doi: [10.1038/nsmb.2348](#); pmid: [22820988](#)
48. X. Lu, A. W. Gross, H. F. Lodish, Active conformation of the erythropoietin receptor: Random and cysteine-scanning mutagenesis of the extracellular juxtamembrane and transmembrane domains. *J. Biol. Chem.* **281**, 7002–7011 (2006). doi: [10.1074/jbc.M512638200](#); pmid: [16414957](#)
49. N. Seubert *et al.*, Active and inactive orientations of the transmembrane and cytosolic domains of the erythropoietin receptor dimer. *Mol. Cell* **12**, 1239–1250 (2003). doi: [10.1016/S1097-2765\(03\)00389-7](#); pmid: [14636581](#)
50. J. Staerk *et al.*, Orientation-specific signalling by thrombopoietin receptor dimers. *EMBO J.* **30**, 4398–4413 (2011). doi: [10.1038/emboj.2011.315](#); pmid: [21892137](#)
51. E. Ishizaka-Ikeda, R. Fukunaga, W. I. Wood, D. V. Goeddel, S. Nagata, Signal transduction mediated by growth hormone receptor and its chimeric molecules with the granulocyte colony-stimulating factor receptor. *Proc. Natl. Acad. Sci. U.S.A.* **90**, 123–127 (1993). doi: [10.1073/pnas.90.1.123](#); pmid: [7678333](#)
52. P. Saharinen, O. Silvennoinen, The pseudokinase domain is required for suppression of basal activity of Jak2 and Jak3 tyrosine kinases and for cytokine-inducible activation of signal transduction. *J. Biol. Chem.* **277**, 47954–47963 (2002). doi: [10.1074/jbc.M205156200](#); pmid: [12351625](#)
53. F. Giordanetto, R. T. Kroemer, Prediction of the structure of human Janus kinase 2 (JAK2) comprising JAK homology domains 1 through 7. *Protein Eng.* **15**, 727–737 (2002). doi: [10.1093/protein/15.9.727](#); pmid: [12456871](#)
54. W. Guo, L. Shi, M. Filizola, H. Weinstein, J. A. Javitch, Crosstalk in G protein-coupled receptors: Changes at the transmembrane homodimer interface determine activation. *Proc. Natl. Acad. Sci. U.S.A.* **102**, 17495–17500 (2005). doi: [10.1073/pnas.0508950102](#); pmid: [16301531](#)
55. D. Abankwa, H. Vogel, A FRET map of membrane anchors suggests distinct microdomains of heterotrimeric G proteins. *J. Cell Sci.* **120**, 2953–2962 (2007). doi: [10.1242/jcs.001404](#); pmid: [17690305](#)

**Acknowledgments:** This work was supported by grants from the National Health and Medical Research Council of Australia (511120, 1002893, and 102082) and the Australian Research Council to M.J.W., A.J.B., A.E.M., and M.W.P. Infrastructure funding from the Victorian Government to St Vincent's Institute is gratefully acknowledged. W.D. and M.D. acknowledge financial support by the NSF (USA) Chemical, Bioengineering, Environmental, and Transport Systems Division (grant number 1067356) and central processing unit time by the University of Houston Research Computing Center. G.A.G. acknowledges financial support by the Kids Cancer Project of the Oncology Research Foundation. We thank W. A. Johnston for optimizing the *Leishmania*-based cell-free lysate expression system used in the single-molecule and Alpha screen interaction studies. Confocal imaging was performed at the IMB/ACRF Cancer Biology Imaging Facility, established with the support of the Australian Cancer Research Foundation.

# Supplementary Materials

[www.sciencemag.org/content/344/6185/1249783/suppl/DC1](http://www.sciencemag.org/content/344/6185/1249783/suppl/DC1)

Materials and Methods

Supplementary Text

Figs. S1 to S9

References (56–87)

16 December 2013; accepted 1 April 2014

10.1126/science.1249783



# Border Control—A Membrane-Linked Interactome of *Arabidopsis*

Alexander M. Jones,<sup>1</sup> Yuanhu Xuan,<sup>1\*</sup> Meng Xu,<sup>1</sup> Rui-Sheng Wang,<sup>2</sup> Cheng-Hsun Ho,<sup>1</sup> Sylvie Lalonde,<sup>1</sup> Chang Hun You,<sup>1</sup> Maria I. Sardi,<sup>1†</sup> Saman A. Parsa,<sup>1</sup> Erika Smith-Valle,<sup>1‡</sup> Tianying Su,<sup>1§</sup> Keith A. Frazer,<sup>1</sup> Guillaume Pilot,<sup>1,3</sup> Réjane Pratelli,<sup>1,3</sup> Guido Grossmann,<sup>1||</sup> Biswa R. Acharya,<sup>4</sup> Heng-Cheng Hu,<sup>5¶</sup> Cawas Engineer,<sup>6</sup> Florent Villiers,<sup>5</sup> Chuanli Ju,<sup>5</sup> Kouji Takeda,<sup>5</sup> Zhao Su,<sup>4</sup> Qunfeng Dong,<sup>7</sup> Sarah M. Assmann,<sup>4</sup> Jin Chen,<sup>1,8</sup> June M. Kwak,<sup>5,9</sup> Julian I. Schroeder,<sup>6</sup> Reka Albert,<sup>2</sup> Seung Y. Rhee,<sup>1#</sup> Wolf B. Frommer<sup>1‡</sup>

Cellular membranes act as signaling platforms and control solute transport. Membrane receptors, transporters, and enzymes communicate with intracellular processes through protein-protein interactions. Using a split-ubiquitin yeast two-hybrid screen that covers a test-space of  $6.4 \times 10^6$  pairs, we identified 12,102 membrane/signaling protein interactions from *Arabidopsis*. Besides confirmation of expected interactions such as heterotrimeric G protein subunit interactions and aquaporin oligomerization, >99% of the interactions were previously unknown. Interactions were confirmed at a rate of 32% in orthogonal in planta split-green fluorescent protein interaction assays, which was statistically indistinguishable from the confirmation rate for known interactions collected from literature (38%). Regulatory associations in membrane protein trafficking, turnover, and phosphorylation include regulation of potassium channel activity through abscisic acid signaling, transporter activity by a WNK kinase, and a brassinolide receptor kinase by trafficking-related proteins. These examples underscore the utility of the membrane/signaling protein interaction network for gene discovery and hypothesis generation in plants and other organisms.

**G**enome projects have provided the inventories of genes and predicted proteins, yet we can only begin to understand how organisms function or interact with their environment once we understand the functions of the proteins in the proteome and their wiring di-

agram. Plants, as sessile organisms, are particularly efficient in acclimating to the dynamics of their environments. Plant growth, development, homeostasis, and acclimation require mechanisms that monitor changes in the environment, coordinate cells and compartments, and adjust transport of ions and metabolites across cellular membranes. Sensing, signaling, and transporter regulation are mediated through interactions with membrane proteins. Largely because of technical challenges caused by the hydrophobicity of membrane proteins, only a small number of membrane protein interactions are known. Membranes contain thousands of proteins whose biochemical or physiological functions have not been identified experimentally and are thus classified as “unknowns.” Identification of genetic and molecular interactions is a promising way to assign functions to the unknowns in the genome (1–3).

To uncover membrane protein interactions, we performed a systematic binary interaction screen using a yeast two-hybrid system specifically developed for membrane protein interactions: the mating-based split-ubiquitin system (mbSUS) (4, 5). The split-ubiquitin system identified interactions between integral membrane proteins that form homo- and hetero-oligomeric complexes such as sucrose and ammonium transporters, potassium channels, and aquaporins (4–6). The mbSUS was also instrumental for identifying regulators of yeast ammonium and amino acid transporters (7), interactions among yeast membrane proteins (8), and interactions between plant proteins and pathogen effector proteins (9). Here, we report a binary screen,

covering more than 6.4 million potential interaction pairs from a library of 3286 membrane and signaling proteins from *Arabidopsis thaliana* (*Arabidopsis*) (Fig. 1 and fig. S1) (5). Proteins from the Gene Ontology (GO) biological process categories of *transport*, *signal transduction*, and *response to abiotic or biotic stimulus* are well represented. Our analysis verified expected interactions, such as those between heterotrimeric G protein subunits (10) and aquaporin isoforms (11), and also identified over 12,000 new protein-protein interactions. Of these, 3849 interactions connected proteins lacking experimentally derived functional annotations to interaction partners with experimentally derived functional annotations; these connections may assist in elucidating the functions of the unknown proteins. The results are freely accessible online (www.associomics.org).

## mbSUS Screen for Membrane-Linked Protein-Protein Interactions

A primary mbSUS screen probed pair-wise interactions among 3286 distinct proteins (Fig. 1, table S1, and supplementary materials). For interaction tests in mbSUS, N- and C-terminal halves of ubiquitin (Nub and Cub) are separately fused to proteins of interest (Fig. 1A) (4, 5). The key advantage of mbSUS is its ability to detect protein interactions that occur outside of the yeast nucleus, specifically at membranes that interface the cytosol (5). Besides interactions among membrane proteins, we tested interactions of membrane proteins with soluble proteins predicted to be involved in signaling (as Nub-fusions). Cub-fusions with soluble proteins are prone to self-activation and were therefore excluded. An initial screen identified “auto-activating” or “nonactivatable” Cub-fusions for exclusion, further reducing the number of interaction tests to be performed. The resulting matrix of 3233 Nub-fusions against 1070 Cub-fusions comprised  $>3 \times 10^6$  interaction tests performed in duplicate and at two stringency conditions (a total of four assays per pair), with a quantifiable readout of yeast colony growth assayed for complementation of histidine auxotrophy (Fig. 1B). We created imaging and statistical analysis pipelines based on distribution model-based classification so as to determine interaction confidence scores and thresholds for positive interactions (figs. S2 and S3). A total of 30,426 interactions, less than 1% of the pairs interrogated, were defined as positive in the primary screen based on stringent criteria (supplementary materials 2). We evaluated all positive interactions from the primary screen in a secondary screen with 12 additional interaction tests in yeast: six replicated tests for complementation of histidine auxotrophy at two stringency conditions (fig. S4). A network of 12,102 interactions between 1523 proteins tested positive consistently at both stringency conditions and was termed MIND1 (Membrane-linked Interactome Database version 1) (fig. S5).

<sup>1</sup>Department of Plant Biology, Carnegie Institution for Science, CA 94305, USA. <sup>2</sup>Department of Physics, Pennsylvania State University, University Park, PA 16802, USA. <sup>3</sup>Department of Plant Pathology, Physiology, and Weed Science, Virginia Polytechnic University and State University, Blacksburg, VA 24061, USA. <sup>4</sup>Department of Biology, Pennsylvania State University, University Park, PA 16802, USA. <sup>5</sup>Department of Cell Biology and Molecular Genetics, University of Maryland, College Park, MD 20742, USA. <sup>6</sup>Cell and Developmental Biology Section, Division of Biological Sciences, University of California, San Diego, La Jolla, CA 92093, USA. <sup>7</sup>Department of Biological Sciences, University of North Texas, Denton, TX 76203, USA. <sup>8</sup>Michigan State University—U.S. Department of Energy (MSU-DOE) Plant Research Laboratory and Department of Computer Science and Engineering, Michigan State University, East Lansing, MI 48824, USA. <sup>9</sup>Center for Plant Aging Research, Institute for Basic Science, Department of New Biology, Daegu Gyeongbuk Institute of Science and Technology, Daegu 711-873, Republic of Korea.

\*Present address: College of Pharmaceutical Sciences, Wenzhou Medical University, Wenzhou, Zhejiang, 325035 China.

†Present address: Department of Microbiology Doctoral Training Program, University of Wisconsin-Madison, Madison, WI 53715, USA.

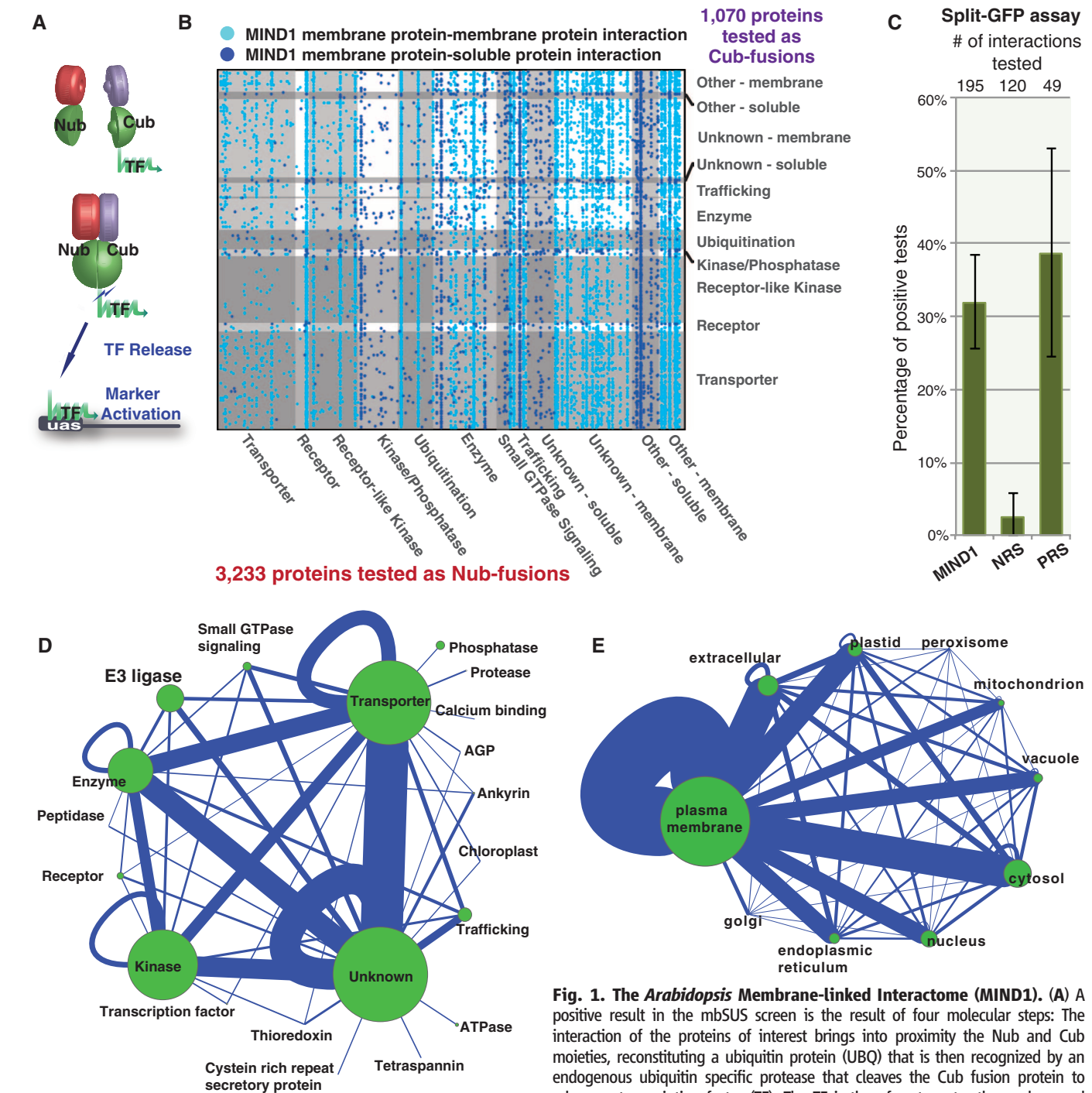
‡Present address: Five Prime Therapeutics, South San Francisco, CA 94080, USA.

§Present address: Department of Biology, Stanford University, Stanford, CA 94305, USA.

||Present address: Centre for Organismal Studies, Universität Heidelberg, 69120 Heidelberg, Germany. Cluster of Excellence CellNetworks, 69120 Heidelberg, Germany.

¶Present address: Department of Agronomy, Iowa State University, Ames, IA 50011, USA.

#Corresponding author. E-mail: wfrommer@stanford.edu (W.B.F.); srhee@carnegiescience.edu (S.Y.R.)



**Fig. 1. The *Arabidopsis* Membrane-linked Interactome (MIND1).** (A) A positive result in the mbSUS screen is the result of four molecular steps: The interaction of the proteins of interest brings into proximity the Nub and Cub moieties, reconstituting a ubiquitin protein (UBQ) that is then recognized by an endogenous ubiquitin specific protease that cleaves the Cub fusion protein to release a transcription factor (TF). The TF is then free to enter the nucleus and activate marker genes whose expression indicates physical interaction between the proteins of interest. (B) 12,102 interactions in MIND1 generated from two rounds of mbSUS screen. Chart displays protein-protein interactions between a membrane protein with another membrane protein or a soluble protein. (C) The results of orthogonal validation of the MIND1 protein-protein interactions by retesting in the split-GFP assay. Error bars show 95% CI estimated with bootstrap analysis (supplementary materials 2.6). (D) Protein family interaction network. Nodes represent family types and edges indicate interactions between two families. Only families that have more than two proteins are included, and only those family pairs that have 10 or more interactions are displayed. (E) Cellular localization interaction network of MIND1<sub>NH</sub>. Nodes represent cellular components; edges indicate interactions between or among proteins localized in the respective compartments.

activate marker genes whose expression indicates physical interaction between the proteins of interest. (B) 12,102 interactions in MIND1 generated from two rounds of mbSUS screen. Chart displays protein-protein interactions between a membrane protein with another membrane protein or a soluble protein. (C) The results of orthogonal validation of the MIND1 protein-protein interactions by retesting in the split-GFP assay. Error bars show 95% CI estimated with bootstrap analysis (supplementary materials 2.6). (D) Protein family interaction network. Nodes represent family types and edges indicate interactions between two families. Only families that have more than two proteins are included, and only those family pairs that have 10 or more interactions are displayed. (E) Cellular localization interaction network of MIND1<sub>NH</sub>. Nodes represent cellular components; edges indicate interactions between or among proteins localized in the respective compartments.

To evaluate the reliability of MIND1, a random subset of 7770 positive interactions from the primary screen was reanalyzed in a tertiary screen (fig. S4). Results from the secondary screen were largely confirmed by the tertiary screen, which included two histidine auxotrophy assays and a LacZ activity assay; only 12% of secondary screen positives failed in all three tertiary screen assays, whereas 80% were positive in at least two assays (fig. S5). Because we tested the interactions of *Arabidopsis* proteins in a single-cell heterologous system, the observed associations are not necessarily relevant in planta. Therefore, we also tested 195 interactions in planta using the orthogonal, low-throughput split-green fluorescent protein (GFP) protein interaction assay (Fig. 1C and supplementary materials 2.6). These pairs tested positive in 31.8% of the split-GFP interaction tests [95% confidence interval (CI) (25.6%, 38.5%), bootstrap analysis]. We estimated the in planta



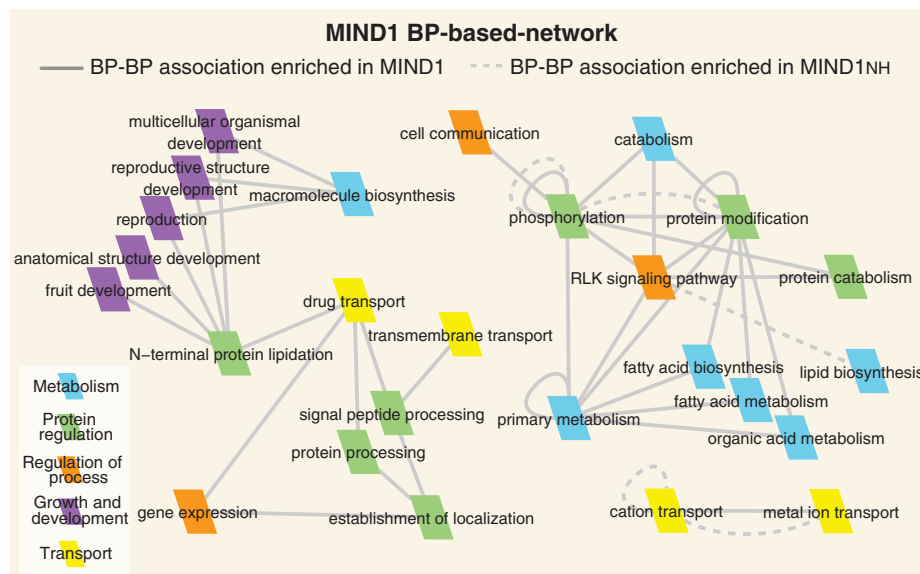
false-positive rate of MIND1 by comparing its split-GFP validation rate to the rate of split-GFP validation for two reference sets of protein pairs (supplementary materials 2.6). A posi-

tive reference set of 49 independently reported interactions—randomly sampled from the subset of primary screen protein pairs that were reported to physically interact in the literature—was

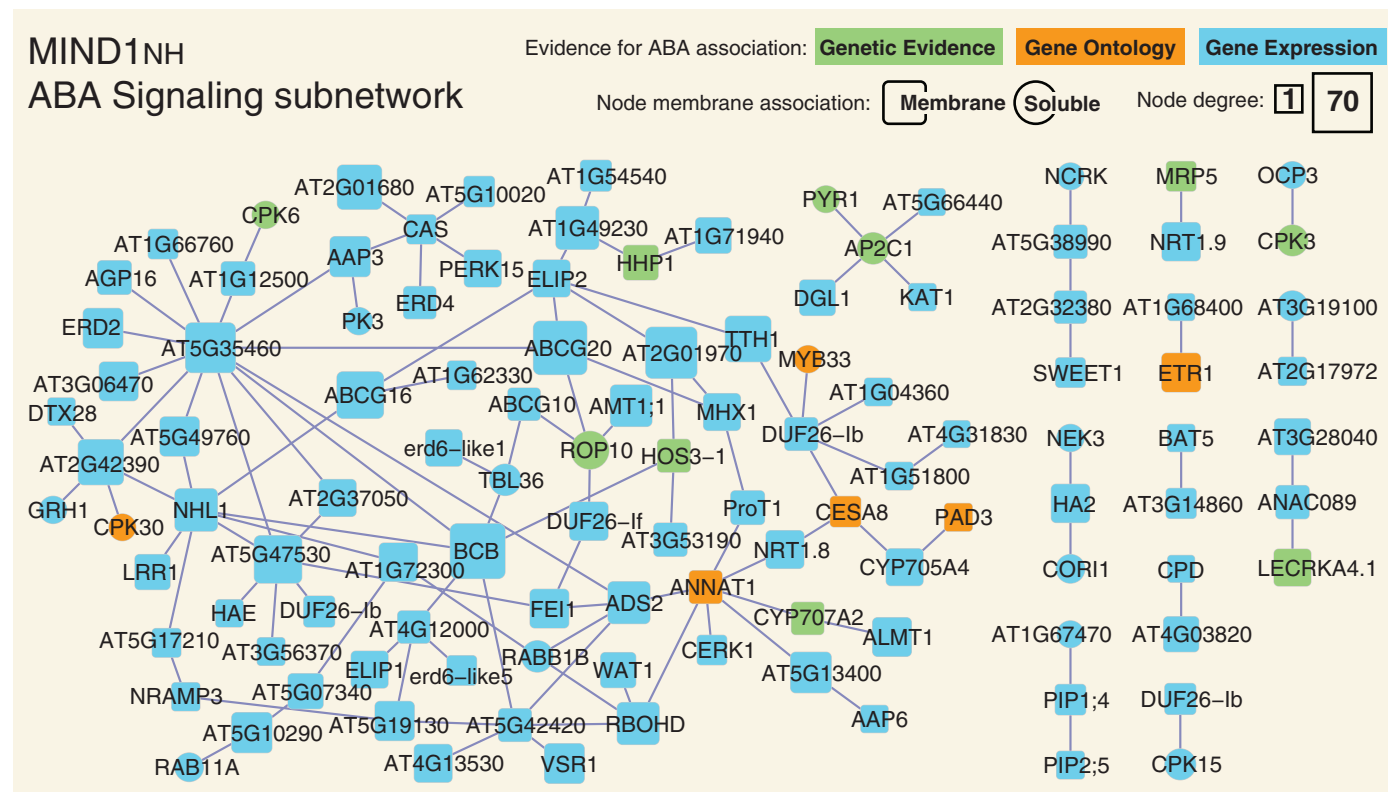
used to estimate the true-positive rate of interactions tested in the split-GFP assay, which was 38.8% [95% CI (24.5%, 53.1%), bootstrap analysis]. A negative reference set of interactions—randomly sampled from the primary screen protein pairs—was used to estimate the false-positive rate of interactions tested in the split-GFP assay, which was 2.5% [95% CI (0, 5.8%), bootstrap analysis]. MIND1 interactions tested positive at a rate that is not significantly different from the independently reported positive interactions (positive reference set,  $P = 0.364$ , permutation test) and over 12-fold higher than noninteracting protein pairs (negative reference set,  $P$  value = 0, permutation test). The MIND1 in planta false-positive rate was estimated to be 19.2% [95% CI (0, 46.6%), bootstrap analysis], although the small fraction of interactions tested in the split-GFP assay precludes a statistically reliable point estimate of the false-positive rate.

## The Potential of Low Stringency Interactions for Discovery

MIND1 does not include interaction pairs that tested positive in only one or two out of the four tests performed in the primary screen. However, we provide these interactions online ([www.associomics.org](http://www.associomics.org)) because they could be biologically relevant. For example, four different SWEET transporter hetero-oligomers were detected in only one out of the four primary screen replicate tests. On the basis of this information, we



**Fig. 2. Enriched connections between GO biological process groups in MIND1.** Nodes represent different GO groups and are color-coded by group type as shown. Edges represent statistically enriched connections between GO groups in the complete MIND1 (solid lines) or in MIND1<sub>NH</sub> (dashed lines) determined by comparing with 10,000 randomized networks and using a false discovery rate  $Q < 0.05$  as threshold.



**Fig. 3. Interactions between abscisic acid signaling-related proteins.** Three types of evidence (genetic evidence, GO annotation, and abscisic acid responsive gene expression) were used to classify

MIND<sub>1NH</sub> nodes as related to abscisic acid signaling. Interactions involving hubs and unconnected abscisic acid-related proteins are not included.

performed a systematic analysis to detect homo- and hetero-oligomerization among all 17 *Arabidopsis* SWEETs and found 8 homo- and 47 hetero-oligomers using the split-ubiquitin system (12). Several of these pairs were confirmed in planta by using the split-GFP assay, suggesting that oligomerization is a general feature of SWEETs and highlighting that pairs that did not yield highly reproducible results may be valuable for inclusion in specific hypothesis-driven studies.

### MIND1 Network Characteristics

MIND1, like other biological networks (13, 14), exhibits small-world properties (short distance among proteins coupled with local order indicated by high clustering coefficient) (supplementary materials 3) and follows a heavy-tailed degree distribution with a reliance on high-degree hubs (proteins with many interactions) (fig. S6). Because hubs have many interaction partners, individual interactions of a hub have low specificity. Thus, hub proteins with degree >70 were removed to generate a non-Hub network (MIND1<sub>NH</sub>) of 3354 interactions (fig. S7). Interacting proteins often share similar expression patterns (15); therefore, we compared expression correlation for MIND1- and MIND1<sub>NH</sub>-interacting protein pairs. Relative to noninteracting pairs, only MIND1<sub>NH</sub> pairs were enriched for expression correlation (fig. S8). However, both MIND1- and MIND1<sub>NH</sub>-interacting protein pairs were enriched for GO functional similarity (fig. S9), indicating that a hub protein was more likely to share a functional annotation with its interaction partners than an expression pattern. MIND1 interactions are complementary to existing interactome networks from *Arabidopsis* in that over 99% of the interactions had not been previously reported (13). This is not unexpected because different interactome assays typically yield complementary data sets (14, 16–18) and because the clone sets analyzed were different (only 212 MIND1 proteins were also screened

by the *Arabidopsis* Interactome Mapping Consortium) (fig. S10) (13).

### MIND1-Derived Functional Predictions

Because 327 proteins (21%) in MIND1 lack GO biological process annotation, the network can potentially contribute to functional predictions (fig. S11). For example, the small, single transmembrane-domain-containing protein AT5G61630 [a potential Ras guanosine triphosphatase (GTPase); www.greenphy1.org] had three interactors that were annotated “water channel activity” (GO:0015250), intimating a role in regulating water transport (table S2). We systematically generated functional predictions for the proteins in MIND1<sub>NH</sub> by identifying functional annotations that were overrepresented among each protein’s interacting partners relative to the proteins present in the network (table S2). For the above example, the annotation “water channel activity” is overrepresented in the interaction partners of AT5G61630 ( $P = 5.68 \times 10^{-6}$ , Fisher’s exact test). We also generated functional predictions for the proteins in MIND1 by first isolating highly connected network clusters (putative functional modules) and then identifying annotations enriched within these clusters. Hierarchical clustering of MIND1 resulted in a large super-cluster dominated by interactions involving hub proteins, whereas hierarchical clustering of MIND1<sub>NH</sub> resulted in numerous smaller clusters (fig. S13). Two additional module detection methods (supplementary materials 3.7) identified MIND1<sub>NH</sub> clusters with enriched GO annotations, potentially indicating functional modules (table S4 and fig. S14). For example, the unknown gene described above, AT5G61630, belongs to a cluster that contains five aquaporin isoforms and is enriched for “water transport” (GO:0006833, Bonferroni-corrected  $P$  value =  $1.36 \times 10^{-4}$ , Fisher’s exact test), a function that may pertain to other members of the cluster, including AT5G61630.

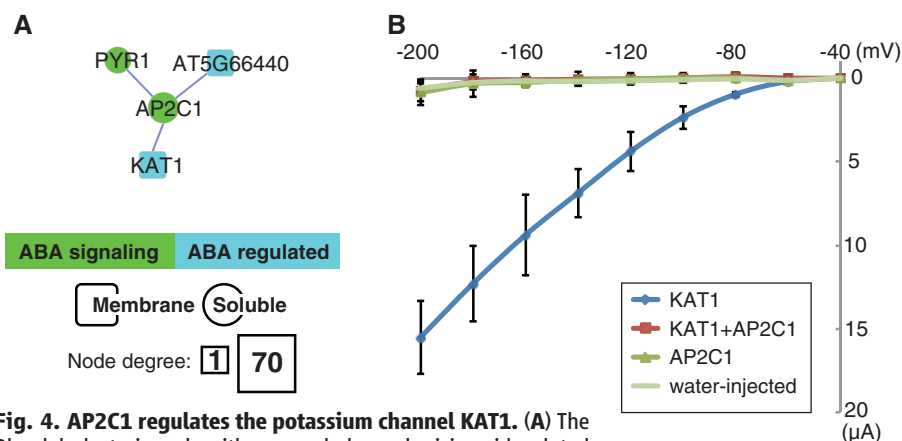
Individual interactions, irrespective of the network context, also guide functional predictions. For example, we found interactions between the nitrate transporter CHL1 (AT1G12110) and the potassium transporter KT2 (AT2G40540) as well as the lysine-deficient protein kinase WNK8 (AT5G41990). CHL1’s transport activity or conformation was affected by these interactions, as demonstrated with the fluorescent transport activity sensor NiTrac1 (19). WNK8 is a key player involved in dose- and duration-dependent sugar signaling, which controls endocytosis of the G protein-coupled receptor RGS1 (20). Interesting parallels exist in the animal kingdom, in which WNK kinases play important roles in controlling ion transport processes (21).

### Characterization of Hubs in MIND1

Disruption of network hubs typically has pleiotropic effects (22). Purifying selection acts more strongly on genes with functions essential for biological fitness and results in reduced evolutionary rates (23). Consistently, MIND1 hubs showed evidence of purifying selection in that  $K_a/K_s$  [the ratio of the number of nonsynonymous substitutions per potential nonsynonymous site ( $K_a$ ) to the number of synonymous substitutions per potential synonymous site ( $K_s$ )] based on *Arabidopsis lyrata* orthologs was low (mean  $K_a/K_s = 0.15$ ) and significantly lower than  $K_a/K_s$  for all *Arabidopsis* proteins with *A. lyrata* orthologs (mean  $K_a/K_s = 0.21$ ,  $P$  value = 0.028, Student’s  $t$  test) (supplementary materials 3.8 and table S3). Although we cannot exclude the possibility that the high number of protein interactions for an individual MIND1 hub could be an artifact, the functions of the hubs are consistent with general roles that require interaction with a large number of target proteins; out of the 33 MIND1 hubs with known or inferred molecular function, 21 have putative functions in protein modification (chaperones/thioredoxins, signal peptidases, or proteases) or protein sorting [soluble *N*-ethylmaleimide-sensitive factor (NSF) attachment protein (SNAP) receptors (SNAREs) or cornichon] (table S3). Moreover, subcellular localization of 16 MIND1 hub GFP-fusions, including nine unknowns, showed that all but one localized to endomembranes, which is consistent with roles in membrane protein modification or sorting (fig. S15 and table S3).

### Analysis of MIND1 at the Level of Protein Families and Biological Processes

Analysis of interactions at the protein family level can be used to predict genetic redundancies, interaction motifs, and potential interactions with paralogs. A gene family-based network (Fig. 1D, figs. S16 and S17, and table S5) revealed overrepresentation of interactions involving proteins of unknown function. The unknowns showed numerous interactions with transporters, indicating undiscovered transport or transport-regulatory functions among these proteins (Fig. 1D).



**Fig. 4. AP2C1 regulates the potassium channel KAT1.** (A) The Blondel clustering algorithm revealed an abscisic acid-related cluster (Blondel cluster 93) in MIND1<sub>NH</sub> that includes KAT1 and AP2C1. (B) Current-voltage relationship of the current in *Xenopus laevis* oocytes injected with KAT1 or AP2C1 or with both cRNAs upon perfusion with 100 mM KCl. In all recordings, the holding potential was set at  $-40$  mV, and voltage steps were applied to potentials ranging between  $-40$  and  $-200$  mV with  $-20$ -mV decrements. Data are means  $\pm$  SE from at least three different individual oocytes.



Aggregating interactions by predicted subcellular localization yielded a location-based network of connections between different cellular compartments predicting higher-level association patterns (Fig. 1E). MIND1<sub>NH</sub> proteins are predominantly plasma membrane-localized, and these plasma membrane proteins show abundant interactions with other plasma membrane proteins and with cytosolic partners (Fig. 1E).

To investigate potential interaction motifs among biological processes, we examined interactions at the level of GO biological processes. Intrabiological process interactions are less abundant in MIND1 as compared with other published networks (fig. S18) (13). We generated a meta-network comprising enriched interactions between biological processes. This network revealed potential interaction motifs such as “Receptor-like Kinase/Pelle (RLK) signaling pathway” linking to “protein catabolism” (Fig. 2).

### Regulation of Transport Activity by Hormones

To strengthen functional predictions from MIND1, the protein interaction network was overlaid

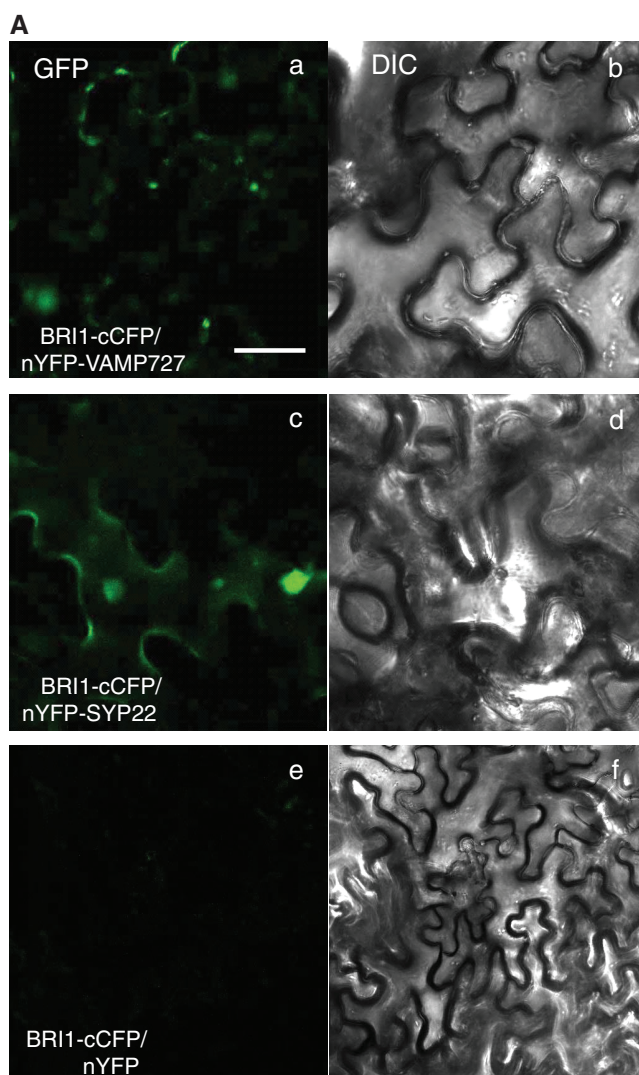
with transcriptome and other annotation data. For example, 311 proteins in MIND1 are related to the hormone abscisic acid according to transcriptomic, genetic, or other experimental evidence (24). MIND1 interactions connected many of these proteins into an abscisic acid-related subnetwork (Fig. 3 and fig. S19). Similar subnetworks obtained for other hormones also represent interaction sets that are strengthened by multiple data sources (figs. S19 to S26).

Transport is highly regulated at the transcriptional and posttranscriptional levels, and hormone signaling often targets membrane-related processes. The activity of potassium channels—which contribute to potassium acquisition from soil, regulation of enzyme activities, adjustment of membrane potential and turgor, and regulation of cellular homeostasis and electrical signaling—is regulated by protein kinases and phosphatases (25). A key mechanism by which abscisic acid promotes stomatal closure is through inhibition of transporters such as the potassium channel KAT1 (26). Abscisic acid responses are mediated by a co-receptor complex that consists of abscisic acid receptors (PYR/PYL/RCAR proteins) and

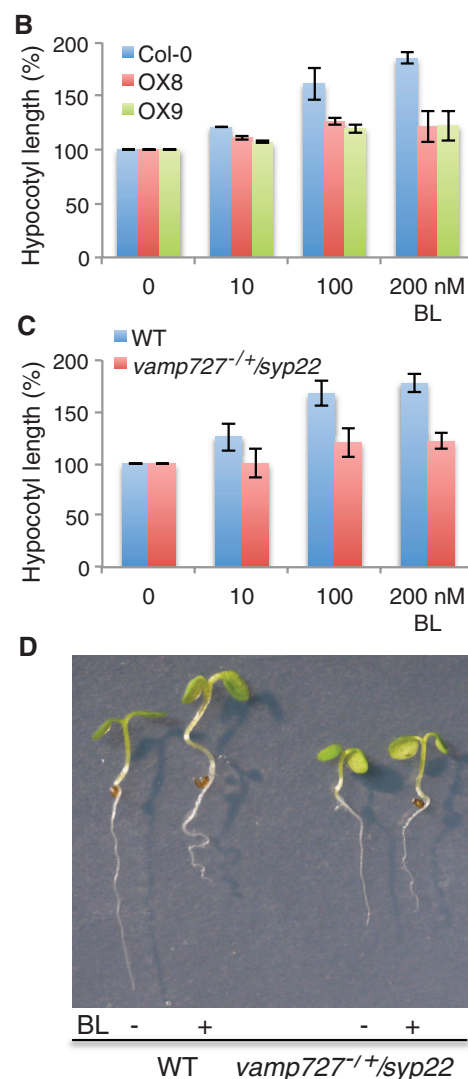
clade-A protein phosphatase 2Cs (PP2C) (27). Although much of abscisic acid signaling proceeds through clade-A PP2C regulation of SnRK2 kinases and SnRK2 regulation of transcription factors, cladeA PP2Cs and SnRK2 kinases can also directly regulate the activity of K<sup>+</sup> channels (28, 29).

Abscisic acid signaling proteins in MIND1 share extensive connections with transporters and other membrane proteins (Fig. 3 and fig. S19). For example, the clade-B PP2C, AP2C1, interacts with the K<sup>+</sup> channel KAT1 in a cluster enriched for abscisic acid-related GO annotations (Fig. 4A); Blondel cluster 93 (table S4) is enriched for GO:0009738—“abscisic acid signaling pathway” (Bonferroni-corrected  $P = 1.25 \times 10^{-2}$ , Fisher’s exact test)—and GO:0071215—“cellular response to abscisic acid stimulus” (Bonferroni-corrected  $P = 1.41 \times 10^{-2}$ , Fisher’s exact test). Although clade-B PP2Cs are not canonical abscisic acid coreceptor components and are not known to regulate potassium channels, when coexpressed with KAT1 in oocytes, AP2C1 completely inhibited channel activity (Fig. 4B). KAT1 functions in stomatal opening;

**Fig. 5. Functional interaction of BRI1 with trafficking proteins.** Split-GFP assay for VAMP727, SYP22, and BRI1, and brassinolide (BL) hyposensitivity of *vamp727*<sup>-/-</sup>; *syp22* and VAMP727 overexpressed (OX) plants. (A)



(A) Yellow fluorescent protein (YFP) fluorescence and bright field images (left, fluorescence channel; right, bright field). (a and b) Reconstitution of YFP fluorescence from nYFP-VAMP727+ BRI1-cCFP; (c and d) nYFP-SYP22+BRI1-cCFP; (e and f) BRI1-cCFP+nYFP (negative control). Scale bars, 20  $\mu$ m. (B) VAMP727 overexpression plants were grown under indicated concentrations of BL, and hypocotyl lengths were measured. (C) Seedlings were grown under various concentrations of BL, and hypocotyl lengths were measured. (B and C) Error bars indicate SE. Experiments were repeated at least three times. (D) Wild type and *vamp727*<sup>-/-</sup>; *syp22* were grown for 5 days with 100 nM or without BL. BL-mediated hypocotyl elongation and primary root growth inhibition (coiling) were affected in *vamp727*<sup>-/-</sup>; *syp22* compared with wild-type plants.



thus, AP2C1 could promote stomatal closure and drought responses by inhibiting KAT1. Indeed, an *ap2c1,pp2c5* double mutant has increased stomatal aperture (30), and we speculate that clade-B PP2Cs such as AP2C1 and PP2C5 may reduce stomatal opening by directly modifying KAT1.

### Receptor Kinase Signaling and Regulation

The RLK family of transmembrane receptors is larger in plants as compared with animals and likely serves as a predominant mechanism of communication across membranes. However, characterization of RLKs is complicated by apparent genetic redundancy (31). MIND1 contains 554 interactions for 175 full-length RLK proteins, extending RLK associations within membranes and with soluble signaling proteins (fig. S27). MIND1<sub>NH</sub> contains >20 RLK interactions with small GTPases (fig. S27). At present, no canonical pathway for intracellular RLK signaling analogous to the metazoan G protein-coupled receptor (GPCR) transmembrane signaling through intracellular heterotrimeric G proteins has been defined in plants. However, small GTPases and related proteins have been identified as intracellular RLK signaling components (32). RLK-GTPase signaling could act in several ways—for example, via direct signal transduction from RLK activation to ROP activation. We observed numerous RLK interactions with Rab-GTPases, proteins involved in trafficking (33), potentially indicating Rab involvement in trafficking of RLKs as shown for RabF2b regulation of FLS2 endocytosis (34). Extending RLK-GTPase associations by using MIND1 and additional interactome data sets (13) reveals additional potential GTPase interaction motifs that could help advance the understanding of the role of small GTPases (fig. S27).

### Regulation of Brassinosteroid Signaling by Trafficking Proteins

Membrane proteins are maintained at appropriate steady-state levels by a balance of delivery to the plasma membrane and recycling through endocytosis. Receptor endocytosis plays a key role in controlling activation and signal termination (35). For example, upon activation by ligands, mammalian RLKs are subject to accelerated lysosomal degradation (36). In *Arabidopsis*, brassinosteroids such as brassinolide are perceived by the RLK BRI1 and its coreceptor BAK1. Ligand-independent trafficking of BRI1 between plasma membrane and early endosomes and degradation in the vacuole has been observed (37, 38), and the Membrane Steroid Binding Protein (MSBP1) was shown to trigger BAK1 endocytosis in a brassinolide-independent manner (39). Although considerable evidence implicates BRI1-trafficking in brassinosteroid signaling, the underlying mechanisms are still ambiguous (40), and the interactions found in MIND1 may help solve some of the open questions regarding RLK trafficking. Here, we found that BRI1 interacts with the R-SNARE VAMP727,

a candidate for regulating BRI1 trafficking (table S1). We confirmed this interaction using the split-GFP assay and also identified SYP22, a VAMP727 interacting Q-SNARE (41), as a BRI1-interactor (Fig. 5A). VAMP727 and SYP22 accumulate at late endosomes/multivesicular bodies (41). Overexpression of VAMP727 in *Arabidopsis* resulted in partial insensitivity to brassinolide (Fig. 5B); overexpression of SYP22 in *bri1-5*, a weak *bri1* mutant, enhanced its dwarf phenotype (fig. S28). The phenotypes of VAMP727 and SYP22 overexpressors are consistent with inhibitory roles in brassinosteroid signaling, perhaps by promoting BRI1-trafficking to the vacuole for degradation. However, although *vamp727* and *syp22* single mutants did not show altered brassinolide responses (fig. S29), *vamp727<sup>-/-</sup>;syp22* mutants were partially insensitive to brassinolide (Fig. 5, C and D), indicating a role for VAMP727 and SYP22 in promoting brassinosteroid signaling. We hypothesize that overexpression and mutation of VAMP727 and SYP22 might result in aberrant BRI1 localization because both result in an apparent reduction in brassinosteroid signaling. VAMP727 had also been observed at the plasma membrane (42), implicating additional functions of VAMP727 in trafficking from plasma membrane to vacuole. Although further experiments are required to fully understand the role of trafficking in BRI1 endocytosis and signaling, we provide genetic and molecular evidence that VAMP727 and SYP22 interact with BRI1 and affect brassinosteroid signaling, potentially through modulation of steady-state levels of BRI1 at the plasma membrane or in endosomes (fig. S29).

### Membrane Protein and Signaling Protein Interactome for Functional Genomics

Membrane proteins are central components of many cellular processes, often through coordinated action with either membrane or soluble interaction partners. The 12,102 protein-protein interactions in MIND1 (www.associomics.org) expand the functional genomics knowledge base for the reference plant *Arabidopsis* and serve as a resource for gene discovery and hypothesis generation. Analysis of MIND1 in conjunction with other data sources has not only confirmed known interactions but also has uncovered connections that shed light on how membrane proteins are regulated at the levels of trafficking, accumulation, and activity.

#### References and Notes

1. S. Lalonde *et al.*, *Plant J.* **53**, 610–635 (2008).
2. C. Boone, H. Bussey, B. J. Andrews, *Nat. Rev. Genet.* **8**, 437–449 (2007).
3. M. C. Jonikas *et al.*, *Science* **323**, 1693–1697 (2009).
4. P. Obrdlik *et al.*, *Proc. Natl. Acad. Sci. U.S.A.* **101**, 12242–12247 (2004).
5. S. Lalonde *et al.*, *Front. Physiol.* **1**, 24 (2010).
6. W. X. Schulze, A. Reinders, J. Ward, S. Lalonde, W. B. Frommer, *BMC Biochem.* **4**, 3 (2003).
7. G. Van Zeebroeck, M. Kimpe, P. Vandormael, J. M. Thevelein, *PLOS ONE* **6**, e24275 (2011).
8. J. P. Miller *et al.*, *Proc. Natl. Acad. Sci. U.S.A.* **102**, 12123–12128 (2005).

9. J. D. Lewis *et al.*, *BMC Genomics* **13**, 8 (2012).
10. Y. Trusov *et al.*, *Plant Cell* **19**, 1235–1250 (2007).
11. G. P. Bienert *et al.*, *Biochem. J.* **445**, 101–111 (2012).
12. Y. H. Xuan *et al.*, *Proc. Natl. Acad. Sci. U.S.A.* **110**, E3685–E3694 (2013).
13. M. Dreze *et al.*, *Science* **333**, 601–607 (2011).
14. H. Yu *et al.*, *Science* **322**, 104–110 (2008).
15. J. L. Sevilla *et al.*, *IEEE/ACM Trans. Comput. Biol. Bioinformatics* **2**, 330–338 (2005).
16. K. Tarassov *et al.*, *Science* **320**, 1465–1470 (2008).
17. J. R. Parrish, K. D. Gulyas, R. L. Finley Jr., *Curr. Opin. Biotechnol.* **17**, 387–393 (2006).
18. N. J. Krogan *et al.*, *Nature* **440**, 637–643 (2006).
19. C. H. Ho, W. B. Frommer, *eLife* **3**, e01917 (2014).
20. Y. Fu *et al.*, *Cell* **156**, 1084–1095 (2014).
21. D. Takahashi *et al.*, *Biosci. Rep.* (2014).
22. H. Jeong, S. P. Mason, A. L. Barabási, Z. N. Oltvai, *Nature* **411**, 41–42 (2001).
23. R. Sterken *et al.*, *Plant Cell* **21**, 2987–2998 (2009).
24. Z. Jiang *et al.*, *Nucleic Acids Res.* **39**, D1123–D1129 (2011).
25. U. Anshütz, D. Becker, S. Shabala, *J. Plant Physiol.* (2014).
26. T. H. Kim, M. Böhmer, H. Hu, N. Nishimura, J. I. Schroeder, *Annu. Rev. Plant Biol.* **61**, 561–591 (2010).
27. S. R. Cutler, P. L. Rodriguez, R. R. Finkelstein, S. R. Abrams, *Annu. Rev. Plant Biol.* **61**, 651–679 (2010).
28. J. Xu *et al.*, *Cell* **125**, 1347–1360 (2006).
29. A. Sato *et al.*, *Biochem. J.* **424**, 439–448 (2009).
30. A. K. Brock *et al.*, *Plant Physiol.* **153**, 1098–1111 (2010).
31. L. A. Gish, S. E. Clark, *Plant J.* **66**, 117–127 (2011).
32. P. Bommert, B. I. Je, A. Goldshmidt, D. Jackson, *Nature* **502**, 555–558 (2013).
33. A. H. Hutagalung, P. J. Novick, *Physiol. Rev.* **91**, 119–149 (2011).
34. M. Beck, J. Zhou, C. Faulkner, D. MacLean, S. Robatzek, *Plant Cell* **24**, 4205–4219 (2012).
35. E. R. Andersson, *Cell. Mol. Life Sci.* **69**, 1755–1771 (2012).
36. L. K. Goh, A. Sorkin, *Cold Spring Harb. Perspect. Biol.* **5**, a017459 (2013).
37. N. Geldner, D. L. Hyman, X. Wang, K. Schumacher, J. Chory, *Genes Dev.* **21**, 1598–1602 (2007).
38. C. Viotti *et al.*, *Plant Cell* **22**, 1344–1357 (2010).
39. L. Song, Q. M. Shi, X. H. Yang, Z. H. Xu, H. W. Xue, *Cell Res.* **19**, 864–876 (2009).
40. A. L. Contento, D. C. Bassham, *J. Cell Sci.* **125**, 3511–3518 (2012).
41. K. Ebine *et al.*, *Plant Cell* **20**, 3006–3021 (2008).
42. K. Ebine *et al.*, *Nat. Cell Biol.* **13**, 853–859 (2011).

**Acknowledgments:** We thank W. Monsell (Pennsylvania State University) and Y. S. Han (University of Maryland) for technical assistance and K. Revanna and V. Desu (University of North Texas) for assistance with the MIND web portal development. This work was made possible by a National Science Foundation (NSF) *Arabidopsis* 2010 grant (MCB-0618402) to W.B.F., S.M.A., R.A., J.M.K., S.Y.R., and J.I.S. and NSF *Arabidopsis* 2010 grant (MCB-1052348) to W.B.F. and S.Y.R., with partial support from NSF-MCB-1021677 (W.B.F.), NSF-MCB-0918220 (J.I.S.) and NSF-MCB-1121612 (S.M.A. and R.A.). Because of the large number of constructs, we are not able to distribute individual clones. We make split-ubiquitin system vectors and an *Arabidopsis* ORF collection available through the *Arabidopsis* Biological Resource Center (<https://abrc.osu.edu>) and split-GFP assay vectors available through AddGene ([www.addgene.org](http://www.addgene.org)). Instructions for acquiring other materials as well as a materials transfer agreement governing plasmids are provided online at [www.associomics.org](http://www.associomics.org). Additional materials are included in the supplementary materials. The authors declare that the research was conducted in the absence of any commercial or financial relationships that could be construed as a potential conflict of interest.

#### Supplementary Materials

[www.sciencemag.org/content/344/6185/711/suppl/DC1](http://www.sciencemag.org/content/344/6185/711/suppl/DC1)  
Materials and Methods  
Supplementary Text  
Figs. S1 to S30  
References (43–83)  
Tables S1 to S6

27 January 2014; accepted 16 April 2014  
10.1126/science.1251358



# Oxidation Products of Biogenic Emissions Contribute to Nucleation of Atmospheric Particles

Francesco Riccobono,<sup>1\*</sup> Siegfried Schobesberger,<sup>2</sup> Catherine E. Scott,<sup>3</sup> Josef Dommen,<sup>1</sup> Ismael K. Ortega,<sup>2†</sup> Linda Rondo,<sup>4</sup> João Almeida,<sup>4</sup> Antonio Amorim,<sup>5</sup> Federico Bianchi,<sup>1</sup> Martin Breitenlechner,<sup>6</sup> André David,<sup>7</sup> Andrew Downard,<sup>8</sup> Eimear M. Dunne,<sup>3‡</sup> Jonathan Duplissy,<sup>2,12</sup> Sebastian Ehrhart,<sup>4</sup> Richard C. Flagan,<sup>8</sup> Alessandro Franchin,<sup>2</sup> Armin Hansel,<sup>6</sup> Heikki Junninen,<sup>2</sup> Maija Kajos,<sup>2</sup> Helmi Keskinen,<sup>9</sup> Agnieszka Kupc,<sup>10</sup> Andreas Kürten,<sup>4</sup> Alexander N. Kvashin,<sup>11</sup> Ari Laaksonen,<sup>9</sup> Katrianne Lehtipalo,<sup>2</sup> Vladimir Makhmutov,<sup>11</sup> Serge Mathot,<sup>7</sup> Tuomo Nieminen,<sup>2,12</sup> Antti Onnela,<sup>7</sup> Tuukka Petäjä,<sup>2</sup> Arnaud P. Praplan,<sup>1</sup> Filipe D. Santos,<sup>5</sup> Simon Schallhart,<sup>2</sup> John H. Seinfeld,<sup>8</sup> Mikko Sipilä,<sup>2,12</sup> Dominick V. Spracklen,<sup>3</sup> Yuri Stozhkov,<sup>11</sup> Frank Stratmann,<sup>13</sup> Antonio Tomé,<sup>5</sup> Georgios Tsakoggeorgas,<sup>13</sup> Petri Vaattovaara,<sup>9</sup> Yrjö Viisanen,<sup>14</sup> Aron Vrtala,<sup>10</sup> Paul E. Wagner,<sup>10</sup> Ernest Weingartner,<sup>1§</sup> Heike Wex,<sup>13</sup> Daniela Wimmer,<sup>4</sup> Kenneth S. Carslaw,<sup>3</sup> Joachim Curtius,<sup>4</sup> Neil M. Donahue,<sup>15</sup> Jasper Kirkby,<sup>4,7</sup> Markku Kulmala,<sup>2,12</sup> Douglas R. Worsnop,<sup>2,16</sup> Urs Baltensperger<sup>1||</sup>

Atmospheric new-particle formation affects climate and is one of the least understood atmospheric aerosol processes. The complexity and variability of the atmosphere has hindered elucidation of the fundamental mechanism of new-particle formation from gaseous precursors. We show, in experiments performed with the CLOUD (Cosmics Leaving Outdoor Droplets) chamber at CERN, that sulfuric acid and oxidized organic vapors at atmospheric concentrations reproduce particle nucleation rates observed in the lower atmosphere. The experiments reveal a nucleation mechanism involving the formation of clusters containing sulfuric acid and oxidized organic molecules from the very first step. Inclusion of this mechanism in a global aerosol model yields a photochemically and biologically driven seasonal cycle of particle concentrations in the continental boundary layer, in good agreement with observations.

**A**erosol particles affect climate both directly by scattering and absorbing solar radiation and indirectly by acting as cloud

condensation nuclei (CCN) (*1*). New-particle formation (nucleation) via gas-to-particle conversion is the largest source of atmospheric particles in the atmosphere (*2*), and it is thought to contribute up to half of the global CCN inventory (*3, 4*). It is therefore important to provide global models with accurate laboratory measurements of nucleation rates as a function of the concentrations of vapor precursors in order to assess the impact of anthropogenic emissions (*5*).

Field measurements have shown that nucleation is strongly associated with the ambient vapor concentration of sulfuric acid ( $\text{H}_2\text{SO}_4$ ), which is therefore considered to be a key component of atmospheric nucleation (*6–9*). Classical nucleation theories (CNTs) of sulfuric acid, water, and ammonia are often used in global aerosol models (*5*). However, they grossly underestimate the ambient nucleation rates  $J$  observed in the planetary boundary layer (BL) at a given  $\text{H}_2\text{SO}_4$  concentration and overestimate the sensitivity of the nucleation rates to  $\text{H}_2\text{SO}_4$  concentration when compared with field observations (*10, 11*). This indicates that additional compounds participate in BL nucleation.

More recently, global aerosol models have shown improved estimation of the particle number concentration in the planetary BL after the CNT nucleation rates were replaced with em-

pirical parameterizations of field measurements using a power-law functional dependence of the form

$$J = k[\text{H}_2\text{SO}_4]^p \quad (1)$$

where the exponent  $p$  ranges between 1 and 2 (*7, 9, 11*). The empirical prefactor  $k$  varies by roughly a factor of 100 at different locations and times, reflecting the variability of the ambient parameters (such as temperature and ionization rates) but also the variability of other unaccounted compounds involved in atmospheric nucleation (*7, 9*). Oxidized biogenic organic vapors, ubiquitous in the BL, may well be important species involved in new-particle formation (*7, 8, 12–15*), but so far the identity of these additional chemical compounds, or class of compounds, remains unknown.

## Observational Background

Identification of the chemical composition of the nucleating clusters in field measurements is difficult for several reasons. Vapor concentrations are extremely low ( $10^7 \text{ cm}^{-3}$  or below), and the clusters contain only a few molecules. The presence of abundant “spectator” molecules and clusters in ambient air can obscure the actively nucleating clusters. Empirical correlations, such as the association of nucleation rates with  $\text{H}_2\text{SO}_4$ , are also strongly affected by the concurrent diurnal variations of other species, which are formed via gas-phase photochemistry.

There is a paucity of studies demonstrating a quantitative overlap between ambient observations and laboratory measurements. Previous comparisons between laboratory experiments and ambient observations have mostly failed to reproduce ambient nucleation rates or to quantify their dependence on  $\text{H}_2\text{SO}_4$  concentration in the presence of pure sulfuric acid and water, or even with the addition of ammonia or organic compounds (*16–22*). A notable exception is the study by Chen *et al.* (*23*) showing a reasonable agreement of predicted nucleation rates with rates measured in Atlanta and Mexico City when including efficient stabilization of the acids by bases such as amines [amine concentrations exceeded 100 parts per trillion by volume (pptv) in Atlanta but were not measured in Mexico City]. Amines strongly enhance nucleation rates already in the low pptv range (*24*). Other studies included biogenic organic compounds but did not show direct evidence that organic compounds participate in the nucleation process itself, because they have been unable to distinguish between an effect of organics on nucleation or on the initial growth after nucleation has taken place (*25, 26*).

A critical limitation is that, until recently, nucleation rates were inferred by the appearance rate of particles at roughly 2-nm diameter. The appearance rate depends on the survival probability of nucleated particles growing to the observed size, which in turn depends strongly

<sup>1</sup>Laboratory of Atmospheric Chemistry, Paul Scherrer Institute, Villigen, Switzerland. <sup>2</sup>Department of Physics, University of Helsinki, Helsinki, Finland. <sup>3</sup>School of Earth and Environment, University of Leeds, Leeds, UK. <sup>4</sup>Institute for Atmospheric and Environmental Sciences, Goethe University of Frankfurt, Frankfurt am Main, Germany. <sup>5</sup>Laboratory for Systems, Instrumentation, and Modeling in Science and Technology for Space and the Environment (SIM), University of Lisbon and University of Beira Interior, Lisbon, Portugal. <sup>6</sup>Ionicon Analytik GmbH and University of Innsbruck, Institute for Ion and Applied Physics, Innsbruck, Austria. <sup>7</sup>CERN (European Organization for Nuclear Research), Geneva, Switzerland. <sup>8</sup>Division of Chemistry and Chemical Engineering, California Institute of Technology, Pasadena, CA 91125, USA. <sup>9</sup>University of Eastern Finland, Kuopio, Finland. <sup>10</sup>Faculty of Physics, University of Vienna, Vienna, Austria. <sup>11</sup>Solar and Cosmic Ray Research Laboratory, Lebedev Physical Institute, Moscow, Russia. <sup>12</sup>Helsinki Institute of Physics, University of Helsinki, Helsinki, Finland. <sup>13</sup>Leibniz Institute for Tropospheric Research, Leipzig, Germany. <sup>14</sup>Finnish Meteorological Institute, Helsinki, Finland. <sup>15</sup>Center for Atmospheric Particle Studies, Carnegie Mellon University, Pittsburgh, PA 15213, USA. <sup>16</sup>Aerodyne Research Incorporated, Billerica, MA 01821, USA.

\*Present address: Joint Research Centre, European Commission, Ispra, Italy.

†Present address: Laboratoire de Physique des Lasers, Atomes et Molécules, Université de Lille 1, Villeneuve d'Ascq, France.

‡Present address: Finnish Meteorological Institute, Kuopio Unit, Kuopio, Finland.

§Present address: Institute for Aerosol and Sensor Technology, University of Applied Sciences, Windisch, Switzerland.

||Corresponding author. E-mail: urs.baltensperger@psi.ch

on their growth rate, making it difficult to disentangle nucleation and growth (27). Thus, there is a critical need for laboratory experiments that mimic the atmosphere under carefully controlled conditions.

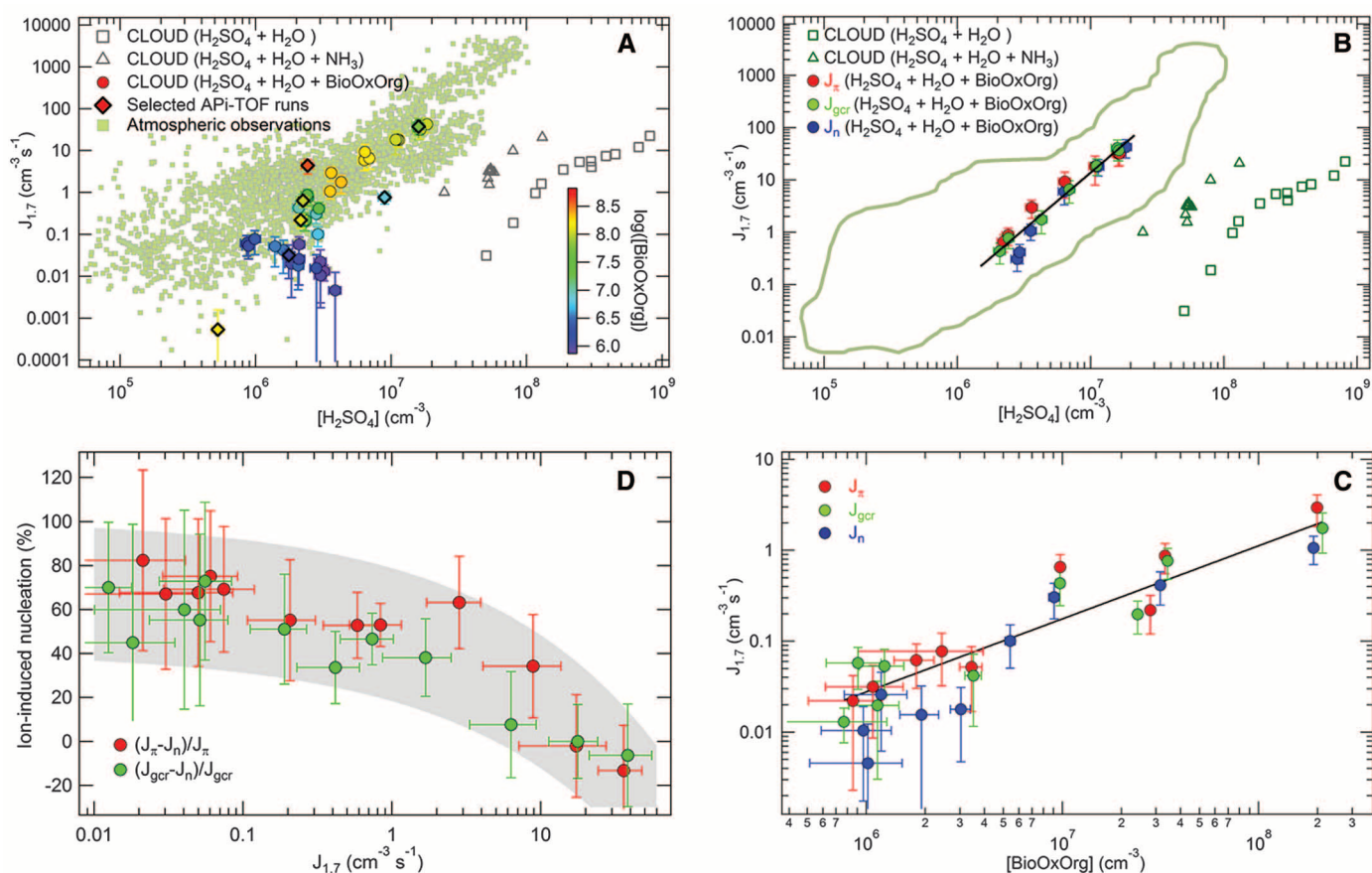
### Experimental Approach

We studied, under well-controlled laboratory conditions, nucleation in the presence of sulfuric acid and biogenic oxidized organic vapors at ionization rates and vapor concentrations spanning atmospheric values. The CLOUD (Cosmics Leaving Outdoor Droplets) experiment at CERN provides a unique facility to measure the evolution from gas molecules to clusters to particles under atmospheric conditions. The CLOUD chamber is a 26-m<sup>3</sup> stainless-steel vessel that enables nucleation experiments to be carried out under extremely stable, reproducible, and essentially contaminant-free conditions (16); a discussion

of minute remaining contamination, which does not influence the measured nucleation rates, is given in (28). The gas and particle phases in the chamber are continuously sampled and analyzed by a comprehensive suite of state-of-the-art instruments (28). In these experiments, condensable vapors were formed by gas-phase reactions of hydroxyl radicals (OH), the dominant oxidant in Earth's atmosphere, with sulfur dioxide (SO<sub>2</sub>) and pinanediol (PD, C<sub>10</sub>H<sub>18</sub>O<sub>2</sub>). Sulfuric acid was formed from oxidation of SO<sub>2</sub>, and a broad range of oxidized biogenic compounds was produced from oxidation of PD. PD is a first-generation oxidation product of  $\alpha$ -pinene; consequently, its oxidation products (in the following called BioOxOrg) closely represent later-generation oxidation products of biogenic monoterpenes. By using the experimental results, we developed a parameterization describing the dependence of nucleation rates on H<sub>2</sub>SO<sub>4</sub>

and BioOxOrg concentrations and implemented it in a global aerosol microphysics model to assess the effect of this process on new-particle formation in the continental BL.

The effects of H<sub>2</sub>SO<sub>4</sub> and BioOxOrg on the nucleation rates were isolated by independently varying the concentration of H<sub>2</sub>SO<sub>4</sub> or BioOxOrg [see (28) for detailed experimental setup and BioOxOrg concentration determination]. The CLOUD facility also benefits from an adjustable pion beam from the CERN Proton Synchrotron (PS) to simulate ionizing cosmic rays and from an electric clearing field of up to 20 kV m<sup>-1</sup> when an ion-free environment is needed. For each set of gas conditions, we measured the nucleation rates  $J$  under three different ion concentrations: (i)  $J_n$  in an ion-free environment (neutral, with the electric field on); (ii)  $J_{gr}$  in a ground-level ionized environment (gcr, with ions naturally generated by galactic cosmic rays); and (iii)  $J_\pi$  in a



**Fig. 1. Exploration of nucleation rates.** (A) Nucleation rates  $J_{1,7}$  as a function of  $H_2SO_4$  concentration for the whole range of BioOxOrg concentrations experimentally explored (color-coded with  $\log[BioOxOrg]$ ), and nucleation rates observed in the BL (small green squares) (7–9). Contaminants NH<sub>3</sub> and dimethylamine are <2 and <1 pptv, respectively. Bold diamonds correspond to those runs for which the API-TOF mass defect plots are shown in Fig. 2 and figs. S2 to S4. (B) Nucleation rates  $J_{1,7}$  as a function of  $H_2SO_4$  concentration for a limited range of BioOxOrg concentration ( $1.0 \pm 0.7 \times 10^8$  cm<sup>-3</sup>, ~4 pptv). The marked area represents the region of BL observations. (C) Nucleation rates as a function of BioOxOrg concentration for a limited range

of  $H_2SO_4$  concentrations ( $1.9 \pm 0.7 \times 10^6$  cm<sup>-3</sup>, ~0.1 pptv). (D) Percentage of ion-induced nucleation as a function of the total nucleation, calculated from the differences of the corresponding experiments under identical conditions. In (B), (C), and (D), blue, green, and red circles correspond to  $J_n$ ,  $J_{gr}$ , and  $J_\pi$ , respectively. The bars represent 1 $\sigma$  total errors, but the overall systematic scale uncertainty on  $H_2SO_4$  (about factor 2) and BioOxOrg concentrations is not shown. In (A) and (B), the binary (H<sub>2</sub>SO<sub>4</sub> and H<sub>2</sub>O, open squares) and ternary (H<sub>2</sub>SO<sub>4</sub>, H<sub>2</sub>O, and NH<sub>3</sub>, open triangles) GCR nucleation rates from CLOUD are also shown (16). The black lines correspond to unconstrained least-squares fits for GCR conditions. The gray band in (D) is shown to guide the eye.



typical high tropospheric environment (pion beam, provided by the CERN PS).

## Results and Discussion

Figure 1A shows the measured nucleation rates at 1.7-nm mobility diameter ( $J_{1.7}$ ). Despite the scatter in the data (caused mainly by the calculation of the BioOxOrg concentration), at BioOxOrg concentrations  $\geq 3 \times 10^6 \text{ cm}^{-3}$  the nucleation rates are similar to those observed in the ambient atmosphere (small squares in Fig. 1A) over the range of  $\text{H}_2\text{SO}_4$  concentrations typically observed. At lower BioOxOrg concentrations, the  $J_{1.7}$  values decrease, approaching those observed for nucleation from sulfuric acid either with water alone or with water and ammonia (open markers in Fig. 1, A and B) (16).

Figure 1, B and C, shows  $J_{1.7}$  as a function of  $\text{H}_2\text{SO}_4$  and BioOxOrg concentrations, with each other held nearly constant. For quasi-constant concentrations of BioOxOrg ( $\sim 4$  pptv, well within the atmospheric range) (14), we find the same power-law dependency on  $\text{H}_2\text{SO}_4$  concentration (Eq. 1) as observed in field campaigns (marked area in Fig. 1B). The unconstrained least-squares fit (solid line) yields an exponent  $p$  with the corresponding 90% confidence interval of  $2.17 \pm 0.14$  for the GCR conditions (green circles). Figure 1C shows that oxidized organic compounds contribute to  $J_{1.7}$  at atmospheric  $\text{H}_2\text{SO}_4$  mixing ratios (0.1 pptv). The unconstrained least-squares fit of  $J = k [\text{BioOxOrg}]^q$  (solid line) yields an exponent  $q$  with the corresponding 90% confidence interval of  $0.80 \pm 0.23$  for the GCR conditions (green circles).

Last, Fig. 1D reveals the role of ions at atmospheric  $\text{H}_2\text{SO}_4$  and BioOxOrg concentrations. It shows the percentage of the nucleation rate attributable to ions as a function of the total nucleation rate under GCR and pion-beam conditions (shown in green and red, respectively). At lower-tropospheric GCR conditions, the ion-induced fraction is about 60% at low nucleation rates ( $J_{1.7} \leq 0.01 \text{ cm}^{-3} \text{ s}^{-1}$ ), falling to below 10% at high nucleation rates ( $> 10 \text{ cm}^{-3} \text{ s}^{-1}$ ). For upper-tropospheric ionization (pion-beam conditions), the ion-induced fraction is about 10% higher than for GCR conditions. This decreasing ion contribution with increasing total nucleation rate (i.e., at higher  $\text{H}_2\text{SO}_4$  and BioOxOrg concentrations) is consistent with an emerging picture that charge, bases, and oxidized organics all compete in stabilizing small  $\text{H}_2\text{SO}_4$  clusters (16, 24). This picture suggests that ambient new-particle formation may involve any, or several, of these stabilizing agents, along with  $\text{H}_2\text{SO}_4$ , depending on meteorological conditions and trace gas levels.

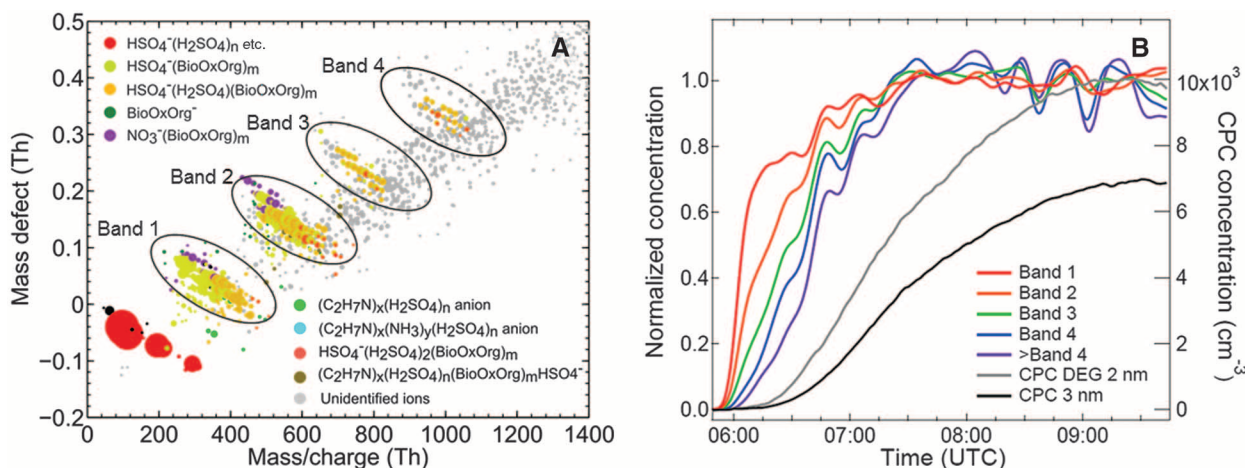
The dependence of  $J$  on  $\text{H}_2\text{SO}_4$  and BioOxOrg concentration can be summarized in terms of a multicomponent power law

$$J = k_m [\text{H}_2\text{SO}_4]^p [\text{BioOxOrg}]^q \quad (2)$$

where  $k_m$  is the multicomponent prefactor. Nucleation occurs through a sequence of collisions between the growing clusters and vapor molecules where only a fraction of the BioOxOrg compounds are able to form stabilized clusters. We label the clusters with  $(n, m)$ , where  $n$  and

$m$  correspond to the number of molecules of  $\text{H}_2\text{SO}_4$  and BioOxOrg, respectively, present in the cluster. In the absence of coagulation or wall losses, the survival probability of a cluster  $(n, m)$  will depend on the competition between its evaporation rate (which depends on the cluster composition) and the collision rate of the cluster with a condensable vapor molecule (which depends on the vapor concentration). A critical cluster is often defined to have a size at which it is equally likely to grow or to evaporate. According to the first nucleation theorem for multicomponent systems (29), the critical cluster composition is directly linked to the exponents  $p$  and  $q$  of Eq. 2.

However, the critical cluster does not apply to systems where highly stabilized clusters are formed from the beginning: the slopes (exponents  $p$  and  $q$  of Eq. 2) are then defined by other, more important loss processes (i.e., the chamber walls in the CLOUD experiment or the preexisting aerosol in the ambient atmosphere) (30). This also means that different conditions would yield different slopes. At very low condensing molecule concentrations, the time to reach 1.7 nm is increased, and the wall loss or coagulation effects are accordingly enhanced (30), resulting in steeper slopes. At high concentrations, saturation effects similar to those found for amine concentrations (24) may be expected, resulting in shallower slopes or even complete saturation. Nevertheless, because our concentrations of  $\text{H}_2\text{SO}_4$  and BioOxOrg are within the atmospheric range and our condensation sink ( $\sim 3 \times 10^{-3} \text{ s}^{-1}$ ) is similar to typical pristine BL values



**Fig. 2. Experimental growth in cluster sizes.** (A) Mass-defect plot of negative clusters measured by the API-TOF and (B) the time series of the normalized concentration of growing clusters grouped in bands and the time series of the particle concentration measured with the diethylene glycol condensation particle counter (DEG CPC) with  $D_{50} = 2$  nm and the CPC with  $D_{50} = 3$  nm. The experiment was started by turning the electric clearing field off at 06:02 and the ultraviolet lights on at 06:11, so most of the observed growth (especially of the larger bands) is caused by formation of BioOxOrg, rather than by diffusional charging of already existing BioOxOrg. This is different from the experiments shown in Fig. 1, B and C, where the sequence neutral  $\rightarrow$  GCR  $\rightarrow$  pion beam was always followed. The clusters are grouped in bands,

from 1 to 4, according to the number  $m$  of BioOxOrg molecules present in the clusters of band  $m$ . In the mass-defect plot, the sulfuric acid monomers, dimers, and trimers,  $(\text{H}_2\text{SO}_4)_{0-2}\text{HSO}_4^-$ , are shown in red.  $m$  oxidized organic molecules bound to  $\text{HSO}_4^-$  (1,  $m$ ) are shown in yellow.  $m$  oxidized organic molecules bound to sulfuric acid dimers (2,  $m$ ) and trimers (3,  $m$ ) are shown in lighter and darker orange, respectively. In (A), the circle diameters are proportional to (count rates) $^{1/2}$ . The unidentified ions are shown in gray and nitrate-BioOxOrg clusters in dark violet. Water molecules evaporate rapidly in the API-TOF and are not detected, as described in (31, 32). The experimental conditions for this specific run were  $J = 4.38 \text{ cm}^{-3} \text{ s}^{-1}$ ,  $[\text{H}_2\text{SO}_4] = 2.41 \times 10^6 \text{ cm}^{-3}$ ,  $[\text{BioOxOrg}] = 3.81 \times 10^8 \text{ cm}^{-3}$ , temperature = 278 K, relative humidity = 39%.

(8), we conclude that our slopes are representative of atmospheric nucleation. However, this hypothesis will need to be tested in future experiments.

Confirmation that BioOxOrg compounds participate in nucleation from the very first step is provided by API-TOF (atmospheric pressure interface time-of-flight) mass spectrometer data (28). Figure 2A shows an API-TOF mass-defect plot where the deviation from the nominal (integer) mass (i.e., the “mass defect”) of a compound is plotted versus the exact mass (31, 32). This plot reveals the molecular composition of the nucleating negatively charged clusters (up to ~1400 Th) and shows the presence of heteromers composed of various numbers of H<sub>2</sub>SO<sub>4</sub> and BioOxOrg molecules ( $n, m$ ), in addition to sulfuric acid monomers, dimers, and trimers (red circles). Especially prominent are (1, 1) (H<sub>2</sub>SO<sub>4</sub>, BioOxOrg) (yellow circles, first band), (2, 1) (orange circles, first band), (1, 2) and (2, 2) (yellow and orange circles, respectively, second band). These heteromers dominate the negative ion signals during the nucleation events. Pure sulfuric acid clusters above the trimer are absent. Several other mass-defect plots for different conditions are shown in (28).

The API-TOF measurements confirm that the negatively charged clusters grow with time. Figure 2B shows the time series of the normalized cluster concentration of the four bands seen in Fig. 2A. The number  $m$  of the band corresponds to the number of BioOxOrg molecules present in the clusters of that band. The clusters additionally contain mainly one or two sulfuric acid molecules (one of which accommodates the negative charge by deprotonation to HSO<sub>4</sub><sup>−</sup>). Each new band appears with a delay of 3 to 10 min relative to the previous band, indicating that the clusters grow by the consecutive addition of BioOxOrg molecules. However, the preferential pathway for growing clusters will depend on the collision and

evaporation rates, which in turn depend on the relative vapor concentrations, the oxidation state of the BioOxOrg molecules, and the charge on the cluster. Figure 2B also shows the appearance of 2- and 3-nm particles, providing evidence that the nucleated clusters indeed grow into larger particles sequentially detected by particle counters with higher cut-offs. The API-TOF measured only negatively charged clusters, and the pathways for neutral clusters could be different. However, Schobesberger *et al.* (32) showed similar growth rates for charged and neutral clusters involving BioOxOrg molecules, which explains the good agreement with the particle counters in Fig. 2B.

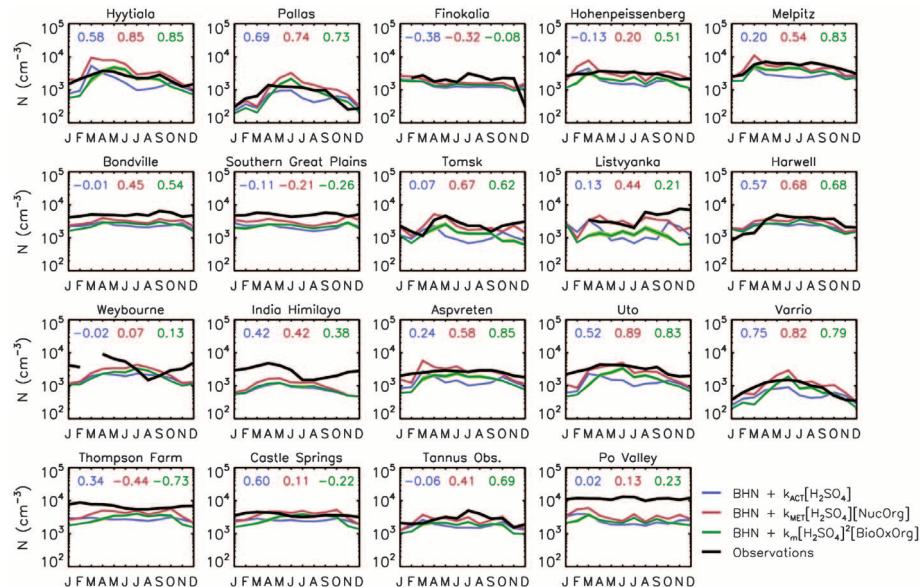
The large enhancement of the nucleation rate with BioOxOrg is due to the formation of clusters with much lower evaporation rates than those of binary sulfuric acid clusters. Quantum chemical calculations (28) indicate that the evaporation rate of a neutral sulfuric acid dimer is much higher than that of a highly oxidized BioOxOrg molecule [with an oxygen-to-carbon ratio (O:C) of up to 1 (28)] clustered in a heterodimer with one sulfuric acid molecule (e.g., by a factor of 10<sup>4</sup> for a 3-methyl-1,2,3-butane-tricarboxylic acid molecule). Zhang *et al.* (2009) (18) investigated heterodimers with *cis*-pinonic acid; however, because of the lower O:C of 0.3, these clusters are substantially less stabilized (28), and therefore much higher concentrations were needed to observe nucleation.

Notwithstanding the caveats on the slopes of the nucleation rates versus H<sub>2</sub>SO<sub>4</sub> and BioOxOrg concentrations, which may vary with experimental conditions, we have parameterized these dependencies to investigate the resulting particle production in a global aerosol model. Setting  $p = 2$  and  $q = 1$  in Eq. 2, we obtain  $k_m = 3.27 \times 10^{-21} \text{ cm}^6 \text{ s}^{-1}$ , with a 90% confidence interval of  $1.73 \times 10^{-21}$  to  $6.15 \times 10^{-21} \text{ cm}^6 \text{ s}^{-1}$ . A nucleation rate in the form  $J = k_m [\text{H}_2\text{SO}_4]^2 [\text{BioOxOrg}]$  can

be compared to rates in the form  $J = k' [\text{H}_2\text{SO}_4]^2$  that have been fitted empirically to ambient measurements (7, 9), which yield an effective prefactor  $k'$  that lies in the range of 0.01 to  $10 \times 10^{-12} \text{ cm}^3 \text{ s}^{-1}$ . For example, with  $\alpha$ -pinene mixing ratios of 200 pptv [e.g., (33)], a condensation sink rate of monomers of  $10^{-3} \text{ s}^{-1}$ , and  $[\text{OH}] = 10^6 \text{ cm}^{-3}$ , we estimate  $k' = 1.3 \times 10^{-12} \text{ cm}^3 \text{ s}^{-1}$ , which is well within measured values (28). Although both parameterizations are consistent with ambient observations (7, 9), our new parameterization contains an explicit dependence on organics. The parameterized CLOUD data can thus be used to quantitatively test the hypothesis that organic-sulfuric acid nucleation plays an important role in the planetary BL, with relatively few assumptions, because the parameterization has its basis in laboratory measurements made under realistic, albeit limited, atmospheric conditions.

We included this parameterization in a three-dimensional global aerosol model, GLOMAP (34, 35). The concentration of BioOxOrg was calculated assuming that it derives from a two-stage oxidation of  $\alpha$ -pinene to first-generation products and then to BioOxOrg, with the  $\alpha$ -pinene emitted from the terrestrial biosphere (36). The new parameterization resulted in a 57% (90% confidence interval range from 46 to 70%) increase in the global annual mean particle (>3 nm in diameter) number concentration in the BL compared with a control simulation that included only binary homogenous nucleation, BHN [from a global annual mean value of  $450 \text{ cm}^{-3}$  for BHN to  $706 \text{ cm}^{-3}$  (range from 654 to  $765 \text{ cm}^{-3}$ ) for the new parameterization]. The increase in particle concentrations occurs mostly over land areas, where  $\alpha$ -pinene is emitted; the mean fractional increase in particle number concentration is 97% (range from 78 to 119%) over land and 49% (range from 40 to 60%) over the ocean. In contrast, when the nucleation rate in the BL is

**Fig. 3. Simulated and observed monthly mean total particle number concentration ( $N$ ) across 19 Northern Hemisphere continental BL locations.** Multiannual observations, represented by the black line, are derived from measurements with minimum cut-off diameters ranging from 3 to 14 nm (11). Simulations using three different nucleation mechanisms are shown as colored lines: blue represents BHN plus activation BL nucleation ( $\text{BHN} + k[\text{H}_2\text{SO}_4]$ ); red represents BHN plus Metzger *et al.* (25) in the BL; dark green represents BHN plus our mechanism (Eq. 2) in the BL [see (28) for a definition of these experiments]. Light green shading around the dark green line for our mechanism represents simulated particle concentrations at the edge of the 90% confidence interval for the value of  $k_m$ . Pearson correlation coefficient ( $R$ ) given for each site (colored according to nucleation mechanism) at the top of each individual plot.





defined as  $J = k_{\text{ACT}}[\text{H}_2\text{SO}_4]$  the enhancement is 79% over land and 137% over oceans, which is likely to be an unrealistic marine/land contrast because it neglects the modulation caused by lower organic compound concentrations over remote marine regions.

Figure 3 shows the seasonal cycle in simulated and observed particle number concentrations across 19 locations in the Northern Hemisphere continental BL (11); see (28) for further details. Model simulations based on the assumption that only  $\text{H}_2\text{SO}_4$  controls nucleation in the boundary layer [ $J = k_{\text{ACT}}[\text{H}_2\text{SO}_4]$ , with rate coefficients determined from ambient data as in Fig. 1A (7, 9)] tend to predict peak particle concentrations in early spring and autumn, with summer nucleation being suppressed by the higher condensation sink. Our parameterization (dark green line in Fig. 3) improves both the simulated magnitude and the seasonal variation of particle concentration (table S3), including the summer peak caused by the strong seasonal variation in biogenic emissions and OH concentration (OH concentration appears to the power of three in the experimentally determined rate because it accounts for the oxidation both of organics to BioOxOrg and of  $\text{SO}_2$  to  $\text{H}_2\text{SO}_4$ ). This difference in seasonality between  $J = k_{\text{ACT}}[\text{H}_2\text{SO}_4]$  and our mechanism is especially apparent at sites located in or near forests (table S3) but less apparent at polluted sites where biogenic emissions play a smaller role. At the forest sites, the mean correlation coefficient between the modeled and observed monthly mean concentrations is 0.7 using our mechanism but only 0.35 using  $J = k_{\text{ACT}}[\text{H}_2\text{SO}_4]$ . Our mechanism can therefore explain about 50% of the temporal variability in particle concentrations, but activation nucleation can explain only 12%. The Metzger *et al.* (25) mechanism ( $J = k_{\text{MET}}[\text{H}_2\text{SO}_4][\text{NucOrg}]$ ) also improves the seasonal cycle, but it assumes that the anthropogenic organic compound used in those experiments is representative of  $\alpha$ -pinene in the model, which may not be the case.

There are many other uncertain model processes that could control the seasonality of particle concentrations. However, in a model study sampling from the 28-dimensional uncertainty space of model processes and emissions (37, 38), the summer dip in particle concentrations was shown to be a robust feature of the model when nucleation is driven only by  $\text{H}_2\text{SO}_4$ . This problem seems to be overcome here by including a biogenically controlled nucleation mechanism. Figure 3 shows a remaining model-observation bias in particle concentrations in winter, which may reflect other uncertain processes or emissions (37) or may indicate that other nucleation mechanisms are operating that are controlled by nonbiogenic compounds. However, at present, there are no measurements that enable the competing effects of compounds like ammonia, amines, and oxidized organics to be accounted for in a model.

## Conclusions

Recent experimental results and quantum chemical calculations have shown that amines and ions can also effectively stabilize the sulfuric acid clusters, reducing evaporation rates and enhancing the nucleation rates at low  $\text{H}_2\text{SO}_4$  concentrations (24, 39, 40). Thus, the dominant nucleation pathway may ultimately depend on the local atmospheric concentration of  $\text{H}_2\text{SO}_4$ , ions, and amines and on the concentration and functionalization of BioOxOrg, all of which vary considerably over time and space. At present, these compounds cannot be combined in a single mechanism because of the unknown way in which they compete with each other to stabilize clusters. Challenging laboratory and field measurements, as well as accurate modeling, of all these variables are required to predict the dominant nucleation pathway at different locations and eventually to understand the global effect of new-particle formation on climate. However, our model simulations show that the nucleation of sulfuric-acid and oxidized biogenic organic compounds (BioOxOrg) explains some features of the observed seasonal cycle of new particles in the continental BL that cannot be explained by sulfuric acid alone. Given the experimental evidence and modeling results presented here, it appears that highly oxidized biogenic organic vapors and sulfuric acid together play a major role in new-particle formation in the BL.

## References and Notes

- Intergovernmental Panel on Climate Change, *Climate Change 2007: The Physical Science Basis. Contribution of Working Group I to the Fourth Assessment Report of the Intergovernmental Panel on Climate Change*, S. Solomon *et al.*, Eds. (Cambridge Univ. Press, New York, 2007).
- M. Kulmala *et al.*, *J. Aerosol Sci.* **35**, 143–176 (2004).
- F. Yu, G. Luo, *Atmos. Chem. Phys.* **9**, 7691–7710 (2009).
- J. Merikanto, D. V. Spracklen, G. W. Mann, S. J. Pickering, K. S. Carslaw, *Atmos. Chem. Phys.* **9**, 8601–8616 (2009).
- R. Zhang, A. Khalizov, L. Wang, M. Hu, W. Xu, *Chem. Rev.* **112**, 1957–2011 (2012).
- R. J. Weber *et al.*, *J. Geophys. Res.* **102**, 4375 (1997).
- S. L. Sihto *et al.*, *Atmos. Chem. Phys.* **6**, 4079–4091 (2006).
- I. Riipinen *et al.*, *Atmos. Chem. Phys.* **7**, 1899–1914 (2007).
- C. Kuang, P. H. McMurry, A. V. McCormick, F. L. Eisele, *J. Geophys. Res.* **113**, D10209 (2008).
- R. J. Weber *et al.*, *Chem. Eng. Commun.* **151**, 53–64 (1996).
- D. V. Spracklen *et al.*, *Atmos. Chem. Phys.* **10**, 4775–4793 (2010).
- R. J. Weber *et al.*, *J. Geophys. Res.* **103**, 16385 (1998).
- F. L. Eisele *et al.*, *J. Geophys. Res.* **111**, D04305 (2006).
- P. Paasonen *et al.*, *Atmos. Chem. Phys.* **10**, 11223–11242 (2010).
- M. Kulmala *et al.*, *Science* **339**, 943–946 (2013).
- J. Kirkby *et al.*, *Nature* **476**, 429–433 (2011).
- R. Zhang *et al.*, *Science* **304**, 1487–1490 (2004).
- R. Zhang *et al.*, *Proc. Natl. Acad. Sci. U.S.A.* **106**, 17650–17654 (2009).

- S. M. Ball, D. R. Hanson, F. L. Eisele, P. H. McMurry, *J. Geophys. Res.* **104**, 23709 (1999).
- L. H. Young *et al.*, *Atmos. Chem. Phys.* **8**, 4997–5016 (2008).
- A. Laaksonen *et al.*, *Atmos. Chem. Phys.* **8**, 7255–7264 (2008).
- A. Sorokin, F. Arnold, *Atmos. Environ.* **41**, 3740–3747 (2007).
- M. Chen *et al.*, *Proc. Natl. Acad. Sci. U.S.A.* **109**, 18713–18718 (2012).
- J. Almeida *et al.*, *Nature* **502**, 359–363 (2013).
- A. Metzger *et al.*, *Proc. Natl. Acad. Sci. U.S.A.* **107**, 6646–6651 (2010).
- F. Riccobono *et al.*, *Atmos. Chem. Phys.* **12**, 9427–9439 (2012).
- M. Sipilä *et al.*, *Science* **327**, 1243–1246 (2010).
- Materials and methods are available as supplementary materials on Science Online.
- D. W. Oxtoby, D. Kashcheyev, *J. Chem. Phys.* **100**, 7665–7671 (1994).
- S. Ehrhart, J. Curtius, *Atmos. Chem. Phys.* **13**, 11465–11471 (2013).
- M. Ehn *et al.*, *Atmos. Chem. Phys.* **10**, 8513–8530 (2010).
- S. Schobesberger *et al.*, *Proc. Natl. Acad. Sci. U.S.A.* **110**, 17223–17228 (2013).
- H. Hakola, H. Hellen, M. Hemmila, J. Rinne, M. Kulmala, *Atmos. Chem. Phys.* **12**, 11665–11678 (2012).
- D. V. Spracklen, K. J. Pringle, K. S. Carslaw, M. P. Chipperfield, G. W. Mann, *Atmos. Chem. Phys.* **5**, 2227–2252 (2005).
- G. W. Mann *et al.*, *Geosci. Model Dev.* **3**, 519–551 (2010).
- A. Guenther *et al.*, *J. Geophys. Res.* **100**, 8873–8892 (1995).
- L. A. Lee *et al.*, *Atmos. Chem. Phys.* **13**, 8879–8914 (2013).
- K. S. Carslaw, L. A. Lee, C. L. Reddington, G. W. Mann, K. J. Pringle, *Faraday Discuss.* **165**, 495–512 (2013).
- A. B. Nadykto, F. Q. Yu, *Chem. Phys. Lett.* **435**, 14–18 (2007).
- T. Kurtén, V. Loukonen, H. Vehkamäki, M. Kulmala, *Atmos. Chem. Phys.* **8**, 4095–4103 (2008).

**Acknowledgments:** We thank CERN for supporting CLOUD with important technical and financial resources and providing a particle beam from the CERN PS; J.-L. Agostini, P. Carrie, L.-P. De Menezes, F. Josa, I. Krasin, R. Kristic, O. S. Maksumov, S.V. Mizin, R. Sitals, A. Wasem, and M. Wilhelmsson for their important contributions to the experiment; and C. Kuang and V.-M. Kerminen for providing the observational data sets used in Fig. 1A and the authors that contributed to them. This research was funded by the European Commission Seventh Framework Programme (Marie Curie Initial Training Network “CLOUD-ITN,” grant no. 215072), the European Research Council Advanced Grant “ATMNUCLE” (no. 227463), the Academy of Finland via the Centre of Excellence program (project no. 1118615) and grant no. 1133872, the German Federal Ministry of Education and Research (project no. 01LK0902A), the Swiss National Science Foundation (project no. 206621\_125025 and 206620\_130527), the Austrian Science Fund (project no. P19546 and L593), the Portuguese Foundation for Science and Technology (project no. CERN/FP/116387/2010), the Russian Foundation for Basic Research (grant N08-02-91006-CERN), the Davidow Foundation, the Royal Society Wolfson Award, and the NSF (grants AGS1136479 and CHE1012293). The data reported in this paper are available online as .txt files in the supplementary materials.

## Supplementary Materials

www.sciencemag.org/content/344/6185/717/suppl/DC1  
Materials and Methods  
Figs. S1 to S8  
Tables S1 to S4  
References (41–71)  
Data S1 to S4

22 July 2013; accepted 21 April 2014  
10.1126/science.1243527

# Transverse Demagnetization Dynamics of a Unitary Fermi Gas

A. B. Bardon,<sup>1</sup> S. Beattie,<sup>1</sup> C. Luciuk,<sup>1</sup> W. Cairncross,<sup>1</sup> D. Fine,<sup>1</sup> N. S. Cheng,<sup>1</sup> G. J. A. Edge,<sup>1</sup> E. Taylor,<sup>2</sup> S. Zhang,<sup>3</sup> S. Trotzky,<sup>1</sup> J. H. Thywissen<sup>1,4\*</sup>

Understanding the quantum dynamics of strongly interacting fermions is a problem relevant to diverse forms of matter, including high-temperature superconductors, neutron stars, and quark-gluon plasma. An appealing benchmark is offered by cold atomic gases in the unitary limit of strong interactions. Here, we study the dynamics of a transversely magnetized unitary Fermi gas in an inhomogeneous magnetic field. We observe the demagnetization of the gas, caused by diffusive spin transport. At low temperatures, the diffusion constant saturates to the conjectured quantum-mechanical lower bound  $\approx \hbar/m$ , where  $m$  is the particle mass. The development of pair correlations, indicating the transformation of the initially noninteracting gas toward a unitary spin mixture, is observed by measuring Tan's contact parameter.

Short-range interactions reach their quantum-mechanical limit when the scattering length that characterizes interparticle collisions diverges. A well-controlled model system that realizes this unitary regime is provided by ultracold fermionic alkali atoms tuned to a Fano-Feshbach resonance (1). These scale-invariant gases are characterized by universal parameters relevant to diverse systems such as the crust of neutron stars at 25 orders of magnitude higher density (2, 3). Experiments with ultracold atoms have already greatly contributed to the understanding of equilibrium properties of unitary gases (4–6). Progress has also been made in the study of unitary dynamics (7–11), including observations of suppressed momentum transport (7) and spin transport (8–10) due to strong scattering.

Spin diffusion is the transport phenomenon that relaxes magnetic inhomogeneities in a many-body system. At low temperature, where Pauli blocking suppresses collision rates, one must distinguish between diffusion driven by gradients in either the magnitude or the direction of magnetization, and quantified by longitudinal spin diffusivity  $D_s^{\parallel}$  or transverse spin diffusivity  $D_s^{\perp}$ , respectively (12, 13). A measurement of  $D_s^{\parallel}$  in a three-dimensional (3D) unitary Fermi gas yielded a minimum trap-averaged value of  $6.3(3)\hbar/m$  (9). This is consistent with a dimensional argument, in which diffusivity is a typical velocity ( $\hbar k_F/m$  for a cold Fermi gas, where  $\hbar k_F$  is the Fermi momentum) times the mean free path between collisions. In the absence of localization, the mean-free path in a gas cannot be smaller

than the interparticle spacing  $\sim 1/k_F$ , which translates into a quantum lower bound of roughly  $\hbar/m$  (9, 14, 15). However,  $D_s^{\perp}$  as low as  $0.0063(8)\hbar/m$  was recently observed in a strongly interacting 2D Fermi gas (10). This thousand-fold range in transport coefficients remains unexplained by theory.

We measure the transverse demagnetization dynamics of a 3D Fermi gas that is initially fully spin-polarized. All of our measurements are carried out with samples of ultracold  $^{40}\text{K}$  atoms in a harmonic trap. Each atom is prepared in an equal superposition of two resonantly interacting internal states, labeled  $|\uparrow\rangle$  and  $|\downarrow\rangle$  (16), which corresponds to a gas with full transverse magnetization  $M_y = 1$  (Fig. 1). Initially, interactions between these identical ultracold fermions is inhibited by the Pauli exclusion principle. The states we use also block any local mechanism for spin relaxation, unlike the scenario typical in liquids or solids. However, the differential magnetic moment  $\Delta\mu$  between the internal states allows a magnetic field gradient  $B' = \partial B_z/\partial z$  to twist the magnetization across the cloud into a spiral pattern, leading to a gradient in transverse magnetization. This gradient drives diffusive spin transport that erodes the coherence irreversibly. In contrast, for a weakly interacting Fermi gas, collisionless spin waves lead to reversible dynamics (17). For

the strongly interacting Fermi gas probed here, the evolution of transverse magnetization  $M_{\perp} = M_x + iM_y$  is modeled with  $\partial_t M_{\perp} = -i\alpha z M_{\perp} + D_s^{\perp} \nabla^2 M_{\perp}$ , neglecting trap effects, where  $\alpha = \Delta\mu B'/\hbar$  (18). This equation is solved by  $M_{\perp}(\vec{r}, t) = i\exp[-i\alpha z t - D_s^{\perp} \alpha^2 t^3/3]$ , such that  $(D_s^{\perp} \alpha^2)^{-1/3}$  gives the time scale of demagnetization. Because there is no spatial gradient in the magnitude of magnetization, the dynamics do not probe  $D_s^{\parallel}$ .

The effect of spin diffusion on magnetization is measured using the spin-echo technique described in Fig. 1. The spin-refocusing  $\pi$  pulse at  $t_{\pi}$  swaps the population of the states  $|\uparrow\rangle$  and  $|\downarrow\rangle$ , which causes the spin spiral to start untwisting. This partial rephasing also reduces the rate of diffusion. At  $t = 2t_{\pi}$ , the model anticipates a spin echo with

$$M_{\perp}(t) = -i\exp[-D_s^{\perp} \alpha^2 t^3/12] \quad (1)$$

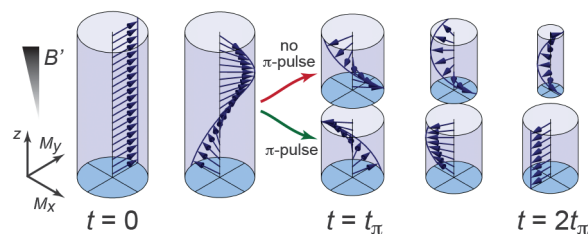
The final cloud-averaged  $|M_{\perp}|$  is indicated by the contrast in  $|\uparrow\rangle$  and  $|\downarrow\rangle$  atom number after a final  $\pi/2$  pulse with variable phase (16).

We observe that demagnetization occurs in several milliseconds (Fig. 2A, inset). Fitting  $|M_{\perp}(t)|$  with an exponential decay function  $\exp[-(t/\tau_M)^{\eta}]$ , we find a range of  $2.5 \leq \eta \leq 4.0$ , compatible with  $\eta = 3$  in Eq. 1. Constraining  $\eta = 3$ , we extract  $\tau_M$  across a wide range of gradients (Fig. 2A) and fit it to find that the  $(B')^{-2/3}$  scaling of Eq. 1 holds even for the case of the trap-averaged magnetization. At an initial temperature  $(T/T_F)_i = 0.25(3)$ , where  $T_F$  is the Fermi temperature of the spin-polarized gas (16), a single-parameter fit of  $\tau_M = (D_s^{\perp} \alpha^2/12)^{-1/3}$  to the data yields  $D_s^{\perp} = (1.08 \pm 0.09_{-0.13}^{+0.17})\hbar/m$ , where the uncertainties are the statistical error from the fit and the systematic error from the gradient calibration, respectively. This is a direct measurement of the time- and trap-averaged diffusivity that does not rely on any calibration other than that of the gradient.

In Fig. 2B, we choose a constant gradient and vary  $(T/T_F)_i$ . Diffusivity is larger in hotter clouds, as both the typical velocity and the mean free path increase with temperature. At lower temperatures, we observe that  $D_s^{\perp}$  does not continue to decrease but appears to saturate. Careful examination of the demagnetization dynamics at our lowest initial temperatures (see insets to Fig. 2B)

## Fig. 1. Magnetization dynamics.

A  $\pi/2$  pulse at  $t = 0$  initializes the system with a homogeneous magnetization ( $M_y = 1$  in the rotating frame) perpendicular to the magnetic field, which is along  $z$ . A spin spiral develops because of a magnetic field gradient and drives diffusive spin currents. The upper and lower sequences show evolution with out and with a  $\pi$  pulse, respectively.



<sup>1</sup>Department of Physics, University of Toronto, M5S 1A7 Canada.

<sup>2</sup>Department of Physics and Astronomy, McMaster University, L8S 4M1 Canada. <sup>3</sup>Department of Physics, Center of Theoretical and Computational Physics, University of Hong Kong, China.

<sup>4</sup>Canadian Institute for Advanced Research, Toronto, Ontario, M5G 1Z8 Canada.

\*Corresponding author. E-mail: joseph.thywissen@utoronto.ca



also suggests an acceleration of demagnetization at later times. An apparently time-dependent  $D_s^\perp$  could be due to its polarization dependence, as is predicted below the so-called anisotropy temperature, where  $D_s^\perp$  differs from  $D_s^\parallel$  (13, 19). It might also arise from spin-rotation effects (20, 21). However, we find the deviations from Eq. 1 to be small, and we are unable to distinguish between

these possibilities and other systematics. Within the probed range of temperature, the trap- and time-averaged  $D_s^\perp$  is consistent with a quantum lower bound of  $\approx \hbar/m$ .

Demagnetization transforms the system of  $N$  particles in a single spin state to a mixture of two spin states, each with  $N/2$  particles. The final Fermi energy of the trapped system  $E_{F,f}$

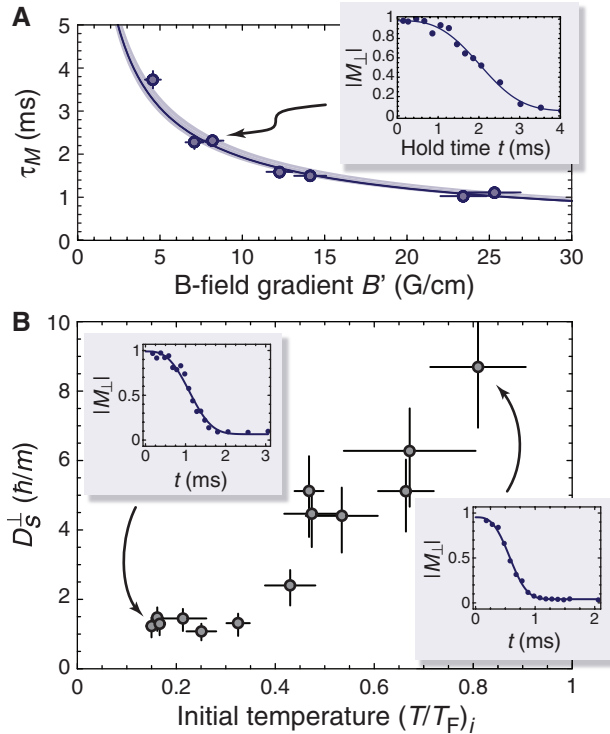
therefore is reduced by a factor of  $2^{1/3}$  compared with the initial  $E_{F,i}$ . Furthermore, demagnetization releases attractive interaction energy. Together these effects increase temperature (16), so that each measurement of  $D_s^\perp$  has to be understood as a time average over a range in temperatures. The intrinsic heating, together with the initial polarization of the cloud, ensures that the gas remains in the normal phase throughout the evolution (22).

The observation of suppressed spin transport indicates strong interparticle scattering but does not reveal how a thermodynamic interaction energy emerges. In a complementary set of measurements, we study the microscopic transformation of the gas by following the dynamical evolution of pair correlations that are enabled by demagnetization. Instead of measuring  $|M_\perp|$ , we probe the gas with a pulse that couples  $|\uparrow\rangle$  to  $|\text{p}\rangle$ , an initially unoccupied internal state that interacts only weakly with  $|\uparrow\rangle$  and  $|\downarrow\rangle$  (16). The transfer rate to  $|\text{p}\rangle$  is measured as a function of the frequency detuning  $\delta$  above the single-particle resonance. In a strongly interacting gas in equilibrium, the high-frequency tail of such a spectrum is known to be proportional to Tan's contact parameter  $C$  [ $\text{d}r C(r)$  times  $\delta^{-3/2}$  (23–30)]. The contact density  $C(r) = \langle g^2 \psi_\uparrow^\dagger(r) \psi_\downarrow^\dagger(r) \psi_\downarrow(r) \psi_\uparrow(r) \rangle$  is a local measure of the pair correlation, that is, the number of pairs of opposite spins at short distance, where  $g$  is the coupling constant and  $\psi_\sigma$  is the annihilation operator with spin  $\sigma$ . As is clear from its definition,  $C$  is also proportional to the local interaction energy. Although contact has been shown to relate various thermodynamic and many-body properties of a short-range interacting gas, it has so far been studied only in equilibrium and only with an unmagnetized gas (25, 30–33).

Figure 3A shows that after a short hold time, the spectrum exhibits only the single-particle peak, whereas after a longer hold time, the spectrum develops a high-frequency tail. Similar spectroscopic measurements starting from a polarized Fermi gas have shown the emergence of mean-field shifts after decoherence (34). Here, we study the high-frequency tail of the spectrum, finding that it has a  $\delta^{-3/2}$  scaling at  $\delta \gtrsim 4E_{F,f}/\hbar$  for each hold time  $t$ , which indicates that pair correlations can be described with a contact parameter throughout the dynamics (Fig. 3B).

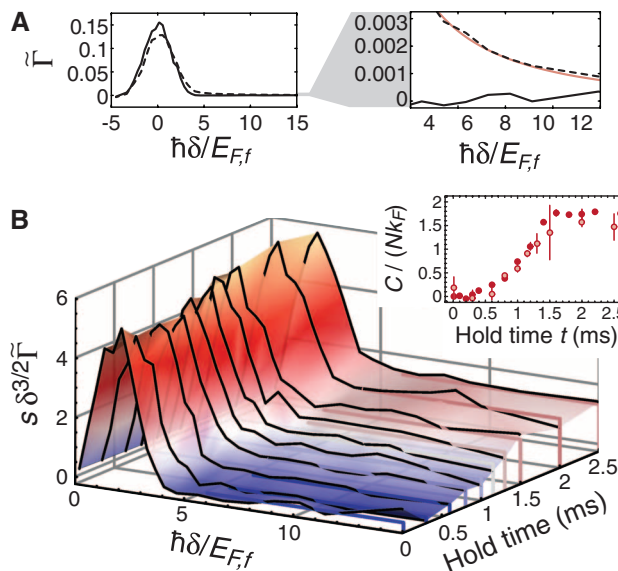
Figure 4A shows that, under various protocols, the contact starts at zero and grows in time toward a maximal value of  $C_{\text{max}}/(k_F N) = 1.53(4)$ , where  $\hbar k_F = \sqrt{2mE_{F,f}}$  is the Fermi momentum in the final state of the trapped gas and  $N$  is the total number of atoms. This is comparable to equilibrium values observed previously at  $T/T_F \approx 0.35$  in (33), which lies between the initial and final temperatures of these data (16). At longer times ( $t > 5$  ms), Fig. 4A shows a slow reduction of contact, which is likely due to heating; however, in this work, we focus on the short-time dynamics. A fit using an empirical rise function  $f(t) = C_{\text{max}}(1 - \exp[-(t/\tau_C)^\eta])$  to the short-time

**Fig. 2. Spin diffusion.** (A) Magnetization decay times  $\tau_M$  at various gradients at an initial temperature of  $(T/T_F)_i = 0.25(3)$ . Horizontal and vertical error bars reflect the systematic error in the gradient calibration and the fit error, respectively. The solid line is a single-parameter fit of  $\tau_M = (D_s^\perp \alpha^2/12)^{-1/3}$  to the data, and the shaded area denotes the combined statistical and systematic uncertainty. The inset shows a sample of  $|M_\perp(t)|$  at  $B' = 8.2(7)$  G/cm with a fit using Eq. 1. (B) Measured  $D_s^\perp$  for various initial temperatures at a single gradient  $B' = 18(1)$  G/cm. To achieve temperature control, the data were collected with  $N = (1 - 7) \times 10^4$ . Horizontal error bars are statistical uncertainty; vertical error bars combine gradient-calibration and fit uncertainty. The insets show sample data for  $|M_\perp(t)|$  at two initial temperatures with a fit using Eq. 1.



**Fig. 3. Time-resolved spectroscopy to measure Tan's contact** at  $B' = 8.2(7)$  G/cm and  $(T/T_F)_i \approx 0.2$ .

(A) The normalized rate  $\tilde{\Gamma}$  of atom transfer (16) from  $|\uparrow\rangle$  to  $|\text{p}\rangle$  is shown after 10  $\mu\text{s}$  (solid line) and 2.5 ms (dashed line), both without a spin-refocusing pulse. The red line in the right panel is a fit of a power-law  $\propto \delta^{-3/2}$  to the high-frequency tail for  $t = 2.5$  ms. (B) The transfer rate  $\tilde{\Gamma}$  rescaled with  $s\delta^{3/2}$  versus hold time, where  $s = \pi^2(2\hbar/E_{F,f})^{3/2}$ , revealing a plateau for large positive detunings  $\delta \gtrsim 4E_{F,f}/\hbar$ . The inset compares contact values extracted from these full spectra (open circles) and those measured at a fixed detuning  $\delta/2\pi = 125$  kHz (filled circles). The latter method allows single-shot study of contact dynamics, and thus reduced statistical noise, as seen here. The contact is normalized by the final Fermi momentum in the trap and the total number of atoms. Error bars in (B) show one standard deviation of repeated measurements.



data yields an exponent of  $\eta = 3.6(3)$  with a spin-reversal and  $\eta = 2.8(2)$  without a spin-reversal, reminiscent of the magnetization loss function  $\propto \exp[-(t/\tau^M)^3]$ . Further connection between contact and magnetization is demonstrated by Fig. 4B, which traces the contact during a spin-reversal sequence: The rise of  $C/(k_F N)$  is slowed by the refocusing pulse and plateaus at the spin-echo time, around which transverse spin diffusion is suppressed.

Figure 4C compares  $\tau_M$  and  $\tau_C$ , both with and without an echo. A linear relationship is found, which is surprising at first, since magnetization is a one-body vector observable and contact is a two-body scalar observable. The connection comes from the Pauli exclusion principle, which requires that if two particles are in the same location, as is required for a contact interaction, their spin state must be the antisymmetric spin-singlet state. For uncorrelated spin pairs, the probability to be in a spin-singlet state is  $\rho_{ss} = (1 - |M_\perp|^2)/4$ . Combining this assumption with the diffusion model for magnetization predicts  $\tau_C = \tau_M/2^{1/3}$  and  $\tau_C = \tau_M/2$  with and without an echo, respectively. The maximum singlet probability for a given magnetization is  $\rho_{ss} = 1 - |M_\perp|^2$  and would instead give  $\tau_C/\tau_M$  that is  $2^{1/3}$  larger. Data in Fig. 4C show an approximately linear relation whose slope is between these two limits.

Comparing the full range of measured values for normalized  $C$  and  $|M_\perp|$  at various times and gradients in Fig. 4D also shows a functional form between the uncorrelated  $C \sim 1 - |M_\perp|^2$  and the

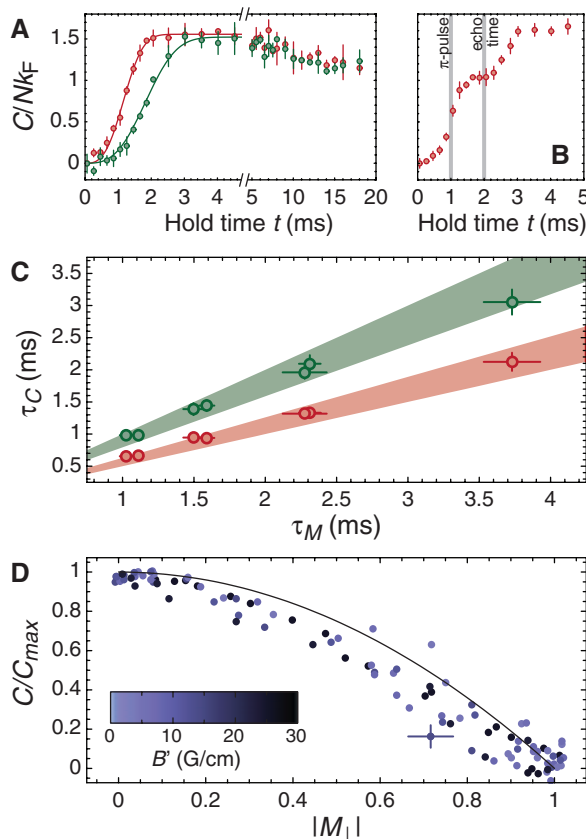
fully paired  $C \sim 1 - |M_\perp|$ . A calculation based on a large- $N$  expansion (35–37) predicts that  $C(M_\perp)$  changes between these limiting behaviors as  $T$  goes from  $2T_c$  to  $T_c$ , where  $T_c$  is the critical temperature for pair superfluidity (16). Because a singlet pair has no net spin, the observation of enhanced  $\rho_{ss}$  is also consistent with previous observations of reduced magnetic susceptibility due to strong attractive interactions in the normal state (38, 39).

Alternatively, an apparent reduction in  $C(M_\perp)$  might arise from a lag in the evolution of  $C$  behind  $|M_\perp|$ . However, we find no statistically significant dependence on gradient, which is evidence for a local equilibration of  $C$  on a faster time scale than the system-wide demagnetization. A true steady-state transport measurement, on the other hand, would suffer from an inhomogeneous magnetization due to imbalanced chemical potentials in the trap. Our dynamic measurement avoids this problem, because longitudinal spin transport is strongly suppressed on the millisecond time scale (8, 9).

In conclusion, we have shown how a transversely spin-polarized Fermi gas decoheres and becomes strongly correlated at an interaction resonance. A diffusion constant of  $\approx \hbar/m$  challenges a quasiparticle-based understanding of transport by implying the necessity of maximally incoherent quasiparticles. A similar limit to the quasiparticle lifetime would explain the ubiquitous  $T$ -linear resistivity in metals (40) and a quantum-limited shear viscosity (7).

#### Fig. 4. Linking contact and magnetization.

The time evolution of contact is studied using single-shot spectroscopy, as illustrated by the inset of Fig. 3B. (A) Contact versus hold time  $t$  with (in green) and without (in red) a spin-refocusing  $\pi$  pulse at  $t/2$ . Solid lines show a fit to  $C_{\max}(1 - \exp[-(t/\tau_C)^3])$ . (B) Contact versus hold time  $t$  with a  $\pi$  pulse applied at  $t_\pi = 1$  ms. At the echo time, the spin spiral has untwisted and no longer drives a diffusive spin current. Error bars in (A) and (B) show statistical error across repeated measurements, and both data sets were taken under the same conditions as Fig. 2A. (C) Contact growth time,  $\tau_C$ , versus demagnetization time,  $\tau_M$  [colors as in (A)], measured at various gradients. Shaded areas are bounded by the limits of fully paired and uncorrelated spins. (D) Normalized contact versus magnetization obtained by relating measurements of  $|M_\perp(t)|$  and  $C(t)$  for all sampled gradients  $B'$ . The solid line shows the behavior of uncorrelated spins. A typical statistical error bar is shown on a single point.



#### References and Notes

- I. Bloch, J. Dalibard, S. Nascimbène, *Nat. Phys.* **8**, 267–276 (2012).
- G. A. Baker, *Phys. Rev. C Nucl. Phys.* **60**, 054311 (1999).
- T.-L. Ho, *Phys. Rev. Lett.* **92**, 090402 (2004).
- S. Nascimbène, N. Navon, K. J. Jiang, F. Chevy, C. Salomon, *Nature* **463**, 1057–1060 (2010).
- M. Horikoshi, S. Nakajima, M. Ueda, T. Mukaiyama, *Science* **327**, 442–445 (2010).
- M. J. Ku, A. T. Sommer, L. W. Cheuk, M. W. Zwierlein, *Science* **335**, 563–567 (2012).
- C. Cao *et al.*, *Science* **331**, 58–61 (2011).
- Y. A. Liao *et al.*, *Phys. Rev. Lett.* **107**, 145305 (2011).
- A. Sommer, M. Ku, G. Roati, M. W. Zwierlein, *Nature* **472**, 201–204 (2011).
- M. Koschorreck, D. Pertot, E. Vogt, M. Köhl, *Nat. Phys.* **9**, 405–409 (2013).
- L. A. Sidorenkov *et al.*, *Nature* **498**, 78–81 (2013).
- A. Meyerovich, *Phys. Lett. A* **107**, 177–180 (1985).
- J. W. Jeon, W. J. Mullin, *Phys. Rev. Lett.* **62**, 2691–2694 (1989).
- D. Wulin, H. Guo, C.-C. Chien, K. Levin, *Phys. Rev. A* **83**, 061601 (2011).
- T. Enss, R. Haussmann, *Phys. Rev. Lett.* **109**, 195303 (2012).
- Supplementary materials are available on Science Online.
- X. Du, Y. Zhang, J. Petricka, J. E. Thomas, *Phys. Rev. Lett.* **103**, 010401 (2009).
- A. Abragam, *The Principles of Nuclear Magnetism* (Oxford University Press, London, 1961).
- T. Enss, *Phys. Rev. A* **88**, 033630 (2013).
- A. J. Leggett, *J. Phys. C* **3**, 448–459 (1970).
- C. Lhuillier, F. Laloe, *J. Phys.* **43**, 225–241 (1982).
- M. W. Zwierlein, A. Schirotzek, C. H. Schunck, W. Ketterle, *Science* **311**, 492–496 (2006).
- S. Tan, *Ann. Phys.* **323**, 2952–2970 (2008).
- E. Braaten, L. Platter, *Phys. Rev. Lett.* **100**, 205301 (2008).
- S. Zhang, A. J. Leggett, *Phys. Rev. A* **79**, 023601 (2009).
- F. Werner, Y. Castin, *Phys. Rev. A* **86**, 013626 (2012) and references therein.
- E. Braaten, D. Kang, L. Platter, *Phys. Rev. Lett.* **104**, 223004 (2010).
- W. Schneider, M. Randeria, *Phys. Rev. A* **81**, 021601 (2010).
- P. Pieri, A. Perali, G. C. Strinati, *Nat. Phys.* **5**, 736–740 (2009).
- J. T. Stewart, J. P. Gaebler, T. E. Drake, D. S. Jin, *Phys. Rev. Lett.* **104**, 235301 (2010).
- G. B. Partridge, K. E. Strecker, R. I. Kamar, M. W. Jack, R. G. Hulet, *Phys. Rev. Lett.* **95**, 020404 (2005).
- F. Werner, L. Tarruell, Y. Castin, *Eur. Phys. J. B* **68**, 401–415 (2009).
- E. D. Kuhnle *et al.*, *Phys. Rev. Lett.* **106**, 170402 (2011).
- S. Gupta *et al.*, *Science* **300**, 1723–1726 (2003).
- P. Nikolic, S. Sachdev, *Phys. Rev. A* **75**, 033608 (2007).
- M. Y. Veilleux, D. E. Sheehy, L. Radzihovsky, *Phys. Rev. A* **75**, 043614 (2007).
- T. Enss, *Phys. Rev. A* **86**, 013616 (2012).
- C. Sanner *et al.*, *Phys. Rev. Lett.* **106**, 010402 (2011).
- S. Nascimbène *et al.*, *Phys. Rev. Lett.* **106**, 215303 (2011).
- J. A. N. Bruin, H. Sakai, R. S. Perry, A. P. Mackenzie, *Science* **339**, 804–807 (2013).

**Acknowledgments:** We thank B. Braverman, I. Kivlichan, L. LeBlanc, and T. Pfau for experimental assistance; D. DeMille, T. Enss, L. Jiang, A. Leggett, and A. Paramekanti for discussions; A. Aspect for manuscript comments; and M. Ku and M. Zwierlein for sharing their unitary equation-of-state data. S.T. acknowledges support from the Centre for Quantum Information and Quantum Control. G.J.A.E. acknowledges support from Ontario. This work was supported by NSERC, CIFAR, the University of Hong Kong, and AFOSR under agreement no. FA9550-13-1-0063.

#### Supplementary Materials

www.sciencemag.org/content/344/6185/722/suppl/DC1  
Materials and Methods  
Figs. S1 and S2  
References (41–47)

21 October 2013; accepted 11 April 2014  
10.1126/science.1247425



# Electrically Switchable Chiral Light-Emitting Transistor

Y. J. Zhang,<sup>1\*</sup> T. Oka,<sup>1</sup> R. Suzuki,<sup>1</sup> J. T. Ye,<sup>1,2,3</sup> Y. Iwasa<sup>1,3\*</sup>

Tungsten diselenide (WSe<sub>2</sub>) and related transition metal dichalcogenides exhibit interesting optoelectronic properties owing to their peculiar band structures originating from the valley degree of freedom. Although the optical generation and detection of valley polarization has been demonstrated, it has been difficult to realize active valley-dependent functions suitable for device applications. We report an electrically switchable, circularly polarized light source based on the material's valley degree of freedom. Our WSe<sub>2</sub>-based ambipolar transistors emit circularly polarized electroluminescence from *p-i-n* junctions electrostatically formed in transistor channels. This phenomenon can be explained qualitatively by the electron-hole overlap controlled by the in-plane electric field. Our device demonstrates a route to exploit the valley degree of freedom and the possibility to develop a valley-optoelectronics technology.

Circularly polarized light is used in various fields, ranging from three-dimensional displays to technologies involving effective spin sources in spintronics (1) and information carriers in quantum computation (2), as well as to induce exotic quantum phenomena such as the Floquet topological state (3, 4). There is a strong demand for circularly polarized light sources having both compactness for achieving

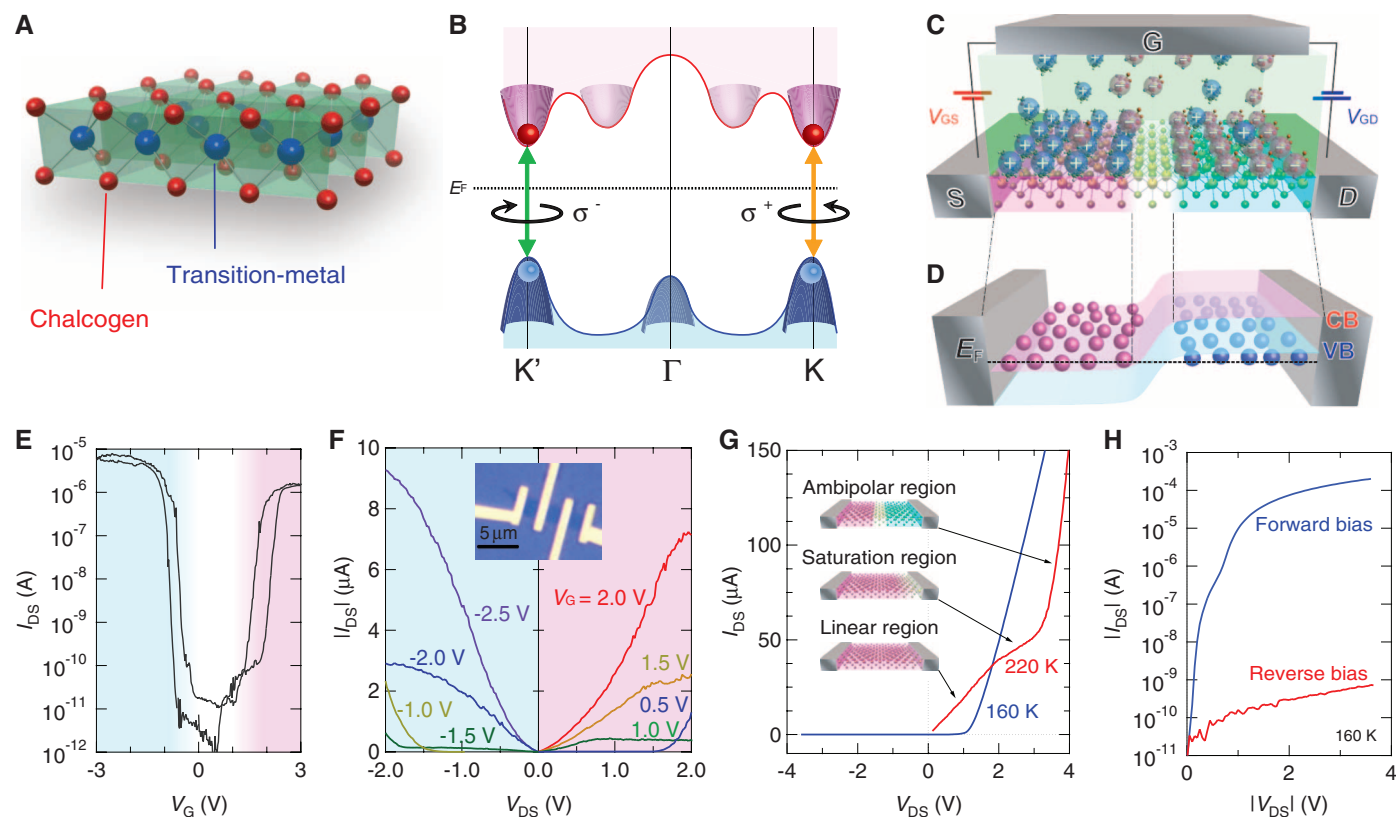
a high level of integration and electrical controllability of the polarization. However, currently available light sources are incapable of meeting these requirements. For example, optical filters (composed of a polarizer and a quarter-wave plate) require mechanical movement to change the polarization; spin light-emitting diodes (LEDs) (5) do not work without an external magnetic field; and metamaterials (6) or chiral polymer

LEDs (7) can produce only a fixed circular polarization, with a specific material configuration. Circularly polarized luminescence from solids is known to be a consequence of direct-gap interband transitions of electrons from the conduction band to the valence band with a total angular momentum shift of  $\pm 1$ . Thus, in order to achieve electrical controllability of the polarization of the luminescence, the minimum requirement is that these transitions must be associated with a degree of freedom that responds to an electric field.

Transition-metal dichalcogenides (TMDs), especially in the monolayer limit, is a promising candidate for such devices because two interband transitions are associated with not only the spin degree of freedom but also the momentum degree of freedom (8), which is indeed related to the electrical current. Monolayers of TMDs consist of a triangularly aligned transition metal [typically molybdenum (Mo) or tungsten (W)]

<sup>1</sup>Quantum-Phase Electronics Center (QPEC) and Department of Applied Physics, University of Tokyo, Tokyo 113-8656, Japan. <sup>2</sup>Zernike Institute for Advanced Materials, University of Groningen, Nijenborgh 4, 9747 AG, Groningen, Netherlands. <sup>3</sup>RIKEN Center for Emergent Matter Science (CEMS), Wako 351-0198, Japan.

\*Corresponding author. E-mail: yzhang@mp.t.u-tokyo.ac.jp (Y.J.Z.); iwasa@ap.t.u-tokyo.ac.jp (Y.I.)



**Fig. 1. EDLTs in action.** (A) Crystal structure of monolayer TMD. (B) Illustration of the band structure of monolayer TMD. (C) Device structure of TMD EDLT under ambipolar charge accumulation. (D) Schematic band structure of EDLT-induced *p-i-n* junction under equilibrium. (E) Transfer curve ( $I_{DS}$  versus  $V_G$ ) of monolayer WSe<sub>2</sub> EDLT. (F) Output curve ( $I_{DS}$  versus  $V_{DS}$ ) of WSe<sub>2</sub> EDLT. (Inset)

Typical optical micrograph of the device. (G)  $I$ - $V$  characteristics of WSe<sub>2</sub> EDLT at 220 K and 160 K, which are higher and lower than the glass transition temperature of *N,N*-diethyl-*N*-(2-methoxyethyl)-*N*-methylammonium bis(trifluoromethylsulfonyl)imide (DEME-TFSI), respectively. Illustrations show charging status at 220 K. (H) Log  $I_{DS}$  versus  $|V_{DS}|$  plot of the blue curve in (G).

plane sandwiched by two triangularly aligned chalcogen [typically sulfur (S) or selenium (Se)] planes. Each metal atom is surrounded by six chalcogen atoms, forming a trigonal prismatic structure (Fig. 1A). Monolayer TMD shares many properties with graphene-like materials with different A- and B-site atoms, in which inversion symmetry is broken (9). In monolayer TMD, electron and hole valleys exist at K and K' points in the hexagonal Brillouin zone, leading to a direct-gap semiconductor nature (Fig. 1B). Because the electronic states of the two valleys have different chiralities because of the inversion asymmetric crystal structure, interband transitions at K and K' points are allowed for  $\sigma_+$  and  $\sigma_-$  circularly polarized light, respectively (valley circular dichroism) (8). These features are suppressed in bulk single crystals because the inversion symmetry is recovered while the band structure changes from direct gap to indirect gap (10).

Circularly polarized photoluminescence (PL) from TMDs has been experimentally observed for monolayers (11–15) and for biased bilayers (16) when they were pumped with circularly

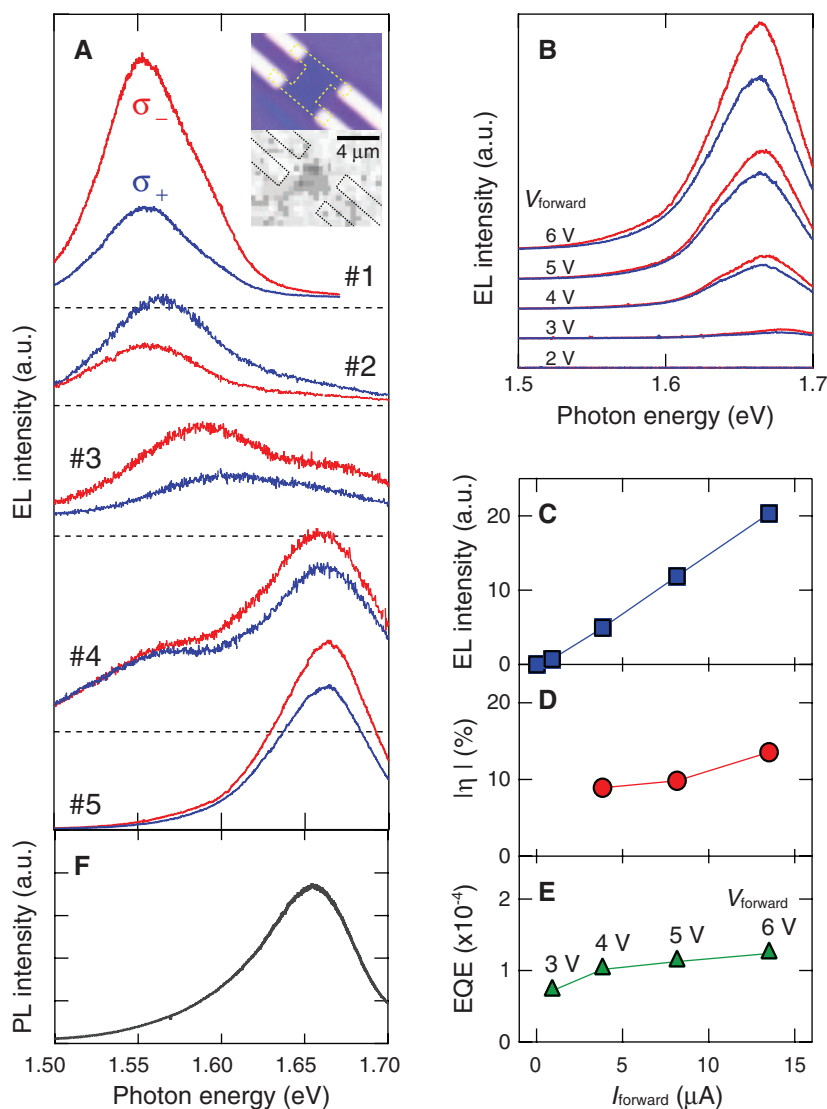
polarized incident light. Here, we report current-induced circularly polarized electroluminescence (EL) from *p-i-n* junctions in monolayer and multilayer tungsten diselenide (WSe<sub>2</sub>) (17). Moreover, the polarization was found to be electrically controllable by changing the current direction.

We formed *p-i-n* junctions using an electric-double-layer transistor (EDLT) structure with WSe<sub>2</sub> thin flakes having thicknesses of 0.6 to 2.6 nm as the channel material (18). Because TMD–field-effect transistors (FETs) show ambipolar transistor behavior (19–24), controlling the potential difference between the gate, source, and drain electrodes enables the simultaneous accumulation of both electrons and holes inside the channel (Fig. 1C), leading to light emission from the *p-i-n* junction, as demonstrated in organic ambipolar FETs (25, 26). EDLT-induced carriers in the channels can be electrostatically fixed when the device is cooled down under such bias conditions, forming a bias-independent *p-i-n* junction (Fig. 1D) (19).

EDLT has an additional benefit of eliminating the strong limitation of monolayers (27–30).

Naïvely thinking, multilayers (bulk material) are not suited for realizing circularly polarized EL. The restored inversion symmetry suppresses valley circular dichroism. In addition, multilayers are indirect-gap semiconductors, in which the conduction band minimum and the valence band maximum locate at T and  $\Gamma$  points, respectively (10). EDLTs can overcome these difficulties. First, the gate electric field breaks the inversion symmetry (16, 24). This recovers the peculiar features of monolayers, including valley circular dichroism (16). Second, because EDLTs produce an electric field one order of magnitude stronger than do conventional FETs, drastic band modulations occur: The valence band top is replaced by K points, and the energy difference between T and K points of the conduction band gets smaller (24). By combining these band structure changes with the large carrier accumulation capability of EDLTs ( $\sim 1 \times 10^{14} \text{ cm}^{-2}$ ), not only holes but also electrons can populate the K points. Therefore, multilayers under an EDLT operates in a similar manner as monolayers (24).

**Fig. 2. Circularly polarized electroluminescence.** (A) Polarized EL spectra from five devices. Spectra of device 1 were measured at 40 K. (Inset) Optical micrograph of device 2 and charge-coupled device image of EL. The yellow dotted curves denote WSe<sub>2</sub> thin flakes. (B) Voltage dependence of EL spectra of device 5. (C) Current dependence of total EL intensity extracted from Fig. 2B. (D) Current dependence of EL polarization extracted from Fig. 2B. (E) Current dependence of external quantum efficiency extracted from Fig. 2B. (F) PL spectrum of monolayer WSe<sub>2</sub> pumped with a He-Ne laser (1.97 eV).





Typical transistor characteristics of our WSe<sub>2</sub> EDLTs are displayed in Fig. 1E (transfer curve) and Fig. 1F (output curve), showing clear ambipolar operation. The carrier density and carrier mobility are estimated to be of the order of  $10^{13} \text{ cm}^{-2}$  and  $10^2 \text{ cm}^2 \text{ V}^{-1} \text{ s}^{-1}$ , respectively. As demonstrated in (19), we controlled gate voltage ( $V_G$ ) and source-drain voltage ( $V_{DS}$ ) to drive our transistor into the ambipolar region in the output curve measurement (Fig. 1G, red curve) and cooled it down to 160 K in order to freeze the gate dielectric, forming a bias-independent  $p$ - $i$ - $n$  junction. Source-drain current ( $I_{DS}$ ) showed a contrasting response at 160 K, with a clear rectifying operation (Fig. 1G, blue curve). The rectification was further confirmed with a log-scale plot (Fig. 1H).

When the WSe<sub>2</sub>  $p$ - $i$ - $n$  junction was forward-biased, clear EL was observed (Fig. 2A). To enhance the EL efficiency, all spectra were recorded at 100 K unless otherwise specified. Two features should be emphasized. First, all EL spectra showed net circular polarization. The degree of circular polarization, defined as  $\eta = [I(\sigma_+) - I(\sigma_-)]/[I(\sigma_+) + I(\sigma_-)]$ , reached as high as 45% (device 1 at 40 K), which is comparable with that of PL from monolayers (12–14). Second, such circularly polarized EL was clearly observed even in multilayer samples (devices 2, 3, and 5), as explained above (18). The EL intensity increased with increasing bias voltage (Fig. 2B). The total intensity depended linearly on the forward current (Fig. 2C), whereas  $\eta$  and the external quantum efficiency (EQE) showed smaller current dependence (Fig. 2, D and E). The EQE value depended on the samples and ranged from  $2 \times 10^{-5}$  to  $6 \times 10^{-4}$ , which is larger than that of the emissions from contact Schottky diodes (27), possibly because of the location of the emission zone in our devices, which is away from the contacts.

The EL spectral shape depended on the samples (Fig. 2A), and all of them can be considered as a superposition of exciton emission around 1.66 eV (by comparing with the PL spectrum in Fig. 2F) and trion emission at lower energies, which have been observed in PL from electrostatically charged TMDs (14, 15, 31). The variation of the trion emission energy can be ascribed to the difference in doping concentrations among the samples (14). The emission type is expected to be controlled by means of carrier injection into the  $i$ -region (18).

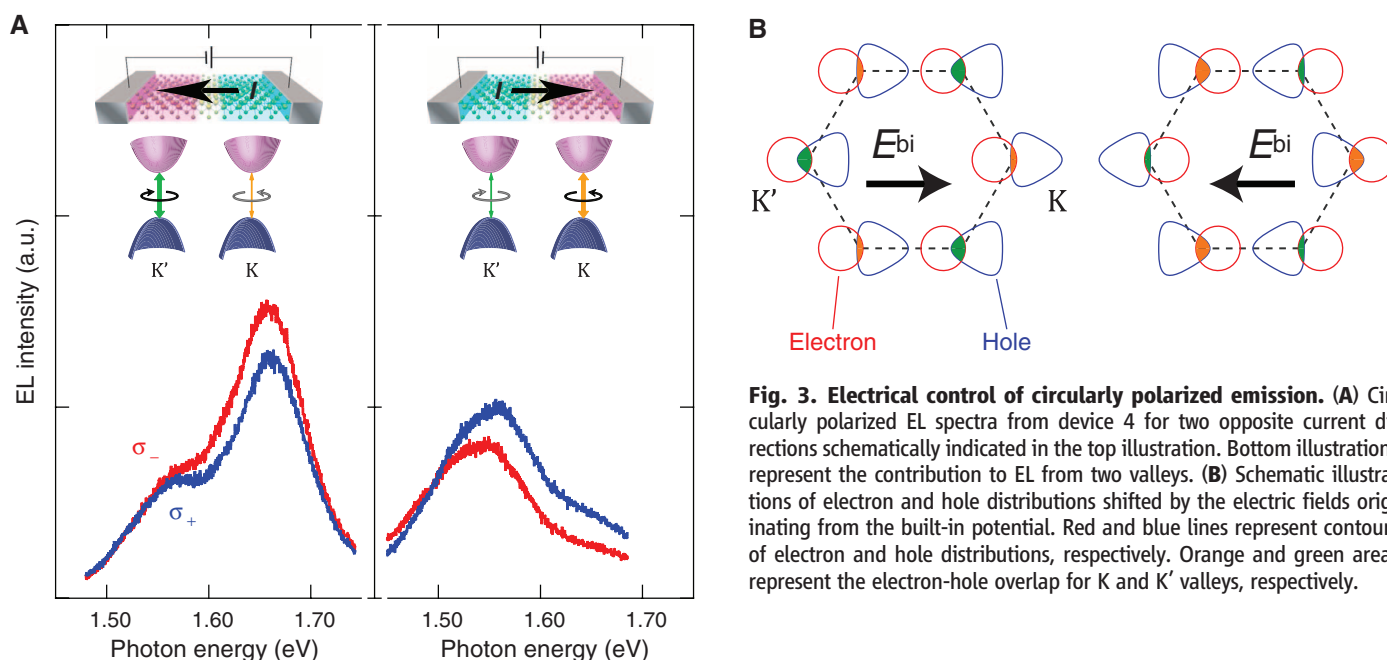
The EL spectra of a single device for two opposite current directions is shown in Fig. 3A. Because the ionic liquid freezes at 100 K, the source and drain biases were exchanged after the device was warmed up to 220 K, followed by another cooling before the next EL measurement (32). The circular polarization was reversed when the source-drain bias was exchanged. This is the first demonstration of electrical control of circularly polarized luminescence. The EL spectral shape was also changed from an exciton-dominant one to a trion-dominant one, possibly because of the difference in doping profiles between the two bias directions (18).

According to the band structure of monolayer TMDs (Fig. 1B), circularly polarized luminescence only occurs when K and K' valleys make inequivalent contributions. Here, we suggest a possible model from the viewpoint of semiclassical transport theory (33), which gives information on the carrier distribution under an electric field. Under a static electric field, the hole distribution shifts parallel to the field in the momentum space, whereas the electron distribution shifts to the opposite direction. As a result, the electron-hole overlap shown in Fig. 3B differs between the two valleys [valley overlap polarization (VOP)] because the carrier distributions in TMDs are not isotropic

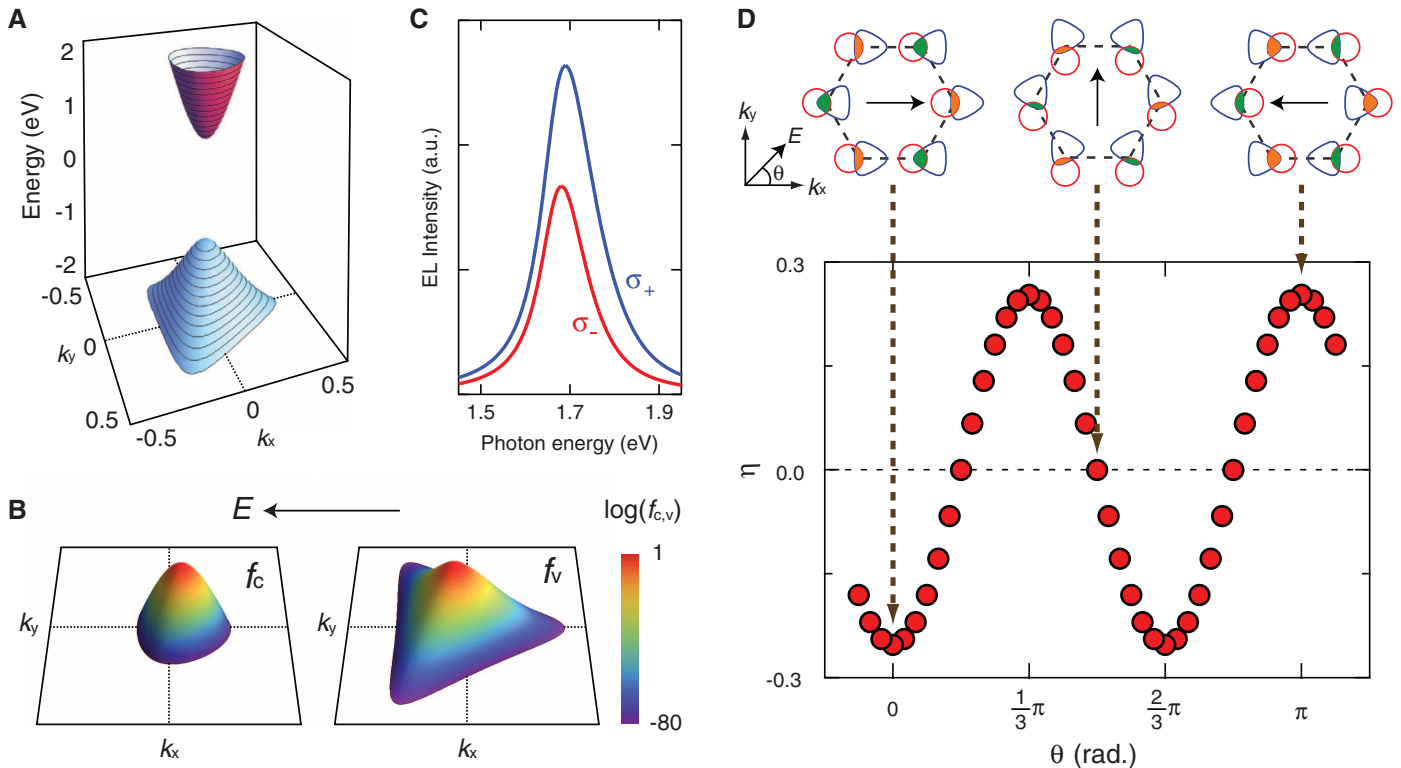
owing to trigonal warping (34). The shift discussed here is much larger than the Fermi surface shift in metals because the carrier density in the  $i$ -region is substantially low and the field strength is much stronger. VOP provides an intensity difference in the luminescence from two valleys, leading to circularly polarized luminescence. The above scenario is widely applicable to TMDs that have two isolated anisotropic valleys with different chiralities. In addition to the observations in WSe<sub>2</sub>, circularly polarized EL has also been observed in MoSe<sub>2</sub> and MoS<sub>2</sub> (18).

A numerical calculation was performed according to this model (18). To understand the carrier distribution in the momentum space, we combined the Boltzmann equation (33) and the charge distribution equation for a  $p$ - $n$  junction (for simplicity, a  $p$ - $n$  junction model was used rather than a  $p$ - $i$ - $n$  junction) (35). The effects of excitons and trions were ignored because we are only interested in the asymmetry. As shown in Fig. 4A, the band dispersions, especially that of the valence band, is anisotropic owing to trigonal warping (34). When an in-plane electric field is applied, the charge distribution is shifted from its equilibrium position (Fig. 4B). The consequent electron-hole overlap differs between K and K' points, giving rise to VOP. Simulated luminescence spectra from K and K' points, corresponding to  $\sigma_+$  and  $\sigma_-$ , respectively, are shown in Fig. 4C. The obtained polarization is qualitatively consistent with the experimental results.

Because trigonal warping is related to the crystal symmetry ( $C_3$ ), this scenario indicates that  $\eta$  and the luminescence intensity are quite sensitive to the relative angle between the crystal orientation and the field direction, exhibiting three-fold symmetry with respect to the rotation of the electric field direction, as clearly shown in the



**Fig. 3. Electrical control of circularly polarized emission.** (A) Circularly polarized EL spectra from device 4 for two opposite current directions schematically indicated in the top illustration. Bottom illustrations represent the contribution to EL from two valleys. (B) Schematic illustrations of electron and hole distributions shifted by the electric fields originating from the built-in potential. Red and blue lines represent contours of electron and hole distributions, respectively. Orange and green areas represent the electron-hole overlap for K and K' valleys, respectively.



**Fig. 4. Simulation of circularly polarized electroluminescence.** (A) Schematic band structure around K point. Momentum along the  $x$  direction ( $k_x$ ) and along the  $y$  direction ( $k_y$ ) are measured from K point. (B) Color plot of charge distribution for electron at conduction band ( $f_c$ ) and hole at valence band ( $f_v$ )

around K point. Dotted lines denote  $k_x = 0$  and  $k_y = 0$ . (C) Simulated EL spectra from K point ( $\sigma_+$ ) and K' point ( $\sigma_-$ ). (D)  $\eta$  versus electric field direction. The angle  $\theta$  is measured from the  $k_x$  direction. VOPs are shown in top illustrations for three electric field directions along  $\Gamma$ -K ( $\theta = 0^\circ$ ),  $\Gamma$ -M ( $90^\circ$ ), and  $\Gamma$ -K' ( $180^\circ$ ).

simulated results in Fig. 4D. Hence, if the current path is not perpendicular to the contact,  $\eta$  does not completely reverse its sign when the electrodes are exchanged, as shown in fig. S6. On the other hand, this feature will enable fine tuning of  $\eta$  by using a multiterminal device to apply biases in directions that are nonparallel to the  $p$ - $i$ - $n$  junction (fig. S7). To maximize the luminescence intensity, the degree of polarization (value of  $\eta$ ), and the polarization tunability (tunability of  $\eta$ ), it will be necessary to improve the device fabrication processes in order to accurately align the crystal orientation and electrode configuration.

Circularly polarized EL is a direct indication of the breakdown of valley symmetry. In our experiment, this was induced purely by the electric field, and we had to go beyond linear response theory in order to understand this phenomenon; for example, we were not able to explain this with the valley Hall effect (8). Therefore, we proposed a model that incorporates nonlinear processes from the carrier distribution shift, which becomes asymmetric from trigonal warping, leading to VOP.

Owing to their spin-valley coupled band structure (8), TMD-based spin LEDs can also exhibit circularly polarized EL. However, such devices cannot work without an external magnetic field (1). Our results, on the other hand, provide a new direction in the quest for electrically switchable circularly polarized light sources and extend the functionality of valley-based optoelectronics.

#### References and Notes

1. I. Žutić, J. Fabian, S. Das Sarma, *Rev. Mod. Phys.* **76**, 323–410 (2004).
2. J. F. Sherson *et al.*, *Nature* **443**, 557–560 (2006).
3. T. Oka, H. Aoki, *Phys. Rev. B* **79**, 081406(R) (2009).
4. Y. H. Wang, H. Steinberg, P. Jarillo-Herrero, N. Gedik, *Science* **342**, 453–457 (2013).
5. R. Fiederling *et al.*, *Nature* **402**, 787–790 (1999).
6. K. Konishi *et al.*, *Phys. Rev. Lett.* **106**, 057402 (2011).
7. Y. Yang, R. C. da Costa, D. M. Smilgies, A. J. Campbell, M. J. Fuchter, *Adv. Mater.* **25**, 2624–2628 (2013).
8. D. Xiao, G. B. Liu, W. Feng, X. Xu, W. Yao, *Phys. Rev. Lett.* **108**, 196802 (2012).
9. Z. Y. Zhu, Y. C. Cheng, U. Schwingenschlögl, *Phys. Rev. B* **84**, 153402 (2011).
10. A. Splendiani *et al.*, *Nano Lett.* **10**, 1271–1275 (2010).
11. K. F. Mak, K. He, J. Shan, T. F. Heinz, *Nat. Nanotechnol.* **7**, 494–498 (2012).
12. H. Zeng, J. Dai, W. Yao, D. Xiao, X. Cui, *Nat. Nanotechnol.* **7**, 490–493 (2012).
13. T. Cao *et al.*, *Nat. Commun.* **3**, 887 (2012).
14. A. M. Jones *et al.*, *Nat. Nanotechnol.* **8**, 634–638 (2013).
15. K. F. Mak *et al.*, *Nat. Mater.* **12**, 207–211 (2013).
16. S. Wu *et al.*, *Nat. Phys.* **9**, 149–153 (2013).
17. Y. Song, H. Dery, *Phys. Rev. Lett.* **111**, 026601 (2013).
18. Materials and methods are available as supplementary materials on Science Online.
19. Y. J. Zhang, J. T. Ye, Y. Yomogida, T. Takenobu, Y. Iwasa, *Nano Lett.* **13**, 3023–3028 (2013).
20. V. Podzorov, M. E. Gershenson, Ch. Kloc, R. Zeis, F. Bucher, *Appl. Phys. Lett.* **84**, 3301–3303 (2004).
21. Y. Zhang, J. Ye, Y. Matsuhashi, Y. Iwasa, *Nano Lett.* **12**, 1136–1140 (2012).
22. J. T. Ye *et al.*, *Science* **338**, 1193–1196 (2012).
23. D. Braga, I. Gutiérrez Lezama, H. Berger, A. F. Morpurgo, *Nano Lett.* **12**, 5218–5223 (2012).
24. H. T. Yuan *et al.*, *Nat. Phys.* **9**, 563–569 (2013).
25. J. Zausseil, R. H. Friend, H. Sirringhaus, *Nat. Mater.* **5**, 69–74 (2006).

26. S. Z. Bisri *et al.*, *Adv. Mater.* **23**, 2753–2758 (2011).
27. R. S. Sundaram *et al.*, *Nano Lett.* **13**, 1416–1421 (2013).
28. A. Pospischil, M. M. Furchi, T. Mueller, *Nat. Nanotech.* **9**, 257–261 (2014).
29. B. W. H. Baugher, H. O. H. Churchill, Y. Yang, P. Jarillo-Herrero, *Nat. Nanotech.* **9**, 262–267 (2014).
30. J. S. Ross *et al.*, *Nat. Nanotechnol.* **9**, 268–272 (2014).
31. J. S. Ross *et al.*, *Nat. Commun.* **4**, 1474 (2013).
32. This process is not essential for circularly polarized EL and polarization reversal. Also, electrical switching can be achieved with solid gate devices, in principle.
33. N. W. Ashcroft, N. D. Mermin, *Solid State Physics* (Thomson Learning, Stamford, CN, 1976), chap. 12.
34. A. Kormányos *et al.*, *Phys. Rev. B* **88**, 045416 (2013).
35. S. M. Sze, *Physics of Semiconductor Devices* (Wiley, New York, 1981), chaps. 1 and 2.

**Acknowledgments:** We thank Y. Saito, H. Shioya, Y. Kasahara, T. Hatano, and Y. Segawa for experimental help and R. Akashi, R. Arita, T. Takenobu, H. Aoki, and B. P. Zhang for discussions. Y.J.Z. is supported by the Japan Society for the Promotion of Science (JSPS) through a research fellowship for young scientists. This research was supported by the Strategic International Collaborative Research Program (SICORP-LEMSUPAR) of the Japan Science and Technology Agency, Grant-in-Aid for Specially Promoted Research (25000003), and the “Funding Program for World-Leading Innovative R&D on Science and Technology (FIRST Program)” from JSPS.

#### Supplementary Materials

www.sciencemag.org/content/344/6185/725/suppl/DC1

Materials and Methods

Supplementary text

Fig. S1 to S7

References (36–40)

27 January 2014; accepted 4 April 2014

Published online 17 April 2014;

10.1126/science.1251329



# In Situ Imaging of Silicalite-1 Surface Growth Reveals the Mechanism of Crystallization

Alexandra I. Lupulescu and Jeffrey D. Rimer\*

The growth mechanism of silicalite-1 (MFI zeolite) is juxtaposed between classical models that postulate silica molecules as primary growth units and nonclassical pathways based on the aggregation of metastable silica nanoparticle precursors. Although experimental evidence gathered over the past two decades suggests that precursor attachment is the dominant pathway, direct validation of this hypothesis and the relative roles of molecular and precursor species has remained elusive. We present an in situ study of silicalite-1 crystallization at characteristic synthesis conditions. Using time-resolved atomic force microscopy images, we observed silica precursor attachment to crystal surfaces, followed by concomitant structural rearrangement and three-dimensional growth by accretion of silica molecules. We confirm that silicalite-1 growth occurs via the addition of both silica molecules and precursors, bridging classical and nonclassical mechanisms.

Optimizing the physicochemical properties of zeolites for applications ranging from catalysts for fuel and chemicals production to porous substrates for separations and diagnostics can be leveraged by a molecular-level understanding of crystallization. For more than two decades, silicalite-1 (siliceous ZSM-5) has been a prototype for mechanistic studies of zeolites. Efforts to elucidate the mechanism of growth have predominantly focused on identification of the primary building unit, which is most often presumed to be silica nanoparticles that assemble with remarkably uniform size during tetraethylorthosilicate (TEOS) hydrolysis in aqueous solutions. Nonclassical pathways of crystal nucleation and growth involving the aggregation and attachment of nanoparticles are recognized mechanisms for many biogenic and natural crystals, including iron oxyhydroxide (1, 2), magnetite (3), gypsum (4), noble metals (5, 6), proteins (7), and calcium minerals (8–11). This is in stark contrast to the classical view of crystallization by spontaneous nucleation and growth from the addition of atoms or molecules—a pathway that is perceived by many to play a marginal role in silicalite-1 crystallization. Although both classical and nonclassical pathways have been proposed for silicalite-1 crystallization, in situ evidence has proven to be elusive because of the challenges associated with time-resolved imaging of surface growth.

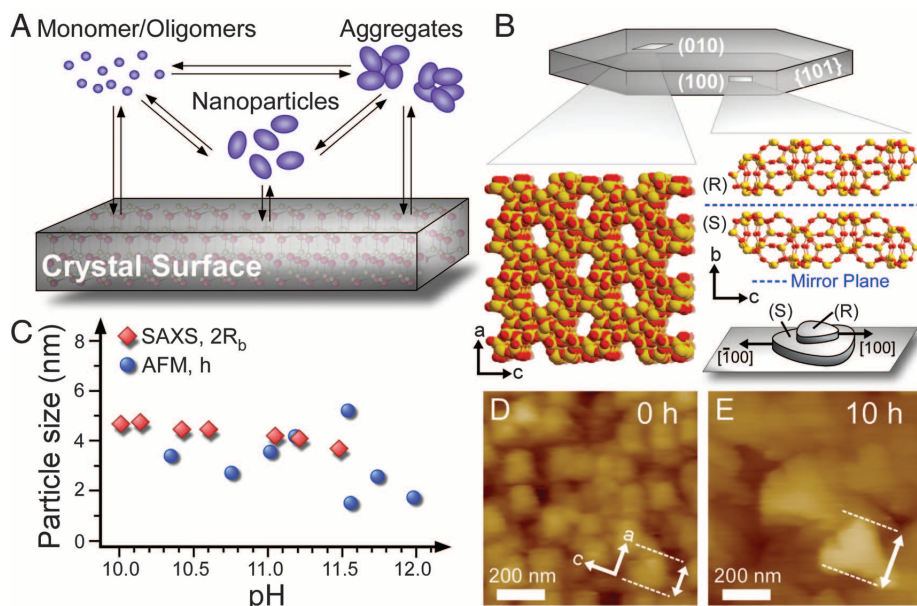
Silicalite-1 precursors are nanoparticles with dimensions of 1 to 6 nm (12–14) that form metastable core-shells, which have a disordered siliceous core and a shell of a physisorbed organic structure-directing agent (OSDA) (14). During nucleation, a fraction of nanoparticles grows at the expense of others via Ostwald ripening with simultaneous structural transformations, which lead to partially ordered OSDA-silica primary units

(15–17) with indistinct noncrystalline microstructure. Tsapatsis and co-workers provided evidence that silicalite-1 nucleation occurs by the aggregation and subsequent restructuring of evolved nanoparticles (17, 18). Their studies have also suggested that silicalite-1 growth occurs by precursor attachment, which is a hypothesis gleaned from ex situ transmission electron microscope measurements that identified ~5-nm protrusions on crystal exteriors (19). The persistence of precursors in growth solutions throughout silicalite-1 crystallization has led to theories and models postulating their involvement as the primary growth unit (20). To a lesser extent, it has been suggested (21, 22) that nanoparticles are metastable species that contin-

ually supply soluble silica molecules (i.e., monomers and oligomers) as viable growth units. Only in the final stage of crystallization, when the concentration of precursors is negligible, is molecule addition proposed as the predominant mechanism (23, 24). The schematic in Fig. 1A depicts the landscape of mechanistic pathways that exemplifies both classical and nonclassical theories of silicalite-1 crystallization from molecule addition and nanoparticle attachment, respectively.

We used in situ atomic force microscopy (AFM) to monitor the growth of the (010) face of silicalite-1 crystals under realistic synthesis conditions. Silicalite-1 crystals amenable for AFM measurements were synthesized with large (010) surface area (~30 × 10 μm<sup>2</sup>) (25) and oriented in the plane of imaging by mounting crystals in epoxy on AFM sample disks. We used a retrofitted AFM liquid sample cell (Asylum Research) equipped with a heating peltier capable of achieving high temperatures (25° to 300°C) and custom-designed components that can withstand caustic solutions (pH 10 to 13). The liquid cell is equipped with inlet/outlet ports (fig. S1) used to supply freshly prepared and degassed growth solution at a rate of 0.2 ml/hour (with a 7-hour residence time). Silicalite-1 growth solutions prepared with TEOS and tetrapropylammonium as the OSDA produced optically transparent solutions for AFM imaging at 80°C and atmospheric pressure.

A mechanical artifact of AFM that needed to be addressed was the lateral drift of the cantilever within the *x/y* plane, which results in a progressive temporal shift and eventual loss of the initial imaging area. This phenomenon has proven to be less critical when imaging materials that readily



**Fig. 1. Precursor attachment to silicalite-1 crystals.** (A) Pathways of silicalite-1 crystallization. (B) Topology of the (010) face, [010] mirror plane, and [100] inversion center of silicalite-1 crystals (MFI type;  $a = 2.01$ ,  $b = 1.97$ ,  $c = 1.31$  nm). (C) Dimensions of silica precursors from SAXS (minor axis,  $2R_b$ ) and AFM (deposit height,  $h$ ) after 7 hours at 80°C in growth solutions of pH 10 to 12 (table S1). (D and E) In situ AFM height mode images reveal the temporal growth of surface features, as indicated by the dashed lines (movie S1).

Department of Chemical and Biomolecular Engineering, University of Houston, 4800 Calhoun Road, Houston, TX 77204–4004, USA.

\*Corresponding author. E-mail: jrimer@central.uh.edu

crystallize at ambient conditions (e.g., 25°C), such as biogenic crystals (26, 27), zeotypes (28), and select metal-organic frameworks (29) in which lower activation barriers for growth unit attachment facilitate rapid time-resolved imaging of surface growth on the order of minutes. High activation energies and concomitant slow rates of zeolite growth necessitate imaging times on the order of hours at high temperatures, which exacerbates lateral drift. To overcome this, we used an AFM scanner with a feedback controller and drift correlation software developed by Asylum Research to achieve small drift rates of ~5 nm/hour, which corresponds to less than 0.3%/hour loss of the imaging area (fig. S2). Analysis of AFM images must also take into account the temporal change in tip geometry due to a gradual deposition of silica that produces a 1.1-nm/hour increase in tip diameter (figs. S3 to S5). Calibration of AFM tips subjected to 20 hours of continuous imaging reveals a less than 2.2% error in height data. As such, mechanistic behavior was evaluated using (010) height data rather than <100> lateral dimensions, which are subject to larger error from tip geometry corrections (~12%, fig. S6) and/or tip artifacts.

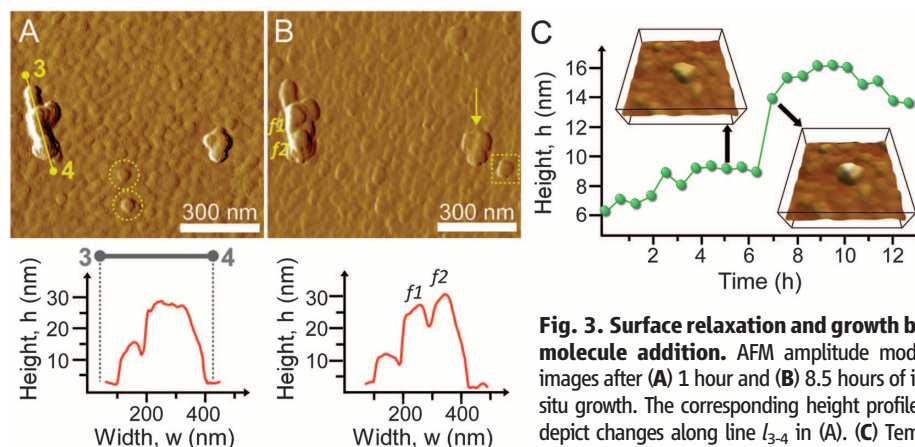
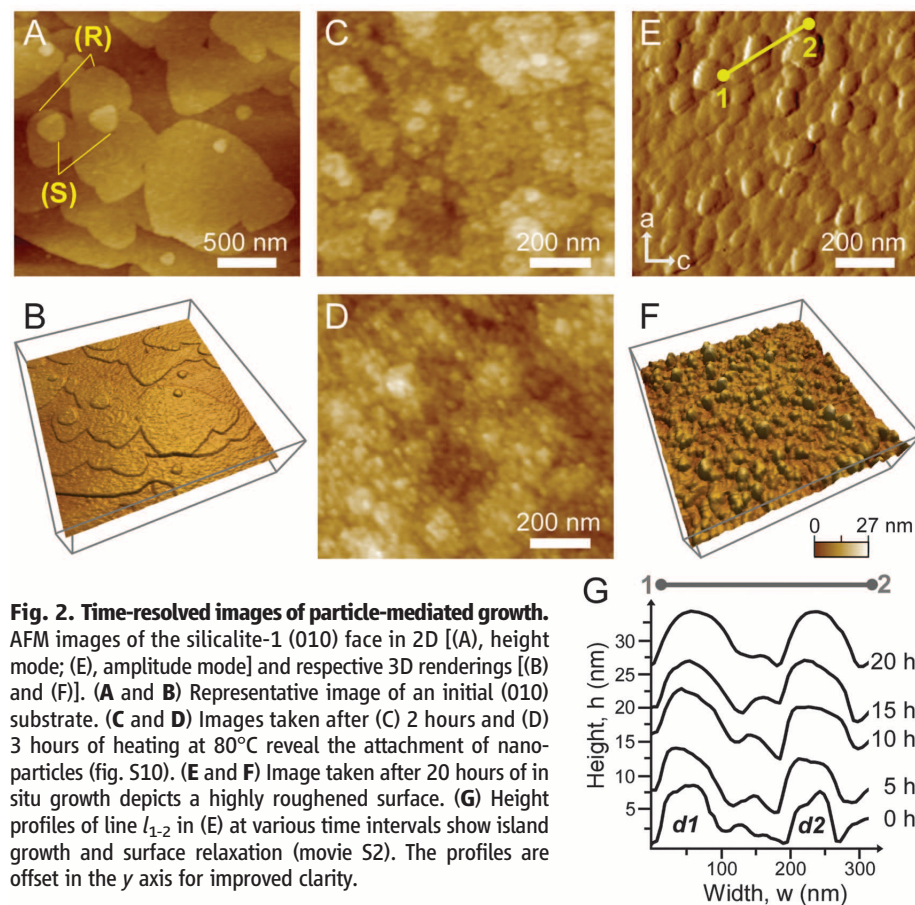
We collected AFM images of the (010) face at discrete time points and observed the appearance of deposits with shapes and dimensions resembling those of nanoparticle precursors (Fig. 1, C and D). In order to confirm this, we performed small-angle x-ray scattering (SAXS) on growth solutions to measure precursor size. An oblate ellipsoid form factor provided the best fit of SAXS data (fig. S7 and table S2), in agreement with literature (14). We compared ellipsoid *b*-axis ( $2R_b$ ) and *a*-axis ( $2R_a$ ) dimensions from SAXS to those of surface deposits from AFM, measured as the average height *h* (Fig. 1C and fig. S8) and width *w* (fig. S9), respectively. The overlap of nanoparticle and deposit size over a range of growth solution pH provides evidence of nanoparticle attachment to crystal surfaces. Continuous AFM imaging of (010) faces reveals that once adsorbed to the silicalite-1 surface, nanoparticle deposits grow in size (Fig. 1, D and E). In order to minimize the potential dislodgement of deposits caused by the movement of the AFM tip, all images were collected in tapping mode, using a scan rate of 1.4 Hz.

Sequential snapshots of surface growth at 80°C (Fig. 2) show (010) interfaces laden with deposits of nearly uniform size. Terraces on the initial substrate (Fig. 2, A and B) are gradually populated with nanoparticles within the first several hours of heating (Fig. 2, C and D). After 5 hours, the substrate is nearly covered with nanoparticles (Fig. 2, E and F). Continuous imaging was initiated after 7 hours of heating, which equals the liquid residence time in the AFM sample cell (see the supplementary materials for details). Inspection of island height contours, such as line scan  $l_{1-2}$  (Fig. 2E), at various time points reveals three-dimensional (3D) growth. Tracking of individual deposits, such as *d1* in  $l_{1-2}$  (Fig. 2G), shows a progressive increase in island width, reflecting

growth in the <100> directions, and a gradual increase in height along the [010] direction. We recorded several movies that capture the dynamics of island growth. Analysis of successive images from movie S2 reveals that the changes in island dimensions are in increments less than the size of precursors, which is consistent with a mechanism of silica molecule addition. AFM images also reveal processes akin to surface relaxation, which

may occur by post-attachment dissolution of precursors and silicate reprecipitation (Ostwald ripening) or by solid-state rearrangement of partially ordered deposits. For instance, the surfaces of *d1* and nearby deposit *d2* in Fig. 2G undergo morphological transformations from initially rough to smooth features during growth.

A long-held mechanistic view that growth occurs by the oriented attachment of fully crystalline





precursors (30) to silicalite-1 surfaces was supplanted by evidence that precursors are noncrystalline (15, 31); however, pathways involving oriented attachment of partially ordered (evolved) precursor segments can still be envisioned. Moreover, full integration of precursors into the underlying crystal topology necessitates some degree of post-attachment restructuring. Recent studies of minerals have demonstrated multiple pathways for particle-mediated growth, including oriented attachment of crystalline iron oxyhydroxide nanoparticles (2) as well as the attachment and rearrangement of disordered nanoparticles in magnetite (3). Silicalite-1 disordered-to-ordered surface relaxation is qualitatively consistent with the latter findings; however, if silica precursors align before attachment to the (010) surface, this process is not evident from in situ AFM. Restructuring of disordered deposits may be governed in part by the Ostwald step rule, whereas the creation of highly strained grain boundaries from misaligned precursors would similarly drive particle dissolution or recrystallization, analogous to recent observations by Li *et al.* (2). Any loss of translational symmetry during precursor restructuring could lead to crystal defects, such as commonly observed twins, or the misoriented domains detected in aggregates of precursors that become silicalite-1 nuclei (17).

Time-resolved images of silicalite-1 crystallization (Fig. 3, A and B) capture the birth, dissolution/rearrangement, and growth of islands. AFM snapshots of surface growth reveal the disappearance of features (Fig. 3A, circles), the emergence of new islands (Fig. 3B, square), and the reduction of feature height due to surface relaxation (Fig. 3B, arrow). For instance, height profiles of line  $I_{3,4}$  (Fig. 3A) depict the partitioning of flattened regions into multiple layers,  $f_1$  and  $f_2$  (Fig. 3B).

The representative profile tracking the temporal change of island height in Fig. 3C captures all of the dynamic phenomena of silicalite-1 growth. During the first 6 hours of imaging, molecule addition results in a linear increase in height analogous to the [010] growth rate reported in literature (32). After 6 hours of growth, there is a step change in height consistent with the attachment of a single nanoparticle precursor. Height mode images (Fig. 3C, inset) show the emergence of a nanoparticle deposit on the island terrace, which is followed by a monotonic decrease in height attributed to post-attachment surface relaxation.

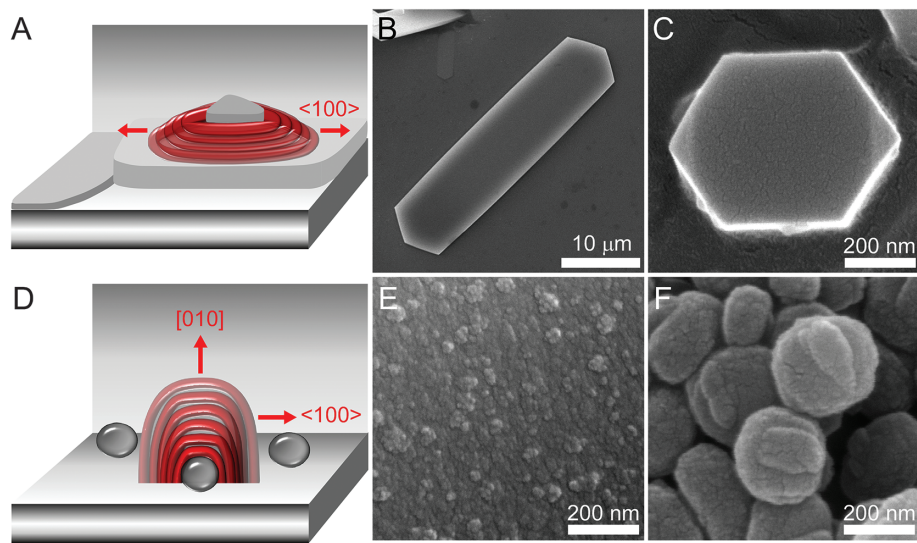
Crystallization mechanisms often involve 2D nucleation and stepwise advancement of layers (Fig. 4A). Anderson and co-workers (33) provided evidence of layer growth for silicalite-1 and other zeolites (32). Our experiments confirmed that synthesis at 160°C produced faceted silicalite-1 crystals (Fig. 4, B and C) and (010) surfaces composed of steps with heights equal to  $b/2$  (~1 nm) or multiples thereof (Fig. 2A). The MFI crystal structure features a [010] mirror plane (Fig. 1B), where the 180°-reversed orientation of anisotropic islands (Fig. 2A) reflects alternating (*R,S*)-pentasil layers. Earlier ex situ studies of silicalite-1 growth revealed rough (010) faces at high silica supersaturation and the appearance of steps as the concentration of silica approached solubility (32). This is consistent with our in situ AFM measurements in supersaturated solutions that reveal surface roughening due to precursor attachment; however, crystallization at 80°C does not yield surfaces with well-defined layers, suggesting a high activation barrier for 2D nucleation and spreading. Silicalite-1 crystallization at low temperature appears to proceed by a 3D mechanism (Fig. 4D and fig. S11). Scanning electron

microscopy (SEM) and AFM images collectively confirm that the lower synthesis temperature yields rounded (i.e., nonfaceted) crystals with roughened surfaces (Fig. 4, E and F). Faceted silicalite-1 crystals have previously been observed at low temperature, but after much longer synthesis times (23, 24) via a mechanism that is presumably driven by molecule addition (or Ostwald ripening).

Molecular-level details gleaned from time-resolved in situ AFM measurements provide evidence of silicalite-1 growth by concerted processes that bridge two schools of thought: a classical mechanism based on the addition of silica molecules and a nonclassical route involving the direct attachment of nanoparticles. Although the exact microstructure of precursors and the molecular-level events governing their structural rearrangement have yet to be reconciled, the dynamic processes of silicalite-1 surface growth identified by in situ AFM reveal a complex series of events that transcend conventional mechanisms involving 2D layer nucleation and spreading. The techniques applied here can be extended to a broader class of zeolite structures, and may also prove to be a valuable tool for elucidating the growth mechanism of other materials synthesized by either hydrothermal or solvothermal methods, which include (but are not limited to) metal oxides, minerals, and metal-organic frameworks.

#### References and Notes

1. J. F. Banfield, S. A. Welch, H. Z. Zhang, T. T. Ebert, R. L. Penn, *Science* **289**, 751–754 (2000).
2. D. S. Li *et al.*, *Science* **336**, 1014–1018 (2012).
3. J. Baumgartner *et al.*, *Nat. Mater.* **12**, 310–314 (2013).
4. A. E. S. Van Driessche *et al.*, *Science* **336**, 69–72 (2012).
5. H. G. Liao, L. K. Cui, S. Whitlam, H. M. Zheng, *Science* **336**, 1011–1014 (2012).
6. H. M. Zheng *et al.*, *Science* **324**, 1309–1312 (2009).
7. S. T. Yau, P. G. Vekilov, *J. Am. Chem. Soc.* **123**, 1080–1089 (2001).
8. D. Gebauer, A. Völkel, H. Cölfen, *Science* **322**, 1819–1822 (2008).
9. W. Habraken *et al.*, *Nat. Commun.* **4**, 1507 (2013).
10. E. M. Pouget *et al.*, *Science* **323**, 1455–1458 (2009).
11. A. F. Wallace *et al.*, *Science* **341**, 885–889 (2013).
12. P. de Moor, T. P. M. Beelen, B. U. Komarschek, O. Diat, R. A. van Santen, *J. Phys. Chem. B* **101**, 11077–11086 (1997).
13. J. N. Watson, L. E. Iton, J. W. White, *Chem. Commun. (Camb.)* **1996**, 2767–2768 (1996).
14. J. M. Fedeyko, J. D. Rimer, R. F. Lobo, D. G. Vlachos, *J. Phys. Chem. B* **108**, 12271–12275 (2004).
15. J. D. Rimer, O. Trofymuk, A. Navrotsky, R. F. Lobo, D. G. Vlachos, *Chem. Mater.* **19**, 4189–4197 (2007).
16. J. D. Rimer, D. G. Vlachos, R. F. Lobo, *J. Phys. Chem. B* **109**, 12762–12771 (2005).
17. T. M. Davis *et al.*, *Nat. Mater.* **5**, 400–408 (2006).
18. S. Kumar, Z. P. Wang, R. L. Penn, M. Tsapatsis, *J. Am. Chem. Soc.* **130**, 17284–17286 (2008).
19. S. Kumar, T. M. Davis, H. Ramanan, R. L. Penn, M. Tsapatsis, *J. Phys. Chem. B* **111**, 3398–3403 (2007).
20. V. Nikolakis, E. Kokkoli, M. Tirrell, M. Tsapatsis, D. G. Vlachos, *Chem. Mater.* **12**, 845–853 (2000).
21. B. J. Schoeman, *Microporous Mesoporous Mater.* **22**, 9–22 (1998).
22. S. L. Burkett, M. E. Davis, *Chem. Mater.* **7**, 920–928 (1995).
23. S. Kumar, R. L. Penn, M. Tsapatsis, *Microporous Mesoporous Mater.* **144**, 74–81 (2011).
24. A. Aerts *et al.*, *Phys. Chem. Chem. Phys.* **13**, 4318–4325 (2011).
25. A. I. Lupulescu, J. D. Rimer, *Angew. Chem. Int. Ed. Engl.* **51**, 3345–3349 (2012).
26. J. D. Rimer *et al.*, *Science* **330**, 337–341 (2010).
27. C. A. Orme *et al.*, *Nature* **411**, 775–779 (2001).



**Fig. 4. Different pathways of layered growth.** Schematics of 2D layer growth (A) and 3D island growth (D) depict proposed mechanisms of silicalite-1 crystallization at high and low temperature, respectively. (B and C) SEM images of faceted silicalite-1 crystals prepared at 160°C using pH 12.7 (B) and 11.4 (C) growth solutions. (E and F) SEM images of crystals prepared at lower temperature (80°C, pH 11.4) by either seeded (E) or nonseeded (F) crystallization exhibit rough surfaces and spheroidal shapes.



28. M. A. Holden, P. Cubillas, M. P. Attfield, J. T. Gebbie, M. W. Anderson, *J. Am. Chem. Soc.* **134**, 13066–13073 (2012).
29. P. Cubillas, M. W. Anderson, M. P. Attfield, *Chemistry* **19**, 8236–8243 (2013).
30. C. E. A. Kirschhock, R. Ravishanker, P. A. Jacobs, J. A. Martens, *J. Phys. Chem. B* **103**, 11021–11027 (1999).
31. C. T. G. Knight, J. P. Wang, S. D. Kinrade, *Phys. Chem. Chem. Phys.* **8**, 3099–3103 (2006).
32. L. I. Meza *et al.*, *J. Am. Chem. Soc.* **129**, 15192–15201 (2007).
33. M. W. Anderson, J. R. Agger, L. I. Meza, C. B. Chong, C. S. Cundy, *Faraday Discuss.* **136**, 143–156, discussion 213–229 (2007).

**Acknowledgments:** We acknowledge support from NSF (grants CAREER-1151098 and BRIGE-1032621), the American Chemical Society (grant PRF 52422-DN15), and the Welch Foundation (grant E-1794). SAXS measurements were performed on an instrument that was purchased with support from NSF (grant MRI-1040446). We are grateful to J. Li and M. Rutgers at Asylum Research for technical assistance.

## Supplementary Materials

www.sciencemag.org/content/344/6185/729/suppl/DC1  
Materials and Methods  
Supplementary Text  
Figs. S1 to S11  
Tables S1 and S2  
References (34–73)  
Movies S1 and S2

17 January 2014; accepted 28 March 2014  
10.1126/science.1250984

# Recyclable, Strong Thermosets and Organogels via Paraformaldehyde Condensation with Diamines

Jeannette M. García,<sup>1\*</sup> Gavin O. Jones,<sup>1</sup> Kumar Virwani,<sup>1</sup> Bryan D. McCloskey,<sup>1,2</sup> Dylan J. Boday,<sup>3</sup> Gijs M. ter Huurne,<sup>4</sup> Hans W. Horn,<sup>1</sup> Daniel J. Coady,<sup>1</sup> Abdulmalik M. Bintaleb,<sup>5</sup> Abdullah M. S. Alabdulrahman,<sup>5</sup> Fares Alsewailem,<sup>5</sup> Hamid A. A. Almegren,<sup>5</sup> James L. Hedrick<sup>1\*</sup>

Nitrogen-based thermoset polymers have many industrial applications (for example, in composites), but are difficult to recycle or rework. We report a simple one-pot, low-temperature polycondensation between paraformaldehyde and 4,4'-oxydianiline (ODA) that forms hemiaminal dynamic covalent networks (HDCNs), which can further cyclize at high temperatures, producing poly(hexahydrotriazine)s (PHTs). Both materials are strong thermosetting polymers, and the PHTs exhibited very high Young's moduli (up to ~14.0 gigapascals and up to 20 gigapascals when reinforced with surface-treated carbon nanotubes), excellent solvent resistance, and resistance to environmental stress cracking. However, both HDCNs and PHTs could be digested at low pH (<2) to recover the bisaniline monomers. By simply using different diamine monomers, the HDCN- and PHT-forming reactions afford extremely versatile materials platforms. For example, when poly(ethylene glycol) (PEG) diamine monomers were used to form HDCNs, elastic organogels formed that exhibited self-healing properties.

Nitrogen-containing thermosets, such as poly(amide)s, poly(imide)s, and poly(benzimidazole)s, are used to manufacture adhesives, coatings, foams, automotive and aerospace parts, and electronic devices owing to their high mechanical strength and durability. Despite their widespread commercial use and practical utility, there has been little recent success in the synthesis and design of new high-performance thermosets because of their at-times challenging production. The development of new synthetic platforms that allow for structural modification to impart a variety of useful materials properties, such as high strength or self-healing, is therefore of considerable interest. Furthermore, all known thermosetting polymers are difficult to recycle because they cannot be remolded once cured and thermally decompose upon heating to

high temperatures. As a result, a thermoset that can be inherently depolymerized would afford a useful route for thermoset recyclability and redeployment.

We have developed two new related classes of thermosets. The first class, hemiaminal dynamic covalent networks (HDCNs; Fig. 1B, 1.5) (1), was prepared by polymerizing monomers containing two –NH<sub>2</sub> units, such as 4,4'-oxydianiline (ODA, 1.4) or diamine-terminated poly(ethylene glycol) (PEG, 4.2), with paraformaldehyde at low (~50°C) temperatures. HDCNs exhibited highly versatile properties depending on the diamine monomer used during the polymerization, and properties range from high-strength, chemically robust materials to self-healing organogels that exhibited chemical reversibility in physiological pH regimes. Furthermore, a specific class of HDCNs prepared from ODA underwent a chemical rearrangement when heated to ~200°C and formed the second class of materials, poly(1,3,5-hexahydro-1,3,5-triazines) (PHTs; Fig. 1B, 1.6), which are highly cross-linked polymer networks.

This work was partially inspired by the synthesis of small-molecule 1,3,5-hexahydro-1,3,5-triazines (HTs; Fig. 1A, 1.3) (2–7), which involves the condensation of amines with formaldehyde proceeding through a hemiaminal (HA) intermedi-

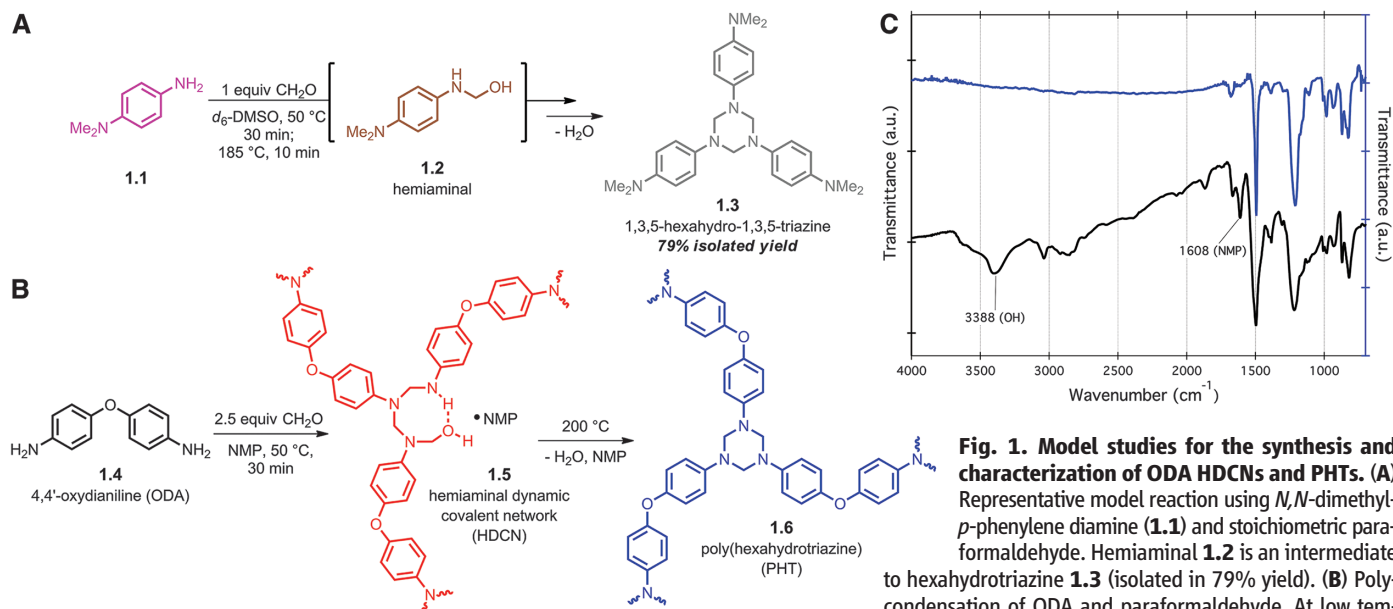
ate (8). To probe the viability of HT formation as a polymer-forming reaction, we studied the trimerization of monofunctional, electron-rich *N,N*-dimethyl-*p*-phenyleneamine with paraformaldehyde as a small-molecule model system by <sup>1</sup>H nuclear magnetic resonance (<sup>1</sup>H NMR) analysis (Fig. 1A). HAs formed within 30 min at 50°C, and at 185°C, the corresponding HT was cleanly synthesized (>98% conversion) within 10 min in deuterated dimethyl sulfoxide (*d*<sub>6</sub>-DMSO, fig. S14). Thus, <sup>1</sup>H NMR analysis confirmed successful conditions for both HA and HT formation in the model system at different temperatures. Motivated by these results, we explored the condensation reaction of the electron-rich bisaniline monomer, ODA, with paraformaldehyde as a possible route to synthesize HDCNs and PHTs. Experiments were performed to determine if the reaction between ODA and paraformaldehyde could form the requisite HA intermediate, which could then undergo cyclotrimerization.

The condensation of ODA with paraformaldehyde in *N*-methyl pyrrolidone (NMP, 50°C for 30 min) yielded an intractable polymer powder that was characterized by solid-state <sup>13</sup>C NMR. Signals corresponding to aliphatic and aromatic carbons were consistent with reported values for HT, but line broadening inherent in the method made it difficult to differentiate between HDCN and PHT polymers (figs. S3 and S4). Thus, we performed solid-state infrared (IR) measurements on the polymer film after casting at 50°C (Fig. 1C). The sharp signal representative of the NH<sub>2</sub> stretch in ODA was no longer present after heating (fig. S12), and a new set of C–H IR stretching frequencies had been generated, indicative of sp<sup>2</sup>-hybridized methylene groups incorporated into the structure. In addition to these expected changes in IR signals, a broad signal at ~3300 cm<sup>-1</sup>, characteristic of an OH stretching signal expected for an HDCN, was measured. Also observed by IR was the carbonyl stretching frequency corresponding to NMP, which presumably remained bound to the polymer (9). However, upon ramping the cure temperature to 200°C, the solid-state IR spectrum of the resulting material lacked the broad signal at ~3300 cm<sup>-1</sup>, suggesting that the OH group was no longer present after heating. In addition, <sup>1</sup>H NMR and gel permeation chromatography (GPC) analysis of a soluble polymer was consistent with the construction of an ODA HDCN at 50°C, whereas at 200°C a PHT was formed (fig. S16).

These structural results were supported with calculations using density functional theory (DFT)

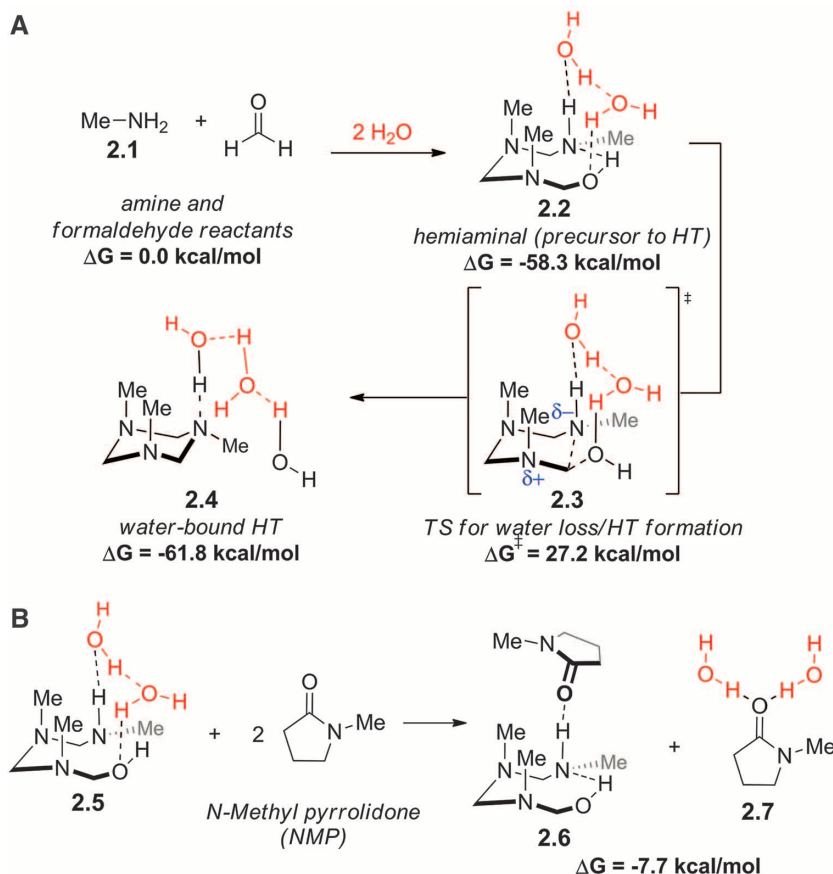
<sup>1</sup>IBM Almaden Research Center, 650 Harry Road, San Jose, CA 95120, USA. <sup>2</sup>University of California, Berkeley, Department of Chemical and Biomolecular Engineering, 201 Gilman Hall, Berkeley, CA 94720, USA. <sup>3</sup>IBM Tucson, 9000 South Rita Road, Tucson, AZ 85744, USA. <sup>4</sup>Eindhoven University of Technology, Post Office Box 513, 5600 MB Eindhoven, Netherlands. <sup>5</sup>King Abdulaziz City for Science and Technology, Post Office Box 6086, Riyadh 11442, Saudi Arabia.

\*Corresponding author. E-mail: hedrick@us.ibm.com (J.L.H.); jmgarcia@us.ibm.com (J.M.G.)



**Fig. 1. Model studies for the synthesis and characterization of ODA HDCNs and PHTs.** (A) Representative model reaction using *N,N*-dimethyl-*p*-phenylene diamine (**1.1**) and stoichiometric paraformaldehyde. Hemiaminal **1.2** is an intermediate to hexahydrotriazine **1.3** (isolated in 79% yield). (B) Polycondensation of ODA and paraformaldehyde. At low temperatures, an HDCN formed, plasticized with ~27% NMP. At higher temperatures, the PHT formed. (C) Solid-state IR spectra for ODA films cured at 50°C (black trace) exhibited a broad signal at ~3300 cm<sup>-1</sup> compared to a film cured at 200°C (blue trace), which lacked the signal corresponding to the OH stretch. The hydrogen-bonded NMP-related carbonyl stretching frequency is not observed after a 200°C curing process. (a.u., arbitrary units)

and water. At higher temperatures, the PHT formed. (C) Solid-state IR spectra for ODA films cured at 50°C (black trace) exhibited a broad signal at ~3300 cm<sup>-1</sup> compared to a film cured at 200°C (blue trace), which lacked the signal corresponding to the OH stretch. The hydrogen-bonded NMP-related carbonyl stretching frequency is not observed after a 200°C curing process. (a.u., arbitrary units)



**Fig. 2. Mechanism and DFT studies of the water-promoted formation of HT from the reaction of methylamine with formaldehyde.** (A) Structures and free energies, in kcal/mol, for the water-promoted conversion of methylamine and formaldehyde into the HA and eventual formation of the HT. The transition structure and barrier for HT formation is shown. (B) Displacement of water from the water-bound HA by NMP and formation of an NMP-bound HA precursor to HT. TS, transition state.

(10–13) on the water-promoted reaction of methylamine (**2.1**) with formaldehyde, which indicated that the formation of HA (**2.2**) was exergonic by about 58 kcal/mol (Fig. 2A). Moreover, the barrier for water loss from this intermediate, leading to cyclization and spontaneous HT formation, was >27 kcal/mol. DFT calculations also predicted that the HA was further stabilized by NMP. The displacement of bound water molecules from the HA precursor (**2.5**) to the HT by NMP solvent produced a complex (**2.6**) in which NMP is hydrogen-bonded to the HA precursor; this process was calculated to be exergonic by 7.7 kcal/mol (Fig. 2B and fig. S30). Thus, the total free energy required for HT formation after exposure to NMP must be a combination of the free energy required to displace the solvent and that required to eliminate water, which was 34.9 kcal/mol. Together, these calculations suggested that the polycondensation between ODA and formaldehyde at low temperature resulted in the formation of a solvent-stabilized intractable PHT precursor (i.e., the NMP/water-bound HDCN), and that PHT formation will only occur at higher temperatures at which the HDCN can be converted to the water-bound PHT through a high-energy transition state. A first-order glass transition temperature (*T<sub>g</sub>*) was observed in the differential scanning calorimetric (DSC) measurements (193°C, fig. S9 and table S2), and swelling measurements of the PHTs in NMP showed no solvent uptake, substantiating a highly cross-linked network.

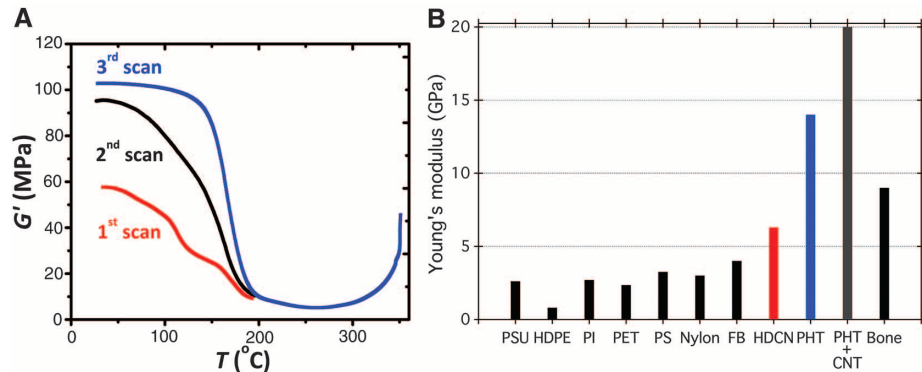
These unreinforced polymers exhibited high Young's moduli [*E*], ~14.0 GPa by nanoindentation (*14*), 10.3 GPa by Instron analysis], placing them among the strongest amorphous thermosets known (Fig. 3B and figs. S25 and S26). Carbon



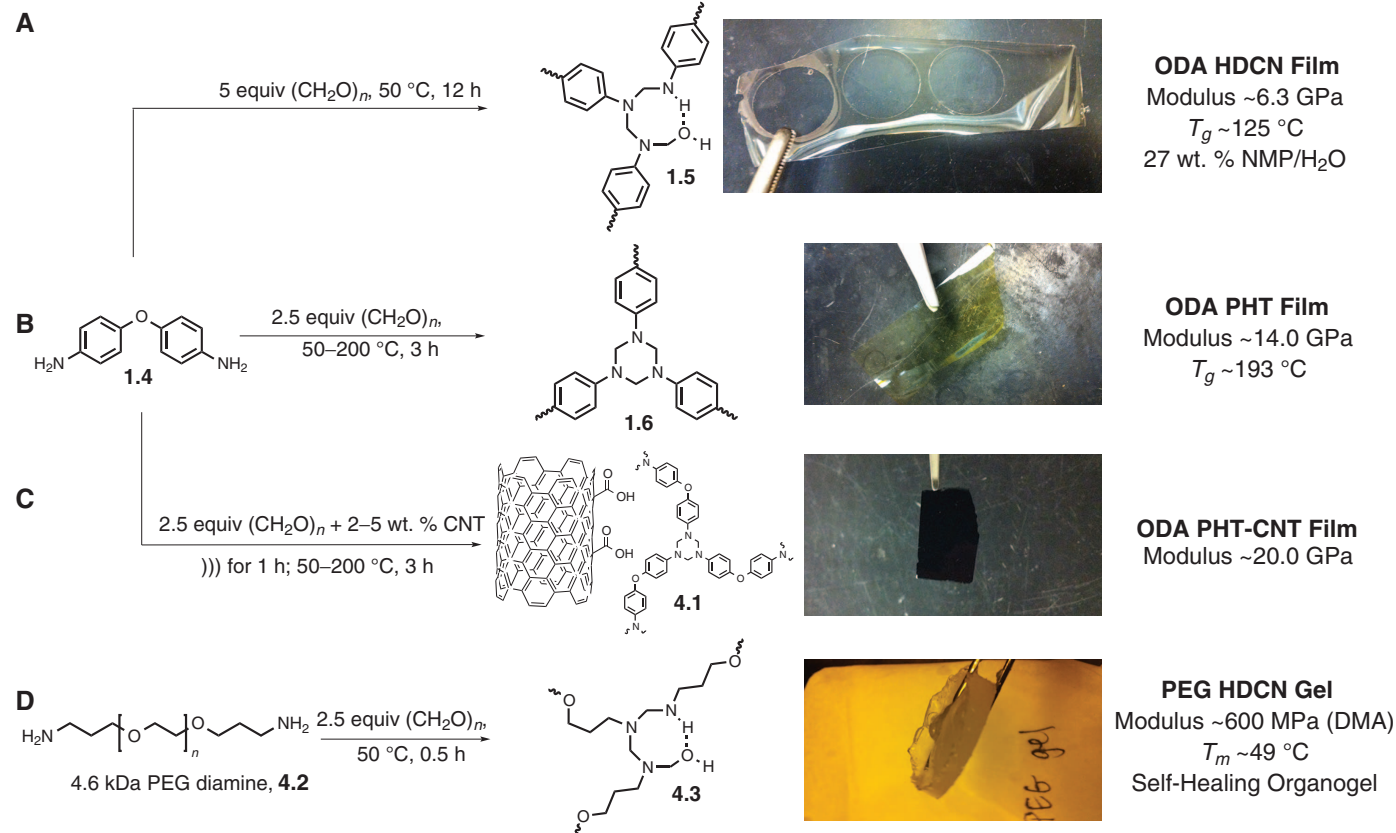
nanotube (CNT)-reinforced composites (**4.1**) were also studied to determine the effect of the matrix resin on the ODA PHT modulus. Carboxylic acid-functionalized CNTs were prepared and loaded in-

to ODA PHT monomer solutions in 2 and 5 weight percent (wt %). Films were cured according to a temperature-ramping procedure to form the ODA PHT (details are provided in the supplementary

materials). Although CNT loading conditions were not optimized, the Young's modulus improved from ~14.0 GPa in the unreinforced film to ~20.0 GPa in the CNT dispersed films, as measured with nanoindentation (Figs. 3B and 4). The Young's modulus value obtained for the ODA PHT-CNT composite approaches moduli for epoxy, polyester, and nylon composites. Although PHTs and their composites show distinctive mechanical properties and exceptional stability to organic solvents and solutions with pH >3, they could be easily depolymerized at pH <2, allowing the recovery of monomers for reuse. The Young's moduli for the ODA HDCN was determined to be ~6.3 GPa with a hardness value (H) of 0.86 GPa, which is surprisingly high considering that these films are stabilized by, and partly composed of, ~30 wt % NMP and water. This modulus value is also high when compared to values for other cross-linked, high-modulus polymers: Poly(imide)s typically have a Young's modulus value of 2.5 to 3.2 GPa, and values range between 2.0 and 4.0 GPa for nylon (Fig. 3B) (15). ODA PHTs were entirely stable in aqueous solutions, except in strongly acidic solutions (pH < 2), where they could be completely depolymerized, albeit at a slower rate than the HDCN (24 hours for 25.0 mg of ODA PHT versus 56 min for



**Fig. 3. Determination of modulus of materials.** (A) The ODA HDCN was partially identified using dynamic mechanical analysis (DMA). Starting materials were heated at 50°C for 1 hour and cycled from 22° to 200°C. The first scan showed two thermal transitions, the  $T_g$  at ~125°C corresponding to the HDCN. By the third scan, a single  $T_g$  just under 200°C of the fully cured PHT was visible. (B) Nanoindentation measurements determined Young's modulus for ODA HDCN, PHT, and composite PHT materials (ODA-PHT Young's modulus was determined to be 10.3 GPa with Instron testing; see data in fig. S28). Mechanical properties of the PHT were enhanced through CNT addition (~20.0 GPa from ~14.0 GPa). This increased strength-to-weight ratio is commonly strived for in epoxy carbon fiber composites (19, 20). PSU, polysulfone; HDPE, high-density polyethylene; PI, polyimide; PET, poly(ethylene terephthalate); PS, polystyrene; FB, fiberboard.



**Fig. 4. Tunable HDCN/PHT platforms.** (A) ODA HDCNs are cross-linked polymer networks plasticized with NMP and water that exhibit high modulus (~6.3 GPa), are flexible, and processable. The  $T_g$  was ~125°C and films decompose to monomer in strongly acidic solutions (pH <2) within an hour. (B) ODA PHTs exhibited a modulus of ~14.0 GPa, are robust materials, and are resistant to bases, oxidants, and

solvents. Rigid PHTs exhibited a  $T_g$  of ~192°C and decomposed at ~300°C. PHTs decompose to monomer after long exposure (>24 hours) to strong acid. (C) PHT film reinforced with 2 wt % of multiwalled, surface-oxidized CNTs exhibited a Young's modulus of ~20.0 GPa. (D) An HDCN derived from 4.6-kD PEG diamine formed a self-healing organogel, which was reversible in neutral water after 24 hours.

27.3 mg of ODA HDCN in 10 ml of 0.5 M H<sub>2</sub>SO<sub>4</sub>, pH = 0); PHTs were insensitive to weak acids, neutral water, and basic conditions (table S4).

The exceptional Young's modulus of aromatic PHTs, combined with the observed reversibility of the reaction in strongly acidic conditions, makes the PHTs an unprecedented new class of thermosets, as most high-modulus materials are completely chemically inert and often very difficult, if not impossible, to rework or recycle. Given their high stability toward organic solvents, ODA PHTs could be used in environments where robust, solvent-resistant materials are necessary; moreover, they resist catastrophic failure associated with environmental stress cracking (fig. S27). The acid-promoted reversibility of ODA PHTs would allow them to become the first thermosets that are easily repolymerized or recycled. The ability to depolymerize the fully cured PHTs opens numerous applications such as reworkable encapsulates (16), which have been explored extensively for recovery of high-value components such as in microelectronics, although approaches commonly sacrifice the mechanical properties of the resin. This rework can lead to substantial cost savings, as often in high-value applications, thermoset components with a single defect can result in the entire part being scrapped because the intractability of traditional thermosets prevents their removal to effect repairs.

PEG oligomers (4.2) were also studied for their reactivity with paraformaldehyde. Although PEG PHTs were not formed at high temperature, PEG HDCNs (4.3) that formed at low temperature exhibited properties that were markedly different from those of the high-modulus ODA HDCNs and PHTs. HDCNs based on oligomeric PEG diamines formed elastic organogels with a melting temperature ( $T_m$ ) of ~49°C by DSC, that com-

pletely reverted back to their original starting components in neutral water, which makes them promising candidates for reversible covalent constructs for a wide variety of applications that require reversible assemblies such as materials for cargo delivery. In addition to reversibility, PEG HDCN organogels exhibited self-healing properties; images and a video of its self-healing ability can be found in the supplementary materials (movie S1 and fig. S23). Previously reported polymerizations attempting to form PHTs focused on low-temperature reactions (50° to ~100°C) and used soluble aliphatic diamine monomers, or targeted PHTs, as reactive intermediates (17). These intermediate aliphatic diamine-based homopolymers were not extensively considered as useful thermosets because they exhibited poor mechanical properties (18). We believe, given the high rate of the reaction to its gelling point (within minutes) and difficulties we encountered to spectroscopically characterize ODA PHTs and HDCNs, that at these lower temperatures, low cross-link density, low-modulus HDCNs were most likely formed.

#### References and Notes

1. T. F. De Greef *et al.*, *Chem. Rev.* **109**, 5687–5754 (2009).
2. A. K. Singh, S. K. Shukla, M. A. Quraishi, *J. Mater. Environ. Sci.* **2**, 403–406 (2011).
3. M. Ghandi, F. Salimi, A. Olyaei, *Molecules* **11**, 556–563 (2006).
4. H. Ulrich, J. Rubinfeld, *J. Org. Chem.* **26**, 1637–1638 (1961).
5. J. Barluenga *et al.*, *J. Chem. Soc. Perkin Trans. 1* **1988**, 1631–1636 (1988).
6. A. Dandia, K. Arya, M. Sati, P. Sarawgi, *J. Fluor. Chem.* **125**, 1273–1277 (2004).
7. Z. Brunovska, J. P. Liu, H. Ishida, *Macromol. Chem. Phys.* **200**, 1745–1752 (1999).
8. A. G. Giumanini, G. Verardo, L. Randaccio, N. Bresciani-Pahor, P. Traldi, *J. Prakt. Chem.* **327**, 739–748 (1985).

9. E. A. Ponzio, R. Echevarria, G. M. Morales, C. Barbero, *Polym. Int.* **50**, 1180–1185 (2001).
10. A. D. Becke, *J. Chem. Phys.* **98**, 5648–5652 (1993).
11. M. W. Schmidt *et al.*, *J. Comput. Chem.* **14**, 1347–1363 (1993).
12. C. Lee, W. Yang, R. G. Parr, *Phys. Rev. B* **37**, 785–789 (1988).
13. V. Barone, M. Cossi, *J. Phys. Chem. A* **102**, 1995–2001 (1998).
14. K. R. Virwani, A. P. Malshe, W. F. Schmidt, D. K. Sood, *Smart Mater. Struct.* **12**, 1028–1032 (2003).
15. [www.engineeringtoolbox.com/young-modulus-d\\_417.html](http://www.engineeringtoolbox.com/young-modulus-d_417.html); accessed 10 August 2013.
16. J.-S. Chen, C. K. Ober, M. D. Poliks, *Polymer (Guildf.)* **43**, 131–139 (2002).
17. A. Chermikh, J. Liu, H. Ishida, *Polymer (Guildf.)* **47**, 7664–7669 (2006).
18. M. Hiller, S. E. Evsyukov, *Mater. Res. Innov.* **6**, 179–184 (2002).
19. L. S. Schadler, S. C. Giannaris, P. M. Ajayan, *Appl. Phys. Lett.* **73**, 3842–3844 (1998).
20. S. Chou, H. C. Chen, H. E. Chen, *Compos. Sci. Technol.* **45**, 23–35 (1992).

**Acknowledgments:** This work was performed under a joint development agreement between IBM Research and King Abdulaziz City for Science and Technology (KACST) through the KACST-IBM Nanotechnology Center of Excellence ([www.nce-kacst-ibm.org](http://www.nce-kacst-ibm.org)). Experimental procedures, NMR spectra, DFT Cartesian coordinates, x-ray diffraction data, nanoindentation data, and GPC traces can be found in the supplementary materials. We gratefully acknowledge J. Frommer for atomic force microscopy images, M. Sherwood for solid-state <sup>13</sup>C NMR experiments, T. Magbitang for thermal analysis, C. Fox for 4.6-kD PEG diamine synthesis, L. Randall for Instron data characterization, and R. King for assistance in nanoindentation measurements.

#### Supplementary Materials

[www.sciencemag.org/content/344/6185/732/suppl/DC1](http://www.sciencemag.org/content/344/6185/732/suppl/DC1)  
Materials and Methods  
Figs. S1 to S30  
Tables S1 to S4  
References (21–26)  
Movie S1

29 January 2014; accepted 2 April 2014  
10.1126/science.1251484

## Marine Ice Sheet Collapse Potentially Under Way for the Thwaites Glacier Basin, West Antarctica

Ian Joughin, Benjamin E. Smith, Brooke Medley

Resting atop a deep marine basin, the West Antarctic Ice Sheet has long been considered prone to instability. Using a numerical model, we investigated the sensitivity of Thwaites Glacier to ocean melt and whether its unstable retreat is already under way. Our model reproduces observed losses when forced with ocean melt comparable to estimates. Simulated losses are moderate (<0.25 mm per year at sea level) over the 21st century but generally increase thereafter. Except possibly for the lowest-melt scenario, the simulations indicate that early-stage collapse has begun. Less certain is the time scale, with the onset of rapid (>1 mm per year of sea-level rise) collapse in the different simulations within the range of 200 to 900 years.

Glaciers along the Amundsen Coast of Antarctica are thinning (1, 2), producing the majority of Antarctica's contribution to sea-level rise (3, 4). Much of this thinning is probably a response to the increased presence of warm modified Circumpolar Deep Water (CDW)

on the adjacent continental shelf (5, 6), which is melting and thinning the floating ice shelves that buttress the ice sheet (7–9). Thinner ice shelves are less able to restrain flow from the interior, contributing to feedbacks that increase ice discharge to the ocean (10–14). Thwaites and Haynes

Glaciers, which hereafter we refer to collectively as Thwaites Glacier, produce just under half (52 Gt/year in 2007) of the Amundsen Coast losses (105 Gt/year in 2007) (3, 4, 15, 16), making it one of the largest contributors to sea-level change. This glacier and the immediately adjacent and rapidly thinning Pine Island Glacier (2, 3) were identified as potentially unstable several decades ago (17).

The present Thwaites grounding line—the location where ice reaches the ocean and goes afloat—rests on a coastal sill ~600 m below sea level (bsl) (Fig. 1) (18). At ~60 to 80 km farther inland, this sill gives way to a deep (>1200 m bsl) marine basin, yielding the potential for marine ice-sheet instability (13, 17, 19–21). Ice discharge is nonlinearly proportional to grounding-line thickness. Hence the potential for instability exists where the ice-sheet bed lies below sea level and steepens toward the interior, so that an initial retreat into deeper water creates a feedback,

Polar Science Center, Applied Physics Lab, University of Washington, 1013 NE 40th Street, Seattle, WA 98105–6698, USA.



leading to more thinning and retreat. Thus, with ongoing thinning and only tens of kilometers separating the grounding line from the marine basin's deepest regions, collapse of Thwaites Glacier may have already begun, albeit for now at a relatively moderate rate. To explore this possibility, we used a basin-scale ice-flow model to evaluate whether collapse is under way or if instead retreat may be limited by stabilizing factors.

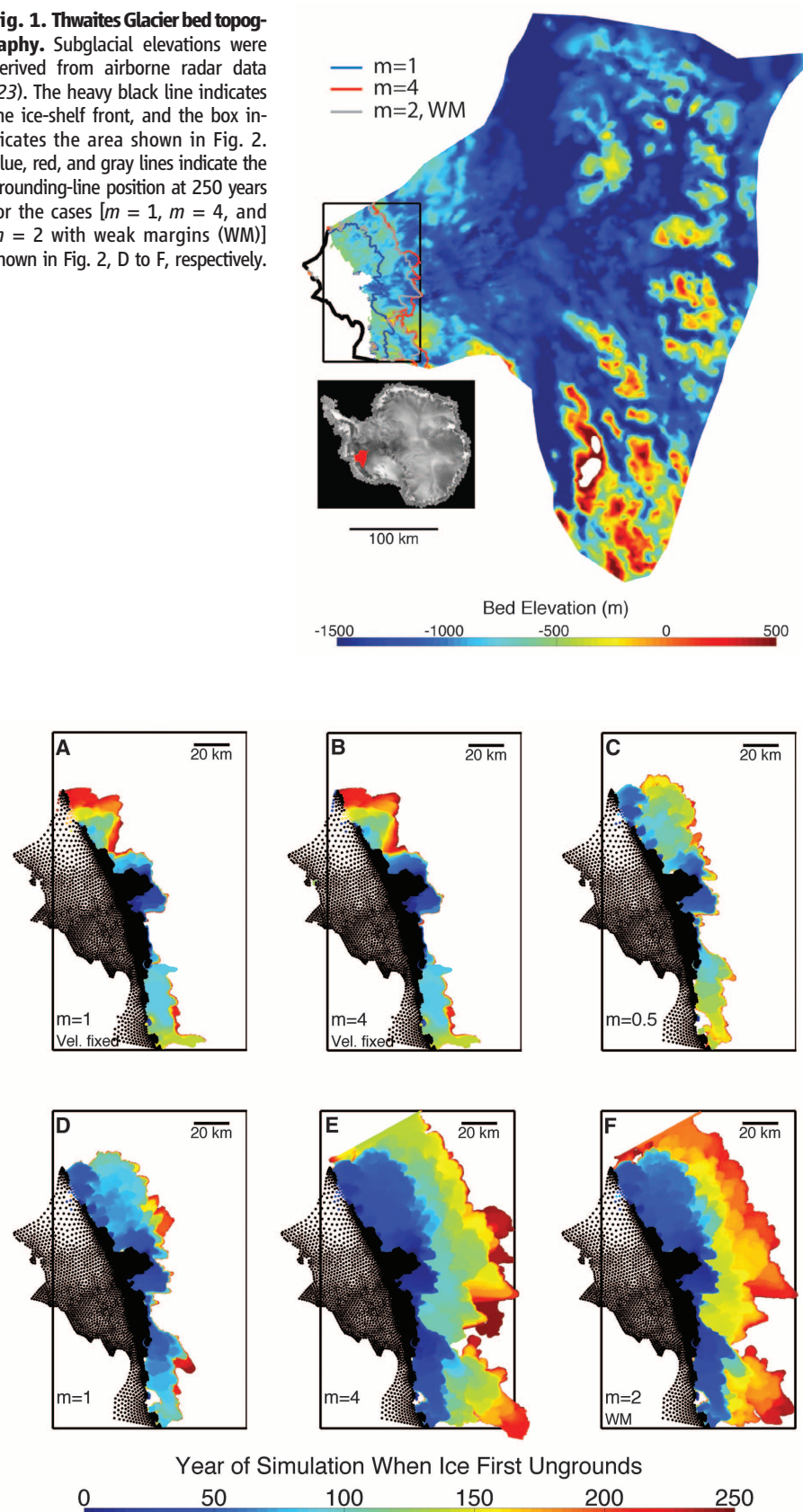
We simulated Thwaites Glacier's response to subshelf melt using a prognostic, finite-element, depth-averaged, shallow-shelf model (12, 22, 23). We initialized the model by determining the basal shear stress and the ice-shelf rheological parameters that best matched the circa 1996 (1994–1996) observed velocity (12, 24) and grounding line (25). At the ice/ocean interface, we used a simple depth-parameterized melt function scaled by a coefficient,  $m$ . With  $m = 1$ , this function produced steady-state behavior for neighboring Pine Island Glacier (12). For the Thwaites Ice Shelf, maximum melt rates with  $m = 1$  are just over 200 m/year in the deepest regions, and total melt is 32 Gt/year when the simulation commences, making it comparable to a 1992–1996 steady-state estimate of 31 Gt/year for the shelf's highest-melt area (26).

Because the Amundsen Coast thinning appears to be driven by increased ice-shelf melting (10, 11), many of our experiments are designed to examine this sensitivity to melt. First we examined the direct influence of melt on grounding-line position, with no feedback or response from the glacier, by fixing the velocity at its initial value throughout the simulation. These experiments reveal that grounding-line position is relatively insensitive to the direct effect of melting (14, 19), producing nearly the same pattern of retreat for  $m = 1$  and 4 (Fig. 2, A and B). The retreat that does occur is largely driven by the non-steady-state fixed velocity imposed at the start of the simulation.

Next we evaluated the model's response to melt ( $m = 0.5$  to 4) with coupling (i.e., freely evolving velocity) to the ice sheet (Fig. 2, C to E). For these cases, there is a much greater sensitivity to melt, with the grounding line approaching the deepest parts of the trough for the higher-melt simulations (Fig. 2E). Strong melt ( $m = 2$  to 4) produces ice loss at rates of  $<0.25$  mm/year of sea-level equivalent (sle) for the first century, beyond which there is a period in each strong-melt simulation when the grounding line retreats abruptly, producing greater ice loss (0.25 to 0.5 mm/year of sle). Except for a few decades in the  $m = 1$  simulation, ice loss for the lower melt simulations ( $m = 0.5$  and 1) was less than observed in 2010 (Fig. 3A).

Antarctic accumulation rates are projected to increase over the 21st century (27). To evaluate any stabilizing effect such a change might have, we simulated a 20% linear increase in accumulation rate over the first 100 years, with a fixed rate thereafter (Fig. 3B). The higher accumulation moves the low-melt ( $m = 0.5$  to 1)

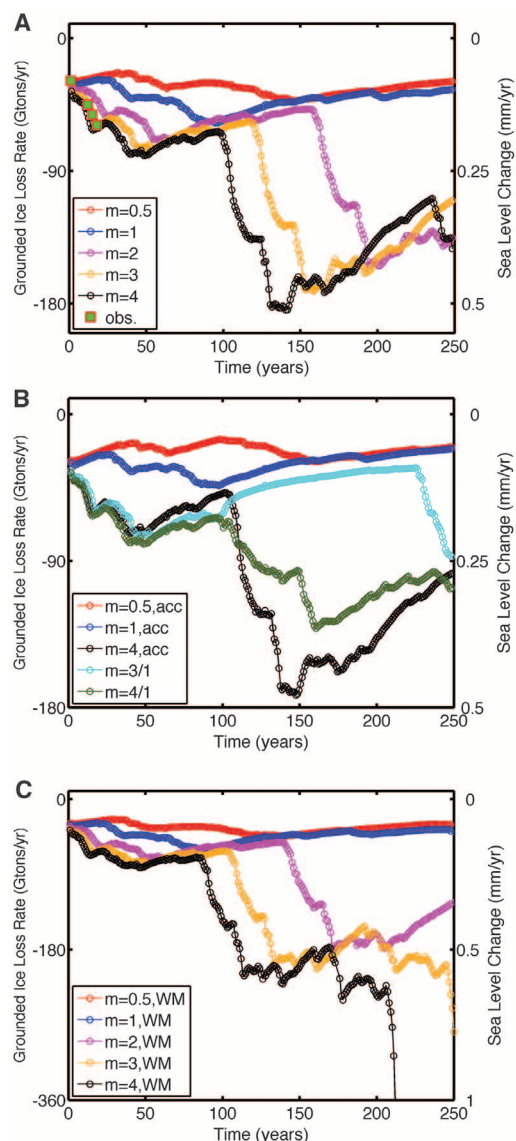
**Fig. 1. Thwaites Glacier bed topography.** Subglacial elevations were derived from airborne radar data (23). The heavy black line indicates the ice-shelf front, and the box indicates the area shown in Fig. 2. Blue, red, and gray lines indicate the grounding-line position at 250 years for the cases [ $m = 1$ ,  $m = 4$ , and  $m = 2$  with weak margins (WM)] shown in Fig. 2, D to F, respectively.



**Fig. 2. Simulated ground line retreat for Thwaites Glacier.** Time of ungrounding for simulations with fixed velocity for (A)  $m = 1$  and (B)  $m = 4$ . The ungrounding time for freely evolving velocity with (C)  $m = 0.5$ , (D)  $m = 1$ , and (E)  $m = 4$  is also shown. (F) Simulation with  $m = 2$  for a shelf with weak margins. Black dots indicate ice-shelf nodes at the beginning of the simulation.

**Table 1. Year in simulation when losses first exceed 1 mm/year of sle for standard and weak-margin models.**

<i>m</i>	Standard model (year)	Weak-margin model (years)
0.5	>1000	>1000
1.0	870	573
2.0	460	342
3.0	343	253
4.0	292	212

**Fig. 3. Simulated ice losses for Thwaites Glacier.** Annual rates of grounded ice loss (i.e., ice above flotation) for (A) initial model runs with  $m = 0.5$  to 4. Green squares with red borders show observed losses for 1996 (1994–1996), 2007, 2010, and 2013 plotted as years 1, 12, 15, and 18, respectively (15, 16). (B) Losses for experiments with a linear increase in accumulation by 20% over the first 100 years (acc) and high-melt cases for only the first 100 years (3/1 and 4/1). (C) Model runs with weakened ice-shelf margins for  $m = 0.5$  to 4.

simulations closer to balance. For the higher-melt case ( $m = 4$ ), it delays the transition to large losses ( $>90$  Gt/year) by just under a decade.

Currently, elevated melt rates on the Amundsen Coast are largely driven by increased transport of warm CDW onto the continental shelf rather than by direct warming of the CDW (6). If the conditions responsible for this transport abate, melting should lessen. Thus, we simulated 100 years of high melt ( $m = 3$  and 4) followed by

reduced melt ( $m = 1$ ) for the remainder of the simulation (Fig. 3B). Although the reduction in melt slowed the rate of loss, at the end of these 250-year simulations, losses were substantially greater relative to the sustained  $m = 1$  simulation.

Inversions for the strength of ice-shelf shear margins often reveal substantial weakening due to either rheological softening (e.g., fabric or strain heating) (28) or mechanical damage (e.g., crevassing or rifting) (29). Our model includes

weaker margins on the initial ice shelf, but as the shelf expands into the originally grounded ice, the newly formed ice-shelf margins remain strong. To evaluate the sensitivity to margin weakening, we implemented an ad hoc weakening scheme (23) and repeated our standard set of experiments. For the  $m = 3$  simulation, weakening of the margins produces more extensive grounding-line retreat (Fig. 2F). For the highest-melt case ( $m = 4$ ), at about 212 years into the simulation (Table 1), the grounding line recedes rapidly to the basin's deepest regions, yielding a sea-level contribution of more than 1 mm/year.

When simulated losses exceed 1 mm/year of sle, much greater losses generally follow within a few years. Using our basin-scale model, however, such rapid collapse is difficult to model, especially because interaction with other basins becomes increasingly important. Thus, we take 1 mm/year of sle to be a threshold that, once crossed, marks the onset of rapid (decades) collapse as the grounding line reaches the deepest regions of the marine basin. In our 250-year simulations, only the highest-melt, weak-margin simulation reaches this critical threshold. Therefore, we have extended the remaining simulations to determine when this threshold is reached (fig. S2 and Table 1). For all but the lowest-melt simulations ( $m = 0.5$ ), the onset of rapid collapse begins within a millennium.

The observed losses from 1996 to 2013 (Fig. 3A) fall between the results from our highest-melt ( $m = 3$  and 4) simulations. Over this period, the average simulated melt of 84 Gt/year for  $m = 4$  agrees well with recent melt estimates of 69 to 97 Gt/year (7, 8), indicating that the higher-melt simulations' early stages reasonably approximate present conditions. Thus, the close agreement between model and observation strengthens the argument that recent losses are melt-driven (10). Specifically, melt-induced ice-shelf thinning reduces buttressing, causing an initial speedup. In turn, this initial speedup causes the grounding line to retreat, resulting in loss of traction and far greater speedup and retreat. The ice stream was already out of balance before 1996, which may have been the result of thinning that caused the ice to unground several decades or more ago from a ridge seaward of the present grounding line (3, 30).

Our simulations are not coupled to a global climate model to provide forcing nor do they include an ice-shelf cavity-circulation model to derive melt rates. Few if any such fully coupled models presently exist (13). As such, our simulations do not constitute a projection of future sea level in response to projected climate forcing. The results, however, indicate the type of behavior that is likely to occur. In particular, all the simulations show the grounding line stepping back in stages with concurrent increases in discharge, consistent with other models and observations of paleo-ice-stream retreat (31, 32). The intensity of melt in our simulations regulates the time scale over which this pattern of retreat



occurs. Thus, although cavity-circulation models driven by regional ocean circulation models coupled to global climate models might yield differing spatiotemporal variations in melt, they should produce patterns of retreat similar to those we have simulated, but with tighter constraints on the timing.

An important feature of our numerical simulations is that they reveal a strong sensitivity to mechanical and/or rheological weakening of the margins, which can accelerate the rate of collapse by decades to centuries. Thus, future models will require careful treatment of shear margins to accurately project sea-level rise. Our simulations also assume that there is no retreat of the ice-shelf front. Full or partial ice-shelf collapse should produce more rapid retreat than we have simulated. In addition, we have not modeled ocean-driven melt that extends immediately upstream of the grounding line, which could also accelerate retreat (32).

Our simulations provide strong evidence that the process of marine ice-sheet destabilization is already under way on Thwaites Glacier, largely in response to high subshelf melt rates. Although losses are likely to be relatively modest over the next century (<0.25 mm/year of sle), rapid collapse (>1 mm/year of sle) will ensue once the grounding line reaches the basin's deeper regions, which could occur within centuries. Such rapid collapse would probably spill over to adjacent catchments, undermining much of West Antarctica (18). Similar behavior also may be under way on neighboring Pine Island Glacier (12, 33). Unless CDW recedes sufficiently to reduce melt well below present levels, it is dif-

ficult to foresee a stabilization of the Thwaites system, even with plausible increases in surface accumulation. Although our simple melt parameterization suggests that a full-scale collapse of this sector may be inevitable, it leaves large uncertainty in the timing. Thus, ice-sheet models fully coupled to ocean/climate models are required to reduce the uncertainty in the chronology of a collapse. Nonetheless, the similarity between our highest melt rates and present observations suggests that collapse may be closer to a few centuries than to a millennium.

## References and Notes

- H. D. Pritchard, R. J. Arthern, D. G. Vaughan, L. A. Edwards, *Nature* **461**, 971–975 (2009).
- A. Shepherd, *Geophys. Res. Lett.* **29**, 1364 (2002).
- E. Rignot, *Geophys. Res. Lett.* **35**, L12505 (2008).
- A. Shepherd et al., *Science* **338**, 1183–1189 (2012).
- S. S. Jacobs, A. Jenkins, C. F. Giulivi, P. Dutrieux, *Nat. Geosci.* **4**, 519–523 (2011).
- M. Thoma, A. Jenkins, D. Holland, S. Jacobs, *Geophys. Res. Lett.* **35**, L18602 (2008).
- E. Rignot, S. S. Jacobs, J. Mouginot, B. Scheuchl, *Science* **341**, 266–270 (2013).
- M. A. Depoorter et al., *Nature* **502**, 89–92 (2013).
- H. D. Pritchard et al., *Nature* **484**, 502–505 (2012).
- A. Shepherd, D. Wingham, E. Rignot, *Geophys. Res. Lett.* **31**, L23402 (2004).
- A. Payne, A. Vieli, A. Shepherd, D. Wingham, E. Rignot, *Geophys. Res. Lett.* **31**, L23401 (2004).
- I. Joughin, B. E. Smith, D. M. Holland, *Geophys. Res. Lett.* **37**, L20502 (2010).
- I. Joughin, R. B. Alley, D. M. Holland, *Science* **338**, 1172–1176 (2012).
- O. Gagliardini, G. Durand, T. Zwinger, R. C. A. Hindmarsh, E. Le Meur, *Geophys. Res. Lett.* **37**, L14501 (2010).
- B. Medley et al., *Cryosphere Discuss.* **8**, 953–998 (2014).
- J. Mouginot, E. Rignot, B. Scheuchl, *Geophys. Res. Lett.* **41**, 1576–1584 (2014).

- T. J. Hughes, *J. Glaciol.* **27**, 518–525 (1981).
- J. Holt et al., *Geophys. Res. Lett.* **33**, L09502 (2006).
- C. Schoof, *J. Geophys. Res. Earth Surf.* **112**, F03528 (2007).
- J. Weertman, *J. Glaciol.* **13**, 3–11 (1974).
- J. H. Mercer, *Nature* **271**, 321–325 (1978).
- D. R. MacAyeal, *J. Geophys. Res. Solid Earth* **94**, 4071–4087 (1989).
- Model details are provided in the supplementary materials.
- I. Joughin et al., *J. Glaciol.* **55**, 245–257 (2009).
- E. Rignot, J. Mouginot, B. Scheuchl, *Geophys. Res. Lett.* **38**, L10504 (2011).
- E. Rignot, S. S. Jacobs, *Science* **296**, 2020–2023 (2002).
- C. Genthon, G. Krinner, H. Castebrunet, *Ann. Glaciol.* **50**, 55–60 (2009).
- E. Larour, E. Rignot, I. Joughin, D. Aubry, *Geophys. Res. Lett.* **32**, L05503 (2005).
- C. P. Borstad, E. Rignot, J. Mouginot, M. P. Schodlok, *Cryosphere Discuss.* **7**, 3567–3610 (2013).
- K. J. Tinto, R. E. Bell, *Geophys. Res. Lett.* **38**, L20503 (2011).
- S. S. R. Jamieson et al., *Nat. Geosci.* **5**, 799–802 (2012).
- B. R. Parizek et al., *J. Geophys. Res.* **118**, 638–655 (2013).
- L. Favier et al., *Nat. Clim. Change* **4**, 117–121 (2014).

**Acknowledgments:** Comments by M. Maki, D. Shapero, and four anonymous reviewers improved the manuscript. NSF supported I.J. and B.M.'s contribution (grants ANT-0424589 and ANT-0631973), and B.E.S. was supported by NASA (grant NNX09AE476). We acknowledge NASA's Operation IceBridge, which provided much of the data used to constrain the model. The data used to constrain the model are archived at the University of Washington Library (<http://dx.doi.org/10.6069/H5CC0XMK>).

## Supplementary Materials

[www.sciencemag.org/content/344/6185/735/suppl/DC1](http://www.sciencemag.org/content/344/6185/735/suppl/DC1)  
Materials and Methods  
Supplementary Text  
Figs. S1 and S2  
References (34–37)

27 November 2013; accepted 21 April 2014  
10.1126/science.1249055

# Stick Insect Genomes Reveal Natural Selection's Role in Parallel Speciation

Víctor Soria-Carrasco,<sup>1\*</sup> Zachariah Gompert,<sup>2\*</sup> Aaron A. Comeault,<sup>1</sup> Timothy E. Farkas,<sup>1</sup> Thomas L. Parchman,<sup>3</sup> J. Spencer Johnston,<sup>4</sup> C. Alex Buerkle,<sup>5</sup> Jeffrey L. Feder,<sup>6</sup> Jens Bast,<sup>7</sup> Tanja Schwander,<sup>8</sup> Scott P. Egan,<sup>9</sup> Bernard J. Crespi,<sup>10</sup> Patrik Nosil<sup>1†</sup>

Natural selection can drive the repeated evolution of reproductive isolation, but the genomic basis of parallel speciation remains poorly understood. We analyzed whole-genome divergence between replicate pairs of stick insect populations that are adapted to different host plants and undergoing parallel speciation. We found thousands of modest-sized genomic regions of accentuated divergence between populations, most of which are unique to individual population pairs. We also detected parallel genomic divergence across population pairs involving an excess of coding genes with specific molecular functions. Regions of parallel genomic divergence in nature exhibited exceptional allele frequency changes between hosts in a field transplant experiment. The results advance understanding of biological diversification by providing convergent observational and experimental evidence for selection's role in driving repeatable genomic divergence.

Whether evolution is predictable and repeatable is difficult to test yet central to our understanding of biological diversification (1–6). Instances of repeated, parallel evolution in response to similar environmental pressures provide evidence of evolution by natu-

ral selection and can involve repeated divergence at specific genes (7–9). Indeed, parallel evolution of individual phenotypic traits has been estimated to involve the same genomic regions 30 to 50% of the time (8). Parallel evolution can also result in replicate species formation (i.e., paral-

lel speciation) (10), but the genome-wide consequences of this process are unclear (7, 8, 11). Although some genomic regions will likely diverge repeatedly during parallel speciation, many might show idiosyncratic patterns because of contingencies such as the order in which mutations arise (7, 8, 10, 11).

Even if repeated divergence occurs for some genomic regions (7, 12, 13), the underlying causes of this parallelism often remain speculative because it is difficult to disentangle the

<sup>1</sup>Department of Animal and Plant Sciences, University of Sheffield, Sheffield S10 2TN, UK. <sup>2</sup>Department of Biology, Utah State University, Logan, UT 84322, USA. <sup>3</sup>Department of Biology, University of Nevada, Reno, NV 89557, USA. <sup>4</sup>Department of Entomology, Texas A&M University, College Station, TX 77843, USA. <sup>5</sup>Department of Botany, University of Wyoming, Laramie, WY 82071, USA. <sup>6</sup>Department of Biology, Notre Dame University, South Bend, IN 46556, USA. <sup>7</sup>J. F. Blumenbach Institute of Zoology and Anthropology, University of Göttingen, 37073 Göttingen, Germany. <sup>8</sup>Department of Ecology and Evolution, University of Lausanne, Lausanne CH-1015, Switzerland. <sup>9</sup>Department of Ecology and Evolutionary Biology, Rice University, Houston, TX 77005, USA. <sup>10</sup>Department of Biological Sciences, Simon Fraser University, Burnaby, BC V5A 1S6, Canada.

\*These authors contributed equally to this work.

†Corresponding author. E-mail: p.nosil@sheffield.ac.uk



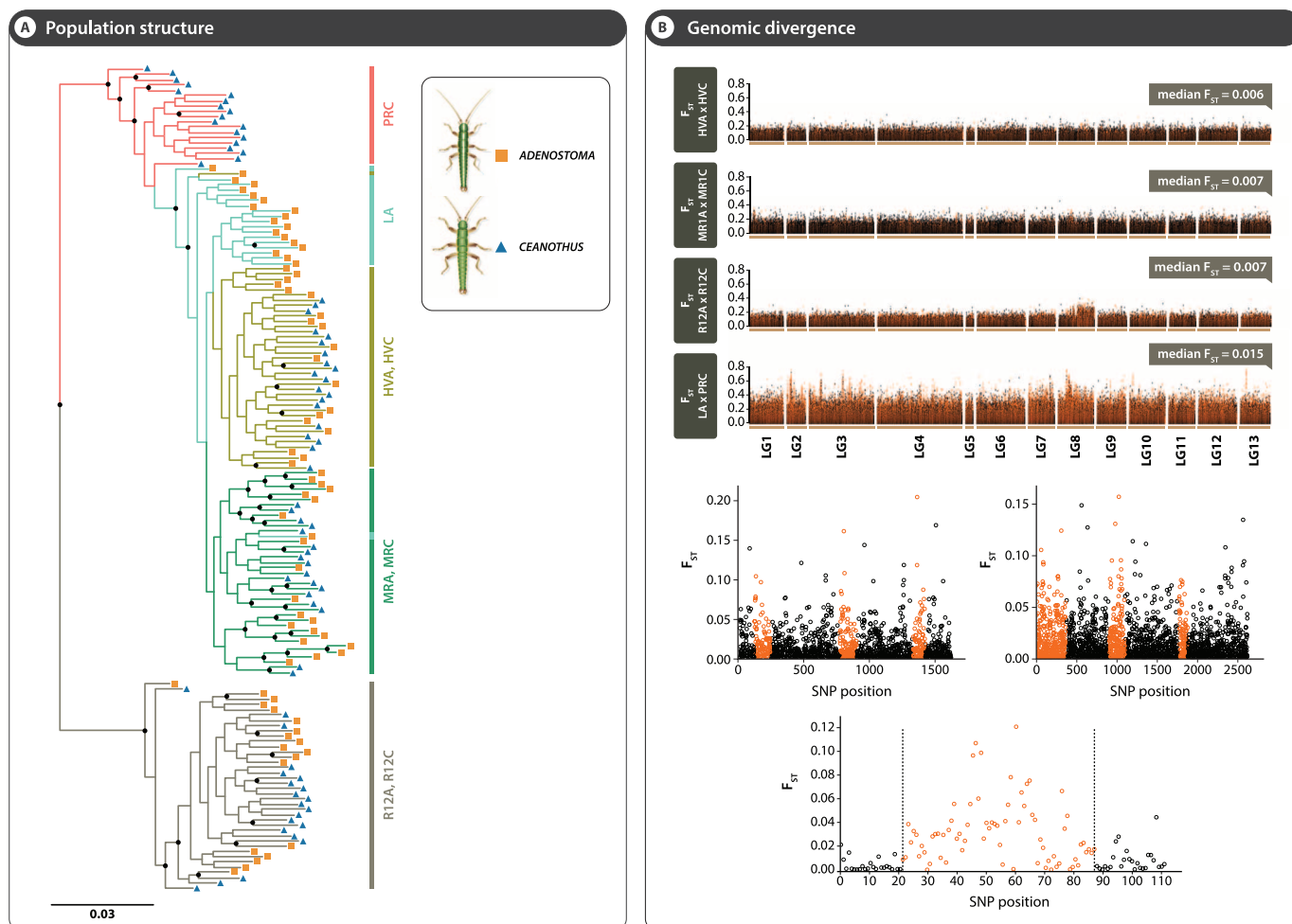
contributions of the many factors that can be involved, such as selection, mutation, recombination, gene flow, population size, and the genetic architecture of traits (2, 11, 14). We chose to study these questions with a wingless, herbivorous stick insect (*Timema cristinae*) endemic to California that has repeatedly evolved ecotypes adapted to different host plant species: *Adenostoma fasciculatum* and *Ceanothus spinosus* (Fig. 1). Populations of this species exhibit high gene flow between adjacent populations on different hosts, little or no gene flow between more distant geographic localities, and repeated evolution of partial reproductive isolation between different ecotype pairs (15–17). Consistent with the main prediction of parallel speciation, pairs of populations in different localities on the same host exhibit weaker reproductive isolation than do different ecotypes, independent from genetic distance. Thus, the

ecotypes of *T. cristinae* are in the early stages of parallel ecological speciation and have evolved increased sexual isolation through reinforcement.

We annotated the reference genome for this species (18) [assembly length of 1,027,063,217 base pairs (bp), 50% of assembly in scaffolds at least 312,000 bp long (N50)] and used sequence data from genetic crosses to assemble it into linkage groups (19). We then resequenced 160 additional whole genomes from replicate ecotype pairs and compared patterns of genomic divergence to allele frequency changes in populations experimentally transplanted to different host plants. These data allowed us to analyze the effects of adaptation on genomic divergence, experimentally test the hypothesis that accentuated and parallel genetic divergence between natural populations is driven by parallel divergent selection, rigorously quantify divergence in both coding and noncoding regions, rule out undetected

genetic differences because of low coverage across the genome, and quantify the repeatability of genetic divergence for individual loci and the genome as a whole.

Our data indicate that parallel speciation can involve both repeatable and idiosyncratic divergence at the genetic level and that the repeated component involves many regions affected by divergent selection. We examined four replicate population pairs on *Ceanothus* versus *Adenostoma* ( $n = 8$  populations) to characterize genomic divergence between ecotypes ( $n = 19$  to 21 individuals per population). Three of these pairs were directly adjacent to one another, and the fourth was separated by 6.4 km (Table 1 and fig. S1). We discovered many rare genetic variants (e.g., 2,526,553 single-nucleotide variants with minor allele frequency, MAF, <1%) and retained 4,391,556 single-nucleotide polymorphisms (SNPs) with MAF >1% that mapped to linkage



**Fig. 1. Population structure and whole-genome divergence between host-plant ecotypes of *T. cristinae*.** (A) A maximum likelihood tree from whole-genome data from individuals from *T. cristinae* populations (rooted with other species of *Timema* not shown). Black circles depict nodes with >80% bootstrap support (100 replicates). Populations LA, HVA, MRC, and R12A were collected from *Adenostoma*. Populations PRC, HVC, MRC, and R12C were collected from *Ceanothus*. The geographic locations of the populations are depicted in fig. S1. (B) Patterns of genetic divergence ( $F_{ST}$ ) along the genome. LG indicates linkage group. Colors denote whether SNPs occur

in moderately (black) or highly (red/orange) divergent genetic regions, delimited with a HMM approach (weakly differentiated regions in blue are too sparse to see). Results are shown at three different scales. (Top)  $F_{ST}$  estimates at all ~4.4 million SNPs for each of the four population pairs. (Middle) Genomic divergence for two scaffolds (scaffolds 1271 on LG7 and 2230 on LG6 from HVA x HVC). (Bottom) Magnified view of genomic divergence for one parallel HMM divergence region that harbored a SNP showing parallel allele frequency divergence between hosts upon transplantation (scaffold 556 on LG4 from R12A x R12C; see also Fig. 3). [Credit: courtesy of R. Ribas.]

**Table 1. Characteristics of the four pairs of natural populations of *T. cristinae* on different host-plant species.** *N<sub>e</sub>m* values are from (16).

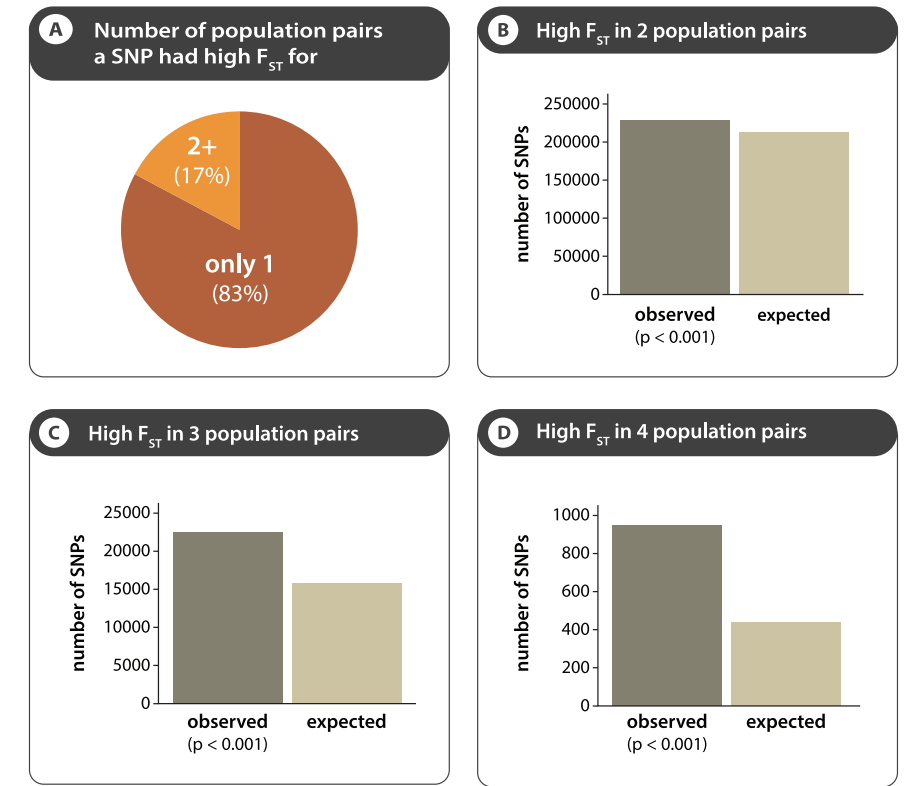
Population Pair	HVA × HVC	MR1A × MR1C	R12A × R12C	LA × PRC
<i>Population characteristics</i>				
Geography	adjacent	adjacent	adjacent	separated
Gene flow ( <i>N<sub>e</sub>m</i> )	28	37	93	11
No. individuals sequenced (per individual population)	20, 20	20, 20	21, 21	19, 19
<i>Genome characteristics from all SNPs</i>				
Mean MAF	17%	20%	19%	20%
Mean <i>F<sub>ST</sub></i>	0.013	0.015	0.015	0.031
Median <i>F<sub>ST</sub></i>	0.006	0.007	0.007	0.015
Range of <i>F<sub>ST</sub></i>	0.000–0.358	0.000–0.461	0.000–0.398	0.000–0.8000
90th quantile	0.035	0.041	0.041	0.083
95th quantile	0.050	0.058	0.056	0.116
<i>Characteristics of HMM divergence regions</i>				
Number	7041	3800	10,628	18,135
% of all SNPs in HMM divergence regions	13%	8%	19%	30%
Mean (median) size in bp	10,460 (4729)	6276 (2278)	10,580 (4830)	7255 (2411)
SD of size in bp	15,514	9942	15,462	12,106
Mean <i>F<sub>ST</sub></i>	0.022	0.028	0.039	0.051

groups for further analysis (across all SNPs, mean coverage per individual per SNP is 5.0).

Genomic divergence between ecotype pairs varied geographically. A phylogenomic tree grouped *T. cristinae* individuals by geographic locality and rejected grouping by host [*P* < 0.00001, approximately unbiased test (Fig. 1 and fig. S2)] (19). This finding was supported by principal components (PC) analysis [variance partitioning of PC1 is 93.7% by geography and 0.2% by host (fig. S1)]. The average genome-wide fixation index (*F<sub>ST</sub>*) for the geographically separated pair was twice that of the adjacent pairs, with all three adjacent pairs exhibiting similarly low average *F<sub>ST</sub>* [median ~0.007; mean ~0.015 (Fig. 1 and Table 1)]. No fixed differences were observed between ecotype pairs. These levels of population differentiation are lower than those found in many studies that analyzed the genomic consequences of divergence (12, 20, 21), emphasizing that we are examining the early stages of speciation.

Patterns of divergence between ecotype pairs also varied across the genome, with *F<sub>ST</sub>* for the most differentiated SNPs being about 60 times greater than the median value (Table 1 and fig. S3). A hidden Markov model (HMM) (22) classified the majority of the genome as moderately divergent, but we observed numerous small- to modest-sized regions of high divergence (hereafter referred to as HMM divergence regions) distributed across all linkage groups. Across population pairs, HMM divergence regions varied in number from 3800 to 18,135, comprising 8 to 30% of the genome with mean size from 6276 to 10,580 bp (standard deviation 9942 to 15,514) (Fig. 1 and fig. S4).

We tested whether divergence between replicate population pairs frequently involved the same genomic regions. To increase precision, we focused these analyses on SNPs. We identified SNPs that were highly divergent between each population pair (those above the 90th empirical quantile of the *F<sub>ST</sub>* distribution; divergent SNPs



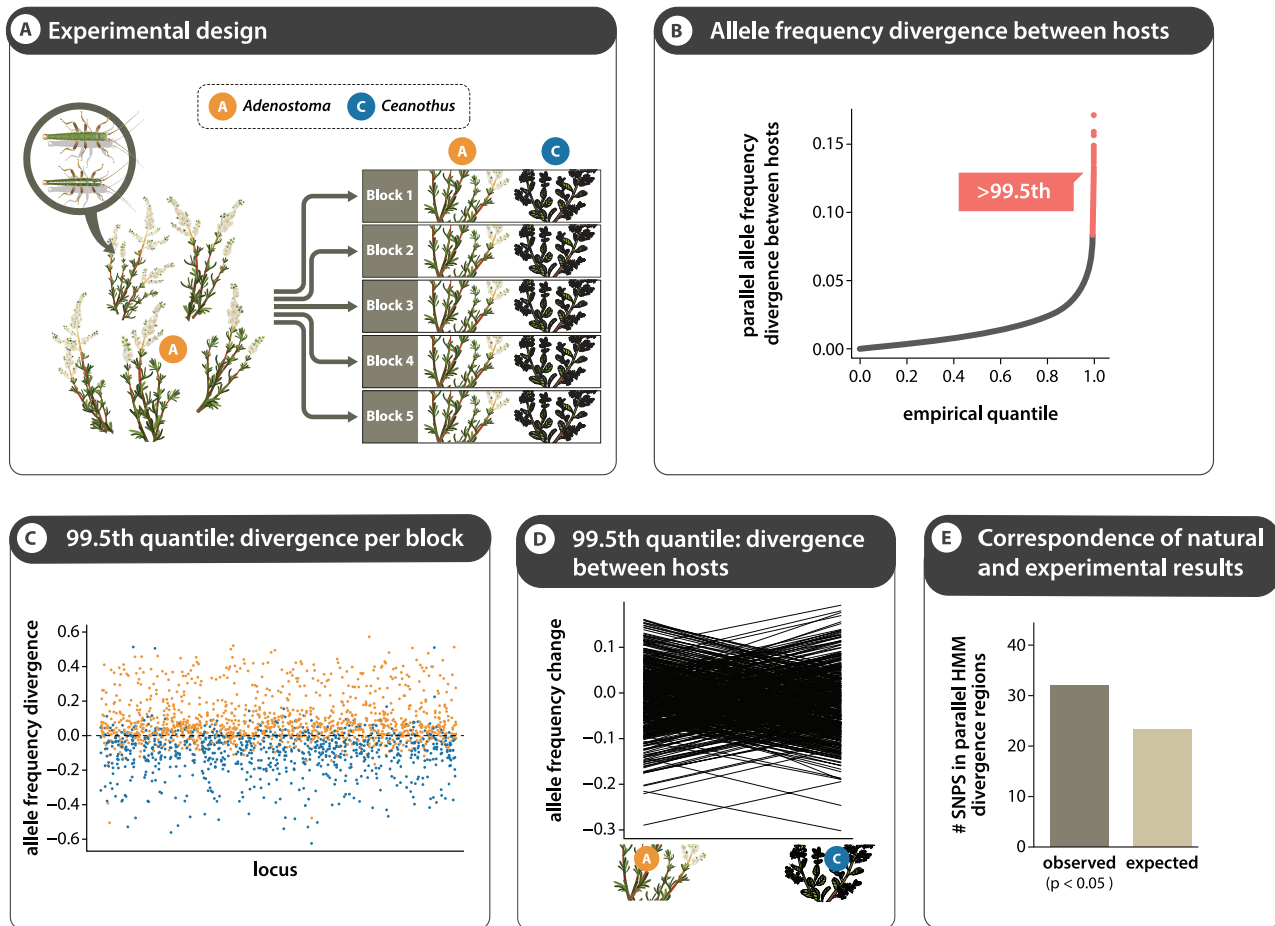
**Fig. 2. Quantification of parallel and nonparallel divergence across population pairs.** (A) The majority of divergent SNPs (those above the 90th quantile of the empirical *F<sub>ST</sub>* distribution) were so only in a single comparison, indicative of largely nonparallel genetic divergence across the genome (pie chart; see table S1 for full results, including those from the 99th quantile). Nonetheless, a significant enrichment of parallelism was observed (bar plots, all *P* < 0.0001, permutation tests of observed versus expected numbers of parallel divergent SNPs). (B) High *F<sub>ST</sub>* in two population pairs. (C) High *F<sub>ST</sub>* in three population pairs. (D) High *F<sub>ST</sub>* in four population pairs. [Credit: courtesy of R. Ribas.]

hereafter). The majority of divergent SNPs (83%) were divergent only in a single population pair. Thus, accentuated divergence was largely nonparallel, supporting repeated and largely independent evolutionary divergence of ecotype pairs in different localities. Nonparallel divergence could

reflect different selective pressures acting on ecotypes in different localities, geographically variable trait genetic architecture, independent genetic drift, or a combination of these factors.

Nonetheless, 17% of divergent SNPs were divergent in two or more population pairs. This





**Fig. 3. Allele frequency changes across the genome in a field transplant experiment.** (A) The experimental design, where individuals from population LA were transplanted to a nearby location of five paired blocks that contained a single plant individual of each host species. (B) An empirical quantile plot of the mean divergence in allele frequencies between hosts for all SNPs. (C) SNPs showing the largest parallel divergence between hosts

(>99.5th quantile) for individual blocks (orange, greater change on *Adenostoma*; blue, greater change on *Ceanothus*). (D) SNPs showing the largest parallel divergence between hosts (>99.5th quantile) averaged across blocks. (E) SNPs showing parallel divergence between hosts in the experiment were in parallel HMM divergence regions between natural population pairs more often than expected by chance ( $P < 0.05$ , randomization test). [Credit: courtesy of R. Ribas.]

degree of parallelism was greater than expected by chance (Fig. 2) (all  $P < 0.001$ , permutation test) and most pronounced for SNPs that were highly divergent in all population pairs [i.e., twofold greater than null expectations; congruent results were obtained for divergent SNPs above the 99th quantile (table S1)]. Last, these SNPs that were divergent in multiple population pairs were in HMM divergence regions that occurred between multiple population pairs more often than expected by chance [all  $P < 0.001$ , randomization test (table S2 and fig. S5)], demonstrating congruence between SNP-based and HMM results. The observed parallelism is consistent with repeatable genetic divergence by natural selection.

Even parallel genetic divergence can be affected by factors other than divergent selection, such as background selection and reduced recombination (2, 11). We thus tested whether HMM divergence regions occurring in multiple population pairs (i.e., parallel HMM divergence regions) harbor SNPs exhibiting divergent allele-frequency changes between multiple experimental population pairs transplanted to different plant species

in the field. In a paired blocks design, we transplanted *T. cristinae* from population LA onto nearby *Ceanothus* and *Adenostoma* plants that were devoid of *T. cristinae* [ $n = 2000$  individuals and 5 blocks (Figs. 1 and 3 and fig. S6)]. There was little or no dispersal after transplantation (19). Thirty-one individuals from LA were not transplanted and preserved as representative “ancestors” of the experimental populations [genomic data from these individuals provide a good representation of genetic variation in LA, particularly given low linkage disequilibrium (16) in this population (fig. S3)]. We collected the first-generation descendants of the transplanted insects 1 year later (these insects feature a single generation per year with a long egg diapause through summer, fall, and winter).

By sequencing these descendants ( $n = 418 F_1$  individuals) and their ancestors ( $n = 31$ ), we observed variable allele frequency changes between hosts across the genome, with most SNPs exhibiting weak to moderate divergence between hosts across a generation (Fig. 3). Numerous SNPs exhibited larger allele frequency changes

between hosts that were remarkably consistent across experimental replicates (i.e., blocks). Thirty-two of the 213 SNPs showing the greatest parallel and divergent allele frequency changes between hosts in the experiment (i.e., those above the 99.5th empirical quantile of such changes) were in parallel HMM divergence regions inferred for natural population pairs, which was more than the 23 expected by chance ( $P < 0.05$ , randomization test). These 32 SNPs were widely distributed across the genome (e.g., found on 32 different scaffolds and 12 of 13 linkage groups). These results are consistent with the hypothesis that parallel HMM divergence regions in natural populations are enriched for loci affected by host-related divergent selection. Our analyses focused on genomic responses to selection, and thus the role of recombination and correlations among loci in such responses warrants future work.

We examined the function of genomic regions exhibiting parallel divergence. We identified the 0.01% of SNPs with the greatest evidence of parallel divergence on the basis of

a metric that combines information on  $F_{ST}$  levels and the direction of allele frequency differences between the four natural population pairs on *Adenostoma* and *Ceanothus* [hereafter referred to as parallel divergence SNPs,  $n = 439$  SNPs; these results are robust to different metrics of parallelism and quantile cutoffs (table S3)]. These parallel divergence SNPs exhibited a 1.5-fold enrichment for being in coding regions of genes compared with expectations from all SNPs (13 and 8%, respectively,  $P < 0.001$ , randomization test), consistent with a role for coding changes even early in speciation.

Gene ontology (GO) analyses revealed that parallel divergence SNPs reside in regions containing genes involved in a range of putative biological processes, including metabolism and signal transduction, and exhibiting various molecular functions [we used GO annotations from the nearest gene on the same scaffold for each parallel divergence SNP (table S4)]. Metal ion binding and calcium ion binding were the two statistically overrepresented molecular functions in regions harboring the parallel divergence SNPs (seven- and threefold enrichment relative to all SNPs,  $P < 0.00001$  and  $P = 0.01$ , respectively, randomization test). Specifically, almost half of the parallel divergence SNPs with molecular function GO annotations (20 of 41 = 48.8%) were in regions harboring genes implicated in metal ion binding, compared with only 6.6% of all SNPs. Consistent with these results from SNPs, the 32 parallel HMM divergence regions associated with parallel divergence in the experiment contained genes related to binding of metals (e.g., iron) and calcium (table S5). Local adaptation to balance the nutritional versus toxic effects of metals has been described in other insects (23), and metals are known to affect traits that differ between the *T. cristinae* ecotypes, such as pigmentation and mandible morphology (24, 25).

Last, we examined the function of SNPs that were divergent between only a single population pair (i.e., nonparallel divergence SNPs,  $n = 440$ ) (19). These SNPs were in regions significantly enriched for genes exhibiting several functions, including one that involved metal binding [i.e., zinc ion binding,  $P < 0.05$ , randomization test (table S6)]. This finding raises the possibility that nonparallel genetic divergence is sometimes the result of adaptive divergence between host ecotypes and that it includes cases of parallelism at the functional level, although further work is required to test these hypotheses.

Our data show that early stages of parallel speciation in *T. cristinae* involve mostly nonparallel genetic divergence between ecotypes. However, numerous regions of the genome have diverged in parallel, and these include more coding genes than expected by chance and harbor loci showing experimentally induced allele frequency changes between hosts. These results indicate that divergent selection plays a role in repeated genomic divergence between ecotypes. Furthermore,

our results suggest that, although repeated evolutionary scenarios (i.e., replaying the tape of life) would likely result in idiosyncratic outcomes, there may be a repeatable component driven by selection that can be detected, even at the genome-wide level and during the complex process of speciation.

## References and Notes

1. D. L. Stern, *Nat. Rev. Genet.* **14**, 751–764 (2013).
2. R. D. H. Barrett, H. E. Hoekstra, *Nat. Rev. Genet.* **12**, 767–780 (2011).
3. M. K. Burke, *Proc. R. Soc. London Ser. B* **279**, 5029–5038 (2012).
4. D. M. Weinreich, N. F. Delaney, M. A. Depristo, D. L. Hartl, *Science* **312**, 111–114 (2006).
5. J. R. Meyer *et al.*, *Science* **335**, 428–432 (2012).
6. J. B. Losos, *Lizards in an Evolutionary Tree: Ecology and Adaptive Radiation of Anoles* (Univ. California Press, Berkeley, CA, 2009).
7. F. C. Jones *et al.*, *Nature* **484**, 55–61 (2012).
8. G. L. Conte, M. E. Arnegard, C. L. Peichel, D. Schluter, *Proc. R. Soc. London Ser. B* **279**, 5039–5047 (2012).
9. Heliconius Genome Consortium, *Nature* **487**, 94–98 (2012).
10. D. Schluter, L. M. Nagel, *Am. Nat.* **146**, 292–301 (1995).
11. J. L. Feder, S. P. Egan, P. Nosil, *Trends Genet.* **28**, 342–350 (2012).
12. H. Ellegren *et al.*, *Nature* **491**, 756–760 (2012).
13. S. H. Martin *et al.*, *Genome Res.* **23**, 1817–1828 (2013).
14. H. Ellegren, *Trends Ecol. Evol.* **29**, 51–63 (2014).
15. P. Nosil, *Am. Nat.* **169**, 151–162 (2007).
16. P. Nosil *et al.*, *Proc. R. Soc. London Ser. B* **279**, 5058–5065 (2012).
17. P. Nosil, B. J. Crespi, C. P. Sandoval, *Nature* **417**, 440–443 (2002).
18. Z. Gompert *et al.*, *Ecol. Lett.* **17**, 369–379 (2014).
19. Materials and methods are available as supplementary materials on Science Online.
20. M. K. N. Lawnczak *et al.*, *Science* **330**, 512–514 (2010).
21. S. Renaud *et al.*, *Nature Commun.* **4**, 1827 (2013).
22. T. Hofer, M. Foll, L. Excoffier, *BMC Genomics* **13**, 107 (2012).
23. T. van Ooik, M. J. Rantala, *Ann. Zool. Fenn.* **47**, 215–222 (2010).
24. J. F. V. Vincent, *Structural Biomaterials* (Princeton Univ. Press, Princeton, NJ, 1990).
25. N. T. Dittmer, M. R. Kanost, *Insect Biochem. Mol. Biol.* **40**, 179–188 (2010).

**Acknowledgments:** The work was funded by the European Research Council (grant R/129639) and Utah State University start-up funds. We thank J. Slate, A. Beckerman, D. Schluter, and two anonymous reviewers for constructive feedback and the High-Throughput Genomics Group at the Wellcome Trust Centre for Human Genetics (funded by Wellcome Trust grant reference 090532/Z/09/Z and Medical Research Council Hub grant G0900747 91070) for generation of the sequencing data. O. Simakov and A. Kapusta provided scripts for transposable elements annotation. The data reported in this paper are tabulated in the supplementary materials and archived at the following databases. The raw sequencing reads are in the NCBI short read archive (BioProject ID: PRJNA243533), and the whole genome assembly and annotation at <http://nosil-lab.group.shef.ac.uk/resources>. Additional data and computer source code have been deposited in the Dryad repository, [datadryad.org](http://datadryad.org), and are also available from the authors upon request. The authors declare no conflicts of interest.

## Supplementary Materials

[www.sciencemag.org/content/344/6185/738/suppl/DC1](http://www.sciencemag.org/content/344/6185/738/suppl/DC1)  
Materials and Methods  
Supplementary Text  
Figs. S1 to S6  
Tables S1 to S6  
References (26–80)

12 February 2014; accepted 18 April 2014  
10.1126/science.1252136

# NMR Spectroscopy of Native and in Vitro Tissues Implicates PolyADP Ribose in Biomineralization

W. Ying Chow,<sup>1</sup> Rakesh Rajan,<sup>2</sup> Karin H. Muller,<sup>3</sup> David G. Reid,<sup>1</sup> Jeremy N. Skepper,<sup>3</sup> Wai Ching Wong,<sup>1</sup> Roger A. Brooks,<sup>2</sup> Maggie Green,<sup>4</sup> Dominique Bihan,<sup>5</sup> Richard W. Farndale,<sup>5</sup> David A. Slatter,<sup>5</sup> Catherine M. Shanahan,<sup>6</sup> Melinda J. Duer<sup>1\*</sup>

Nuclear magnetic resonance (NMR) spectroscopy is useful to determine molecular structure in tissues grown in vitro only if their fidelity, relative to native tissue, can be established. Here, we use multidimensional NMR spectra of animal and in vitro model tissues as fingerprints of their respective molecular structures, allowing us to compare the intact tissues at atomic length scales. To obtain spectra from animal tissues, we developed a heavy mouse enriched by about 20% in the NMR-active isotopes carbon-13 and nitrogen-15. The resulting spectra allowed us to refine an in vitro model of developing bone and to probe its detailed structure. The identification of an unexpected molecule, poly(adenosine diphosphate ribose), that may be implicated in calcification of the bone matrix, illustrates the analytical power of this approach.

Understanding the atomic-level structure of the extracellular matrix (ECM) of tissues is a prerequisite for detailed understanding of both biological and mechanical functions of those tissues. However, while nanoscopic and longer structural length scales can be studied by various forms of microscopy (1–3), there is a

paucity of techniques able to probe atomic-level structures in such complex and heterogeneous materials as the ECM. Multidimensional nuclear magnetic resonance (NMR) spectroscopy is capable in principle of yielding structural information (4–6), even in such a difficult situation, but only if <sup>13</sup>C and <sup>15</sup>N labeling of the molecular

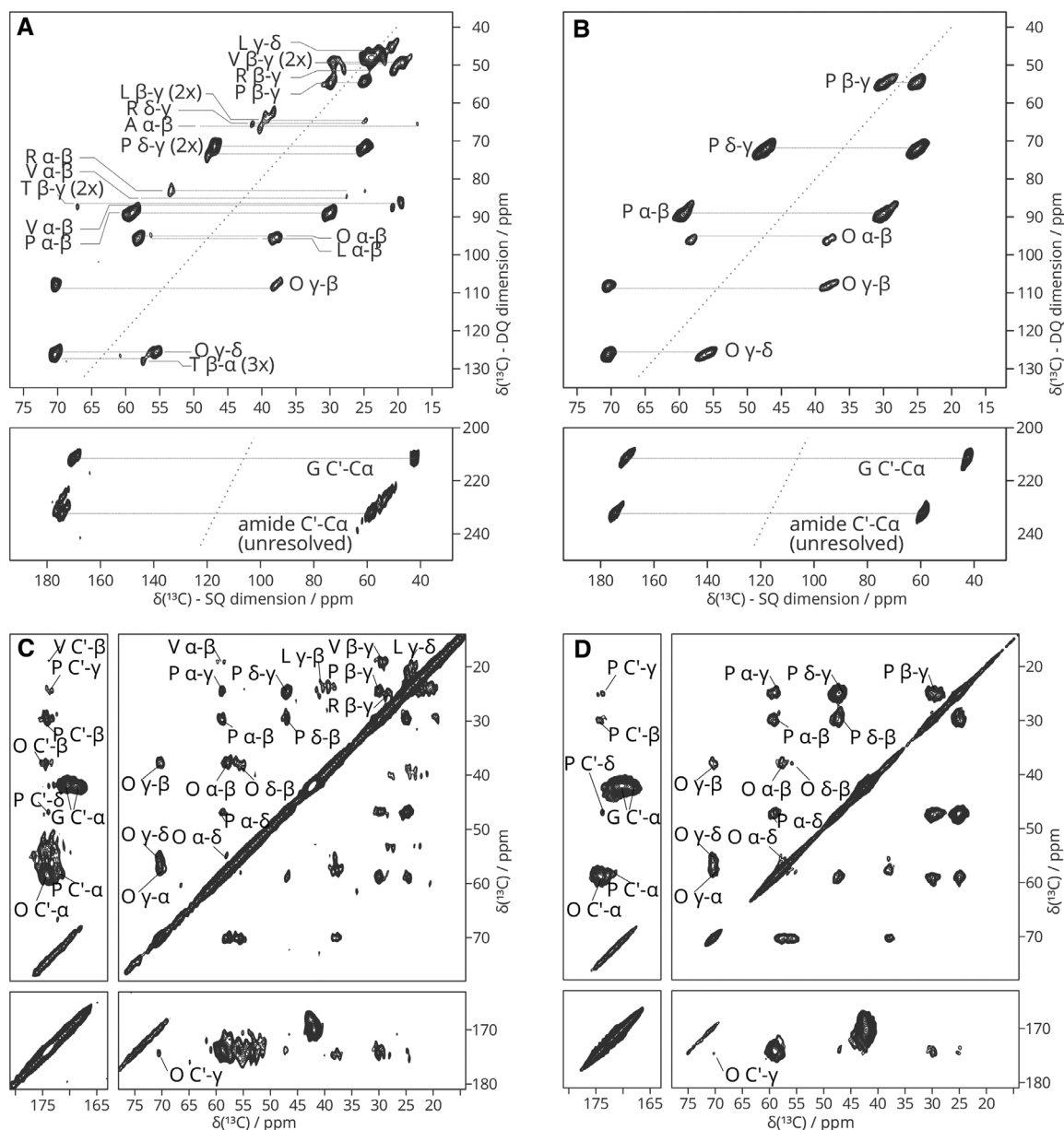
components of interest can be achieved. Specific isotope labeling is difficult *in vivo*, but there are, at least in principle, many more possibilities for such labeling *in vitro*. The problem is that there is no certainty that an *in vitro*-grown tissue will have atomic-level structures representative of

those *in vivo* and, worse, there are currently no ways of directly checking the similarity of *in vivo* and *in vitro* tissues on this length scale. We show here that the structural sensitivity of multidimensional solid-state NMR spectra can solve both of these problems, allowing us to refine as well as validate the atomic structure of an *in vitro* model of developing bone. Probing the atomic structures and composition of the ECM by NMR requires no *a priori* knowledge; this feature, in combination with the feasibility of specific isotope labeling in our *in vitro* model that is not possible *in vivo*, has allowed us to detect the presence of an unexpected sugar species at the calcification front in developing bone that could also be important in pathological calcification.

Our first step was to develop a heavy mouse in which the protein components of its tissues are ubiquitously enriched in  $^{13}\text{C}$  and  $^{15}\text{N}$  (~20%), so

that we could record reference multidimensional NMR spectra of native tissues that act as fingerprints for the underlying molecular structures.  $^{13}\text{C}$ -enriched collagen has previously been produced through feeding with single isotope-enriched amino acids ( $1\text{-}^{13}\text{C}$ -Gly,  $^{15}\text{N}$  Gly, and Pro-2- $d_2$ ) (7, 8), and  $^{15}\text{N}$  enrichment of tissues is now common practice for quantitative mass spectroscopy. Here, though, we require enrichment of many amino acid types with both  $^{13}\text{C}$  and  $^{15}\text{N}$ , so our protocol took account of the fact that isotope-labeling may adversely affect metabolism. It resulted in a mouse with significant isotopic enrichment of all collagenous tissues. (See the supplementary materials for a description of materials and methods.) These tissues allowed high-quality two-dimensional (2D)  $^{13}\text{C}$ - $^{13}\text{C}$  and  $^{13}\text{C}$ - $^{15}\text{N}$  correlation spectra to be recorded on intact tissues (Fig. 1), without need for further

**Fig. 1. 2D solid-state NMR (ssNMR) spectra of labeled mouse bone and *in vitro* ECM.**  $^{13}\text{C}$ - $^{13}\text{C}$  DQ-SQ correlation spectra from mouse calvarial bone (A) and *in vitro* fetal ovine osteoblast ECM cultured in the presence of U- $^{13}\text{C}$  Gly, Pro (B) (spinning rate, 10 kHz; mixing sequence, 14 POST-C7 blocks). The dotted line indicates the double-quantum diagonal.  $^{13}\text{C}$ - $^{13}\text{C}$  PDSQ correlation spectra from bone (C) and osteoblast ECM as in (B) (spinning rate, 10 kHz; mixing time, 20 ms) (D). These spectra are symmetric about the diagonal, and hence only half the observed signals are labeled. Other signals are not visible at the current displayed contour level but are shown in fig. S1 and listed and assigned in table S1.





sample preparation. For example, in mouse calvarial bone, ~20% of amino acid residues incorporated are fully  $^{13}\text{C}$ ,  $^{15}\text{N}$ -labeled.

As shown in Fig. 1, two different NMR spectral analyses were performed on each tissue sample:

(i)  $^{13}\text{C}$ - $^{13}\text{C}$  double-quantum–single-quantum (DQ-SQ) spectrum (9) (Fig. 1A), which consists of pairs of  $^{13}\text{C}$  signals from pairs of close, i.e., bonded, carbons (within 2 Å) in the so-called SQ spectral dimension, which are centered at the sum of their respective signal frequencies in the DQ dimension. This type of spectrum resolves the detailed  $^{13}\text{C}$  chemical shift distributions for each carbon signal; in turn, the chemical shift distribution reflects the distribution of molecular geometries present in the sample.

(ii)  $^{13}\text{C}$ - $^{13}\text{C}$  proton-driven spin diffusion (PDS) spectrum (Fig. 1C), which correlates pairs of  $^{13}\text{C}$  spins via through-space dipolar coupling (10), potentially allowing correlations between more distant (up to ~10 Å) carbon pairs than the DQ-SQ spectrum to be observed.

Two-dimensional  $^{13}\text{C}$ - $^{15}\text{N}$  spectrum can also be recorded on these tissues, giving  $^{15}\text{N}$  chemical shift distributions and their correlation with those of neighboring  $^{13}\text{C}$  sites (fig. S1).

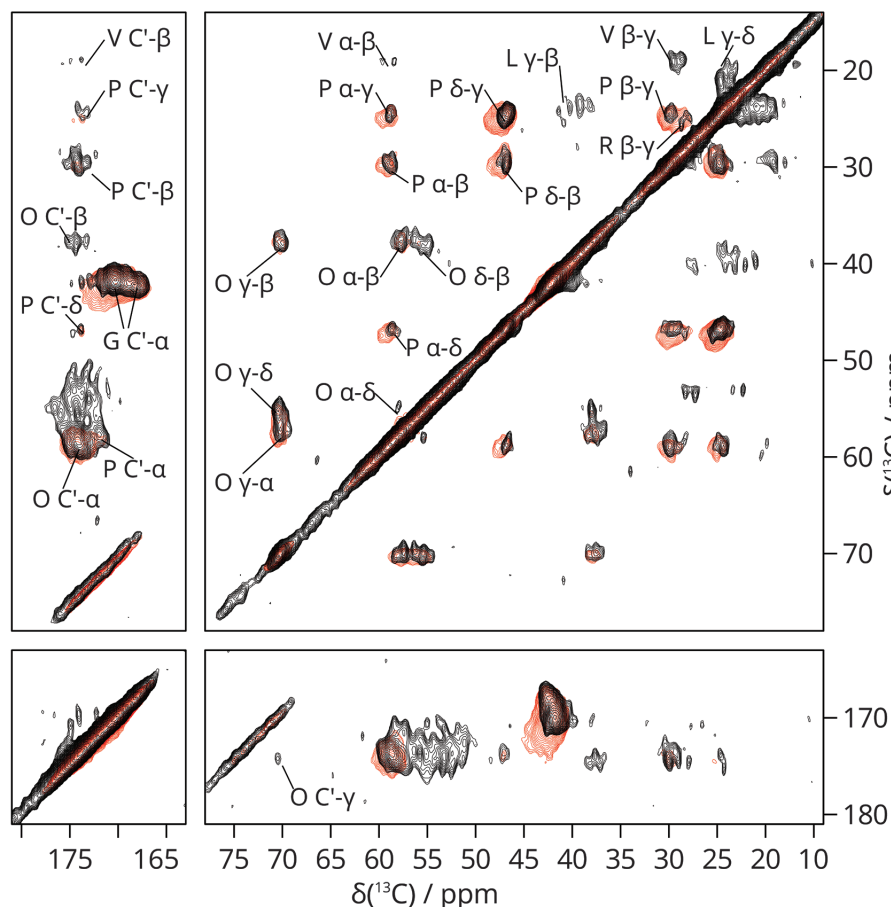
The fibril-forming collagens that are the major component of mammalian tissues are trimeric triple-helical proteins consisting of G-X-Y repeats, where X is often proline (Pro, P) and Y hydroxyproline (Hyp, O), a collagen-specific post-translational modification. Collagen signals, in particular those from Gly, Pro, and Hyp, dominate all our heavy mouse tissue correlation spectra.

The DQ-SQ spectrum (Fig. 1A) allows resolution of signals that were previously overlapped in 1D spectra of pure collagen (11), enabling measurement of separate  $^{13}\text{C}$  signals for Pro Ca [59.1 parts per million (ppm)] and Hyp Ca (57.8 ppm). The DQ-SQ spectrum further allows resolution and assignment of  $^{13}\text{C}$  signals for almost all amino acid types in collagen (see fig. S1C and table S1). It is to be noted that the  $^{13}\text{C}$  chemical shifts of all the main-chain carbons are considerably lower than generally found for the same residues in other proteins; these low chemical shifts are diagnostic of the collagen triple helical motif and occur because the  $^{13}\text{C}$  chemical shift is highly sensitive to local molecular geometry, i.e., to peptide dihedral angles (5) and chemical bonding as well as primary sequence (12). As well as resolving the full  $^{13}\text{C}$  chemical shift distribution for each amino acid residue type, the DQ-SQ spectrum displays the correlations between the chemical shift distributions of neighboring carbon atoms and so serves as a sensitive monitor of the detailed local environments for each residue type in the collagen structure. For instance, the glycine  $\text{C}_\alpha$  and  $\text{C}'$  signals in the DQ-SQ spectrum each show a distribution of chemical shifts, and these are linearly correlated with each other as indicated in Fig. 1A; each pair of correlated  $\text{C}_\alpha$  and  $\text{C}'$  Gly chemical shifts within this distribution represents a particular molecular Gly microenvironment, the relative intensity of the correlation indicating the relative

abundance of that molecular microenvironment in the overall protein structure.

These 2D NMR spectra thus represent “fingerprints” of the underlying atomic structures within the native mouse tissue. Our second step is to use these fingerprints to determine the fidelity of an in vitro bone model. In vitro tissue was grown from low-passage fetal sheep primary osteoblasts in medium containing U- $^{13}\text{C}$ ,  $^{15}\text{N}$ -labeled glycine and proline and 2D NMR correlation spectra recorded as above. [This results in the hydroxyprolines (posttranslationally modified from prolines) also being  $^{13}\text{C}$  and  $^{15}\text{N}$  enriched, so that more than 50% of the total amino acid residues in the collagens are likely to be labeled.] Comparison of these spectra with those from the heavy mouse bone tissue allowed an immediate assessment of the similarity of the atomic structures between the in vitro and in vivo tissues. Detailed comparison indicated in what respects the two tissues differed on the atomic length scale and so suggested ways of improving the cell culture protocol, generating the in vitro tissue to produce more native-like tissue. The main spectral differences are some signal intensity to the high-frequency side of the Pro, Hyp,

and Gly signals for the in vitro tissue that are lacking for native tissue (fig. S2A). The higher frequency of these signals indicates that they are from residues not in a collagen triple-helical motif. The signals are more intense after the sample has been sonicated (fig. S2B) and therefore most likely arise from Pro, Hyp, and Gly in unfolded or misfolded collagen-like proteins or fragments, which is consistent with their higher chemical shift values. These signals were reduced by minimizing the shear stress on the cells in culture while they were laying down ECM, by reducing the frequency of culture medium renewal and minimizing disturbance of the cells during this process (fig. S2, C and D). The in vitro tissue was judged to be optimal when the 2D spectra showed a high degree of similarity to those of the native mouse tissue (Fig. 1, B and D), indicating that the molecular geometries in the two tissues are very similar. Furthermore, scanning electron microscopy (SEM) of the optimized in vitro ECM (to examine nanoscale structure) showed a highly organized matrix of parallel fibrils, similar to native bone (fig. S3, A and B), and atomic force microscopy (AFM) showed correct assembly of triple helices into the characteristic



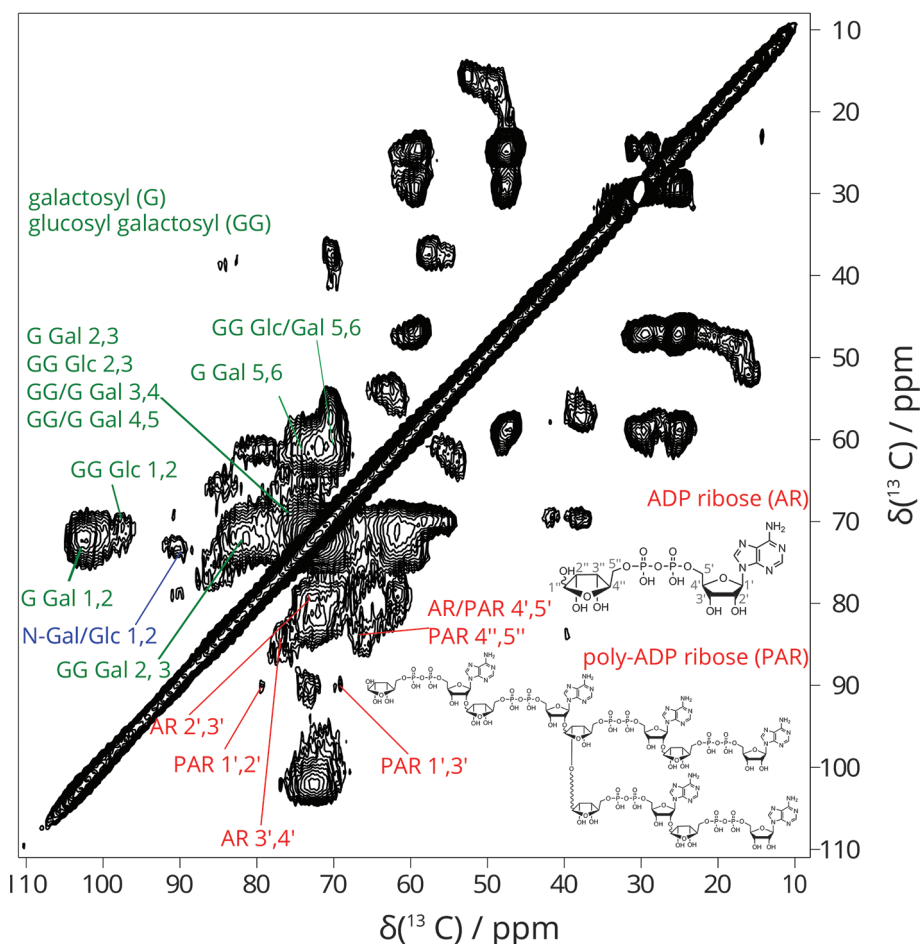
**Fig. 2. Overlay of ssNMR PDS spectra for in vivo and in vitro tissues, highlighting spectral regions where they differ.** PDS spectra of labeled mouse calvarial bone (black) and in vitro fetal ovine osteoblast ECM (red) cultured in the presence of U- $^{13}\text{C}$  Gly, Pro. Differences between the spectra in the range of chemical shift values shown in the red spectrum are likely to arise from unfolded or misfolded proteins in the in vitro sample (see also fig. S2A).

67-nm banded fibril (fig. S3C) and, based on these results, would also be judged as representative of native tissue at a nanoscopic level. There is still

some signal from unfolded or misfolded collagen proteins in the optimized tissue (Fig. 2). Such species may cause deleterious immune responses in

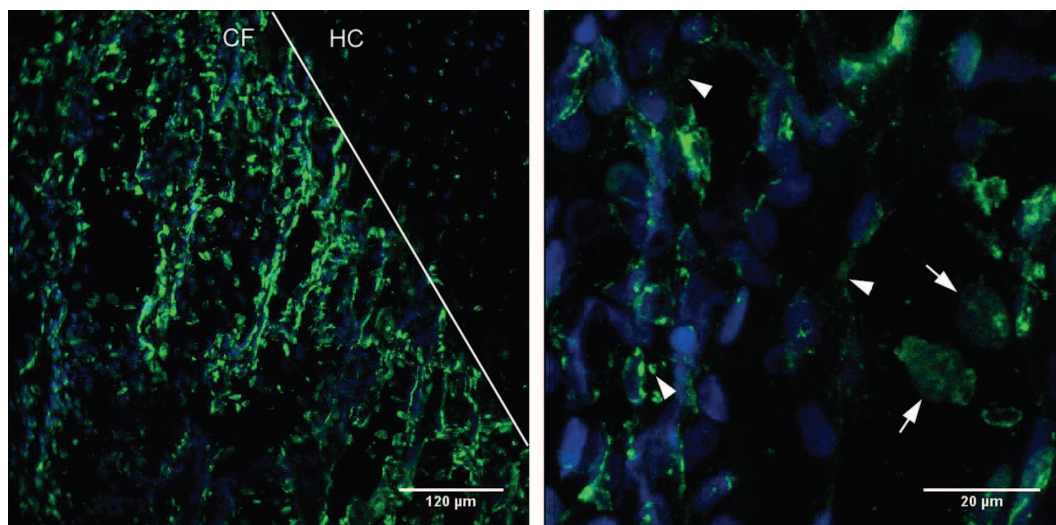
tissue grown in vitro for implants, for instance, so knowledge of their presence is important. These species cannot be detected by microscopy without a suitable immune label and, by implication, a priori knowledge of these species, nor would such proteins be expected to affect the collagen fibril structure; thus, they would not be apparent under SEM or AFM.

Our refined in vitro tissue model allows us to study the sugar components of a tissue as well as the collagen proteins. The sugars in matrix glycoproteins and proteoglycans are essential parts of the ECM structure—collagen glycosylation, for instance, is necessary for proper fibril formation—yet atomic structures of sugars in intact tissue are understudied in comparison to proteins, largely because of a lack of methods to probe them. Moreover, we have previously shown that a sugar species yet to be identified is important in the organic-inorganic interface in bone (13), so we decided to monitor the sugar species present in developing bone and examine how far collagen glycosylation might be involved in the organic-inorganic interface. Isotope-enriching tissue sugars in an animal model would be extremely challenging because sugars are rapidly metabolized, but it is feasible in our in vitro model. Thus, our next step was to generate  $^{13}\text{C}$  enrichment of the sugar species in our in vitro ECM, achieved by addition of  $\text{U-}^{13}\text{C}$ -glucose to the cell culture medium. This procedure resulted in extensive  $^{13}\text{C}$  enrichment of collagen glycosylations (14), which were assigned using typical chemical shifts for the expected glycosylation products of collagen type I supported by information from spectral through-space correlations (Fig. 3A), plus the spectra in figs. S4 to S8, as detailed in tables S3 and S4. The molecular species previously identified at the organic-inorganic interface in bone have signals in the range 72 to 78 ppm (and include a component from mineral-associated citrate at ~76 ppm). Moreover, it has been shown that all of these signals are due to carbons closer in space to phosphorus (and, by implication, mineral phosphate) than collagen protein



**Fig. 3. Identifying PAR in our in vitro model of developing bone.**  $^{13}\text{C}$ - $^{13}\text{C}$  PDS correlation spectrum of in vitro fetal sheep osteoblast ECM grown in the presence of  $\text{U-}^{13}\text{C}$ -glucose, Gly, and Pro. Signals assigned: O-linked galactosyl (G), O-linked glucosyl galactosyl (GG), both native collagen glycosylation species (green labels, structures not shown). The remaining signals are assigned to glycation species (blue labels, structures not shown) and ribosyl phosphate species (red labels). (Inset) The structures of ADP ribose (AR) and PAR.

**Fig. 4. Immunostaining of fetal sheep growth plate shows the presence of PAR.** Maximum intensity projection of Z stacks. Frozen tissue sections of fetal sheep bone growth plate were stained for nuclei (Hoechst staining, blue) and PAR (clone 10H antibody to PAR, green). (Left) The white line marks the boundary between the zone of hypertrophic cartilage (HC) and the calcification front (CF). Strong PAR staining is visible in the CF, whereas the adjoining zone of HC is stained weakly. (Right) In the CF, some PAR staining is colocalized with Hoechst in the nuclei (arrowheads). In addition, PAR staining is also found in the cytoplasm and probably the extracellular space (arrows).





carbons (fig. S9) (13, 15). The spectrum in Fig. 3A shows that the main signal intensity from the collagen glycosylation here occurs between 72 and 75 ppm; thus, we conclude that collagen glycosylation species are predominantly closer to mineral crystals in bone than is the collagen protein itself. Because the mineral crystals in bone are close-packed between the collagen fibrils (16), this implies that the collagen glycosylation must lie between the collagen fibrils and mineral crystals—i.e., that the collagen glycosylation must lie predominantly on the collagen fibril surfaces. However, there is further signal intensity due to carbons close in space to phosphorus in bone, in particular a weaker signal at ~66 ppm, as shown in fig. S9 and elsewhere (13, 15). There is a broad signal at ~66 ppm in our 2D correlation spectra, but it does not correlate with any signals from collagen glycosylation carbons; furthermore, we noted that there were other signals in the sugar region of the  $^{13}\text{C}$  2D correlation spectra (Fig. 3A) not assignable to collagen glycosylation, nonenzymatic protein glycation, or typical tissue proteoglycans. Detailed analysis of the signal frequencies and their correlations in 2D  $^{13}\text{C}$ - $^{13}\text{C}$  PDS and DQ-SQ correlation spectra (Fig. 3B) show that these correspond closely to the signals that might be expected for poly[adenosine diphosphate (ADP) ribose] (PAR) and ADP ribose (ADPR) (assignment in tables S6 and S7 and figs. S10 and S11). If these signals are indeed from such species, then they must be in an extracellular environment, because all cells have been removed from the in vitro ECMs before the NMR experiments, as verified by SEM. Furthermore, they must be immobilized in the ECM to give signals in the correlation spectra and sufficiently well bound not to be removed by repeated washing during sample preparation.

PAR is a post-translational modification of cellular, particularly nuclear, proteins and is involved in DNA repair and the regulation of cell survival and death. Neither PAR nor ADPR have been previously reported as components of the ECM, nor to the best of our knowledge has there been any suggestion that they might exist in, or form persistent attachments to, the ECM. The largely nuclear role documented to date for these species meant that their presence in our in vitro tissue was unexpected. Accordingly, we examined an ex vivo model of developing bone, fetal sheep growth plate, for the presence of PAR by staining and confocal laser fluorescence microscopy (Fig. 4). The images in Fig. 4 show the presence of substantial quantities of PAR in the calcifying region of the growth plate in comparison with the adjoining unmineralized hypertrophic cartilage. The PAR appears both in close proximity to cell nuclei, i.e., intracellular, and in regions where there are no cell nuclei, i.e., presumably extracellular. Thus, its presence in our in vitro tissue models has been confirmed in a comparable native tissue model.

PAR is generated in cells from nicotinamide adenine dinucleotide ( $\text{NAD}^+$ ) by PAR polymer-

ase (PARP) enzymes (17, 18). Overactivation of PARPs leads to cellular ATP and  $\text{NAD}^+$  depletion and drives cell necrosis (17, 19). Osteoblast necrosis is an essential part of bone mineralization in vivo (20), with 65 to 85% of bone osteoblasts suffering this fate within mineralizing zones (21). Osteoblast necrosis is thought to be necessary to make space for the forming mineral crystals, but our results here suggest it may have an additional purpose. Cell necrosis results in release of cell contents into the surrounding ECM, and this process is presumably how PAR ends up in the ECM in developing bone. That PAR binds to the ECM at the same time as the matrix is beginning to mineralize is potentially important. The charged pyrophosphate groups of PAR have high calcium affinity, and its polymeric structure makes it a candidate as a scaffold for mineral formation. Moreover, PAR has a binding affinity for collagen type XII (22), a FACIT (fibril-associated collagens with interrupted triple helices) collagen that decorates the surface of collagen type I fibrils, the majority collagen type in bone; because it is between such fibrils that the bulk of bone mineral forms, we conclude that bound PAR can also be in the right place to act as a scaffold for mineral formation. Furthermore, previous work has shown that if organic phosphate esters are removed from demineralized bone, the bone cannot be remineralized (23), which suggests that the species responsible for nucleating bone mineral crystals has been removed by this process. The organic phosphate esters concerned have been assumed to be phosphorylated proteins, but our work shows that there is another possible species, namely the PAR polysaccharide. Other work has shown that polyanions such as polyaspartate can induce biomimetic mineralization of collagen matrices by stabilizing a mineral precursor phase (24, 25), but no such polyanion has yet been reported in the context of native bone ECM. PAR, however, fits the description. Moreover, we have previously shown that the same distribution of sugar species at the organic-inorganic interface in bone occurs in pathological calcification in arteries as well (26), and cell death and necrosis always precedes these pathologies (27), so PAR may be a feature in pathological calcification also.

In conclusion, NMR comparisons of  $^{13}\text{C}$ ,  $^{15}\text{N}$ -enriched in vivo and in vitro tissues allows the fidelity of the atomic structure of the in vitro model to be ascertained. Our first application of a dual in vivo-in vitro NMR-based approach toward understanding the atomic structures of tissues has led to the identification of a molecule in the ECM of developing bone likely to be relevant to matrix calcification and capable of binding mineral to the collagen matrix. This molecule, PAR, is more commonly associated with nuclear proteins but most likely to be present in the ECM of forming bone due to cell necrosis associated with bone development. PAR may also be relevant to the initiation of pathological vascular calcification, which we have previously shown involves similar sugar species to those

in bone (26). In addition, having the ability to understand differences between an in vitro and in vivo tissue in terms of their respective molecular structures—here, the presence of misfolded collagen proteins in the in vitro tissue—raises the possibility of more rational refinement of in vitro tissue models.

## References and Notes

1. S. Weiner, H. D. Wagner, *Annu. Rev. Mater. Sci.* **28**, 271–298 (1998).
2. S. Bertazzo, T. von Erlach, S. Goldoni, P. L. Çandarlıoğlu, M. M. Stevens, *Nanoscale* **4**, 2851–2854 (2012).
3. W. Denk, H. Horstmann, *PLoS Biol.* **2**, e329 (2004).
4. D. S. Wishart, B. D. Sykes, *J. Biomol. NMR* **4**, 171–180 (1994).
5. S. Spera, A. Baj, *J. Am. Chem. Soc.* **113**, 5490–5492 (1991).
6. A. Böckmann, *C. R. Chim.* **9**, 381–392 (2006).
7. S. K. Sarkar, C. E. Sullivan, D. A. Torchia, *J. Biol. Chem.* **258**, 9762–9767 (1983).
8. D. A. Torchia, Y. Hiyama, S. K. Sarkar, C. E. Sullivan, P. E. Young, *Biopolymers* **24**, 65–75 (1985).
9. M. Hohwy, H. J. Jakobsen, M. Edén, M. H. Levitt, N. C. Nielsen, *J. Chem. Phys.* **108**, 2686–2694 (1998).
10. N. M. Szeverenyi, M. J. Sullivan, G. E. Maciel, *J. Magn. Reson.* **47**, 462–475 (1982).
11. A. E. Aliev, *Biopolymers* **77**, 230–245 (2005).
12. D. S. Wishart, C. G. Bigam, A. Holm, R. S. Hodges, B. D. Sykes, *J. Biomol. NMR* **5**, 67–81 (1995).
13. E. R. Wise *et al.*, *Chem. Mater.* **19**, 5055–5057 (2007).
14. R. G. Spiro, *J. Biol. Chem.* **244**, 602–612 (1969).
15. O. Nikel *et al.*, *J. Phys. Chem. C. Nanomater. Interfaces* **116**, 6320–6331 (2012).
16. E. A. McNally, H. P. Schwarcz, G. A. Botton, A. L. Arsenault, *PLoS ONE* **7**, e29258 (2012).
17. P. Jagtap, C. Szabó, *Nat. Rev. Drug Discov.* **4**, 421–440 (2005).
18. A. Hakmé, H.-K. Wong, F. Dantzer, V. Schreiber, *EMBO Rep.* **9**, 1094–1100 (2008).
19. H. C. Ha, S. H. Snyder, *Proc. Natl. Acad. Sci. U.S.A.* **96**, 13978–13982 (1999).
20. B. Zimmermann, *Cell Tissue Res.* **275**, 345–353 (1994).
21. S. C. Manolagas, *Endocr. Rev.* **21**, 115–137 (2000).
22. J.-P. Gagné *et al.*, *Nucleic Acids Res.* **40**, 7788–7805 (2012).
23. M. J. Glimcher, *Anat. Rec.* **224**, 139–153 (1989).
24. L. B. Gower, *Chem. Rev.* **108**, 4551–4627 (2008).
25. A. Dey *et al.*, *Nat. Mater.* **9**, 1010–1014 (2010).
26. M. J. Duer *et al.*, *Arterioscler. Thromb. Vasc. Biol.* **28**, 2030–2034 (2008).
27. F. Otsuka, K. Sakakura, K. Yahagi, M. Joner, R. Virmani, *Arterioscler. Thromb. Vasc. Biol.* **34**, 724–736 (2014).

**Acknowledgments:** The authors appreciate advice from M. Norman and J. Keeley; technical support from S. Thomas and R. Westwood (Central Biological Services, University of Cambridge); helpful interactions with D. Martel (SAFE, Augy, France); and advice and assistance with AFM from R. Oliver and C. Grover (University of Cambridge). The authors acknowledge funding from BBSRC for D.A.S., D.G.R. (BB/G021392/1), M.J.D., R.R., and R.W.F.; from BHF for D.A.S. and R.W.F. (PG/08/011/24416), K.H.M. (PG/10/43/28390), M.J.D., J.N.S., and C.M.S.; from EPSRC for W.Y.C. and W.C.W.; from MRC for D.B. and R.W.F. (G0500707); and from the National Institute of Health Research for R.A.B.

## Supplementary Materials

www.sciencemag.org/content/344/6185/742/suppl/DC1  
Materials and Methods  
Supplementary Text  
Figs. S1 to S11  
Tables S1 to S6  
References (28–52)

6 November 2013; accepted 9 April 2014  
10.1126/science.1248167



# Genomic Diversity and Admixture Differs for Stone-Age Scandinavian Foragers and Farmers

Pontus Skoglund,<sup>1\*</sup>† Helena Malmström,<sup>1\*</sup> Ayça Omrak,<sup>2</sup> Maanasa Raghavan,<sup>3</sup> Cristina Valdiosera,<sup>4</sup> Torsten Günther,<sup>1</sup> Per Hall,<sup>5</sup> Kristiina Tambets,<sup>6</sup> Jüri Parik,<sup>6</sup> Karl-Göran Sjögren,<sup>7</sup> Jan Apel,<sup>8</sup> Eske Willerslev,<sup>3</sup> Jan Storå,<sup>2</sup> Anders Götherström,<sup>2,†</sup> Mattias Jakobsson<sup>1,9,†</sup>

Prehistoric population structure associated with the transition to an agricultural lifestyle in Europe remains a contentious idea. Population-genomic data from 11 Scandinavian Stone Age human remains suggest that hunter-gatherers had lower genetic diversity than that of farmers. Despite their close geographical proximity, the genetic differentiation between the two Stone Age groups was greater than that observed among extant European populations. Additionally, the Scandinavian Neolithic farmers exhibited a greater degree of hunter-gatherer-related admixture than that of the Tyrolean Iceman, who also originated from a farming context. In contrast, Scandinavian hunter-gatherers displayed no significant evidence of introgression from farmers. Our findings suggest that Stone Age foraging groups were historically in low numbers, likely owing to oscillating living conditions or restricted carrying capacity, and that they were partially incorporated into expanding farming groups.

The impact of the adoption of agriculture in Europe—the Neolithic transition—has long been debated in archaeology (1) and was one of the first historical questions to be addressed by population geneticists (2). There are contrary schools of thought of the relative importance of migration versus cultural diffusion as the Neolithic lifestyle dispersed across Europe. Farming appeared in the Near East at least 10,000 years before present (B.P.) and spread into Europe via the Balkan and Mediterranean regions, arriving in Scandinavia ~6000 years B.P. (3). Analyses of mitochondrial DNA (4–6) and genomic sequences (7–9) from Stone Age human remains provide evidence that farming and foraging groups were genetically distinct and that admixture between these groups played a role in forming the genetic landscape of modern-day Europe. However, most studies so far have focused on the comparison of ancient individuals to recent groups, and the degree of direct genetic relatedness between ancient groups, gene flow, and within-group genomic variation remains unaddressed.

We generated between 0.01- and 2.2-fold genome-wide coverage for six Neolithic hunter-gatherers from the Pitted Ware Culture context (PWC), four Neolithic farmers from the Funnel Beaker culture context (TRB), and one late Mesolithic hunter-gatherer (Table 1). All of the Neolithic individuals were excavated in Sweden and were dated either directly or contextually to ~5000 years B.P. The late Mesolithic hunter-gatherer individual, directly dated to ~7500 years B.P., was excavated in Sweden in close proximity to the Neolithic hunter-gatherers. All generated sequence data showed evidence of nucleotide misincorporations (figs. S1 to S3) characteristic of postmortem degradation.

The mitochondrial genome was covered to an average depth of at least 23-fold for seven of the individuals, and estimates of contamination were low (Table 1). All six Neolithic hunter-gatherers and the late Mesolithic hunter-gatherer were assigned to haplogroups U or V (Table 1), similar to other Mesolithic and Paleolithic hunter-gatherers (4, 8, 10). The four TRB individuals were assigned to haplogroups H and K, similar to previous results (5) and as observed in other Neolithic farmers in Europe

(6). The Y chromosome of the Ajvide58 individual (Neolithic hunter-gatherer) was assigned to haplogroup I2a1 (table S5), a specific subhaplogroup uncommon in current-day Scandinavia (11). Recent studies suggest that variants associated with phenotypes and immune system genes differ between Stone Age hunter-gatherers and farmers, often from ancestral to derived variants (8, 9). However, we found little evidence of differentiation for these variants (tables S6 to S10) between Neolithic Scandinavian hunter-gatherers and farmers, except for the SLC24A5 locus involved in pigmentation. Ajvide58, like the Mesolithic Iberian LaBran1 (8), carried the ancestral allele, and both the Tyrolean Iceman (9) and Gökhem2 carried the derived allele (table S8), which is associated with light pigmentation and nearly fixed in current-day Europe and common in current-day South Asia (12).

To investigate the ancient individuals' relationship to the modern-day genetic landscape, we used principal component (PC) analysis with a set of 57 Western Eurasian populations (table S11), including individuals across modern-day Sweden, and projected the 11 Scandinavian Stone Age individuals together with the Mesolithic Iberian LaBran1 (8), the Paleolithic Siberian MA1 (13), and the Chalcolithic (~5300 years B.P.) Tyrolean Iceman (Fig. 1A) (9). All six Neolithic hunter-gatherers clustered outside the variation

<sup>1</sup>Department of Evolutionary Biology, Uppsala University, Uppsala 752 36, Sweden. <sup>2</sup>Department of Archaeology and Classical studies, Stockholm University, Stockholm 106 91, Sweden. <sup>3</sup>Centre for GeoGenetics, Natural History Museum of Denmark, University of Copenhagen, Copenhagen 1350, Denmark. <sup>4</sup>Department of Archaeology, Environment and Community Planning, La Trobe University, Melbourne VIC 3086, Australia. <sup>5</sup>Department of Medical Epidemiology and Biostatistics, Karolinska Institutet, Stockholm 171 77, Sweden. <sup>6</sup>Evolutionary Biology Group, Estonian Biocentre and University of Tartu, Tartu 51010, Estonia. <sup>7</sup>Department of Historical Studies, University of Gothenburg, Gothenburg, 405 30, Sweden. <sup>8</sup>Department of Archaeology and Ancient History, Lund University, Lund, 221 00, Sweden. <sup>9</sup>Science for Life Laboratory, Uppsala University, Uppsala 752 36, Sweden.

\*These authors contributed equally to this work.

†Present address: Department of Genetics, Harvard Medical School, Boston, MA 02115, USA.

‡Corresponding author. E-mail: tsarapkin@googlemail.com (A.G.); mattias.jakobsson@ebc.uu.se (M.J.)

**Table 1. Ancient genomic sequence data.** Only sequences with mapping quality of at least 30 were used. mtDNA, mitochondrial DNA; hg, haplogroup; Contam., Contamination estimate; CI, confidence interval; cal years BP, calibrated years BP. Dashes indicate no reliable estimate.

Sample	Context	Genome coverage	mtDNA coverage	mtDNA hg	Contam. (95% CI)	Source	Age (cal years B.P.)*	Genetic sex
StoraFörvar11	Mesolithic	0.09	25.6	U5a1	0 to 22.2%	This study	7500 to 7250	Male
Ajvide52	PWC	0.09	49.4	V	0 to 3.7%	This study and (7)	4900 to 4600	Male
Ajvide53	PWC	0.03	2.5	U4d	—	This study	4900 to 4600	Female
Ajvide58	PWC	2.22	161.7	U4d	0 to 0.6%	This study	4900 to 4600	Male
Ajvide59	PWC	0.01	1.3	U	—	This study	4900 to 4600	Male
Ajvide70	PWC	0.16	52.5	U4d	1.5 to 7.7%	This study and (7)	4900 to 4600	Male
Ire8	PWC	0.04	43.2	U4d	1.6 to 9.6%	This study and (7)	5100 to 4150	Male
Gökhem2	TRB	1.33	91.9	H1c	0 to 2.7%	This study	5050 to 4750	Female
Gökhem4	TRB	0.04	6.5	H	0 to 25.9%	(7)	5280 to 4890	Male
Gökhem5	TRB	0.02	26.2	K1e	0 to 4%	This study	5050 to 4750	Female
Gökhem7	TRB	0.01	32.8	H24	0 to 7.6%	This study	5050 to 4750	Female

\*Details and references for the radiocarbon dating can be found in (17).

of modern populations, which is consistent with a previous study (7). The Mesolithic Scandinavian and the Mesolithic Iberian sample also clustered together in this PC space, which is consistent with population continuity from late Mesolithic groups to Neolithic Scandinavian hunter-gatherers. The Mesolithic and the Scandinavian Neolithic hunter-gatherers do not cluster particularly close to any individuals self-identifying as Swedish Saami (14) or indigenous populations from central Russia. All Scandinavian farmer individuals clustered among southern and central European populations.

To test whether the North-South difference between farmers and hunter-gatherers was consistent for different individuals from each cultural context, we examined which modern-day population had the greatest genetic affinity to particular ancient individuals by identifying the modern-day population with the greatest shared genetic drift with each ancient individual using an outgroup  $f_3$ -statistic (13, 15). The greatest shared genetic drift with Ajvide58 was observed for Lithuanians, whereas the greatest shared genetic drift with Gökhem2 was

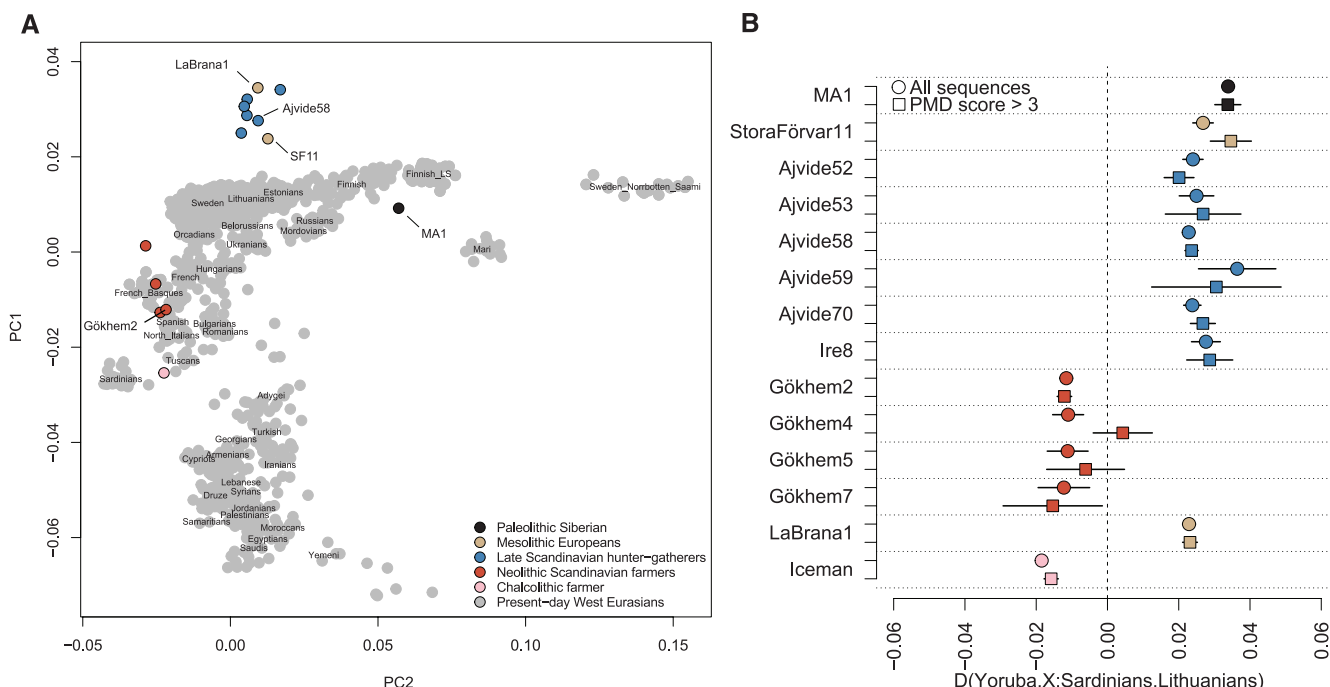
observed for Sardinians (Fig. 1, C and D). Both of these higher-coverage Neolithic individuals show negligible levels of contamination (Table 1).

We also computed  $D$ -statistics (15) to test whether each single Stone Age individual was closer to Lithuanians or Sardinians and found statistically significant segregation between all Stone Age farmers and hunter-gatherers (Fig. 1B); we found the same results when we restricted the analyses to sequences that displayed clear evidence of postmortem damage (16). Focusing on modern-day Swedish groups, which are intermediate to the two Scandinavian Neolithic groups (7), direct tests indicate that modern-day Swedish populations are closer to Ajvide58 (table S14). In addition to Sardinians, many current-day groups from the Near East and southern Europe are significantly closer to Gökhem2 than to Ajvide58 (17).

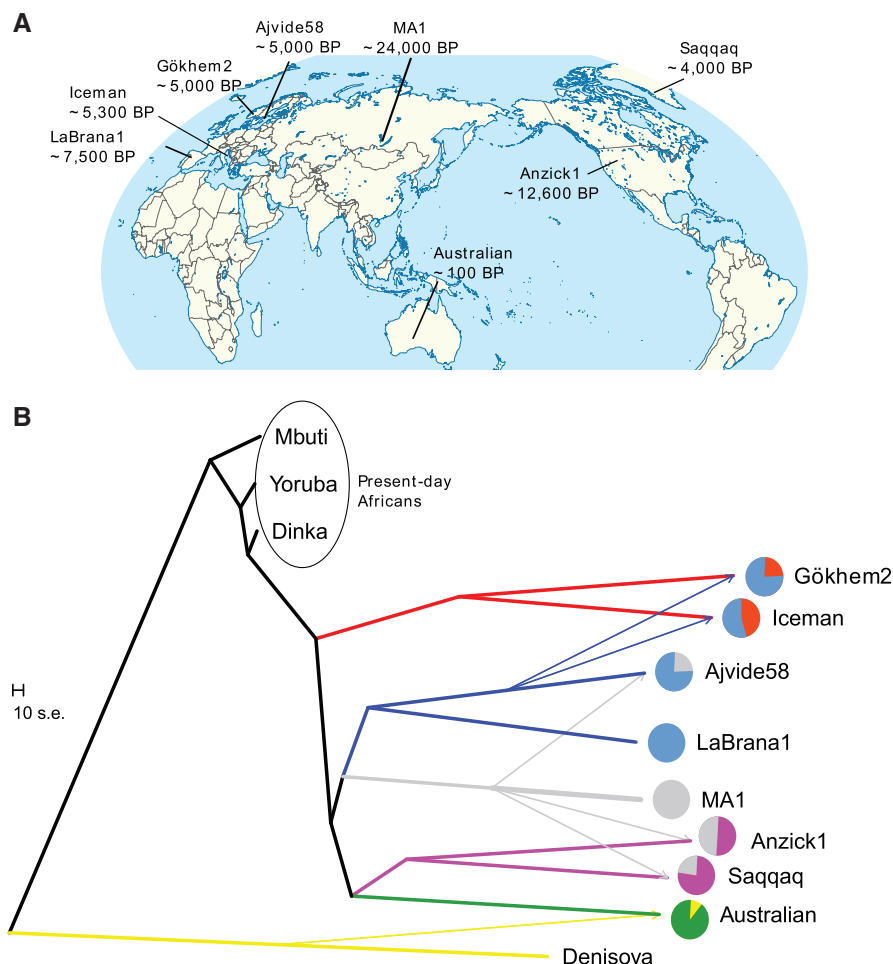
Because both Stone Age farmers and hunter-gatherers contributed genetic material to modern-day European groups (7), we investigated whether this putative admixture between ancestral populations had already begun in the Neolithic. We

tested symmetry between ancient genomes (table S13) and found that although the Tyrolean Ice-man is consistent with forming a group with modern-day Sardinians to the exclusion of Stone Age hunter-gatherers ( $D$ -statistics,  $|Z| < 2$ ), the Scandinavian early farmer Gökhem2 is significantly closer to hunter-gatherers ( $2 < |Z| < 8$  for all comparisons with  $>100,000$  loci). In contrast, the Scandinavian hunter-gatherer Ajvide58, which postdates the arrival of agriculture in Scandinavia, shows no significant evidence of admixture ( $|Z| < 2$ ) from early farmers when contrasted with an Iberian Mesolithic individual [LaBran1, which predates agriculture in Iberia (table S13)]. This suggests that the ancestors of the group represented by Gökhem2 admixed with individuals from hunter-gatherer groups during the northward expansion, whereas the Scandinavian Neolithic hunter-gatherers show no meaningful evidence of admixture with incoming farmers despite at least 40 generations of coexistence in Scandinavia.

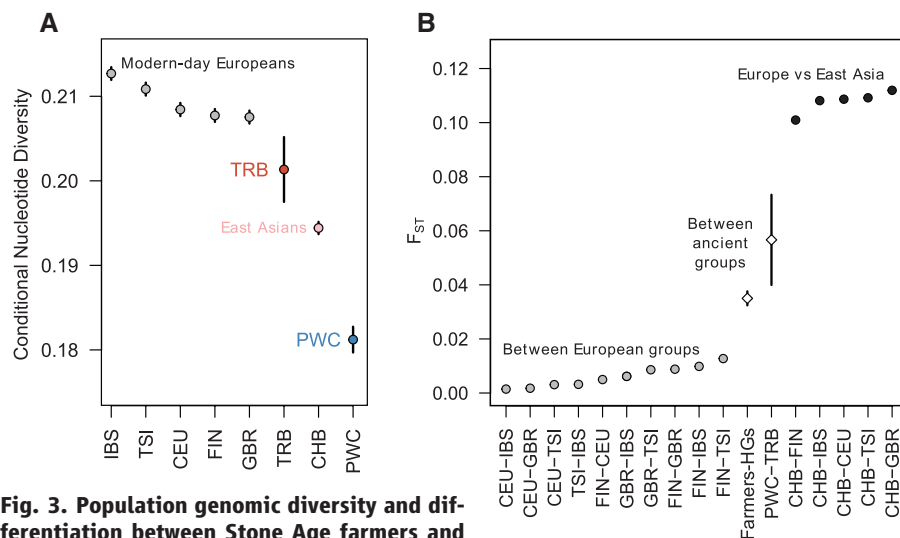
We fitted an admixture graph population model (17) to all publicly available ancient



**Fig. 1. Population structure and genetic affinities of ancient Eurasians.** (A) Ancient individuals were projected on PCs computed on 57 modern-day Western Eurasian groups. (B)  $D$ -statistics assessing affinity to either Lithuanians or Sardinians show stratification between all sequenced ancient Eurasian individuals (circles), which is robust for when only sequences with clear evidence of degradation are used (squares). Error bars represent 1 SE on each side (total 2 SEs). (C) Shared genetic drift between Western Eurasian populations and Ajvide58, a Neolithic hunter-gatherer from Scandinavia. (D) Shared genetic drift between Western Eurasian populations and Gökhem2, an early farmer from Scandinavia.



**Fig. 2. Sample locations and population history model.** (A) Sample locations of ancient human remains that are included in the population history model. (B) Admixture graph of population history fitted to ancient genomes, showing more hunter-gatherer admixture in Neolithic Scandinavian farmers than in central European farmers (table S15).



**Fig. 3. Population genomic diversity and differentiation between Stone Age farmers and hunter-gatherers contrasted with modern-day groups.** (A) Nucleotide diversity estimated as the average pairwise difference at transversion single-nucleotide polymorphisms (SNPs) identified in an African Yoruba individual. (B) Wright's  $F_{ST}$  estimated at transversion SNPs identified in African Yoruba and Mbuti individuals. Error bars represent 1 SE on each side (total 2 SEs), estimated by using a block jackknife procedure across the genome, with 5 Mb in each block. IBS, Spanish; TSI, Tuscan; CEU, Northern and Western European ancestry; FIN, Finnish; GBR, British; CHB, Chinese.

genomes of at least one-fold coverage [as well as a version including modern-day individuals from Sardinia and France (17)] and incorporated the gene-flow events identified in the  $D$ -tests above as well as in previous studies (Fig. 2A). Ancestry related to the Upper Paleolithic Siberian MA1 is estimated to ~15% in Ajvide58 (table S15), which is not found in the more southerly LaBrana1, suggesting gene-flow or shared ancestry among Northern Eurasian hunter-gatherer populations. Gökhem2 and the Tyrolean Iceman had ancestry from a basal group separated from all other ancient genomes (Fig. 2B) (17, 18). However, the early farmers also have a substantial amount of ancestry related to European hunter-gatherers, which is significantly higher in Gökhem2 ( $77.2 \pm 6.1\%$ ) as compared with the Tyrolean Iceman ( $56.0 \pm 3.0\%$ ), which is consistent with the  $D$ -statistics results above.

A possible contact phase in Northern Europe between expanding farming populations and hunter-gatherers that may explain the admixture in Gökhem2 is the period between ~7500 and 6000 years B.P., when the hunter-gatherer Ertebølle culture coexisted for more than a millennium with the early farming Linearbandkeramik (LBK) complex (19, 20). Hunter-gatherers and farmers also coexisted during the Early Neolithic expansion of agriculture into Scandinavia, which may have involved admixture between groups, but little is known about the populations from this period because skeletal remains are scarce.

Comparison of relative levels of genetic diversity in populations can provide information on effective population sizes because smaller populations often have reduced levels of diversity. We computed “conditional nucleotide diversity” (a relative measure of genetic diversity) for the Neolithic Scandinavian groups based on positions that are variable in single African individuals sequenced to high coverage (21) in order to avoid effects of post mortem degradation and sequence errors (17). To avoid effects of potential inbreeding, we always compared variants from separate individuals (17). The Scandinavian Neolithic hunter-gatherer group had significantly lower conditional nucleotide diversity ( $0.181 \pm 0.0015$ ) as compared with that of the Scandinavian Neolithic farmer group ( $0.201 \pm 0.0038$ ) (Fig. 3A and fig. S9). Although the specific properties of ancient DNA may still affect comparisons with sequence data from modern-day individuals, the conditional nucleotide diversity in the hunter-gatherers was also lower than in any modern-day European and a Chinese population (22) analyzed by using the same approach as for the ancient groups. In contrast, the diversity of the TRB is more similar to the level observed in modern-day populations (Fig. 3A).

The conditional approach also allowed us to estimate population genetic differentiation, Wright's  $F_{ST}$ , to  $0.057 \pm 0.017$  between TRB and PWC, and to  $0.035 \pm 0.0026$  between pan-European hunter-gatherers (Ajvide52 and LaBrana1) and farmers (Gökhem2 and Iceman). Both of these values are larger than the maximum



observed pairwise  $F_{ST}$  between European populations in the 1000 Genomes project, which was  $0.013 \pm 0.00059$  between Finnish and Italian individuals (Fig. 3B). These estimates suggest greater genetic stratification among Stone Age European groups as compared with current-day groups of European ancestry (7) but that this stratification in Stone Age Europe was correlated with the mode of subsistence instead of geography, as in current-day Europe (23).

The distinct features of the two Neolithic Scandinavian groups—nonsymmetric gene-flow into farmers, low level of diversity among hunter-gatherers, and strong differentiation between groups—have important implications for our understanding of the demographic histories of these groups. The greater diversity in the farmer population may have been influenced by gene flow from hunter-gatherers. However, the low level of genetic diversity in Neolithic hunter-gatherers likely has a demographic explanation, similar to that of the Iberian Mesolithic individual (8). Although we cannot exclude that this low diversity is a feature restricted to the Gotland island hunter-gatherer population, the low diversity may be due to the fact that hunter-gatherer ancestors resided in ice-free refugia in Europe during the Last Glacial Maximum (LGM), potentially causing population bottlenecks. Climatic changes and occasional population crashes also likely affected the population sizes of hunter-gatherers (24, 25). Furthermore, mobility may have decreased among late hunter-gatherer groups, especially when settling in coastal areas (20). Meanwhile, the population ancestral to the Neolithic farmers, that later were to expand across Europe, resided in warmer areas that could sustain larger population sizes during the LGM. Although it is possible that climate also affected populations in southern Eurasia, it may have been in a different manner (26), and farming economies are associated with greater carrying capacity than those of hunter-gatherer economies. It is likely that several factors contributed to the different levels of genetic diversity, and disentangling these processes and assessing their generality in prehistoric Europe may be possible as more genomic data from a wider geographic and temporal range becomes available.

## References and Notes

- V. G. Childe, *The Dawn of European Civilization* (Kegan Paul, London, 1925).
- P. Menozzi, A. Piazza, L. Cavalli-Sforza, *Science* **201**, 786–792 (1978).
- M. P. Malmer, *The Neolithic of South Sweden: TRB, GRK, and STR*. (Almqvist & Wiksell International, Stockholm, 2002).
- B. Bramanti *et al.*, *Science* **326**, 137–140 (2009).
- H. Malmström *et al.*, *Curr. Biol.* **19**, 1758–1762 (2009).
- G. Brandt *et al.*, *Science* **342**, 257–261 (2013).
- P. Skoglund *et al.*, *Science* **336**, 466–469 (2012).
- I. Olalde *et al.*, *Nature* **507**, 225–228 (2014).
- A. Keller *et al.*, *Nat. Commun.* **3**, 698 (2012).
- Q. Fu *et al.*, *Curr. Biol.* **23**, 553–559 (2013).
- A. O. Karlsson, T. Wallerström, A. Götherström, G. Holmlund, *Eur. J. Hum. Genet.* **14**, 963–970 (2006).
- C. Basu Mallick *et al.*, *PLOS Genet.* **9**, e1003912 (2013).
- M. Raghavan *et al.*, *Nature* **505**, 87–91 (2014).
- K. Tambets *et al.*, *Am. J. Hum. Genet.* **74**, 661–682 (2004).
- N. Patterson *et al.*, *Genetics* **192**, 1065–1093 (2012).
- P. Skoglund *et al.*, *Proc. Natl. Acad. Sci. U.S.A.* **111**, 2229–2234 (2014).
- Materials and methods are available as supplementary materials on Science Online.
- I. Lazaridis *et al.*, <http://arxiv.org/abs/1312.6639> (2013).
- L. Klassen, in *The Neolithisation of Denmark: 150 Years of Debate*, A. Fischer, K. Kristiansen, Eds. (J. R. Collis, Sheffield, UK, 2002), pp. 305–317.
- G. Bailey, in *Mesolithic Europe*, G. Bailey, P. Spikings, Eds. (Cambridge Univ. Press, Singapore, 2008), chap. 14.
- M. Meyer *et al.*, *Science* **338**, 222–226 (2012).
- G. R. Abecasis *et al.*, *Nature* **491**, 56–65 (2012).
- J. Novembre *et al.*, *Nature* **456**, 98–101 (2008).
- F. Riede, *Hum. Biol.* **81**, 309–337 (2009).
- S. Shennan, K. Edinborough, *J. Archaeol. Sci.* **34**, 1339–1345 (2007).
- B. Weninger *et al.*, *Quat. Res.* **66**, 401–420 (2006).
- Acknowledgments:** We thank L. Gattepaille, M. Metspalu, T. Naidoo, M. Rasmussen, S. Rasmussen, D. Reich, E. Salmela, and P. Wallin for technical assistance and discussions. The SNP data for the modern-day Swedish individuals is available from P. Hall at the Karolinska Institute under a materials transfer agreement. We thank the late L. Beckman for contributing the Saami samples; K.T. (ktambets@gmail.com) retains governance over the Saami and the Mari samples. This project was supported by grants from the Nilsson-Ehle Foundation (P.S.), Helge Ax:son Foundation (P.S.), Royal Swedish Academy of Science (FOA12H-177 to P.S.), Danish National Research Foundation (E.W. and M.R.), Swedish Research Council (J.A. and J.S.), Berit Wallenberg Foundation (J.A. and J.S.), Wenner-Gren Foundations (T.G.) and European Research Council (M.J.). P.S., H.M., A.G., and M.J. conceived and designed the study. E.W., J.S., A.G., and M.J. supervised the study. H.M., A.O., M.R., and C.V. generated DNA sequence data from ancient human remains. P.S. processed and prepared the data. P.S., H.M., and T.G. analyzed the genetic data, supervised by M.J. with the following contributions: mtDNA and Y-chromosome (H.M. and P.S.); functional SNPs (T.G. and P.S.); and contamination, biological sex, and population genetic analyses (P.S.). K.-G.S., J.S., and J.A. provided archaeological information and interpretation. P.H., K.T., and J.P. contributed samples. P.S., H.M., J.S., A.G., and M.J. wrote the manuscript with input from all authors. Data are available from the European Nucleotide Archive under accession no. PRJEB6090, and data aligned to the human reference genome are available at [www.ebc.uu.se/Jakobsson](http://www.ebc.uu.se/Jakobsson). The authors declare no competing interests.
- Supplementary Materials**  
[www.sciencemag.org/content/344/6185/747/suppl/DC1](http://www.sciencemag.org/content/344/6185/747/suppl/DC1)  
Materials and Methods  
Supplementary References  
Figs. S1 to S9  
Tables S1 to S16  
References (27–101)  
17 March 2014; accepted 16 April 2014  
Published online 24 April 2014;  
10.1126/science.1253448

# Late Pleistocene Human Skeleton and mtDNA Link Paleoamericans and Modern Native Americans

James C. Chatters,<sup>1\*</sup> Douglas J. Kennett,<sup>2</sup> Yemane Asmerom,<sup>3</sup> Brian M. Kemp,<sup>4</sup> Victor Polyak,<sup>3</sup> Alberto Nava Blank,<sup>5</sup> Patricia A. Beddows,<sup>6</sup> Eduard Reinhardt,<sup>7</sup> Joaquin Arroyo-Cabrales,<sup>8</sup> Deborah A. Bolnick,<sup>9</sup> Ripan S. Malhi,<sup>10</sup> Brendan J. Culleton,<sup>2</sup> Pilar Luna Erreguerena,<sup>11</sup> Dominique Rissolo,<sup>12</sup> Shanti Morell-Hart,<sup>13</sup> Thomas W. Stafford Jr.<sup>14</sup>

Because of differences in craniofacial morphology and dentition between the earliest American skeletons and modern Native Americans, separate origins have been postulated for them, despite genetic evidence to the contrary. We describe a near-complete human skeleton with an intact cranium and preserved DNA found with extinct fauna in a submerged cave on Mexico's Yucatan Peninsula. This skeleton dates to between 13,000 and 12,000 calendar years ago and has Paleoamerican craniofacial characteristics and a Beringian-derived mitochondrial DNA (mtDNA) haplogroup (D1). Thus, the differences between Paleoamericans and Native Americans probably resulted from in situ evolution rather than separate ancestry.

Genetic studies of contemporary Native Americans and late prehistoric skeletal remains from the Americas have consistently supported the idea that Native Americans are descended from Siberian ancestors who moved into eastern Beringia between 26,000 and 18,000 years ago (26 to 18 ka), spreading southward into the Americas after 17 ka (1). A complete genome analysis of the 12.6-ka Anzick infant from Montana (2), and mitochondrial DNA (mtDNA) from the 14.1-ka coprolites from Paisley Caves in Oregon (3) and mtDNA from other early (10.5 to 10.2 ka) remains from Nevada and Alaska (4, 5) support this hypothesis. With Anzick linked to the Clovis culture and Paisley Caves to the West-

ern Stemmed tradition—North America's two widespread early archaeological complexes—the genetic evidence for a Beringian origin of the earliest inhabitants of western North America is compelling.

The ancestry of the earliest Americans is still debated, however, because the oldest skeletal remains from the Americas (>9 ka, the Paleoamericans) consistently fail to group morphometrically with modern Native Americans, Siberians, and other northeast Asians (6). Paleoamericans exhibit longer, narrower crania and smaller, shorter, more projecting faces than later Native Americans (7). In nearly all cases, they are morphologically most similar to modern peoples of Africa,

Australia, and the southern Pacific Rim (7–9). Polymorphic dental traits currently found in East Asia also distinguish later Native Americans (10),

<sup>1</sup>Applied Paleoscience and DirectAMS, 10322 NE 190th Street, Bothell, WA 98011, USA. <sup>2</sup>Department of Anthropology and Institutes of Energy and the Environment, Pennsylvania State University, University Park, PA 16802, USA. <sup>3</sup>Department of Earth and Planetary Sciences, University of New Mexico, Albuquerque, NM 87131-0001, USA. <sup>4</sup>Department of Anthropology and School of Biological Sciences, Washington State University, Pullman, WA 99164, USA. <sup>5</sup>Bay Area Underwater Explorers, Berkeley, CA, USA. <sup>6</sup>Department of Earth and Planetary Sciences, Northwestern University, Evanston, IL 60208, USA. <sup>7</sup>School of Geography and Earth Sciences, McMaster University, Hamilton, Ontario L8S 4K1, Canada. <sup>8</sup>Instituto Nacional de Antropología e Historia, Colonia Centro Histórico, 06060, Mexico City, DF, Mexico. <sup>9</sup>Department of Anthropology and Population Research Center, University of Texas at Austin, Austin, TX 78712, USA. <sup>10</sup>Institute for Genomic Biology, University of Illinois, Urbana-Champaign, IL 61801, USA. <sup>11</sup>Subdirección de Arqueología Subacuática, Instituto Nacional de Antropología e Historia, 06070 Mexico City, Mexico. <sup>12</sup>Waitt Institute, La Jolla, CA 92038-1948, USA. <sup>13</sup>Department of Anthropology, Stanford University, Stanford, CA 94305, USA. <sup>14</sup>Centre for AMS <sup>14</sup>C, Department of Physics and Astronomy, Aarhus University, Aarhus, Denmark, and Centre for GeoGenetics, Natural History Museum of Denmark, Geological Museum, Copenhagen, Denmark.

\*Corresponding author. E-mail: paleosci@gmail.com

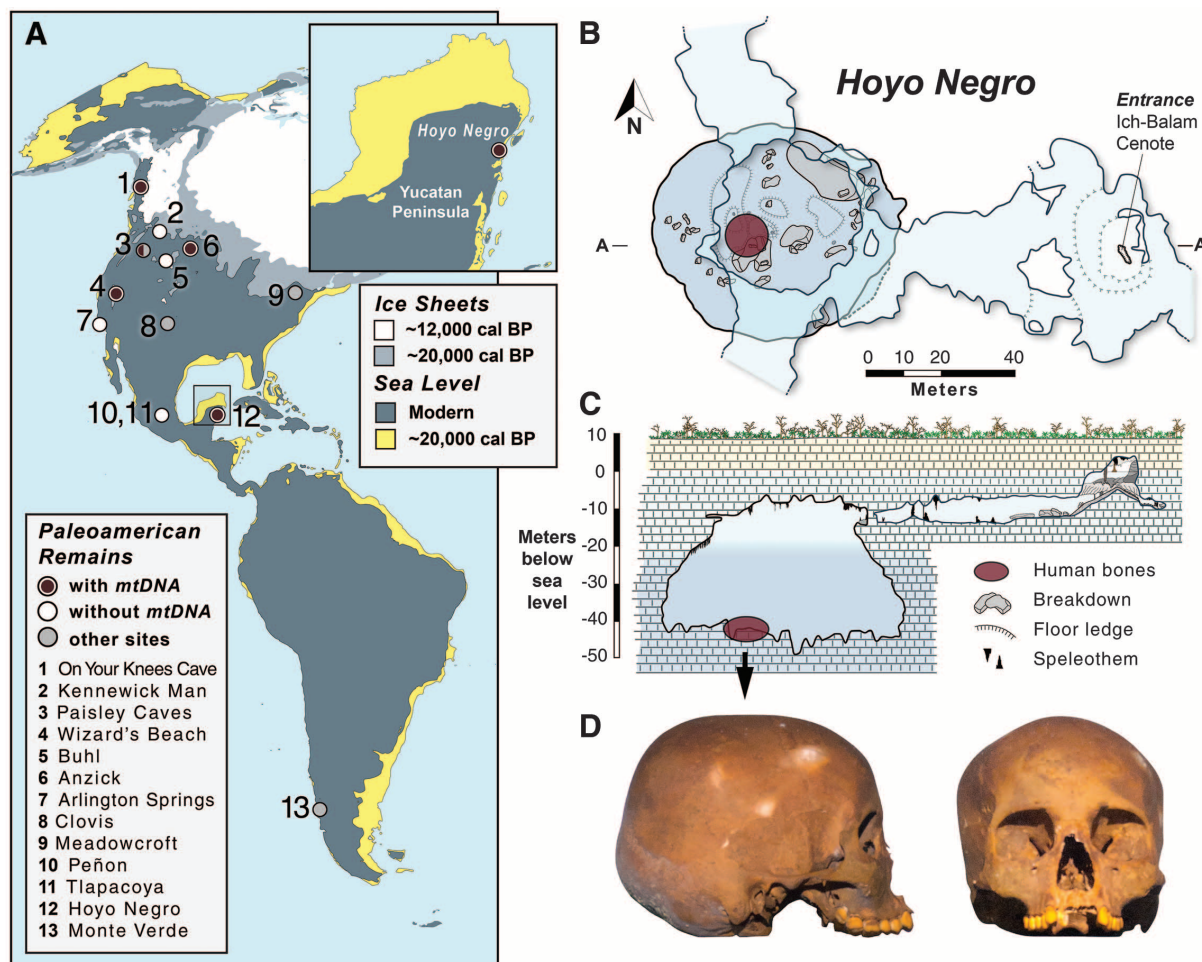
who tend to exhibit such specialized (Sinodont) traits as winged, shovel-shaped upper incisors, three-rooted lower first molars, and small or absent third molars; from Paleoamericans, who exhibit a less specialized (Sundadont) morphology (7). These differences suggest that America was colonized by separate migration events from different parts of Eurasia (11) or by multiple colonization events from Beringia (12), or that evolutionary changes occurred in the Americas after colonization (13).

To date, most genetic data are from immature individuals, such as the Anzick infant (2); fragmentary material, such as the remains from On Your Knees Cave (5); or human byproducts, such as the Paisley Cave coprolites (3). The one complete skull associated with ancient DNA (aDNA), Wizard's Beach (4), is a single early Holocene individual that groups morphometrically with modern Native Americans (9). Furthermore, genetic evidence from the earliest Americans—those predating 10 ka—is limited to northwestern North America (Fig. 1 and Table 1), leaving open the possibility of different geographic origins for Paleoamericans elsewhere in the hemisphere.

Resolution of this issue has also been hindered by the rarity of Paleoamerican skeletons. Remains

of no more than 30 individuals from North America, most of them fragmentary, predate 10 ka, and only 12 are directly dated (table S1). Furthermore, just 20 skeletons in this age range are reported for South America (14). Only five individuals, all from North America, securely predate 12 ka (Table 1). Of these five, only two have intact skulls and none possesses a complete dental assemblage.

Here we report a nearly complete, Late Pleistocene-age human skeleton (HN5/48) with intact dentition from Hoyo Negro (HN), a submerged collapse chamber in the Sac Actun cave system, eastern Yucatan Peninsula, Mexico (Fig. 1). HN lies at the confluence of three horizontal passages formed within a Cenozoic limestone platform (fig. S1). This and other cave systems in the Yucatan were accessible via sinkholes for much of the last glacial period, serving as natural traps for people and animals. They became inundated between 10 and 4 ka (15), as the glaciers melted. Sea-level change was predominantly eustatic in this tectonically stable region (16), with a moderate offset imposed by a global glacial isostatic adjustment (17). The remains of Pleistocene megafauna and pre-Maya humans occur in other cave systems, including eight partial human skeletons



**Fig. 1. The site and skull form of the HN human remains.** HN5/48 was found far to the southeast of other ancient American skeletons from which DNA has been obtained (A). HN5/48 lies at the bottom of HN, a submerged

chamber shown in plan and profile (B and C). Paleoamerican features are visible in this view of the cranium (D). Paisley Cave is an early site with DNA but without Paleoamerican skeletal remains.

**Table 1. Paleoamerican skeletons directly dated to >12 ka\*† and all >10 ka skeletons from which aDNA has been extracted.**

Skeleton	Location	<sup>14</sup> C age	Age (calendar yr B.P.)	Skeletal assemblage	aDNA	aDNA reference
On Your Knees Cave	AK, USA	9200 <sup>‡§</sup>	~10,500–10,250	Mandible, carnivore-damaged skeletal fragments	mtDNA: D4h3a; Y: Q1a3a1a	(5)
Wizard’s Beach	NV, USA	9225 ± 60	10,560–10,250	Skull with partial dentition, partial skeleton	mtDNA: C1	(4)
Tlapacoya I	Mexico, EUM	10,200 ± 65	12,150–11,610	Calotte	No	—
Buhl	ID, USA	10,675 ± 95	12,740–12,420	Skull with partial dentition, partial skeleton (reburied)	No	—
Anzick 1	MT, USA	10,680 ± 50 <sup>‡</sup>	12,707–12,556	Neurocranium, four bones of infant	mtDNA: D4H3a Y: Q-L54(xM3)	(2)
Peñon III	Mexico, EUM	10,755 ± 75	12,770–12,560	Skull with partial dentition, partial skeleton	No	—
Arlington Springs	CA, USA	10,960 ± 80	13,010–12,710	Partial femora	No	—
HN	Quintana Roo, EUM	10,976 ± 20 <sup>‡</sup>	12,910–11,750 <sup>  </sup>	Skull with complete dentition, largely complete skeleton	mtDNA: D1	This article

\*Claims of >13 ka for Naharon (Mexico) and Lapa Vermelha IV (Brazil) are not supported by evidence (table S1 footnotes). †For references, see table S1. ‡Mean of multiple measurements. §No standard deviation provided. ||Age range constrained by <sup>14</sup>C and U-Th dates. Calibrations were computed in OXCAL 4.2, based on Reimer *et al.* (25).

found 20 km south of HN in the Tulum region. These individuals are inferred to predate 10 ka on the basis of their depth below sea level, but reliable radiometric dates on the skeletons are lacking.

HN is a 62-m-diameter, subterranean, bell-shaped, collapsed dissolution chamber (pit) containing the skeletons of one human and at least 26 large mammals (Fig. 1 and table S2). The three passages joining HN are 10 m below sea level (mbsl); the pit drops to a maximal depth of 55 mbsl. The bottom is strewn with roof-collapse boulders and marked by guano, accumulations of calcite raft sediment, and a few stalagmites. HN contains layered fresh and saltwater, with a halocline at 15 to 22 mbsl. This permeable aquifer tracks sea level to within 1 to 2 m. The skeletal material lies at the base of the pit, 600 m from the nearest entrance when it was a dry cave. HN is now accessible only by technical dive teams. Information collected to date has been derived primarily through videography, photography, minimal sampling, and three-dimensional modeling from remote images.

The faunal assemblage in the bottom of HN is composed of extinct taxa, including sabertooth (*Smilodon fatalis*), gomphothere (*Cuvieronius* cf. *tropicus*, a proboscidean), Shasta ground sloth (*Nothrotheriops shastensis*), and an unnamed megalonychid ground sloth, along with extant species, including puma, bobcat, coyote, Baird’s tapir, collared peccary, white-nosed coati, and a bear of the genus *Tremarctos* (table S2 and fig. S2). Animal bones are concentrated on the south side of the floor on wall projections or sloping boulders between 40 and 43 mbsl (28 to 31 m below the pit rim; figs. S3 and S4). The distribution and condition of elements are probably explained by the decomposition of the carcasses in water, which scattered bones toward the walls of the room during episodic flooding of the chamber (fig. S4).

Subaerial conditions existed in this room above 42 mbsl before inundation or recurred after short-lived episodes of water table rise, because some

bones of the human and one gomphothere are covered with patches of calcite speleothems in the form of 0.5 to 5-cm bushy crystals referred to here as florets. Florets develop from dripping water in a manner similar to stalagmites, growing from the mist/aerosol created by drip water hitting the cave floor.

Directly dating HN5/48 and the associated faunal assemblage is challenging because the conditions do not favor bone collagen preservation. Attempts to extract collagen from bone and tooth specimens for accelerator mass spectrometry (AMS) radiocarbon (<sup>14</sup>C) dating were unsuccessful. Multiple lines of evidence, however, indicate that the human remains and much of the faunal assemblage date to the latest Pleistocene. HN5/48 is associated by position and depth with the remains of multiple species of mega-fauna (sabertooth, gomphothere, and ground sloths) that were largely extinct in North America by 13 ka (18, 19). HN, therefore, trapped the animals before flooding. The age of the human skeleton is thus constrained by sea-level history after the Last Glacial Maximum (LGM) (17). Identifying the florets as subaerial deposits is consistent with the inundation of HN5/48 after 10 to 9.5 ka on the basis of global sea-level reconstructions (20, 21) and our independent evidence of cave flooding.

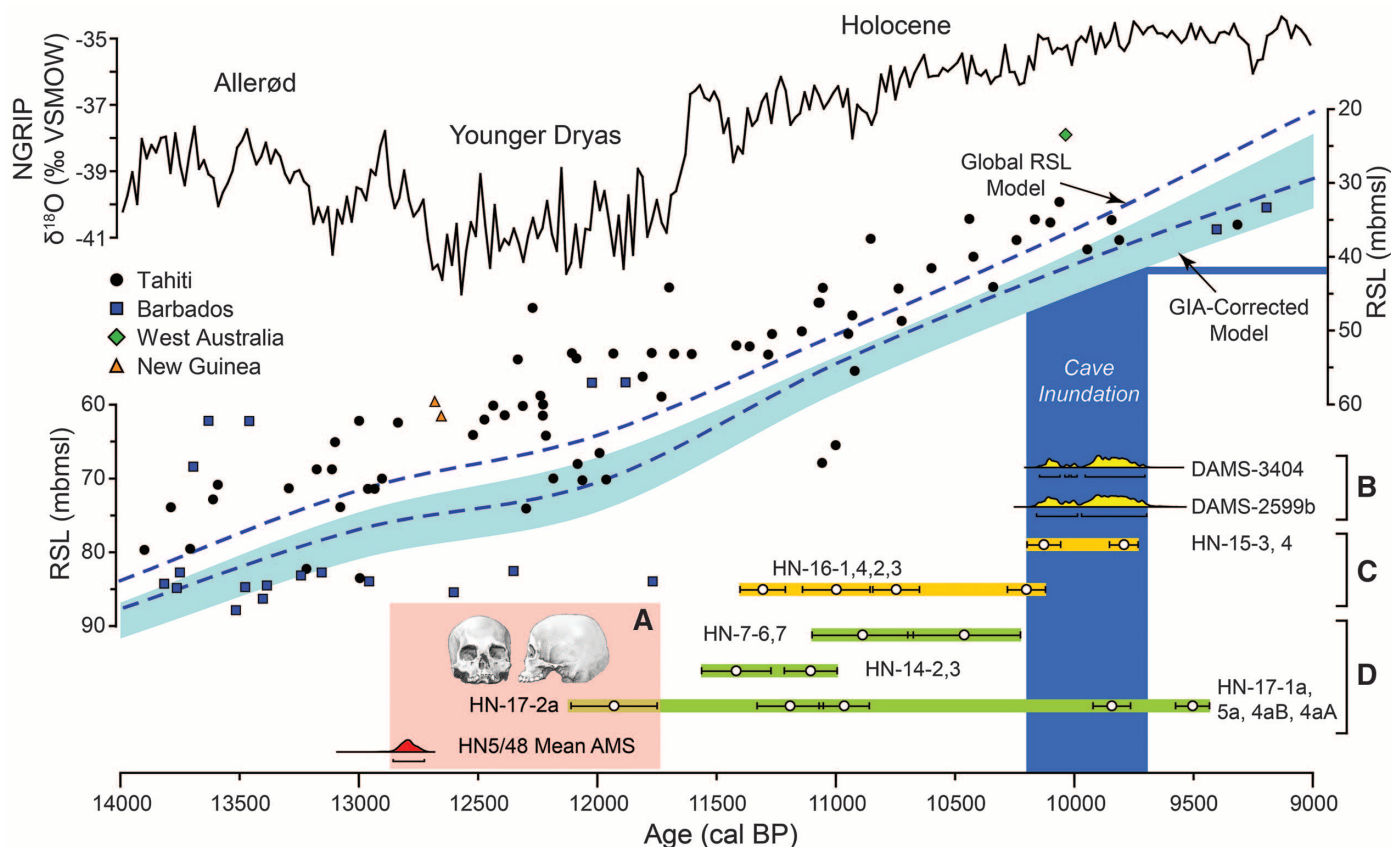
In 2013, our dive team collected florets formed on the surfaces of human bones (Fig. 2) for absolute age determinations with the uranium-thorium (U-Th) method. Nine U-Th dates on florets removed directly from the upper surfaces of these bones range from 12.0 ± 0.2 to 9.6 ± 0.1 ka (tables S3 and S4). This establishes a minimum age of ~12 ± 0.2 ka for the human skeleton. Independent AMS <sup>14</sup>C measurements on enamel bioapatite from an upper third molar yielded statistically identical <sup>14</sup>C ages of 10,970 ± 25 [Stafford Research sample no. 8205, University of California-Irvine AMS (UCIAMS) sample no. 119438] and 10,985 ± 30 years before the present (<sup>14</sup>C yr B.P.)

(Pennsylvania State University sample no. 5493, UCIAMS sample no. 123541), suggesting a calibrated age for the skeleton of ~12.9 to 12.7 ka. Bioapatite is subject to contamination by dissolved inorganic carbon (DIC) in groundwater, however. A 16,160 ± 78 <sup>14</sup>C yr B.P. date on bioapatite from a rib of HN5/48 indicates that the rib was contaminated by fossil carbon, which may also have affected the enamel age. The 13-ka date must therefore be considered a maximum age for the skeleton. Furthermore, there could be a small reservoir effect if this individual consumed marine foods, but that appears unlikely because of light dental wear, severe dental caries, and paleoecological evidence for a terrestrial emphasis in the diet of the earliest Central Americans. Thus, we argue that this individual entered the cave system between 13.0 and 12.0 ka.

To determine whether the human bones and the associated gomphothere (fig. S5) are the same age, we obtained U-Th ages of florets from the larger animal’s pelvis and femur and <sup>14</sup>C dates on its tooth enamel (table S3). Five U-Th dates range between 18.8 ± 0.3 and 11.9 ± 0.3 ka and indicate the the gomphothere was deposited by at least ~19 ka. Two AMS <sup>14</sup>C dates on its tooth enamel suggest an age as early as 41.6 to 36.4 ka, but these teeth are heavily mineralized, and we cannot rule out DIC affecting this age estimate. Regardless, the U-Th and AMS <sup>14</sup>C data are consistent with the hypothesis that HN trapped animals during the latest Pleistocene, when the upper horizontal passages were accessible, with western Caribbean sea level below 10 mbsl. The U-Th dates also indicate that HN was largely subaerial and primarily dry above 42 mbsl between 19.0 and 9.5 ka.

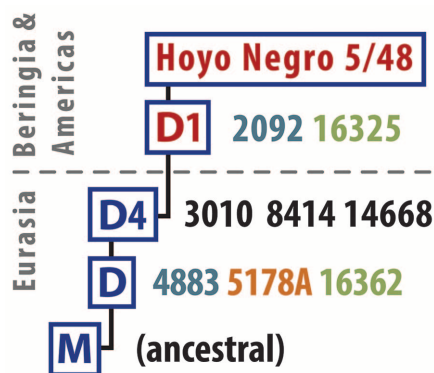
<sup>87</sup>Sr/<sup>86</sup>Sr and δ<sup>234</sup>U values demonstrate that the florets precipitated under relatively stable vadose, subaerial conditions throughout this interval (tables S4 and S5). Floret formation below 42 mbsl terminated at 9.6 ± 0.1 ka, consistent with the hypothesis that inundation of the cave





**Fig. 2. Radiocarbon and U-Th dates from HN compared to relative sea level (RSL).** Radiocarbon dates on a human tooth (red histogram) and U-Th dates from calcite florets on human bones [green bars in (D)] place HN5/48 between 12,910 and 11,750 calendar yr B.P. [pink bar in (A)]. Calcite florets (C and D) and guano deposits [yellow histograms in (B)] ceased forming when

rising sea level surpassed 42 mbmsl and permanently inundated the human remains (blue bar). The global RSL model presented is from corals with a  $^{234}\text{U}/^{238}\text{U}$  activity range of 1.137 to 1.157 (21), modified by an estimated glacial isostasy adjustment (GIA) of 3.5 m (20). Measurement standards: NGRIP, North Greenland Ice Core Project; VSMOW, Vienna standard mean ocean water.



**Fig. 3. Base-pair substitutions (numbers) confirming the presence of mtDNA haplogroups D and D1 in HN5/48.** Colors represent substitutions confirmed in multiple extracts with restriction fragment length polymorphism and DNA sequencing (orange), multiple extracts with DNA sequencing (green), and a single extract with DNA sequencing (blue).

between 10.2 and 9.5 ka, which is also consistent with these reconstructions (table S3). Thus, the age range for HN5/48 (13 to 12 ka) is supported by this larger geochronological framework.

HN5/48 is the largely complete, well-preserved skeleton of a gracile, small-statured ( $149 \pm 4$  cm) female estimated to have been 15 to 16 years old. All skeletal elements are intact, except for apparent perimortem fractures of pubic bones, trauma that is consistent with a fall into a shallow pool from one of the upper passages. Cranial and dental characteristics are comparable to those of other, less complete pre-10-ka Paleoamerican skeletons, including Peñon, Buhl, and Wilson-Leonard [(7, 8) table S1], and to those of Upper Paleolithic humans across Eurasia (22). Measurements from a three-dimensional digital model show the cranium to be long and high, with a pronounced forehead and projecting, sharply angled occipital (Fig. 1 and fig. S6). The upper face is short, broad, and small relative to the neurocranium, with low, wide-set eye orbits and a broad nose. It exhibits moderate alveolar prognathism and lacks the broad, everted zygomatics characteristic of late Holocene and contemporary Native Americans. The palate is long and parabolic, with moderately shoveled upper central incisors (a Sinodont

trait), a lack of double shoveling, no deflecting wrinkle on the lower first molar, third molars approximately equal in size to the second molars (Sundadont traits), and a strongly developed Carabelli's cusp on the upper first molar.

HN5/48 is among the small group of Paleoamerican skeletons, a group that is morphologically distinct from Native Americans. We extracted DNA from the skeleton's upper right third molar and analyzed the mtDNA using methods developed for poorly preserved skeletal elements, with independent replication. The mtDNA haplogroup for the HN skeletal remains was determined through restriction fragment analysis, direct Sanger sequencing, and second-generation sequencing after target enrichment. The Alu1 5176 site loss, in combination with Sanger and Illumina sequence data, confirm its placement in haplogroup D, subhaplogroup D1 (Fig. 3). Subhaplogroup D1 is derived from an Asian lineage but occurs only in the Americas, having probably developed in Beringia after divergence from other Asian populations (1).

D1 is one of the founding lineages in the Americas (1). Subhaplogroup D1 occurs in 10.5% of extant Native Americans (23), with a high frequency of 29% in indigenous people from Chile and Argentina (24). This suggests that HN5/48

occurred in parallel with rising sea levels (Fig. 2). AMS  $^{14}\text{C}$  dates of seeds from nearby ostracod-bearing guano deposited in shallow water range

descended from the population that carried the D1 lineage to South America. The discovery of a member of subhaplogroup D1 in Central America, ~4000 km southeast of any other pre-10-ka DNA in the Americas, greatly extends the geographic distribution of Pleistocene-age Beringian mtDNA in the Western Hemisphere.

HN5/48 shows that the distinctive craniofacial morphology and generalized dentition of Paleoamericans can co-occur with a Beringian-derived mtDNA haplogroup. This 13- to 12-ka Paleoamerican skeleton thus suggests that Paleoamericans represent an early population expansion out of Beringia, not an earlier migration from elsewhere in Eurasia. This is consistent with hypotheses that both Paleoamericans and Native Americans derive from a single source population, whether or not all share a lineal relationship. In light of this finding, the differences in craniofacial form between Native Americans and their Paleoamerican predecessors are best explained as evolutionary changes that postdate the divergence of Beringians from their Siberian ancestors.

#### References and Notes

1. E. T. Tamm *et al.*, *PLOS ONE* **2**, e829 (2007).
2. M. Rasmussen *et al.*, *Nature* **506**, 225–229 (2014).
3. D. L. Jenkins *et al.*, *Science* **337**, 223–228 (2012).
4. F. A. Kaestle, D. G. Smith, *Am. J. Phys. Anthropol.* **115**, 1–12 (2001).
5. B. M. Kemp *et al.*, *Am. J. Phys. Anthropol.* **132**, 605–621 (2007).
6. J. A. Raff, D. A. Bolnick, *Nature* **506**, 162–163 (2014).
7. D. G. Steele, J. F. Powell, in *Who Were the First Americans?*, R. Bonnichsen, Ed. (Center for the Study of the First Americans, Oregon State University, Corvallis, OR, 1999), pp. 25–40.
8. R. González-José *et al.*, *Am. J. Phys. Anthropol.* **128**, 772–780 (2005).
9. J. F. Powell, W. A. Neves, *Am. J. Phys. Anthropol.* **110** (suppl. 29), 153–188 (1999).
10. C. G. Turner 2nd, *Am. J. Phys. Anthropol.* **82**, 295–317 (1990).
11. M. M. Lahr, *Evol. Anthropol.* **6**, 2–6 (1997).
12. J. C. Chatters, in *Human Variation in the Americas: The Integration of Archaeology and Biological Anthropology*, B. M. Auerbach, Ed. (Occasional Paper 38, Center for Archaeological Investigations, Southern Illinois Univ., Carbondale, IL, 2010), pp. 51–76.
13. J. F. Powell, *The First Americans: Race, Evolution, and the Origin of Native Americans* (Cambridge Univ. Press, Cambridge, 2004).
14. W. A. Neves *et al.*, in *Paleoamerican Odyssey*, K. E. Graff, C. V. Ketron, M. R. Waters, Eds. (Center for the Study of the First Americans, College Station, TX, 2013), pp. 397–412.
15. W. R. Peltier, R. G. Fairbanks, *Quat. Sci. Rev.* **25**, 3322–3337 (2006).
16. B. J. Szabo, W. C. Ward, A. E. Weidie, M. J. Brady, *Geology* **6**, 713–715 (1978).
17. G. A. Milne, M. Peros, *Global Planet. Change* **107**, 119–131 (2013).
18. R. W. Graham, in *The World of Elephants (La Terra degli Elefanti)—Proceedings of the 1st International Congress (Atti del 1° Congresso Internazionale)*, G. Cavarretta *et al.*, Eds. (Consiglio Nazionale delle Ricerche, Rome, 2001), pp. 707–709.
19. G. Haynes, *Quat. Int.* **285**, 89–98 (2013).
20. E. Bard, B. Hamelin, D. Delanghe-Sabatier, *Science* **327**, 1235–1237 (2010).
21. M. Medina-Elizalde, *Earth Planet. Sci. Lett.* **362**, 310–318 (2013).
22. M. M. Lahr, *Evolution of Modern Human Diversity* (Cambridge Univ. Press, Cambridge, 1996).
23. U. A. Perego *et al.*, *Genome Res.* **20**, 1174–1179 (2010).
24. M. de Saint Pierre *et al.*, *PLOS ONE* **7**, e43486 (2012).
25. P. J. Reimer *et al.*, *Radiocarbon* **55**, 1869–1887 (2013).

**Acknowledgments:** Data reported here are available in tables S2 to S5 and at GenBank (accession no. KJ710435). Support was provided by the National Geographic Society, the Archaeological Institute of America, the Waitt Institute, the Instituto Nacional de Antropología e Historia, NSF (Y.A., V.P., and D.K.), Pennsylvania State University, the University of New Mexico, the University of Texas at Austin, the University of Illinois, Urbana-Champaign, and DirectAMS.

#### Supplementary Materials

www.sciencemag.org/content/344/6185/750/suppl/DC1

Materials and Methods

Figs. S1 to S13

Tables S1 to S5

Additional Acknowledgments

References (26–107)

25 February 2014; accepted 18 April 2014

10.1126/science.1252619

# Neurosensory Perception of Environmental Cues Modulates Sperm Motility Critical for Fertilization

Katherine McKnight,<sup>1</sup> Hieu D. Hoang,<sup>2</sup> Jeevan K. Prasain,<sup>3</sup> Naoko Brown,<sup>4</sup> Jack Vibbert,<sup>2</sup> Kyle A. Hollister,<sup>5</sup> Ray Moore,<sup>3</sup> Justin R. Ragains,<sup>5</sup> Jeff Reese,<sup>4,6</sup> Michael A. Miller<sup>2\*</sup>

Environmental exposures affect gamete function and fertility, but the mechanisms are poorly understood. Here, we show that pheromones sensed by ciliated neurons in the *Caenorhabditis elegans* nose alter the lipid microenvironment within the oviduct, thereby affecting sperm motility. In favorable environments, pheromone-responsive sensory neurons secrete a transforming growth factor- $\beta$  ligand called DAF-7, which acts as a neuroendocrine factor that stimulates prostaglandin-endoperoxide synthase [cyclooxygenase (Cox)]-independent prostaglandin synthesis in the ovary. Oocytes secrete F-class prostaglandins that guide sperm toward them. These prostaglandins are also synthesized in Cox knockout mice, raising the possibility that similar mechanisms exist in other animals. Our data indicate that environmental cues perceived by the female nervous system affect sperm function.

Diet and environment have profound, yet largely unexplained effects on fertility in many animals (1, 2). Essential components of the mammalian diet include the polyunsaturated fatty acids (PUFAs), which are oxidized into labile signaling molecules called prostaglandins (fig. S1). The F-class prostaglandins are among the most abundant and ubiquitous members. Prostaglandins are critical for reproduction (3), but their functions and regulatory mechanisms are incompletely understood. For instance, in vitro studies have shown that prostaglandins induce  $\text{Ca}^{2+}$  influx into human sperm via the CatSper channel (4, 5).

The biological role of this mechanism is not clear, largely because monitoring sperm behavior in the female reproductive tract is difficult.

Cyclooxygenase (Cox) enzymes, the targets of nonsteroidal anti-inflammatory drugs, are thought to be the exclusive enzymatic initiators of prostaglandin synthesis (3). Prostaglandin species are also formed nonenzymatically under conditions of high oxidative stress (6). These latter prostaglandins, which are esterified to phospholipids, lack biological regulation and stereoselective generation. The nematode *Caenorhabditis elegans* generates specific F-class prostaglandins, including prostaglandin

F1 $\alpha$  (PGF1 $\alpha$ ) and PGF2 $\alpha$  stereoisomers independent of Cox (7, 8) (fig. S1). Prostaglandin metabolism is regulated and has an important function in fertilization (8–10). Hence, *C. elegans* possesses an alternative metabolic pathway for F-class prostaglandin synthesis.

Oocytes synthesize numerous F-class prostaglandins from PUFA precursors provided in yolk lipoprotein complexes (8, 9). These prostaglandins function collectively to guide sperm to the spermatheca, the fertilization site (Fig. 1A) (7). The worm's transparent epidermis facilitates direct tracking of fluorescently labeled motile sperm. More than 90% of sperm target the spermatheca (Z3) successfully 1 hour after mating (Fig. 1B).

We previously found that mutations in the *daf-7* transforming growth factor- $\beta$  (TGF- $\beta$ ) ligand cause sperm-targeting defects (8). *daf-7*, which is expressed in amphid single (ASI) sensory neurons (Fig. 1A), functions in a population density sensing mechanism (11–13). DAF-7 signals are transmitted through DAF-1 type I and DAF-4 type II receptors (Fig. 1C) (14). Mutations in *daf-7*, the *daf-1* and *daf-4* receptors, or downstream *daf-8*

<sup>1</sup>Division of Reproductive Endocrinology and Infertility, Department of Obstetrics and Gynecology, University of Alabama at Birmingham, Birmingham, AL 35294, USA. <sup>2</sup>Department of Cell, Developmental and Integrative Biology, University of Alabama at Birmingham, Birmingham, AL 35294, USA. <sup>3</sup>Department of Pharmacology and Toxicology, University of Alabama at Birmingham, Birmingham, AL 35294, USA. <sup>4</sup>Department of Pediatrics, Vanderbilt University, Nashville, TN 37232, USA. <sup>5</sup>Department of Chemistry, Louisiana State University, Baton Rouge, LA 70803, USA. <sup>6</sup>Department of Cell and Developmental Biology, Vanderbilt University, Nashville, TN 37232, USA.

\*Corresponding author. E-mail: mamiller@uab.edu



and *daf-14* R-Smads impair wild-type (WT) sperm targeting to the spermatheca (Fig. 1B and tables S1 and S2). Moreover, loss of the antagonistic co-Smad *daf-3* suppresses these defects (Fig. 1B and table S1). We conclude that the DAF-7/TGF- $\beta$  pathway is essential for sperm targeting. The mechanism is specific to the DAF-7 pathway, as sperm reach the spermatheca efficiently in other TGF- $\beta$  pathway mutants (fig. S2).

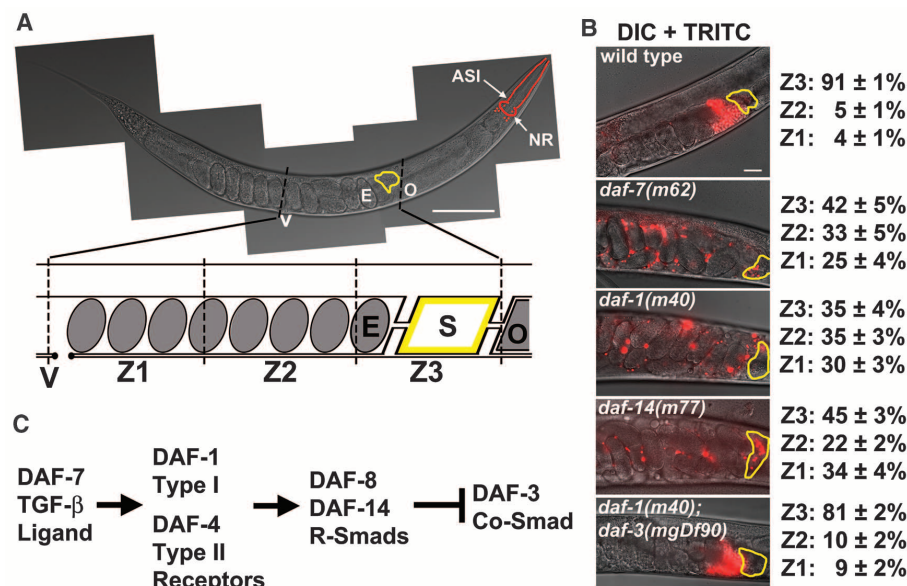
During larval development, the DAF-7/TGF- $\beta$  pathway regulates dauer stage entry (11). In contrast to dauer, the sperm-targeting mechanism is not sensitive to temperature (tables S1 and S2). At 16°C, TGF- $\beta$  mutants complete gonad development, generate oocytes that undergo meiotic maturation and ovulation, and are fertile (fig. S3). Sperm targeting is abnormal and brood size is reduced (15), probably due to sperm loss.

To test whether TGF- $\beta$  functions in adults, we used the RNA interference (RNAi) feeding method to temporally inactivate *daf-1* or *daf-4* receptors (see supplementary materials and methods). Down-regulating TGF- $\beta$  signaling in young adults causes sperm-targeting defects (fig. S4). Therefore, DAF-7/TGF- $\beta$  promotes sperm targeting independent of earlier roles.

The *daf-7* promoter drives gene expression in ASI neurons (11), which extend cilia through the nose to perceive ascaroside pheromones (13). Ascarosides accumulate as population density rises, triggering reduced *daf-7* expression (12, 13). To test whether *daf-7* functions in ASI for sperm guidance, we expressed *daf-7* cDNA in *daf-7* mutants under the ASI-specific *gpa-4* promoter (16). The *gpa-4p::daf-7* transgene rescues the sperm guidance defects (Fig. 2A). The ascarosides asc-C6-MK and asc- $\Delta$ C9, components of dauer pheromone, repress *daf-7* expression in ASI neurons (12). Synthetic asc-C6-MK and asc- $\Delta$ C9 application to adult hermaphrodites causes sperm-targeting defects dependent on the *daf-7* promoter and *daf-3* Co-Smad (fig. S5). We also observed sperm-targeting defects in *daf-19* mutant hermaphrodites lacking sensory cilia, as well as in hermaphrodites exposed to high population density (fig. S6). Collectively, the data indicate that DAF-7/TGF- $\beta$  couples ascaroside perception to sperm function.

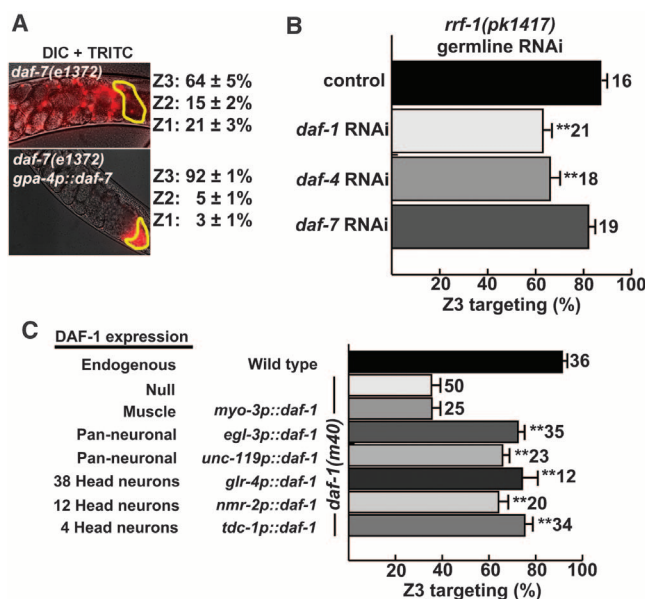
Sperm do not directly transduce TGF- $\beta$  signals because WT sperm fail to target the spermatheca efficiently in receptor and Smad mutants (Fig. 1B and tables S1 and S2). To determine the cell type that transduces TGF- $\beta$  signals, we conducted genetic mosaic analysis on the *daf-1* receptor. *daf-1* loss in the germline or neuronal lineages causes sperm-targeting defects, whereas loss in somatic gonadal, muscle, intestinal, or epidermal lineages does not appreciably affect sperm guidance (fig. S7). Loss of germline or neuronal *daf-1* expression is not as severe as complete *daf-1* loss, suggesting that both cell types transduce DAF-7 signals in parallel. As an alternative test, we used an RNAi mosaic strategy to restrict receptor inactivation to the adult germ line. Germline *daf-1* or *daf-4* receptor inactivation causes sperm-targeting defects, whereas germline *daf-7* ligand inactivation does not (Fig. 2B). These results support the model that DAF-7 functions in part as a neuroendocrine factor that transmits signals directly to oögonia. We also identified a group of head interneurons that perceive DAF-7 signals for sperm guidance (Fig. 2C). These neurons regulate feeding rate and fat metabolism in a DAF-7-dependent manner (17). In contrast to feeding and metabolism, interneuron TGF- $\beta$  signaling to the gonad appears to be mediated by insulin and steroid ligands (fig. S8).

Given that DAF-7 receptors function in oögonia, we hypothesized that TGF- $\beta$  promotes sperm-guiding F-class prostaglandin synthesis. Inhibiting oöcyte prostaglandin synthesis causes sperm to move with reduced velocity, little directional velocity, and high reversal frequency (7, 8). Similar motility parameters are observed in *daf-7* and



**Fig. 1. *C. elegans* sperm guidance and DAF-7/TGF- $\beta$  pathway.** (A) Anatomy of an adult hermaphrodite, showing ASI sensory neurons, nerve ring (NR), and proximal gonad. The oocytes (O), which synthesize F-class prostaglandin sperm guidance cues, lie adjacent to the spermatheca (S, outlined in yellow). Males inject sperm into the uterus through the vulva (V). Sperm migrate around fertilized eggs (E) toward the anterior or posterior spermathecae. The uterus is divided into zones Z1, Z2, and Z3 for quantification. Sperm distribution is measured 1 hour after mating, whereas sperm motility is measured immediately. Scale bar, 100  $\mu$ m. (B) Fluorescent [tetramethylrhodamine isothiocyanate (TRITC)] WT sperm distribution in control and selected TGF- $\beta$  pathway mutants 1 hour after mating. Average zone distributions  $\pm$  SEM are shown. See tables S1 to S3 for complete data. Scale bar, 25  $\mu$ m. (C) Major DAF-7/TGF- $\beta$  pathway components.

**Fig. 2. TGF- $\beta$  pathway sites of action.** (A) Fluorescent (TRITC) WT sperm distribution in *daf-7* transgenic mutants. The spermatheca (yellow) is outlined. Average zone distributions  $\pm$  SEM are shown. (B) Spermatheca (Z3) targeting after adult germline-restricted TGF- $\beta$  ligand and receptor inactivation using *rff-1* mutants (20). (C) Z3 targeting in *daf-1* mutants expressing *daf-1* cDNA under tissue-specific promoters. The *glr-4*, *nmr-2*, and *tdc-1* promoters drive expression in nerve-ring interneurons (Fig. 1A). The common target among these promoters is RIM/RIC interneurons (17). Error bars denote SEM preceding trial number. \*\* $P < 0.001$ .





*daf-1* mutants (table S3). To directly test the hypothesis, we used liquid chromatography–tandem mass spectrometry (LC-MS/MS) operated in multiple reaction monitoring (MRM) mode to measure prostaglandin levels in WT and *daf-1* mutant extracts. Oocytes synthesize a mixture of F-class prostaglandins derived from dihomo- $\gamma$  linolenic (F1 subclass), arachidonic and  $\Omega$ -3 arachidonic (F2 subclass), and eicosapentaenoic acids (F3 subclass) (7). *C. elegans* PGF1 (CePGF1) and CePGF2 are mixtures of co-eluting PGF1 $\alpha$  and PGF2 $\alpha$  stereoisomers, respectively, including the mirror-image stereoisomer of PGF2 $\alpha$  called *ent*-PGF2 $\alpha$  (Fig. 3A). *daf-1* mutant extracts contain strongly reduced levels of all F-class isomers (Fig. 3B). CePGF1 and CePGF2 are reduced by ~75% in *daf-1* mutants (Fig. 3C), similar to mutants lacking germ cells (7). We conclude that DAF-7/TGF- $\beta$  signaling promotes oocyte prostaglandin synthesis essential for sperm guidance.

PGF2 $\alpha$  is prevalent in mammalian follicular fluid, although its functions are incompletely understood. Because DAF-7 regulates Cox-independent CePGF2 synthesis, we tested whether mice lacking Cox enzymes synthesize F-class prostaglandins. The mouse genome contains two *Cox* genes called *Cox-1* (*ptgs1*) and *Cox-2* (*ptgs2*). *Cox-1*<sup>-/-</sup>; *Cox-2*<sup>-/-</sup> double knockout (dKO) mouse pups appear similar to WT pups at birth but die within 12 hours due to a patent ductus arteriosus (18). To directly test whether Cox-independent prostaglandin synthesis occurs in mice, we extracted lipids from mutant and control pups delivered at term. MRM indicates that 6-keto PGF1 $\alpha$ , a stable metabolite of prostacyclin (see fig. S9 for prostaglandin structures, retention times, and MRM transitions), is eliminated in dKO mouse extracts (Fig. 4A and fig. S10A). In contrast, PGF2 $\alpha$  and/or co-eluting *ent*-PGF2 $\alpha$  are present (Fig. 4A and fig. S11). The PGF2 $\alpha$  stereoisomer 8-*epi*-PGF2 $\alpha$  and/or co-eluting 8-*epi*-15(R) PGF2 $\alpha$  are increased in the double mutants (Fig. 4A and fig. S11), and an unidentified PGF2 $\alpha$  isomer is unaffected by *Cox* genotype (fig. S11). More than 50% of total PGF2 $\alpha$  isomer levels remain in *Cox* dKO pups. PGD2 and PGE2 levels were slightly above the detection limit in WT pups. The absence of 6-keto PGF1 $\alpha$ , PGD2, and PGE2 isomers in *Cox* knockout extracts indicates that free-radical-induced lipid peroxidation, which generates a nonselective mixture of prostaglandin isomers (6), is inconsequential (fig. S10). These data indicate that Cox enzymes are not essential for mouse F-class prostaglandin synthesis.

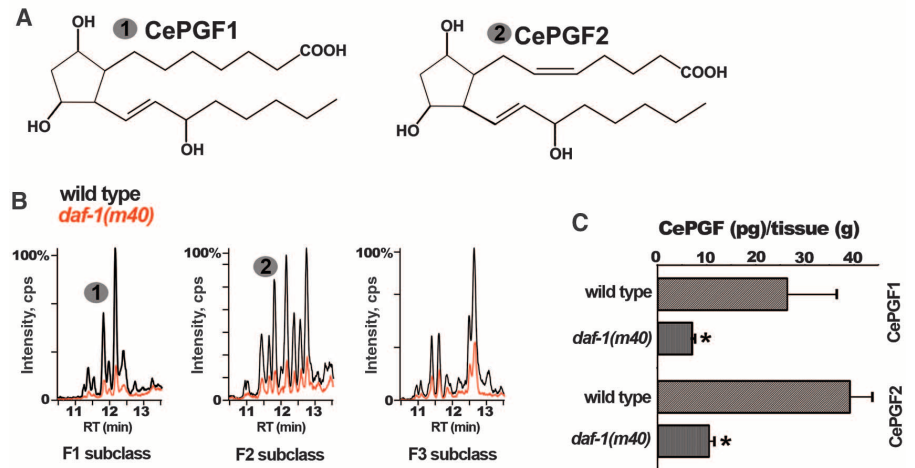
Our LC-MS/MS method separates most PGF2 $\alpha$  stereoisomers (7, 8, 19) (fig. S9). The retention times of the three major PGF2 $\alpha$  peaks in *Cox* dKO mouse extracts are markedly similar to those in *C. elegans* extracts. When mouse and worm extracts are run consecutively, the three PGF2 $\alpha$  isomer retention times are indistinguishable (Fig. 4B). We also found these PGF2 $\alpha$  isomers in brain, stomach, and small intestine tissues from a rare *Cox* dKO adult mouse that survived devel-

opment (fig. S12), as well as in WT adult mouse and zebrafish tissues (fig. S13). These results support the idea that Cox-independent prostaglandin synthesis is evolutionarily ancient.

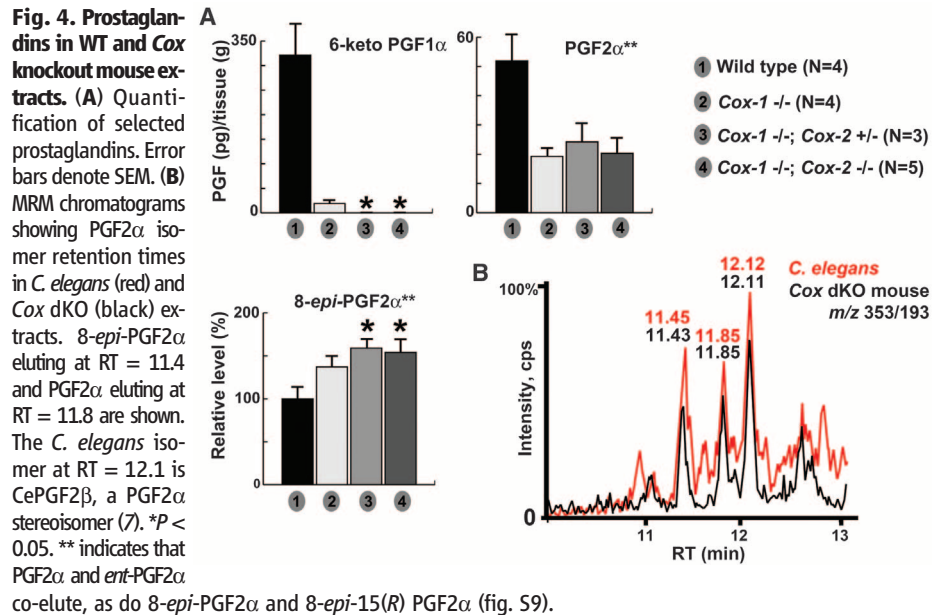
In summary, we delineate a *C. elegans* signaling pathway by which environmental cues are relayed from head sensory neurons to the gonad. As population density rises and food decreases, reduced DAF-7/TGF- $\beta$  levels in ASI neurons down-regulate R-Smad activity in developing oocytes and head interneurons that modulate feeding rate and fat metabolism. These disrupted neuroendocrine pathways converge on oocytes to inhibit the Cox-independent conversion of PUFAs into F-class prostaglandins. Consequently, sperm fail to locate the spermatheca efficiently, reducing the fertilization

rate. This mechanism enables *C. elegans* adults to modulate reproductive output in response to a dynamic external environment.

This study has two important implications: First, female environmental perception can have strong effects on sperm function. Disrupting the neuroendocrine mechanisms that mediate these effects—through genetic mutation, dietary changes, or environmental exposures—impairs fertility. These mechanisms might be relevant to infertile human couples and internally fertilizing animals with disappearing or changing habitats. Second, an alternative Cox-independent pathway for F-class prostaglandin synthesis emerged early in animal evolution. These prostaglandins probably modulate numerous biological processes, perhaps



**Fig. 3. Prostaglandins in WT and *daf-1* mutant extracts.** (A) Planar structures of *C. elegans* prostaglandins CePGF1 and CePGF2. CePGF2 is predominantly *ent*-PGF2 $\alpha$  (7). (B) MRM chromatograms of WT and *daf-1* mutant extracts. Worms were grown at 16°C and shifted to 25°C for 24 hours. The F1 class was detected with mass transition  $m/z$  (mass/charge ratio) = 355/311, the F2 class with  $m/z$  = 353/193, and the F3 class with  $m/z$  = 351/193 (7, 19). RT, retention time; cps, counts per second. (C) Quantification of CePGF1 and CePGF2 (\* $P$  < 0.05,  $N$  = 3 replicates). Error bars denote SEM.



**Fig. 4. Prostaglandins in WT and *Cox* knockout mouse extracts.** (A) Quantification of selected prostaglandins. Error bars denote SEM. (B) MRM chromatograms showing PGF2 $\alpha$  isomer retention times in *C. elegans* (red) and *Cox* dKO (black) extracts. 8-*epi*-PGF2 $\alpha$  eluting at RT = 11.4 and PGF2 $\alpha$  eluting at RT = 11.8 are shown. The *C. elegans* isomer at RT = 12.1 is CePGF2 $\beta$ , a PGF2 $\alpha$  stereoisomer (7). \* $P$  < 0.05. \*\* indicates that PGF2 $\alpha$  and *ent*-PGF2 $\alpha$  co-elute, as do 8-*epi*-PGF2 $\alpha$  and 8-*epi*-15(R) PGF2 $\alpha$  (fig. S9).

together with Cox-dependent prostaglandins. As prostaglandins are oxidative stress markers and therapeutic targets for many human disorders, the implications are far reaching.

## References and Notes

1. A. Cariboni, R. Maggi, J. G. Parnavelas, *Trends Neurosci.* **30**, 638–644 (2007).
2. D. A. Crain *et al.*, *Fertil. Steril.* **90**, 911–940 (2008).
3. C. D. Funk, *Science* **294**, 1871–1875 (2001).
4. T. Strünker *et al.*, *Nature* **471**, 382–386 (2011).
5. P. V. Lishko, I. L. Botchkina, Y. Kirichok, *Nature* **471**, 387–391 (2011).
6. G. L. Milne, H. Yin, J. D. Morrow, *J. Biol. Chem.* **283**, 15533–15537 (2008).
7. H. D. Hoang, J. K. Prasain, D. Dorand, M. A. Miller, *PLOS Genet.* **9**, e1003271 (2013).
8. J. W. Edmonds *et al.*, *Dev. Cell* **19**, 858–871 (2010).
9. H. M. Kubagawa *et al.*, *Nat. Cell Biol.* **8**, 1143–1148 (2006).
10. J. W. Edmonds, S. L. McKinney, J. K. Prasain, M. A. Miller, *Dev. Biol.* **359**, 47–58 (2011).
11. P. Ren *et al.*, *Science* **274**, 1389–1391 (1996).
12. K. Kim *et al.*, *Science* **326**, 994–998 (2009).
13. A. H. Ludewig, F. C. Schroeder, "Ascaroside signaling in *C. elegans*." in *WormBook*, The *C. elegans* Research Community, Ed. (WormBook, 2013); doi:10.1895/wormbook.1.155.1; www.wormbook.org.
14. T. L. Gumienny, C. Savage-Dunn, "TGF- $\beta$  signaling in *C. elegans*." in *WormBook*, The *C. elegans* Research Community, Ed. (WormBook, 2013); doi:10.1895/wormbook.1.22.2; www.wormbook.org.
15. D. Dalfó, D. Michaelson, E. J. Hubbard, *Curr. Biol.* **22**, 712–719 (2012).
16. Y. J. You, J. Kim, D. M. Raizen, L. Avery, *Cell Metab.* **7**, 249–257 (2008).
17. E. R. Greer, C. L. Pérez, M. R. Van Gilst, B. H. Lee, K. Ashrafi, *Cell Metab.* **8**, 118–131 (2008).
18. J. Reese *et al.*, *Proc. Natl. Acad. Sci. U.S.A.* **97**, 9759–9764 (2000).
19. J. K. Prasain, H. D. Hoang, J. W. Edmonds, M. A. Miller, *J. Vis. Exp.* **76**, e50447 (2013).
20. T. Sijen *et al.*, *Cell* **107**, 465–476 (2001).

**Acknowledgments:** We thank K. Ashrafi, R. Butcher, J. Parant, I. Kadisha, and T. van Groen for reagents or technical

assistance and the NIH-supported *Caenorhabditis* Genetics Center (P40 OD010440) for strains. This work was supported by NIH grants (GM085105 to M.A.M.; HL096967 and HL109199 to J.R.) and the University of Alabama at Birmingham (UAB) Reproductive Endocrinology and Infertility Fellowship Program. The UAB Targeted Metabolomics and Proteomics Laboratory has been supported by the UAB Skin Disease Research Center (P30 AR050948), UAB–University of California San Diego O'Brien Acute Kidney Injury Center (P30 DK079337), UAB Lung Health Center (HL114439 and HL110950), UAB Center for Free Radical Biology, and a National Center for Research Resources Shared Instrumentation grant (S10 RR19261). All data are provided in the main paper and supplementary materials. We declare no conflicts of interest.

## Supplementary Materials

www.sciencemag.org/content/344/6185/754/suppl/DC1  
Materials and Methods  
Figs. S1 to S13  
Tables S1 to S3  
References (21–34)

8 January 2014; accepted 23 April 2014  
10.1126/science.1250598

# Sulfur Oxidation Genes in Diverse Deep-Sea Viruses

Karthik Anantharaman,<sup>1</sup> Melissa B. Duhaime,<sup>2</sup> John A. Breier,<sup>3</sup> Kathleen A. Wendt,<sup>4</sup> Brandy M. Toner,<sup>4</sup> Gregory J. Dick<sup>1,2,5\*</sup>

Viruses are the most abundant biological entities in the oceans and a pervasive cause of mortality of microorganisms that drive biogeochemical cycles. Although the ecological and evolutionary effects of viruses on marine phototrophs are well recognized, little is known about their impact on ubiquitous marine lithotrophs. Here, we report 18 genome sequences of double-stranded DNA viruses that putatively infect widespread sulfur-oxidizing bacteria. Fifteen of these viral genomes contain auxiliary metabolic genes for the  $\alpha$  and  $\gamma$  subunits of reverse dissimilatory sulfite reductase (*rdsr*). This enzyme oxidizes elemental sulfur, which is abundant in the hydrothermal plumes studied here. Our findings implicate viruses as a key agent in the sulfur cycle and as a reservoir of genetic diversity for bacterial enzymes that underpin chemosynthesis in the deep oceans.

Chemolithoautotrophic bacteria are ubiquitous in the dark oceans (1), where they serve as a sink for CO<sub>2</sub> (2) through primary production that equals up to 53% of the particulate organic carbon exported from the photic zone (3). Uncultured sulfur-oxidizing bacteria of the SUP05 clade are among the most abundant and widespread marine chemolithoautotrophs, fixing carbon and oxidizing reduced sulfur species and hydrogen in diverse marine environments such as hydrothermal vent plumes (4), hydrothermal vent-associated animals (5, 6), and oxygen minimum zones (7), where they underpin cryptic links

between the sulfur and nitrogen cycles (8). Although viruses are abundant in these deep-sea ecosystems (9), little is known about viruses that infect lithotrophic primary producers.

We conducted shotgun metagenomic sequencing on samples from five different hydrothermal vent plumes and associated deep ocean waters at the Eastern Lau Spreading Center (Lau Basin) in the western Pacific Ocean and one plume at Guaymas Basin in the Gulf of California (10, 11) (table S1). De novo assembly of sequence reads and binning by tetranucleotide signatures (12) revealed discrete genomic "bins" (fig. S1). Five bins (henceforth Lau77, Lau85, Lau87, Lau218, and Lau220) contained 18 viral genome sequences of putative SUP05 viruses. Phylogeny of the viral large terminase gene (*terL*) (fig. S2) [which reflects phage DNA packaging mechanisms (13)], synteny with well-characterized phages of known taxonomy (fig. S3), and results of protein sequence similarity searches against public sequence databases (fig. S4) indicated that the five viruses belonged to three marine viral families of the orders

*Caudovirales* (double-stranded DNA viruses, no RNA stage), *Podoviridae*, *Siphoviridae*, and *Myoviridae* (table S2).

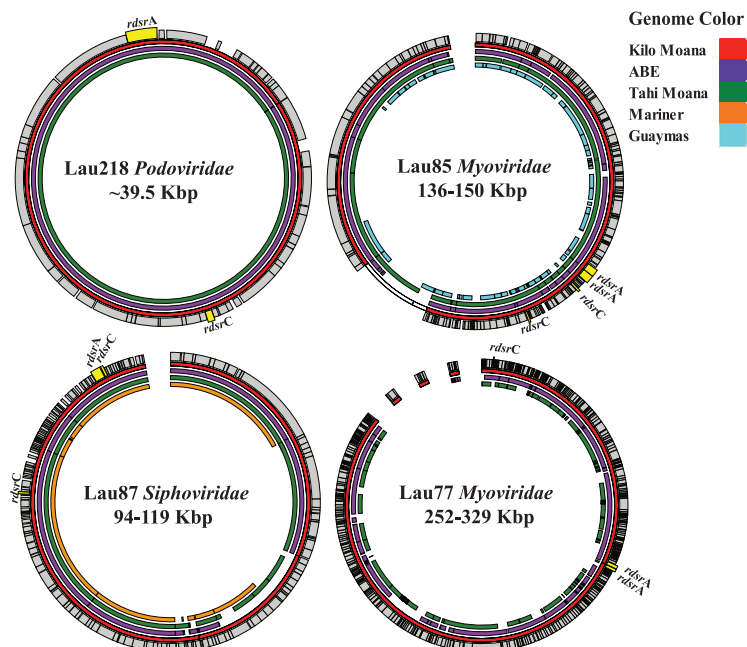
Fifteen of the 18 viral genomes (from four of the five SUP05 viral genomic bins) contained genes encoding the  $\alpha$  (*rdsrA*) and  $\gamma$  (*rdsrC*) subunits of the reverse-acting dissimilatory sulfite reductase (*Rdsr*) complex for elemental sulfur oxidation (Fig. 1). No other *rdsr* genes or other sulfur oxidation genes were present on the viral genomes. Analysis of bacterial genome bins recovered from Lau and Guaymas metagenomes revealed colocalized *rdsr* genes in the order *rdsrABEFHCMKLJOPN* in the Gammaproteobacteria Lau10 (SUP05), Lau62 (EC-01-9C-26), and Lau60 (unclassified). The Deltaproteobacterium Lau20 (Sar324) (14) possessed only *rdsrAB*. Regions flanking the bacterial *rdsr* genes showed no similarity to the viral genome sequences, suggesting that viral *rdsr* genes were derived from selective retention rather than recent homologous recombination with bacterial genomic DNA.

Phylogenetic analyses indicated that all viral *rdsrA* genes recovered were affiliated with SUP05 Gammaproteobacteria (74 to 96% amino acid identity) (fig. S5) and distinct from *rdsrA* genes of other bacteria (Fig. 2). We identified two distinct groups of *rdsrA* sequences that each included both viral and bacterial sequences. All viral *rdsrA* genes fall into group one, except for Lau85, which contained two copies of *rdsrA* with one representative in each group. Bacterial representatives of group one included the SUP05 GB-1 and GB-2 from Guaymas, as well as *Bathymodiolus* mussel symbionts (6). Group two was populated by SUP05 from oxygen minimum zones (7) and symbionts of deep-sea clams (5). The tight phylogenetic clustering of *rdsrA* gene sequences of three distinct phage families with SUP05 bacteria in two separate lineages suggests that the phage *rdsrA* genes originated from SUP05 and were transferred to viruses. These observations are analogous to those

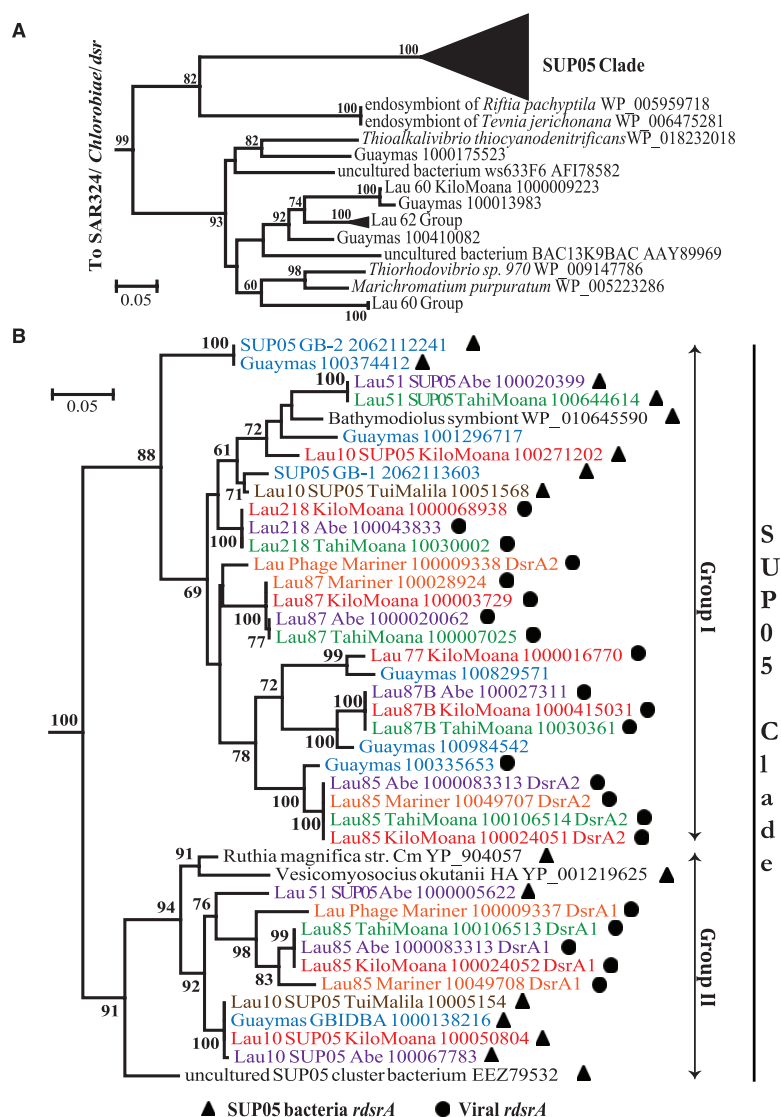
<sup>1</sup>Department of Earth and Environmental Sciences, University of Michigan, Ann Arbor, MI 48109, USA. <sup>2</sup>Department of Ecology and Evolutionary Biology, University of Michigan, Ann Arbor, MI 48109, USA. <sup>3</sup>Applied Ocean Physics and Engineering, Woods Hole Oceanographic Institution, Woods Hole, MA 02543, USA. <sup>4</sup>Department of Soil, Water, and Climate, University of Minnesota–Twin Cities, St. Paul, MN 55108, USA. <sup>5</sup>Center for Computational Medicine and Bioinformatics, University of Michigan, Ann Arbor, MI 48109, USA.

\*Corresponding author. E-mail: gdick@umich.edu

**Fig. 1. Gene content of 15 phage genomes from three viral families retrieved from Lau and Guaymas basins.** Colored nested circles represent syntenous viral genomes and contiguous genomic fragments from locations indicated in the legend. Gray boxes on the outermost circles indicate predicted genes from the Kilo Moana viruses. *rdsrA* and *rdsrC* genes are highlighted in yellow. Kbp, thousand base pairs.



**Fig. 2. Phylogeny of *rdsrA* genes from Lau and Guaymas basins inferred by Maximum Likelihood. (A)** Phylogenetic tree showing the SUP05 *rdsrA* gene clade in relation to closely related sequences. **(B)** Detailed view of the SUP05 *rdsrA* clade. Group one and group two subclades are shown on the right. Sequences are colored by geographical origin: blue, Guaymas Basin; red, Kilo Moana (Lau Basin); green, Tahi Moana (Lau Basin); purple, ABE (Lau Basin); brown, Tui Malila (Lau Basin); orange, Mariner (Lau Basin).





of core photosynthesis genes in cyanobacterial phages and other microbe-derived auxiliary metabolic genes (15, 16) (e.g., *psbA*, *psbD*, *mazG*) that are similar but not identical to known hosts, forming subclusters distinct from host proteins (17, 18).

The amino acid sequences deduced from the viral *rdsrA* and *rdsrC* genes indicated the capacity to serve as functional sulfur-oxidizing enzymes. Phage RdsrA contained all conserved sulfite reductase residues and secondary structure elements for  $\alpha$  helix and  $\beta$  sheets (fig. S6). Similarly, a multiple alignment of RdsrC amino acid sequences indicated highly conserved residues across two distinct groups (fig. S7). We also identified other genes in the viral genomes with high sequence identity to SUP05, including iron-sulfur cluster proteins, cytochromes, and sulfur relay proteins (table S3). The existence of these additional SUP05-like genes on viral genomes supports their specificity to SUP05 bacteria and suggests a role for viral genes in supplementing host metabolism.

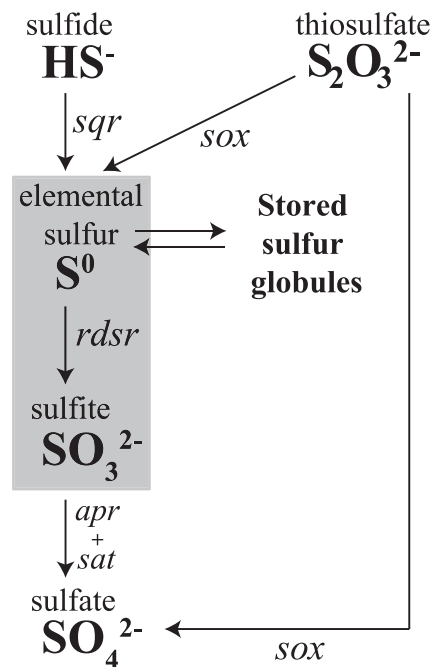
Elemental sulfur is a key and stable intermediate of bacterial oxidation of reduced sulfur compounds and constitutes a “bottleneck” in the sulfur cycle (19). Sulfur-oxidizing bacteria with an incomplete Sox pathway, such as SUP05, form intracellular or extracellular globules of elemental sulfur that serve as an electron-donor reserve for energy metabolism (Fig. 3) (4, 19–21). The presence of *rdsrA* and *rdsrC* on viral genomes may offer selective advantages to the viruses by sup-

plementing host pathways for oxidation of this sulfur during infection. First, enhanced expression of *rdsrA* could replenish proteins involved in a rate-limiting reaction in the host, as previously demonstrated with cyanobacterial phage D1 proteins involved in photosynthesis (22). Second, phage *rdsrC* could maintain or increase high transcription levels to ensure efficient delivery of sulfur substrate to the RdsrAB complex during infection. Thus, phage auxiliary metabolic genes that can supplement or sustain sulfur oxidation metabolism in their hosts may ensure continued viral infection and replication.

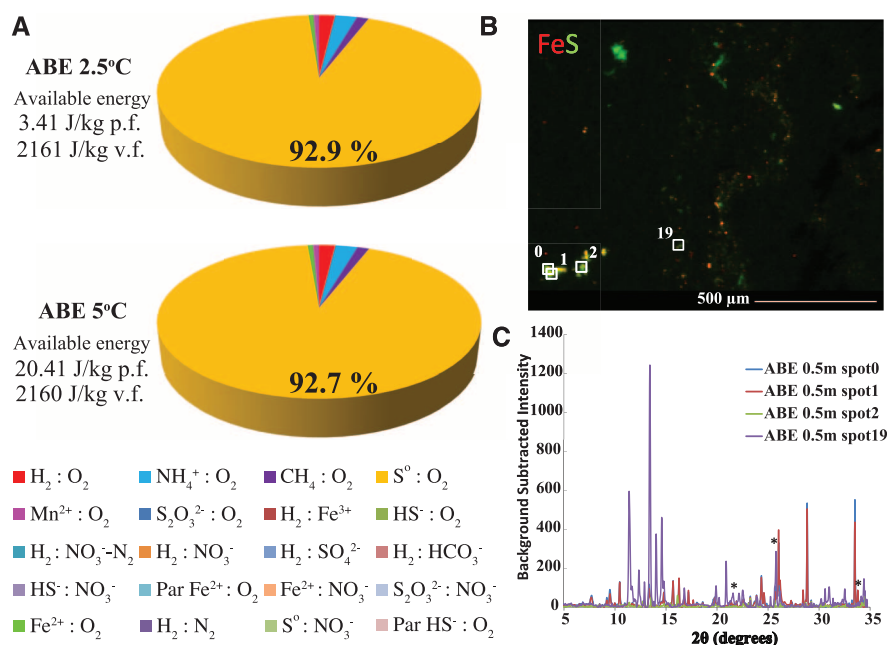
A coupled bioenergetic-thermodynamic reaction path model (23) indicated that aerobic elemental sulfur oxidation potentially accounted for 80 to 93% of the total lithotrophic energy available in the ABE and Mariner hydrothermal plumes at Lau Basin at two temperatures that were representative of the plumes studied here (Fig. 4A and fig. S8). The model predicted a minor role for 19 other lithotrophic microbial metabolisms, including oxidation of other reduced sulfur species such as hydrogen sulfide, sulfite, and thiosulfate. These results were consistent with a previous model of hydrothermal plumes that found elemental sulfur to be the most abundant source of chemosynthetic energy (24), as well as with our previous work (4, 25, 26), which was based on the same approach. Our model predicted greater relative energy yields for more energetically favored metabolisms, such as sulfur oxidation, because we

assumed that metabolic reactions occurred in sequence from most to least energetically favored. Our model also enabled reactions to explicitly modify the product and reactant pools. Although there is some uncertainty regarding the speciation of sulfur present in the plume, elemental sulfur is a central intermediate in the oxidation of other reduced forms of sulfur used by SUP05 (Fig. 3). X-ray fluorescence maps showed that sulfur was abundant in the plumes (Fig. 4B and fig. S8), whereas microprobe x-ray diffraction showed that elemental sulfur was widely present in particle aggregates with other crystalline phases, such as pyrite (Fig. 4C and fig. S8). Although we did not conclusively identify intracellular elemental sulfur, our results showed that elemental sulfur presented an abundant source of energy for SUP05 bacteria in hydrothermal plumes and deep ocean waters of Guaymas and Lau basins.

The abundance and diversity of viruses infecting SUP05 bacteria in hydrothermal plumes suggests that chemolithoautotrophs in the deep sea face viral predation pressures similar to photosynthetic microbes in the surface waters (27). The marked synteny and conservation of the four viruses studied here (95 to 99% genome nucleotide identity) across hydrothermal vent environments and ocean basins suggests that these viruses are ubiquitous in marine environments dominated by SUP05 bacteria. Analyses of the Pacific Ocean Virome data set (28) (fig. S9), which notably contains viral communities from oxygen minimum



**Fig. 3. Schematic of the sulfur oxidation pathway in SUP05 bacteria.** The gray box indicates the reaction affected by SUP05 viruses. Key genes are shown in italics: *sqr* (sulfide quinone reductase), *sox* (sulfur oxidation), *rdsr* (reverse dissimilatory sulfite reductase), *apr* (adenosine 5'-phosphosulfate reductase), and *sat* (sulfate adenyltransferase).



**Fig. 4. Bioenergetics and occurrence of sulfur in the ABE hydrothermal plume.** (A) Modeled free energies of catabolic reactions as a percentage of total available free energy in the ABE hydrothermal plume at 2.5° and 5°C. Total available free energy in the plume is normalized per kilogram of plume fluid (p.f.) and per kilogram of vent fluid (v.f.). (B) Distribution of iron (red) and sulfur (green) in particles collected at 0.5 m above the ABE vent. Locations where elemental sulfur was detected by microprobe x-ray diffraction measurements are indicated as spots 0, 1, 2, and 19. (C) Radially integrated diffractograms with elemental sulfur peaks annotated (asterisks) at 22.0°, 25.7°, and 34.1° 2 $\theta$ .

zones dominated by SUP05 (7), revealed the presence of *rdsrA* and *rdsrC* genes (table S5), consistent with the prevalence of phage-encoded sulfur oxidation beyond hydrothermal plumes and in the wider pelagic oceans.

To date, deep-sea SUP05 has evaded growth in laboratory cultures; thus, direct host-phage manipulations and validation of the underlying mechanisms of phage-influenced sulfur oxidation remain a challenge. Yet, this study demonstrates the sequence-based elucidation of microbial community dynamics through the discovery of phages that infect a widespread deep-sea bacterium. The existence of *rdsr* genes in viral genomes reveals a mechanism for horizontal transfer of genes associated with sulfur cycling (29) and implicates viruses in the evolutionary dynamics of a central step in the planetary cycling of sulfur.

## References and Notes

- B. K. Swan *et al.*, *Science* **333**, 1296–1300 (2011).
- J. Aristegui, J. M. Gasol, C. M. Duarte, G. J. Herndl, *Limnol. Oceanogr.* **54**, 1501–1529 (2009).
- T. Reinthaler, H. M. van Aken, G. J. Herndl, *Deep-Sea Res. II* **57**, 1572–1580 (2010).
- K. Anantharaman, J. A. Breier, C. S. Sheik, G. J. Dick, *Proc. Natl. Acad. Sci. U.S.A.* **110**, 330–335 (2013).
- I. L. Newton *et al.*, *Science* **315**, 998–1000 (2007).
- J. M. Petersen *et al.*, *Nature* **476**, 176–180 (2011).
- D. A. Walsh *et al.*, *Science* **326**, 578–582 (2009).
- D. E. Canfield *et al.*, *Science* **330**, 1375–1378 (2010).
- S. Hara, I. Koike, K. Terauchi, H. Kamiya, E. Tanoue, *Mar. Ecol. Prog. Ser.* **145**, 269–277 (1996).
- G. J. Dick, B. M. Tebo, *Environ. Microbiol.* **12**, 1334–1347 (2010).
- R. A. Lesniewski, S. Jain, K. Anantharaman, P. D. Schloss, G. J. Dick, *ISME J.* **6**, 2257–2268 (2012).
- G. J. Dick *et al.*, *Genome Biol.* **10**, R85 (2009).
- S. R. Casjens *et al.*, *J. Bacteriol.* **187**, 1091–1104 (2005).
- C. S. Sheik, S. Jain, G. J. Dick, *Environ. Microbiol.* **16**, 304–317 (2014).
- M. Breitbart, L. R. Thompson, C. A. Suttle, M. B. Sullivan, *Oceanography* **20**, 135–139 (2007).
- M. Breitbart, *Annu. Rev. Mar. Sci.* **4**, 425–448 (2012).
- J. C. Ignacio-Espinoza, M. B. Sullivan, *Environ. Microbiol.* **14**, 2113–2126 (2012).
- D. Lindell *et al.*, *Proc. Natl. Acad. Sci. U.S.A.* **101**, 11013–11018 (2004).
- W. Ghosh, B. Dam, *FEMS Microbiol. Rev.* **33**, 999–1043 (2009).
- D. Hensen, D. Sperling, H. G. Trüper, D. C. Brune, C. Dahl, *Mol. Microbiol.* **62**, 794–810 (2006).
- K. T. Marshall, R. M. Morris, *ISME J.* **7**, 452–455 (2013).
- D. Lindell, J. D. Jaffe, Z. I. Johnson, G. M. Church, S. W. Chisholm, *Nature* **438**, 86–89 (2005).
- Materials and methods are available as supplementary materials on Science Online.
- T. M. McCollom, *Deep-Sea Res. I* **47**, 85–101 (2000).
- J. A. Breier *et al.*, *Geochim. Cosmochim. Acta* **88**, 216–236 (2012).
- M. Li *et al.*, *Nat. Commun.* **5**, 3192 (2014).
- S. Avrani, O. Wurtzel, I. Sharon, R. Sorek, D. Lindell, *Nature* **474**, 604–608 (2011).
- B. L. Hurwitz, M. B. Sullivan, *PLOS ONE* **8**, e57355 (2013).
- M. Klein *et al.*, *J. Bacteriol.* **183**, 6028–6035 (2001).

**Acknowledgments:** This project is funded in part by the Gordon and Betty Moore Foundation (grant GBMF2609) and the NSF (grants OCE1038006, OCE1038055, OCE1037991, and OCE1029242). We thank the University of Michigan Rackham Graduate School Faculty Research Fellowship Program for their support and M. Li and S. Jain for their assistance. DNA sequencing was conducted at the University of Michigan DNA Sequencing Core. We acknowledge the captain and crew of *R/V Thomas G. Thompson*, Chief Scientist A.-L. Reysenbach, and J. Sylvan for sampling and logistical support. For assistance with synchrotron measurements at BL10.3.2, we thank K. J. Edwards, J. V. Sorensen, M. A. Marcus, and S. C. Fakra. The Advanced Light Source is supported by the Director, Office of Science, Office of Basic Energy Sciences, of the U.S. Department of Energy (DOE) under contract no. DE-AC02-05CH11231. The nucleotide sequences are available from DOE JGI-IMG/MER (Taxon Object IDs: Kilo Moana, 3300001680; ABE, 3300001681; Mariner, 3300001678; Tahiti Moana, 3300001679; Tui Malila, 3300001676; Guaymas, 3300001683) and the National Center for Biotechnology Information (BioProject: PRJNA234377). We declare no competing financial interests.

## Supplementary Materials

www.sciencemag.org/content/344/6185/757/suppl/DC1  
Materials and Methods  
Supplementary Text  
Figs. S1 to S10  
Tables S1 to S6  
References (30–78)  
Data S1

14 February 2014; accepted 16 April 2014  
Published online 1 May 2014;  
10.1126/science.1252229

# Positive Feedback Within a Kinase Signaling Complex Functions as a Switch Mechanism for NF- $\kappa$ B Activation

Hisaaki Shinohara,<sup>1\*</sup> Marcelo Behar,<sup>2,3\*</sup> Kentaro Inoue,<sup>1</sup> Michio Hiroshima,<sup>4,5</sup> Tomoharu Yasuda,<sup>6†</sup> Takeshi Nagashima,<sup>1‡</sup> Shuhei Kimura,<sup>7</sup> Hideki Sanjo,<sup>6§</sup> Shiori Maeda,<sup>6</sup> Noriko Yumoto,<sup>1</sup> Sewon Ki,<sup>1</sup> Shizuo Akira,<sup>8</sup> Yasushi Sako,<sup>5</sup> Alexander Hoffmann,<sup>2,3||</sup> Tomohiro Kurosaki,<sup>6,9||</sup> Mariko Okada-Hatakeyama<sup>1||</sup>

A switchlike response in nuclear factor- $\kappa$ B (NF- $\kappa$ B) activity implies the existence of a threshold in the NF- $\kappa$ B signaling module. We show that the CARD-containing MAGUK protein 1 (CARMA1, also called CARD11)—TAK1 (MAP3K7)—inhibitor of NF- $\kappa$ B ( $\text{I}\kappa\text{B}$ ) kinase- $\beta$  (IKK $\beta$ ) module is a switch mechanism for NF- $\kappa$ B activation in B cell receptor (BCR) signaling. Experimental and mathematical modeling analyses showed that IKK activity is regulated by positive feedback from IKK $\beta$  to TAK1, generating a steep dose response to BCR stimulation. Mutation of the scaffolding protein CARMA1 at serine-578, an IKK $\beta$  target, abrogated not only late TAK1 activity, but also the switchlike activation of NF- $\kappa$ B in single cells, suggesting that phosphorylation of this residue accounts for the feedback.

The transcription factor nuclear factor- $\kappa$ B (NF- $\kappa$ B) has a central role in determining cellular outcomes (1–3). Stimulus-driven NF- $\kappa$ B activity is highly dynamic and shows oscillations due to transcriptionally inducible negative feedback of inhibitor of NF- $\kappa$ B ( $\text{I}\kappa\text{B}$ ) (3–6). When examined at the single-cell level, NF- $\kappa$ B activity is triggered in a switchlike manner, and the number of fully activated cells underlies a

shallow population dose response (6). The switchlike response in NF- $\kappa$ B activity implies the existence of a threshold in the receptor-proximal signaling module, but this mechanism has not been elucidated.

In B cell receptor (BCR) signaling, NF- $\kappa$ B activity determines multiple B cell functions (7) (Fig. 1A). BCR stimulation by cognate antigen first induces activation of protein kinase C  $\beta$  (PKC $\beta$ ),

which phosphorylates serine-668 (S668) of CARD-containing MAGUK protein1 (CARMA1, also called CARD11). This modification causes a conformational change in CARMA1, allowing recruitment and activation of both the protein

<sup>1</sup>Laboratory for Integrated Cellular Systems, RIKEN Center for Integrative Medical Sciences (IMS-RCI), Tsurumi-ku, Yokohama, Kanagawa 230-0045, Japan. <sup>2</sup>Signaling Systems Laboratory, Department of Chemistry and Biochemistry, University of California, San Diego, La Jolla, CA 92093, USA. <sup>3</sup>Institute for Quantitative and Computational Biosciences (QC Bio) and Department of Microbiology, Immunology, and Molecular Genetics, University of California, Los Angeles, Los Angeles, CA 90025, USA. <sup>4</sup>Laboratory for Cell Signaling Dynamics, RIKEN Quantitative Biology Center (QBC), 6-2-3, Furuedai, Suita, Osaka 565-0874, Japan. <sup>5</sup>Cellular Informatics Laboratory, RIKEN, 2-1 Hirosawa, Wako 351-0198, Japan. <sup>6</sup>Laboratory for Lymphocyte Differentiation, RIKEN Center for Integrative Medical Sciences (IMS-RCI), Tsurumi-ku, Yokohama, Kanagawa 230-0045, Japan. <sup>7</sup>Graduate School of Engineering, Tottori University 4-101, Koyama-minami, Tottori 680-8552, Japan. <sup>8</sup>Laboratory of Host Defense, WPI Immunology Frontier Research Center, Osaka University, 3-1 Yamada-oka, Suita, Osaka 565-0871, Japan. <sup>9</sup>Laboratory for Lymphocyte Differentiation, WPI Immunology Frontier Research Center, Osaka University, 3-1 Yamada-oka, Suita, Osaka 565-0871, Japan.

\*These authors contributed equally to this work.

†Present address: Max-Delbrück-Center for Molecular Medicine, 13125 Berlin, Germany.

‡Present address: Division of Cell Proliferation, Tohoku University Graduate School of Medicine, Sendai, Miyagi 980-8575, Japan.

§Present address: Department of Molecular and Cellular Immunology, Shinshu University School of Medicine, 3-1-1 Asahi, Matsumoto, Nagano 390-8621 Japan.

||Corresponding author. E-mail: ahoffmann@ucla.edu (A.H.); kurosaki@rci.riken.jp (T.K.); marikoh@rci.riken.jp (M.O.-H.)

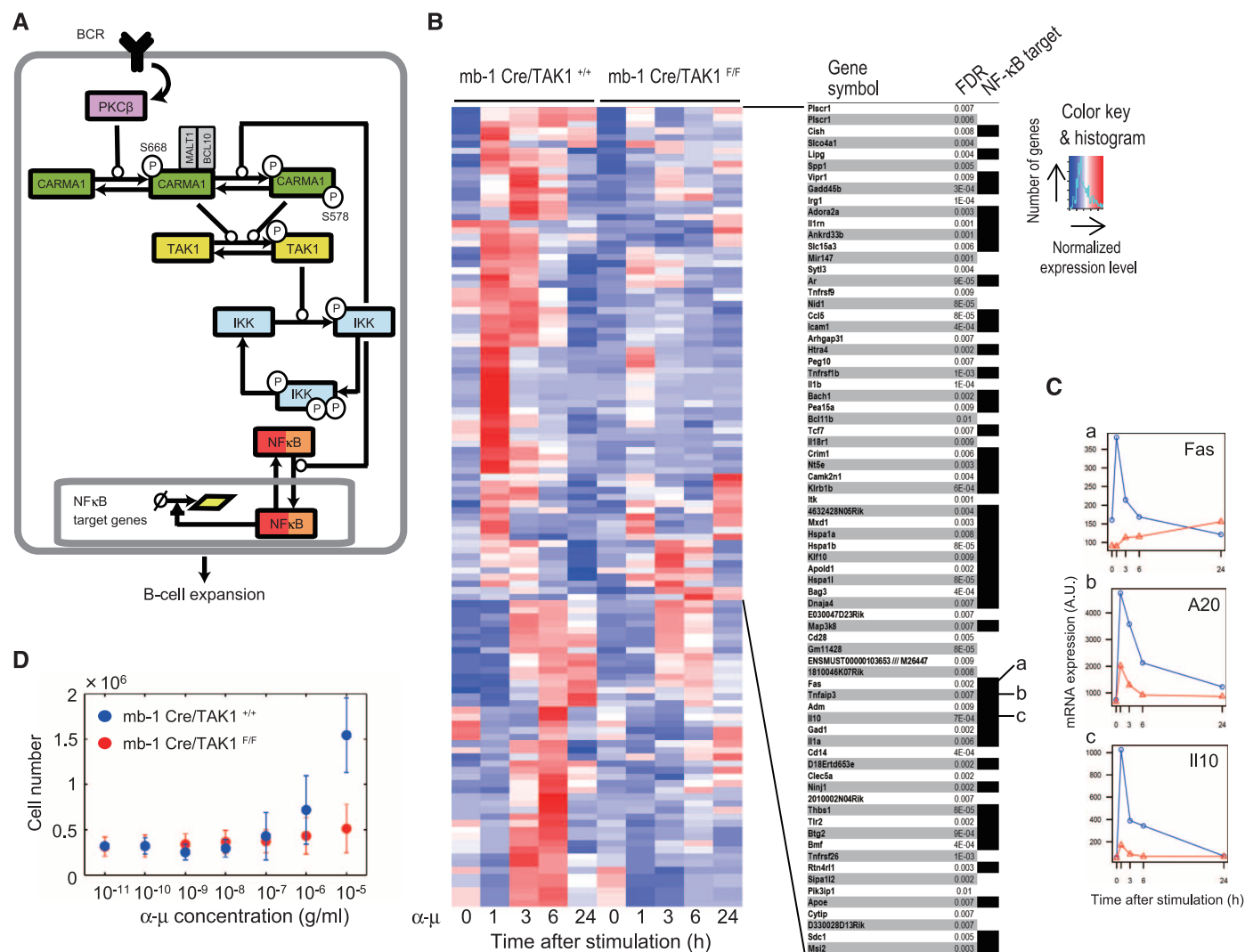
kinase TAK1 (also called MAP3K7) and the adapter protein Bcl10, the caspase-like protein MALT1 (CBM complex), and the associated I $\kappa$ B kinase (IKK) complex (7, 8). These interactions cause IKK $\beta$  activation, allowing for I $\kappa$ B phosphorylation and degradation, resulting in nuclear translocation of NF- $\kappa$ B and increased transcription of target genes. The assembly of the CARMA1 complex is regulated via multiple mechanisms (9–12). Notably, the activated IKK $\beta$  phosphorylates CARMA1 at S578, thereby serving as a positive modifier to enhance the assembly of the CARMA1 complex, which increases IKK $\beta$  activity (13). Regulatory motifs involving positive feedback may enhance and prolong stimulus-induced activities and, in some cases, provide the

basis for switchlike behavior in signaling pathways (14, 15). We used iterative quantitative experiments and mathematical modeling to show that TAK1-IKK $\beta$  engages in positive feedback through CARMA1 and that this positive feedback loop can produce switchlike activation of NF- $\kappa$ B.

TAK1 may be critical for induction of NF- $\kappa$ B activity through the regulation of IKK activity (7). Indeed, we found that upon BCR stimulation, splenic B cells obtained from mice after conditional deletion of TAK1 (TAK1-cKO) showed very little nuclear translocation of RelA and NF- $\kappa$ B1 (fig. S1A), IKK $\beta$  activation, phosphorylation of I $\kappa$ B (fig. S1, B and C), and expression of NF- $\kappa$ B target genes (e.g., *Fas*, *A20*, and *Il10*)

(Fig. 1, B and C). Steep induction of cellular proliferation in response to stronger stimuli observed in wild-type cells [Hill coefficient, 1.88; median effective concentration ( $EC_{50}$ ),  $1.46 \times 10^{-6}$  g/ml] was abolished in the TAK1-cKO cells (Fig. 1D). Thus, TAK1 appears to be indispensable for BCR-mediated activation of NF- $\kappa$ B and cell proliferation.

To further investigate the regulation of NF- $\kappa$ B activity in response to BCR-stimulation, we assessed TAK1 and IKK $\beta$  activities in chicken DT40 B cells. We used an ultrafine, 90-s-interval time-course analysis of TAK1 activity to resolve two maxima at 1.5 and 6 min after BCR stimulation (Fig. 2A and fig. S2A). By contrast, IKK $\beta$  activity showed an initial plateau followed by a peak at 6 min (Fig. 2B and fig. S2B). When knock-in



**Fig. 1. IKK $\beta$ -NF- $\kappa$ B activation in BCR signaling.** (A) The NF- $\kappa$ B activation pathway in BCR signaling. The circled letter P indicates phosphorylated state of the amino acid residue. Arrows show functional modifications of the protein or protein complex. Lines ended by an open circle indicate activation of the component. (B to D) Role of TAK1 in NF- $\kappa$ B activation in mouse primary B cells. (B) Gene expression analysis. Splenic B cells from control mice (mb-1Cre/TAK1<sup>+/+</sup>) or TAK1 B cell knockout mice (mb-1Cre/TAK1<sup>F/F</sup>) were stimulated with anti-IgM (10  $\mu$ g/ml) ( $\alpha$ - $\mu$ ) for the indicated time periods. Up-regulated genes

in control mice with compatible genes in TAK1 knockout mice are shown. NF- $\kappa$ B target gene is shown as a black box (NF- $\kappa$ B target), and *Fas* (a), *A20* (b), and *Il-10* (c) represent typical target genes. FDR, false discovery rate. (C) TAK1-deficient splenic B cells showed significantly decreased expression of typical NF- $\kappa$ B-target genes; *Fas* (a), *A20* (b), and *Il-10* (c) in response to anti-IgM ( $\alpha$ - $\mu$ ) stimulation; control (blue), TAK1 knockout (red). (D) B cell proliferation dose response. Data are mean  $\pm$  SD [ $n = 5$  mice for control (blue);  $n = 3$  mice for TAK1 knockout (red)].



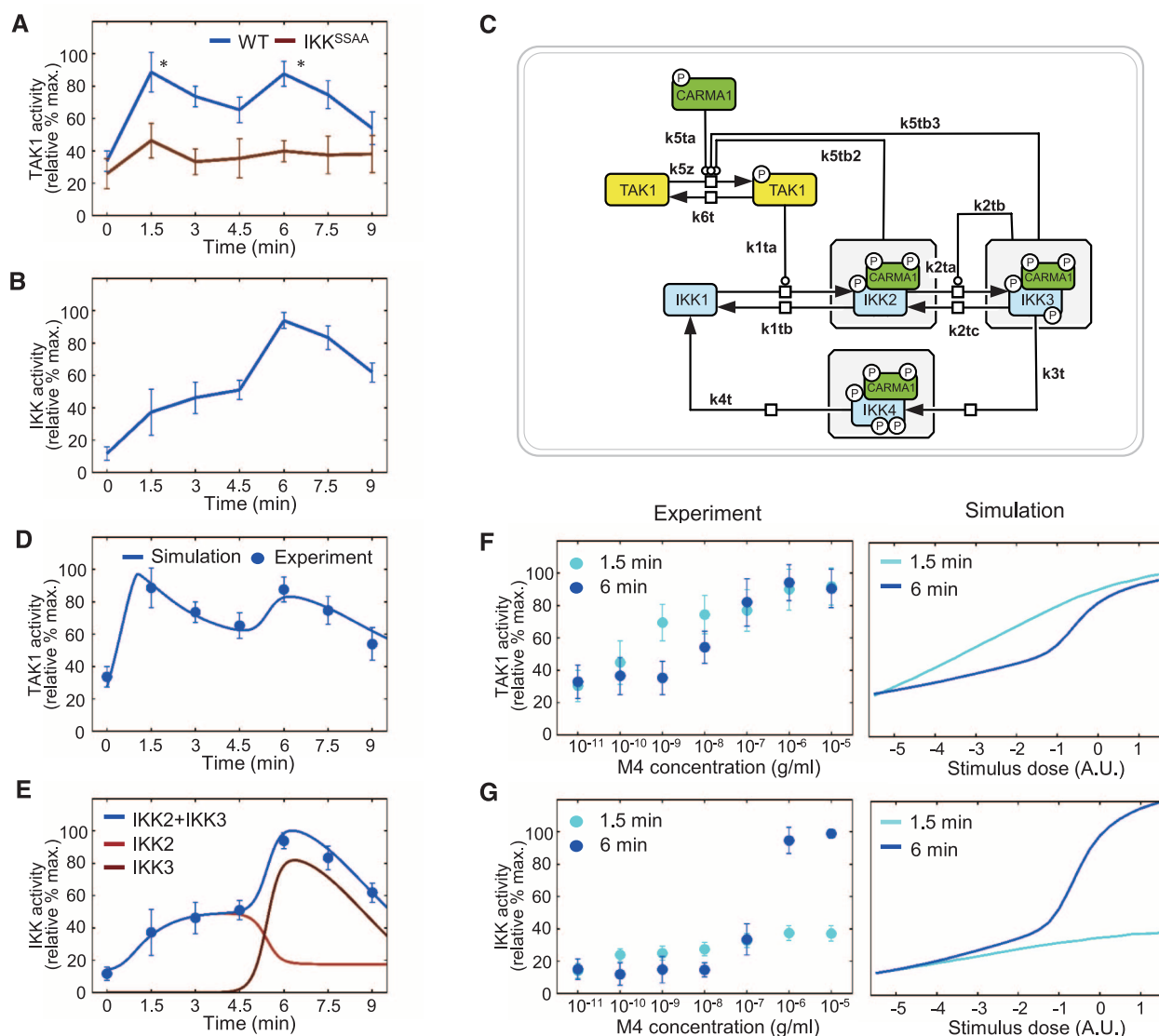
cells expressing catalytically inactive IKK $\beta$  (IKK $\beta^{SSAA}$ , S176A and S181A mutated) B cells (13) were examined, TAK1 activity was significantly reduced and the second peak was completely absent (Fig. 2A and fig. S2A). Mutation of IKK $\beta$  also decreased the interaction of TAK1 with CARMA1 (fig. S3, A and C). The lack of correspondence between time-course patterns of TAK1 and IKK $\beta$  activities, as well as the reduced TAK1 activity in IKK $\beta^{SSAA}$  cells, hinted at a positive-feedback regulation from IKK $\beta$  to TAK1.

To rigorously analyze the observed signaling dynamics, we constructed a mathematical model depicting the activity states of TAK1 and IKK $\beta$

with phosphorylation of CARMA1 S668 (P668) as an input (Fig. 2C and fig. S4). The model includes two IKK $\beta$  activation states, IKK2 and IKK3 (potentially reflecting oligomerization or different phosphorylation states), whose formation is mediated by trans-autophosphorylation (16), and an inactivated form (IKK4) likely mediated by further phosphorylation and subsequent breakdown of the complex containing NF- $\kappa$ B essential modifier (IKK $\gamma$ , also called NEMO) (17) (Fig. 2C and table S1). In the absence of IKK $\beta$  self-activation and phosphorylation processes, the model failed to show late TAK1 and IKK $\beta$  activities and termination of the signals, respectively

(fig. S5). After parameterization, the model simulations showed an excellent correspondence with the experimental time course (Fig. 2, D and E, and fig. S2) and dose-response profiles (Fig. 2, F and G, and figs. S6 and S7) of TAK1 and IKK $\beta$  activity. The high Hill coefficient of IKK $\beta$  at 6 min but not at 1.5 min (1.92 and 0.34, respectively;  $EC_{50}$ ,  $1.83 \times 10^{-7}$  g/ml) in dose-response profiles is characteristic of a positive-feedback regulation.

Analysis of the model trajectory in the phase space showed that TAK1 operates close to quasi-equilibrium and that its initial activity is mainly driven by the input signal (but still helped by IKK



**Fig. 2. Mathematical model of TAK1-IKK $\beta$  positive feedback.** (A) Time course of TAK1 activity in DT40 B cells after stimulation with the monoclonal antibody (mAb) to chicken IgM (M4). Results are mean  $\pm$  SD ( $n = 8$ ). Wild type (WT, blue), IKK<sup>SSAA</sup> (brown). \* denotes statistical significant difference ( $P < 0.01$ , Welch's  $t$  test) from the value at 4.5 min. (B) Time course of IKK $\beta$  activity after stimulation with M4. Results are mean  $\pm$  SD ( $n = 6$ ). (C) Diagram of the TAK1-IKK $\beta$  feedback model. Each activation state of IKK $\beta$  is depicted: IKK1 (basal), IKK2 (phosphorylated), IKK3 (trans-activated, highly active), and IKK4 (hyperphosphorylated, inactive). Parameters shown on the arrows correspond to

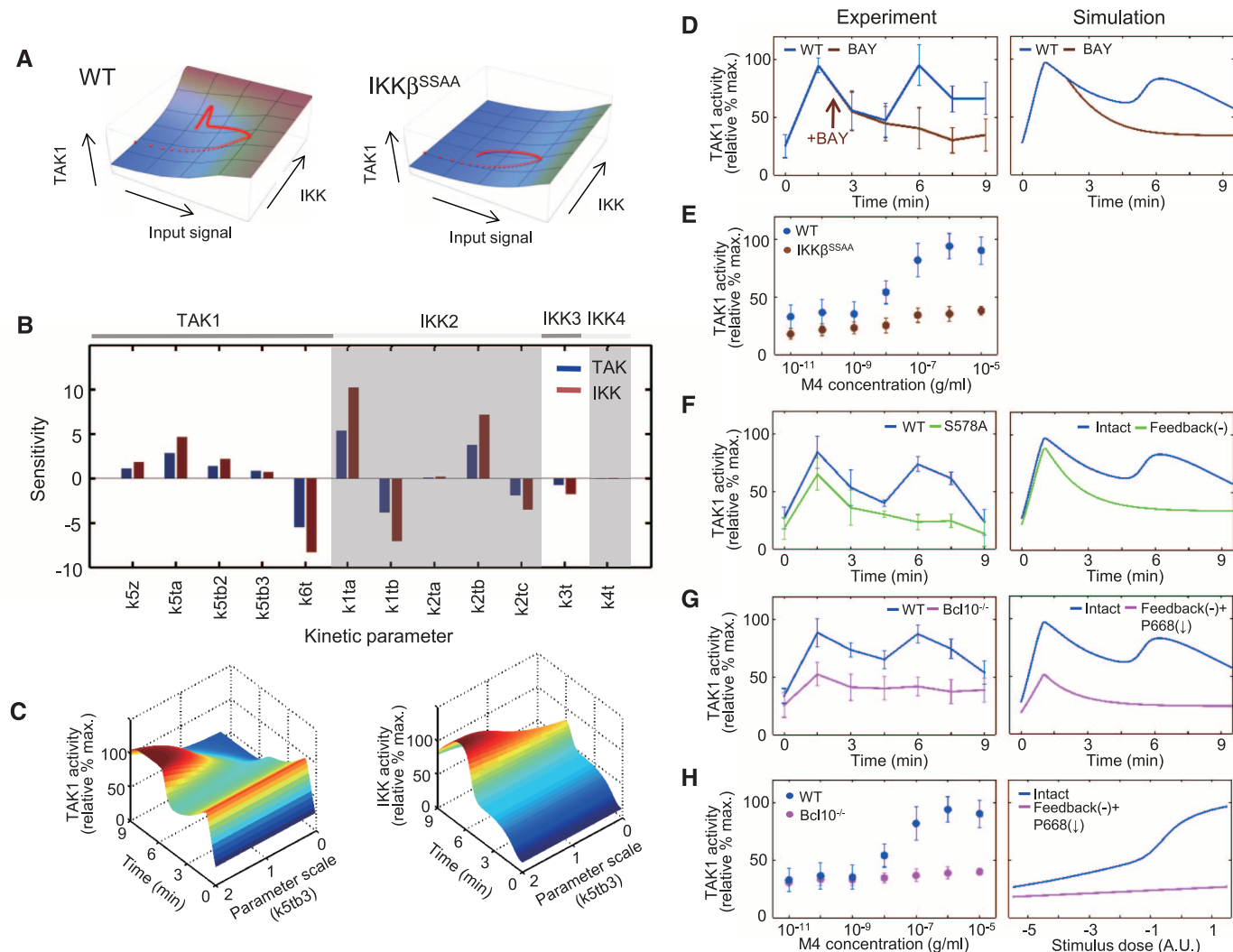
those in the sensitivity analysis in Fig. 3, B and C. The circled letter P denotes phosphorylation state. Lines with an open circle represent activation. (D and E) Simulation (lines) and experimental data (dots) of the time-course responses. Values of TAK1 (D) and IKK $\beta$  (E) activities are shown as median relative to the maximum change measured in M4-stimulated cells, so that the maximum values equal 100 (see fig. S2 and supplementary methods) ( $n = 8$ ). (F and G) Experimental (dots) and simulation (lines) data of dose responses. TAK1 (F) and IKK $\beta$  (G) activities were examined at 1.5 (aqua) and 6 min (blue) after stimulation with the indicated concentrations of M4 ( $n = 8$  to 10).

activity) but becomes driven by IKK $\beta$  as the event progresses (Fig. 3A). This explains loss of the second peak of TAK1 activity and reduced initial peak in IKK $\beta^{SSAA}$  cells (Fig. 2A). The model predicted that late TAK1 activity is only possible in the presence of persistent input signal (Fig. 3A, right), which is consistent with the loss of the second peak in the presence of a PKC inhibitor after 2 min of BCR stimulation (fig. S8). Likewise, IKK2 activation mediated by the TAK1 activity (k1ta) is the most sensitive parameter for IKK $\beta$  activation (Fig. 3B). A positive-feedback loop from IKK3 to TAK1 (k5tb3) controls the amplitude of IKK $\beta$  and late TAK1 activities (Fig. 3C). We confirmed in mouse splenic B cells that the second wave of TAK1 activity was abolished by addition of an IKK $\beta$  inhibitor (BAY11-7985)

after 2 min of BCR stimulation (Fig. 3D, fig. S9, and table S2). These results suggest that the IKK $\beta$ -mediated sustained activation of TAK1 is a common mechanism for TAK1 activation. Thus, IKK $\beta$  activity is essential for the steep dose response of TAK1 activity (Fig. 3E and fig. S6).

Deletion of TAK1 severely reduced phosphorylation of S578 in CARMA1 (fig. S3, B and F), without having any effect on the PKC $\beta$ -dependent phosphorylation of S668 (fig. S10), suggesting that an upstream feedback target is unlikely. By contrast, the second peak of TAK1 activity was completely abrogated in this CARMA1<sup>S578A</sup> mutant (Fig. 3F and fig. S11). Suppressing the IKK $\beta$ -driven feedback in the mathematical model resulted in a TAK1 activity profile that recapitulated the experimental data (Fig. 3F and table S3).

We investigated the role of the Bcl10 adaptor protein in the CARMA1 complex for IKK-dependent TAK1 activation. Bcl10 positively regulates NF- $\kappa$ B activation in antigen receptor signaling (18); however, negative regulation of Bcl10 by IKK $\beta$  is also implicated after T cell receptor (TCR) engagement (10–12). The time course profile of TAK1 activity in Bcl10<sup>-/-</sup> cells (fig. S12) was similar to that of IKK $\beta^{SSAA}$  cells (Figs. 2A and 3G and fig. S2), suggesting that Bcl10 has a positive role in IKK $\beta$  feedback regulation in this time frame. However, the overall reduction of TAK1 activity in these mutants raised the additional possibility that both Bcl10 and IKK $\beta$  may facilitate the initial activation of TAK1. Simulations with attenuated inputs of both CARMA1-P668 and IKK $\beta$  feedback (table S4) recapitulated



**Fig. 3. Role of TAK1-IKK $\beta$  feedback loop in switchlike activation of TAK1 and IKK $\beta$ .** (A) Equilibrium surface of TAK1 activity in WT and IKK $\beta^{SSAA}$  cells obtained by simulation. (B) Sensitivity analysis of TAK1 activity and IKK $\beta$  activity on each kinetic parameter. (C) Simulated effects of various degrees (0.02 to 2 times that of the wild type) of the positive-feedback strength (k5tb3) from IKK3 to TAK1 (left) and IKK $\beta$  (right) activities. (D) Time course of TAK1 activity in mouse B cells. The IKK $\beta$  inhibitor BAY11-7985 (BAY) was added 2 min after stimulation with anti-IgM (10  $\mu$ g/ml) (left). The simulation represents the attenuation of IKK $\beta$  2 min after signal input (right). (E) TAK1

dose response from experimental data in WT and IKK $\beta^{SSAA}$  cells at 6 min after ligand stimulation ( $n = 8$  to 10). (F) Time-course experiment of TAK1 activation in WT and CARMA1<sup>S578A</sup> DT40 B cells ( $n = 3$ ) (left). Simulation of TAK1 time-course activities under feedback attenuated conditions (right). (G) Time-course experiment of TAK1 activation in WT and Bcl10<sup>-/-</sup> DT40 B cells ( $n = 8$ ) (left). Simulation of TAK1 time-course activities under feedback and input attenuated conditions (right). (H) Experimental data for TAK1 activity in an M4 dose-response study in Bcl10<sup>-/-</sup> cells ( $n = 8$ ) (left). Simulation of the dose response of TAK1 activities under feedback and input attenuated conditions (right).

the time-course dynamics of TAK1 activity in Bcl10<sup>-/-</sup> cells (Fig. 3G and fig. S2A). The model's dose response of TAK1 activity to BCR stimulation in this hypothetical condition accurately captured the experimental observations in the Bcl10<sup>-/-</sup> (Fig. 3H and fig. S13) and IKKβ<sup>SSAA</sup> cells (Fig. 3E and fig. S6). In support of the simulation, phosphorylation of CARMA1 at S668 (input signal) was reduced in cells deficient in IKKβ or Bcl10 (fig. S14). Bcl10 and MALT1 binding in the CARMA1 complex was also reduced in the IKKβ-deficient cells (fig. S3, B to E). Taken together, these data indicate that Bcl10 and IKKβ mediate feedback regulation of TAK1, but may also function in initial activation of TAK1 in the CARMA1 complex, as shown in T cells (10).

To determine whether the CARMA1-TAK1-IKKβ positive-feedback loop that functions to amplify IKKβ activity in BCR signaling also functions to induce switchlike activation of NF-κB, we examined nuclear translocation of RelA in cell populations (fig. S15A). In the steep dose-dependent RelA translocation profile at 45 min, peak maxima exhibited positive cooperativity (Hill coefficient, 2.46; EC<sub>50</sub>,  $1.48 \times 10^{-6}$  g/ml) (Fig. 4B and fig. S15C) and closely resembled that of the IKKβ activity at 6 min (Fig. 4A). The analysis showed that the dose response of RelA translocation is shifted and more gradual in the

CARMA1 S578 mutant cells (Fig. 4B and fig. S15C), suggesting a lack of positive cooperativity in this mutant.

We tested whether the switchlike activation of NF-κB observed at the cell population level also existed at the single-cell level. Live cell images showed that the RelA labeled with green fluorescent protein (GFP) in the cytosol in the resting state began to translocate into the nucleus at 10 min after BCR stimulation and remained until ~60 min in wild-type cells (Fig. 4C). Activated cells showing a high ratio of nuclear to cytosolic (N/C > 1) RelA-GFP were observed under various dosage conditions, although the frequency of such active cells decreased along with decreased concentrations of antibodies against immunoglobulin M (anti-IgM) ( $10^{-4}$  g/ml, 78%;  $10^{-5}$  g/ml, 90%;  $10^{-6}$  g/ml, 64%;  $10^{-7}$  g/ml, 26%;  $10^{-8}$  g/ml, 20%) at 45 min after BCR stimulation (Fig. 4D). The apparent Hill coefficient was 7.03 (EC<sub>50</sub>,  $9.1 \times 10^{-7}$  g/ml) for wild type, whereas CARMA1<sup>S578A</sup> mutant cells exhibited a more graded response even at high antibody concentrations.

Our study provides evidence that the TAK1-IKKβ positive-feedback loop mediated by phosphorylation of CARMA1 at S578 serves as a basis for switchlike activation of NF-κB, thereby determining an activation threshold in BCR signaling. A switchlike response is not always pro-

duced by simple positive feedback. Additional conditions, such as low activity before stimulation, should also be met to produce a large difference in the kinetic rates (19). The stoichiometry of the CARMA1 scaffolding protein and the binding kinases must also be optimal to present a switchlike effect (20, 21). By this means, various modifications of CARMA1 may allow different thresholds of NF-κB to be set and thereby shape NF-κB signaling dynamics.

## References and Notes

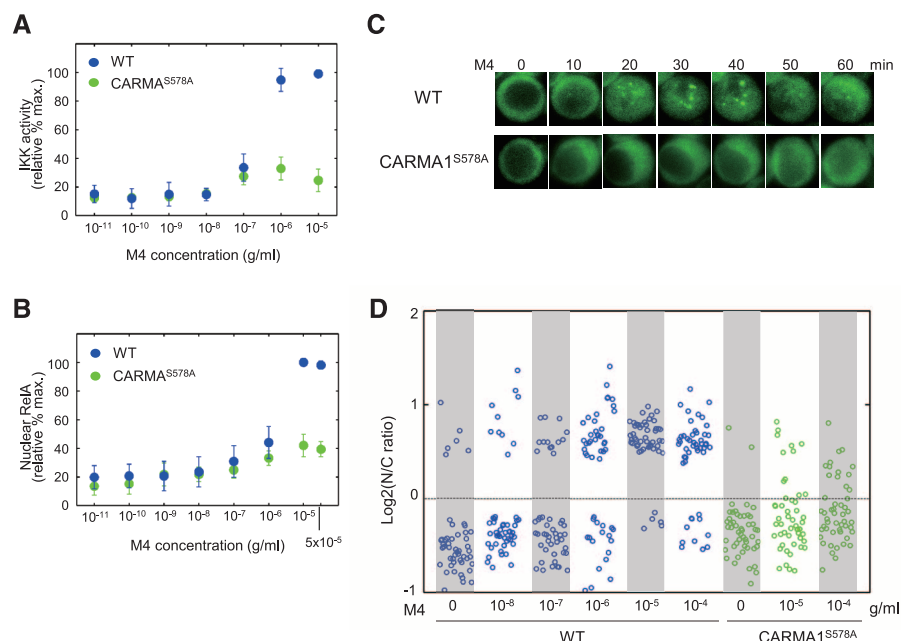
1. M. S. Hayden, S. Ghosh, *Genes Dev.* **26**, 203–234 (2012).
2. S. Basak, M. Behar, A. Hoffmann, *Immunol. Rev.* **246**, 221–238 (2012).
3. L. Ashall *et al.*, *Science* **324**, 242–246 (2009).
4. A. Hoffmann, A. Levchenko, M. L. Scott, D. Baltimore, *Science* **298**, 1241–1245 (2002).
5. T. Y. Tsai *et al.*, *Science* **321**, 126–129 (2008).
6. S. Tay *et al.*, *Nature* **466**, 267–271 (2010).
7. H. Shinohara, T. Kurosaki, *Immunol. Rev.* **232**, 300–318 (2009).
8. M. Thome, J. E. Charton, C. Pelzer, S. Hailfinger, *Cold Spring Harb. Perspect. Biol.* **2**, a003004 (2010).
9. R. L. Lamason, A. Kupfer, J. L. Pomerantz, *Mol. Cell* **40**, 798–809 (2010).
10. E. Wegener *et al.*, *Mol. Cell* **23**, 13–23 (2006).
11. C. Lobry, T. Lopez, A. Israël, R. Weil, *Proc. Natl. Acad. Sci. U.S.A.* **104**, 908–913 (2007).
12. H. Zeng *et al.*, *Mol. Cell. Biol.* **27**, 5235–5245 (2007).
13. H. Shinohara, S. Maeda, H. Watarai, T. Kurosaki, *J. Exp. Med.* **204**, 3285–3293 (2007).
14. S. D. Santos, P. J. Verwee, P. I. Bastiaens, *Nat. Cell Biol.* **9**, 324–330 (2007).
15. J. E. Ferrell Jr., E. M. Machleder, *Science* **280**, 895–898 (1998).
16. S. Polley *et al.*, *PLOS Biol.* **11**, e1001581 (2013).
17. H. Häcker, M. Karin, *Sci. STKE* **2006**, re13 (2006).
18. J. Ruland *et al.*, *Cell* **104**, 33–42 (2001).
19. A. J. Ninfa, A. E. Mayo, *Sci. STKE* **2004**, pe20 (2004).
20. A. Levchenko, J. Bruck, P. W. Sternberg, *Proc. Natl. Acad. Sci. U.S.A.* **97**, 5818–5823 (2000).
21. E. C. O'Shaughnessy, S. Palani, J. J. Collins, C. A. Sarkar, *Cell* **144**, 119–131 (2011).

**Acknowledgments:** We thank T. Takemori, M. Nomura, S. Magi, A. Imamoto, and P.D. Burrows for advice and review of the manuscript and M. Reth for providing mb1-Cre mice. The study is supported by a RIKEN RCAT project for Interdisciplinary Research to H.S., and in part by Cell Innovation Program, Ministry of Education, Culture, Sports, Science and Technology, Japan and the Aihara Innovative Mathematical Modelling Project, FIRST program, Japan Society for the Promotion of Science, to M.O.-H. M.B. was funded by a Postdoctoral Research Fellowship from the Cancer Research Institute and NIH grant 5R01CA141722 to A.H. The microarray data are deposited at Gene Expression Omnibus under accession number GSE41176. The authors declare no competing financial interests. H.S. designed the research; H.S., T.Y., S.M., N.Y., and S.K. performed the experiments; M.B., K.I., and S.K. performed computational analysis; H.S., M.H., and Y.S. performed single-cell imaging analysis; T.N. analyzed the microarray data; H.S. and S.A. provided essential reagents; H.S., M.B., K.I., and M.O.-H. analyzed the data; H.S., M.B., K.I., A.H., and M.O.-H. wrote the paper; and A.H., T.K., and M.O.-H. conceived the study and provided overall direction.

## Supplementary Materials

www.sciencemag.org/content/344/6185/760/suppl/DC1  
Materials and Methods  
Figs. S1 to S15  
Tables S1 to S4  
References (22–34)

20 December 2013; accepted 16 April 2014  
10.1126/science.1250020



**Fig. 4. Switchlike activation of NF-κB at population and single-cell levels.** (A) Dose response of IKKβ activation. IKKβ activities were measured in WT (blue) and CARMA1<sup>S578A</sup> (green) DT40 B cells ( $n = 5$ ) by kinase assay at 6 min after stimulation with the indicated concentration of mAb to chicken IgM (M4). (B) Dose response of NF-κB activation. NF-κB activity was examined in WT (blue) and CARMA1<sup>S578A</sup> (green) DT40 B cells ( $n = 5$ ) by RelA translocation into the nucleus at 45 min after stimulation with the indicated concentration of M4. (C and D) Single-cell imaging analysis of GFP-tagged RelA nuclear translocation. (C) A representative time-course response in WT (top) and CARMA1<sup>S578A</sup> (bottom) cells. Live-cell snapshots up to 60 min after M4 ( $10^{-5}$  g/ml) stimulation. (D) Dose response. Cells were stimulated with M4 at the indicated concentration in WT (blue) and CARMA1<sup>S578A</sup> (green) cells. Nuclear-to-cytoplasmic ratio (N/C) of fluorescence at 45 min after stimulation was calculated (50 cells per experiment).





**cell sciences**  
cytokine center



www.cellsciences.com

## Buy one, get one free

Stock up now on select cytokines, growth factors and chemokines.

### Order any two vials from this list for just \$235

Enter promo code CYT241 when you place your order on-line or mention the promo code to get your discount when calling our toll-free number 888-769-1246.

These recombinant proteins are low endotoxin, carrier-free, highly pure, biologically active and suitable for cell culture and animal studies. Get two of the same item or pick any two different items from the list.\* See our web site for complete product specifications.

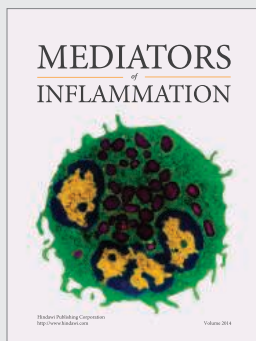
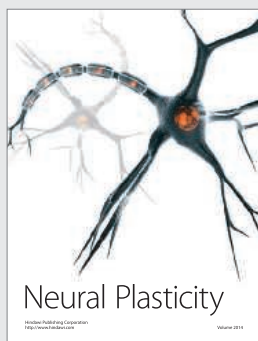
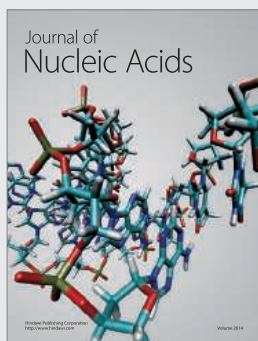
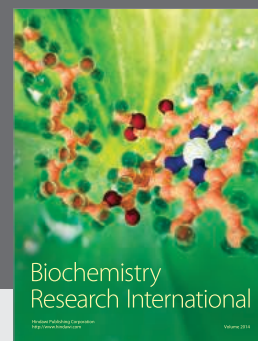
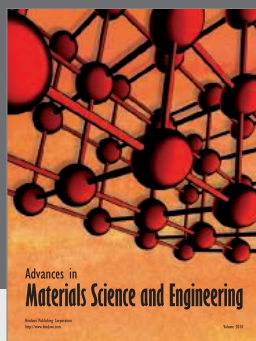
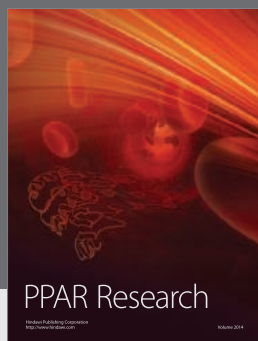
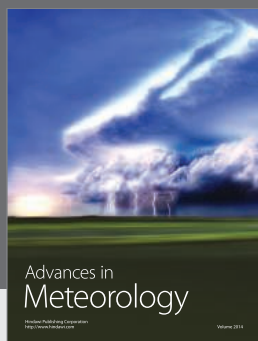
Browse our web site of recombinant proteins, including hundreds more cytokines, growth factors, chemokines and neurotrophins. Bulk quantities of these proteins are available at competitive pricing. Call or visit our web site for details. Cell Sciences also carries corresponding antibodies and ELISA kits.

Catalog No:	Item:	Size:
CRB100B	Recombinant Human BMP-2	10 µg
CRC400B	Recombinant Human CNTF	20 µg
CRF000B	Recombinant Human FGF-acidic/FGF1	50 µg
CRF001B	Recombinant Human FGF-basic/FGF2	50 µg
CRK300B	Recombinant Human FGF-7/KGF	10 µg
CRG300B	Recombinant Human G-CSF/CSF3	10 µg
CRG100B	Recombinant Human GM-CSF/CSF2	20 µg
CRG101B	Recombinant Mouse GM-CSF/CSF2	20 µg
CRG500B	Recombinant Human GRO-alpha/CXCL1	25 µg
CRG502B	Recombinant Rat GRO-alpha/KC/CXCL1	25 µg
CRI004B	Recombinant Human IFN-alpha 2b	100 µg
CRI000B	Recombinant Human IFN-gamma	100 µg
CRI001B	Recombinant Mouse IFN-gamma	100 µg
CRI002B	Recombinant Rat IFN-gamma	100 µg
CRI500B	Recombinant Human IGF-1	100 µg
CRI100B	Recombinant Human IL-2	50 µg
CRI153B	Recombinant Human IL-10	10 µg
CRI137B	Recombinant Human IL-15	10 µg
CRI162B	Recombinant Human IL-17	25 µg
CRI172B	Recombinant Human IL-21	10 µg
CRI225B	Recombinant Human IL-33	10 µg
CRM151B	Recombinant Human M-CSF/CSF1	10 µg
CRR000B	Recombinant Human RANTES/CCL5	20 µg
CRS000B	Recombinant Human SDF-1 alpha	10 µg
CRS002B	Recombinant Human SDF-1 beta	10 µg
CRT100B	Recombinant Human TNF-alpha	50 µg
CRT192B	Recombinant Mouse TNF-alpha	20 µg
CRV000B	Recombinant Human VEGF 165	10 µg
CRV014B	Recombinant Mouse VEGF 165	10 µg

\* Good on orders in US and Canada only. This offer may not be combined with other offers or discounts. All products for research use only.

CELL SCIENCES INC • 480 NEPONSET STREET, BUILDING 12A, CANTON, MA 02021 • INFO@CELLSCIENCES.COM

TOLL FREE: (888) 769-1246 • TEL: (781) 828-0610 • FAX: (781) 828-0542 • WEB WWW.CELLSCIENCES.COM



Hindawi

Submit your manuscripts at  
<http://www.hindawi.com>



# Make ends meet.



## Gibson Assembly<sup>®</sup> Cloning Kit

New England Biolabs has revolutionized your laboratory's standard cloning methodology. The Gibson Assembly Cloning Kit combines the power of the Gibson Assembly Master Mix with NEB 5-alpha Competent *E. coli*, enabling fragment assembly and transformation in just under two hours. Save time, without sacrificing efficiency.

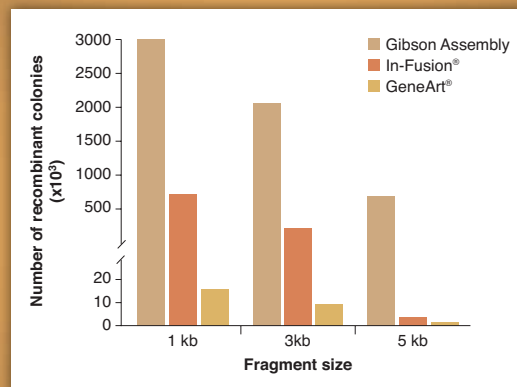
Making ends meet is now quicker and easier than ever before, with the Gibson Assembly Cloning Kit from NEB.

**NEBuilder**<sup>™</sup>  
for Gibson Assembly

Visit [NEBGibson.com](http://NEBGibson.com) to view the latest tutorials and to try our primer design tool.

IN-FUSION<sup>®</sup> is a registered trademark of Clontech Laboratories, Inc.  
GENEART<sup>®</sup> is a registered trademark of Life Technologies, Inc.  
GIBSON ASSEMBLY<sup>®</sup> is a registered trademark of Synthetic Genomics, Inc.

Gibson Assembly Cloning Kit provides robust transformation efficiencies

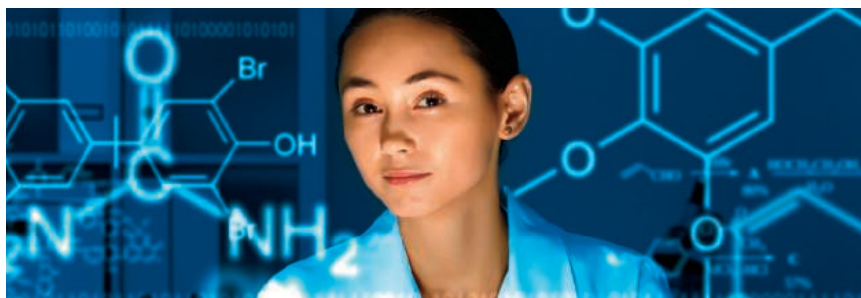


Assembly reactions containing 25 ng of linear pUC19 vector and 0.04 pmol of each fragment were performed following individual suppliers' recommended protocols and using the competent cells provided with the kit. The total number of recombinant colonies was calculated per 25 ng of linear pUC19 vector added to the assembly reaction.

**SGIDNA**

Some components of this product are manufactured by New England Biolabs, Inc. under license from Synthetic Genomics, Inc.





## STOP WRITING GRANTS. AND START WRITING HISTORY.

With five- to seven- year grants of \$1.625 million, Pathway to Stop Diabetes® is a radical new road for diabetes research. Now in its second year, the Pathway program focuses on brilliant minds at the peak of their creativity, and provides the freedom, autonomy and professional mentoring to drive new breakthroughs in the fight to Stop Diabetes. Learn more about Pathway today. And focus your time and talent on diabetes research.

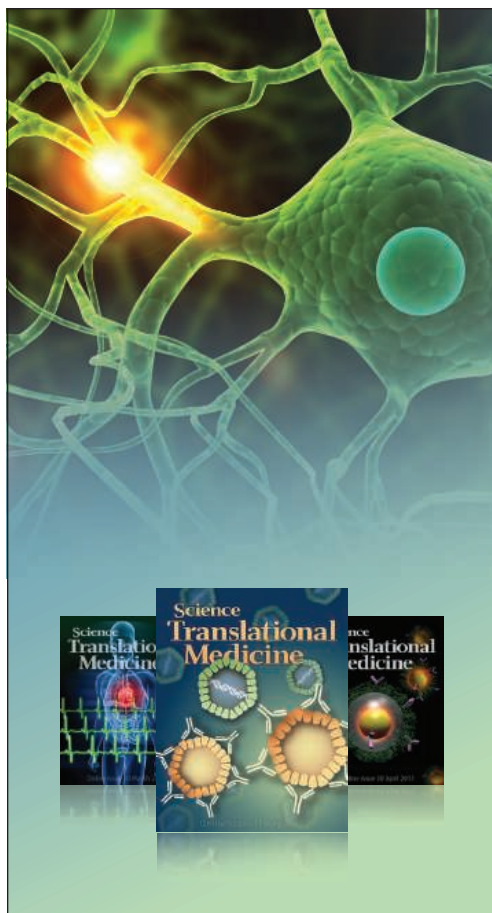


## PATHWAY TO STOP DIABETES®

 American Diabetes Association.  
RESEARCH FOUNDATION

APPLICATIONS BY  
NOMINATION ONLY.  
DEADLINE: JULY 1, 2014.  
FIND OUT MORE AT  
[DIABETES.ORG/PATHWAY](http://DIABETES.ORG/PATHWAY)

### PATHWAY SPONSORS



# Science Translational Medicine

**Integrating Science, Engineering, and Medicine**

Publishing results that harness the basic sciences  
to advance human health in all areas of medicine

**Submit your research**

[ScienceTranslationalMedicine.org](http://ScienceTranslationalMedicine.org)

**Recommend to your library**

[ScienceOnline.org/recommend](http://ScienceOnline.org/recommend)



[scitranslmededitors@aaas.org](mailto:scitranslmededitors@aaas.org)



2013 Winner  
Dr. Michael Yartsev  
CV Starr Research Fellow  
Princeton Neuroscience  
Institute

# Call for Entries

**Application Deadline  
June 15, 2014**

## **Eppendorf & Science Prize for Neurobiology**

The annual Eppendorf & Science Prize for Neurobiology, an international award, honors young scientists for their outstanding contributions to neurobiological research based on methods of molecular and cell biology.

The winner and finalists are selected by a committee of independent scientists, chaired by Science's Senior Editor, Dr. Peter Stern. To be eligible, you must be 35 years of age or younger.

## **You could be next to win this prize and to receive**

- > Prize money of US\$25,000
- > Publication of your work in Science
- > Full support to attend the Prize Ceremony held in conjunction with the Annual Meeting of the Society for Neuroscience in the USA
- > An invitation to visit Eppendorf in Hamburg, Germany

It's easy to apply!

Learn more at: [www.eppendorf.com/prize](http://www.eppendorf.com/prize)



# immunogenomics

## 2014

**September 29 - October 1, 2014**  
**HudsonAlpha Biotechnology Campus**  
**Huntsville, Alabama, USA**

*Join us at the intersection of  
Immunology and Genomics!*

#### Keynote Speakers

**Christophe Benoist**, Harvard Medical School

**Mary Ellen Conley**, University of Tennessee, College of Medicine, Memphis

**Mark Davis**, Howard Hughes Medical Institute;  
Stanford University School of Medicine

#### Session Chairs

**Lou Bridges**, University of Alabama at Birmingham, AL, USA • **Jean-Laurent Casanova**, Howard Hughes Medical Institute, Rockefeller • **Alain Fischer**, Imagine Institute, Necker Hospital, Paris, France • **Dan Littman**, New York University, NY, USA

• **Sara Marsal**, University of Barcelona, Spain • **Kristen Mueller**, Science • **Harlan Robins**, University of Washington/Fred Hutchinson Cancer Research Center

#### Session Speakers

**Scott Boyd**, Stanford University School of Medicine, CA • **Zhijian James Chen**, UT Southwestern, TX • **Yanick Crow**, University of Manchester, UK • **Malek Faham**, Sequentia, CA • **Wendy Garrett**, Harvard University School of Public Health, MA

• **Peter Gregersen**, Feinstein Institute for Medical Research, NY • **Jian Han**, HudsonAlpha Institute for Biotechnology, AL • **Lionel Ivashkiv**, Hospital for Special Surgery, NY • **Thirumala-Devi Kanneganti**, St. Jude Children's Research Hosp. •

**Julian Knight**, Merton College, University of Oxford, UK • **Mike Lenardo**, National Institutes of Health, Washington D.C. •

**Xochitl Morgan**, Harvard University School of Public Health, MA • **Barbara Methe**, J. Craig Venter Institute, MD •

**Kees Murre**, University of California, San Diego, CA • **Richard M. Myers**, HudsonAlpha Institute for Biotechnology, AL •

**Soumya Raychaudhuri**, Broad Institute, MA • **Lars Steinmetz**, European Molecular Biology Laboratory, Germany •

**Barbara Stranger**, University of Chicago, IL USA

Register today at

**immunogenomics.com**

presented by



#### Platinum Sponsors

**BAY CITY CAPITAL**



#### Gold Sponsors



#### Silver Sponsors



#### Bronze Sponsors

**SEQUENTA**

follow

@immunogenomics  
on





## ALGAE PROTEIN EXPRESSION KITS

The new algae engineering kits contain features requested by algae biologists and are designed to make work with algae simpler and faster. The GeneArt kits represent the first commercially available genetic modification and expression systems for photosynthetic microalgae *Chlamydomonas reinhardtii* and *Synechococcus elongatus*. The GeneArt *Chlamydomonas* Protein Expression Kits and GeneArt *Synechococcus* Protein Expression Kits contain high-expression vectors capable of driving production of genes of interest to as much as 10% of total cellular protein. The kits also contain new proprietary transformation reagents that can boost introduction of DNA into cells by as much as a thousandfold over what is typically achieved with current techniques. The new GeneArt kits also contain reagents and a protocol enabling researchers to freeze and store *Chlamydomonas* strains at  $-80^{\circ}\text{C}$ . Algal researchers have traditionally relied on passing strains indefinitely, which makes the cultures subject to genetic drift, and shipping live cultures on agar slants, which frequently become contaminated.

### Life Technologies

For info: 800-955-6288 | [www.lifetechnologies.com](http://www.lifetechnologies.com)



## 3-D CELL CULTURE PLATES

The new Alvetex Scaffold 3-D cell culture plates provide biopharmaceutical companies with a new tool to improve the predictive accuracy, productivity, and biological relevance of their cell-based high throughput testing. The new 384-well plates allow scientists to grow tumor cells in a way that better mimics how these cells grow in vivo. It is then very simple to test the cytotoxic effects of novel or existing anti-cancer compounds using standard cell health assays such as MTT, XTT, extracellular oxygen consumption, and many others. Researchers can then easily retrieve RNA and protein from the drug-treated cells to study mechanism of action and look for biomarkers. Alvetex Scaffold plates work seamlessly with liquid handling robotic systems further enhancing the high throughput potential of your cell-based testing. Alvetex Scaffold is also available in other formats including a 12-well culture plate, 24-well culture plate, and 96-well plate as well as 6-well and 12-well inserts.

### AMS Biotechnology

For info: +44-(0)-1235-828200 | [www.amsbio.com](http://www.amsbio.com)

## KIM-1 ELISA KIT

The most sensitive KIM-1 (human) enzyme-linked immunosorbent assay (ELISA) kit is designed for detection of acute kidney injury, diabetes, and toxicity. This quantitative ELISA kit offers ultrasensitive detection enabling quantification of both normal and disease state levels of KIM-1, detecting as little as 1.2 pg/mL of KIM-1 in human urine. The assay provides quantitative results with excellent reproducibility between experiments, and offers efficiency over Western blotting by requiring less sample input, and analysis of up to 38 duplicate samples in less than two hours. The ELISA displays high specificity to human KIM-1 with low cross-reactivity to similar molecules such as TIM-3 and TIM-4. The KIM-1 ELISA kit is complete, flexible, and put through rigorous fit-for-purpose validation and stability testing to ensure high precision, accuracy, sensitivity, and specificity. It is supplied with an easy-to-follow protocol, precoated microtiter plate, and liquid color-coded reagents to save the user time and reduce errors.

### Enzo Life Sciences

For info: 800-942-0430 | [www.enzolifesciences.com](http://www.enzolifesciences.com)

## SEMI-AUTOMATIC MICROPLATE SEALER

The MiniSeal II semiautomatic microplate sealer comes complete with adapters enabling it to process deep-well, shallow-well, low-profile deep-well, filter, and assay plates that conform to the ANSI/SLAS standard format. MiniSeal II plate adaptors not currently in use are ingeniously designed to stack on top of the unit to keep them readily available. The MiniSeal II heat sealer operates with a very high force, that together with a powerful 450W heater ensures high-integrity sealing of almost any type of microplate. With so much available power, sealing times for most polypropylene plates with Porevair seals are less than three seconds each. Sealed plates are automatically ejected from the MiniSeal II. The compact footprint, about the size of a sheet of A4 paper, means that MiniSeal II will fit just about anywhere—on your lab bench or inside a fume hood if required.

### Porvair Sciences

For info: +44-(0)-1978-666240 | [www.porvair-sciences.com](http://www.porvair-sciences.com)

## NUCLEIC ACID DYE SYSTEM

The QuantiFluor ONE dsDNA System is a sensitive, dsDNA-specific fluorescent dye suitable for use in both research and clinical workflows. The new dye system is integrated into the new Promega Quantus Fluorometer and GloMax detection instruments, but is compatible with any fluorometer capable of measuring the appropriate fluorescence excitation and emission spectra. The QuantiFluor ONE dsDNA System is supplied in “add-and-read” format, enabling users to simply quantitate even low-concentration samples with confidence, and without dilutions or additional tubes. The dye system has significantly increased sensitivity compared with absorbance-based systems and is highly specific to dsDNA, showing minimal binding to ssDNA, RNA, protein, and interfering compounds. The QuantiFluor ONE dsDNA System expands the company’s range of nucleic acid quantitation reagents and instrumentation, which includes the recently launched Quantus Fluorometer for highly sensitive (up to 40,000x higher than absorbance-based methods) quantitation of dsDNA, ssDNA, and RNA.

### Promega

For info: 800-356-9526 | [www.promega.com/quantus](http://www.promega.com/quantus)

Electronically submit your new product description or product literature information! Go to [www.sciencemag.org/products/newproducts.dtl](http://www.sciencemag.org/products/newproducts.dtl) for more information. Newly offered instrumentation, apparatus, and laboratory materials of interest to researchers in all disciplines in academic, industrial, and governmental organizations are featured in this space. Emphasis is given to purpose, chief characteristics, and availability of products and materials. Endorsement by Science or AAAS of any products or materials mentioned is not implied. Additional information may be obtained from the manufacturer or supplier.

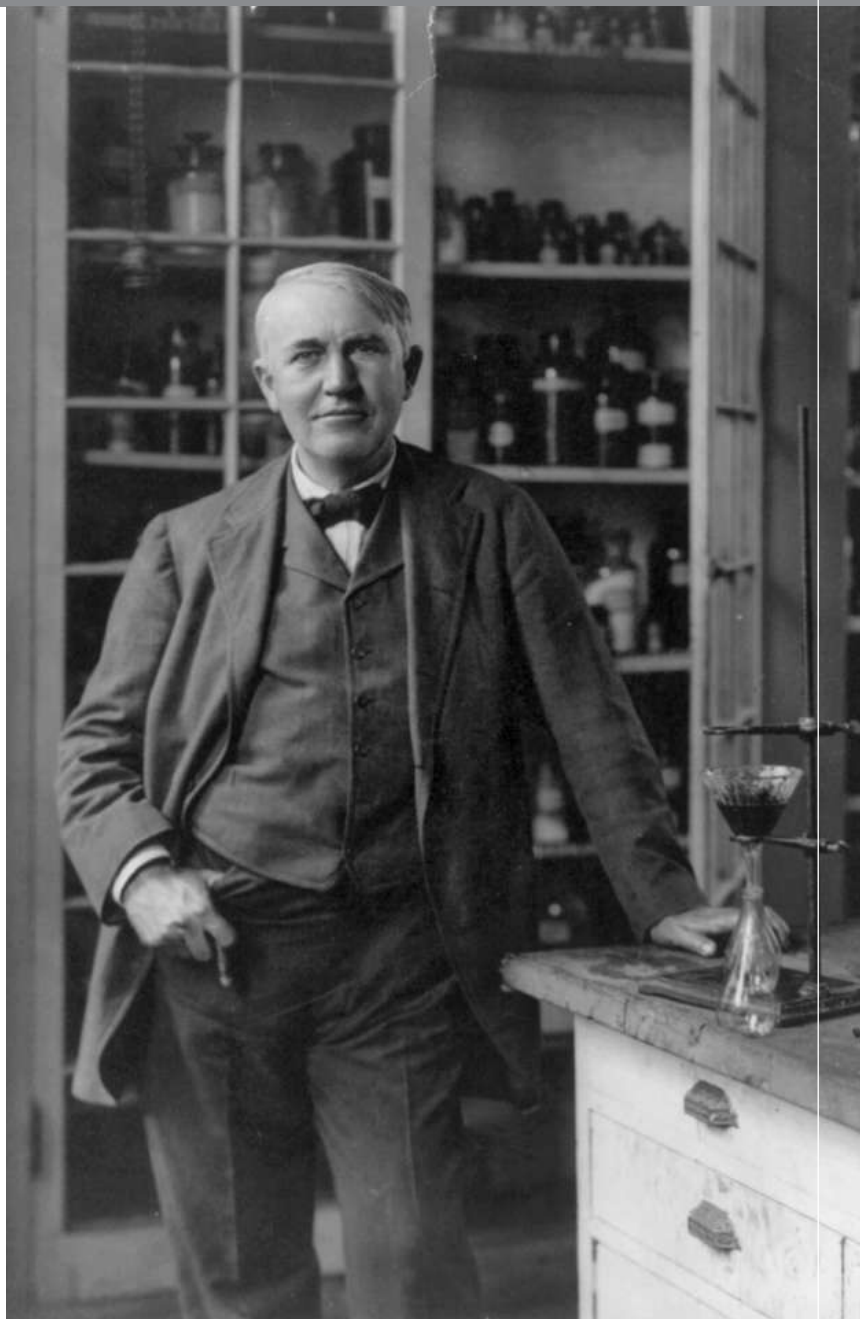
# WHAT DO YOU AND THOMAS EDISON HAVE IN COMMON?

## AAAS.

By investing in AAAS you join Thomas Edison and the many distinguished individuals whose vision led to the creation of AAAS and our world-renowned journal, *Science*, more than 150 years ago.

Like Edison, you can create a legacy that will last well into the future through planned giving to AAAS. By making AAAS a beneficiary of your will, trust, retirement plan, or life insurance policy, you make a strong investment in our ability to advance science in the service of society for years to come.

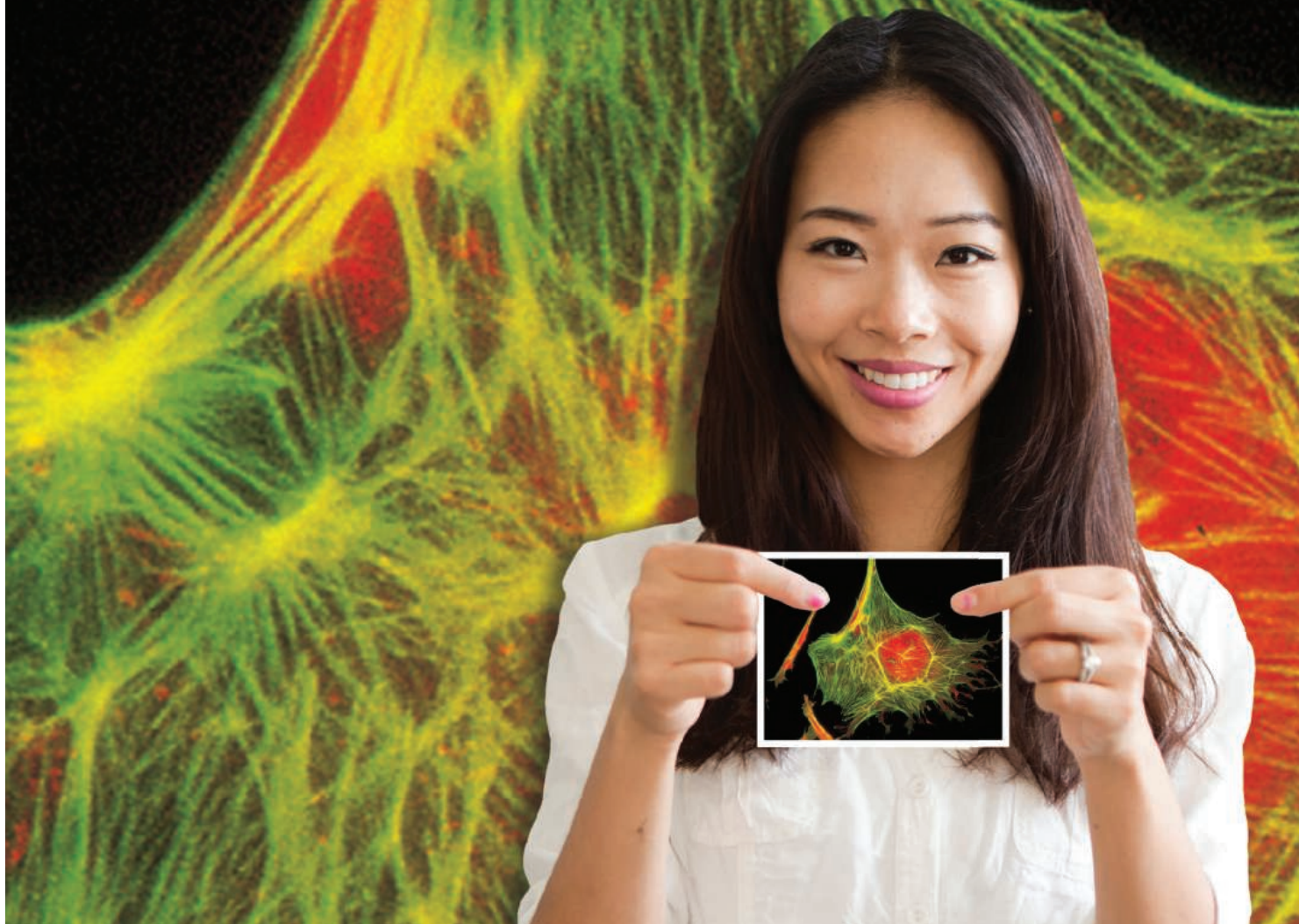
To discuss your legacy planning, contact Juli Staiano, Director of Development, at (202) 326-6636, or [jstaiano@aaas.org](mailto:jstaiano@aaas.org), or visit [www.aaas.org/1848](http://www.aaas.org/1848) for more information.



"I feel great knowing that I will leave behind a legacy that will be channeled through the AAAS. It also means a lot to me to be able to honor my late parents, too."

—PETER ECKEL  
Member, 1848 Society and AAAS Member since 1988

# This. Is. Molecular Probes.



Molecular Probes®

## We wrote the book. You published the papers.

Since it was first printed in 1975, the Molecular Probes® Handbook has served as a reference guide for fluorescent probes and labeling technologies.

Thanks to your publications, it now describes the most peer-referenced fluorescent reagents used in life science research.

Find out why Molecular Probes® reagents are preferred by researchers worldwide at [lifetechnologies.com/probes](http://lifetechnologies.com/probes)

*life*  
technologies

A Thermo Fisher Scientific Brand

For Research Use Only. Not for use in diagnostic procedures. Life Technologies is a Thermo Fisher Scientific brand. © 2014 Thermo Fisher Scientific Inc. All rights reserved. All trademarks are the property of Thermo Fisher Scientific and its subsidiaries. C009359 0414





There's only one  
**Science**

## Science Careers Advertising

For full advertising details, go to ScienceCareers.org and click For Employers, or call one of our representatives.

### Tracy Holmes

Worldwide Associate Director  
Science Careers  
Phone: +44 (0) 1223 326525

### THE AMERICAS

E-mail: [advertise@sciencecareers.org](mailto:advertise@sciencecareers.org)  
Fax: 202-289-6742

### Tina Burks

Phone: 202-326-6577

### Nancy Toema

Phone: 202-326-6578

### Marci Gallun

Sales Administrator  
Phone: 202-326-6582

### Online Job Posting Questions

Phone: 202-312-6375

### EUROPE / INDIA / AUSTRALIA / NEW ZEALAND / REST OF WORLD

E-mail: [ads@science-int.co.uk](mailto:ads@science-int.co.uk)  
Fax: +44 (0) 1223 326532

### Axel Gesatzki

Phone: +44 (0)1223 326529

### Sarah Lelarge

Phone: +44 (0) 1223 326527

### Kelly Grace

Phone: +44 (0) 1223 326528

### JAPAN

### Yuri Kobayashi

Phone: +81-(0)90-9110-1719  
E-mail: [ykobayas@aaas.org](mailto:ykobayas@aaas.org)

### CHINA / KOREA / SINGAPORE / TAIWAN / THAILAND

### Ruolei Wu

Phone: +86-1367-1015-294  
E-mail: [rwu@aaas.org](mailto:rwu@aaas.org)

All ads submitted for publication must comply with applicable U.S. and non-U.S. laws. Science reserves the right to refuse any advertisement at its sole discretion for any reason, including without limitation for offensive language or inappropriate content, and all advertising is subject to publisher approval. Science encourages our readers to alert us to any ads that they feel may be discriminatory or offensive.

**Science Careers**

From the journal Science



ScienceCareers.org



## THE CHINESE UNIVERSITY OF HONG KONG

Applications are invited for:-

### Department of Microbiology

The Department has a wide range of research facilities and access to a large comprehensive teaching hospital. The establishment provides a good environment for basic as well as clinical research and facilitates collaboration with other disciplines. Further information about the Department is available at <http://www.cuhk.edu.hk/med/mic/>. The Department is seeking for suitable candidates to fill the below posts.

### (1) Professor / Associate Professor / Assistant Professor

(Ref. 1314/159(665)/2) (Closing date: June 30, 2014)

Applicants should have (i) a PhD degree or equivalent; (ii) a strong track record of research in the field of microbiology or virology; and (iii) commitment to undergraduate teaching and postgraduate students supervision. Applicants for Professorship / Associate Professorship should also have a strong record on external funding support, international recognition and leadership. Experience in cutting-edge techniques such as bioinformatics and genomics will be an advantage.

The appointee will (a) deliver teaching and related educational activities for undergraduate and postgraduate students; (b) apply for competitive research grants and related funding; (c) conduct high-standard research projects independently and in collaboration with other parties; and (d) supervise MPhil and PhD students. Appointment will normally be made on contract basis for up to three years initially commencing July 2014, which, subject to mutual agreement, may lead to longer-term appointment or substantiation later. Competitive start-up package may be provided.

### (2) Research Assistant Professor

(Ref. 1314/160(665)/2) (Closing date: June 30, 2014)

Applicants should have (i) a PhD degree or equivalent; and (ii) a strong track record of research in the field of microbiology or virology. Experience in tumour virology, microbial genomics and bioinformatics will be an advantage.

The appointee will (a) apply for competitive research grants and related funding; and (b) conduct high-standard research projects independently and in collaboration with other parties. Appointment will initially be made on contract basis for up to three years commencing July 2014, renewable subject to mutual agreement.

### Salary and Fringe Benefits

Salary will be highly competitive, commensurate with qualifications and experience. The University offers a comprehensive fringe benefit package, including medical care, a contract-end gratuity for appointments of two years or longer, and housing benefits for eligible appointees. Further information about the University and the general terms of service for appointments is available at <http://www.per.cuhk.edu.hk>. The terms mentioned herein are for reference only and are subject to revision by the University.

### Application Procedure

Please send full resume, together with copies of academic credentials, a publication list and/or abstracts of selected published papers, and names, addresses and fax numbers/e-mail addresses of three referees to whom the applicants' consent has been given for their providing references (unless otherwise specified), to the Personnel Office, The Chinese University of Hong Kong, Shatin, N.T., Hong Kong [fax: (852) 3943 1462] by the closing date. The Personal Information Collection Statement will be provided upon request. Please quote the reference number and mark 'Application - Confidential' on cover.



## Sitlington Endowed Chair in Infectious Diseases

The Center for Veterinary Health Sciences (CVHS), Department of Veterinary Pathobiology (VPB), Oklahoma State University requests applications and nominations for a faculty position and the Sitlington Endowed Chair in Infectious Diseases. This Chair carries an endowment of \$3 million for the development of the Chair's research program. The appointee is expected to develop and sustain an extramurally funded research program in the area of infectious diseases, ranging from molecular to applied aspects of infection. The CVHS and VPB have a distinguished and active research program committed to infectious diseases of animals and humans. While the specific research area of the candidate is open, a focus complementing existing research departmental programs of viral and bacterial pathogenesis, microbial/viral genomics, vector-borne infections, pathogen host interaction, host immunity, and vaccinology would be preferred. Remodeled BSL-2 and BSL-3 laboratories, as well as start-up and relocation support, will be provided. OSU and the CVHS have excellent research support facilities including flow cytometry; confocal and electron microscopy, microbial fermentation, animal care facilities for conventional and biocontainment housing of research animals, including laboratory and food animals, and excellent molecular biology support facilities including nucleic acid and protein sequencing and synthesis, mass spectrometry, micro-array and NMR. Other responsibilities of the successful candidate will include graduate student and postdoctoral training and collaborative research with other faculty. A qualification for the Chair includes an earned PhD. Those with a DVM or equivalent degree and advanced degree are encouraged to apply. The successful candidate should have a proven record of current research productivity and sustained research support from NIH, NSF, DoD, or other federal agencies. Appointment will be at the associate or full professorial rank, and salary will be competitive with the rank.

Nominations and applications by interested applicants should include a curriculum vitae, description of the research program, plans for further program development, and the names and addresses of five references addressed to **Dr. Robert W. Fulton, Chair, Search Committee for the Sitlington Chair in Infectious Diseases, Department of Veterinary Pathobiology, Center for Veterinary Health Sciences, Oklahoma State University, Stillwater, OK 74078.** [Robert.fulton@okstate.edu](mailto:Robert.fulton@okstate.edu). Review of applications will begin **July 1, 2014**, and will continue until a suitable candidate is identified. College information is available at [www.cvhs.okstate.edu](http://www.cvhs.okstate.edu) and inquiries can be made at **405-744-8170** to **Dr. Fulton**.

*Oklahoma State University is an Affirmative Action/Equal Opportunity/E-verify Employer committed to diversity. All qualified applicants will receive consideration for employment and will not be discriminated against based on race, color, religion, sex, national origin, disability or protected veteran status. OSU-Stillwater is a tobacco-free campus.*



The University of Konstanz, belongs to the universities in Germany whose "future concepts for top-class research at universities" is promoted within the framework of the Excellence Initiative of the German federal and state governments.

The *Zukunftskolleg* of the University of Konstanz is offering:

### up to five ZIF Marie Curie 5-year Research Fellowships and

### up to four Zukunftskolleg 5-year Research Fellowships

in any discipline represented at the University of Konstanz for the development and implementation of individual research projects (Salary Scale 14 TV-L).

**Fellowships will begin on May 1, 2015, and end on April 30, 2020.**

**Reference number 2014 / 069**

Applications, supporting materials, and two letters of reference should be submitted in English **by August 31, 2014 using the Online Application Platform:** [www.zukunftskolleg.uni-konstanz.de/online-application](http://www.zukunftskolleg.uni-konstanz.de/online-application)

Details concerning application requirements and information about the Zukunftskolleg are available on our website:  
<http://www.zukunftskolleg.uni-konstanz.de>

**Contact:** Help Desk, [zukunftskolleg-application@uni-konstanz.de](mailto:zukunftskolleg-application@uni-konstanz.de),  
Anda Lohan, e-mail: [a.lohan@uni-konstanz.de](mailto:a.lohan@uni-konstanz.de).



The University of Konstanz, belongs to the universities in Germany whose "future concepts for top-class research at universities" is promoted within the framework of the Excellence Initiative of the German federal and state governments.

The *Zukunftskolleg* of the University of Konstanz is offering:

Up to **six ZIF Marie Curie 2-year Postdoctoral Fellowships in any discipline represented at the University of Konstanz** (Salary Scale 13 TV-L) for researchers in the early stage of their career, so as to enable them to develop and implement individual and independent research projects.

**Fellowships will begin on March 1, 2015, and end on February 28, 2017.**

**Reference number 2014 / 068**

Applications, supporting materials, and two letters of reference should be submitted in English **by August 31, 2014 using the Online Application Platform:** [www.zukunftskolleg.uni-konstanz.de/online-application](http://www.zukunftskolleg.uni-konstanz.de/online-application)

Details concerning application requirements and information about the Zukunftskolleg are available on our website:  
<http://www.zukunftskolleg.uni-konstanz.de>

**Contact:** Help Desk, [zukunftskolleg-application@uni-konstanz.de](mailto:zukunftskolleg-application@uni-konstanz.de),  
Anda Lohan, e-mail: [a.lohan@uni-konstanz.de](mailto:a.lohan@uni-konstanz.de).



The University of Pennsylvania, School of Dental Medicine invites applications for a tenured Professor and Chair of the Department of Biochemistry. Candidates are sought who have a strong record in research and extramural funding, particularly in the areas of structural biology, as it relates to cancer biology, including oral and head and neck cancers, or metabolic sciences. Experience in and commitment to interdisciplinary teaching is essential.

The Department Chair will have the opportunity to build new and enhance existing research areas. The School of Dental Medicine is situated on a walkable campus that includes the Schools of Medicine, Veterinary Medicine, Nursing, Engineering, and the Children's Hospital of Philadelphia, and has a vibrant and interdisciplinary research program. The School is committed to education of dental health professionals in order to prepare graduates to become leaders in the delivery of dental care and in oral health research. The Department is responsible for teaching biochemistry to dental students and for the ongoing development of these courses to meet the educational needs of new generations of oral health professionals. Responsibilities of the Chair include: recruitment and retention of faculty, provision of leadership in the areas of faculty research, teaching and service; and oversight of departmental activities such as budget development and administration.

Individuals with a PhD or dual degree including DMD/DDS, MD, DVM or equivalent are invited to submit a statement of research and teaching interests, curriculum vitae and a vision statement related to departmental leadership. Review of applications will begin immediately and continue until the position is filled. Applicants should apply online at:

<http://facultysearches.provost.upenn.edu/postings/220>

For further information regarding the above position, contact the Search Committee at [BioCH@dental.upenn.edu](mailto:BioCH@dental.upenn.edu).

*The University of Pennsylvania is an Affirmative Action/Equal Opportunity Employer. All qualified applicants will receive consideration for employment and will not be discriminated against on the basis of race, color, religion, sex, sexual orientation, gender identity, creed, national or ethnic origin, citizenship status, age, disability, veteran status, or any other characteristic protected by law.*



EMBL-EBI



EMBL-EBI and Wellcome Trust Sanger Institute share the Wellcome Trust Genome Campus near Cambridge. This proximity fosters close collaborations and contributes to an international and vibrant campus environment.

## ESPOD fellowships

### Call for applications 2014

The EMBL-EBI – Sanger Postdoctoral (ESPOD) Programme builds on the strong collaborative relationship between the two institutes, offering projects which combine experimental (wet lab) and computational approaches.

Select from pre-defined projects:

- Detection of somatic mutations in normal cells
- Creating phenotype variation through epigenetics: DNA methylation variability in populations and individual cells
- Rational selection of therapeutic gut bacteria
- Functional genomics of cancer evolution
- Discovery/validation of splicing at the proteome level in cancer
- Modelling and engineering of cytokine-receptor interactions
- Identification of novel anti-obesity therapies stimulating brown/beige adipocytes

For further information on the ESPOD fellowships and how to apply please visit [www.ebi.ac.uk/research/postdocs/espods](http://www.ebi.ac.uk/research/postdocs/espods)

**Closing date:** 25 July 2014 [www.embl.org/jobs](http://www.embl.org/jobs)



## AAAS is here – helping scientists achieve career success.

Every month, over 400,000 students and scientists visit ScienceCareers.org in search of the information, advice, and opportunities they need to take the next step in their careers.

A complete career resource, free to the public, *Science Careers* offers a suite of tools and services developed specifically for scientists. With hundreds of career development articles, webinars and downloadable booklets filled with practical advice, a community forum providing answers to career questions, and thousands of job listings in academia, government, and industry, *Science Careers* has helped countless individuals prepare themselves for successful careers.

As a AAAS member, your dues help AAAS make this service freely available to the scientific community. If you're not a member, join us. Together we can make a difference.

To learn more, visit  
[aaas.org/plusyou/sciencecareers](http://aaas.org/plusyou/sciencecareers)



## FUNDING OPPORTUNITIES

### U.S. Department of Defense Defense Medical Research and Development Program Peer Reviewed Medical Research Program

The Peer Reviewed Medical Research Program (PRMRP) funds exceptional research with the goal to improve the health and well-being of all military service members, Veterans, and beneficiaries. The PRMRP received **\$200 million** in fiscal year 2014 (FY14), and seeks grant applications in the following **topic areas**:

Acupuncture	Food Allergies	Neuroprosthetics
Arthritis (other than post-traumatic osteoarthritis and rheumatoid arthritis)	Fragile X Syndrome	Pancreatitis
Chronic Migraine and Post-Traumatic Headaches	Hereditary Angioedema	Polycystic Kidney Disease
Congenital Heart Disease	Illnesses Related to Radiation Exposure (excludes cancer)	Post-Traumatic Osteoarthritis
DNA Vaccine Technology for Post-Exposure Prophylaxis	Inflammatory Bowel Disease	Psychotropic Medications
Dystonia	Interstitial Cystitis	Respiratory Health (excludes lung cancer and mesothelioma)
Epilepsy	Lupus	Rheumatoid Arthritis
	Malaria	Segmental Bone Defects
	Metabolic Disease	Tinnitus

The FY14 PRMRP Program Announcements and General Application Instructions are anticipated to be posted on Grants.gov by **May 1, 2014**:

- Clinical Trial Award
- Discovery Award
- Focused Program Award
- Investigator-Initiated Research Award
- Technology/Therapeutic Development Award

All applications must conform to the Program Announcements and General Application Instructions that will be available for electronic downloading from the Grants.gov website (all viewable under CFDA number 12.420). Execution management support will be provided by the Congressionally Directed Medical Research Programs.

<http://cdmrp.army.mil>  
<http://cdmrp.army.mil/funding/prmrp.shtml>

## Introducing the new *Science Careers Jobs* app from Science



**Jobs are updated 24/7**

**Search thousands of jobs on your schedule**

**Receive push notifications per your job search criteria**

### Get a job on the go.

Search worldwide for thousands of scientific jobs in academia, industry, and government. Keep your finger on the pulse of your field—set up an alert for the type of job you are looking for and receive push notifications when jobs are posted that meet your criteria. The application process is seamless, linking you directly to job postings from your customized push notifications.



Scan this code to download app or visit [apps.sciencemag.org](http://apps.sciencemag.org) for information.

**Science Careers**

From the journal *Science* AAAS

[ScienceCareers.org](http://ScienceCareers.org)





## Post-doctor in experimental endocrinology at Lund University, Sweden

Lund University Diabetes Centre is seeking a highly motivated and talented postdoc for investigating the molecular mechanisms underlying type 2 diabetes with the long-term goal of finding new anti-diabetic treatments. The successful applicant will have a key role in a project that is in the front line of metabolic research. The project builds on a strategy to identify novel disease genes for complex diseases as described in Mahdi T et al., *Cell Metabolism* 2012, and Rosengren AH et al., *Science* 2010. The applicant must have a PhD degree and is expected to have extensive experimental background in cell physiology and/or cell biology and a very strong record of scientific productivity in international journals.

Lund University is one of Europe's foremost universities, and Lund University Diabetes Centre forms one of the strongest diabetes research environments world-wide.

Additional information on this post can be found at <http://www.ludc.med.lu.se/research-units/translational-diabetes-research/>

The application containing a cover letter, a CV and a list of scientific publications should be addressed to Dr. Anders Rosengren, Department of Clinical Sciences, Malmö at anders.rosengren@med.lu.se.

**Closing date: 15 June 2014.**

## FRED HUTCHINSON CANCER RESEARCH CENTER

### FACULTY POSITION

The Clinical Research Division of the Fred Hutchinson Cancer Research Center is currently seeking outstanding scientists for a faculty position at the Assistant or Associate Member level specializing in translational hematopoietic cell gene therapy and engineering. We seek scientists with established research experience in hematopoietic cell gene therapy, with emphasis in molecular studies leading to a better understanding of engraftment of gene-modified hematopoietic stem/progenitor cells, insertional mutagenesis and malignancy in cellular targets of gene therapy. Specific areas of interest include characterization of clonality of gene-modified repopulating cells, insertion patterns of various retroviral gene transfer systems in preclinical and clinical studies, mechanistic studies of gene vector insertion to improve tools for advanced hematopoietic cell therapy and investigation of gene networks that regulate gene-modified cell fitness and clonal homeostasis. These findings will have important consequences for the fields of hematology, oncology, immunology and regenerative medicine. Thus, this position will complement and synergize with ongoing basic and clinical research programs in the Clinical Research Division, as well as with basic research conducted in the Human Biology Division. Interested candidates should have an MD, PhD or MD/PhD degree, and a strong academic record. All applicants should have substantial peer-reviewed publications that demonstrate research productivity and the ability to perform cutting edge research in translational gene therapy. Preference will be given to established investigators in translational cell and gene therapy already well-funded by extramural grants and with publications in high-impact journals. Early stage investigators with outstanding accomplishments in these areas will also be considered. Appointment is available at the Assistant Member level and competitive packages will be offered based on qualifications.

Please send a curriculum vitae, a letter summarizing research goals and career plans, and the names of four references to <https://careers-fhrc.icims.com/jobs/4054/associate-member/job>

*The Fred Hutchinson Cancer Research Center is an Equal Opportunity Employer; committed to workforce diversity.*



## Max Planck Institute for Gravitational Physics (Albert Einstein Institute)

### NOMINATIONS SOUGHT FOR THE POSITION OF DIRECTOR

at the Max Planck Institute for Gravitational Physics (or Albert Einstein Institute), Potsdam-Colm, Germany

The Albert Einstein Institute (AEI), with approximately 400 scientists, employees, and students, is the world's largest research organization devoted to the study of the general theory of relativity (GR) and gravity. The AEI campus has three divisions (Astrophysical and Cosmological Relativity, Quantum Gravity and Unified Theories, and Mathematical Relativity) located in Potsdam-Colm, near Berlin, and two divisions (Laser Interferometry and Gravitational Wave Astronomy, Observational Relativity and Cosmology) located in Hannover.

The AEI is seeking a new Director following the departure of Prof. Gerhard Huisken, former Director of the Mathematical Relativity division. The successful candidate will have established a record of original and creative research at the highest international level, and will have demonstrated the ability to inspire and lead a substantial group of younger scientists. The search will span the following areas: Mathematical Relativity, Classical General Relativity and Gravity, Theoretical Cosmology, and Quantum Gravity.

Nominations can be submitted with a deadline of 1 July 2014 by registering at the following link: <http://NewDirector.aei.mpg.de>

Upon registration nominators will receive a password that will allow them to enter their nomination (multiple nominations are possible). Nominations must include a short description of the nominee's background and most significant scientific accomplishments. Self-nominations are not permitted. All nominations will be treated confidentially.

The Max Planck Society is an equal opportunity employer, and seeks to increase the percentage of female Directors. It is also committed to employing more individuals with disabilities. Nominations in these categories are particularly welcome.



## Fondazione Meru - Medolago Ruggeri - per la ricerca biomedica Meru Foundation for biomedical research - [www.fondazionemeru.org](http://www.fondazionemeru.org) CALL FOR AWARD APPLICATIONS

Meru Foundation announces the first call for award applications. A four-year post-doctoral fellowship - limited to individuals not older than 35 years of age at the time of application - and a two-year junior faculty grant will be awarded to conduct research relevant to vascular biology at The Scripps Research Institute (TSRI) in La Jolla, California.

Applicants must hold an MD or PhD degree. The post-doctoral fellowship awardee will work under the mentorship of a TSRI Principal Investigator. The junior faculty grant awardee will also be associated with a TSRI mentor, but will be expected to be on the path to independence as a principal investigator and in a position of obtaining extramural grant support by completion of the award. Salaries will be in accordance with TSRI compensation for equivalent positions. In addition, the junior faculty grant awardee will receive \$25,000 as a contribution towards research supplies.

Applications should include: (1) Extended CV; (2) a statement of personal goals that the award will help achieve; (3) a research plan - maximum three, single-spaced US letter-size pages, 11 pt Arial font, including figures and legends but excluding bibliography - addressing basic questions relevant to mechanisms of thrombosis, hemostasis, inflammation and vascular disease; (4) three letters of recommendation highlighting the applicant's qualifications for the specific Meru award.

Submit applications as a single pdf document to: [ruggeri@scripps.edu](mailto:ruggeri@scripps.edu), cc [robertt@scripps.edu](mailto:robertt@scripps.edu), by the deadline of **July 31, 2014**; inquires on the application process can be sent to the same address. Applications will be evaluated by a panel of internationally recognized peers in the field of vascular biology. The panel roster will be disclosed in the evaluation letter that all applicants will receive by October 31, 2014. The award initiation date should be no later than February 15, 2015.

In the future, Meru Foundation expects to announce calls for applications on a regular yearly schedule alternating one post-doctoral fellowship and one junior faculty grant award. TSRI is an Equal Opportunity Employer.



**THE COLTON PROFESSOR of  
Autoimmunity  
Endowed Professorship  
NYU Division of Rheumatology**

The NYU School of Medicine has established an endowed Professorship, the Colton Professor of Autoimmunity, in the Division of Rheumatology and a newly created Colton Center for Autoimmunity. The Colton Professor will be a leader in the field of autoimmunity who will work with a team of scientists across the disciplines of immunology, microbiology, genetics, and bioinformatics to advance translational science in the field of rheumatic diseases. The candidate should be a recognized leader in the field and have a strong track record of NIH funding. To apply or for additional information, contact: **Jill P. Buyon, M.D.**, Professor Director, Division of Rheumatology NYU School of Medicine, Department of Medicine e-mail: [jill.buyon@nyumc.org](mailto:jill.buyon@nyumc.org), telephone: 212-598-6110.

**TENURE-TRACK FACULTY POSITION  
Georgia Institute of Technology  
School of Chemistry and Biochemistry  
Atlanta, GA 30332-0400**

The Georgia Institute of Technology, School of Chemistry, and Biochemistry seeks to fill a tenure-track faculty position in the development of any aspect of chemistry or biochemistry related to feedstocks from renewable and sustainable sources. Research areas of interest include, but are not limited to, functional biomaterials, catalysis, energy harvesting and storage, efficient syntheses and processes, and plant bioengineering and synthetic biology. Opportunities for significant interaction with and support from the Institute for Paper Science and Technology at Georgia Tech (website: <http://ipst.gatech.edu>) will be available. Candidates with interdisciplinary research programs may be considered for joint appointments with other campus units.

Exceptional candidates at all levels are encouraged to apply. **ASSISTANT PROFESSOR** candidates should submit a cover letter, curriculum vitae, description of research plans, description of teaching interests and philosophy, and arrange for the submission of three letters of recommendation. Candidates at advanced levels should submit a cover letter, curriculum vitae, and the names and contact information of three references. All materials and requests for information should be submitted electronically, as per the instructions found at website: <https://academicjobsonline.org/ajo/jobs/4045>.

The application deadline is September 15, 2014, with application review continuing until the position is filled. *Georgia Tech is an Equal Education/Employment Opportunity Institution.*

Find your  
future here.



**Science Careers**

From the journal *Science* AAAS

[www.ScienceCareers.org](http://www.ScienceCareers.org)

**Download  
your free copy  
today.**

**ScienceCareers.org/booklets**



From technology specialists to patent attorneys to policy advisers, learn more about the types of careers that scientists can pursue and the skills needed in order to succeed in nonresearch careers.

**Science Careers**

From the journal *Science* AAAS